Modelling of water and energy fluxes in the Seine basin

Deniz Kilic

▶ **To cite this version:**

Deniz Kilic. Modelling of water and energy fluxes in the Seine basin. Biodiversity and Ecology. Université Paris sciences et lettres, 2022. English. ⟨NNT : 2022UPSLM092⟩. ⟨tel-04249468⟩

HAL Id: tel-04249468

https://pastel.hal.science/tel-04249468v1

Submitted on 19 Oct 2023

HAL is a multi-disciplinary open access archive for the deposit and dissemination of scientific research documents, whether they are published or not. The documents may come from teaching and research institutions in France or abroad, or from public or private research centers.

L'archive ouverte pluridisciplinaire **HAL**, est destinée au dépôt et à la diffusion de documents scientifiques de niveau recherche, publiés ou non, émanant des établissements d'enseignement et de recherche français ou étrangers, des laboratoires publics ou privés.

HAL Authorization

PSL UNIVERSITÉ PARIS

THÈSE DE DOCTORAT
DE L'UNIVERSITÉ PSL

Préparée à MINES Paris - PSL

Modeling water and energy fluxes in the Seine basin

Modélisation des flux d'eau et d'énergie dans le bassin de la Seine

Soutenue par

Deniz KILIC

Le 30 09 2022

École doctorale n°398

Géosciences, Ressources Naturelles et Environnement

Spécialité

Géosciences et géo-ingénierie

Composition du jury :

Dr. Florentina MOATAR Directrice de Recherche, INRAE RiverLy	*Président*
Dr. Sandrine ANQUETIN Directrice de Recherche CNRS, IGE, Université Grenoble-Alpes	*Rapporteur*
Dr. Christopher BRADLEY Senior Lecturer, University of Birmingham	*Rapporteur*
Dr. Laurent LONGUEVERGNE Directeur de Recherche, Geosciences Rennes	*Examinateur*
Dr. Philippe BLANC Directeur de Recherche, Mines Paris - PSL	*Examinateur*
Dr. Nicolas FLIPO Directeur de Recherce, MINES Paris - PSL	*Directeur de thèse*
Dr. Agnés RIVIERE Chargée de recherche, MINES Paris - PSL	*Directrice de thèse*

MINES PARIS | PSL

ACKNOWLEDGEMENT

With immense pleasure and a deep sense of gratitude, I wish to express my sincere thanks to my thesis director Dr Nicolas Flipo, for his dynamism and endless support; my co-supervisor Dr Agnès Riviére, for trusting me with this project after the research internship and for encouraging me at every step. Also, Dr Agnès Ducharne, from the beginning until the end, was supportive and encouraging, which hepled me to overcome the challenges during the project. Without their support and continuous encouragement, this research would not have been successfully completed. I want to thank the jury: the reporters, Dr Sandrine Anquetin and Dr Christopher Bradley; the jury president, Dr Florentina Moatar; and examiners, Dr Laurent Longuevergne and Dr Philippe Blanc. Their observations, recommendations, and our discussions on this thesis have enriched the manuscript immensely. I want to sincerely thank Dr Philippe Peylin and Dr Patrick Goblet, who enriched this work with their expertise and know-how on various critical aspects of this study. Thanks to Nicolas Gallois for his constant support on the software development part of this project and for encouraging me to dive into code development.

This work was funded by the Mines Paris and the PIREN Seine project. I am grateful to the Mines Paris and the Geosciences centre for providing me with infrastructural facilities and many other resources needed for my research.

My thesis would not have been the same without the constructive contributions of Dr Faiçal Rejiba, William Thomas, and Dr Jean-Louis Roujean. I express my sincere gratitude and thanks to William Thomas for providing us with the river temperature dataset. I sincerely thank the ORCHIDEE team, Josefin Ghattas, Dr Nina Raoult, and Vladislav Bastrikov, for their support throughout my research. I want to thank my colleagues at the Geosciences centre of Mines Paris, especially our team SHR: Shuaitao, Matthias, Pierre, Jonathan, Aurélien, Masihullah, Joao, Fulvia, Elisabeth, Dominique, Pascal, Alexandra, Jacques for sharing this journey with me. Also, I would like to thank the secretary team, V. Lachasse and S. Motte who helped me to overcome many bureaucratic challenges.

I am extending my profound gratitude to my family, whom I could always count on, for all the sacrifices they made during my research and for providing me with moral support and encouragement whenever required, along with patience and understanding.

Contents

ACKNOWLEDGEMENT i
LIST OF FIGURES vii
LIST OF TABLES xix
LIST OF TERMS AND ABBREVIATIONS xxiv

Résumé **1**

1 General introduction **30**
1.1 Climate change 32
1.2 Scientific questions and objectives 37
1.3 Research outlines 39

2 Past trends in the Seine basin under the impact of climate change **41**
2.1 Introduction 41
2.2 Description of The seine hydrosystem 44
2.2.1 The aquifer system 44
2.2.2 The surface water 47
2.2.3 Soil and land cover distribution in the basin 48
2.3 Water and thermal uses of resources 51
2.3.1 Uses of water resources 51
2.3.2 Thermal use 53
2.4 Brief analyses of hydrothermal observations 54
2.4.1 Seasonal description of hydrological variables 55
2.4.2 Historical events in the Seine basin 56
2.4.3 Temperature evolution of the Seine hydrosystem 57
2.5 Conclusion and perspectives 62

3 Energy and water fluxes in the hydrosystem **64**

3.1 Introduction . . . 64
3.2 Energy fluxes . . . 64
3.2.1 Surface processes . . . 65
3.2.2 River . . . 69
3.2.3 Ground heat transfer . . . 71
3.3 The link between water and energy fluxes . . . 72
3.4 Water fluxes . . . 72
3.4.1 Surface processes . . . 73
3.4.2 River . . . 78
3.4.3 Groundwater Flow . . . 80
3.5 Synthesis: a coupled framework . . . 81

4 Hydrosystem modelling 83
4.1 Introduction . . . 83
4.2 SVAT . . . 83
4.3 River . . . 93
4.4 Groundwater . . . 98
4.4.1 Ground heat transfer . . . 99
4.4.2 Overland flow and routing . . . 100
4.4.3 Synthesis: Groundwater . . . 101
4.5 Integrated modeling approaches . . . 105
4.5.1 SVAT-aquifer interface . . . 105
4.5.2 SVAT-stream interface . . . 106
4.5.3 Stream-aquifer interface . . . 107
4.5.4 Aquifer-aquifer interface . . . 108
4.6 Synthesis: Integrated modelling . . . 109

5 Modelling the hydrosystem fluxes at the regional scale 112
5.1 Introduction . . . 112
5.2 Models . . . 113
5.2.1 ORCHIDEE . . . 113
5.2.2 CaWaQS . . . 116
5.2.3 Coupling strategy . . . 119

5.3 Conclusion . . . 120

6 Application of ORCHIDEE-CaWaQS: hydrological modeling 122

6.1 Introduction . . . 122

6.2 Data and methods . . . 125

6.2.1 Construction of the Seine model . . . 125

6.2.2 Soil information . . . 127

6.2.3 Vegetation . . . 134

6.2.4 Slope map . . . 138

6.2.5 Introduction of a new soil class: urban . . . 139

6.2.6 Water abstraction . . . 139

6.2.7 Technical considerations of the Seine application . . . 141

6.2.8 CaWaQS setup . . . 143

6.2.9 Calibration strategy . . . 144

6.2.10 Validation criteria . . . 145

6.2.11 Model evaluation and data . . . 147

6.2.12 Calibration procedure . . . 149

6.3 Results and discussion . . . 154

6.3.1 Surface water balance (ORCHIDEE) . . . 154

6.3.2 ORCHIDEE-CaWaQS coupled application . . . 174

6.4 Conclusions and perspectives . . . 181

7 Assessing water and energy fluxes in a regional hydrosystem: case study of the Seine basin 187

7.1 Introduction . . . 188

7.2 Material and methods . . . 192

7.2.1 Study area: The Seine hydrosystem . . . 192

7.2.2 Numerical tools and model development . . . 193

7.3 Results and discussions . . . 203

7.3.1 Calibration of the surface water cycle . . . 203

7.3.2 Performance of the ORCHIDEE-CaWaQS coupled simulation . . . 205

7.4 Hydrological and thermal functioning of the Seine Hydrosystem . . . 207

7.4.1 Pluri-annual water budget . . . 207

7.4.2 Pluri-annual heat budget 208
7.4.3 Seasonal heat fluxes in the river network 210
7.4.4 Implications on the Water-Energy-Food Nexus 212
7.5 Conclusions and perspectives 213
7.5.1 Performance of the ORCHIDEE-CaWaQS coupling: hydrology . . 215

8 An assessment of the water budget and energy balance of the Seine Basin: current and future trends 217
8.1 Introduction 217
8.2 Methods and materials 219
8.2.1 ORCHIDEE-CaWaQS Seine model 219
8.2.2 Climate change scenarios 221
8.2.3 Experiments setup 222
8.2.4 Analysis of hydrological and temperature regimes 223
8.3 Results and discussion 224
8.3.1 Projected changes in the Seine basin 224
8.3.2 Changes in the temperature regime in the basin 226
8.3.3 Projected seasonal changes in the river heat fluxes 227
8.3.4 Projected changes in the energy balance 228
8.4 Conclusions and perspectives 231

9 Conclusion and perspectives 234
9.1 Coupled water and energy budget at the regional scale 234
9.2 Perspectives 237
References 239

Appendices

Appendix A Development of the heat transport in the CaWaQS platform 300
A.1 Introduction 300
A.2 Les outils de modélisation du transfert de chaleur dans les bassins 302
A.2.1 CaWaQS: CAtchment WAter Quality Simulator 302
A.2.2 *libttc*: librairie de transport de chaleur et de solutés 304

A.3 Solution analytique des échanges thermiques cours d'eau-aquifère et aquifère-aquitard-aquifère 310
A.4 Validation des développements 314
A.4.1 Validation du transfert de chaleur en rivière 316
A.4.2 Validation du transfert de chaleur en aquifère 317
A.4.3 Validation du transport de chaleur transitoire en régime hydraulique transitoire 329
A.4.4 Validation du transport de chaleur au travers du lit de la rivière et au travers des aquitard 337

Appendix B Water and energy budgets from MIROC reanalysis simulations 342

List of Figures

1 Schématisation de la structure de la plateforme CaWaQS3.X de modélisation de flux d'eau et de chaleur. 8

2 Vue d'ensemble du bassin de la Seine (78 650 km^2). L'occupation des sols, utilisée comme fond de carte, est fournie par la base de données *CorineLandCover* de 2018 . Les triangles bleus et les cercles jaunes représentent les positions de mesure du débit et de la température des rivières, respectivement. Les lignes pointillées de couleur indiquent l'étendue de l'ensemble du système aquifère. Les stations de mesure de la température des aquifères sont regroupées en fonction de l'ensemble aquifère auquel elles sont associées. 9

3 Composantes du bilan annuel moyen des eaux de surface calculées par ORCHIDEE en mm y^{-1}. Le biais a été calculé sur le débit moyen pluriannuel à la station de mesure de Vernon après que le retrait des prélèvements d'eau annuels moyens. La colonne CaWaQS représente le bilan hydrique calculé par l'application CaWaQS-Seine. 16

4 Comparaison sur la période août 2001-juillet 2018 entre a) le débit simulé (rouge) et observé (bleu) à la sortie du bassin versant de la Seine (Vernon) ; b) la température simulée (rouge) et observée (bleu) du fleuve à Paris (Austerlitz). Les années sont indiquées au 1er janvier. KGE : Coefficient d'efficacité de Kling-Gupta ; CC : coefficient de corrélation ; $PBIAS$: Pourcentage de biais ; $RMSE$: Erreur quadratique moyenne. 19

5 Bilan d'eau de l'hydrosystème de la Seine sur la période 2001-2018 tel que simulé par l'application ORCHIDEE-CaWaQS. Le système d'eau souterraine englobe toute l'étendue des aquifères. ITB : Flux d'infiltration pour les unités aquifères affleurantes au-delà des limites du bassin de la Seine. Les flux hors limites (ITB) sont au-delà de l'étendue du bassin de la Seine. Les flux sont exprimés en valeurs moyennes inter-annuelles en $\mathrm{m^3\,s^{-1}}$. Pluie = 760mm/an*, ETR* = 559mm/an*, Ruissellement = 69mm/an*, Recharge des aquifères = 132mm/an*. Couches aquifères : 'Alluvion' : Dépôts alluvionnaires, 'Beauce' : Ensemble des calcaires de Beauce, 'Brie' : Calcaires de Brie et sables de Fontainebleau, 'Champigny' : Calcaires de Champigny, 'Lutétien' : Calcaires du Lutétien, 'Thanétien' : Sables du Thanétien, 'Chalk' : aquifère crayeux du Crétacé supérieur, 'JLC. ens.' : Ensemble du Crétacé inférieur et du Jurassique. 22

6 Bilan thermique de l'hydrosystème Seine sur la période 2001-2018 simulé par l'application ORCHIDEE-CaWaQS . Les quantités d'énergie sont exprimées en valeurs moyennes pluriannuelles en $\mathrm{GW\,h}$ par jour et la température moyenne annuelle quotidienne de l'air et du sol à $2\,\mathrm{m}$ de profondeur sont indiquées en $^\circ\mathrm{C}$. SW : Rayonnement net à courte longueur d'onde, LW : Rayonnements à grande longueur d'onde, SH : Chaleur sensible, LH : Chaleur latente. Couches aquifères : 'Alluvion' : Dépôts alluvionnaires, 'Beauce' : Ensemble des calcaires de Beauce, 'Brie' : Calcaires de Brie et sables de Fontainebleau, 'Champigny' : Calcaires de Champigny, 'Lutétien' : Calcaires du Lutétien, 'Thanétien' : Sables du Thanétien, 'Chalk' : aquifère crayeux du Crétacé supérieur, 'JLC. ens.' : Ensemble du Crétacé inférieur et du Jurassique. 23

7 Flux de chaleur saisonniers ($\mathrm{W\,m^{-2}}$) dans le réseau hydrographique de la Seine sur la période 2001-2018. 25

1.1 Flows and changes in the hydrosystem that influence groundwater resources (figure from IPCC (2007)) 31

1.2 Historical and projected changes in the annual average CO_2 concentrations. The black line combines the reconstructed values from 1880-1958 and Mauna Loa observations from 1959-2019. The coloured lines are the four Representative Concentration Pathway (RCP) scenarios used in the CMIP5 (figure from (Stocker et al., 2013)). 33
1.3 Past global surface temperature trends along with future projections. The black line indicates past temperature trends before 2005. Coloured lines indicate surface temperature projections under different CO_2 emission levels. Shades indicate uncertainty ranges. (figure from Knutti and Sedláček (2013)) 34
1.4 Surface temperature anomalies in France from 1900 until 2010. Future projections are also shown in red line with an uncertainty range in orange colour. The smaller figure indicates the reanalysis of the past data with anthropological forcing and natural forcing (without anthropological stresses). (figure from Terray and Boé (2013)) 35
2.1 The succession and extent of the aquifer layers. The river network and the extension of the Seine basin are superposed on the aquifer layers. . . 46
2.2 The surface topography and the river network in the Seine River basin. Thicker lines indicate a higher Strahler order. The major cities (red dots) are evolved around the river network, with Paris being at the confluence of the Seine and Marne rivers. 49
2.3 Soil cover map from the basin. Source INRA InfoSol (Jolivet et al., 2006). 50
2.4 The Seine River basin land use map. Source: Corine Land Cover (Büttner et al., 2004). 51
2.5 Distribution of major water abstraction locations in the Seine basin. The size of the point indicates the amount withdrawn, source: AESN. 52
2.6 Local observations from the Seine River Basin. Temperature data is from the river network. 56
2.7 The climatological state of the Seine basin throughout 1980-2018, shown by monthly mean temperature and precipitation. 57
2.8 Evolution of the water temperatures and associated trend lines in the Seine basin (source: William Thomas, DRIEE, 2020). 58

2.9 Long-term seasonal Theil-Sen trends (°C of the soil horizon at 100cm depth. Filled dots indicate a statistically significant trend ($p < 0.05$), and empty dots indicate an insignificant trend according to the Mann-Kendall test. Overall shows the average temperature trend. No dots indicate insufficient data to establish a trend. 60
2.10 Spatial distribution of Theil-Sen trends (°C.yr^{-1}) of the soil horizon at 100cm depth during summer. All soil stations show a positive trend at 100 cm depth; Fontaine, Bretigny and Coucy do not show a significant trend based on the Mann-Kendall trend test. 61
3.1 Processes in the water cycle and models that capture the processes. Rectangles indicate components of the water cycle, and arrows indicate processes of the water cycle. (Figure modified from De la Torre (2014)) 65
3.2 The heat and water flux processes in the vegetation layer based on the description by Krinner et al. (2005). 69
3.3 Representation of the energy and hydrological fluxes controlling river water temperature. 71
3.4 A categorised representation of water and energy fluxes in the hydrosystem. 73
3.5 The inherent connection between water and energy fluxes. Above formulation describes the water balance, whereas, lower formulation describes the energy balance 74
3.6 Groundwater processes with connection to surface. 81
5.1 Impact of c_K on dominant soil textures i.e. a) Clay Loam, b) Loam, c) Loamy Sand in the Seine basin. KSref indicates the saturated hydraulic conductivity of the soil texture defined in ORCHIDEE. 114
5.2 The structure of the CaWaQS3.XX platform with distinct compartments of the hydrosystem (Gallois et al., 2020b) 119
5.3 a) The atmospheric and surface processes that control thermal regimes, b) the flowchart for integrating SVAT models and groundwater flow and heat transport models) and c) The flow chart of ORCHIDEE-CaWaQS integration. (Figure adapted from Kurylyk et al. (2014).) 120

6.1 The simulated domain by ORCHIDEE. Main sub-basins in the basin are shown. River network is not simulated by ORCHIDEE. Evaluation data locations are noted: piezometers (triangle), and major gauging stations (circle). 126
6.2 Ternary diagram of the USDA soil classification system (Grey) USDA, 1993) overlapped by European Ternary Diagram (red). (Cl = Clay, SiCl = Silt Clay, SaCl = Sandy clay, ClLo = Clay loam, SiClLo = Silty Clay Loam, SaClLo = Sandy Clay Loam, Lo = Loam, SiLo = Silty Loam, Si = Silt, SaLo = Sandy Loam, LoSa = Loamy Sand, Sa = Sand; VF = Very Fine, F = Fine, M = Medium, MF = Medium Fine, C = Coarse) . . 131
6.3 The soil classification maps from INRA, LUCAS, Reynolds, SoilGrids . 132
6.4 Soil distribution of different soil maps per sub-catchment in the Seine basin 133
6.5 ESA-CCI 2015 land cover map over the ORCHIDEE Seine Basin grid (resolution = 300 m) 135
6.6 Distribution of vegetation by sub-catchment in the Seine basin 136
6.7 PFT type variation in the period 1992-2015 of the Seine Basin 137
6.8 The slope map transformed from an IGN 25m DEM database 138
6.9 Various soil texture distribution maps with new urban soil texture class. 140
6.10 ORCHIDEE grid structure intersected with unsaturated zone thickness from a previously validated CaWaQS model application 142
6.11 Evolution of soil moisture distribution over the period 1980-1990. . . . 155
6.12 Evolution of soil temperature evolution over the period 1980-1990. . . . 156
6.13 The comparison of pluri-annual mean discharge between simulated and observed of the experiments. Pluri-annual mean simulated fluxes were calculated and a withdraw rate was uniformly applied. 159
6.14 Monthly observed and simulated total (EXP1-11) surface runoff dynamics of in mm/d from main sub-catchments 160
6.15 Comparison of observed discharge at Poses station with simulated total surface runoff fluxes from ORCHIDEE. The comparison shows the daily (upper figure) and 30-day moving averaged fluxes (lower figure). . 161

6.16 Mean yearly surface water budget components of EXP1-13 calculated by ORCHIDEE in $mm.y^{-1}$. Bias was calculated on the multi-year mean discharge at Vernon gauging station after the adjustments on the mean yearly water abstractions are taken into account . CaWaQS column represents the water balance calculated by CaWaQS-Seine application including water abstractions. 162
6.17 Monthly variation of LAI over the period 1982-2010. The comparison is between GIMMS-LAI product and the set of experiments 166
6.18 Monthly variation of LAI ($m^2.m^{-2}$over the period 1982-2010 from EXP6. The comparison is between GIMMS-LAI product and the set of experiments 167
6.19 Monthly variation of actual evapotranspiration. The comparison is between GLEAM-AET product and the set of experiments 168
6.20 Monthly variation of actual evapotranspiration. The comparison is between GLEAMv3 product and EXP6 simulation in $mm.d^{-1}$ 169
6.21 Monthly dynamics of the EXP12 (NoUrban) and EXP13 (Urban) compared to the observed discharge at the main sub-catchments of the Seine basin. 171
6.22 The surface water balance in the ORCHIDEE from EXP10. Positive scale shows the precipitation variation, whereas the negative scale shows the components of the surface water balance. Fluxues in $mm.y^{-1}$ 172
6.23 Distributed a) runoff, b) recharge maps obtained from the ORCHIDEE simulations. The yearly values are averaged for the period of 1990-2018. 173
6.24 Spatial distribution of calculated KGE at the gauging stations simulated by ORCHIDEE-CaWaQs Seine application throughout the catchment. Coloured areas indicate the main sub-catchments of the basin. The thickness of river reaches varies as a function of Strahler order no. . . . 174
6.25 The simulated and observed discharges at the Vernon station. KGE= 0.77, Correlation coefficient: 0.82, PBIAS: 1.6% 176
6.26 Comparison of the simulated and the observed discharges at each gauging station of the catchment. Period of averaging: 2001-2018 177

6.27 Spatial distribution of calculated RMSE on 292 piezometers over the period 2001-2018. 178
6.28 Comparison of the simulated and the observed piezometric heads at each observation well in the catchment. 179
6.29 Time series illustration of hydraulic head during the examined period of the Beauce aquifer (Layer 2). The number of daily observations, RMSE, KGE, CC and standard deviation metrics are noted. 180
6.30 Time series illustration of hydraulic head during the examined period of the Champigny aquifer (Layer 4). The number of daily observations, RMSE, KGE, CC and standard deviation metrics are noted. 181
6.31 Time series illustration of hydraulic head during the examined period of the Chalk (Craie) aquifer (Layer 7). The number of daily observations, RMSE, KGE, CC and standard deviation metrics are noted. 182
6.32 Comparison of standalone ORCHIDEE, standalone CaWaQS, the coupled model and the observed discharge at Seine Poses. A 30-day moving average was applied to discharge values 183
7.1 General overview of the Seine basin area ($\simeq$ 78,650 km^2). Land use as provided by the 2018 *CorineLandCover* database is used as map background. Triangles and square points represent river discharge and temperature measurements, respectively. Colored dashed lines indicate the extent of the entire aquifer system. Aquifer temperatures stations are grouped according to the main aquifer ensemble they are associated with. 193
7.2 Mean yearly surface water budget components calculated by ORCHIDEE in mm y^{-1}. Bias was calculated on the multi-year mean discharge at Vernon gauging station after the adjustments on the mean yearly water abstractions are taken into account for EXP1-10. CaWaQS column represents the water balance calculated by the CaWaQS-Seine application including water abstractions. 202

7.3 Comparison between a) simulated (red) and observed (blue) discharge at the outlet of Seine watershed (Vernon); b) simulated (red) and observed (blue) river temperature at Paris (Austerlitz). From August 2001 to July 2018. Years indicate 1st of January. KGE: Kling-Gupta Efficiency coefficient; CC: correlation coefficient; $PBIAS$: Percent bias; $RMSE$: Root mean squared error. 206

7.4 Water budget of the Seine hydrosystem over the period 2001-2018 as simulated by ORCHIDEE-CaWaQS application. Groundwater system encompasses the full extent of the aquifers. ITB: Infiltration flux for outcropping aquifer units beyond the Seine basin limits. Flows outside boundaries (OTB) are beyond the extent of the Seine basin. Flows are expressed in inter-annual average values in $\mathrm{m^3\,s^{-1}}$. Model layers : 'Alluvium': Alluvial deposits, 'Beauce': Beauce limestones ensemble, 'Brie': Brie limestones and Fontainebleau sands, 'Champigny': Champigny limestones, 'Lutetian': Lutetian limestones, 'Thanetian': Thanetian sands, 'Chalk' : Upper Cretaceous chalk aquifer, 'JLC. ens.': Lower Cretaceous and Jurassic ensemble. 208

7.5 Heat budget of the Seine hydrosystem over the period 2001-2018 as simulated by ORCHIDEE-CaWaQS application. Groundwater system encompasses the entire aquifer extents. Flows outside boundaries are beyond the extent of the Seine basin. Energy amounts are expressed in multi-annual average values in $\mathrm{GW\,h}$ per day and mean annual daily air temperature and soil temperature at $2\,\mathrm{m}$ depth are shown in $^{\circ}\mathrm{C}$. $\Delta Heat$: net thermal load variation in the river network. SW: Net shortwave radiation, LW: Long-wave radiation, SH: Sensible heat, LH: Latent heat. Model layers : 'Alluvium': Alluvial deposits, 'Beauce': Beauce limestones ensemble, 'Brie': Brie limestones and Fontainebleau sands, 'Champigny': Champigny limestones, 'Lutetian': Lutetian limestones, 'Thanetian': Thanetian sands, 'Chalk' : Upper Cretaceous chalk aquifer, 'Jurassic': Lower Cretaceous and Jurassic ensemble. 209

8.1 a) Physical processes that control the surface and subsurface temperature regimes; b) The flowchart that combines the atmospheric climate models used for future projections to surface and groundwater models c) The simulation protocol with models and data used in this application. (Step 1a.), Simulation of GCM model (Step1b) Downscaling of the GCM results at appropriate basin scale. (Step 2) Simulation of ORCHIDEE to estimate surface water budget and energy balance (Step 3) Simulation of CaWaQS coupled with the fluxes from ORCHIDEE. Adapted from Kurylyk et al. (2014). 220
8.2 Global temperature change projections up to 2100 based on CMIP3 (left) and CMIP5 (right) frameworks. Lines represent the mean temperature anomaly increase based on the projections, and past observations (dark); shaded areas indicate the degree of uncertainty (source: IPCC (2019)) 222
8.3 Changes in the regime of hydrological and energy fluxes. a) The monthly precipitation regime, b) the monthly air temperature regime at the surface boundary; 224
8.4 Changes in the temperature regime in the Seine hydrosystem. a) the average water temperatures in the Seine river, b) the riverbed temperatures at the river-aquifer interface. 226
A.1 Schématisation de la structure de la plate-forme CaWaQS3.X de modélisation de flux d'eau (d'après Gallois et al. (2020a)). 304
A.2 La configuration de la solution analytique dans a) l'interface aquifère-aquitard-aquifère et b) l'interface nappe-rivière. 315
A.3 Géométrie du cas-test : A). Couverture des mailles SAFRAN and ORCHIDEE, les zones 1 et 2 représentent des cellules SAFRAN différentes; B). Les lignes bleues correspondent aux tronçons de rivière; les sections (verte, bleue, rouge) correspondent aux unités de production d'eau et de chaleur dont les flux journaliers sont calculés par ORCHIDEE 316
A.4 Températures de l'eau simulées pour la maille à l'exutoire (tronçon de rivière 3) 317

A.5 A) La géométrie de la colonne de sol en 1-D. B) Températures initiales et conditions aux limites utilisées sur la colonne de sol. 318
A.6 Comparaison de la solution analytique (Stallman, 1965) et de la simulation CaWaQS3.X , dans le cas du transport de chaleur en colonne gigogne en 1-D. 320
A.7 Géométrie du cas test “bassin versant” et condition initiales et limites associées. La variation de température de la cellule rouge sera étudiée, par la suite, en section A.4.3.2. 321
A.8 Évolution de la température simulée en régime permanent, pour le bassin versant avec un flux de chaleur orienté Nord-Sud. 322
A.9 Maillage irrégulier associé au cas de simulation test en milieu poreux. La résolution de la cellule est 1 m. 323
A.10 Évolution de la température simulée en régime permanent pour le cas-test “bassin versant”. 323
A.11 A) Géométrie de la colonne de sol en 1-D. B) Températures initiales et conditions aux limites de la colonne de sol Goto et al. (2005). 325
A.12 Variations spatio-temporelles des réponses thermiques d’un flux de l’eau descendant (cas 1) dans la colonne de sol à partir a)de la solution numérique libttc, b) de la solution analytique Goto. Chaque ligne représente le profil de température d’un jour en différentes couleurs pendant la période de simulation. 327
A.13 Variations spatio-temporelles des réponses thermiques d’un flux de chaleur conductif pur (cas 2) dans la colonne de sol à partir de a)la solution numérique libttc, b) la solution analytique Goto. Chaque ligne représente le profil de température d’un jour en différentes couleurs pendant la période de simulation. 328
A.14 Variations spatio-temporelles des réponses thermiques du flux de l’eau ascendant (cas 3) dans la colonne de sol à partir a) de la solution numérique libttc, b) de la solution analytique Goto. Chaque ligne représente le profil de température d’un jour en différentes couleurs pendant la période de simulation 329

A.15 Variations temporelles des d'un flux d'eau: Flux d'eau descendant jusqu'au jour 30, pas de flux d'eau entre le jour 30 et 60) et flux d'eau ascendant à partir du jour 60), dans la colonne de sol. 330
A.16 Variations de température à $0.5\mathrm{m}$ profondeur. Goto-Conduction : Goto en conduction pur ; Goto-Downflow : Goto avec flux d'eau descendant ($U = 5\ 10^{-6}\mathrm{m\,s^{-1}}$). Goto-Upflow : Goto avec flux d'eau ascendant ($U = -5\ 10^{-6}\mathrm{m\,s^{-1}}$). 331
A.17 Variations de température à $5\mathrm{m}$ profondeur. Goto-Conduction : Goto en conduction pur ; Goto-Downflow : Goto avec flux d'eau descendant ($U = 5\ 10^{-6}\mathrm{m\,s^{-1}}$). Goto-Upflow : Goto avec flux d'eau ascendant ($U = -5\ 10^{-6}\mathrm{m\,s^{-1}}$). 331
A.18 Variations de température à 9.5 m profondeur. Goto-Conduction : Goto en conduction pur ; Goto-Downflow : Goto avec flux d'eau descendant ($U = 5\ 10^{-6}\mathrm{m\,s^{-1}}$). Goto-Upflow : Goto avec flux d'eau ascendant ($U = -5\ 10^{-6}\mathrm{m\,s^{-1}}$). 332
A.19 Variations temporelles des réponses thermiques d'un flux de l'eau variable dans la colonne de sol à $0.5\mathrm{m}$, $5\mathrm{m}$, 9.5 m profondeur. La ligne violet indique la condition limite en haut de la colonne. Les lignes verticales indiquent les jours où la vitesse change. 333
A.20 Variation de la vitesse pour 1 an de période de simulation. Une fort vitesse de Darcy uniforme est appliquée dans EXP1and2. Tous les 120 jours, la vitesse est modifiée de manière progressive pour l'EXP3-4. EXP3 signifie une simulation avec un écoulement de l'eau plus lent dans la direction Nord-Sud. EXP4 signifie une simulation avec un flux d'eau plus fort. L'EXP4 est censée être dominée le terme advectif. . . . 335

A.21 Évolution de la température de la cellule rouge du cas synthétique aquifère triangulaire (Fig. A.7). EXP1 a une vitesse de $1e{-}4\mathrm{m\,s^{-1}}$ vers Sud-Nord, et EXP2 a une vitesse de $1e{-}4\mathrm{m\,s^{-1}}$ vers Nord-Sud. a) Advection signifie une simulation avec seulement le transport de chaleur advectif activé, b) Conduction signifie une simulation avec seulement le transport de chaleur conductif activé, c) Advection + Conduction signifie une simulation avec les deux composantes du transport de chaleur activées. 336

A.22 Évolution de la température de la cellule rouge du cas synthétique aquifère triangulaire (Fig. A.7). EXP3 a une vitesse de $1e{-}6\mathrm{m\,s^{-1}}$ dans différentes directions, et EXP4 a une vitesse de $1e{-}5\mathrm{m\,s^{-1}}$. a) Advection signifie une simulation avec seulement le transport de chaleur advectif activé, b) Conduction signifie une simulation avec seulement le transport de chaleur conductif activé, c) Advection + Conduction signifie une simulation avec les deux composantes du transport de chaleur activées. 337

A.23 Résultats de la solution de transport de chaleur au centre de la cellule du lit de la rivière en utilisant différents champs d'écoulement. Les points rouges sont le résultat de la simulation CaWaQS avec les mêmes températures limites du cours d'eau et de l'aquifère. 338

A.24 Résultats de la solution de transport de chaleur au centre de la cellule aquitard en utilisant différents champs d'écoulement. Les points rouges sont le résultat de la simulation CaWaQS avec les mêmes températures limites de l'aquifère. 339

List of Tables

1 Jeu de paramètres appliqué aux 10 expériences pour calibrer le modèle ORCHIDEE (- : même valeur que la précédente, R : Reynolds, SG : SoilGrids, L : Lucas, I : INRA, pLAI : LAI prescrit, ST : STOMATE activé, TeBS : Temperature Boreal Summerreen Trees, TeBe : Temperate Boreal Evergreen Trees, NC3 : Natural C_3 grass, AC3 : Agricultural C_3 crops) 14

2 Critères statistiques (période 2001-2018) de 48 sondes de température de cours d'eau réparties dans le bassin. Tableau supérieur : Erreur quadratique moyenne ($RMSE$), erreur absolue moyenne (MAE). Tableau inférieur : Coefficient de corrélation de Pearson (CC), et coefficient d'efficacité de Kling-Gupta (KGE). 20

3 Critères statistiques (période 2001-2018) à partir de 211 sondes de température de l'aquifère réparties dans le bassin. Erreur quadratique moyenne ($RMSE$), erreur absolue moyenne (MAE) 21

4 Flux de chaleur saisonniers ($\mathrm{W\,m^{-2}}$) dans le réseau hydrographique de la Seine sur la période 2001-2018. La longueur totale du fleuve est de 28378 km, la surface totale du réseau hydrographique d'ordre de Strahler supérieur à 3 est de 369 km^2. Les flux nets sont le bilan thermique total du réseau hydrographique. Le signe négatif (-) indique une perte de chaleur par la rivière. . . . 26

2.1 The thermal properties of the Seine aquifer system provided in the literature. . 47

2.2 Summary of the observed variables from the Seine river network and available global satellite-derived products. 54

4.1 Comparison of existing SVAT models by their processes: part 1 89

4.2 Comparison of existing SVAT models by their processes: part 2 90

4.3 Comparison of existing SVAT models by their processes: part 3 91

4.4 Comparison of existing SVAT models by their processes: part 4 92

4.5 A compilation of numerical river models: part 1 96

4.6 A compilation of numerical river models: part 2 97
4.7 Existing groundwater models, a synthesis: part 1 102
4.8 Existing groundwater models, a synthesis: part 2 103
4.9 Existing groundwater models, a synthesis: part 3 104
4.10 A synthesis of integrated models 111
5.1 Soil texture properties of USDA soil classes based on Carsel and Parrish (1988). Dry soil heat capacities are defined following Pielke (2013) 117
6.1 The lookup table used to transform European soil classification to USDA soil classification according to Figure 6.2 130
6.2 List of evaluation data sets. 149
6.3 Parameter set applied to the 10 experiments to calibrate the ORCHIDEE model (-: same value than the previous one, R: Reynolds, SG: SoilGrids, L: Lucas, I : INRA, pLAI: prescribed LAI, ST: STOMATE activated, TeBS: Temperature Boreal Summergreen Trees, TeBe: Temperate Boreal Evergreen Trees, NC3: Natural C_3 grass, AC3: Agricultural C_3 crops) 152
6.4 Results of the calculated percent bias for each sub-catchment from EXP11. The bias was estimated after the water withdrawal rates were applied to the simulated discharge. 158
6.5 Performance of standalone ORCHIDEE, CaWaQS and coupled ORC-CaW vs observations at Seine Vernon. PBIAS: Percent bias, KGE: Kling-Gupta Efficiency, NSE: Nash-Sutcliffe Efficiency, CC: Correlation coefficient. Period: 2001-2018. 181
7.1 Parameter set applied to the 10 experiments to calibrate the ORCHIDEE model (-: same value than the previous one, R: Reynolds, SG: SoilGrids, L: Lucas, I : INRA, pLAI: prescribed LAI, ST: STOMATE activated, TeBS: Temperature Boreal Summergreen Trees, TeBe: Temperate Boreal Evergreen Trees, NC3: Natural C_3 grass, AC3: Agricultural C_3 crops) 201

7.2 Statistical criteria (2001-2018 period) from 48 stream temperature probes distributed in the basin. Upper Table: Root Mean Square Error ($RMSE$), Mean Absolute Error (MAE). Lower table: Pearson correlation coefficient (CC), and Kling-Gupta Efficiency (KGE) coefficient. 207

7.3 Statistical criteria (2001-2018 period) from 211 aquifer temperature probes distributed in the basin. $RMSE$: Root Mean Square Error, MAE: Mean Absolute Error 207

7.4 Seasonal heat fluxes ($\mathrm{W\,m^{-2}}$) in the Seine river network over the 2001-2018 period. The total river length is 28378 km, The total surface area of the river network is 369 km^2. The streambed fluxes are the heat exchanges between river and aquifer. Outflows are the heat loss of the river network via discharge. Negative sign (-) indicates loosing fluxes by the river. Inflows indicate the overflow towards the river network from the aquifer layer not linked to an active river-aquifer exchange calculation. 211

7.5 Statistical criteria (2001-2018 period) from 267 piezometers distributed in the basin. Upper table: Root Mean Square Error ($RMSE$), Mean Absolute Error (MAE). Lower Table: Pearson correlation coefficient (CC), and Kling-Gupta Efficiency coefficient (KGE). 216

8.1 Heat fluxes ($\mathrm{W\,m^{-2}}$) in the Seine river network from current, mid-century and end-century scenarios. The total river length is 28378 km, The total surface area of the river network is 369 km^2. Outflows are the heat flow from the river network via discharge. Inflows indicate the overflow towards the river network from the aquifer layer not linked to an active river-aquifer exchange calculation. Reanalysis: MIROC5 forcing. Negative sign (-) indicates losing fluxes by the river. Units are $\mathrm{W\,m^{-2}}$. 228

8.2 Estimation of the heat balance under the current state, mid-century, and end-century scenarios on the behaviour of the Seine hydrosystem. RV: Relative variation of scenarios from current reanalysis; RV*: Relative variation of GCM ref. from SAFRAN; Basin: Seine basin domain; ITB: Infiltration outside the basin boundaries; OTB: Outflows through the basin boundaries. Negative sign (-) indicates losses. Units are GWh/d 229

8.3 Average soil temperatures (surface and soil at 2 meter depth) by simulated by ORCHIDEE and aquifer temperatures simulated by CaWaQS under different climate change scenarios. Values are given in °C. Current period is the average temperature over 1993-2010, Mid-century is the average temperature over 2043-2060, End-century is the average temperature over 2083-2100 231
A.1 Paramètres utilisés pour la modélisation de transport. Les propriétés sont considérées homogènes 305
A.2 Propriétés thermiques du problème du transport de la chaleur en colonne 1-D avec un maillage irrégulier 319
A.3 Propriétés thermiques du problème du transport de la chaleur dans un bassin avec maillage régulier. 321
A.4 Propriétés thermiques de la colonne de sol utilisée pour les trois cas testés pour le transport de chaleur: 1) Flux advectif-conductif vers le bas, 2) Cas conductif pur, pas de flux d'eau, 3) Flux advectif-conductif vers le haut de la colonne. 326
A.5 Valeurs des conditions aux limites et initiales des trois cas tests. U_{cas1} est la simulation advectif-conductif avec un flux de l'eau descendant, U_{cas2} indique le test conductif pur, U_{cas3} est la simulation d'un flux de l'eau descendant. Les conditions aux limites et initiales thermiques $T_{initiale}$, $T_{surface}$, T_{bas} sont les mêmes pour les trois cas. 326
A.6 Performances de simulation: coefficient de corrélation, MAE (°C), RMSE (°C), biais (%), et KGE calculé pour les cas de test de la solution numérique vs Goto et al. (2005). 1) Cas 1 a un flux descendant avec une vitesse U de $1e{-}6\ \mathrm{m\,s^{-1}}$; 2) Cas 2 est une simulation en conductif pur $\mathrm{m\,s^{-1}}$; 3) Cas 3 a un flux ascendant U de $-1e{-}6\ \mathrm{m\,s^{-1}}$. 328
A.7 Propriétés thermiques d'une colonne de sol pour résoudre le transport de chaleur avec une hydraulique variable. 330
B.1 The water balance of the hydrosystem from current, mid-century, and end-century simulations described in Chapter 8. Fluxes are defined in $\mathrm{m^3\,s^{-1}}$. . . 343
B.2 The water balance the aquifer layers from current, mid-century, and end-century simulations described in Chapter 8. Fluxes are defined in $\mathrm{m^3\,s^{-1}}$. 344

B.3 Intra-aquifer exchanges of the aquifer system from current, mid-century, and end-century simulations described in Chapter 8.Fluxes are defined in $m^3\,s^{-1}$. . 345
B.4 Heat balance of the hydrosystem from current, mid-century, and end-century simulations described in Chapter 8. Heat flow amounts are defined in GWh/d. 346
B.5 Heat balance of the aquifer layers from current, mid-century, and end-century simulations described in Chapter 8. Heat flow amounts are defined in GWh/d. 347
B.6 Intra-aquifer heat exchanges and the geothermal gradient of the hydrosystem from current, mid-century, and end-century simulations described in Chapter 8. Fluxes are defined in GWh/d. 348

Simulations des flux d'eau et de chaleur au sein de l'hydrosystème Seine

Deniz Kilic

Résumé

Ce chapitre résume l'essentiel du travail de thèse. Les résultats de cette étude ont été préparés sous forme d'un rapport annuel du PIREN Seine:

Rivière, A., Kilic, D., Gallois, N., Ducharne, A., Wang, S., Peylin, P., Flipo. N., 2022. Simulations des flux d'eau et de chaleur au sein de l'hydrosystème Seine.

Introduction

La gestion durable des hydrosystèmes sera sous-tendue dans le futur par notre capacité à anticiper les effets du changement climatique, l'évolution des demandes en eau et des usages énergétiques de l'eau et les nouveaux systèmes de gouvernance relatifs à la gestion des milieux anthropisés (gestion des infrastructures, politiques de développement territorial). Ainsi, il est impératif de décrire aussi précisément que possible les évolutions temporelles et spatiales des transferts de solutés, de chaleur et d'eau dans les différents compartiments tout en tenant compte des changements globaux. Des premières simulations ont été mises en œuvre afin de prédire une évolution possible de l'hydrosystème Seine dans le futur (Boé et al., 2007; Ducharne, 2008; Ducharne et al., 2009; Flipo et al., 2020a). Cependant, la compréhension précise de l'impact du changement climatique sur le cycle de l'eau nécessite l'inclusion du bilan énergétique, car les processus inhérents au cycle de l'eau sont dépendants de celui-ci (Maxwell and Kollet, 2008a).

Dans ce cadre, un outil de modélisation intégrée a été développé visant à simuler

des échanges hydriques et thermiques entre l'atmosphère et la surface (sol, rivière et lac) et les systèmes aquifères en passant par les interfaces (zone non saturée, interface nappe-rivière et aquitards). Ces développements ont permis le couplage entre ORCHIDEE (*ORganizing Carbon and Hydrology in Dynamic EcosystEms*), dévelopée par l'IPSL (Krinner et al., 2005; Ducharne et al., 2000, 2020) et CaWaQS [1].(*CAtchment WAter Quality Simulator*, développée par Mines Paris, PSL Université, (Labarthe, 2016; Flipo et al., 2023). ORCHIDEE est utilisé pour résoudre le bilan hydrique et énergétique des compartiments sol-végétation-atmosphère au pas de temps horaire, tandis que CaWaQS est utilisé pour déterminer les flux d'eau et d'énergie dans les aquifères et les rivières ainsi que les flux d'échange via leurs différentes interfaces (aquitard, interface, nappe-rivière, atmosphère-rivière). Ce couplage est appliqué à l'hydrosystème Seine. Un travail de déclinaison régionale d'ORCHIDEE à l'échelle de l'hydrosystème Seine, non présenté ici, a d'ores et déjà été réalisé (Kilic et al., 2019, 2021a). Ce travail se base sur l'application CaWaQS-Seine (Flipo et al., 2023) qui a récemment été améliorée via l'inclusion de l'ensemble du système aquifère de la frange orientale de l'hydrosystème Seine (Gallois and Flipo, 2021), et l'ajustement des paramètres du système (Flipo et al., 2023), notamment le fractionnement hydrologique de la pluie efficace en ruissellement et infiltration.

La philosophie du couplage ORCHIDEE-CaWaQS est d'appliquer les températures de surface et les flux de recharge et de ruissellement simulés par ORCHIDEE comme forçages CaWaQS pour simuler explicitement les flux d'eau et de chaleur au sein des rivières et du système aquifère. Dans ce but, une bibliothèque de transport libttc originale basée sur la résolution de l'équation de transport de diffusion/advection a été développée pour simuler le transfert de chaleur dans les réseaux hydrographiques en 1D et les systèmes aquifères en pseudo-3D (Kilic et al., 2021b). Une solution analytique est utilisée pour simuler la réactivité thermique des interfaces telles que les aquitards et le lit des cours d'eau (Kurylyk et al., 2017).

Dans ce résume, l'outil est brièvement présenté, ainsi que la calibration du bi-

[1] disponible sous licence *open-source* EPL v2, CaWaQS est accessible à l'adresse https://gitlab.com/cawaqs/cawaqs

lan hydrique de surface. La dynamique et les ordres de grandeur des bilans d'eau et d'énergie sont détaillés dans le cas d'une simulation à long terme, afin de répondre à trois questions de recherche : **(i)** quel est le fonctionnement hydrologique et thermique de l'hydrosystème de la Seine dans les conditions climatiques actuelles ? **(ii)** Quelles sont les sources de chaleur prédominantes dans le réseau hydrographique de la Seine ? **(iii)** Quel est le rôle du ruissellement de surface et des échanges nappe-rivière dans le bilan énergétique de la Seine ?

Les outils de modélisation du transfert de chaleur dans les hydrosystèmes

ORCHIDEE (tag 2.2, rev. 6533)

ORCHIDEE est un modèle SVAT (« *Soil-Vegetation-Atmosphere-Transfer* »), initialement conçu pour être couplé à un modèle atmosphérique de circulation globale (Krinner et al., 2005), mais il peut également être utilisé en mode autonome, en utilisant un jeu de données météorologiques d'entrée. ORCHIDEE tag 2.2 a été développé dans le cadre du modèle IPSL-CM6 (Boucher et al., 2020) pour contribuer à la sixième phase du *Coupled Model Intercomparison Project* (CMIP6) (Eyring et al., 2016).

La résolution horizontale est imposée par la grille atmosphérique, et les bilans énergétiques et hydriques de la surface terrestre sont calculés dans chaque maille à un pas de temps infrahoraire (15 min dans le modèle couplé, 30 min en mode autonome) pour tenir compte des variations diurnes du rayonnement entrant. Ces bilans dépendent fortement de l'occupation du sol, décrite dans chaque maille comme une mosaïque de 15 types fonctionnels de plantes différents (TFP) comprenant le sol nu, les arbres à feuilles persistantes et à feuilles caduques, les prairies C3 et C4 et les cultures. Tous les TFP partagent les mêmes équations, mais avec des paramètres différents. La proportion de chaque TFP est prescrite dans chaque cellule de la grille à partir de cartes d'occupation du sol dérivées d'observations satellitaires, avec des mises à jour annuelles (Lurton et al., 2020). Deux options sont comparées dans ce travail en ce qui concerne l'évolution de l'indice de surface foliaire (LAI), qui peut être soit prescrit via des cartes d'entrée du LAI mensuel, soit calculé dynamiquement à un pas de temps journalier

par le module STOMATE, qui redistribue la production primaire nette (photosynthèse moins respiration autotrophe) en raison de règles d'allocation et de phénologie dépendantes des TFP.

La redistribution verticale de l'humidité du sol est modélisée par une solution multicouche de l'équation de Richards, utilisant un sol de 2 m discrétisé en 11 couches de sol, avec un drainage libre comme condition limite inférieure. L'infiltration et le ruissellement de surface sont dérivés d'une paramétrisation inspirée du modèle de Green-Ampt (D'Orgeval et al., 2008). La diffusivité hydraulique dans la zone non saturée est décrite par les relations de Van Genuchten-Mualem décrivant la variation de saturation en fonction de la pression capillaire dans les sols et la variation de la perméabilité en fonction de la saturation. Dans chaque cellule du modèle, les paramètres correspondants (y compris la perméabilité à saturation K_{sat} et la porosité) sont déduits de la texture du sol comme détaillé dans Tafasca et al. (2019). La $\mathrm{K_{sat}}$ $[\mathrm{m/s}]$ subit en outre une décroissance exponentielle verticale pour tenir compte des effets de compaction des sols et de la bioturbation :

$$K_{\mathrm{sat}}(z) = K^{*}_{\mathrm{sat}} \, \exp\left(-c_K(z - z_{\mathrm{lim}})\right), \tag{0.1}$$

où z est la profondeur du sol $[\mathrm{m}]$, K^{*}_{sat} est la valeur de référence de la perméabilité K_{sat} basée sur la texture du sol $[\mathrm{m/s}]$, z_{lim} est la profondeur à laquelle la diminution de K_{sat} commence (par défaut, égale à 0. 3 m), et c_K est le facteur de décroissance [en m^{-1}] (égal à 2 par défaut). L'évapotranspiration est composée de quatre sous flux : la sublimation, la perte par interception, l'évaporation du sol et la transpiration, étroitement couplées à la photosynthèse. L'évaporation et la transpiration du sol dépendent de l'humidité du sol via des facteurs de stress réduisant les taux effectifs par rapport au taux potentiel, qui dépend lui-même d'une résistance aérodynamique (et stomatique pour la transpiration) et du gradient de vapeur d'eau entre la surface et l'atmosphère. L'évapotranspiration E $[\mathrm{kg/m^2/s^1}]$ et son équivalent énergétique, le flux de chaleur latente LE $[\mathrm{Wm^{-2}}]$, couplent les bilans hydrique et énergétique, calculés à l'échelle de

la maille donnée par :

$$C_p \frac{\partial T_s}{\partial t} = (1 - \alpha_s)\, R_{\mathrm{SWd}} + R_{\mathrm{LWd}} - \varepsilon \sigma T_s^4 - LE - H - G. \tag{0.2}$$

La température de surface T_s est la variable pronostique [K], t est le temps [s], C_p est la capacité calorifique de la couche de surface [$\mathrm{J/K/m^3}$], tandis que R_{SWd} et R_{LWd} sont les flux de rayonnement descendant d'entrée [$\mathrm{w/m^2}$] dans les longueurs d'onde visibles et infrarouges, respectivement. L'albédo de surface α_s dépend de l'albédo du sol et de chaque TFP, qui sont des paramètres prescrits, et de l'albédo de la neige, calculé en fonction de l'âge de la neige par un module de neige à trois couches (Wang et al., 2013). Enfin, H est le flux de chaleur sensible [$\mathrm{w/m^2}$], et G est le flux de chaleur du sol [$\mathrm{w/m^2}$], qui couple le bilan énergétique de surface au profil de température du sol, résultant d'une équation de diffusion de chaleur en 1D. Le gel du sol est négligé puisque le bassin de la Seine est situé dans un climat tempéré. La discrétisation verticale pour la diffusion de la chaleur est identique à celle adoptée pour les flux d'eau jusqu'à 2 m, puis étendue à 18 m où un flux de chaleur nul est supposé en bas de la colonne de sol. Les propriétés thermiques du sol (capacité calorifique et conductivité thermique) de chaque couche dépendent de l'humidité du sol (en supposant un profil uniforme en dessous de 2 m) et de la texture du sol (Wang et al., 2016b).

CaWaQS (*v* 3.17)

La plateforme CaWaQS [2] est un outil numérique permettant la simulation spatio-temporelle de flux d'eau à diverses échelles, en régime permanent et/ou transitoire, au sein d'un hydrosystème (Flipo, 2005; Labarthe, 2016; Flipo et al., 2023). Cet outil a hérité de nombreux concepts de la plateforme de modélisation MODCOU-NEWSAM (de Marsily et al., 1978; Ledoux, 1980). Son application permet de couvrir un large éventail de problématiques, de la prospective sur les impacts du changement climatique sur la trajectoire hydrologique du bassin de la Seine aux enjeux de remontées de nappe en

[2] Développé au Centre de Géosciences, Mines Paris - PSL, disponible sous licence *open-source* EPL v2, CaWaQS est accessible à l'adresse https://gitlab.com/cawaqs/cawaqs. Pour plus d'informations, une fiche 'outils du PIREN-Seine' dédiée est consultable sur le site du PIREN-Seine.

agglomération parisienne (Maillot, 2019), en passant par l'étude d'impacts environnementaux autour de l'exploitation des gravières (Wang et al., 2016b) ou encore de la pollution diffuse d'origine agricole (Beaudoin et al., 2018; Gallois and Viennot, 2018). CaWaQS couple un ensemble de bibliothèques autonomes, offrant une structure modulaire à l'utilisateur qui peut sélectionner les compartiments de l'hydrosystème qu'il souhaite modéliser. Quatre librairies dédiées à ces compartiments constituent le cœur de la plateforme CaWaQS :

- Le module *libfp* (cf. Fig 1.A) calcule le bilan hydrique de surface au pas de temps journalier. Cette librairie permet de calculer l'évapotranspiration réelle, d'évaluer le stock d'eau dans le sol, de caractériser l'infiltration et le ruissellement à partir de données de précipitation et d'évapotranspiration potentielle. Le ruissellement est transféré jusqu'au réseau hydrographique de manière directe. Cette conceptualisation tend à négliger le temps de transfert entre le point de production du ruissellement hypodermique et le tronçon du réseau hydrographique le plus proche. Pour ce faire, le maillage de surface, support du transfert d'eau de surface, correspond à celui de bassins versants unitaires dont le temps de transfert est supposé inférieur au pas de temps de calcul (pas de temps journalier)

- le module *libhyd* (cf. Fig 1.B) simule les écoulements au sein du réseau rivière, selon le schéma de Muskingum (Cunge, 1969) (cf. Fig 1.D). Le ruissellement produit localement est distribué de manière homogène le long de chaque tronçon du réseau. L'épaisseur de la colonne d'eau dans la rivière est calculée par la méthode de Manning-Strickler.

- Le module *libnsat* (cf. Fig 1.C) transfère verticalement, dans la zone non saturée, les flux d'eau infiltrés calculés par le module de surface. Le transfert vertical est conceptualisé par une succession de réservoirs, de volumes et de coefficients de vidange renseignés basée sur la méthodologie développée par Nash (1959). Les flux calculés en base de ce compartiment sont par suite transférés comme recharge à la zone saturée (aquifère), soit par transfert vertical direct soit après routage.

- Le module *libaq* simule (cf. Fig 1.E) l'écoulement de l'eau dans un système aquifère multicouche, selon une discrétisation semi-implicite, par différences finies. L'équation de diffusivité est résolue sous une forme pseudo-3D. Un support de cette résolution par maillage gigogne est possible pour affiner la résolution en relation avec les couches supérieures et inférieures. Le lien entre les couches du système aquifère est établi par le concept de drainance (cf. Fig 1.H), analogue à celui de conductance, utilisé dans la simulation des échanges nappe-rivière (cf. Fig 1.G).

- Le module *libseb* simule, à partir de données météorologiques spatio-temporelles, le bilan global des échanges thermiques à l'interface eau/atmosphère.

- Le module *libttc* (cf. Fig 1.F) simule le transport d'énergie et de soluté dissous en milieu poreux (aquifères) et également en écoulement à surface libre (cours d'eau et rivières). Il permet le transport simultané, dans les différents compartiments des hydrosystèmes, de n espèces dissoutes. Cette fonctionnalité est essentielle, notamment dans une optique future d'intégration du transport réactif entre espèces et en relation avec la température. Ce module permet un niveau de flexibilité additionnel sur le pas de temps de simulation. Celui-ci est adaptable dans le but d'obtenir une meilleure représentation des processus physiques de chaque compartiment des hydrosystèmes en tenant compte de leurs temps caractéristiques.

Dans le cadre du présent travail, la possibilité a été programmée de coupler CaWaQS avec un modèle de surface terrestre (LSM - *Land Surface Model*) en définissant les cartes de forçages de recharge et de ruissellement, de concentration et/ou de température à partir de ces modèles de surface.

Stratégie de couplage des modèles

Le couplage est réalisé *via* une procédure de forçage "*offline*", par laquelle les modèles impliqués sont exécutés de manière séquentielle, ne permettant ainsi qu'une interaction

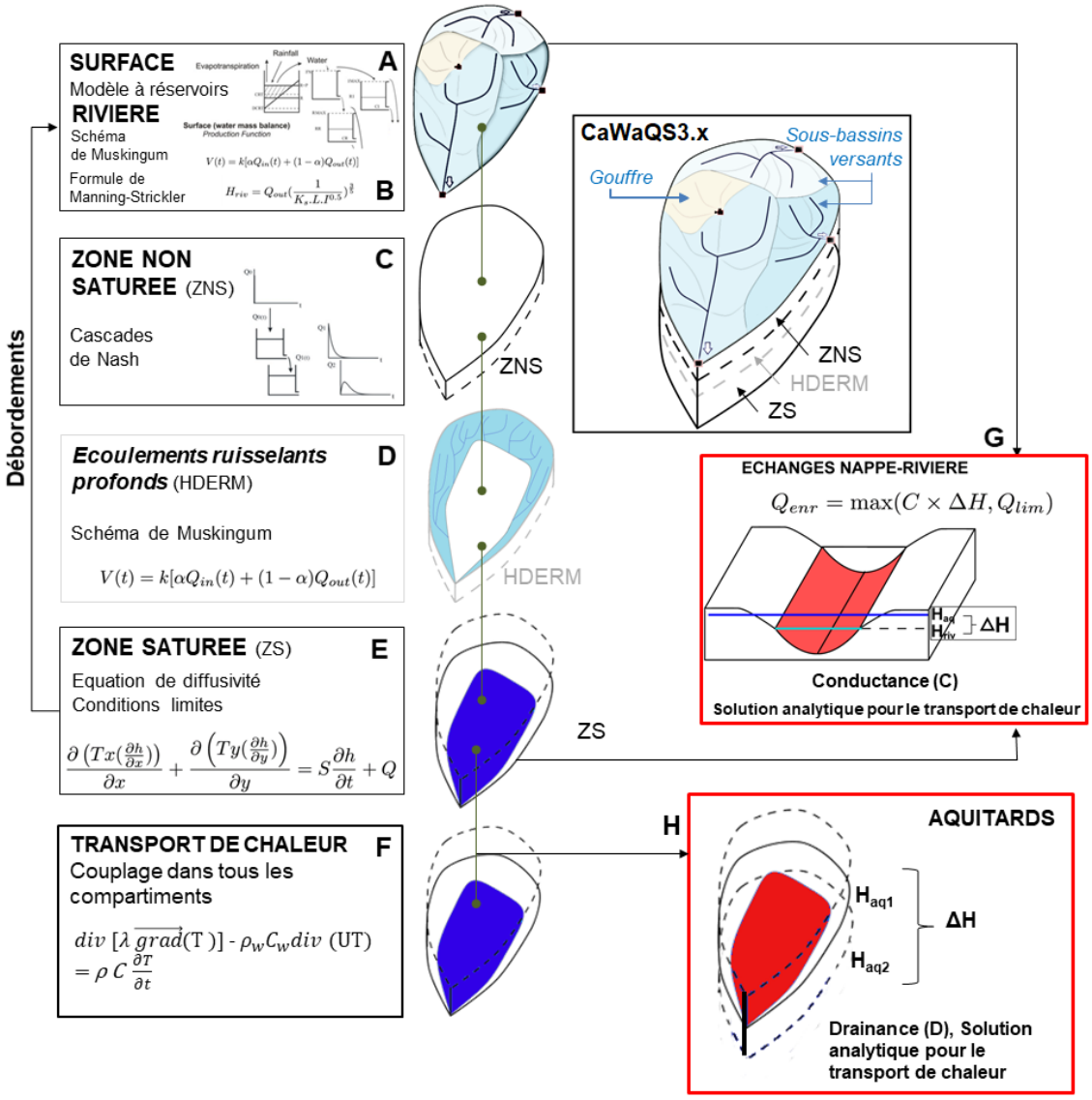

Figure 1 Schématisation de la structure de la plateforme CaWaQS3.X de modélisation de flux d'eau et de chaleur.

monodirectionnelle, d'ORCHIDEE vers CaWaQS. Les flux de drainage simulés par ORCHIDEE sont prescrits comme une recharge de l'aquifère dans CaWaQS, avec une température égale à celle du sol à 2 m de profondeur, tandis que le ruissellement de surface est acheminé vers le réseau hydrographique, en supposant que sa température est en équilibre avec celle de la surface du sol (0,001 m de profondeur, couche supérieure).

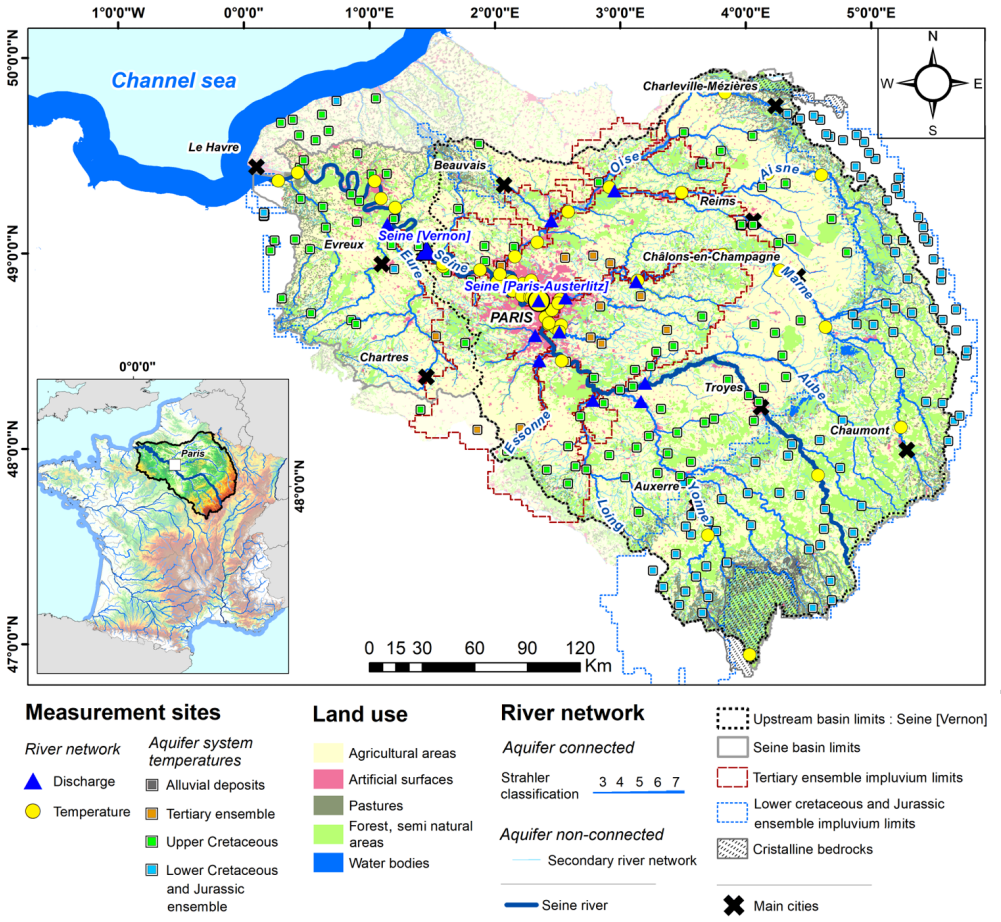

Figure 2 Vue d'ensemble du bassin de la Seine (78 650 km^2). L'occupation des sols, utilisée comme fond de carte, est fournie par la base de données *CorineLandCover* de 2018 . Les triangles bleus et les cercles jaunes représentent les positions de mesure du débit et de la température des rivières, respectivement. Les lignes pointillées de couleur indiquent l'étendue de l'ensemble du système aquifère. Les stations de mesure de la température des aquifères sont regroupées en fonction de l'ensemble aquifère auquel elles sont associées.

L'hydrosystème Seine

L'hydrosystème Seine ($\simeq$ 78 650 km^2) est situé dans le bassin sédimentaire de Paris. Le contexte géologique est constitué de formations sédimentaires du Tertiaire (alternance d'argile, de grès et de calcaire), de craie du Crétacé et de calcaires du Jurassique reposant sur un socle cristallin, affleurant principalement à l'extrême limite sud-est (Morvan) et nord-est (Ardennes) du bassin. L'altitude la plus élevée est de 856 m et 90 % du bassin est situé en dessous de 300 m d'altitude. Le réseau hydrographique présente des pentes douces.

Le régime climatique est tempéré, modulé par les variations saisonnières de l'évapotranspiration.

Le taux de précipitations annuel moyen est de 825 mm sur la période 1980-2020 (jeu de données SAFRAN, Vidal et al. (2010a)). Le débit moyen de la Seine aval à la station de jaugeage de Vernon avant l'estuaire était de 490 $\mathrm{m^3\,s^{-1}}$ sur la période 1980-2020 (base de données HYDRO).

Actuellement, le bassin de la Seine est le bassin le plus urbanisé et le plus industrialisé de France. La population est constituée de 17 millions d'habitants (25 $\%$ de la population nationale), dont 10 millions pour la seule agglomération parisienne. Le bassin concentre 40 $\%$ des activités industrielles nationales, tandis qu'une large zone autour de l'immense agglomération parisienne est orientée vers la production industrielle de culture de céréales (Figure 2). Ces activités présentent une demande énergétique conséquente. De plus, compte tenu de l'importance de la population et de la production alimentaire du bassin de la Seine, les ressources en eau sont stratégiques, près de 1 million de mètres cubes d'eau souterraine étant extraits chaque année sur l'ensemble du bassin (Flipo et al., 2023).

Conception de l'application ORCHIDEE-CaWaQS de l'hydrosystème Seine

La plateforme ORCHIDEE-CaWaQS a été appliquée sur la période 2001-2018, qui a été marquée par des événements de crue remarquables (ex. hiver/printemps 2001, hiver 2016-2018) ainsi que par des périodes de débit extrêmement faible/sécheresse et des vagues de chaleur (ex. été 2003, été 2006-2007).

Application ORCHIDEE de l'hydrosystème Seine

ORCHIDEE est forcée avec le jeu de données météorologiques de la base de données SAFRAN (Vidal et al., 2010a). Les forçages utilisés sont les variables atmosphériques à un pas de temps horaire, sur une grille régulière de 8 km x 8 km . Cette grille définit le maillage de l'application Seine. Un total de 1 490 cellules est utilisé pour décrire le domaine de l'hydrosystème Seine. Une concentration constante de dioxyde de carbone (370 ppm) sur la période 1980-2018 a été appliquée.

La carte de distribution de la végétation a été dérivée à une résolution de 0,5 degré à partir du jeu de données ESA-CCI Land Cover à une résolution de 300 m, pour la

période 1992-2015 (voir les détails dans Lurton et al. (2020)). La distribution de la végétation en dehors de cette période a été fixée à celle de l'année disponible la plus proche avec une distribution de végétation constante. Les valeurs mensuelles de l'indice foliaire (LAI) ont été obtenues à partir de la simulation globale existante sur 40 ans réalisée en mode autonome à 0,5 ° (55 km de résolution). La carte de l'albédo du sol a été dérivée de l'ensemble de données MODIS agrégées à une résolution de 0,5 degré. Les cartes de distribution de la couverture du sol ont été obtenues à partir de quatre sources : Reynolds (Reynolds et al., 2000), SoilGrids (Hengl et al., 2017), LUCAS (Ballabio et al., 2016), et INRA (Jolivet et al., 2006). L'état initial a été obtenu après une période d'initialisation de cinq ans (1980-1985) afin d'atteindre l'état d'équilibre du modèle de surface de l'humidité et de la température du sol.

Application CaWaQS-Seine

L'application CaWaQS préexistante de l'hydrosystème Seine développée par Flipo et al. (2023) est utilisée. Celle-ci considère les principales unités aquifères en interaction avec la Seine et ses principaux affluents (Ordre de Stralher >3). Du plus ancien au plus récent, ces aquifères peuvent être regroupés selon quatre grands ensembles : **(i)** un ensemble d'unités aquifères et aquitardes, allant du Jurassique inférieur (étage de Hettangien) au Crétacé inférieur (étage de l'Albien), **(ii)** le grand aquifère crayeux du Crétacé supérieur, **(iii)** un complexe d'aquifères du tertiaire comprenant cinq couches aquifères datant de l'époque du Paléocène à l'époque du Miocène et **(iv)** des dépôts alluviaux récents (Pléistocène, Holocène). La résolution des cellules des CaWaQS aquifères varie entre 100 m et 3 200 m en utilisant une approche de grille gigogne. La géométrie du réseau hydrographique a été obtenue à partir de la base de données SYRAH-CE (Chandesris et al., 2008). Les entrées d'eau du réseau hydrographique tiennent compte du ruissellement de subsurface, des débordements de l'aquifère vers la surface du sol ainsi que des échanges nappe-rivière. Principalement pour des raisons de temps de calcul, les calculs d'échanges nappe-rivière ont été limités au réseau hydrographique principal, qui correspond aux tronçons de rivière avec un ordre de Strahler supérieur ou égal à 3 (Figure 2). La paramétrisation thermique (conductivités thermiques, capacités calori-

fiques et porosités) du bassin de la Seine a été extraite de Dentzer (2016) et Rivière (2012). Le transport de chaleur a également été simulé dans les tronçons de rivière avec un ordre de Strahler supérieur ou égal à 3 (Figure 2). Les températures de surface du sol simulées avec ORCHIDEE ont été imposées aux tronçons de rivière inférieurs à l'ordre de Strahler 3. L'état initial de température du système aquifère a été obtenu en faisant tourner le modèle couplé pendant 40 ans en simulant 2 fois la période 1985-2005.

Les forçages de CaWaQS ont été définis comme suit : **(i)** un flux nul en écoulement est imposé aux limites inférieures et aux limites du domaine, sauf pour les mailles rivière où la hauteur d'eau de la maille rivière adjacente est imposée ; **(ii)** Les prélèvements d'eau souterraine sont pris en compte sous la forme d'un débit de pompage journalier, les valeurs provenant des données annuelles de prélèvement d'eau souterraine de l'Agence de l'eau Seine-Normandie (AESN) pour les besoins domestiques, industriels et agricoles ; **(iii)** Les prélèvements agricoles sont supposés avoir lieu uniquement pendant la période estivale (*i.e.* le volume d'eau d'irrigation est distribué temporellement comme suit : 20% en mai, 30% en juin et juillet, et 20% en août) ; **(iv)** Un flux nul de chaleur est imposé aux limites horizontales du domaine; **(v)** des températures sont imposées selon la méthodologie de couplage décrite précédemment aux systèmes de surfaces ; **(vi)** Un flux géothermique est imposé pour la limite inférieure du domaine (75 mWm^{-2}, Dentzer (2016)).

Calibration de la plateforme ORCHIDEE-CaWaQS

Une procédure de calibration en deux étapes a été utilisée pour calibrer le bilan d'eau et de chaleur de l'hydrosystème Seine: d'abord le bilan de surface et ensuite le bilan sous-terrain. Compte tenu de l'impact de l'oscillation nord-atlantique (NAO) sur la variation des eaux souterraines (Flipo et al., 2012; Massei et al., 2010), une période de moyenne de 17 ans entre 2001-2018 a été sélectionnée pour mener la première étape de calibration.

Calibration du bilan de surface

L'étape de calibration du bilan d'eau de surface consiste en des ajustements itératifs par essais et erreurs des paramètres d'ORCHIDEE afin de minimiser le biais entre le débit moyen pluriannuel simulé et observé aux différentes stations de jaugeage (Figure 2) et de garantir une contribution des eaux souterraines à l'exutoire du bassin d'environ $\frac{2}{3}$, telle que récemment réévaluée par Flipo et al. (2023). Le débit moyen pluriannuel est estimé en multipliant le ruissellement total par la superficie du bassin ainsi que la recharge des aquifères corrigée des prélèvements annuels d'eau souterraine (équivalent à une moyenne annuelle de 37 $m^3\,s^{-1}$ pendant la période 2008-2012, AESN).

Un ensemble de 10 simulations ORCHIDEE a été choisi pour illustrer ce processus itératif (Tableau 1). Tout d'abord, EXP1 à EXP4 nous permettent d'évaluer l'influence de la carte de distribution des sols (avec une carte LAI prescrite et des paramètres par défaut, tels qu'utilisés à l'échelle globale pour CMIP6). Ensuite, les deux options disponibles pour tenir compte des variations du LAI (carte prescrite vs simulation dynamique par le module STOMATE) peuvent être évaluées en comparant EXP4 et EXP5. Enfin, EXP5 à EXP10 ne diffèrent que par certains paramètres ORCHIDEE jugés pertinents par plusieurs analyses de sensibilité (par ex. Raoult et al. (2021)) : la perméabilité à saturation (K_{sat}) attribuée aux différents types de sol dominant dans le bassin de la Seine (sable silteux, silt, argile silteuse) et leur facteur de diminution de la perméabilité c_K (Eq. 0.1) ; l'albédo foliaire dans le visible et le proche infrarouge et le LAI maximum des principales TFP du bassin. Il faut noter qu'aucune calibration n'a été effectuée pour améliorer les flux thermiques. Les températures des couches inférieures et supérieures du sol ont été supposées être en équilibre avec les températures de la recharge (drainage) et du ruissellement de surface, respectivement.

Calibration du bilan souterrain

Les paramètres géométriques et physiques du réseau hydrographique et du système aquifère de la Seine sont fournis par Flipo et al. (2023). Aucune calibration supplémentaire des paramètres hydrogéologiques n'a été réalisée. La distribution et la valeur

Table 1 Jeu de paramètres appliqué aux 10 expériences pour calibrer le modèle ORCHIDEE (- : même valeur que la précédente, R : Reynolds, SG : SoilGrids, L : Lucas, I : INRA, pLAI : LAI prescrit, ST : STOMATE activé, TeBS : Temperature Boreal Summerreen Trees, TeBe : Temperate Boreal Evergreen Trees, NC3 : Natural C_3 grass, AC3 : Agricultural C_3 crops)

Experiment		EXP1	EXP2	EXP3	EXP4	EXP5	EXP6	EXP7	EXP8	EXP9	EXP10
Distribution des sols		I	SG	L	R	R	R	R	R	R	R
Modèle de végétation		pLAI	pLAI	pLAI	pLAI	ST	ST	ST	ST	ST	ST
Parametre	Classe										
c_K		2	-	-	-	-	4	-	-	10	-
K_{sat} ($m\,s^{-1}$)	Loamy Sand	4.05×10^{-5}	-	-	-	-	-	-	1.73×10^{-5}	-	-
	Silt	2.88×10^{-6}	-	-	-	-	-	-	1.50×10^{-6}	-	-
	Argile Silt	7.22×10^{-7}	-	-	-	-	-	-	4.62×10^{-7}	-	-
Proche-Infrarouge Albedo foliaire	TeBE	0.22	-	-	-	-	-	0.2	-	-	-
	TeBS	0.22	-	-	-	-	-	0.2	-	-	-
	NC3	0.3	-	-	-	-	-	0.25	-	-	-
	AC3	0.3	-	-	-	-	-	0.1	-	-	-
Rayonnement-Visible Albedo foliaire	TeBE	0.06	-	-	-	-	-	0.04	-	-	-
	TeBS	0.06	-	-	-	-	-	0.04	-	-	-
	NC3	0.1	-	-	-	-	-	0.05	-	-	-
	AC3	0.1	-	-	-	-	-	0.04	-	-	-
Maximum LAI	TeBE	4.5	-	-	-	-	-	-	-	-	5.5
	TeBS	4	-	-	-	-	-	-	-	-	5
	NC3	2	-	-	-	-	-	-	-	-	3
	AC3	2	-	-	-	-	-	-	-	-	3

des paramètres thermiques utilisés ont été tirés de Dentzer (2016) et Rivière (2012) an moyennant les valeurs par couche aquifère. Le bilan thermique de la rivière a été calibré en modifiant le facteur d'ombrage uniforme allant de 0 $\%$ à 50 $\%$ appliqué sur le rayonnement net entrant (Beaufort et al., 2016a). Un ombrage uniforme de 30 $\%$, cohérent avec les valeurs rapportées dans Loicq et al. (2018), a été sélectionné après une série de simulations.

Méthodologie d'évaluation

Pour valider les performances de la plateforme ORCHIDEE-CaWaQS, les résultats de l'application ont été comparés à l'ensemble des niveaux piézométriques et des débits mesurés sur le réseau hydrographique, ainsi qu'à des données de température de la rivière, répartie sur l'ensemble de l'hydrosystème Seine (Figure 2). Le coefficient de Kling-Gupta (KGE), l'erreur quadratique moyenne ($RMSE$), l'erreur absolue moyenne (MAE), le pourcentage de biais ($PBIAS$) et le coefficient de corrélation de Pearson (CC) ont été calculés pour évaluer quantitativement l'application Seine sur la période 2001-2018. Les variables collectées sont les données de débit de 183 stations de jaugeage ; les données de niveaux piézométriques de 267 piézomètres ont été utilisées

pour évaluer les statistiques de performance de la partie hydrologie. Les chroniques ont été obtenues à partir des bases de données ADES et HYDRO.

Les données sur la température de l'eau des rivières ont été rassemblées par William Thomas de la DRIEAT, à partir de diverses agences opérant dans le bassin ; l'ensemble de données comprend des observations horaires et quotidiennes provenant de 62 sites (Rivière et al., 2021). Pendant la période de simulation (2001-2018), 48 stations avec des observations horaires ont été sélectionnées. Les données de température des aquifères utilisées ont été obtenues à partir de la base de données nationale ADES. Bien que cette dernière fournisse une grande quantité de données, les enregistrements sont souvent incomplets et hétérogènes. La majorité des données de température en aquifère ne sont malheureusement pas consolidées. Un pré-traitement a donc été appliqué à l'ensemble des données en utilisant la méthode de l'écart inter-quartile (IQR), comme décrit dans Hemmerle et al. (2019). Sur le jeu de données initial de 9 179 stations sur la région Seine-Normandie, il restait après le pré-traitement 211 stations avec un minimum de 40 observations sur la période de simulation.

Résultats et discussions

Calibration du bilan de surface

Le bilan d'eau de surface des différentes expériences obtenues est présenté dans la figure 3. Les résultats montrent l'influence des paramètres (Tableau 1) dans le partage des précipitations en évapotranspiration réelle (ETR) et en pluie efficace, qui est composée du ruissellement de surface et de la recharge des aquifères (drainage de la colonne de sol). Il a été choisi de présenté les simulations qui ont le plus d'impact sur les bilans d'eau.

Distribution des sols

Les quatre premières simulations (EXP1-4) montrent l'impact de la distribution des sols, qui induit une variation de 6% de l'ETR (valeurs moyennes comprises entre 469 et 497 mm y^{-1}), et une modification de la pluie efficace. La distribution des sols a égale-

ment un impact sur le partage de la pluie efficace entre le drainage et le ruissellement de surface, qui varie entre 20 et 47% de la pluie efficace entre EXP4 (Reynolds) et EXP2 (SoilGrids). Ceci s'explique par la composition des distributions de sols : en effet, les cartes SoilGrids et INRA comprennent une fraction importante de sols limoneux qui augmentent le ruissellement de surface au détriment du drainage (Tafasca et al., 2019). Le biais des débits de Vernon est le plus faible dans l'EXP4 qui utilise la carte de texture de sol de Reynolds. Par concéquent, cette carte a été retenue comme référence pour les autres expériences de calibration.

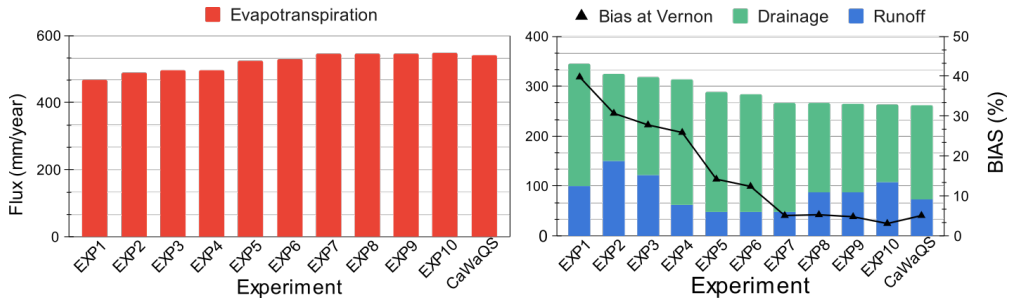

Figure 3 Composantes du bilan annuel moyen des eaux de surface calculées par ORCHIDEE en mm y^{-1}. Le biais a été calculé sur le débit moyen pluriannuel à la station de mesure de Vernon après que le retrait des prélèvements d'eau annuels moyens. La colonne CaWaQS représente le bilan hydrique calculé par l'application CaWaQS-Seine.

Influence de la végétation

Le calcul de la dynamique de la végétation par le module STOMATE (EXP5) permet une nouvelle représentation de l'évapotranspiration réelle (ETR =+26 mm y^{-1}) par rapport aux simulations avec LAI prescrit (EXP1-4). STOMATE calcule un LAI plus élevé que celui prescrit, ce qui permet d'augmenter l'évapotranspiration via une biomasse plus importante pendant la saison de croissance. La diminution de la pluie efficace qui en résulte entraîne une réduction du biais du débit de Vernon, qui passe de 25,9 % à 14,2 %. La faible diminution de la contribution du ruissellement de surface à la pluie efficace (-3%) peut être attribuée au compromis entre le ruissellement de surface, l'effet de la végétation et le prélèvement d'eau par les racines dans la couche arable. La ré-

duction de l'albédo des feuilles dans le proche infrarouge et dans le visible (de l'EXP6 à l'EXP7) entraîne également une augmentation significative de l'évapotranspiration réelle (+6,16 mm y^{-1}, c'est-à-dire +5$\%$), car elle augmente l'énergie nette disponible. Cela entraîne une diminution du biais du débit de Vernon (5,1$\%$ dans l'EXP7).

En revanche, la mise en œuvre d'une décroissance verticale plus marquée de la perméabilité K_{sat} en dessous de 30 cm dans la colonne de sol (de EXP5 à EXP6) a montré un faible impact : l'ETR s'est en effet légèrement amélioré de seulement 4 mm y^{-1}, le biais du débit a diminué 1,8$\%$. Cette faible sensibilité aux modifications du profil vertical de K_{sat} montre l'importance des 30 premiers cm de la colonne de sol sur le bilan d'eau de surface (de Rosnay et al., 2000).

Influence des valeurs des propriétés physiques des sols

La diminution de K_{sat} pour toutes les textures de sol dominantes (EXP7 à EXP8) a eu un impact encore plus faible sur l'évapotranspiration, sur la pluie efficace et sur le biais du débit (même légèrement aggravé). La diminution de K_{sat} a toutefois eu un impact significatif sur la répartition de la pluie efficace, puisqu'elle a presque doublé la contribution du ruissellement de surface (de 18$\%$ à 33 $\%$). La diminution supplémentaire de K_{sat} dans la partie inférieure du sol en augmentant le facteur de décomposition c_K à 10 (EXP9) n'a eu aucun impact sur le bilan d'eau de surface, et l'augmentation du LAI maximum (EXP 10) a eu un effet très limité sur l'ETR et le ruissellement total bien qu'elle ait augmenté la proportion du ruissellement de surface (+ 10 $\%$). Les valeurs maximales du LAI dans toutes les simulations, y compris EXP10, correspondent aux plages de LAI observées dans l'ensemble du réseau FluxNET pour des biomes et des climats similaires (Krinner et al., 2005). Une calibration détaillée des propriétés de la végétation dépasse le cadre de cette étude, bien que les moyens d'améliorer la représentation de la biosphère terrestre et les processus énergétiques dans les modèles SVAT soient des domaines de recherche actifs (Peylin et al., 2016). En définitive, ces résultats montrent que la surestimation du débit à la sortie de Vernon résulte d'une sous-estimation de l'ETR. Les calculs dynamiques de l'indice LAI ont permis d'améliorer considérablement le débit, ce qui peut être attribué en partie à la résolution grossière de

la carte LAI d'entrée dans les simulations pLAI, et à un meilleur cycle saisonnier du LAI (comparaison avec le produit GiMMS (Zhu et al., 2013) non montré), plus cohérent avec le forçage météorologique SAFRAN. Bien que les prélèvements d'eau souterraine soient pris en compte dans le calcul du biais de décharge d'ORCHIDEE (voir section), l'absence d'irrigation dans les simulations peut également contribuer à la sous-estimation de l'ETR et à la surestimation de la décharge des rivières puisque l'augmentation de l'ETR par les prélèvements d'eau de surface est négligée. Si l'on considère que ORCHIDEE simule un bassin naturel contrairement au bassin de la Seine fortement réglementé et irrigué, un biais de 3,1% (EXP10) à la sortie du bassin (Vernon) est très satisfaisant. Cependant, lorsque les proportions d'infiltration et de ruissellement de surface sont considérées (voir section), EXP9 est plus performant avec près de deux tiers de la recharge contribuant au ruissellement total.

Performance de la plateforme ORCHIDEE-CaWaQS

La simulation ORCHIDEE la plus performante en termes de biais de débit de rivière et de partitionnement de la pluie effective (EXP9) a été sélectionnée pour forcer la simulation CaWaQS. Une simulation couplée a été réalisée sur la période de 17 ans (août 2001 - juillet 2018). Le débit simulé est comparé de manière satisfaisante au débit observé dans 14 sous-bassins versants principaux, comme illustré à l'exutoire du bassin de la Seine (Vernon) dans la figure 4.a. Bien que les faibles débits soient légèrement surestimés par le modèle couplé, celui-ci capture correctement la dynamique annuelle (KGE = 0,77, CC = 0,82) et le volume moyen ($PBIAS$ = 1,6%), sachant que l'erreur de mesure du débit du fleuve peut atteindre 20% (Sauer and Meyer, 1992).

La température des cours d'eau est également bien simulée le long du bassin de la Seine, comme l'illustre la station de Paris-Austerlitz (Figure 4.b). Les températures simulées correspondent aux températures observées (CC = 0,98) avec un $PBIAS$ de -0,3% et une $RMSE$ de 1,52°C, bien que les températures simulées soient généralement sous-estimées en été comme en hiver. Une partie de cette incertitude peut être attribuée au facteur d'ombrage uniforme ou à l'absence de structures urbaines qui modifient artificiellement le régime thermique sur les berges (Ferguson and Woodbury, 2007). Le

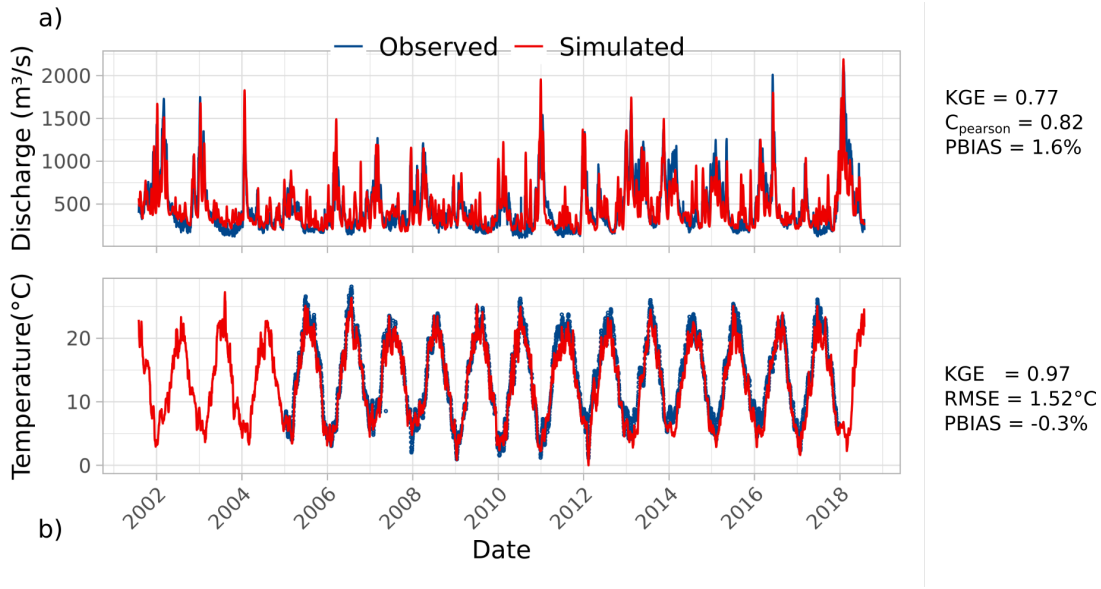

Figure 4 Comparaison sur la période août 2001-juillet 2018 entre a) le débit simulé (rouge) et observé (bleu) à la sortie du bassin versant de la Seine (Vernon) ; b) la température simulée (rouge) et observée (bleu) du fleuve à Paris (Austerlitz). Les années sont indiquées au 1er janvier. KGE : Coefficient d'efficacité de Kling-Gupta ; CC : coefficient de corrélation ; $PBIAS$: Pourcentage de biais ; $RMSE$: Erreur quadratique moyenne.

modèle utilise également un facteur d'ombrage uniforme et constant dans le temps qui s'écarte de la dynamique saisonnière et de la distribution spatiale de la végétation dans le bassin de la Seine (Figure 2). Les performances du modèle évaluées respectivement par rapport aux sondes de température des cours d'eau et des aquifères sur la période de simulation sont fournies dans les tableaux 2 et 3.

La dynamique du transport de chaleur dans le réseau hydrographique est bien représentée (CC > 0,7 pour 100% des stations) et MAE est inférieur à 2°C pour 65% des stations. 96% des stations de température de rivière ont une $RMSE$ inférieure à 4°C. Les températures de l'eau dans les ruisseaux et les petites rivières (< 10 000 km^2) présentent une $RMSE$ moyenne plus élevée (2,58 °C) que les stations en aval (< 10 000 km^2) (1,58 °C). Les températures imposées sur les tronçons de rivière dont l'ordre de Strahler est inférieur à 3 influencent fortement les températures des cours d'eau et des petites rivières et contribuent ainsi à obtenir une RMSE plus élevée, car la proportion de tronçons avec une température prescrite est plus importante que celle des tronçons en aval. Une $RMSE$ relativement élevée indique une inadéquation entre les températures

simulées et observées à l'échelle quotidienne. Globalement, la dynamique saisonnière est bien représentée dans le réseau hydrographique (figure 4.b). Le transport de chaleur dans la rivière est comparable à d'autres études à l'échelle régionale utilisant la méthode de la température d'équilibre (Beaufort et al., 2016a) en termes de $RMSE$.

Table 2 Critères statistiques (période 2001-2018) de 48 sondes de température de cours d'eau réparties dans le bassin. Tableau supérieur : Erreur quadratique moyenne ($RMSE$), erreur absolue moyenne (MAE). Tableau inférieur : Coefficient de corrélation de Pearson (CC), et coefficient d'efficacité de Kling-Gupta (KGE).

Intervalle [°C]	Nombre de station		Pourcentage cumulé [%]	
	$RMSE$	MAE	$RMSE$	MAE
[0.0-2.0[	31	42	65	88
[2.0-4.0[	15	1	96	90
[4.0-6.0[	2	2	100	94
[6.0-8.0[	0	3	100	100
Intervalle [°C]	Nombre de station		Pourcentage cumulé [%]	
	CC	KGE	CC	KGE
]0.7-1.0]	48	43	100	90
]0.5-0.7]	0	2	100	94
]0.4-0.5]	0	1	100	96
]0.2-0.4]	0	2	100	100

Les températures des eaux souterraines montrent une bonne adéquation puisque la $RMSE$ est inférieure à 2°C pour 49% des stations. La RMSE médiane calculée pour les observations de l'aquifère était de 2,12°C (variant entre 20,2 et 0,01°C). Les RMSE élevées sont concentrées sur l'aquifère jurassique, ce qui est dû en grande partie à un décalage entre la profondeur du puits et la profondeur de la cellule. Seulement 22% des stations présentent un CC supérieur à 0,5 et seuls 3 % des stations présentent une performance KGE supérieure à 0,5. Le facteur limitant en termes de dynamique est le manque de séries temporelles suffisantes dans le système aquifère. En ce qui concerne les hypothèses pour les estimations des conditions aux limites supérieures du transport de chaleur dans le système d'eau souterraine, les températures du sol simulées à 2 m de profondeur à partir d'ORCHIDEE ont été appliquées à la limite supérieure du système d'eau souterraine, qui sont assez différentes des températures réelles de l'eau souterraine à la nappe phréatique (Anderson, 2005).

Table 3 Critères statistiques (période 2001-2018) à partir de 211 sondes de température de l'aquifère réparties dans le bassin. Erreur quadratique moyenne ($RMSE$), erreur absolue moyenne (MAE) .

Intervalle [°C]	Nombre de piézomètres [-]		Pourcentage cumulé [%]	
	$RMSE$	MAE	$RMSE$	MAE
[0.0-2.0[	93	115	44	49
[2.0-4.0[	58	59	71	74
[4.0-6.0[	16	17	79	81
[6.0-8.0[	17	17	87	88
[8.0-10.0[	8	9	91	92
>=10	20	19	100	100

Fonctionnement hydrologique et thermique de l'hydrosystème de la Seine

Les résultats de la meilleure simulation ORCHIDEE-CaWaQS ont été utilisés pour calculer le bilan hydrique (Fig. 5) et le bilan énergétique (Fig. 6) de l'ensemble du bassin de la Seine, y compris les contributions des eaux souterraines, sur la période 2001-2018.

Pluri-annual water budget

La figure 5 présente un bilan hydrique pluriannuel du bassin de la Seine. L'ETR y représente 73,5 % (559 mm y^{-1}) des précipitations (760 mm y^{-1}). Le reste de la pluie effective (201 mm y^{-1}) est réparti entre le ruissellement de surface et la recharge des nappes phréatiques, ce qui représente respectivement 34,6 % et 65,3 % de la pluie effective. Un flux d'infiltration total de 449,2 $m^3 s^{-1}$ transite par la zone non saturée, rechargeant l'ensemble du système aquifère.

27,8 % de la recharge de l'aquifère est perdue par des flux d'eau régionaux à travers les limites du bassin de la Seine (21,6 % de la recharge) ou retirée du système par des pompages (6,2 % de la recharge). Au sein du bassin de la Seine, les échanges fleuve-aquifère pour les ordres de Strahler supérieurs à 3 fournissent environ la moitié du débit (248,7 $m^3 s^{-1}$) enregistré à la sortie du réseau hydrographique (Figure 5). Ce que l'on appelle le débordement correspond principalement au drainage du système d'eau souterraine par les ordres de Strahler bas (un et deux). Il correspond donc également aux échanges nappe-rivière, et s'élève à 91,3 $m^3 s^{-1}$ (17,6 % du débit total). Enfin, le ruissellement de surface contribue à hauteur de 177,9 $m^3 s^{-1}$ (34,4 % du débit total).

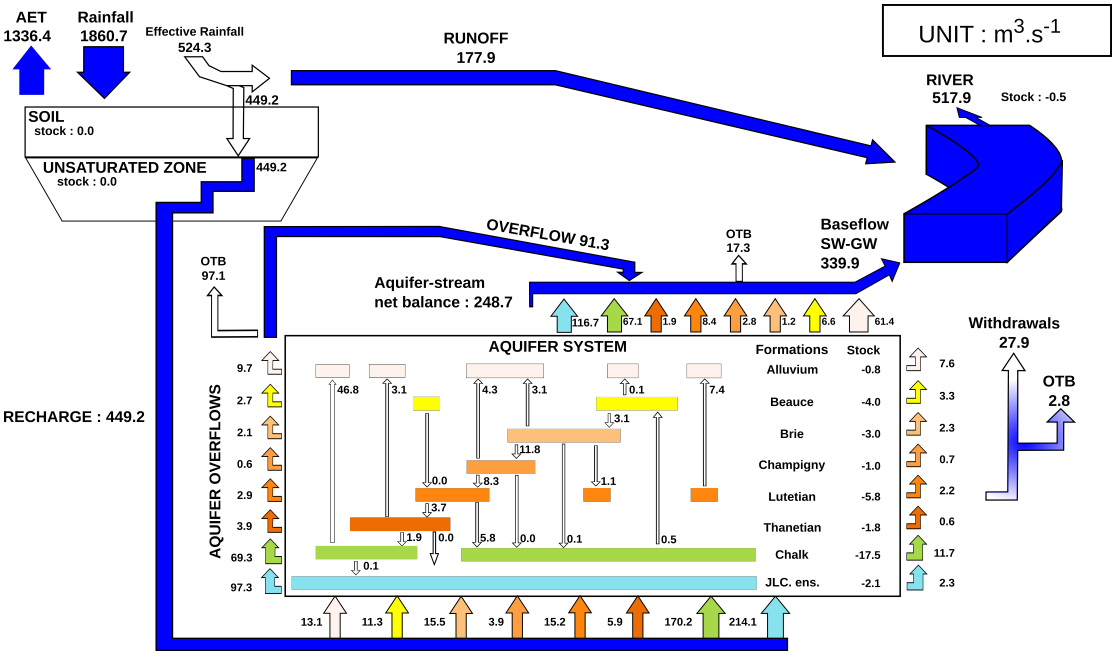

Figure 5 Bilan d'eau de l'hydrosystème de la Seine sur la période 2001-2018 tel que simulé par l'application ORCHIDEE-CaWaQS. Le système d'eau souterraine englobe toute l'étendue des aquifères. ITB : Flux d'infiltration pour les unités aquifères affleurantes au-delà des limites du bassin de la Seine. Les flux hors limites (ITB) sont au-delà de l'étendue du bassin de la Seine. Les flux sont exprimés en valeurs moyennes interannuelles en $\mathrm{m^3\,s^{-1}}$. Pluie = 760mm/an*, ETR* = 559mm/an*, Ruissellement = 69mm/an*, Recharge des aquifères = 132mm/an*. Couches aquifères : 'Alluvion' : Dépôts alluvionnaires, 'Beauce' : Ensemble des calcaires de Beauce, 'Brie' : Calcaires de Brie et sables de Fontainebleau, 'Champigny' : Calcaires de Champigny, 'Lutétien' : Calcaires du Lutétien, 'Thanétien' : Sables du Thanétien, 'Chalk' : aquifère crayeux du Crétacé supérieur, 'JLC. ens.' : Ensemble du Crétacé inférieur et du Jurassique.

Bilan thermique pluriannuel

Le bilan thermique pluriannuel sur la période 2001-2018 est illustré par la figure 6. La température moyenne pluriannuelle de l'air est de 10,6°C dans le bassin de la Seine, et la température moyenne pluriannuelle de la surface du sol est de 11,3°C (*i.e.* la température associée au ruissellement de surface). La température du sol à 2 m de profondeur est estimée à 10,7°C. La température moyenne quotidienne de la rivière est estimée à 12,1°C (Figure 6). Les températures moyennes annuelles de l'aquifère varient entre 10,6°C pour l'aquifère alluvial peu profond et 23,8°C pour l'aquifère jurassique plus profond. Les gains de chaleur les plus importants dans le système aquifère sont dus aux flux de recharge (182,5 TW h) et au gradient géothermique (63,2 TW h) au fond du bassin (Figure 6). Le premier représente les flux d'advection tandis que le second

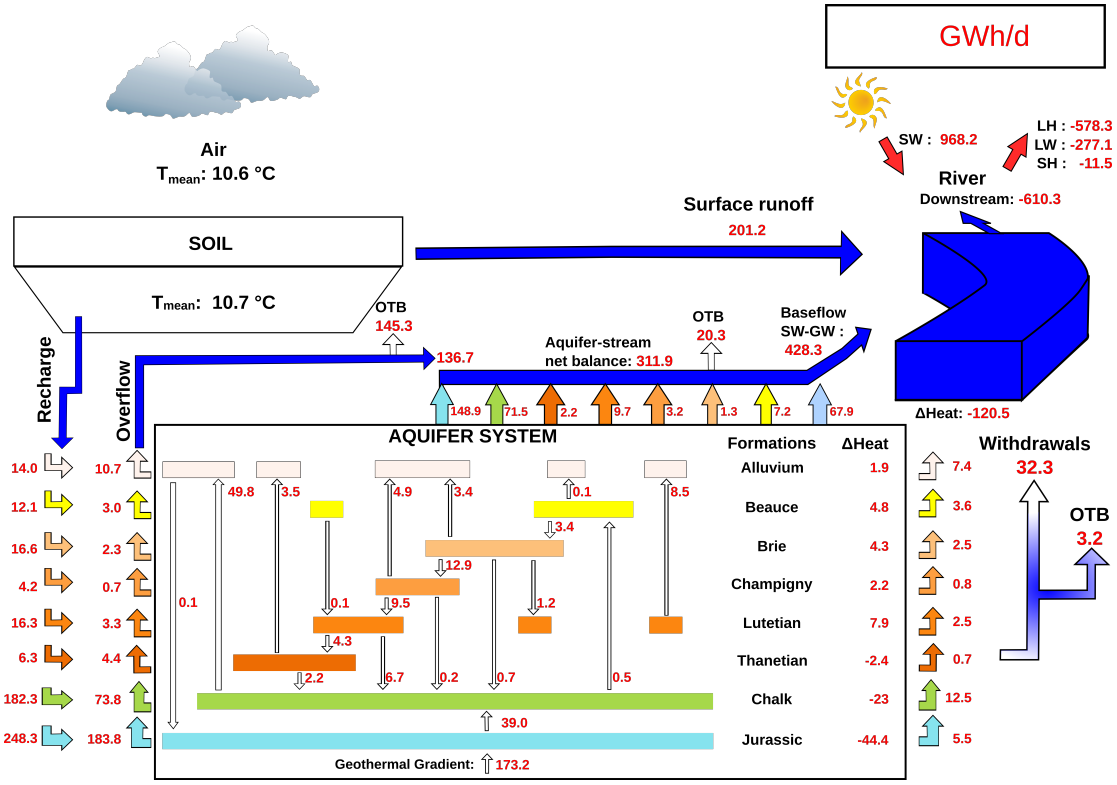

Figure 6 Bilan thermique de l'hydrosystème Seine sur la période 2001-2018 simulé par l'application ORCHIDEE-CaWaQS . Les quantités d'énergie sont exprimées en valeurs moyennes pluriannuelles en $\mathrm{GW\,h}$ par jour et la température moyenne annuelle quotidienne de l'air et du sol à $2\,\mathrm{m}$ de profondeur sont indiquées en $^{\circ}\mathrm{C}$. SW : Rayonnement net à courte longueur d'onde, LW : Rayonnements à grande longueur d'onde, SH : Chaleur sensible, LH : Chaleur latente. Couches aquifères : 'Alluvion' : Dépôts alluvionnaires, 'Beauce' : Ensemble des calcaires de Beauce, 'Brie' : Calcaires de Brie et sables de Fontainebleau, 'Champigny' : Calcaires de Champigny, 'Lutétien' : Calcaires du Lutétien, 'Thanétien' : Sables du Thanétien, 'Chalk' : aquifère crayeux du Crétacé supérieur, 'JLC. ens.' : Ensemble du Crétacé inférieur et du Jurassique.

représente les flux de conduction. Comme prévu, l'influence de l'advection diminue avec la profondeur, tandis que la conduction devient le processus thermique dominant. Ceci est dû à la diminution des flux d'eau avec la profondeur.

Les principales sources de pertes de chaleur par advection en surface sont dues à : **(i)** les échanges entre la rivière et l'aquifère ($113{,}9\ \mathrm{TW\,h}$), **(ii)** les échanges entre le cours d'eau et l'aquifère pour le réseau secondaire de la rivière (ordres 1 et 2 de Strahler) (c'est-à-dire le débordement, qui s'élève à $102{,}9\ \mathrm{TW\,h}$), **(iii)** et les prélèvements ($11{,}8\ \mathrm{TW\,h}$). Le système aquifère perd le plus d'énergie via les aquifères du Jurassique, de la Craie et des alluvions. Le Jurassique perd les flux de chaleur advectifs les plus importants par le biais du débordement et des échanges entre la rivière et l'aquifère vers la

surface (Figure 6). L'aquifère de la Craie et les alluvions sont les deuxième et troisième termes les plus importants au bilan de la rivière via le terme advectif. L'aquifère de la Craie est également le plus important en termes de pertes thermiques dues au prélèvement d'eau (4,6 $\mathrm{TW\,h}$).

L'énergie provenant du rayonnement à courtes longueurs d'onde (rayonnement net, 353,4 $\mathrm{TW\,h}$) est la principale source non advective de gain de chaleur dans le réseau hydrographique chaque année (Figure 6), contribuant à 60 $\%$ de la charge thermique du fleuve pendant la période d'étude. Comme le montre la figure 5, les échanges nappe-rivière pour la rivière simulée (ordres de Strahler supérieurs à 3) et le trop-plein (ordres de Strahler 1 et 2) sont les plus grands termes au bilan thermique de la rivière. L'incidence du régime hydrologique sur le bilan thermique dans le réseau hydrographique est illustrée par l'important flux de chaleur advectif via le débit de base (156,3 $\mathrm{TW\,h}$ par an), qui constitue la deuxième source de gains de chaleur fluviale. Le ruissellement de surface représente 13% de la charge thermique totale du réseau hydrographique. Les pertes de chaleur non advectives les plus importantes dans le réseau hydrographique sont la chaleur latente et les pertes par rayonnement de grandes ondes, qui représentent respectivement 67% (211,0 $\mathrm{TW\,h}$) et 32 $\%$ (101,1 $\mathrm{TW\,h}$). Environ 1% des pertes de chaleur totales est dû aux pertes de chaleur sensible dans la rivière.

Flux thermique saisonnier dans la Seine à l'échelle du bassin

Les variations saisonnières de chaque terme du bilan thermique dans le réseau hydrographique sont fournies dans le Tableau 4 et la figure 7. Il est important de noter que les échanges thermiques entre la rivière et l'aquifère ne sont pas simulés par le modèle pour les rivières d'ordre de Strahler inférieur à 3. Cela implique que les flux ne sont pas calculés sur la même surface de rivière que les autres compartiments. Le rayonnement à courte longueur d'onde est plus élevé en été et au printemps. Il dépend du rayonnement solaire qui atteint la surface du cours d'eau, de l'albédo, de l'eau et du facteur d'ombrage. Le facteur d'ombrage peut varier en fonction de la morphologie du cours d'eau, de la végétation riparienne, de l'urbanisation ou des nuages (Loicq et al., 2018). Bien qu'un facteur d'ombrage fixe ait été utilisé dans cette étude (30%), des travaux

supplémentaires sont nécessaires pour mettre en œuvre la variabilité spatiale du facteur d'ombrage.

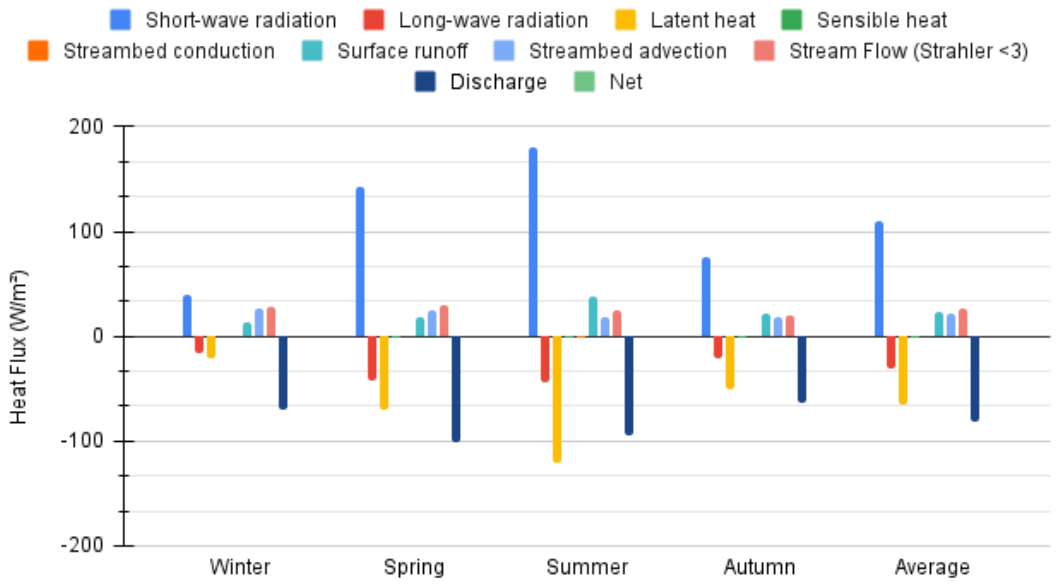

Figure 7 Flux de chaleur saisonniers ($\mathrm{W\,m^{-2}}$) dans le réseau hydrographique de la Seine sur la période 2001-2018.

L'ordre de grandeur des flux non advectifs ne varie pas selon les saisons, la chaleur latente étant la plus grande source de chaleur du système, suivie du rayonnement à grande longueur d'onde, de la chaleur sensible et de la conduction provenant du lit du cours d'eau. La chaleur latente entraîne en moyenne une perte de chaleur de 120,6 $\mathrm{W\,m^{-2}}$ en été et de 20,3 $\mathrm{W\,m^{-2}}$ en hiver. D'après la simulation, les flux de chaleur liés à la conduction dans le lit de la rivière sont négligeables par rapport aux autres termes de flux, quelle que soit la saison.

Au cours de l'année, les gains de chaleur par la Seine sont liés au rayonnement à courte longueur d'onde et les échanges nappe-rivière. Pendant l'hiver, les gains nets de chaleur sont directement fonction du rayonnement à courte longueur d'onde qui représente 22 % des gains de chaleur pendant la période estivale (Tableau 4 et Figure 7). Les échanges nappe-rivière soutiennent les gains de chaleur du réseau hydrographique tout au long des saisons, et deviennent la source de chaleur dominante en hiver. Les contributions des flux de chaleur advectifs de chaque unité aquifère changent chaque saison en raison des variations de température de la rivière et du volume d'eau échangé entre

Table 4 Flux de chaleur saisonniers ($\mathrm{W\,m^{-2}}$) dans le réseau hydrographique de la Seine sur la période 2001-2018. La longueur totale du fleuve est de 28378 km, la surface totale du réseau hydrographique d'ordre de Strahler supérieur à 3 est de 369 km^2. Les flux nets sont le bilan thermique total du réseau hydrographique. Le signe négatif (-) indique une perte de chaleur par la rivière.

Processus	Type de flux	Hiver	Printemps	Été	Automne	Moyenne annuelle
Rayonnement à courtes < longueurs d'onde	Conductif x	39,3	142,0	180,1	75,9	109,3
Rayonnement à grande longueurs d'onde	Conductif	-16,1	-42,9	-44,6	-21,5	-31,3
Chaleur latente	Conductif	-20,3	-69,9	-120,6	-50,4	-65,3
Chaleur sensible	Conductif	-0,2	-1,7	-2,1	-1,1	-1,3
Échanges conductifs avec cours d'eau	Conductif	0,4	-0,2	-0,7	-0,1	0,2
Ruissellement de surface	Advectif	13,3	18,9	37,9	20,8	22,7
Echanges advectifs avec cours d'eau	Advectif	54,0	54,8	44,3	39,5	48,1
Flux nets	Total	69,1	101,5	96,2	63,2	82,5

les nappes et la rivière. Les études partent généralement du principe que la contribution de la conduction du lit de la rivière est négligeable par rapport à l'apport de chaleur advective (Magnusson et al., 2012). Notre étude confirme cette affirmation puisque la conduction du lit de la rivière n'atteint que 1,5 % des flux advectifs nappe-rivière.

Loinaz et al. (2013) ont montré qu'à l'échelle du bassin versant, les échanges nappe-rivière contribuent à une fraction significative des apports de chaleur. De même, dans le bassin de la Seine, les échanges nappe-rivière contribuent significativement au bilan énergétique du fleuve. Localement, les échanges nappe-rivière peuvent dominer le bilan thermique, en particulier en hiver (Tableau 4). Ces échanges peuvent donner lieu à des effets locaux de réchauffement pendant l'hiver et de refroidissement pendant l'été et par conséquent créer des refuges thermiques pour les espèces aquatiques (Kaandorp et al., 2019).

Bien qu'une analyse de sensibilité détaillée n'ait pas été possible dans le cadre de cette première phase du projet, une étude similaire à l'échelle régionale dans le bassin de la Loire a rapporté que les facteurs dominants, par ordre décroissant d'importance, étaient le facteur d'ombrage, les températures des eaux d'amont, le débit des eaux souterraines, le débit des rivières et la géomorphologie de la rivière (Beaufort et al.,

2016a). Notre approche diffère de cette étude, qui reposait sur un concept de température d'équilibre, par la manière dont les processus sont traités explicitement et la température du lit des rivières est estimée par une solution analytique de manière distribuée. Nous avons constaté que l'échange rivière-atmosphère avait le plus grand impact sur le bilan thermique de la rivière à l'échelle régionale.

Conclusions et perspectives

La question des flux d'énergie au sein des hydrosystèmes a d'abord été portée à l'attention de la communauté scientifique par les sciences écologiques. Leur objectif était de comprendre comment la température de l'eau peut réguler le cycle de vie des communautés piscicole. Pour ce faire, de nombreuses études ont été menées sur des cours d'eau de tête de bassin, et des bilans thermiques ont été établis à partir de données *in situ* (Caissie, 2006; Webb et al., 2008). Par la suite, des outils numériques sont apparus pour calculer les flux d'énergie à l'échelle du bassin versant (Loinaz et al., 2013) et de bassin régional, comme la Loire (Beaufort, 2015; Beaufort et al., 2016a; Loicq et al., 2018). L'un des principaux inconvénients de ces avancées significatives était la simplification de la simulation des eaux souterraines sans modélisation explicite de leurs processus. Notre objectif est de quantifier le bilan énergétique à l'échelle régionale en incluant les processus des eaux souterraines et leur interaction avec les autres compartiments de l'hydrosystème grâce à la mise en place de la plateforme ORCHIDEE-CaWaQS selon les développements méthodologiques et techniques suivants :

- Développement des transferts de chaleur dans CaWaQS, notamment avec le couplage avec la librairie *libttc*, dédiée aux rivières et aquifères. Une approche originale pour le transfert dans les aquitards et le lit de la rivière a également été mise en œuvre sur la base de la solution analytique de Kurylyk et al. (2017) ;

- Mise en place d'une application ORCHIDEE régionale ;

- Développement d'une stratégie de calibration en deux étapes. Elle a été adaptée pour forcer ORCHIDEE à reproduire la part des principaux termes du bilan d'eau:

l'ETR, le ruissellement et la recharge des aquifères, à l'échelle du bassin de la Seine et pour 14 sous-bassins principaux.

Une première simulation des flux d'eau et d'énergie à l'échelle régionale (96 204 km^2) a été réalisée sur l'hydrosystème de la Seine afin de quantifier les interactions entre les différents compartiments de l'atmosphère jusqu'aux systèmes souterrains. La plateforme ORCHIDEE-CaWaQS simule le débit moyen des différents sous-bassins versants dans le bassin de la Seine et les niveaux piézométriques de manière correcte. Elle permet de simuler les bilans hydrique et énergétique de l'hydrosystème de manière adéquate, menant à une meilleure compréhension du rôle des eaux souterraines dans le fonctionnement du bassin.

Le bilan thermique du réseau hydrographique est contrôlé par principalement par les échanges avec l'air, et les échanges nappe-rivière et le ruissellement de surface dans le bassin de la Seine en fournissant respectivement 60$\%$, 27$\%$ et 13$\%$ du bilan thermique total. Le principal apport d'énergie au réseau fluvial provient du rayonnement à courte longueur d'onde (356,4 $TWh.y^{-1}$, échange avec l'air). Ces résultats contribuent de manière significative à notre compréhension de la façon dont les échanges de chaleur entre les eaux souterraines contribuent au bilan thermique du réseau hydrographique.

La quantification des flux d'eau et d'énergie ouvre la voie à des études à l'échelle du bassin versant sur le fonctionnement de l'hydrosystème à diverses échelles temporelles et spatiales. Cet outil va permettre d'améliorer la quantification de l'impact du changement climatique sur les ressources en eau et sur les flux d'énergie à l'échelle du bassin régional. Celle-ci fournira des informations utiles pour les stratégies d'adaptation et d'atténuation des impacts des changements globaux et répondre par conséquent au nexus "eau-énergie-alimentation" (De Amorim et al., 2018). Le Nexus "eau-énergie-alimentation" a émergé en 2011 pour permettre d'harmoniser les usages ces ressources nécessaire à nos sociétés et le maintien des écosystèmes. Il existe une compétition entre les usages de l'eau pour la production d'eau, de nourriture et d'énergie. De plus, ces trois éléments sont interdépendants. Par exemple, nous nécessitons de l'énergie pour pomper et acheminer l'eau potable et nous nécessitons de l'eau pour refroidir les centrales nucléaires. Notre modèle couplé ORCHIDEE-CaWaQS peut être mobilisé pour

évaluer l'impact des politiques de gestion de l'eau, de l'énergie et des pratiques agricoles à l'échelle du bassin de manière quantitative et qualitative, en s'appuyant sur les études précédentes décrivant l'effet des pratiques agricoles sur l'hydro-agrosystème de la Seine (Beaudoin et al., 2018).

Chapter 1

General introduction

Water is a critical resource for sustaining natural life and societies, but we are currently facing concerning issues in water sustainability. A large part of the world's population suffers from water scarcity problems, and the absolute number of people facing this challenge is rising every year (Liu et al., 2017). Major factors contributing to this concerning trend are climate change (IPCC, 2021) and land-use-associated degradation (IPCC, 2019), which can be grouped into global changes. Surface energy imbalance caused by the global changes (Von Schuckmann et al., 2020) contributes to the modifications in the water cycle (Sterling et al., 2013), pollution of riverine systems and degradation of water quality (Ducharne, 2008; Bailey and Ahmadi, 2014).

Energy and water cycles are intertwined, so the uneven distribution of energy on Earth is a primary driver of the water cycle. Long-wave and short-wave radiation from the Sun are transformed into latent and sensible energy fluxes that evaporate water and warm the Earth's surface, respectively. The remaining energy is either transferred to the ground or consumed and stored by the interactions in the biosphere, such as photosynthesis. Moreover, the water and energy fluxes in the hydrosystem are affected by numerous (natural and anthropogenic) factors such as geology, geomorphology, climatological conditions, soil characteristics, river-groundwater interactions, and human consumption, and land uses such as urbanisation and agricultural practices (Freeze and Cherry, 1979; de Marsily, 1986; Winter et al., 1998). In return, the energy and water fluxes impact the biota, water quality and quantity (Krause et al., 2017; Hayashi and Rosenberry, 2002; Fleckenstein et al., 2010). Improving the understanding of these factors and processes at the basin scale, especially in the critical zone, is essential for

managing water resources and improving the resilience of the hydrosystem against climate change.

The concept of hydrosystem emerged as a systems approach to the hydrological cycle to systematically study the problems involved in terrestrial aspects of the water cycle (Dooge, 1968). Flipo et al. (2012) describe the hydrosystem as a system "composed of storage components, where large water flows slowly (e.g. aquifers) and conductive components, where large quantities of water flow relatively quickly (e.g. surface water)". In this aspect, the hydrosystem can be seen as a combination of various compartments that form a closed system bounded by the watershed area and the extent of underlying aquifer layers. The hydrosystem might interact with adjacent hydrosystems through lateral flows in and out of the system; it might gain and lose water and energy through the atmosphere processes, and ultimately drain towards the ocean or form a closed lake system.

The processes that control the water fluxes of an hydrosystem with relation to processes of anthropological changes have been summarised in Figure 1.1.

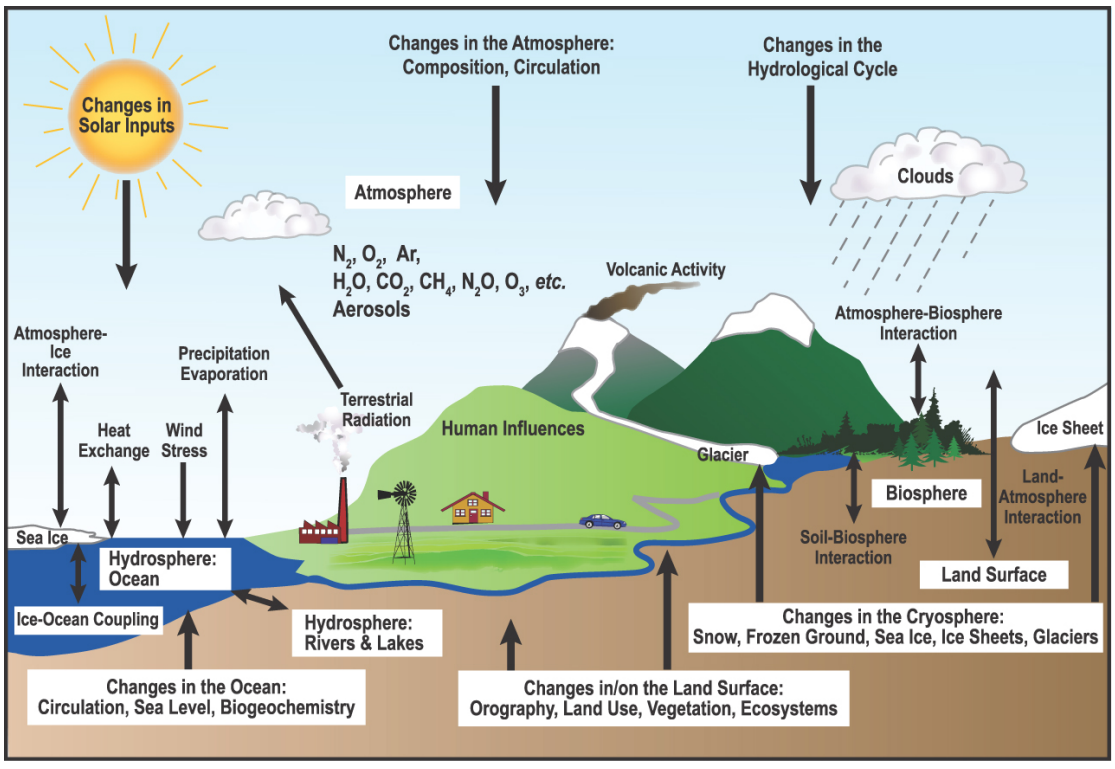

Figure 1.1 Flows and changes in the hydrosystem that influence groundwater resources (figure from IPCC (2007))

Although the links between energy and water fluxes are clear and the processes are well known (Anderson, 2005; Stonestrom and Constantz, 2003; Healy et al., 2007); the studies for water resources often focused on the water fluxes and incorporated heat fluxes only via evapotranspiration term (Singh, 2014). Given that the water resources management scale is between 100 km to 1000 km (Flipo et al., 2014), models that incorporate a complete hydrosystem with water and energy fluxes fully described are either at continental scales (Maxwell and Kollet, 2008b) or local to reach scales (Qiu et al., 2019). Studies on the impact of climate change and surface feedback are usually done at larger scales than the water management scale (Taylor et al., 2013; Viviroli et al., 2011). This causes a mismatch between observed effects of climate change and the translation of this information on water management decisions (Bates et al., 2008). Since groundwater studies often neglect the heat balance, our understanding of the groundwater heat balance and its impact on the surface are limited.

The lack of quantification of the heat balance associated with water budget has policy implications since the energy exchanges at groundwater and its feedback to surface water resources can not be addressed yet. Since 1964, with the Water Law in France, regional scale basins, such as the Seine basin, became the scale for water resources management (Flipo et al., 2020b). Even though hydrological models are well established at this scale, energy fluxes within river basins, including their aquifer system, are poorly understood. There is, therefore, a need to study energy and water fluxes at the hydrosystem scale to assist decision-makers. It is necessary to describe physical process couplings occurring at the local to regional scale.

In the following section, the impact of climate change on the water and energy cycle is addressed, and its implications on the water resources are discussed.

1.1 Climate change

Climate change due to increasing CO_2 concentrations in the atmosphere (Figure 1.2) is effectively changing the current state of the hydrosystem. It increases the uncertainty when planning sustainable water resources practices. Climate change will modify the

water cycle and energy balance processes (Taylor et al., 2013): soil infiltration, groundwater recharge (York et al., 2002), river discharge (Gudmundsson et al., 2021) and groundwater (Benz et al., 2017) and river temperature (Webb and Nobilis, 2007).

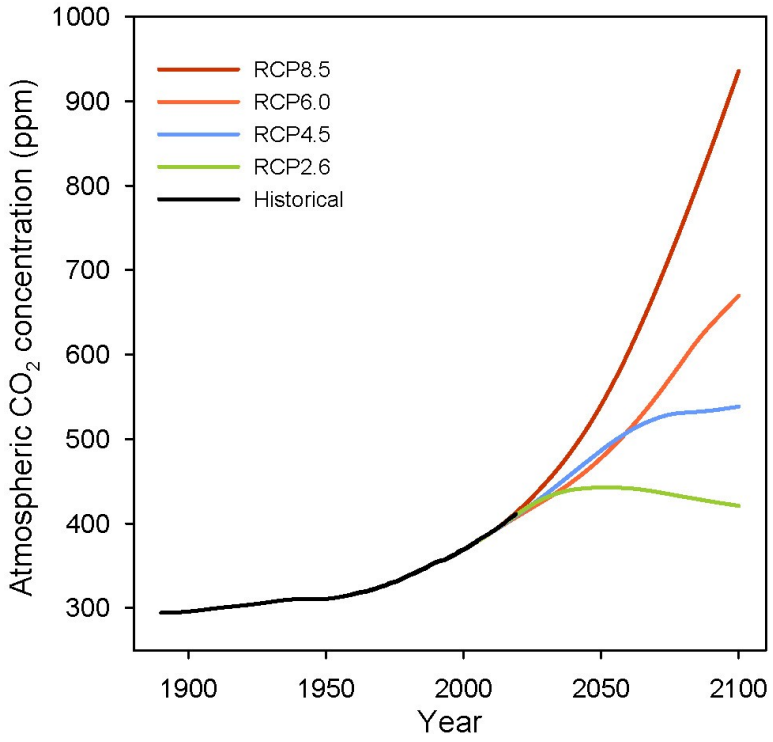

Figure 1.2 Historical and projected changes in the annual average CO_2 concentrations. The black line combines the reconstructed values from 1880-1958 and Mauna Loa observations from 1959-2019. The coloured lines are the four Representative Concentration Pathway (RCP) scenarios used in the CMIP5 (figure from (Stocker et al., 2013)).

Recent projections indicate that while some hydrosystems will be negatively impacted, others will have positive impacts (IPCC, 2021; Wu et al., 2020). Either way, the effect of climate change should be factored into the models for water resources management. Global data trends are derived from a series of sub-continental studies on how global temperature and precipitation change temporally and spatially. The feedback between anthropological activity and climate is factored in the trend studies along with the multi-decadal meteorological variability.

A synthetic representation of global surface warming and future projections can be seen in Figure 1.3. The temperature regime in the past century and projected temperature increase in France can be seen in Figure 1.4 (Terray and Boé, 2013). The reanalysis of the past data with anthropological stress and without it shows clear climate warming

with the anthropological stresses. Depending on various scenarios, average temperatures in the 21^{st} century can increase between 1-4°C (Terray and Boé, 2013). Increases in temperature amplify evapotranspiration activity and reduce the available water in the soil and rivers.

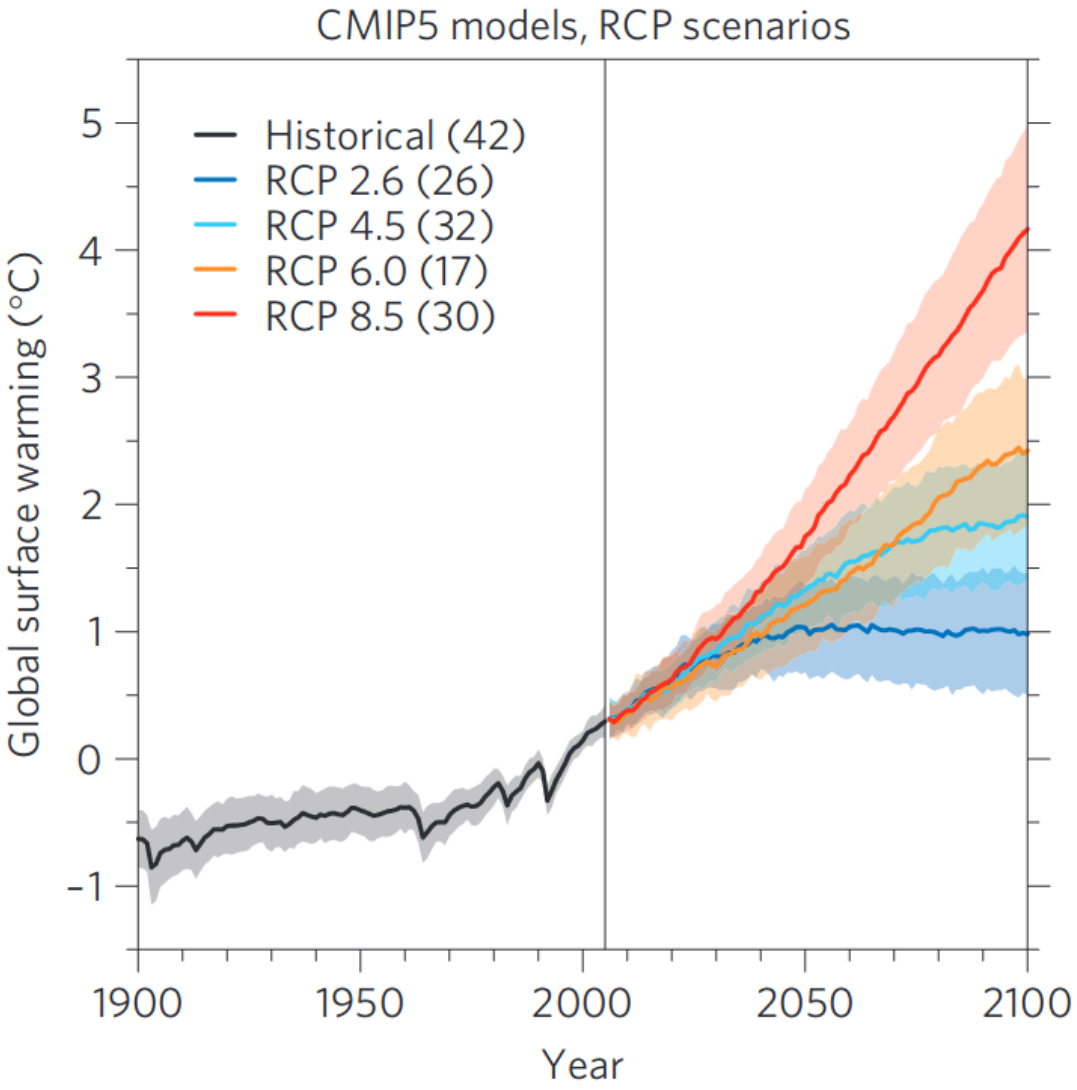

Figure 1.3 Past global surface temperature trends along with future projections. The black line indicates past temperature trends before 2005. Coloured lines indicate surface temperature projections under different CO_2 emission levels. Shades indicate uncertainty ranges. (figure from Knutti and Sedláček (2013))

Evaporation magnitudes also increased in the past century due to an increase in surface temperatures. Studies have shown an increasing trend in different hydrological settings (Duethmann and Blöschl, 2018; Milly and Dunne, 2001; Zhang et al., 2007; Ukkola and Prentice, 2013). Contrary to these findings, a recent study found that evap-

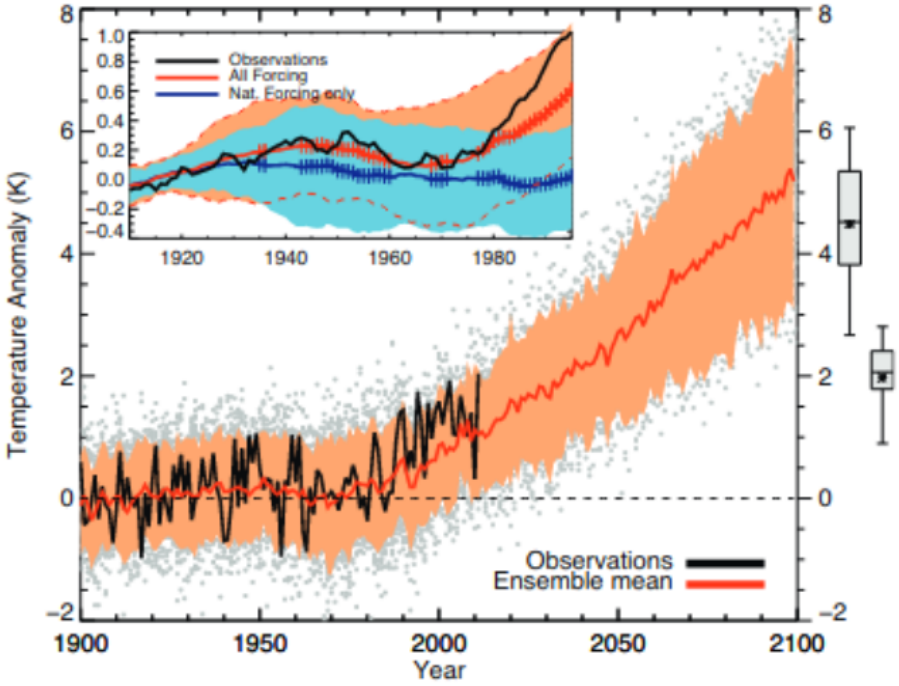

Figure 1.4 Surface temperature anomalies in France from 1900 until 2010. Future projections are also shown in red line with an uncertainty range in orange colour. The smaller figure indicates the reanalysis of the past data with anthropological forcing and natural forcing (without anthropological stresses). (figure from Terray and Boé (2013))

otranspiration is constrained globally due to soil moisture limitations (Jung et al., 2010). In either case, these findings indicate that changes in evapotranspiration are high enough to cause shifts in the water balance of the hydrosystem.

The most recent global climate change assessment report estimates little change in the fraction of precipitation with the climate change (IPCC, 2021). However, at the regional scale, seasonal decreases (Whitehead et al., 2009; Dayon et al., 2018) or increases (Qian et al., 2007) are observed in the precipitation regime. Similar projections are also made for future precipitation(Ducharne et al., 2007). A concerning impact of climate change is the intensification of the water cycle (Christensen and Christensen, 2003, 2004; Milly and Dunne, 2001; Trenberth et al., 2007), causing floods (Milly et al., 2002; Whitehead et al., 2009), loss of life and property. Therefore negative impacts should be factored into the water management studies and projections to stop or mitigate them (Kundzewicz et al., 2008).

Changes in climate patterns influence the discharge regimes and water levels (Lavers et al., 2015; Flipo et al., 2012; Massei et al., 2010). Moreover, possible reductions in the

precipitation influence river water levels enhanced by catchment water use (Dai et al., 2009; Dayon et al., 2018), where reductions can reach up to 40% at some locations. This could be related to increased evaporation, over-exploitation of groundwater, and reduced regional precipitation. All of these factors are influenced by climate change.

Changes in the hydro-climatic conditions are also linked with a higher risk of eutrophication of stream systems (Minaudo et al., 2015). The quality of water is expected to decrease with decreasing discharge levels and increasing stream temperatures (Ducharne, 2008; Whitehead et al., 2009; Zweimüller et al., 2008).

The demand for water is expected to increase in the 21^{st} century due to the population increase (de Marsily, 1986). An increase in the water demand already poses a risk to groundwater due to excessive abstraction (Wada et al., 2010; Gurdak, 2017; Famiglietti and Rodell, 2013). Modifications in the water cycle can limit the water available for agricultural and water supply purposes. Consequently, low-quality water is drawn from deeper aquifer levels, further deteriorating the quality of water that is being used. The reduction of groundwater levels also results in land subsidence, lowering the porosity of the aquifer and the capacity to recharge and increasing runoff generation.

Temperature is a major determinant for drinking water quality (Webb, 1996; Moatar and Gailhard, 2006; Hannah et al., 2008; Isaak et al., 2012; Pekárová et al., 2011; Zweimüller et al., 2008; Ducharne, 2008), since it influences physical, chemical and biological processes, such as absorption, decay (Monteiro et al., 2017), growth and competition (Prest et al., 2016). Many studies have been carried out regarding the effects of climate warming on stream temperature (Ducharne, 2008; Vliet et al., 2013; Webb et al., 2008) and aquatic species (Isaak et al., 2020). Groundwater seepage to streams is known to moderate summer and winter stream temperatures and to create so-called local thermal refugia (Kaandorp et al., 2019) and climate refugia (Briggs et al., 2018) for aquatic biota. The impact of the groundwater on river temperatures at the watershed scale is not quantified yet. Modelling approaches to river temperatures often introduce groundwater temperatures as a function of air temperature at larger scales (Beaufort et al., 2016a), or they neglect it completely (Magnusson et al., 2012) at reach scales.

Most of the studies of climate change are derived from observations or global circulation models (GCMs), which test scenarios of climate projections for the future. There is a limited amount of research at the basin scale, which is at best composed of a few cells of GCM without accounting for groundwater processes. However, the impact of climate change problems on humans is more pronounced on the basin scale, where human-induced stresses are greater (Giordano, 2009; Habets et al., 2013).

To summarise, the trends in the data show unprecedented changes in the water and energy balance, including the modification of the water cycle, limited water availability for agriculture and drinking, and the intensification of extreme events that exacerbates sustainable water management, causing loss of life and property for natural habitats. Moreover, data trends indicate that the anthropological impact is more pronounced at the basin scale. Thence, data-driven process-based applications that model the basin scale water and energy balance are essential to understanding the effect of changing data trends.

1.2 Scientific questions and objectives

The accurate description of physical processes and, subsequently, energy fluxes is fundamental for GCMs, which use Soil-Vegetation-Atmosphere Transfer (SVAT) models that are usually based on the description of energy transfer between the atmosphere and the soil. Even though most of those models attempt to simulate river flow, they are not hydrological models and therefore simplify the physics related to hydrosystems. Through SVAT models, it is possible to evaluate the amount of energy that reaches the surface of a regional basin. Using the energy and water fluxes estimated by SVAT and combining them with a distributed process-based hydrological model, the research question we aim to answer is: "How are energy fluxes modulated within the hydrosystem, which consists of processes at the surface, in the soil, the vadose zone, the aquifer system and the river network?". The evaluation of energy transfer through every compartment of an hydrosystem remains unanswered and a challenging task.

The research objective of this thesis is to establish a first energy budget at a re-

gional basin scale by coupling a SVAT with a distributed process-based hydrological model that explicitly accounts for groundwater processes. Forthcoming from the main objective, several technical challenges need to be answered:

- Which models could be coupled for what *purpose*?
- For a proof of concept, which one is the optimal coupling strategy: on-line coupling or off-line coupling, and what are the advantages and disadvantages of each strategy;
- What are the boundary conditions of our system? This is a typical example of the critical zone ongoing research. Our domain limits are composed of the bedrock downward and the atmosphere upward, with the topographical frontiers of the river basin laterally. What type of boundary conditions should be used, and how to quantify their value;
- What strategy should be developed for calibrating the joint model? How to order the fitting of the large number of processes simulated by the modelling tool? Is it possible to identify a hierarchy of processes that will allow for a step-wise calibration procedure?

We then aim with the developed tool to provide **a quantitative assessment of internal fluxes in the hydrosystem**, such as the quantity of water and energy brought to the river network by various processes: transfer at the air-atmosphere interface, river-aquifer transfer and runoff inputs. This study will be the first explicit evaluation of the contribution of groundwater to the energy budget of a river network at the regional scale. It will refine Beaufort et al. (2016a)'s results which were based on the assumption that groundwater temperature is the average of the air temperature over 365 days, and that the groundwater-river fluxes are oriented upward.

Based on such an evaluation, we will, in a second phase, analyse the potential effect of climate change, allowing us to **evaluate hydrological and thermal trajectories** related to environmental policies represented by scenarios. The functioning of a whole

aquifer system will also be characterised in a more complete way under ongoing climate change.

1.3 Research outlines

This thesis contains nine chapters. The first three chapters synthesise the previous works on the Seine basin, set out the concepts and definitions used in the PhD and present the different ways to model the terms of the water and energy cycle.

Chapter 2 presents the Seine basin and synthesises the previous studies. In addition, the long-term soil, river, and air temperature trends are presented in this chapter.

Chapter 3 defines the concept of hydrosystem and presents the link between water and energy fluxes. Selected surface and groundwater models from the literature are explored in Chapter 4. The surface model ORCHIDEE and the groundwater model CaWaQS used in the PhD are described in Chapter 5. Additionally, the coupling methodologies between the two models are specified.

Chapter 6, details the development of the coupled hydrological model framework and subsequent calibration effort of the surface hydrology and the coupling of ORCHIDEE-CaWaQS models. The results of hydrological simulation were assessed, and the performance of the coupled model was evaluated.

Chapter 7 is a submitted paper to "Comptes Rendus: Geo-Hydrological Data and Models". This paper presents the first simulated heat balance of the whole Seine basin. This study takes advantage of the newly developed ORCHIDEE-CaWaQS framework to couple the heat balance and water budget of the atmosphere, the groundwater and the river. The heat transport module for the CaWaQS model to simulate river and aquifer heat transport is presented in Appendix A.

The future impact of global heat imbalance (Von Schuckmann et al., 2020) at the regional scale is analysed in Chapter 8 to assess the future changes temperature regime of the Seine basin. This study uses ORCHIDEE-CaWaQS application by leveraging recently available bias-corrected climate forcing data from MIROC5 GCM. Changes in the hydrologic and temperature regimes were investigated through two future scenarios

(RCP6.0 and RCP8.5) at mid-century (2043-2060) and end-century (2083-2100). Preliminary results of the changes in the hydrosystem water budget and heat balance are presented. Finally, the implications of this study are summarised and potential future research themes are presented in Chapter 9.

Chapter 2

Past trends in the Seine basin under the impact of climate change

2.1 Introduction

Over the past decades, exceptional hydrological and thermal extremes such as heat waves, floods and droughts have affected France and Europe to a larger extent. These extremes cause concern for the water managers and stakeholders of hydrosystems that depend on the well-being of the hydrosystems. In addition, permanent changes in the water cycle and energy balance prompted by climate change have become more apparent in the literature (IPCC, 2019). Emerging concerns about climate change require an understanding of the processes at the regional scale. A regional scale approach is essential as it is the policy-making scale where stakeholders develop a shared understanding of the available resources. This understanding depends on the hydrological models at regional scales capable of estimating a water budget. As evidenced in the literature (Healy et al., 2007), river water temperature is a key property and variable for physical, chemical and biological processes. Specifically, water quality depends on the temperature profile as the metabolism of pollutants and bacteria depends on it (Billen et al., 2007; Wang et al., 2018b). Although studies state the importance of temperature, studies often focus on local (Cucchi et al., in prep) or reach scales (Le Lay et al., 2019; Bond et al., 2015). In contrast, distributed estimates of the regional temperature calculations often depend on the stochastical (Beaufort et al., 2020) or conceptual approaches (Beaufort et al., 2016a,b). Recently, estimation of heat fluxes by a distributed physically-based model gained interest (Maxwell and Kollet, 2008b; Rousset et al., 2004). However, these approaches estimate energy balance at the surface, and do not

attempt to include the aquifer system even though the groundwater system is explicitly represented for the water cycle. The groundwater system is a key component of the energy balance as it is the lower boundary of the hydrosystem. This impact could be significantly more pronounced in basins with strong baseflow at the river network.

In this framework, the Seine hydrosystem is unique due to the anthropological pressure exerted by the largest metropolis and highly developed agricultural and industrial activities. The Paris agglomeration hosts more than 10 million people. The total population of the Seine basin reaches up to 16 million with the adjacent urban settings and cities. Naturally, the Seine hydrosystem faces many environmental problems linked to agricultural, industrial and domestic activities. Water consumption in the Seine basin reaches up to 3 $\mathrm{Gm^3\,s^{-1}}$ (Flipo et al., 2020a), part of which is used for drinking and electricity generation via nuclear plants to sustain the energy demand. The agriculture, electricity generation, and industrial practices in the basin depend on the sustained water flow in its river network. The waterways navigation in the basin is key to its economic activities. Electricity production also depends on the sustained water flow in the river network as well as manageable river temperatures. The unsustainable water temperatures lead to unavoidable and unpredictable shutdowns of nuclear plants damaging the economy (Boogert and Dupont, 2005). Similarly, increased water temperatures hasten the decay of the urban infrastructure and eventually raise costs. Since the basin is predominantly exploited for agricultural practice, nitrate pollution is significant. In a climate change scenario testing study on the fate of pollutants in the Seine basin, Ducharne (2008) stressed, for example, the increased sensitivity of nitrate mineralisation and organic matter decomposition. European Union directives require proper management of the pollutants of agricultural origin. Although temperature is a key variable for the metabolism of diffuse pollutants, modelling approaches (Beaudoin et al., 2018; Gallois and Viennot, 2018) of these issues in the Seine basin often lack a distributed temperature estimate of the critical zone, the underlying aquifer system and the river network.

The Seine basin contains one of the largest groundwater reservoirs in Europe (90,200 $\mathrm{km^2}$). Being under anthropological stress, the future of the Seine hydrosystem and its

well-being is still uncertain. Given the type of stresses faced by the Seine hydrosystem, modelling approaches often require accurate energy balance and water budget estimations. Since the late-80s, the interdisciplinary research project PIREN-Seine (Flipo et al., 2020b) has many campaigns on different axes in terms of functioning of the hydrosystem, ecological and anthropological aspects. The work of the PIREN-Seine project has shown the precarious state of the river network with respect to anthropogenic activities, water quality issues and subsequent fish species and ecological impairments.

Estimating distributed water temperature in the groundwater system and river network is therefore required to develop accurate strategies against climate change. Such distributed estimates can inform agronomics models (Beaudoin et al., 2018) or river network pollution studies (Ducharne, 2008), or it could help determine ecological evolution, i.e. migration of fish species and subsequent changes in the riparian ecology. Moreover, estimates of temperature can help urban planners with the costs of the maintenance of the infrastructure. Estimating the heat fluxes through the interfaces of the surface-subsurface, between aquifers and at the river-aquifer network can improve the understanding of the dominant processes in the thermal heat budget of the river network as well as the aquifer system. Such information could be leveraged to develop ways to exploit the groundwater thermal energy for cooling and warming households in the Seine basin.

The main objectives of this chapter are to: **(i)** describe the Seine basin watershed in terms of its geography, geological setting, climatology and observations from the basin. **(ii)** define the key historical events **(ii)** discuss previous work in the basin with respect to the prevalent hydrological and temperature regimes. **(iii)** assess if climate change influences the temperatures in the soil horizon that would eventually impact the groundwater system. As part of these objectives, a trend analysis was applied to the soil temperatures at 100 cm horizon from 1981-2001. The hypothesis is that prevalent temperature changes in the local climate influence the temperature regime of the soil horizon. The warming up of the soil would eventually propagate towards the aquifer system; therefore, such a study could help to understand how the temperature regime in the basin might change and thus better identify the future of water resources and water

quality.

2.2 Description of The seine hydrosystem

2.2.1 The aquifer system

The Seine basin covers 78,650 km^2, i.e. 12 $\%$ of the surface area of Northern France. The basin takes its name from the Seine river, which originates from the Langres plateau in the Southeast and flows to Rouen. Geologically, the Seine river flows over the Paris basin. This structure is formed by the sedimentary units, which were deposited by the late-Paleozoic to Tertiary marine transgressions. Quaternary erosion forms the topography of the basin. The Paris basin is bounded by the Manche sea to the North, the Ardennes and the Vosges mountains to the East. It is limited by the Central Massif to the South and Armoricain Massif to the West. Geological structures of the Paris basin are synthesised with an emphasis on hydrology by the thesis work of (Gomez, 2002, Chapter 6).

The sedimentary structure of the Seine basin can be defined in 10 formations which form distinct aquifers in the basin (Labarthe, 2016; Gomez, 2002):

- Lias inferior (Sinemurien, Hettangien, and Rhetien): the formation is a limited porosity and low thickness aquifer at the bottom
- Dogger aquifer: Calcareous aquifer from Bathonien and Bajocien age ranges between 1200 m to 2000 m thickness towards the centre of the Paris basin
- Oxfordian aquifer: Semi-permeable aquifer contains marl and clayey rocks
- Tithonian aquifer: A very heterogeneous calcareous aquifer limited by a semi-permeable Oxfordian marl layer at the bottom and semi-permeable Kimmeridgian marl and calcareous top layer
- Albian aquifer: A sedimentary sand deposit that was originally an artesian aquifer, but heavy exploitation damaged this capacity

- Chalk aquifer: The Chalk aquifer is formed by Montian and Senonian formations. It forms a heterogeneous complex aquifer overlain by the permeable alluvium
- Thanetian aquifer: Includes sands of Bracheux and calcareous layer with marl
- Lutetian aquifer: Middle and inferior Eocene aquifer (Saissonais): Sedimentary aquifer that is exploited towards the Northern part of the Paris basin
- Champigny aquifer (Superior Eocene formation): A complex karstic aquifer towards the centre of the Paris basin
- Brie aquifer: Priabonian "Brie" limestones and "Fontainebleau"sands
- Beauce aquifer: Oligocene formation. This aquifer is situated south of the Paris basin, it underlays the Essone river, and is exploited heavily in the region
- Alluvial aquifer: Neocene alluvium formations are distributed throughout the Paris basin, forming valleys. These formations form the aquifer system within the vicinity of the river network. They are well-developed and exploited aquifers with high permeability

The extent aquifers as mentioned above is shown in Figure 2.1. The Jurassic layer combines the formations below Chalk aquifer i.e. Albian, Tithonian, Oxfordian, Dogger, and Lias aquifers. Several studies on the groundwater resources in the Seine catchment have already shown the functioning of the groundwater system (Flipo et al., 2020a; Pryet et al., 2015; Labarthe, 2016; Rousset et al., 2004; Gomez, 2002). These works treated the Seine basin with 7 distinct aquifers, excluding aquifers below the Chalk aquifer. The work of Rousset et al. (2004) included a coupling of MODCOU with a surface hydrology model ISBA. Although the coupled application included the heat budget, it only treated the surface heat balance without extending to the aquifer system. Gallois and Flipo (2021) recently extended the CaWaQS Seine model application by introducing a Jurassic layer. The Jurassic layer in this work combines the aquifer and aquitard layers starting from the Albian down to Lias as one ensemble.

.

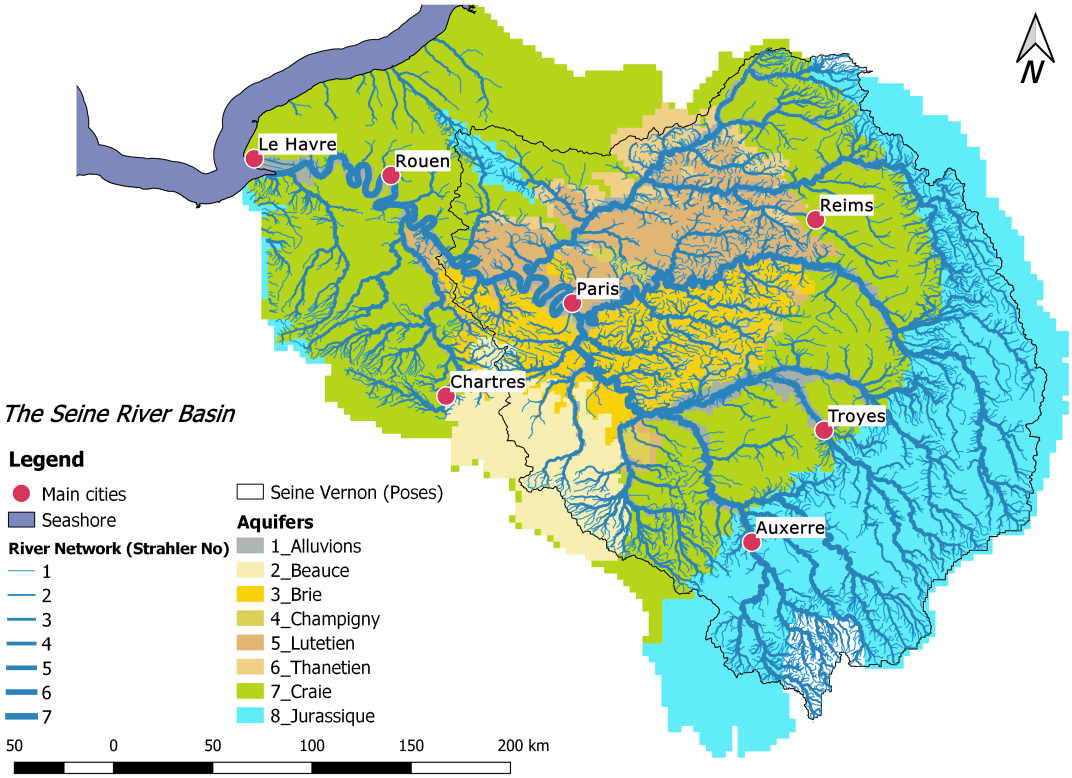

Figure 2.1 The succession and extent of the aquifer layers. The river network and the extension of the Seine basin are superposed on the aquifer layers.

Approximately two-thirds of the effective rainfall feeds the aquifer system via recharge, whereas the remainder drains through the river network as surface runoff. The recharge of the Seine aquifer system is approximately 200 mm/y (Gomez, 2002). Nearly two-thirds of the discharge in the Seine basin is supplied by the aquifer system (Labarthe, 2016). When rainfall is limited, the baseflow contribution to discharge can reach up to 80% during summer seasons (Rousset et al., 2004) .

Approximately a third of total water consumption in the Seine basin depends on groundwater resources, according to the AESN (2013). This consumption adds additional stress to the groundwater system. The groundwater resources are mainly exploited for domestic consumption throughout the basin. Certain sectors of the catchment, mainly the Beauce aquifer and parts of the Chalk aquifer in the East, are used for irrigation during the summer. Industrial usage of the groundwater is concentrated in the Paris metropolitan area and around Rouen city before the estuary. In terms of the water quality, according to AESN (2013), 77% of the aquifer system is classified as average quality. Due to agricultural practices, there is excessive pesticide and nitrate

Table 2.1 The thermal properties of the Seine aquifer system provided in the literature.

Period	Age/stage	Hydrofacies	Thermal conductivity (W/m/K)	Porosity	Mean Heat capacity (J/kg/K)	Density (kg/m³)
Tertiary	Neocene	Alluvium	1.7	0.3	1230	2500
	Oligocene	Beauce	1.6	0.25		
		Brie	1.6	0.25		
	Eocene superior	Champigny	1.6	0.25		
	Lutetian	Lutetian	1.6	0.25		
	Thanetiean	Thanetian	1.6	0.25		
Upper Crateceous	Senonian-Turonian	Craie	1.9	0.28		
Lower Cretaceous	Albian	Albian	1.9	0.3		
	Aptian	Aptian	1.7	0.3		
	Neocomian	Neocomian	1.7	0.28		
	Portlandian	Portlandian	1.8	0.14		
Jurassic	Kimmeridgian	Kimmeridgian	1.8	0.14		
	Lusitanian	Lusitanian	2.1	0.15		
	Oxfordian	Oxfordian	2.2	0.13		
	Callovian	Callovian	2.2	0.13		
	Bathonian	Bathonian	2.0	0.16		
	Lias, Toarcian	Lias	2.1	0.13		
	Aalenian, Bajocian	Bajocian	2.1	0.13		
	Hettancian	Hettancian	2.1	0.14		
	Triassic formations	-	1.6	0.15		
	Bedrock	-	1.8	0.1		

concentration in the groundwater resources (Gomez, 2002). Also, industrial activities exert pressure on the system in terms of heavy metal and chemical concentration.

2.2.1.1 Hydrothermal characterisation of the basin

Interest in the thermal regime of the Paris basin gained popularity on three axes: paleoclimate of the Paris basin (Dentzer, 2016; Rivière et al., 2014; Jost, 2006; Gonçalvès et al., 2003), petroleum studies (Burrus, 1997), and geothermal exploitation (Lopez et al., 2010). The average thermal gradients in the basin range between 2.5-3.5°C$/100m$ (Lopez et al., 2010).

As a result of previous studies, the available information on the thermal properties of the Seine basin accumulated. The thermal properties of the layers of the Seine aquifer system are summarised in Table 2.1. Progressively, the porosities of the basin decrease at deeper layers. Due to the difficulties in establishing the heat capacity and densities of the layers, an average value was often used in these studies. The thermal conductivities in the aquifer system range between 1.6 - 2.2 $\mathrm{W\,m^{-1}\,K^{-1}}$.

2.2.2 The surface water

The Seine river network is formed by a 28000 km long hydrological network of rivers, canals, and reaches. The topography of the basin is given in Figure 2.2. Surface erosion forms a dense drainage system in the basin. The Seine river and its tributaries have a

very gentle slope thanks to the flatness of the surface (Meybeck et al., 1998). Most of the basin has an altitude lower than 300 m, although the maximum altitude reaches 800 m towards the Southeast of the basin. Towards the centre of the Paris basin, the plateaus of Beauce and Picardy are situated. The Seine river discharges into the Manche sea. However, the hydrodynamic influence of the sea starts at Poses (166 km to Manche sea) (Ducharne et al., 2003). The main tributaries of the Seine River are the Oise River, the Marne River, and the Yonne River.

Water regulation in the basin has always been modified to some degree due to the importance of the river network for fish production, agriculture, and water navigation (Lestel et al., 2020). Most significant changes started after the 1830s with the development of industry, and the intensification of agricultural production. Water mills, agricultural drainage structures, and water navigation channels started to emerge in the basin. Since the 1910 flood, flood management has also become an important aspect. As the urban sprawl increasingly more dependent on the sustained water flow in the basin, water reservoirs and dams were developed after the 1940s to regulate the water flow. Most notable water reservoirs were developed within the Yonne, the Upper Seine, the Aube and the Marne rivers. The capacities for these reservoirs are: 80 Mm^3 in the Yonne, 220 Mm^3 in the Upper Seine, 360 Mm^3 in the Marne, and 180 Mm^3 in the Aube. These reservoirs aim to sustain a minimum low flow of 100 $\mathrm{m}^3\,\mathrm{s}^{-1}$that would ensure water navigation. The impact of these reservoirs on the low flow of the Seine basin was evidenced in Flipo et al. (2020a), where the minimum flow in the past two decades did not fall below 100 $\mathrm{m}^3\,\mathrm{s}^{-1}$.

2.2.3 Soil and land cover distribution in the basin

The topsoil distribution map (Figure 2.3) is obtained from the INRA InfoSol database (Jolivet et al., 2006). The land use map (Figure 2.4) is obtained from CORINE Land Cover (Büttner et al., 2004). The map is obtained for 2012 in the form of 1/100 000. The map covers the soil distribution in France at 1/1 000 000 scale. Both of these maps provide high resolution (minimum mapping unit: 25 ha) information of the surface.

The soil at the near surface is formed by a combination of sand, silt and clay parti-

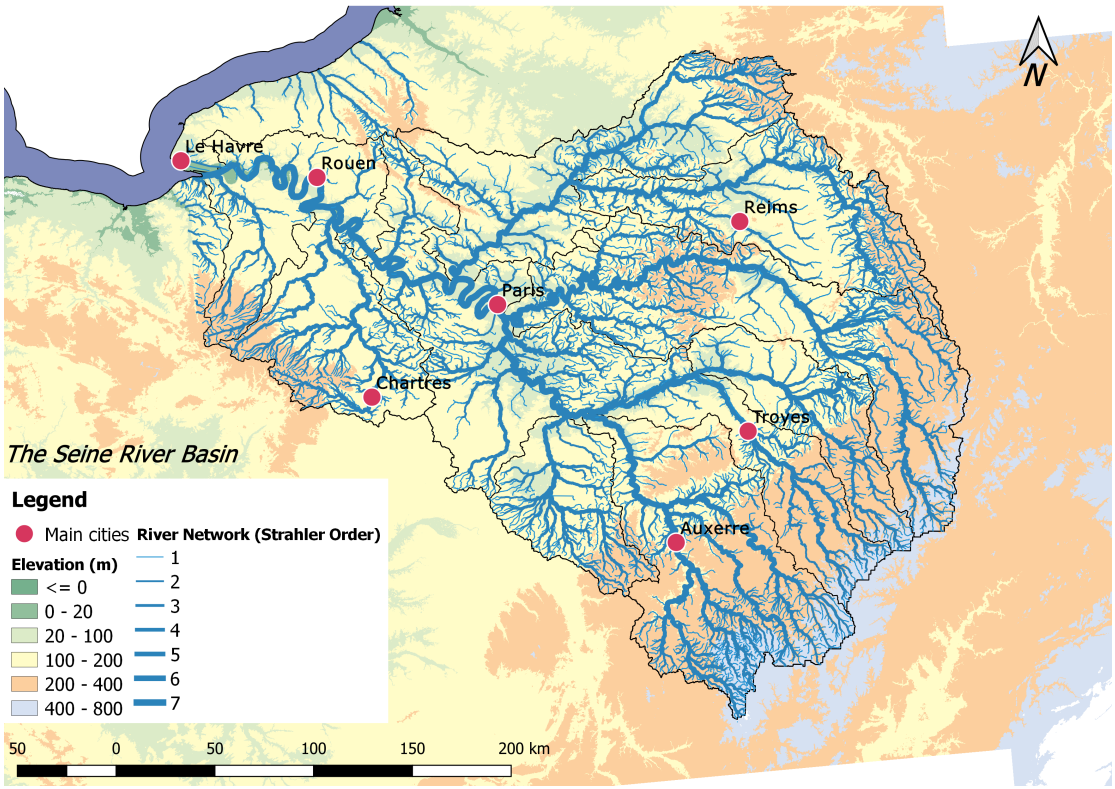

Figure 2.2 The surface topography and the river network in the Seine River basin. Thicker lines indicate a higher Strahler order. The major cities (red dots) are evolved around the river network, with Paris being at the confluence of the Seine and Marne rivers.

cles derived from the weathering of nearby outcrops. Due to biologic activity, organic and inorganic carbon mixes with the soil and modifies soil hydrodynamic and thermal properties. The soil distribution and texture play an important role in the recharge of aquifers (Healy and Scanlon, 2010), the soil moisture profile (Richards and Weaver, 1944), flood generation (Anquetin et al., 2010), and heat transport (Peters-Lidard et al., 1998)in the shallow subsurface domain. The heterogeneity of the soil properties is one of the main sources of uncertainty in recharge estimation (Rushton et al., 2006). Moreover, soil distribution maps and texture are subject to extensive research generally (Dai et al., 2019; Ballabio et al., 2016; Reynolds et al., 2000) because state-of-the-art land surface models require the soil distribution information as well as soil properties in the form of pedo-transfer functions (Vereecken et al., 2010).

The Seine basin surface is mainly covered by silt and Quaternary clay over the Paris basin formations (Figure 2.3). The Southeast of the basin is covered mainly by calcareous soils. Silt or sand-dominated soils also form a considerable part of the Seine

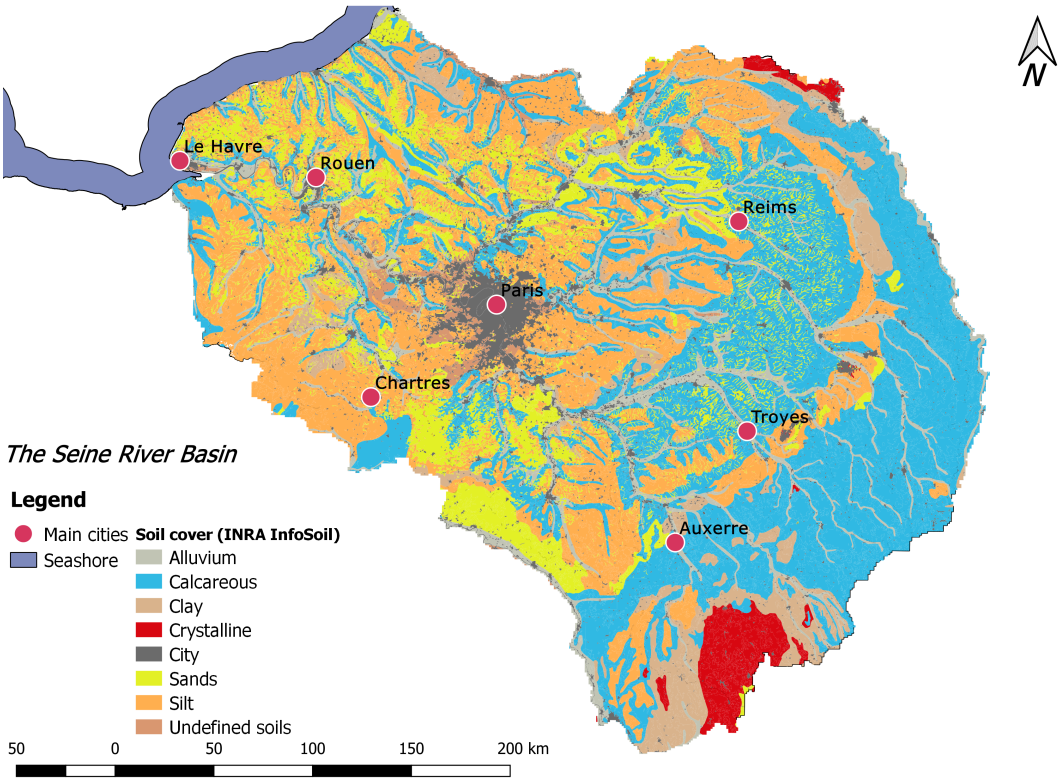

Figure 2.3 Soil cover map from the basin. Source INRA InfoSol (Jolivet et al., 2006).

basin towards the centre and western parts of the basin. The urban cover is mainly at the centre of the basin by the Paris agglomeration covering the bulk of the urban land cover. Hercynian basement outcrops are situated at the southern and northeastern boundaries of the basin, forming crystalline-derived soils.

This cover has a good capacity for holding water and transferring it to the drainage network. Another consideration is the physical properties of these soils covering the surface and underneath. Soil is subject to significant heterogeneity, and physical parameters are hard to obtain (de Marsily, 1986). There have been a series studies on the Paris basin, and its aquifer and soil properties. Dogger aquifer has been closely studied for water management (Lopez et al., 2010; André et al., 2007). Properties of the calcareous soils in the Paris basin were studied for contaminant management (Roulier et al., 2006; Renard and Tognelli, 2016).

The land usage information shows a high proportion of urbanised area (7.6%). Grasslands cover 9.6% of the total area, and forests cover a little over a quarter of the total area (25.6%). Water bodies and wetlands do not cover a significant portion. The

agricultural production includes wheat, oilseed rape, maize, and spring pea. Forests in the basin consist of mainly summer-green trees, while ever-green forests are limited.

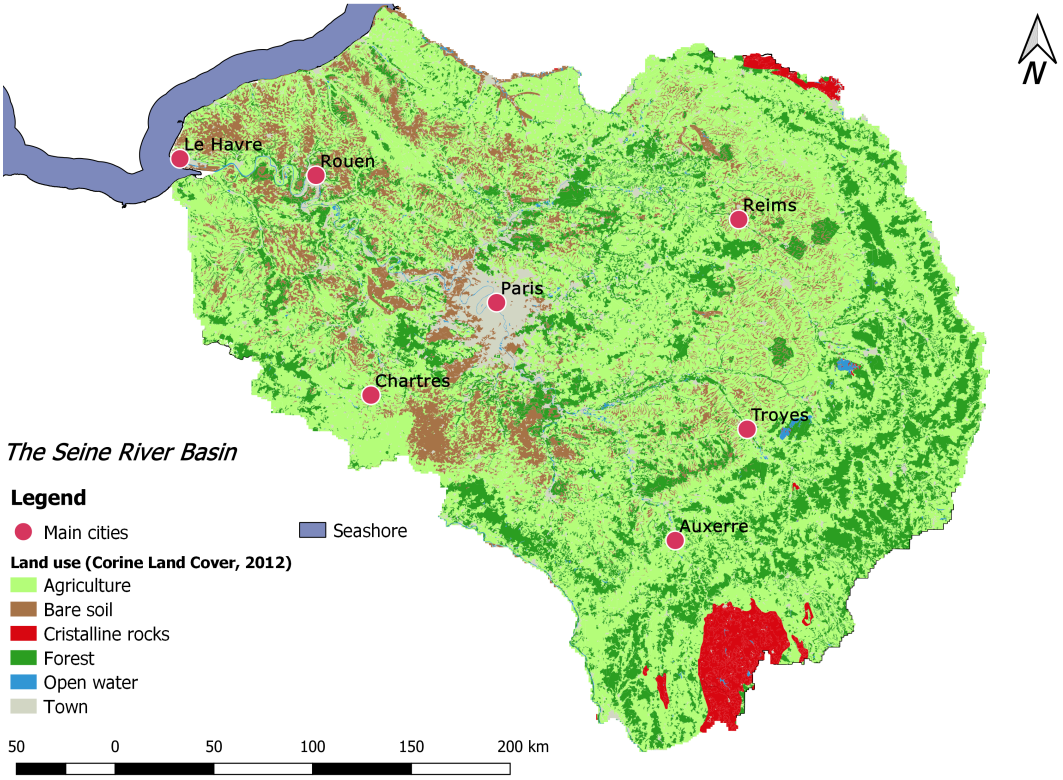

Figure 2.4 The Seine River basin land use map. Source: Corine Land Cover (Büttner et al., 2004).

2.3 Water and thermal uses of resources

2.3.1 Uses of water resources

The watershed supplies major cities and the capital in France, the agricultural practices, and the majority of the French industry. As the basin is agriculturally developed, 56.5% of the basin is dedicated to agricultural practices. The high-intensity agriculture activities in the region mainly produce cereal and industrial crops. There is also high-intensity livestock which augments the nitrate pollution (Meybeck et al., 1998).

Urban zones cover up to 7% of the surface area of the basin. In terms of population, there are 16.7 million inhabitants. 85% of the inhabitants live upstream of Poses station (close to Rouen city), while the remaining lives within the estuaries. The Paris Metropolitan area (2850km^2) is home to 12.4 million inhabitants. This dense popula-

tion negatively factors in terms of water quality and ecological degradation. Moreover, water management becomes an important issue given that the population is expected to increase further.

Water abstraction from the basin reaches up to 1 billion m^3 from the groundwater and 2 billion m^3 from the river network per year (Flipo et al., 2020a). The surface water withdrawal from the river network is mainly for regulation and energy production; hence 97 $\%$ of the water is returned to the catchment. From 2008-2012, the water abstraction from the basin by various sources (Figure 2.5) was equivalent to 37 $\mathrm{m}^3\,\mathrm{s}^{-1}$. Energy production in the Seine basin depends on the sustained river discharge and temperatures within acceptable ranges. Nogent-sur-Seine Nuclear Power plant situated in the basin depends on river water for cooling.

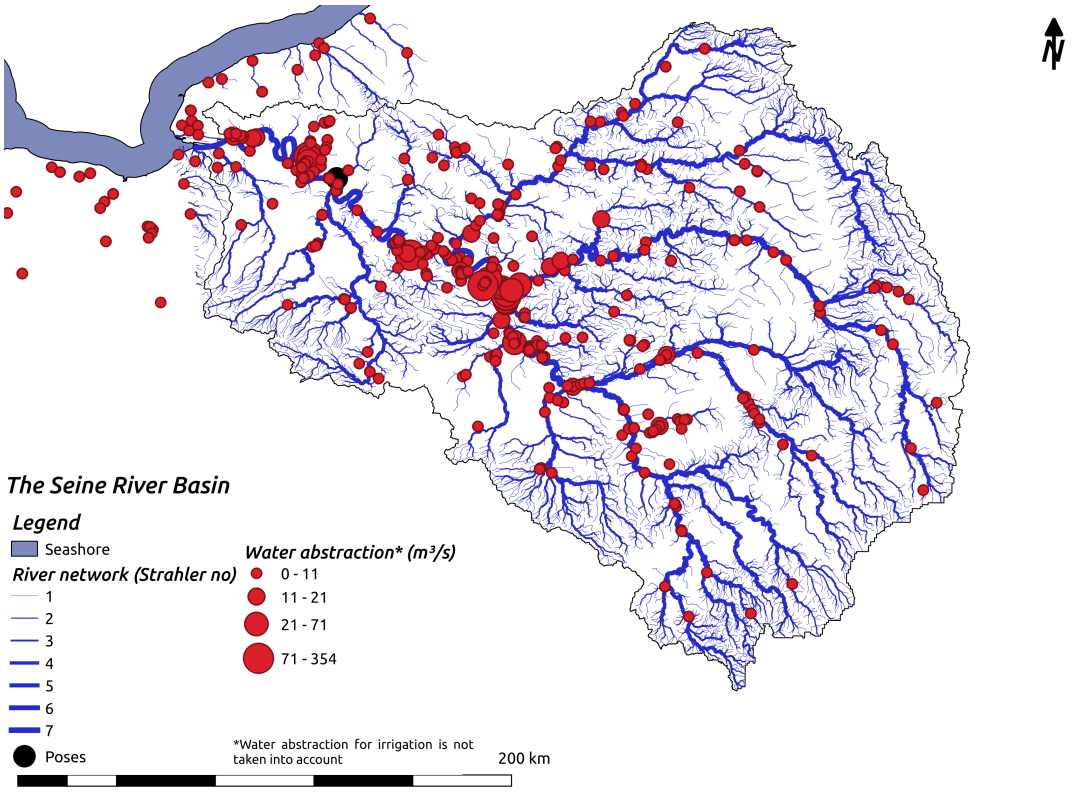

Figure 2.5 Distribution of major water abstraction locations in the Seine basin. The size of the point indicates the amount withdrawn, source: AESN.

2.3.1.1 Quality issues related to water resources

The Seine basin is heavily exploited by industrial, agricultural applications, and urban development (Figure 2.5) that lead to water quality issues in the basin (Meybeck, 2002).

More than 50% of the basin is dedicated to agriculture (Figure 2.4). Intensification of agricultural practices aggravated the nitrate pollution in the Seine basin. This issue prompted a series of modelling activities to understand the extent of the pollution in the groundwater system and the river network (Ledoux et al., 2007; Gallois and Viennot, 2018; Tavakoly et al., 2019). Ledoux et al. (2007) coupled the MODCOU model with an agronomy model STICS to simulate the nitrate transport in the Seine groundwater system. Similarly, Gallois and Viennot (2018) coupled MODCOU with the STICS model to analyse the extent of nitrate pollution under varying climate scenarios. These approaches have shown the suitability of the coupled framework using a distributed hydrological and an agronomy model to show the extent of diffuse nitrate pollution in the basin and its seasonal variations. Finally, Ducharne (2008) has coupled a river water quality model RIVERSTRAHLER with an LSM model CLSM to simulate the pollutant and phytoplankton species in the Seine river network to analyse the future climate change impact on the water quality. They have described the water temperature as a linear function of the lagged moving average of air temperature. They found that the increases in the water temperature increase the growth rate of phytoplankton, but the loss rate is faster during the winter season under climate change conditions. In smaller streams, the pollution is mainly due to diffuse nitrate pollution, whereas point source pollution becomes significant downstream.

2.3.2 Thermal use

The Seine basin has significant geothermal and heat supply potential for the urban uses. The Paris city uses a district cooling system which is connected to the river network to with more than $325\mathrm{MW}$ installed capacity. This approach depends on water from the Seine to take advantage of water temperatures to cool the buildings via heat exchangers. Moreover, water treatment and electricity production plants depend on water temperatures to cool in the basin.

The geothermal potential of the Seine basin is also quite significant (Lopez et al., 2010). The Dogger aquifer's geothermal potential was exploited more than 40 years. The good yield of the sedimentary basin and strong geothermal gradient renders the

Table 2.2 Summary of the observed variables from the Seine river network and available global satellite-derived products.

Variable	Stations (n)	From	To	Temporal resolution	Spatial Resolution	Source
River temperatures	62	1849	2018	Hourly, Daily	Point	William Thomas (DRIEE)
Aquifer Temperatures	211	1978	2020	Daily	Point	SANDRE
Soil Temperature	8	1981	2018	Daily	Point	Meteo France
Piezometers	267	1970	2020	Daily	Point	HYDRO
River Discharge	183	1970	2020	Daily	Point	HYDRO
Water withdrawal	56414	2008	2012	Yearly	Point	SANDRE-AESN
Evapotranspiration	Distributed	2003	2018	Monthly	1/4°	Gleam-ET (Martens, 2019)
Leaf Area Index	Distributed	1982	2011	Monthly	1/12°	GIMMS (Zhu et al., 2013)

Seine basin suitable for geothermal exploitation. Lopez et al. (2010) also emphasised the importance of a detailed estimation of the water and heat budgets of the aquifer layers so that the geothermal potential can be better estimated and exploited.

2.4 Brief analyses of hydrothermal observations

The Seine basin is closely monitored by several campaigns in terms of discharge, piezometric head level, and water and soil temperatures. The water and temperature data and their sources are summarised in Table 2.2.

The river gauging station data was obtained from Eau France - Banque Hydro database. There are 183 stations distributed over the hydrological network of the Seine River basin. These stations capture most of the sub-catchments of the Seine basin. Within the Seine river, multiple gauging stations capture the stream flow upstream, before Paris, after Paris and before the estuary (Seine Vernon).

Piezometric data are obtained from the BRGM database (Gomez, 2002). There are 267 stations with data from different periods, and the record is incomplete. Most piezometric data are obtained from the chalk aquifer (Craie).

River temperature data was obtained from William Thomas (DRIEE) database. The database consists of water temperature observations from various locations in the Seine basin provided by the stakeholders such as water agencies and industrial partners in the Seine river basin. The historical data dates back to 1849 at a few stations, while there are multi-year gaps in the observations. Continuous daily observations date back to 1980, where the bulk of daily observations is recorded until now.

The soil temperature data were obtained from METEO France from 10 stations in

the Seine basin. The dataset is available in daily time steps over the period 1984-2001. The observations are collected from soil horizons at 10, 20, 50, and 100 cm depth.

In terms of validation, remotely sensed observations are the only products that supply sufficient spatial and temporal coverage for regional hydrological models. Recently, estimates of evapotranspiration and leaf area index products were developed with the help of advancements in remote sensing. Martens (2019) provides a global high-resolution gridded evapotranspiration product by combining microwave observations with a water budget model. Similarly, Zhu et al. (2013) provided a global leaf area index dataset derived from the NASA MODIS satellite product with the help of a neural network application. Both datasets are used to evaluate energy balance and vegetation activity in land surface models.

A limitation of satellite-derived products is that they are produced for recent periods, and may not cover the application periods. The second limitation is the inherent problems with the satellite products, such as instrumental bias and scaling (Winsemius, 2009). Due to the nature of the satellite data, the observations are coarser than the simulation scale of regional applications. Hence, these uncertainties should be accounted for when the satellite products are used for calibration and validation.

2.4.1 Seasonal description of hydrological variables

The average monthly precipitation (Figure 2.7) is around 65 mm within the basin from 1985 to 2018. It increases to 80 mm during the winter season and decreases down to 60 mm during summer. The average precipitation reaches above 800 mm/year towards the Normandy region (Northern regions). Towards the centre of the basin, the yearly precipitation ranges between 550 to 800 mm/year. It can reach up to 1300 mm/year in the Morvan area (southern boundary of the basin).

The river flow is regulated by a set of dams and reservoirs. The gauging station before the estuary has an average discharge of 485 $\mathrm{m^3\,s^{-1}}$, but during a high flow period, it can reach up to 2280 $\mathrm{m^3\,s^{-1}}$, whereas it decreases as low as 80 $\mathrm{m^3\,s^{-1}}$ during a low flow period (Flipo et al., 2020a). In addition, the river flow in the basin is associated with a 17-year cycle linked to the North Atlantic Oscillations (NAO), influencing the

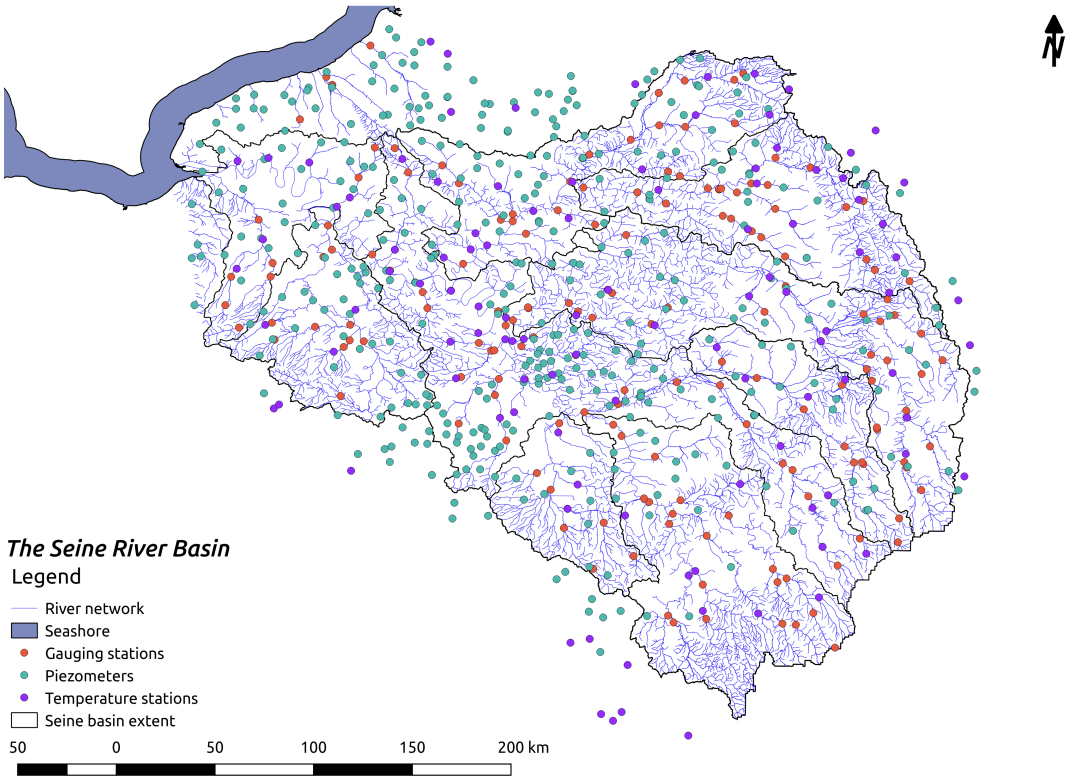

Figure 2.6 Local observations from the Seine River Basin. Temperature data is from the river network.

river discharge (Massei et al., 2010) and groundwater levels (Flipo et al., 2012). The average evapotranspiration is estimated at around 550 mm/year, and the infiltration varies between 30-250 mm/year in the basin (Flipo et al., 2020a).

Mean monthly temperatures range between 2 - 20 °C, which means freezing, and snow precipitation is relatively limited in terms of the water budget. The hydrological regime of the basin is pluvial/oceanic. The rainfall (Figure 2.7) shows spatial variability where the wet season typically starts from October and continues until February. A drier period from February to October follows except for May.

2.4.2 Historical events in the Seine basin

The Seine basin is susceptible to hydrological extremes: floods, heat waves, and droughts. Paris region has witnessed several major flood events over the past centuries. The most destructive one in the record is the great flood of 1910 and 1924, which prompted a series of waterworks to regulate the river basin (Dorchies et al., 2014). These events were followed by the 1949 and 1955 floods and, more recently the 2001 flood. The

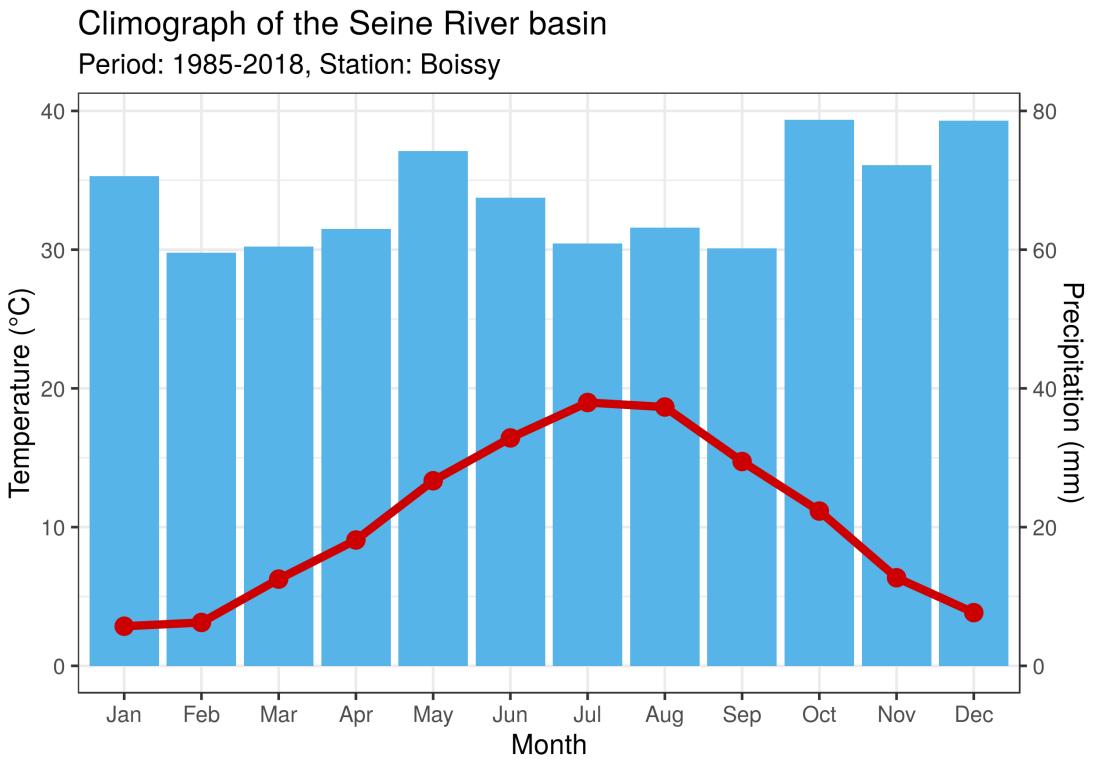

Figure 2.7 The climatological state of the Seine basin throughout 1980-2018, shown by monthly mean temperature and precipitation.

Seine basin also had notable droughts in 2003 and 2005. The heat waves and droughts have started to become more pronounced in recent decades.

2.4.3 Temperature evolution of the Seine hydrosystem

The hydroclimatic variability of several key climate indices in the Paris region was documented by Ringard et al. (2019). Although the precipitation did not show any significant decreasing or increasing trend, the mean, minimum, and maximum air temperatures show an increasing trend. Significant air temperature trends were recorded in the region during the spring and summer seasons. This trend was followed by a decrease in relative humidity. Ringard et al. (2019) attributed the increases in the temperature trends to the Atlantic Low weather regime.

A recent trend study on the water temperatures shows a 1.6 °C increase in the average water temperatures per century (Figure 2.8). Average yearly temperatures show a continuous increase over two centuries. A recent study by Seyedhashemi et al. (2022) found similar water temperature trends in the Loire basin adjacent to the Seine basin.

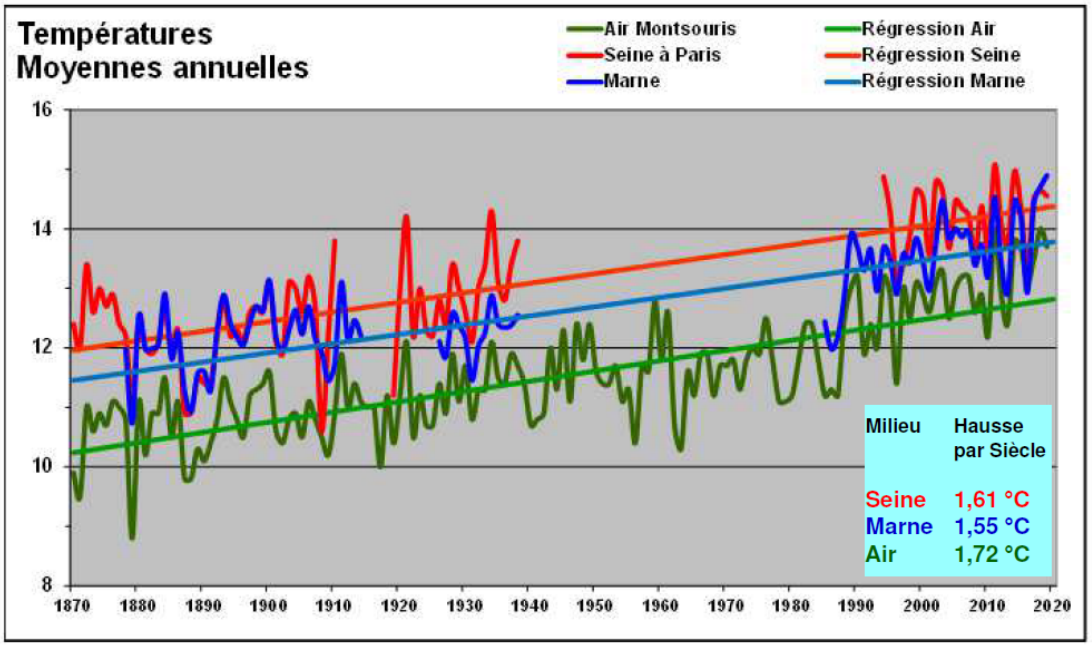

Figure 2.8 Evolution of the water temperatures and associated trend lines in the Seine basin (source: William Thomas, DRIEE, 2020).

A similar analysis of the water temperature regime changes by Rivière et al. (2021) documented an increase of 2°C in temperature during winter over the past century. Moreover, they found that the number of hot days (T > 24 °C) throughout the years constantly increased while the number of cold days (T < 5 °C) decreased. They also estimated future water and air temperatures based on the RCP8.5 and RCP4.5 climate change scenarios. The number of hot days is expected to increase considerably in the RCP8.5 scenario, and they predict that a constant increase in water temperatures might severely restrict water usage for drinking and industrial purposes.

Although several studies analysed the long-term trends of climate variables and water temperatures, potential soil temperature trends were not documented, to our knowledge. However, temperature increases at the surface can alter the temperatures at the shallow subsurface and in the aquifer system (Bense and Kooi, 2004).

The long-term trends were analysed by Mann-Kendall (Kendall, 1955) and Theil-Sen (Sen, 1968) tests. A non-parametric Mann-Kendall (Kendall) test compares the pairs of values to obtain a positive or negative score that signifies an increasing or decreasing trend, respectively. Statistically, a p-value that reflects the probability of no trend is also calculated to test the null hypothesis (no trend). In this study, a p-value

of 0.05 was considered where, p<0.05 was deemed to be a significant trend. Similarly, the Theil-Sen test calculates a linear regression of a time series where an overall slope of the time series could be obtained. These tests were applied to seasonal and yearly averages of the temperature variables.

The results of the Mann-Kendall trend analysis combined with Theil-Sen trend estimations are given in Figure 2.9. Overall, there is a positive trend (significant for spring and summer, not significant for winter and autumn) present in all stations. Seasonally, the soil temperatures have increased for spring (0.11°C.yr^{-1}), summer (0.09°C.yr^{-1}), winter (0.07°C.yr^{-1}, not significant), and autumn (0.06°C.yr^{-1}, not significant). Trends in the Chatillon station could not be assessed as the available data covers only 1981-1985.

None of the winter stations has shown a significant temperature increase by the Mann-Kendall test. During autumn, only Fontaine and Beauvais stations show a significant temperature increase by 0.10°C.yr^{-1}, 0.11°C.yr^{-1}, respectively.

During spring, all the stations show a significant temperature trend increase, with Beauvais showing the strongest trend (0.13°C.yr^{-1}), while Chartres show the lowest temperature trend (0.08°C.yr^{-1}). The strongest temperature trend during summer is recorded in Bonneuil and Boos stations (0.12°C.yr^{-1} each). Fontaine, Courcy, Bretigny stations do not show significant trends.

The spatial distribution of summer temperature trends of the soil horizon at 100cm is shown in Figure 2.10. The strongest trends are recorded in the Paris urban area, and near Rouen and Auxerre. The northeast of the basin does not show any significant trends. Similarly, Bretigny in the south of Paris has no significant trends.

Overall, temperature trends recorded in the basin corroborate with the air temperature trends reported by Ringard et al. (2019). Typically the proximity of the stations near large urban areas could indicate the impact of thermal load trapped due to the urban heat island phenomenon (Ferguson and Woodbury, 2007). The strong temperature trends in soils show that changes in the surface climatology propagate towards the shallow subsurface, then into the aquifer system.

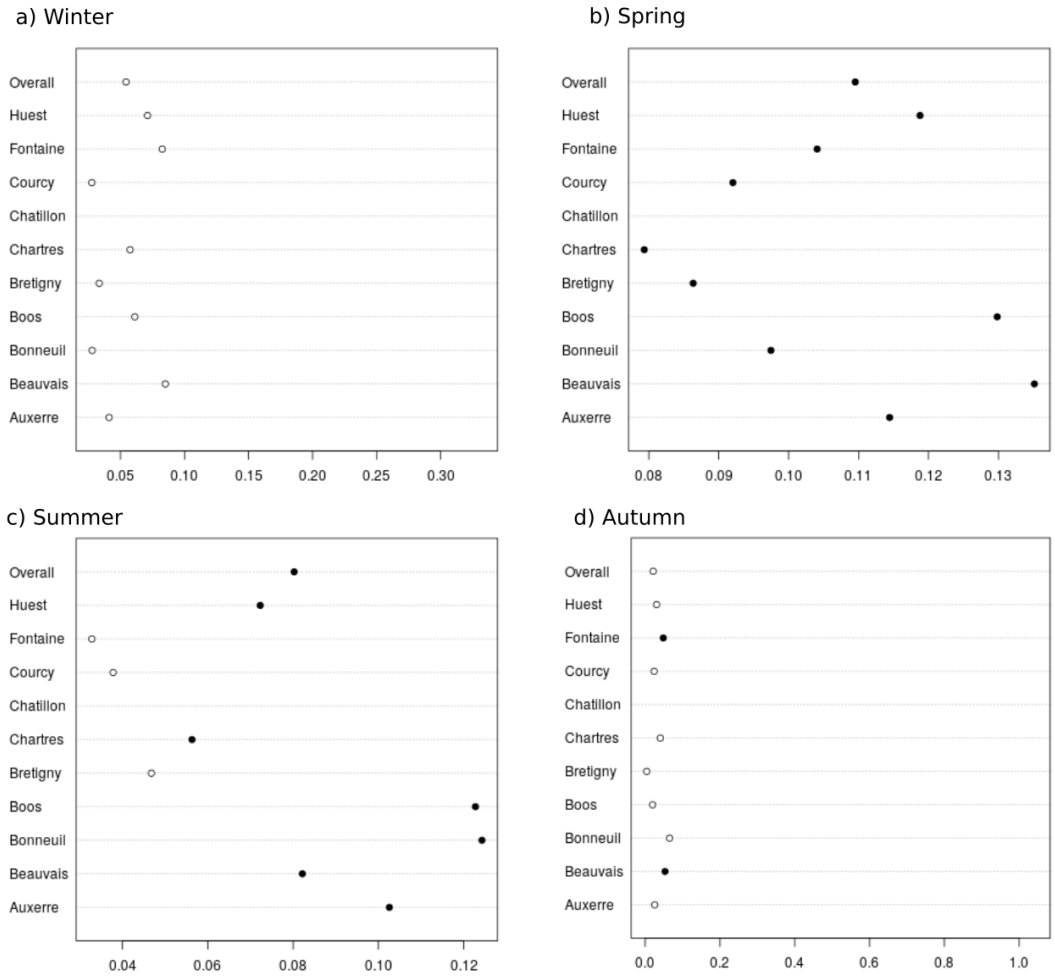

Figure 2.9 Long-term seasonal Theil-Sen trends (°C of the soil horizon at 100cm depth. Filled dots indicate a statistically significant trend ($p < 0.05$), and empty dots indicate an insignificant trend according to the Mann-Kendall test. Overall shows the average temperature trend. No dots indicate insufficient data to establish a trend.

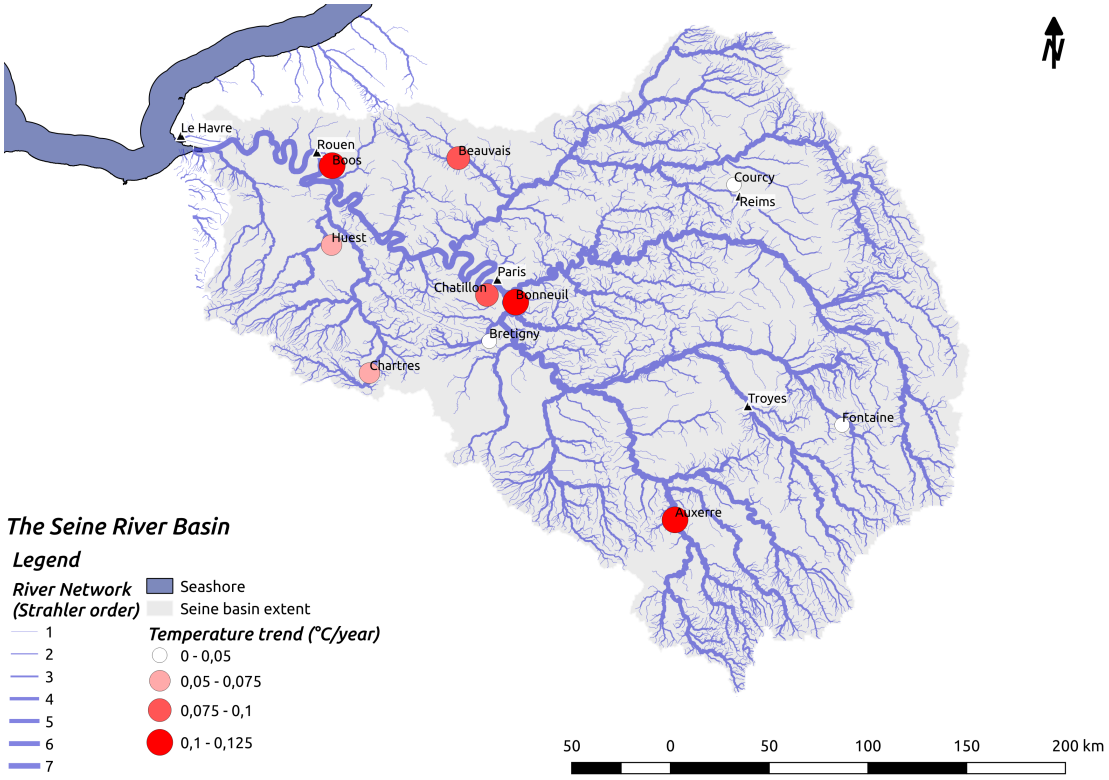

Figure 2.10 Spatial distribution of Theil-Sen trends (°C.yr^{-1}) of the soil horizon at 100cm depth during summer. All soil stations show a positive trend at 100 cm depth; Fontaine, Bretigny and Coucy do not show a significant trend based on the Mann-Kendall trend test.

2.5 Conclusion and perspectives

The Seine hydrosystem is one of the largest groundwater resources in Europe. Several field campaigns, observations since the 20^{th} century and decades of studies show that:

- The basin is advanced in terms of agricultural and industrial activities. It hosts more than 16 million people that exert considerable pressure on the groundwater resources. The hydrosystem supports more than 22% of the national economic activities as the Seine basin is the industrial and agricultural heart of the country (AESN, 2013).

- The geological setting can be grouped into 10 distinct formations, which form 8 aquifer layers in the catchment, from alluvial deposits to Jurassic formations. The thermal properties of these layers are not homogeneous.

- Water sources abstraction reaches up to 3 Gm^3, where approximately 1 Gm^3 of water is sourced from the groundwater system. Agricultural and industrial practices and domestic usage exert pressure on the hydrosystem.

- Century-long hydrological observations show that the hydrosystem is vulnerable in terms of floods as notable events have occurred since the beginning of the 20th century. Since the 21^{st} century, an increase in the frequency of flood events and heat waves has been observed. These events are destructive to human life and economic activities.

- Temperature observations since the beginning of the 19th century indicate an increasing temperature trend in the atmosphere and river. The data shows a warming up trend in the deeper soil horizon, which would eventually modify the heat balance of the aquifer system.

- Soil temperatures are often neglected in the studies of climate change (Qian et al., 2011). However, we demonstrate that the soil temperatures at 100cm horizon show statistically significant trends at various locations in the Seine basin. The spring and summer trends show up to $0.13°\mathrm{C}.yr^{-1}$ warming trend. Implications

of the shallow subsurface warming are the changes in the shallow aquifer temperature trend (Benz et al., 2017). Therefore, aquifer temperatures should also be studied to identify the extent of the warming up trends at the surface (Kurylyk et al., 2015).

- The hydrosystem is under the impact of North Atlantic Oscillations (NAO), which influences the climatological regime of the basin, and there is a link between the water flow in the Seine and the NAO.

- Studies of this vast hydrosystem at the regional scale are essential to understand functioning of the Seine hydrosystem and mitigate the potential risks caused by climate change.

- The functioning of the hydrosystem should be further investigated in terms of surface water and energy fluxes and their interaction with the groundwater system. An energy budget of the hydrosystem at the regional scale would be critical for the decision-making process in the face of global changes.

Chapter 3

Energy and water fluxes in the hydrosystem

3.1 Introduction

A hydrosystem is composed of a set of components. Physical processes between and within these components of the hydrosystem result from the flow of energy and mass. A summary of processes in terms of heat and water flow is given in Figure 3.1.

Processes in the hydrosystem are discussed in this section. Firstly, energy flow through the atmosphere, soil, river, and aquifer are discussed. After that, the link between energy and water fluxes is shown, and water fluxes due to energy transfer is reviewed.

3.2 Energy fluxes

The relationship between different sources of energy is established via the concept of the energy budget. The energy budget includes incoming energy from the Sun as the net income. The net incoming energy is consumed by four main processes: evaporation, surface sensible heat, energy absorbed by the ground, photosynthesis, and transpiration processes by biomass. The resulting energy balance at the surface can be shown as:

$$Rad_{net} = H + LE + H_{soil} + P \tag{3.1}$$

where Rad_{net} is the net radiation that the surface absorbs, H is the sensible heat which translates into temperature, LE is the latent heat which forms the evaporation term, H_{soil} is the energy absorbed and conducted into the soil, and P is the energy absorbed and used for photosynthesis (Pitman, 2003). Terms of the energy budget are

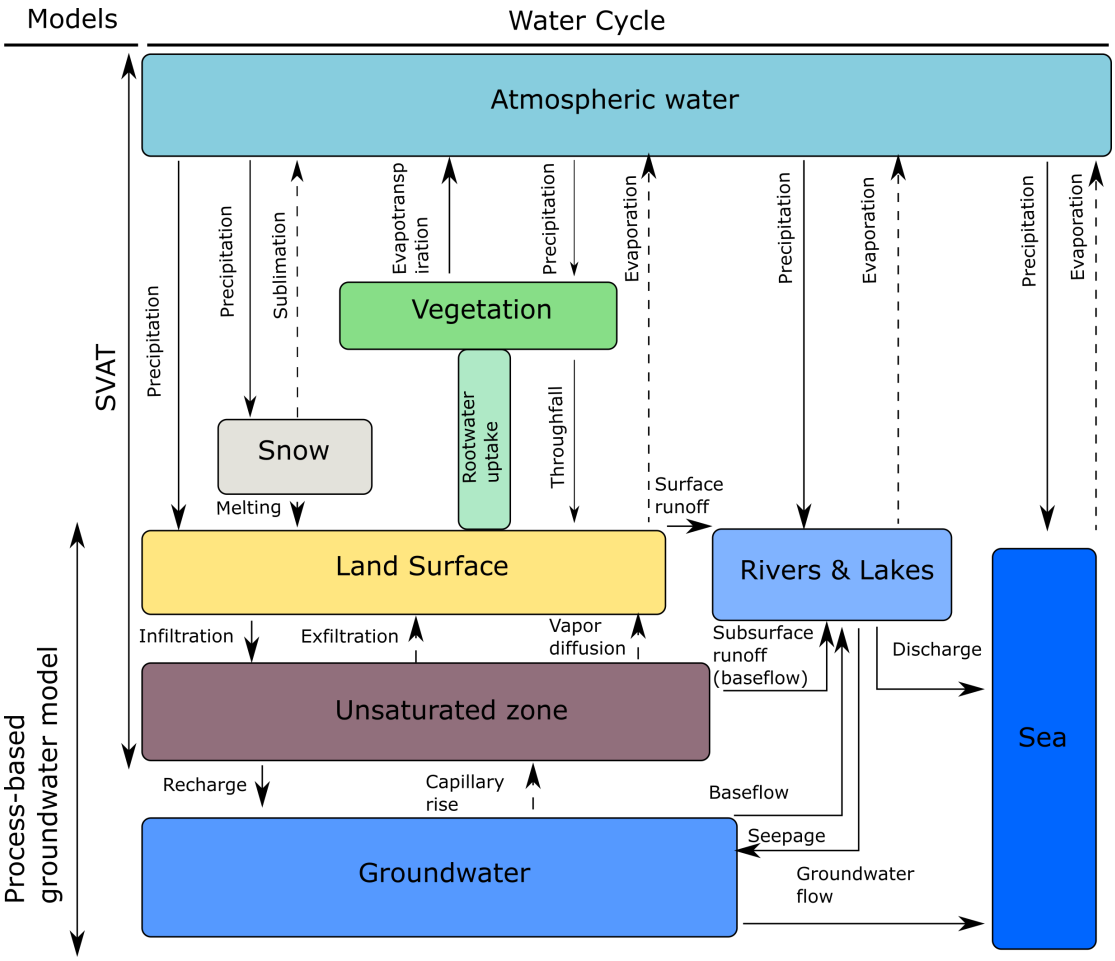

Figure 3.1 Processes in the water cycle and models that capture the processes. Rectangles indicate components of the water cycle, and arrows indicate processes of the water cycle. (Figure modified from De la Torre (2014))

described by $\mathrm{W\,m^{-2}}$ unit.

3.2.1 Surface processes

3.2.1.1 Atmosphere

Atmosphere is the major driver of land surface processes, groundwater heat and water fluxes. Processes defined in the energy budget (Eq. 3.1 are controlled by various factors such as albedo, turbulent air fluxes, surface roughness, vegetation. Recently, anthropological activities (Greenhouse gas emissions) have been confirmed to impact the energy balance alongside natural factors (Stocker et al., 2013).

One of the main processes at the surface is evapotranspiration. Evapotranspiration is controlled by energy fluxes and water availability of the near-surface. The atmospheric

variables such as wind speed and temperature also impact the amount of evapotranspiration generated in the basin. Another control variable is surface and soil moisture for evapotranspiration. These variables are impacted by the vegetation distribution, vegetation cover type and hydrodynamical characteristics of the top soil. Generation of evapotranspiration was first conceptualised by Budyko as either limited by energy (not enough to extract total available moisture) or limited by water (i.e. not enough moisture to transform although energy is ample) (Gentine et al., 2012). The early studies on the evapotranspiration processes started with Penman (1948) and Monteith (1965). Although their initial goal was to understand the impact of evapotranspiration on agricultural management, the practical nature of their methods allowed for them to be later incorporated into hydrological models (Clark et al., 2015). These terms and fluxes include latent heat, sensible heat, bare soil evaporation, incident solar radiation, and the interactions with canopy layer (Pitman, 2003).

Processes in the atmosphere are characterised by aerodynamic resistance r_a ($\mathrm{s\,m^{-1}}$) parameter, i.e. it opposes the transfer of water vapour from the surface-air interface to air at the reference level chosen in the atmosphere (Ducoudré et al., 1993):

$$r_a = \frac{1}{C_d V_a} \tag{3.2}$$

where C_d (-) is the surface drag coefficient and V_a is the wind speed($\mathrm{m\,s^{-1}}$). Two main fluxes at the surface using the aerodynamic resistance are latent heat and sensible heat. Most models estimate the latent and sensible heat in the atmosphere at reference height based on Monin-Obukhov similarity theory i.e. the dimensionless mean horizontal wind speed, mean potential temperature, and mean specific humidity profile gradients depend on unique functions depending on Monin-Obukhov length. This theory forms the basis for estimating kinematic momentum flux, sensible heat flux, and vapour flux, all of which are applied to the surface layer. A detailed description could be found in Oleson et al. (2010).

There are four representations of latent heat ($\mathrm{W\,m^{-2}}$) models that have been summarised by Merlin et al. (2016):

$$LH = \begin{cases} \dfrac{e^*(T_s) - e_r}{r_s + r_a}\dfrac{\rho c_p}{\gamma} & Unmodified\ evaporation \\ \dfrac{\alpha e^*(T_s) - e_r}{r_a}\dfrac{\rho c_p}{\gamma} & Vapour\ pressure\ limited \\ \beta * \dfrac{e^*(T_s) - e_r}{r_a}\dfrac{\rho c_p}{\gamma} & Potential\ evaporation\ limited \\ min(LE_p, \beta * \dfrac{e^*(T_s) - e_r}{r_a}\dfrac{\rho c_p}{\gamma}) & Supply\ demand\ threshold \end{cases} \tag{3.3}$$

where $e^*(T_s)$ (Pa) is the saturated vapour pressure at T_s(K), e_r (Pa)is the vapour pressure at reference height. $\gamma(\mathrm{Pa\,K^{-1}})$ is the psychrometric constant, r_s ($\mathrm{s\,m^{-1}}$) is the surface resistance to heat transfer of water from the surface to air, r_a ($\mathrm{s\,m^{-1}}$) is the air resistance calculated in Equation 3.2, ρ ($\mathrm{kg\,m^{-3}}$) is the density of air, C_p ($\mathrm{J\,kg^{-1}\,K^{-1}}$) is the specific heat capacity of air. The second type of evaporation uses α. It is the factor for scaling saturated vapour pressure down to actual vapour pressure at the soil surface (ranging from 0-1); other terms are the same as the unmodified version. The third type uses β, where β is the factor for scaling potential evaporation down to actual evaporation (ranging from 0-1). The fourth type uses a so-called demand-supply Priestley-Taylor method where LE_p ($\mathrm{W\,m^{-2}}$) is the potential soil evaporation, and LE_{max} ($\mathrm{W\,m^{-2}}$) is the maximum soil-limited water flux from below the surface; the value of LE_{max} can be found either physically or empirically (Merlin et al., 2016). LE_p is estimated using the aerodynamic, Penman, or Priestley-Taylor methods (Merlin et al., 2016).

The sensible heat representation is:

$$H = \frac{T_s - T_r}{r_a}\rho C_p \tag{3.4}$$

where T_s is the surface temperature (K), T_r is the reference temperature (K) at a given height (usually 2 m), ρ is the density of air ($\mathrm{kg\,m^{-3}}$), C_p is the heat capacity of air ($\mathrm{J\,kg^{-1}\,K^{-1}}$).

Latent heat and sensible heat are the two surface energy flux terms. SVAT models typically describe these fluxes (Pitman, 2003; Dickinson et al., 1991; Liang et al., 1994; Famiglietti and Wood, 1991) using the relationships described above, albeit they might

include minor differences as pointed out by Merlin et al. (2016)

3.2.1.2 Vegetation

Vegetation layer is crucial for partitioning of the energy and water at the surface. It forms a pseudo-storage with its canopy layer that can hold water. Hence it impacts the water budget and the energy balance. The processes summarizing the fluxes at the vegetation layer are shown in Figure 3.2. The main impact of vegetation is on the energy balance through canopy layer resistances on the latent heat and sensible heat. There is also incident solar radiation resulting from the radiation reflection. It impacts the surface roughness, hence, the latent heat. In the vegetation layer, absorbed energy and water fluxes are utilised to sustain the life of the vegetation cover. Transpiration and photosynthesis are subject to seasonality and highly variable in capacity due to physiological and phenological differences between different species of vegetation.

Initial work on introducing the vegetation layer into land surface models is done by Deardorff (1978). A set of pedo-transfer functions have been proposed by Bonan et al. (2002) and are now widely used to represent the vegetation layer in SVAT models. Namely: soil resistance, plant resistance, and bulk stomatal resistance (Dickinson et al., 1991). These resistances determine the amount of energy partitioned by the surface, vegetation layer, and ground.

Water flows through stomate of the vegetation. Leaf conductance g_{st} ($\mathrm{mol\,m^{-2}\,s^{-1}}$) (Ball et al., 1987) is used to represent this phenomenon:

$$g_{st} = 1/r_s = m\frac{A_n h_s}{c_s} + b \tag{3.5}$$

Where, A_n ($\mu\mathrm{mol\,m^{-2}\,s^{-1}}$) is the net leaf assimilation rate, c_s (ppm) is the partial pressure of CO_2 at the leaf surface, h_s ($\%$) is the relative humidity at the leaf surface, m is an empirical coefficient, and b is the minimum stomatal conductance (Krinner et al., 2005). The stomatal conductance is integrated over the biomass using Leaf Area Index (LAI). LAI is a variable that evolves throughout the seasons as a function of the vegetation type. Often it is prescribed to SVAT models; however, recent developments

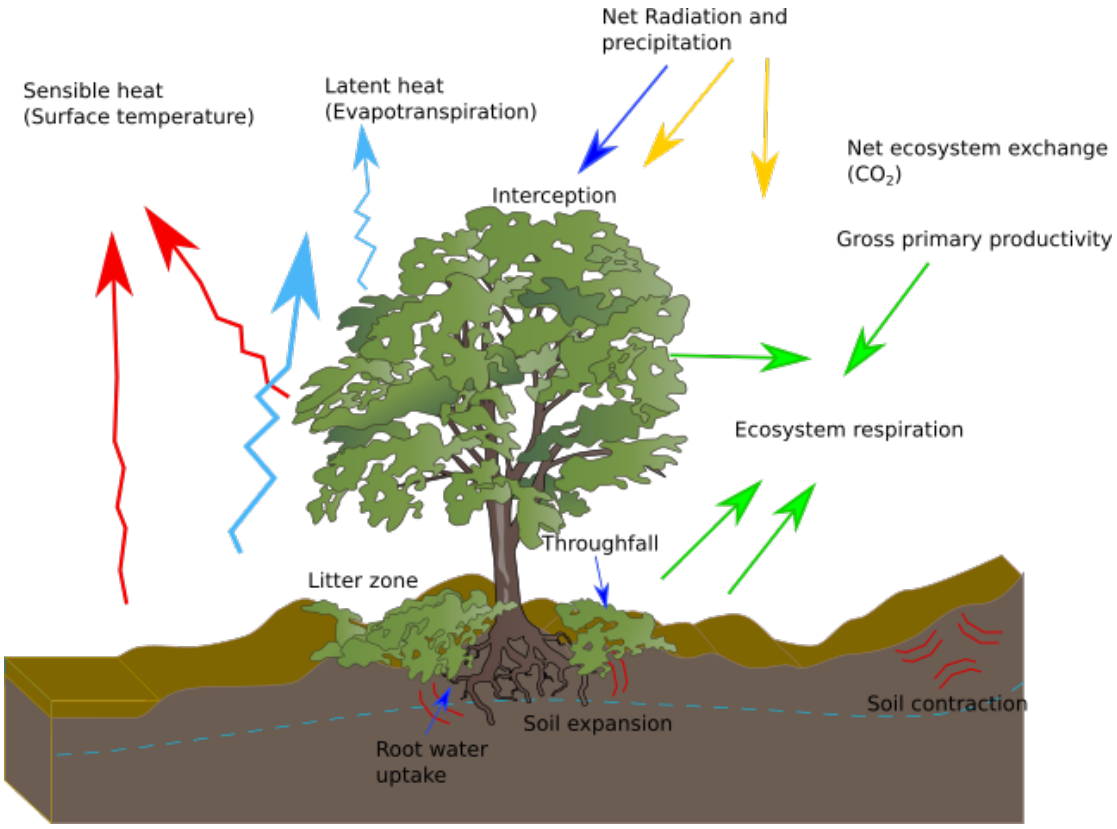

Figure 3.2 The heat and water flux processes in the vegetation layer based on the description by Krinner et al. (2005).

enable LAI to be dynamically simulated and re-evaluated on a yearly basis (Sitch et al., 2003). The canopy resistance (Krinner et al., 2005) is:

$$g_c = \int_0^{LAI} g_{st}(l) * dl \tag{3.6}$$

where l is the cumulative LAI, It increases from the canopy top(l=0) to the canopy bottom (l = LAI).

3.2.2 River

Water and energy fluxes in stream compartment of the hydrosystem depend on various physical processes as shown in Figure 3.3. Processes in the stream are controlled by the river characteristics such as geology, geomorphology, and sinuosity of the river. Climate exerts a first-order influence on the water and energy fluxes in the system, followed by the reach scale and local scale processes (Hannah et al., 2008). Precipitation brings advective energy to the stream, along with the short-wave and long-wave radia-

tion. The main inputs are incident short-wave and long-wave radiation, condensation, friction at channel bed and banks, chemical and biological processes, precipitation, and groundwater input. Losses are the reflection of solar radiation, emission of long-wave radiation, and evapotranspiration. Sensible heat and water column-bed energy transfers may cause gains or losses in the system. Advective energy fluxes are transferred through in and outflow of channel discharge, hyporheic exchange, groundwater up and down-welling, tributary inflows and precipitation. A heat balance concept can be established to describe the energy transfer relationship in the river (Caissie, 2006):

$$H_{total} = H_a + H_{net} + H_l + H_s + H_{bh} + H_f \tag{3.7}$$

where H_a ($\mathrm{W\,m^{-2}}$) is advective heat due to groundwater discharge, precipitation, hyporheic exchange, and longitudinal heat flow in river body, H_{net} ($\mathrm{W\,m^{-2}}$) is the net radiation influx into river, H_l ($\mathrm{W\,m^{-2}}$) is latent heat, H_s ($\mathrm{W\,m^{-2}}$) is sensible heat, H_{bh} ($\mathrm{W\,m^{-2}}$) is heat exchange from the riverbed, H_f ($\mathrm{W\,m^{-2}}$) is friction at the bed and banks.

Modifications to the energy balance equation can be made depending on the availability of the data or the purpose of the study. For example, studies focusing on the air temperature-river temperature often consider no-flux at the riverbed; however, studies on hyporheic zone exchanges include the riverbed heat transfers in the models. Large scale models neglect the advective fluxes at the riverbed and consider only conductive fluxes.

Energy budget is the basis of river temperature description (Eq. 3.7). After the estimation of the net energy influx(or outflux) is done, river temperature is estimated by Advection-dispersion equation (Eq. 3.8). There are many variations to this equation trying to include the variability in river discharge, channel morphology, or compute heat transport in multiple dimensions. Advection-dispersion equation for a one dimensional open channel of a fixed cross-section and flow (Sinokrot and Stefan, 1993) is given as:

$$\frac{\delta T_w}{\delta t} = -U\frac{\delta T_w}{\delta x} + D_L\frac{\delta^2 T_w}{\delta x^2} + \frac{H_{total}}{\rho * c_p * d} \tag{3.8}$$

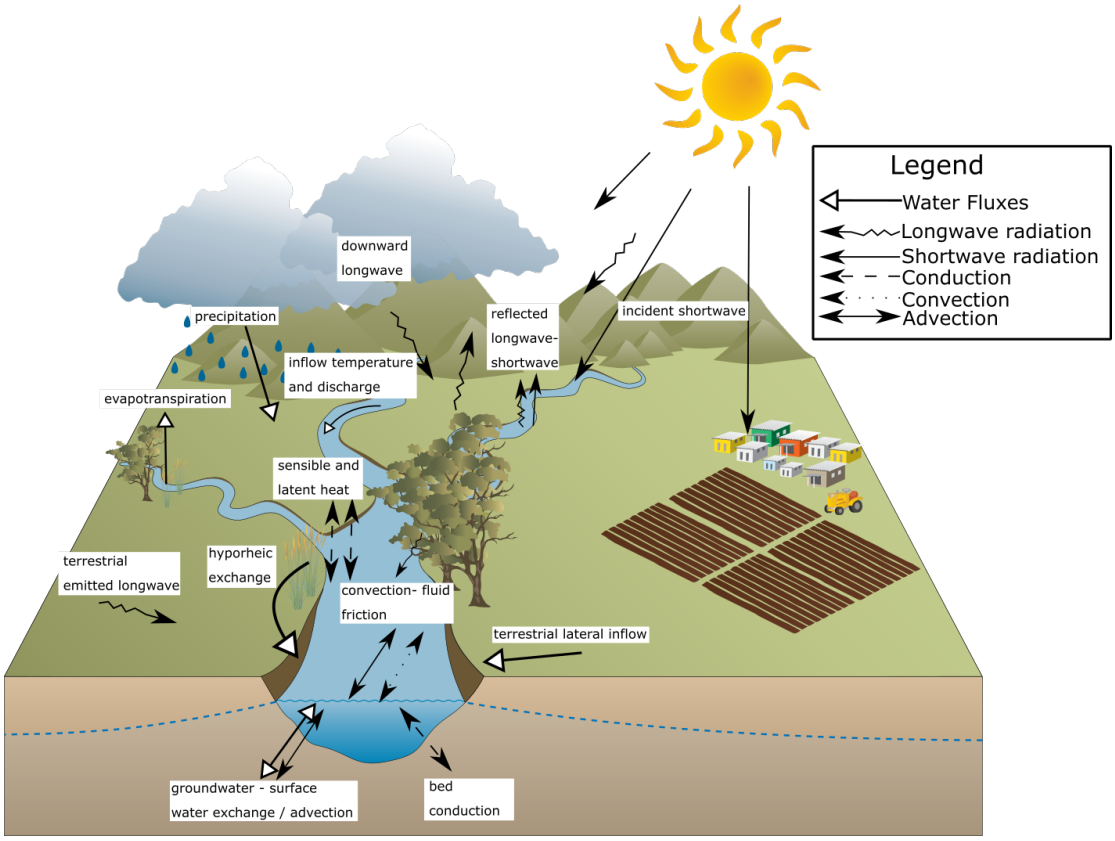

Figure 3.3 Representation of the energy and hydrological fluxes controlling river water temperature.

where T_w is water temperature (°C) at time t, U is the mean channel velocity ($\mathrm{m\,s^{-1}}$), x is the streamwise distance (m), D_L is an empirically derived longitudinal dispersion coefficient ($\mathrm{m\,s^{-2}}$), ρ is the density of water ($\mathrm{kg\,m^{-3}}$), c_p is the specific heat of water and d is the mean channel depth (m). The equation mentioned above (Eq. 3.8) allows for Eularian computation of river temperature, however, it can be rearranged in the form of spatial Lagrangian framework. This equation assumes a well-mixed channel with no notable lateral temperature gradients. Given the assumptions, elucidated equations (Eq. 3.7 and 3.8) can be used to simulate water temperature as a function of hydro-meteorological and geomorphological input.

3.2.3 Ground heat transfer

Heat fluxes at the subsurface can be summarised by two main inputs, the convection from Earth's mantle and crust, and heat input from the surface. The heat input at the surface results from two main sources, advective and conductive heat input. Advective

input is the water that infiltrates and transfers heat from the surface. Conductive heat fluxes result from the transfer of solar radiation into the subsurface through soil, vegetation and river interface. For global-scale studies, the advective heat fluxes at the subsurface are neglected, but at the basin-scale, advective fluxes might play an important role (Clark et al., 2015). At larger scales than hydrosystem, groundwater heat transport is simulated in 1-D to simplify the computing. Hydrosystem and basin scale studies are subject to uncertainties. Therefore, 2-D or 3-D representations of ground heat flow would be better suited. Moreover, recharge and stream-aquifer exchanges contribute to the heat budget through advective fluxes. The heat transfer in the ground (Domenico and Schwartz, 1998) is represented as:

$$G_r = -\lambda_s(x,t,\theta)\frac{\delta T(x,t)}{\delta z} - \rho_w c_w V \delta T \tag{3.9}$$

where $\lambda_s(x,t)$ ($\mathrm{W\,m^{-1}\,K^{-1}}$) depends on the mineral properties of soil and θ $\mathrm{m^3\,m^{-3}}$ is the time-varying water content in the ground, z (m) is the depth, $\delta T(x,t)$ (K) is the change of temperature by depth and time, ρ_w is the density of water ($\mathrm{kg\,m^{-3}}$), c_w is the heat capacity of the water ($\mathrm{J\,kg^{-1}\,K^{-1}}$), V is the groundwater velocity ($\mathrm{m\,s^{-1}}$) over a cross-section of the medium, depending on the hydraulic head distribution. The surface temperature is given as a boundary condition, and heat variation with depth is obtained.

3.3 The link between water and energy fluxes

Energy and water processes are separately shown in Figure 3.4. The inherent link between these fluxes is shown in Figure 3.5 via the energy and water budget. Evapotranspiration is crucial for the water budget and is controlled by the availability of energy and water in the hydrosystem.

3.4 Water fluxes

Water fluxes in the hydrosystem can be represented by the water balance equation:

$$P = E + R + R_{inf} + \delta S \tag{3.10}$$

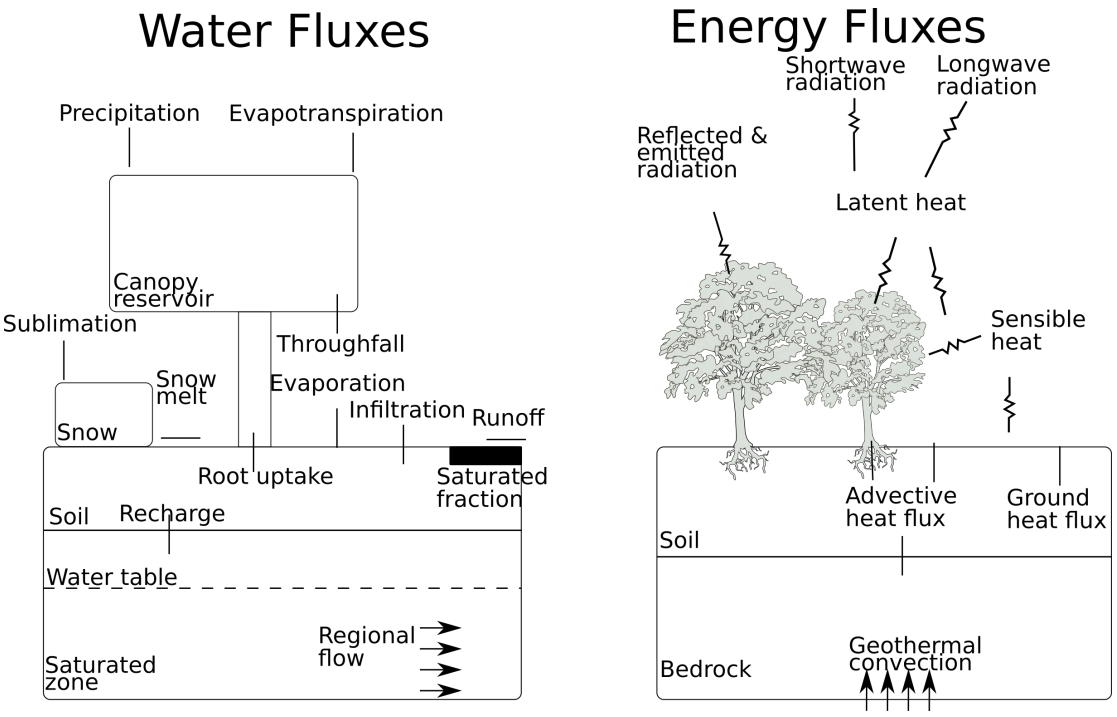

Figure 3.4 A categorised representation of water and energy fluxes in the hydrosystem.

where P is the precipitation, E is the evapotranspiration, R is the runoff component, R_{inf} is recharge, and δS is the change in the water storage as soil moisture. Evapotranspiration is a combination of the evaporation from the bare soil, from the canopy layer, and the transpiration from vegetation. Photosynthesis also consumes water but it is limited and therefore negligible.

3.4.1 Surface processes

3.4.1.1 Atmosphere

Precipitation is the main independent variable that generates runoff, recharge and soil moisture in the unsaturated zone and brings advective energy to the hydrosystem (Figure 3.4). It is conceptualised in two terms: rainfall and snow. Depending on the temperature regime, snow forms storage of water in the solid phase, which eventually melts, and is joined to surface or subsurface water budget. Excess rainfall is partitioned by recharge to the aquifer, runoff to stream, and infiltration to soil moisture. A negligible portion of water is withheld within the canopy layer. Its spatial and temporal distribution plays a vital role in surface processes, aquifer recharge and the water cycle. The

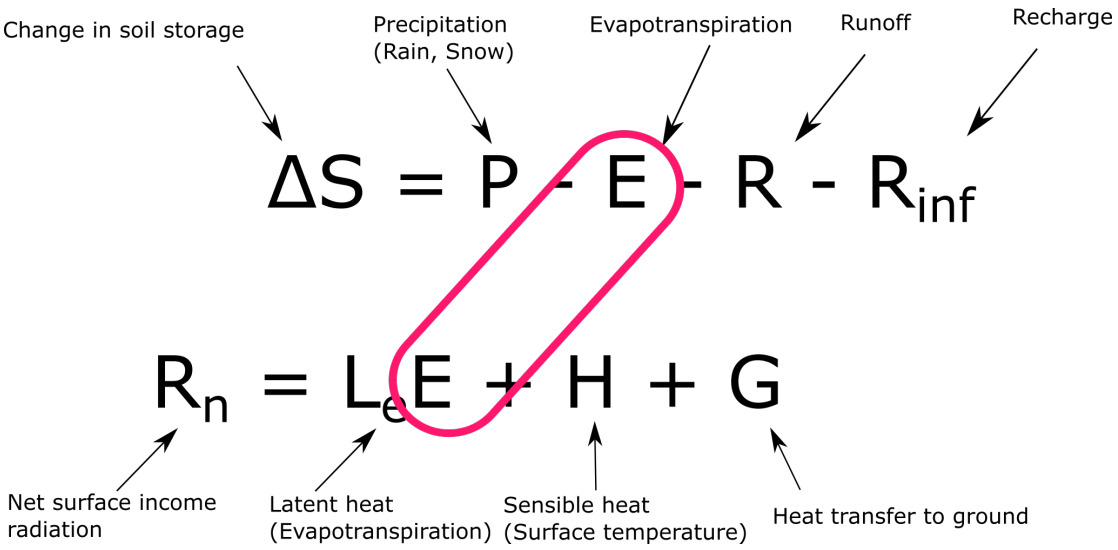

Figure 3.5 The inherent connection between water and energy fluxes. Above formulation describes the water balance, whereas, lower formulation describes the energy balance

amount, intensity, and frequency of precipitation are subject to many factors.

3.4.1.2 Vegetation

Vegetation (i.e. canopy layer) plays an important role in the partition of precipitation, and evapotranspiration as shown in Figure 3.2. Three reasons can explain this importance. First, vegetation forms a canopy layer that holds water as a storage (Dickinson et al., 1993). Second, the stored water is released through plant respiration, transpiration or evaporation. Third, a fraction of water and absorbed energy is used for the photosynthesis of plants. The volume of biomass is subject to seasonal and yearly variations, which modifies the water storage capacity in the canopy layer. Agriculture practices such as irrigation and harvest also modify the vegetation layer and can change the water demand. Therefore, the temporal evolution of the vegetation layer, senescence processes, and litter processes are also crucial for multi-year studies.

Soil moisture is water contained in the soil column (Seneviratne et al., 2010). Groundwater interacts with soil moisture through the water exchanges between the unsaturated zone and the underlying aquifer; however, these processes are not amply presented in SVAT models (Niu et al., 2007). Fan et al. (2007) shows the importance of shallow groundwater levels on the water and energy fluxes at the surface.

Root water uptake is essential when characterizing the impact of vegetation on groundwater level and soil moisture. The root zone is found to have a profound relationship with the groundwater levels which eventually impacts the moisture present in the soil (Fan et al., 2007; Niu et al., 2007). The root water update is represented in general by using a macroscopic approach described by Feddes et al. (2001) (Clark et al., 2015) with the following equation:

$$S_{et,j} = \frac{f_{roots,j}\beta_{v,j}}{\beta_v} \frac{Q^{veg}_{trans}}{L_{vap}\rho_{liq}\delta z_j} \tag{3.11}$$

where Q^{veg}_{trans} ($\mathrm{W\,m^{-2}}$) is the transpiration latent-heat flux, $\beta_{v,j}$ is the soil water stress factor for the jth soil layer, β_v is the total water availability stress factor, $f_{roots,j}$ is the fraction of roots in the jth soil layer, δz_j is the depth of the jth soil layer (m), and L_{vap} ($\mathrm{J\,kg^{-1}}$) and ρ_{liq}($\mathrm{kg\,m^{-3}}$) are the latent heat vaporisation and the intrinsic density of liquid water, respectively. Soil water stress factor in Eq. 3.11 is parameterised as a function of volumetric water content (de Rosnay et al., 2002; Wang et al., 2011):

$$\beta_{v,j} = \frac{\theta_j - \theta_{wlt}}{\theta_{crit} - \theta_{wlt}} \tag{3.12}$$

where θ_{crit} and θ_{wlt} define the soil moisture content when plants become stressed and the residual soil moisture content, respectively. Total water availability defined in Equation 3.11 is:

$$\beta_v = \sum_j f_{roots,j}\beta_{v,j} \tag{3.13}$$

which is used in the parameterisations of stomatal conductance (Clark et al., 2015). The vertical root distribution in these models is parameterised (de Rosnay and Polcher, 1998) as:

$$f_{roots}(z) = e^{-cz} \tag{3.14}$$

where $f_{roots}(z)$ defines the fraction of roots below depth z, and the parameter c is fit for different vegetation types. Another common representation framework for the root zone is presented by Jarvis (1989) and Feddes et al. (2001). Vegetation representation

plays is crucial in correctly estimating canopy layer reservoir, water budget and energy balance. It creates the sub-grid variability for the models as well.

3.4.1.3 Topsoil hydrology

The water that reaches to surface soil might infiltrate to ground, excess water might saturate the underlying ground and generate runoff (Horton, 1931), or intense water infiltration might overload the infiltration capacity of soil and generate runoff (Dunne and Black, 1970). The unsaturated zone is determined by the thickness of soil from the surface to the water table. This zone hosts the vegetation (mainly the root zone) and may host considerable soil moisture. The amount of water available on the surface and within top soil determines the potential of evapotranspiration (Penman, 1948). Hydrological fluxes at the soil column are critical for improving representation of soil moisture-atmosphere feedbacks. Soil moisture, in essence, impacts the partitioning of surface net radiation into sensible and latent heat flux (evaporation), which eventually determines the surface temperature, boundary layer properties, and atmospheric processes such as cloud formation and precipitation (evaporated water as an input to precipitative fluxes) (Seneviratne et al., 2010).

An increase in latent heat reduces the soil moisture levels and raises the water vapour in the atmosphere, forming the clouds for precipitation and increasing the tendency for vegetation formation and soil moisture. If the sensible heat amount increases due to low soil moisture, the humidity in the air decreases, resulting in less rain and reduced plant water uptake. Accurate simulation of soil moisture is also vital for agriculture (de Noblet-Ducoudré et al., 2004). It has been subject to integrated model studies as well.

The available water at the surface to infiltrate is stated as:

$$q(z = 0) = P_x - e_s - q_{rf} \tag{3.15}$$

where P_x is the flux of water ending up at the soil surface ($\mathrm{kg\,m^2\,s^{-1}}$), including throughfall, when there is no snowpack, e_s is the bare soil evaporation loss ($\mathrm{kg\,m^2\,s^{-1}}$),

q_{rf} is the surface runoff ($\mathrm{kg\,m^2\,s^{-1}}$). There are four main approaches used in the expression of runoff processes:

$$q_{rf} = \begin{cases} 0 & Zero\ runoff \\ P_x F_{sat} + (1 - F_{sat}) max(0, P_x - i_{max}) & Mixed\ infiltration\ and\ saturation\ excess \\ \dfrac{P_x^2}{P_x + I_c} & Infiltration\ excess \\ I_0 - K_i^{int}(1 - exp(-I_0/K_i^{int})) & Saturation\ excess \end{cases} \tag{3.16}$$

where i_{max} is the maximum infiltration rate ($\mathrm{kg\,m^2\,s^{-1}}$), parameterised as a function of volumetric water content or liquid water matric potential in the upper soil layer(s). F_{sat} is the saturated fraction of the catchment, and I_c is the infiltration capacity ($\mathrm{kg\,m^2\,s^{-1}}$), parameterised as a function of the soil moisture deficit and the saturated hydraulic conductivity (Clark et al., 2015). The fourth equation is described in ORCHIDEE (Krinner et al., 2005), which it uses the infiltration flux (I_0) from the surface and hydraulic conductivity of each layer (K_i^{int}) to estimate saturation excess runoff.

Rate of change in volumetric liquid water content (Clark et al., 2015) is:

$$\frac{\delta\theta}{\delta t} = -\frac{\delta q}{\delta z} + S_{etr} + S_{lf} \tag{3.17}$$

where θ is the volumetric liquid water content, q is the vertical flux of liquid water ($\mathrm{m\,s^{-1}}$), S_{etr} is the sink term for evapotranspiration (i.e. root water uptake), and S_{lf} is the source-sink term for the lateral flux of liquid water ($\mathrm{s^{-1}}$). In many models, S_{lf} is equal to 0; hence lateral fluxes are not accounted for. Therefore, q (i.e. vertical flux of liquid water) is represented as a function of volumetric liquid water content:

$$q(z) = -K\frac{\delta\phi}{\delta\theta}\frac{\delta\theta}{\delta z} + K \tag{3.18}$$

where $K = f(\theta)$ is the hydraulic conductivity ($\mathrm{m\,s^{-1}}$) and $\phi = f(\theta)$ is the liquid water metric potential (m) (Mualem, 1976; Van Genuchten, 1980).

There is an inherent connection between soil hydraulic conductivity (K), porosity

(θ), and matric potential (ϕ). There are several models describing this relationship in the models such as: Clapp and Hornberger (1978), Van Genuchten (1980), Brooks and Corey (1964). The Van Genuchten-Mualem relationships for saturation-pressure and relative permeability-saturation are:

$$s(p) = \frac{s_{sat} - s_{res}}{[1 + (ap)^n]^{(1-1/n)}} + s_{res} \tag{3.19}$$

$$k_r(p) = \frac{(1 - \frac{(ap)^{n-1}}{[1 + (ap)^n]^{(1-1/n)}})}{[1 + (ap)^n]^{(1-1/n)/2}} \tag{3.20}$$

where a and n are soil parameters, s_{sat} is the saturated water content, and s_{res} is the residual saturation.

The boundary conditions of these equations are the soil surface fluxes such as infiltration of water into soul profile, and soil bottom fluxes such as recharge (drainage). The bottom boundary condition equation (Clark et al., 2015) is given as:

$$q(z = z_{bottom}) = \begin{cases} c_d K_i & flux\ boundary\ condition \\ -K_{sat}\dfrac{-\phi(\theta_i)}{z_u - z_i} + K_{sat} & head\ boundary\ condition \end{cases} \tag{3.21}$$

where z_{bottom} is the depth of the soil (m) (i.e. the depth of the water table for the head boundary condition), z_i is the depth of the lowest soil layer (m), K_i is the hydraulic conductivity of the lowest soil layer ($\mathrm{m\,s^{-1}}$), K_{sat} is the saturated hydraulic conductivity ($\mathrm{m\,s^{-1}}$), θ_i is the volumetric liquid water content of the lowest soil layer, and c_d is a parameter that controls the rate of flow at the lower boundary.

3.4.2 River

Stream modelling at the basin scale focuses on the processes that occur within the stream, at the interface of stream-atmosphere, the interactions between groundwater-stream (hyporheic flow), and stream-surface interactions (agriculture, surface runoff, sewage discharge) (Caissie, 2006; Webb et al., 2008). There are also studies on sedi-

mentary transport, hydrodynamics of the stream, and mechanical processes; however, these processes are not part of this report.

The main hydrological processes within the stream are the surface water inflows, the groundwater baseflow, evaporation from the water surface, hyporheic flows. This is controlled by factors such as the morphology of the stream, the amount of seepage and runoff from the watershed, the loss to evaporation (hence, shading plays a role), bank vegetation. The discharged water is gathered by two main processes: subsurface seepage and surface runoff. Subsurface seepage is driven by the interactions between groundwater and stream, and interactions between unsaturated zone-stream.

Groundwater-stream interacts in three ways (Brunner et al., 2009): streams gain water (the bank water level is higher than the stream water level), streams lose water (the stream water level is higher than the bank water level, connected, or disconnected), or they do both (while connected at some reaches, and disconnected at other reaches in the stream). This set of interactions plays an important role in the river water budget and energy balance. The state of connectedness is a dynamic phenomenon, and it may vary depending on the several factors such as precipitation and hydrological characteristics of the streambed. However, most streams gain water from groundwater. The input of groundwater into the stream is called base flow. Base flow is estimated using mainly hydrograph separation techniques and reflects the seepage processes at the interface.

The percolating water mainly infiltrates into groundwater; however, depending on the relief and proximity to the stream, the percolating water in the unsaturated zone might inflow into the stream. In the case of gaining stream, the unsaturated zone might act as bank storage and hold a significant portion of water as a reservoir due to elevated hydraulic heads.

The input from the surface to the stream is through the surface runoff process, i.e. the flow of excess water that can not percolate through the surface into a stream. It is controlled by a number of factors such as, morphology of the surface, relief difference (higher relief difference causes lower infiltration and higher runoff), hydrodynamical characteristics of the surface and unsaturated zone (low hydraulic permeability generates low infiltration and more surface runoff) and vegetation (which acts as an obstacle

against surface runoff, increases porosity and permeability at unsaturated zone, leading to higher infiltration capacity). This process intensifies during storm events as the limit of infiltration can be reached and excess water runoffs into the stream. The solution for water fluxes in the river is mainly conducted by 1-D Saint-Venant equation, which uses momentum conservation, as:

$$\frac{\delta A}{\delta t} + \frac{\delta Au}{\delta x} = 0 \tag{3.22}$$

$$\frac{\delta u}{\delta t} + u\frac{\delta u}{\delta x} + g\frac{\delta h}{\delta x} + g(S_f - S) = 0 \tag{3.23}$$

where *x* is the space coordinate along the channel axis, *t* denotes time, $A_{x,t}$ is the cross-sectional area of the flow at location x, $u_{x,t}$ is the flow velocity, $h_{x,t}$ is the water elevation, and $\gamma_{x,t}$ is the wall shear stress along the wall perimeter $P_{x,t}$ of the cross-section at x, *S* is the bed slope and S_f is the friction slope; ρ is the fluid density, and g is the gravitational acceleration.

The relationship between the wall shear stress γ and the flow velocity *u* can be related using Darcy-Weisbach equation, Manning formula, or Chézy formula.

3.4.3 Groundwater Flow

The water table is part of the soil where the soil is saturated completely. The volume of soil below the water table is called an aquifer. Water table level is variable between seasons, as a function of climate variability, regional flows, or exploitation. Aquifers provide water supply to the communities mainly in arid and semi-arid regions (Famiglietti, 2014). Therefore, correct estimation of the storage carries essential importance. The water fluxes in aquifer systems are the regional flow of water due to gravitational forces, exchanges between overlying unsaturated zone through recharge and hyporheic exchanges at the basin scale. Major groundwater flows are represented in Figure 3.6. Flow into the ocean and sea also carries importance for aquifers bordering them; however, this concept is not part of this report.

The modelling approach of this compartment is usually treated by a variable water table approach with a mixed form of Richards' equation as follows:

$$\frac{\delta[s(p)\rho\phi]}{\delta t} - \nabla.[\frac{k(x)k_r(p)\rho}{\mu}(\nabla.p - \rho g \nabla.z)] = q \tag{3.24}$$

where s(p) is the water saturation for hydraulic pressure p, ρ is the water density, ϕ is the effective porosity of the medium, k(x) is the absolute permeability of the medium, μ is the viscosity, $k_r(p)$ is the relative permeability, q represents any source terms, and z is the elevation. It can be used to model both unsaturated and saturated fluxes. Depending on the computational resources and aim of the study, this equation can be employed in 1-D or 3-D. The water table is variable in this approach, and water is assumed to be well fixed. This indicates the variation in the water density does not play a role in the flow dynamics.

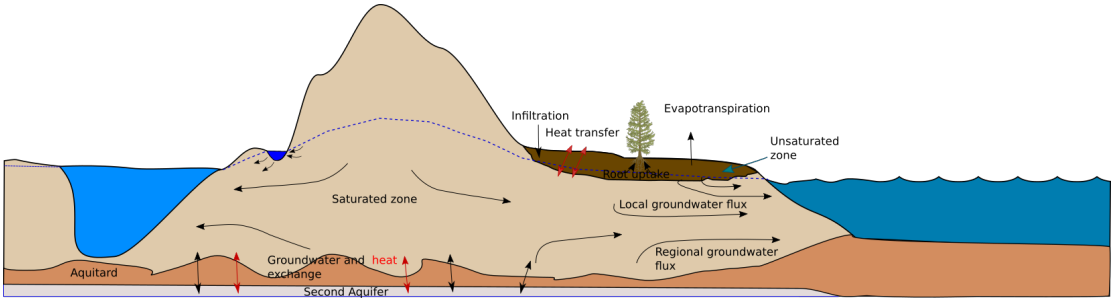

Figure 3.6 Groundwater processes with connection to surface.

3.5 Synthesis: a coupled framework

The processes of water and energy balances are presented in this chapter. There is an inherent link between the energy and water fluxes. The energy at various compartments of the hydrosystem drive the physical processes starting with evapotranspiration for the hydrological cycle.

Decades of research allowed us to explicitly represent the physical processes of both water and energy cycle. Although the studies of surface and atmosphere readily combine water and energy fluxes, the groundwater community uses only the evapotranspiration term to include the energy in the water cycle studies. Similarly river heat transport studies often neglect the groundwater heat part. However, a coupled framework that reconciles water with energy and surface with groundwater and river could enable us

to quantify the interactions of each compartment of an hydrosystem and improve our understanding.

Chapter 4

Hydrosystem modelling

4.1 Introduction

In this chapter, the modelling approaches of hydrosystem are reviewed. Firstly, modelling approaches for each compartment of a hydrosystem are investigated. This chapter describes how processes within each compartment of a hydrosystem are represented in these models. The main compartments of the hydrosystem can be divided into three parts: surface, river, and groundwater. The surface model section is dedicated to Soil-Vegetation-Atmosphere-Transfer (SVAT) models which aim to describe the surface processes in process-based applications. River models are wide-ranging, while the ones that simulate river temperatures can be grouped into regression, stochastic and deterministic models. The groundwater models section is dedicated to process-based groundwater models that can simulate the water budget at the regional scale.

Integrated modelling approaches and their implementations are discussed as well. These approaches include representations of SVAT-aquifer, SVAT-stream, stream-aquifer, and aquifer-aquifer interfaces where interactions between different compartments are described. Finally, a synthesis of integrated modelling approaches is made where different integrated hydrosystem modelling approaches are discussed.

4.2 SVAT

Integration of the physical and thermal fluxes in atmospheric land surface models has long been established in the literature (Manabe, 1969; Pitman, 2003). These models now incorporate the complex interactions on the land surface as well as sub-grid het-

erogeneity and plant processes in SVAT models (Franks et al., 1999; Krinner et al., 2005). They aim to represent physical relations and processes in the atmosphere and land surface by a set of governing equations described in Chapter 3. This process-based description attempts to tackle the problems such as water management, climate change, pollution, and land and crop management by representing the processes separately in the applications. In a review paper, Pitman (2003) explained the need for SVAT models and their evolution in terms of process representation. Clark et al. (2015) compared the different SVAT models in their representation of the surface processes and groundwater representation. In this section, a brief introduction to processes is addressed, several SVAT models are summarised, and their process representations and possible issues related to sub-grid heterogeneities and equifinality are discussed.

Efforts of energy-based land surface model development rely on the evapotranspiration studies of Penman (1948) (later known as the Penman-Monteith approach with the improvement of surface resistance by Monteith (1965)). The earliest land surface models combined this approach with a "bucket" model (Manabe, 1969). Starting with these approaches, different SVAT models emerged from various work groups studying water cycle and atmosphere (Pitman, 2003).

Process representation in SVAT models can be categorised into four groups: atmosphere, vegetation, surface, and unsaturated zone. Recently, some models have taken into account groundwater dynamics; however, these approaches have simple definitions (Clark et al., 2015).

There have been numerous applications of SVAT models (Tables 4.1, 4.2, 4.3, 4.4). Major developments have been carried out in the representation of surface fluxes, the canopy layer and introduction of CO_2 processes such as photosynthesis. Little importance was given to representation of groundwater fluxes since these models were applied to macroscale surface processes and soil layer (Clark et al., 2015). Moreover, SVAT models generally neglect the urban processes such as irrigation even though recent studies have shown the importance for water balance estimations by Pokhrel et al. (2015).

Model improvements are still made to include additional processes. Some inte-

grated models incorporate saturated flow variability (Maxwell et al., 2014) or macropore representation (Milly et al., 2014) into SVAT models. The importance of routing in the representation of surface fluxes and water storage has been noted by many studies (de Rosnay, 2003; Nguyen-Quang et al., 2018; Arora et al., 1999, 2001). Many SVAT models either do not consider routing in their schemes (CABLE (Kowalczyk et al., 2006), Catchment (Ducharne et al., 2000), JULES (Best et al., 2011), Noah (Ek et al., 2003), HIRHAM RCM (Christensen et al., 1998), NEST (Zhang et al., 2003), RegCM3 (Pal et al., 2007), SiSPAT (Braud et al., 1995), SURFEX (Moigne, 2012), ISBA (Noilhan et al., 1995)) or use 1-D linear or diffusive wave equations to describe river routing (ORCHIDEE (Krinner et al., 2005),VIC (Liang et al., 1994), LEAF (Walko et al., 2000), LM3 (Milly et al., 2014), CLM (Dai et al., 2003), TESSEL (Balsamo et al., 2009)) At the global scale, coarse representations of routing might be acceptable, yet, at the basin scale, certain important processes are neglected, such as hyporheic flow and shading, which impacts the water and energy balance of the basin.

The representation of the vegetation has been mainly done with the help of the Plant Functional Types (PFTs) concept. Other applications, such as Vegetation Area Index (VAI) are introduced by SVAT model NEST (Zhang et al., 2003). In this concept, each plant group has a distinct set of parameterisations ranging from stomatal resistance to vegetation height that is used to estimate photosynthesis, water uptake, canopy reservoir, LAI, evaporation, and transpiration. New generation models such as ORCHIDEE (Krinner et al., 2005), LM3 (Milly et al., 2014), and RAMS-Hydro (Miguez-Macho et al., 2007) are coupled with biophysical models such as LPJ (Sitch et al., 2003) or LM3V (Shevliakova et al., 2009) to include full biosphere dynamics with carbon dynamics with hydrological feedback.

These models are created to represent regional and continental hydrology; however, there have been studies to represent catchment scale fluxes (Ducharne and Laval, 2000). SVAT models can have large biases on the discharge estimation at the basin scale. It can be attributed to forcing data input rather than model performance (Zhou et al., 2018) since input resolution is coarser for basin scale. Although great emphasis has been given to continental-scale SVAT modelling, basin scale studies should also be considered to

understand atmospheric feedback on local aquifers (Clark et al., 2015). The SVAT models RegCM3 and HIRHAM RCM (Christensen et al., 1998) aim to estimate the regional climate feedback at regional scale with a high resolution and limited land surface process representation. Since their main focus is not land surface processes, they represent atmospheric fluxes in more detail, but the land surface processes are not as developed as other SVAT models such as ORCHIDEE, CLM.

Naturally, the surface is subject to horizontal heterogeneities resulting from topography, geology, geomorphology, physical properties of the soil, and land use characteristics. Heterogeneities in the surface cause non-linearities in the physical processes that take place at the surface, and in the soil. SVAT models aim to describe the surface domain in large horizontal grids with resolution often ranging 10-200 km, causing a gross simplification of the simulated domain (Wood et al., 1992). The main driver for this simplification was computational feasibility issues with a higher resolution representation of the complex characteristics. This is still an issue despite considerable improvements in computational power. Several approaches have been proposed in the SVAT models to overcome the discrepancy between the real-case surface and the numerical representation, i.e. sub-grid variability. One approach uses multiple tiles to represent sub-grid heterogeneity (Koster and Suarez, 1994), and another estimates energy balance of snow-covered and snow-free surfaces separately (Takata et al., 2003). Models such as TOPMODEL (Beven and Kirkby, 1979) represent the sub-grid variability by a grid-average infiltration for soil moisture and the water table estimations. Essery et al. (2008) developed new parameterisations that represent the aggregate impact of sub-grid heterogeneities on grid-average fluxes. Although these applications are present, Clark et al. (2015) argue that the main gap in current SVAT models is the representation of heterogeneities in the distribution of soil moisture and water table, meaning that the groundwater dynamics are missing or simplified (Maxwell and Miller, 2005).

The properties of soil and vegetation are generally defined by a grid-based approach with multiple tiles. SVAT models use the grid based system; however, grid sizes start from 0.1°, and soil and vegetation might vary considerably. To overcome this, models use tile systems to represent sub-grid variabilities as in CLM (Dai et al., 2003)

or ORCHIDEE (Ducharne, 2018). CLM uses a hierarchical tile system that lets the modeller define the type of vegetation, agriculture, and anthropological input, whereas ORCHIDEE tile system enables the user to define 15 plant functional types (PFTs) or 12 soil texture types. Soils, similar to the vegetation, are represented by Pedo-transfer functions (PTFs) where each soil texture has distinct hydrological and thermal properties. Estimation of soil properties are difficult and is subject to extensive research Wosten et al. (2001); Vereecken et al. (2010); Schaap and Leij (2000).

Models estimate the fluxes based on this sub-grid variability and take weighted averages for each grid. ORCHIDEE also estimates the fluxes based on the vegetation group such as agricultural, tropical etc.

Certain issues with over-parameterisation, or under-parameterisation of the processes might increase the uncertainty and damage model fidelity (Beven and Binley, 1992). SVAT schemes use complex descriptions of the physical processes. They rely on many parameters, making calibration a difficult task. This is due to the increased degree of freedom in these models; fitting model predictions to calibration or validation can be established in more than one area of the parameter space for a given set of parameters. This problem is called equifinality (Franks et al., 1997). At the regional scale, physical processes depend on topography, soil characteristics, vegetation, and land use parameterisation, each of which varies significantly at the sub-grid scale. Therefore, the 'effective' parameters representing the processes at a grid have higher uncertainty, given that it is possible to obtain simulated fluxes with more than one parameter set. This raises the question of how to reduce parameter uncertainty at regional scale applications and how many different observations from different sources are required to reduce the degree of freedom. (Schilling et al., 2019a; Beven, 2006). The current approach to this problem is to reduce the number of parameters by fixing the insensitive parameter and reducing the dimensionality of the parameterisation. This feat is achieved by conducting a sensitivity test. An additional way to reduce the degree of freedom is to provide additional observation information from different sources, such as incorporating temperature observations, evapotranspiration flux tower data, soil moisture products etc., in addition to the discharge observations at the sub-basin scale.

Indeed, recent studies suggest that temperature could be used to constrain and estimate recharge by using temperature as a tracer (Anderson, 2005).

Table 4.1 Comparison of existing SVAT models by their processes: part 1

Processes/Models	**CABLE**	**Catchment**	**CLM**	**TESSEL**
Discretisation	Finite difference	-	Finite difference	Finite difference
Precipitation	Partitioned based on vegetation fraction until saturation for vegetation, then throughfall	Transferred through an analogous conservative scheme	Partitioned based on vegetation fraction until saturation for vegetation, then throughfall	Partitioned based on vegetation fraction until saturation for vegetation, then throughfall
Interception	No interception	Interception as a function of LAI, transferred to runoff after saturation	Interception as a function of LAI, transferred to runoff after saturation	Interception layer accumulates until saturation, excess water is transferred as throughfall
Evapotranspiration (ET)	Combination of evaporation of soil and vegetation and transpiration with single layer canopy	After Deardorff (1978)	Combination of evaporation from soil vegetation and transpiration	Combination of evaporation from soil vegetation and transpiration
Snow processes	No snow process	Three layer snow model with melting and refreezing	Simple explicit scheme, melt transfers to infiltration and Runoff	Single layer of snow present, melt transfers into runoff
Soil water solution	6 layers - Richard's Equation[a]	1 layer Emp. apprx. 1-D Richard's Equation	10 layers Richard's Equation[a]	4 layers Richard's Equation[a]
Runoff and Infiltration	Unlimited	Saturation-excess runoff	Saturation-excess runoff	Saturation-excess runoff
Routing scheme	None	None	Linear storage-outflow	1-D diffusive wave
Groundwater dynamics	No GW dynamics	Base flow based on TOPMODEL concepts	Base flow based on TOPMODEL concepts	None

Table 4.2 Comparison of existing SVAT models by their processes: part 2

Processes/Models	**JULES**	**LEAF**	**LM3**	**MATSIRO**
Discretisation	Finite difference	Finite difference	Finite difference	Finite difference
Precipitation	Partitioned based on vegetation fraction until saturation for vegetation, then throughfall	Partitioned based on vegetation fraction until saturation for vegetation, then throughfall	Partitioned based on vegetation fraction until saturation for vegetation, then throughfall	Partitioned based on vegetation fraction until saturation for vegetation, then throughfall
Interception	No interception bucket	Interception bucket as a function of LAI	Defined after Deardorff (1978)	No interception bucket
Evapotranspiration (ET)	Combination of evaporation from soil vegetation and transpiration	Combination of evaporation from soils and vegetation and transpiration	Combination of evaporation from soil vegetation and transpiration	Combination of evaporation from soil vegetation and transpiration
Snow processes	Zero-layer and multi layer snow representation is present	Snow cover layer is present, water infiltrates to top soil layer	Snow model is present with fixed # of layers, excess transfers to runoff	Snow module is present by 1-3 layers, energy budget is calculated separately for snow-covered and snow-free surface
Soil water solution	4 layers Richard's Equation[b]	2 soil layers Richard's Equation[a,b]	Arbitrary number of vertical layers, Richard's Equation[a]	5 layers Richard's Equation[a]
Runoff and Infiltration	Saturation-excess runoff	Saturation-excess runoff	Infiltration-excess runoff	Unlimited
Routing scheme	None	1-D diffusive wave	1-D routing	1-D diffusive wave in low slope reaches
Groundwater dynamics	Base flow based on TOPMODEL concepts	Grid-to-grid lateral flow based on Darcy's law	Hillslope flow based on Darcy's Law	Base flow based on TOPMODEL concepts

Table 4.3 Comparison of existing SVAT models by their processes: part 3

Processes/Models	**Noah**	**ORCHIDEE**	**VIC**	**ISBA**
Discretisation	Finite difference	Finite difference	Finite Element	Analytical
Precipitation	Partitioned based on vegetation fraction until saturation for vegetation, then throughfall	Partitioned based on vegetation fraction until saturation for vegetation, then throughfall	Partitioned based on vegetation fraction until saturation for vegetation, then throughfall	Partitioned based on vegetation fraction until saturation for vegetation, then throughfall
Interception	No interception bucket	No interception bucket	Defined after Deardorff (1978)	No interception bucket
Evapotranspiration (ET)	Combination of soil and vegetation evaporation, transpiration	Combination of soil and vegetation evaporation, transpiration	Combination of soil and vegetation evaporation, transpiration	Combination of soil and vegetation evaporation, transpiration
Snow processes	Explicit snow module is present, melt is transferred into surface water budget	Snow process present, detailed in (Wang et al., 2013)	Single layer snow accumulation, zero energy flux lower boundary at snow layer	Snow cover layer is present modeled after (Douville et al., 1995)
Soil water solution	4 layers Richard's Equation[a]	2-11 Layers Richard's Equation[a]	2 layers Richard's Equation[b]	2 layers Richard's Equation[a]
Runoff and Infiltration	Saturation-excess runoff	Based on variability in infiltration and precipitation	Saturation-excess runoff	Saturation-excess runoff
Routing scheme	None	1-D routing	Linear storage-outflow	None
Groundwater dynamics	None	None	Conceptual Bucket below the soil profile	None

Table 4.4 Comparison of existing SVAT models by their processes: part 4

Processes/Models	**NEST**	**RegCM3**	**RAMS-Hydro**	**HIRHAM RCM**	**SiSPAT**	**SURFEX**
Discretisation	Finite difference	Finite difference	Finite difference	Eularian	Implicit finite difference	Finite difference
Precipitation	Partitioned between canopy layer and throughfall as a function of vegetation	Partitioned between canopy layer and throughfall as a function of vegetation	Partitioned between canopy layer and throughfall as a function of vegetation	Partitioned between canopy layer and throughfall as a function of vegetation	Partitioned between canopy layer and throughfall as a function of vegetation	Precipitation transfer to canopy layer, excess is transferred to throughfall
Interception	No interception bucket	No interception bucket	Interception bucket as a function of LAI	A bucket of interception is present as a function of LAI, a percentage evaporates and the rest transpires. Excess is transferred to runoff	A bucket of interception is present as a function of LAI, a percentage evaporates and the rest transpires. Excess is transferred to runoff	Interception present as a function of LAI, modeled after Deardorff (1978)
Evapotranspiration (ET)	Penman-Monteith method (Monteith, 1965)	Combination of evaporation from soil vegetation and transpiration	Combination of evaporation from soil vegetation and transpiration	Combination of evaporation from soil vegetation and transpiration	Combination of evaporation from soil vegetation and transpiration	Combination of evaporation from soil vegetation and transpiration
Snow processes	Snow module is present, excess water transfers into soil if soil is not frozen	Modeled after Anderson and Bisal (1969)	Snow layer is present, melt infiltrates to top soil layer	Documentation missing	No representation	2 layer thermodynamic model present, modeled after Douville et al. (1995)
Soil water solution	3 layers Richards' eq.[a]	None	1 layer Richard's Equation[a]	Var. soil layers Mixed form of Richards' eq.[a]	3 layers Mixed form of Richards' eq.[a]	Variable layer Richards' Eq.
Runoff and Infiltration	Saturation-excess runoff	Saturation-excess runoff	Infiltration-excess runoff	-	Saturation-excess runoff	Modeled after Dümenil and Todini (1992)(VIC parameterisation)
Routing scheme	None	None	1-D diffusive wave	None	None	None
Groundwater dynamics	Base flow based on TOPMODEL concepts	Grid-to-grid lateral flow based on Darcy's Law	None	None	Base flow based on TOPMODEL concepts	None

4.3 River

Early river models studied the air temperature-stream temperature relationships (Cluis, 1972) and heat budget (Brown, 1969), following that, models incorporating processes-based deterministic approach (Sinokrot and Stefan, 1993), stochastic (Caissie et al., 1998), and regression models (Stefan and Preud'homme, 1993) were developed. A vast number of stream models can be grouped into two main approaches: stochastic and regression models (Benyahya et al., 2007), and mechanistic models (Dugdale et al., 2017).

These two approaches differ in their purpose and the amount of data required. Statistical-based approaches are mainly used for large spatial scale models in data-poor regions or water quality analysis. On the contrary, process-based models are data-intensive, and they are used with a motive to understand the processes that drive river temperatures (Dugdale et al., 2017). Albeit data-intensive, process-based models are particularly useful for three main reasons: a) providing insights into process-based drivers of river temperature (Caissie, 2006), b) improving the metrics of larger spatial scale statistically based models (Toffolon and Piccolroaz, 2015), c) predicting hydrological and temperature response of hydrosystem under changing climatic (Loinaz et al., 2014) and land-use (Sun et al., 2015) conditions.

Previous studies that use deterministic heat budget models have various goals that can be summarised as: determining dominant heat fluxes to streams (Caissie et al., 2007; Webb and Zhang, 1997), quantifying stream-groundwater interactions (Loheide and Gorelick, 2005), and assessing stream temperature sensitivity to changing climate (Loinaz et al., 2013) and land use (Sun et al., 2015). Although many models use either process-based approaches (Dugdale et al., 2017) or statistical models (Benyahya et al., 2007), there are hybrid applications that combine the power of statistical tools and data-intensive process-based models (Toffolon and Piccolroaz, 2015).

Process-based stream temperature models with hydrological components are summarised in Table 4.5, 4.6. These models vary in their temporal and spatial scales, flow and heat transport formulations, shading, and radiation inflow approaches. One way

they differ is the description of the routing module in these models. For example, certain models derive the formula based on the dynamic wave approach to model transient storms etc., such as HEC RAS (Brunner, 1995) and Mike 11 (DHI, 2003). Another solution is the kinematic wave approach, where the flow is assumed to be uniform, and the friction slope is approximately equal to the slope of the channel, where the terms representing frictions ($S_f - S = 0$) are simplified. The third assumption is the diffusive wave, where the inertial terms are less than the gravity, friction, and pressure terms. Hence, the terms with gravitational force are equal to 0. MIKE SHE (DHI, 2017), and LISFLOOD (Knijff et al., 2010) are models that use diffusive wave assumption. Several models attempt to model the processes that take place in the river environment (Dugdale et al., 2017). Initially, these models aimed to understand the impact of land use and temperature on fish species (Bicknell et al., 1996; Theurer et al., 1984; Allen, 2008). A number of process-based models (Rutherford et al., 1997) have been developed for stream temperature prediction using well-understood energy budget principles. The Stream Network temperature model (SNTEMP, Theurer et al. (1984)) has been widely used to predict longitudinal stream temperature changes as a result of alterations in flow regimes, dam release, and impacts of canopy modification (Bartholow, 1996) as they incorporate dynamics of riparian vegetation and solar heating. It has applications in the large scale Colorado river basin, and smaller catchment Tucannon River in the U.S. The Hydrological Simulation Program Fortran (HSPF, Bicknell et al. (1996)) simulates the hydrologic and associated water quality processes for land surfaces and streams. The model has been applied to assess the effects of land-use changes, reservoir operations, point or non-point source treatment alternatives, and so forth (e.g. Taylor and Stefan (2009)) developed shade and streambed conduction sub-models and incorporated them within HSPF to explore the interaction between riparian forest management and stream temperature. The WET-Temp model (Cox and Bolte, 2007) is a spatially-explicit, network-based stream temperature model that estimates diurnal stream temperatures for 30-meter long sub-reaches. Contrary to SNTEMP, WET-Temp includes the stream network, unlike the 1-D longitudinal application. Furthermore, the authors acknowledge that several global parameter values obtained through calibration (notably

the width-depth ratio and the volume multiplier) potentially compensate or buffer for physical mechanisms (e.g. hyporheic flow) not explicitly accounted for in the model (Cox and Bolte, 2007). Another GIS-based model LISFLOOD (Knijff et al., 2010), incorporates unsaturated zone dynamics (e.g. soil moisture flow into the stream), including vegetation, to determine flood prediction and climate change scenarios. While these models are significant advances over earlier less mechanistic approaches, they also have considerable input data requirements. Qiu et al. (2019) proposes a hydro-thermal process-based river model estimating the heat and water fluxes at the reach scale. The model includes the surface, river, and groundwater components. The aim is to simulate the reach scale processes, the hyporheic exchanges and the reach scale heat budget.

The summary of process-based models is given in Tables 4.5 and 4.6. Many of those models aim to simulate small-scale or reach-scale processes. However, a process-based regional scale model representing the surface-subsurface interactions is lacking in the literature. This gap must be filled to better understand the mechanism between river water and energy balance and other components of the water cycle. Given that the climate change and land use stresses from groundwater to streams still carry uncertainties, it is an important issue. It would result in a better understanding of the river heat and energy input into groundwater as a buffer zone (Allen, 2008)

Table 4.5 A compilation of numerical river models: part 1

Name	Reference	Flow Equation	Transport	Scheme	Min. Temporal Scale	Spatial Structure	Shading Correction
CEQUEAU	Morin and Paquet (2007)	Saint-Venant formulation	1-D Advection Dispersion	Finite difference	Daily	1-D Gridded	-
Delft3D-FLOW	Deltares (2008)	3-D Momentum	3-D Advection Dispersion	Finite Difference	None	Gridded 2D, 3D	-
DHVSM-RBM	Sun et al. (2015)	Brooks-Corey formulation	Quasi 3-D Transport	Eularian-Lagrangian particle tracking	None	1-D Nodes/segments Lagrangian	Yes
SHADE-HSPF	Bicknell et al. (1996)	2-D Flow		Finite difference	Hourly	1-D Nodes/segments	Yes
RIVERSTRAHLER	Ducharne (2008)	Darcy's law		Statistical	10 day	Basin	No
BasinTemp	Allen (2008)	-	1-D heat balance	GIS-based	Hourly	1-D nodes/segments	Yes
CE-QUAL-W2	Cole and Wells (2006)	Horizontal momentum	Turbulent advection-diffusion	Finite difference	None	Cross-sections with vertical cells(2-D)	Yes
CrUSTe	LeBlanc et al. (1997)	-	Brown's Equation	Finite difference	Hourly	1D nodes/segments	Yes
Heat source	Boyd and Kasper (2003)	Darcy's Flow	1-D Advection Dispersion	Finite difference	Minute	1D	Yes
GIS-STRTemp	Sansone and Lettenmaier (2001)	-	1-D Advection Dispersion	Finite difference	Hourly	1D nodes/segments	Yes
HEC-RAS	Brunner (1995)	1-D Flow	1-D Advection-Dispersion	Finite difference	Minute	1D cross-sections	-
MNSTREM	Sinokrot and Stefan (1993)	-	1-D Advection Dispersion	Finite difference	Minute	1D nodes/segments	Yes
Qual2K	Chapra et al. (2008)	-	1-D Advection Dispersion	Finite elements	None	1D	Yes

Table 4.6 A compilation of numerical river models: part 2

Name	Reference	Flow Equation	Heat transport	Scheme	Minimum Temporal Scale	Spatial Structure	Shading Correction
RMA11	King (1997)	Saint-Venant	1D Advection-Dispersion	Finite elements	None	1D nodes or 2,3D gridded	-
SNTemp	Theurer et al. (1984)	-	1D Advection-Dispersion	Finite difference	Daily	1-D nodes/segments	Yes
Streamline	Rutherford et al. (1997)	-	1D Dispersion	4th order Runge-Kutta	15 minutes	1D nodes/segments	Yes
TVA-RMS	Deas et al. (2003)	Saint-Venant	1D Advection-Diffusion	Finite difference/Holly-Preissman	Hourly	1-D cross-sections	Yes
WAIORA	Jowett et al. (2004)	-	1D Advection-Dispersion	Finite difference	Daily	1D nodes/segments	Yes
WASP7	Wool et al. (2008)	-	Advection-Dispersion	Finite difference	None	1D nodes or 2,3D gridded	-
WET-Temp	Cox and Bolte (2007)	-	1D Advection-Dispersion	Finite difference	None	1D nodes/segments	Yes
T-NET	Beaufort et al. (2016a)	-	-	semi-Lagrangian	Daily	Basin 1-D	Yes
SSTEMP	Bartholow (2010)	-	1D Advection-Dispersion	Finite difference	Daily	1D nodes/segments	Yes
RBM	Yearsley (2012)	-	-	semi-Lagrangian	Daily	1-D nodes/segments	Yes
FJQHW97	Foreman et al. (2001)	-	Heat Budget	Finite difference	Daily	1D nodes/segments	Yes
HEATLINK	Tokuda et al. (2019)	1-D Saint -Venant	Advection-Dispersion	Finite difference	Daily	1D nodes/segments	Yes
MODBRANCH	Swain and Wexler (1996)	1-D Saint-Venant	Advection-Dispersion	Finite difference	Daily	1-D nodes/segments	Yes
SIMWAT	Querner (1997)	-	Heat Budget	Finite difference	Daily	1-D nodes/segments	Yes
ECOMAG	Motovilov et al. (1999)	Kinematic wave	-	Finite difference	Daily	1-D nodes/segments	Yes
ParFlow	Maxwell and Miller (2005)	Kinematic wave	-	Finite difference	Daily	1-D nodes/segments	Yes
Flow-3DL	Stamou et al. (2007)	3-D Navier-Stokes	-	Finite difference	Daily	3-D nodes/segments	Yes
Dassflow	Honnorat et al. (1992)	1-D 2-D Saint-Venant	-	Finite difference	Daily	2-D,3-D nodes/segments	Yes
LISFLOOD	Knijff et al. (2010)	Kinematic wave	-	Finite difference	Daily	1-D nodes/segments	Yes

4.4 Groundwater

The first steps toward process-based modelling started with the works of Freeze and Harlan (1969). The saturated flow component of the models is represented by Richards' equation as given in Equation 3.24. Exceptions to using Richards' equation are the model tRIBS (Ivanov et al., 2004b), which uses quasi 3-D cascade groundwater solution based on Darcy's law and PIHM (Qu and Duffy, 2007), which uses an ODE to solve the unsaturated and saturated zone flow. Discretisation schemes differ between finite elements, finite volume, and finite difference. Models such as FEFLOW (DHI, 2009), SUTRA (Voss, 1984), HydroGeoSphere (Aquanty, 2015), and CATHY (Camporese et al., 2010) use finite elements discretisation scheme, PIHM (Qu and Duffy, 2007) model uses a semi-discrete representation for ODE solution. GEOtop (Rigon et al., 2006) uses a finite volume representation to solve subsurface fluxes based on 3-D Richards' equation. CaWaQS (Flipo et al., 2005) solves nonlinear Boussinesq equations with a finite difference numerical scheme. It combines Darcy's law and the mass conversation of bi-dimensional laminar flow in an anisotropic, homogeneous aquifer. tRIBS and MODCOU (Ledoux et al., 1989) use quasi 3-D discretisation for estimation of flow. Models differ in terms of their representation of macro pores, dual porosity and preferential flow regarding the saturated flow. FEFLOW, HydroGeoSphere, MODFLOW (Hughes, 2017), MIKE SHE (DHI, 2017) provide modules for these representations.

Processes of the unsaturated zone are described in the previous chapter. Propriety models such as FEFLOW, MIKE SHE, and HydroGeoSphere have integrated infiltration and evapotranspiration estimation modules where these processes are defined and the input is considered on the flow of the unsaturated zone. Modular groundwater models such as HYDRUS, MODFLOW, SUTRA, and MODCOU have simplified infiltration input, or prescribed input (MODFLOW), and no explicit evapotranspiration description. Therefore, these processes are limited. These models depend on integration with other modules to explicitly include the biophysical processes impacting water fluxes. ParFlow uses a coupled scheme with other models such as CLM to es-

timate these processes. Other models such as tRIBS, CATHY, GEOtop, and PIHM include the surface processes. They estimate the infiltration, evapotranspiration and unsaturated zone flow at various degrees of representation. For example, PIHM includes vegetation layer and processes; however, it does not include root zone. tRIBS includes vegetation layer and root zone, and it produces the distributed actual evapotranspiration and recharge. CATHY does not explicitly include the vegetation layer or root zone. However, these models have integrated applications with SVAT models to include the biophysical processes impacting unsaturated zone flow.

Some models (FEFLOW, MIKE SHE) use 3-D Richards' representation in saturated zone flow and 1-D representation in the unsaturated zone. These models mainly depend on Richards' equation to estimate the unsaturated zone flow. MODCOU, tRIBS us quasi 3-D cascade to estimate the flow in the unsaturated zone. tRIBS uses a simplified Darcian flow after Cabral et al. (1992). CATHY uses 3-D Richards' equation for flow in both mediums. Unsaturated flow is also impacted by soil moisture properties such as saturated water content, field capacity, wilting point, and residual water content. These parameterisations are included in models with vegetation representation such as PIHM, FEFLOW, HydroGeoSphere, and PIHM. However, other models have simplified representations of these properties. These models mainly rely on the Van Genuchten-Mualem relationship (Van Genuchten, 1980; Mualem, 1976) or Clapp-Hornberger relationship (Clapp and Hornberger, 1978) for the characterisation of water retention curves from soils. Various soil characteristics data are available although they are incomplete. A common data set being used by many models is the one provided by Carsel and Parrish (1988), a comprehensive soil dataset from U.S. soils. However, other available data exist, such as Leij et al. (1997).

4.4.1 Ground heat transfer

Some models do not calculate the surface energy fluxes but only include the energy influx or outflux as a boundary condition, such as FEFLOW (DHI, 2009) and Hydrus (Šimůnek et al., 2011). MODFLOW (Hughes, 2017) and SUTRA (Voss, 1984) do not include evapotranspiration calculation in their models. ParFlow (Maxwell and Miller,

2005) takes potential evapotranspiration as a boundary from a land surface model. Exceptions to these models are HydroGeoSphere (Aquanty, 2015) and MIKE SHE (DHI, 2017), both of which include surface characterisation. tRIBS model computes the latent and sensible heat fluxes from radiation input after Bras et al. (1987). The potential evapotranspiration is estimated after the Penman-Monteith method (Penman, 1948; Monteith, 1965). PIHM model uses the Pennman method to estimate the evaporation for soil and vegetation after Bras et al. (1987). The estimation of the potential evapotranspiration is conducted using the Penman-Monteith method (Penman, 1948; Monteith, 1965). Another pivotal approach in GEOtop model by Rigon et al. (2006) is estimating the energy budget, including the net surface radiation, by explicitly representing the direct and diffuse radiation. The direct shortwave radiation is subject to the shading factor, whereas the diffuse radiation is only impacted by the view to sky factor.

4.4.2 Overland flow and routing

The overland flow comprises the runoff generation from subsurface and precipitation excess. In groundwater modelling, there are two main approaches to model; while one type treats hillslope runoff and channel runoff separately, the other type treats both of these processes together. The treatment is mainly done by Saint-Venant formulation as given in Equations 3.22 and 3.23.

Hillslope runoff represents the water flow at the watershed surface, and channel runoff represents the runoff through drainage streams in the watershed. Models such as MODFLOW (Hughes, 2017), SUTRA (Voss, 1984), and HYDRUS (Šimůnek et al., 2011) do not have explicit overland flow and routing representations. Many recent models with a process-based approach include the overland flow and routing through the Saint-Venant formulation of momentum transfer. Overland flow is usually represented as 2-D sheet flow on the surface, whereas the channel flow is represented as 1-D routing in the models FEFLOW (DHI, 2009), HydroGeoSphere (Aquanty, 2015), PIHM (Qu and Duffy, 2007), and MIKE SHE (DHI, 2017). Models that use 1-D routing and overland flow schemes are ParFlow (Maxwell and Miller, 2005) and CATHY (Camporese et al., 2010). Although ParFlow is mainly used for integrated modelling

within the CLM scheme, it also includes the surface routing scheme to estimate the channel fluxes.

These models do not include the energy budget in the streams and shading impact, except GEOtop. There is a lack of representation for complete picture of stream exchanges at basin scale as these hydrogeological models' main goal is to represent the subsurface reservoir and fluxes.

Models such as MODFLOW, HYDRUS, HydroGeoSphere, ParFlow, and MIKE SHE have integrated applications with stream models to explicitly represent the fluxes in the stream. Models use Saint-Venant representation for the channel flow with either kinematic wave or diffusion wave approximation, which are explained in the stream mathematical representation subsection. The point is to simplify the calculation process by simplifying the flow complexity. For runoff generation, models use TOPMODEL conceptualisation after Beven and Kirkby (1979). Richards' equation enables the generation of Hortonian and Dunne type runoff (Rigon et al., 2006), in addition, it allows for water to redistribute laterally and move uphill or exfiltrate according to local suction.

4.4.3 Synthesis: Groundwater

The available process-based groundwater models are summarised in Tables 4.7, 4.8, and 4.9. The summary represents the similarities of the models for the computation of unsaturated zone and saturated zone water fluxes. However, they differ in handling surface fluxes and surface representation. While some models do not include the surface fluxes and only consider the boundary conditions such as MODFLOW, SUTRA, and HYDRUS, new generation models usually include surface fluxes and explicit overland flow and channel flow representations.

Table 4.7 Existing groundwater models, a synthesis: part 1

Process/Model	**HydroGeoSphere**	**Hydrus**	**MIKE SHE**	**MODCOU, CaWaQS**
Reference	Aquanty (2015)	Šimůnek et al. (2011)	DHI (2017)	Labarthe (2016); Ledoux et al. (1989); Flipo et al. (2007b)
Rainfall interception	Intercepted by canopy, throughfall transfers to surface budget	No interception, surface water infiltrates or runoff	No surface interception	No interception
Ground heat flux	1-D,2-D,3-D Advection-Dispersion	Does not include inherently, coupled with other modules	2-D Advection-Dispersion	-
Evapotranspiration	No explicit evapotranspiration calculation	No ETP calculation	No ETP scheme	No ETP scheme
Infiltration	Prescribed infiltration	Infiltration is limited	Limited by interception storage, excess is runoff	Limited by interception storage, excess is transferred to river flow
Flow in unsaturated zone	3-D Richards' Eq.	3-D Mixed form of Richards' Eq.	3-D Boussinesq eq.	Nash cascade
Groundwater flow	2-D,3-D Richards' Eq.	3-D Mixed form of Richards' Eq.	3-D Boussinesq eq.	Diffusivity equation
Overland Flow and Runoff	2-D overland flow based on Saint-Venant Eq.	None	None	-
Hydraulic routing	2-D Manning Eq.	None	None	1-D Routing Muskingum scheme

Table 4.8 Existing groundwater models, a synthesis: part 2

Process/Model	**FEFlow**	**Modflow**	**SUTRA**	**CATHY**
Reference	DHI (2009)	Hughes (2017)	Voss (1984)	Camporese et al. (2010)
Rainfall interception	Intercepted by canopy, throughfall transfers to surface budget	No interception, surface water infiltrates or runoff	No surface interception	No interception bucket
Ground heat flux	1-D,2-D,3-D Advection-Dispersion	Does not include inherently, coupled with other modules	2-D Advection-Dispersion	No heat transport
Evapotranspiration	No explicit evapotranspiration calculation	No ETP calculation	No ETP scheme	Potential evaporation is given as input
Infiltration	Prescribed infiltration	Prescribed infiltration	Prescribed infiltration	Prescribed infiltration
Flow in unsaturated zone	1-D Richards' Eq.	3-D Boussinesq Eq.	1-D,2-D,3-D Richards' Eq.	3-D Richards' Eq.
Groundwater flow	2-D,3-D Richards' Eq.	3-D Boussinesq Eq.	1-D,2-D,3-D Richards' Eq.	3-D Richards' Eq.
Overland Flow and Runoff	2-D overland flow based on Saint-Venant Eq.	None	None	Diffusion wave approximation of Saint-Venant Eq. with finite difference solver
Hydraulic routing	1-D Saint-Venant Eq.	None	None	1-D Saint-Venant Eq.

Table 4.9 Existing groundwater models, a synthesis: part 3

Process/Model	**tRIBS**	**GEOtop**	**PIHM**	**ParFlow**
Reference	Ivanov et al. (2004a)	Rigon et al. (2006)	Qu and Duffy (2007)	Maxwell and Miller (2005)
Rainfall interception	Canopy interception as a function of LAI, excess transfers to surface water	Single layer canopy for interception, excess transfers to surface water	Canopy bucket is present, excess is transferred to surface water	Canopy interception is present, excess transfers to surface water
Ground heat flux	Combination of gradient method and force-restore method are used	Fourier heat diffusion equation	1-D transient heat conduction	1-D transient heat conduction
Evapotranspiration	ETP is a combination of vegetation transpiration, bare soil evaporation, and evaporation from wet canopy	Evaporation is sum of vegetation transpiration, evaporation of wet canopy, soil, and snow surface	Penman Equation after Bras et al. (1987)	ETP is input from SVAT model
Infiltration	Prescribed infiltration	Prescribed infiltration	Prescribed infiltration	Prescribed infiltration
Flow in unsaturated zone	Simplified flow modeled after Cabral et al. (1992)	3-D Richards' Eq.	Richards' Eq.	3-D Richards' Eq.
Groundwater flow	Quasi 3-D cascade groundwater flow based on Darcy's	3-D Richards' Eq.	Richards' Eq.	3-D Richards' Eq.
Overland Flow and Runoff	Non-linear hydrologic routing, no reinfiltration	Kinematic wave approximation of Saint-Venant Eq.	2-D Saint-Venant Eq. solved by Riemann approach	Kinematic wave approximation of Saint-Venant Eq.
Hydraulic routing	1-D river routing via continuity equation for unsteady free surface flow	Hillslope runoff and channel runoff routing is separated	1-D river routing solved with Saint-Venant Eq.	2-D Sheet flow surface routing

4.5 Integrated modeling approaches

4.5.1 SVAT-aquifer interface

Maxwell and Miller (2005) provided an initial work on the combination of surface and subsurface model coupling. Their work shows that the groundwater feedback impacts the surface fluxes and the atmosphere. Therefore, the inclusion of groundwater in SVAT modelling is essential for understanding regional groundwater-surface water interactions. They combined the physically-based SVAT model CLM with the ParFlow subsurface model. ParFlow also solves subsurface for the Richards' equations (Richards, 1931). His approach was an important step in the representation of subsurface water fluxes along with a land surface model.

A similar approach has been made by Sulis et al. (2010). They compared two models, ParFlow, and CATHY, to assess their process representation. They found that the surface fluxes are sensitive to different discretisation schemes. Hence, integrated models should take into account the suitability of discretisation schemes. De Maet et al. (2015) developed a scalable coupled surface-subsurface flow model to estimate the interactions between surface and subsurface; however, the model does not include the temperature transfer scheme. It uses 3-D Richard's equation for subsurface flow and a non-inertia approximation for the surface fluxes. Although the model efficiently simulates the fluxes, it does not consider the physical processes at the surface and the groundwater. Ala-aho et al. (2017) integrated a surface-subsurface model to understand the role of groundwater in catchment runoff generation.

Bisht et al. (2017) evaluated the role of water table fluctuations on land surface variables. Qiu et al. (2019) coupled the SVAT model with aquifer and stream modules to assess the impact of heat fluxes on the stream at the local scale. Although this was one of the first applications to simulate water and energy fluxes, including full hydrosystem representation, it aims to simulate the local to reach scale processes. However, this study captured the main characteristics of a surface-stream-aquifer continuum in terms of temperature modelling so it served as a proof of concept. Habets et al. (2008) proposed an integrated SVAT-groundwater model ISBA-MODCOU to simulate

hydrosystem processes at the regional scale in the Seine basin. This approach provides the complete representation of the hydrosystem processes for water fluxes, but it does not consider the energy fluxes in the hydrosystem.

4.5.2 SVAT-stream interface

Haag and Luce (2008) developed an integrated SVAT-stream heat and water fluxes model and included the atmosphere feedback on the stream model. The model solved the terrestrial water cycle components in hourly time steps. This model is a basin-scale implementation of the integrated model LARSIM. They developed the model on an already calibrated water balance model for the same basin. They assessed the model performance against statistical indicators such as the Nash-Sutcliffe coefficient and RMSE which produced satisfactory results. They used a statistical regression method for the river temperature and conducted a forecast test. Qiu et al. (2019) combined surface, subsurface, and stream modelling frameworks in order to assess the surface fluxes' impact on stream temperature. The developed basin scale model used the CLM SVAT model. The developed model solved quasi 3-D groundwater equation based on Darcy's law. They included two groundwater layers. Stream temperature was solved using 1-D heat transfer equation. They observed a mismatch between the temperature observations in the stream and the simulated temperatures. This was related to a phenology mismatch in the SVAT vegetation representation. However, they have reached statistically adequate temperature simulations for stream. A novelty in this study was including the shading coefficients at basin scale at integrated model framework as well as explicit stream and stream-bed temperature modules. Van Vliet et al. (2012a) coupled a SVAT model with a process-based river (RBM) model to estimate the temporal regime in the river. The authors combined a SVAT model with water temperature regression model and a 1-D heat transport model RBM in their multi-model approach. In their iterative approach, the authors found improved performance in river discharge and temperature estimates to assess the impact of anthropological causes.

4.5.3 Stream-aquifer interface

A comprehensive description of types of process representation in distributed models, the assumptions and limitations of these models, and a discussion of comparison and assessment issues is provided in Kampf and Burges (2007), Clarke (2008), Ek et al. (2003), and Furman (2008). Stream aquifer interactions at a large scale have been extensively reviewed in the work of Flipo et al. (2014). The authors showed that the exchanges at the river corridor are impacted by reach and local scale interactions. Stonestrom and Constantz (2003) showed that the water and heat fluxes are interdependent. For this reason, they can be modelled together to improve the representation of stream aquifer interactions and surface aquifer interactions in general. Heterogeneity in the streambed water fluxes from groundwater into the stream was assessed by Kalbus et al. (2009). Using a stream temperature model, HEATFLOW, they showed that the groundwater inflow into the stream influences the stream discharge, and hydraulic conductivity heterogeneity plays an important role. Gunduz (2004) developed an integrated flow and contaminant transport modelling approach for streams. They used the leakance concept to compute the water flux between the groundwater domain and the stream channels. Händel et al. (2013) developed a regional groundwater heat transport model to assess the impact of groundwater heat pumps.

Loinaz et al. (2013) combined the MIKE SHE groundwater model and the MIKE 11 stream transport model to simulate the stream aquifer interactions on the catchment scale. Following the development of this model, Loinaz et al. (2014) analysed the anthropological stress factors on the stream budget and possible aquifer restoration strategies at the catchment scale. Attard et al. (2016) analysed the urban temperature input into the aquifer by developing a thermal FEFLOW model for transient heat transport.

Bisht et al. (2017) coupled a groundwater-stream integrated model with a SVAT model to analyze the heat and water fluxes in the rivers and groundwater and the atmospheric feedback. The model used TOPFLOW surface runoff generation formulations (Beven and Kirkby, 1979). The model included the CLM SVAT model with PLFORTRAN reactive transport scheme. They compared the estimated fluxes with key hy-

drologic fluxes, and although piezometric head estimation was underrepresented, they obtained feasible results. Mueller et al. (2018) analysed the impact of urban heat buffer in the cities on aquifers.

Qiu et al. (2019) approach also captured the heat and water flow interactions between stream and aquifer. The temperature interactions between stream and aquifer were captured by one-dimensional advection conduction heat transport used by Anderson (2005). Their approach also captured the surface atmosphere input by a SVAT model. The simulated and observed streambed temperatures were in arrangement, and they could use the model to divide the gaining and losing portions of the stream. King and Neilson (2019) developed a river-aquifer exchange framework using tracer experiment data and temperature data to model the heat and water fluxes transport and river-aquifer exchanges at the reach scale. The method shows promising results for the reach scale characterisation.

4.5.4 Aquifer-aquifer interface

Scheck-Wenderoth et al. (2014) analysed the heat transport in the Central European Basin by developing a 3-D heat transfer scheme. Kupfersberger et al. (2017) analysed the impact of different subsurface structures with a 2-D heat transfer model using FEFLOW. The authors found that the groundwater heat fluxes in an urban environment are influenced by groundwater-related parameters rather than surface parameterisation. The procedure shows the impact of groundwater variations on the heat flow regime; however, it does not include the heat flow between aquifers. Rock and Kupfersberger (2018) developed a basin scale heat transport model using a FEFLOW 1-D vertical flow as in Kupfersberger et al. (2017). The developed model captures the impact of soil layer and urbanisation on shallow groundwater in terms of heat flow and temperature; however, the study does not include any intra-aquifer heat flow interaction.

Although studies by Kupfersberger et al. (2017) and Rock and Kupfersberger (2018) show the shallow groundwater are under constant impact by the heat influx, these studies do not include the underlying aquifers. The study of Scheck-Wenderoth et al. (2014) takes into account the different layers below the shallow aquifers, but the study does not

explicitly represent the flow between different aquifer-aquitards underlying the basin. Gringarten and Sauty (1975) studied heat transport within aquifers between re-injection wells and production wells for geothermal heating purposes. The developed analytical approach was able to estimate the temperatures reaching satisfactory results for geothermal purposes. McConnell and Pingen (2012) developed a heat transfer algorithm to explicitly represent the heat transfer in the continuum. The methodology proposed is a pseudo-3D approach to model heat sinks. This approach is analytical to the heat transfer between aquifers since the aquitard acts as a heat sink. Hence, the proposed framework could be used for groundwater aquifer interactions. Another approach to this problem within the hydrological framework was adopted by Zhan et al. (2009). The study provided an analytical solution to aquifer-aquitard-aquifer solute transfer. The solution considers the advective-dispersive transfer and maintains the mass conservation at the interface. Burns et al. (2016) tried to evaluate a steady state linear analytical solution for the transfer among aquifer systems since the problem remains unsolved. Numerous studies are discussed above that solve the heat and water flow between aquifers; however, none are unified within a groundwater model comprising multiple aquifer systems. There is a gap to fill to understand the heat and water fluxes between aquifer systems in adjacent hydrosystem and combine this with a SVAT model in an integrated modelling framework.

4.6 Synthesis: Integrated modelling

There are vast amounts of integrated models for different purposes ranging from surface water-groundwater model integration (Maxwell and Miller, 2005; Loinaz et al., 2013, 2014; Bisht et al., 2017; Tian et al., 2015; De Maet et al., 2015; Ala-aho et al., 2017; Spanoudaki et al., 2009), SVAT-river continuum (Qiu et al., 2019; Haag and Luce, 2008), SVAT-crop modelling (de Noblet-Ducoudré et al., 2004; Van den Hoof et al., 2011) to subsurface-river modelling (Monninkhoff and Li, 2009) as noted in Table 4.10. Although these models use various frameworks and degree of representations, the underlying physics of these models are the same. Variable hydraulic head applica-

tions are common in integrated model applications (Maxwell and Condon, 2016; Loinaz et al., 2013). The surface components and unsaturated zone are mainly integrated by keeping the subsurface modules present in the integrated model (Maxwell and Miller, 2005). This is due to explicit representation of surface flow and unsaturated zone flow in the subsurface models, which improve the representation in the vent of integration (Clark et al., 2015). The integrated models mainly use fully coupled framework with two-way integration. The processes at the interface simultaneously transfer between the surface model and groundwater model, resulting in accurate process description of the hydrosystem for water fluxes.

Table 4.10 A synthesis of integrated models

Reference	SVAT	Hydraulic Model	Heat Model	GW Model	Coupling Method
Maxwell and Miller (2005)	CLM4	3-D Richards'	Advection-Dispersion	ParFlow	Direct, Indirect
Ala-aho et al. (2017)	HydroGeoSphere	3-D Richards'	-	HydroGeoSphere	Direct, Indirect
Qiu et al. (2019)	CLM4	1-D routing	1-D Heat Transport	PAWS	Direct 2-way coupling
Bisht et al. (2017)	CLM4.5	1-D routing	-	PLFORTRAN	Direct
Haag and Luce (2008)	LARSIM	2-D Saint Venant	Advection-Dispersion	LARSIM	Direct, Indirect
Loinaz et al. (2013)	MIKE SHE	MIKE 11 (1-D St. Venant)	1-D Heat Transport	MIKE SHE	Direct
Loinaz et al. (2014)	MIKE SHE	MIKE 11 (1-D St. Venant)	1-D Heat Transport	MIKE SHE	Direct
Fairbairn et al. (2017)	ISBA	1-D routing	-	MODCOU	Direct
Panday and Huyakorn (2004)	MODHMS	1-D,2-D St.Venant	-	MODHMS(3-D Richards')	Direct
Tian et al. (2015)	GSFLOW-SWMM	1-D St. Venant	-	GSFLOW-SWMM	Direct, Indirect
Van Vliet et al. (2012a)	VIC	-	RBM	-	Direct
Spanoudaki et al. (2009)	IRENE	FLOW-3DL	-	3-D Richards' Eq.	Direct
Schilling et al. (2019b)	HydroGeoSphere	-	1-D Heat Transport	HydroGeoSphere	Direct
Shen and Phanikumar (2010)	PAWS	1-D,2-D Diffusive Wave Eq.	-	PAWS(Quasi 3-D)	Direct

Chapter 5

Modelling the hydrosystem fluxes at the regional scale

5.1 Introduction

Hydrological model selection is an essential step in the accurate representation of the hydrological phenomena (Addor and Melsen, 2019). The main processes of an hydrosystem are described in Chapter 3. The link between water and energy fluxes is established via the evapotranspiration term. The vegetation dynamics and transpiration are the main drivers of evapotranspiration in temperate climates (Thornthwaite, 1948). The ensemble of SVAT and groundwater models are described in Chapter 4. The SVAT models described here cover the main processes of the hydrosystem ranging from regional to global scale. Similarly, groundwater models cover the unsaturated and saturated zones in the ground. They mainly focus on water flow. In terms of transport, they usually aim to solve pollutant transport problems.

In this project's scope, the surface model ORCHIDEE and the groundwater model CaWaQS are selected. The selection procedure is based on the conceptual capabilities of the models and their adaptability to the specifications of heat and water flux simulation at the regional scale. The surface model ORCHIDEE describes the processes of the surface water and energy cycle at regional to global scales. It includes the vegetation dynamics, both long-term and short-term processes, including photosynthesis. It is possible to adapt the model at the regional scale with minor modifications, such as urban zones.

CaWaQS groundwater model complements the missing compartments in the ORCHIDEE model by providing an explicit solution for the groundwater flow and the

river flow. CaWaQS describes stream-aquifer exchanges, as well as aquifer-aquitard-aquifer exchanges. This model was extended by developing a heat transport module that can simulate transport in river network and aquifer system (Detailed description in Appendix A). In this chapter, the conceptual details of both models are described.

5.2 Models

5.2.1 ORCHIDEE

ORCHIDEE model is selected to simulate the regional surface hydrology from an ensemble of SVAT models described in Section 4.2. The model was developed by IPSL (Institute Pierre-Simon Laplace) and is detailed in Krinner et al. (2005). Several modules form the ORCHIDEE SVAT model, namely, SECHIBA, LPJ, and STOMATE. ORCHIDEE allows simulation of surface water budget and energy balance at a 15-min time step when coupled with a GCM, or 30-min time steps in standalone (offline) simulation.

SECHIBA module describes the fluxes and exchanges of the energy and water between the atmosphere and the biosphere. The soil hydrology evolved in the SECHIBA module, starting with a simple two-layer bucket-type model (Ducoudré et al., 1993), then moving to a vertical discretisation of a $2\mathrm{m}$ soil column to calculate the unsaturated water flow. The second hydrology module uses Richards (1931) equation at 1D of the soil column using a finite difference method. The soil column thickness and discretisation in the second hydrology module can be modified after the recent improvements by Campoy et al. (2013). Van Genuchten (1980) - Mualem (1976) relationship describes the soil properties. The model can use Zobler or USDA soil classes to describe the soils. Soil properties for the USDA soil classes are described in Carsel and Parrish (1988) using the Van Genuchten-Mualem relationship. It is also possible to reduce the hydraulic conductivity due to soil contraction or increase the hydraulic conductivity due to the expansion of the root zone as a function of depth. The field capacity and wilting point are important parameters for the biomass processes. A soil matric potential of -3.3m (-1m for sandy soils following Richards and Weaver (1944)) and -150m for the permanent wilting point. The transpiration process of the biomass is coupled with the soil moisture

profile via a root density profile (de Rosnay and Polcher, 1998). Bare soil evaporation is also controlled by the top layer soil moisture availability. The interception losses and snow sublimation is not controlled by the soil moisture profile of SECHIBA.

In each grid cell, the corresponding parameters (including saturated hydraulic conductivity K_{sat} and porosity) are deduced from soil texture as detailed in Tafasca et al. (2019). K_{sat} (in m s^{-1}) further undergoes a vertical exponential decay to account for the effects of soil compaction and bioturbation:

$$K_{\mathrm{sat}}(z) = K^{*}_{\mathrm{sat}} \exp(-c_K(z - z_{\mathrm{lim}})), \tag{5.1}$$

where z is the depth below the soil surface (m), K^{*}_{sat} is the reference value of K_{sat} based on soil texture (m s^{-1}), z_{lim} is the depth at which the decrease of K_{sat} starts (by default equal to 0.3 m), and c_K is the decay factor (in m^{-1}, equal to 2 by default). The impact of c_K on the K_{sat} is provided in Figure 5.1. Increase in factor reduces K_{sat} progressively below 30cm depth.

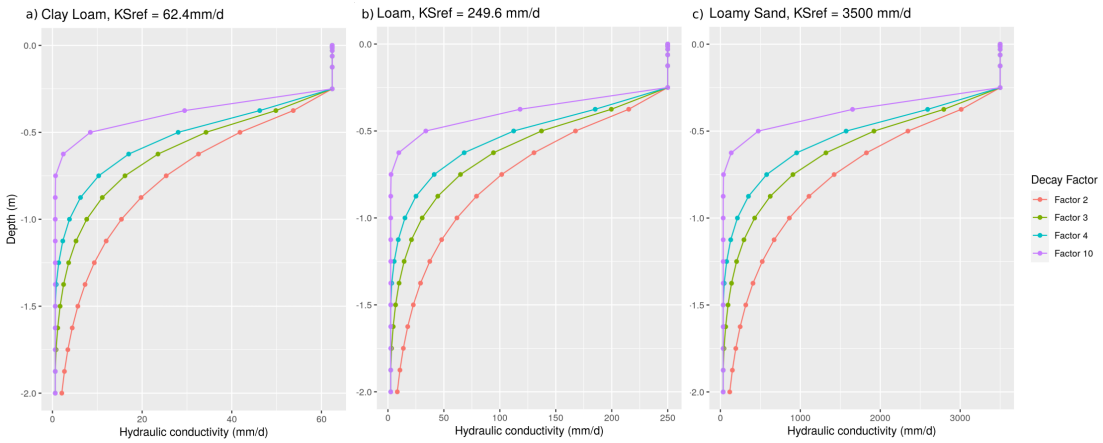

Figure 5.1 Impact of c_K on dominant soil textures i.e. a) Clay Loam, b) Loam, c) Loamy Sand in the Seine basin. KSref indicates the saturated hydraulic conductivity of the soil texture defined in ORCHIDEE.

The infiltration mechanism uses the model of Green and Ampt (1911). The parameterisation of the infiltration processes is described in detail by D'Orgeval et al. (2006, 2008). The runoff mechanism depends on the infiltration excess (Horton, 1933). The soil suction mechanism is neglected; hence infiltration is controlled by the gravitational forces. The infiltration rate depends on the saturated hydraulic conductivity and the

hydraulic conductivity of the unsaturated layer based on Haverkamp et al. (1977). ORCHIDEE allows a fraction of runoff to pond if the soil below is saturated and the slope is below a certain degree. The drainage through the soil column bottom depends on three distinct representations. The first two options depend on the saturation and the hydraulic conductivity governed by the gravitational forces. Additionally, the second option introduces a drainage coefficient which might be used to limit the drainage at the soil bottom. A third condition is introduced by the work of Campoy et al. (2013), which introduces a saturated layer (water table). If the soil moisture drops below the saturation due to root uptake or upward diffusion, a negative drainage saturates the soil bottom.

The heat transport in the soil is described by the 1-D Fourier's law (Ducharne, 2018). The heat diffusion is solved by an implicit finite difference method. A zero-flux boundary condition at the lower boundary of the soil bottom is described. Thermal conductivities and rock densities are obtained from Peters-Lidard et al. (1998). The heat capacity of the solids is obtained from Pielke (2013). The density, heat capacity, and heat conductivity terms are subject to variation based on the saturation degree of soil as thermal properties of water, ice, and soil matrix (quartz and other minerals) are different. The effective density and heat capacity of each layer in the soil column is estimated based on the saturation degree of the soil node since the heat capacity of water is larger than that of the soil matrix. Similarly, the effective heat conductivity of the soil layers is determined after a semi-empirical method proposed by (Johansen, 1977). The effective thermal conductivity of each soil layer is estimated based on the water, ice, quartz and other mineral contents of the soils, proportionate to the saturation degree of the soil. ORCHIDE assumes the heat capacity of air is negligible. The dry soil heat capacity and quartz content of USDA soil textures are provided in Table 5.1. A detailed description of the thermal properties of soils are provided in the technical report by Ducharne (2018).

The vegetation dynamics are defined from the dynamic global vegetation model (DGVM) LPJ (Sitch et al., 2003). The processes include fire, sapling establishment, light competition, tree mortality, and climatic criteria for the introduction or elimination

of plant functional types. The time step of the vegetation dynamics is 1 year. The third module is STOMATE (Saclay Toulouse Orsay Model for Analysis of Terrestrial Ecosystems), which combines the vegetation dynamics and soil hydrology to simulate main surface processes (Krinner et al., 2005). These processes include photosynthesis, carbon allocation, litter decomposition, soil carbon dynamics, maintenance and growth respiration, and phenology. The time step of this module is 1 day. Therefore, the slow vegetative processes are dealt with by the LPJ, whereas STOMATE deals with fast vegetative processes. STOMATE module makes it possible to study the carbon cycle. The ORCHIDEE model relies on the plant functional types to describe the land cover properties (Smith et al., 1998). Twelve distinct vegetation classes are described in the model. More than one PFT can coexist in the same cell. Water reservoirs are calculated for each PFT separately, excluding the lower soil reservoirs.

The parameterisation of the soil column is homogeneous. A system of tiles called "soiltiles" is used to describe the relationship between the soil column of each cell and the various land-cover portions inside the cell. Three main soiltiles are gathered together to represent various land cover types. Bare soil, forest vegetation classes, grasslands, and agricultural crops form the three distinct soiltiles. The water budget and the energy balance is calculated for each soiltiles within a cell.

Table 5.1 synthesises the soil properties defined in ORCHIDEE to describe soil hydrological and thermal properties. The model of Mualem (1976) and Van Genuchten (1980) are used to simulate the unsaturated flow. The used parameters of Van Genuchten (n and α) are obtained from Carsel and Parrish (1988) (Table 5.1).

5.2.2 CaWaQS

The CaWaQS model is a numerical tool that simulates the water flow of a hydrosystem at varying scales either in steady state or transient conditions (Flipo, 2005; Labarthe, 2016; Flipo et al., 2019). It is a physically-based distributed model that simulates the water balance and dynamics of water flow, including the phreatic zone, river drainage system, unsaturated zone and effective rainfall with the help of a conceptual reservoir-based approach. It inherits several concepts from the modelling platform MODCOU-

Table 5.1 Soil texture properties of USDA soil classes based on Carsel and Parrish (1988). Dry soil heat capacities are defined following Pielke (2013)

Parameter Texture	Ks $mm.d^{-1}$	n	α mm^{-1}	θ_s $m^3.m^{-3}$	θ_{fc} $m^3.m^{-3}$	θ_w $m^3.m^{-3}$	θ_r $m^3.m^{-3}$	$C_{v,dry}$ $J.m^{-3}.K-1$	Quartz (-) (-)
Sand	7128.0	2.68	0.0145	0.43	0.0493	0.0450	0.045	1.47e6	0.92
Loamy Sand	3501.6	2.28	0.0124	0.41	0.0710	0.0570	0.057	1.14e6	0.82
Sandy Loam	1060.8	1.89	0.0075	0.41	0.1218	0.0657	0.065	1.34e6	0.6
Silt Loam	108.0	1.41	0.0020	0.45	0.2402	0.1039	0.067	1.27e6	0.25
Silt	60.0	1.37	0.0016	0.46	0.2582	0.0901	0.034	1.21e6	0.1
Loam	249.6	1.56	0.0036	0.43	0.1654	0.0884	0.078	1.21e6	0.4
Sandy Clay Loam	314.4	1.48	0.0059	0.39	0.1695	0.1112	0.100	1.18e6	0.6
Silty Clay Loam	16.8	1.23	0.0010	0.43	0.3383	0.1967	0.089	1.32e6	0.1
Clay Loam	62.4	1.31	0.0019	0.41	0.2697	0.1496	0.095	1.23e6	0.35
Sandy Clay	28.8	1.23	0.0027	0.38	0.2672	0.1704	0.100	1.18e6	0.52
Silty Clay	4.8	01.09	0.0005	0.36	0.3370	0.2665	0.070	1.15e6	0.1
Clay	48.0	01.09	0.0008	0.38	0.3469	0.2707	0.068	1.09e6	0.25

NEWSAM (de Marsily et al., 1978; Ledoux, 1980). CaWaQS is developed to account for groundwater processes, surface processes, and groundwater-surface water interactions. It aims to include the maximum amount of geological, geomorphological, topographical, and physiographical information. It represents the spatial and temporal variations in the hydrosystem's structure and behaviour. The model aims to reconcile complex hydrological processes and practical use by stakeholders to manage the hydrosystems. It has wide range of applications, such as studies of climate change impact at the regional scale (Flipo et al., 2020b), groundwater functioning under flood conditions (Maillot, 2019), and the fate of pollutants from agricultural origins (Wang et al., 2016a).

The model is highly modular; each compartment of a hydrosystem is developed in a stand-alone library. Four distinct libraries form the basis of the CaWaQS model: The components of the CaWaQS3x model are listed below:

1. A surface module *libfp* (cf. Fig 5.2.A) calculates the hydrological budget at the surface in daily time steps. It estimates the actual evapotranspiration from the water in the topsoil. The runoff and infiltration are calculated from precipitation and real evapotranspiration of each hydrological unit. The runoff is instantaneously transferred to the river network, whereas the infiltration passes into the unsaturated zone.

2. A hydraulic module *libhyd* (cf. Fig 5.2.B) simulates the flow in the river network, using the concept of Cunge (1969) (cf. Fig 5.2.D). Locally produced runoff is dis-

tributed homogeneously in each section of the river in the network. The thickness of the water column in the river is calculated by the method of Manning-Strickler (Chow, 1959).

3. An unsaturated module *libnsat* (cf. Fig 5.2.C) simulates vertical flow of water in the unsaturated zone with a succession of Nash reservoirs (Nash, 1959). These successive reservoirs have different emptying coefficients, and the thicknesses might vary spatially. The resulting fluxes are transferred to the saturated zone as recharge either by direct transfer or after routing (Gallois et al., 2020b).

4. A saturated module *libaq* (cf. Fig 5.2.E) solves the pseudo-3D diffusivity equation in a multilayer aquifer system with a semi-implicit finite difference numerical scheme. It is possible to refine the simulated domain in a nested manner, as explained in de Marsily (1986). The link between the neighbouring layers is established with the concept of drainage, which is analogous to the conductance concept used in the stream-aquifer exchanges. The conductance model (cf. Fig. 5.2) calculates stream-aquifer water exchanges.

An ensemble of complementing libraries enables the model to construct (*libio*,*libmesh*), interpolate (*libts*), manage time series (*libchronos*,*libts*), print and couple spatially the fluxes between the compartments (*libspa*) and solve the linear systems with the conjugate gradient method (*libspa*).

The CaWaQS model underwent a set of improvements recently that enabled the model to include forcing fluxes in the compartments of the hydrosystem (river network and aquifers) (Gallois et al., 2020b). Additional improvements include sub-catchment, gauging stations, and river inflows (Gallois et al., 2020a, 2021). These developments make it possible to couple CaWaQS with a land surface model by defining forcing files of runoff and infiltration or transport (pollutants, temperature species) fluxes in the model.

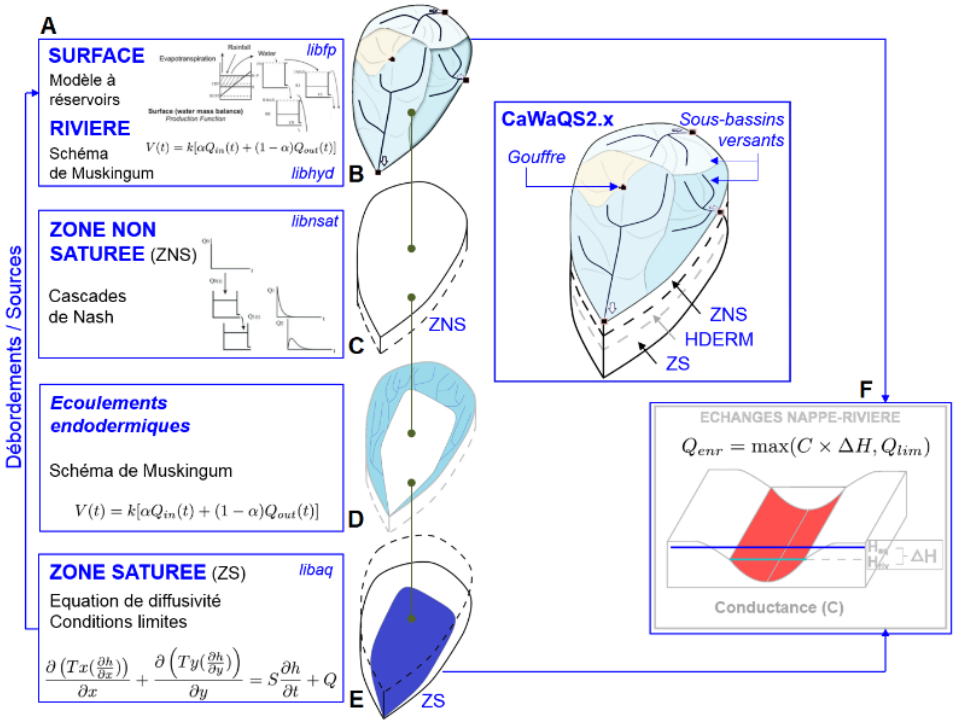

Figure 5.2 The structure of the CaWaQS3.XX platform with distinct compartments of the hydrosystem (Gallois et al., 2020b)

5.2.3 Coupling strategy

The flowchart of ORCHIDEE-CaWaQS model integration to simulate water budget and energy balance of the Seine hydrosystem is given in Figure 5.3. The atmospheric forcing variables from SAFRAN dataset is used to force the ORCHIDEE SVAT model. Surface water budget and energy balance are estimated by ORCHIDEE in the Seine basin. The surface runoff, recharge and the soil temperatures estimated by ORCHIDEE are set as the surface boundary of the CaWaQS Seine model.

In this application we assume that the recharge fluxes is at equilibrium temperature with soil temperatures at $2\mathrm{m}$ depth, whereas the surface runoff temperature is at equilibrium with soil temperatures of the first soil layer ($0.001\ \mathrm{cm}$). Therefore the coupled heat and water fluxes at the interface of water table (recharge) and lateral inflows (surface runoff) can drive CaWaQS to simulate the hydrological and thermal regime in the aquifer system and the river network.

The recently developed driver in CaWaQS allows CaWaQS model to be forced by external water and solute fluxes at the surface boundary. Detailed description of the

forcing driver could be found in Gallois et al. (2020b). Our approach differs in the way that temperature is treated unlike solutes. While the solute transport through the unsaturated zone is treated by a series of Nash cascade reservoirs which are constrained by a reservoir emptying factor, we treat temperature of recharge at equilibrium temperature with the water table, effectively by-passing the nash reservoirs.

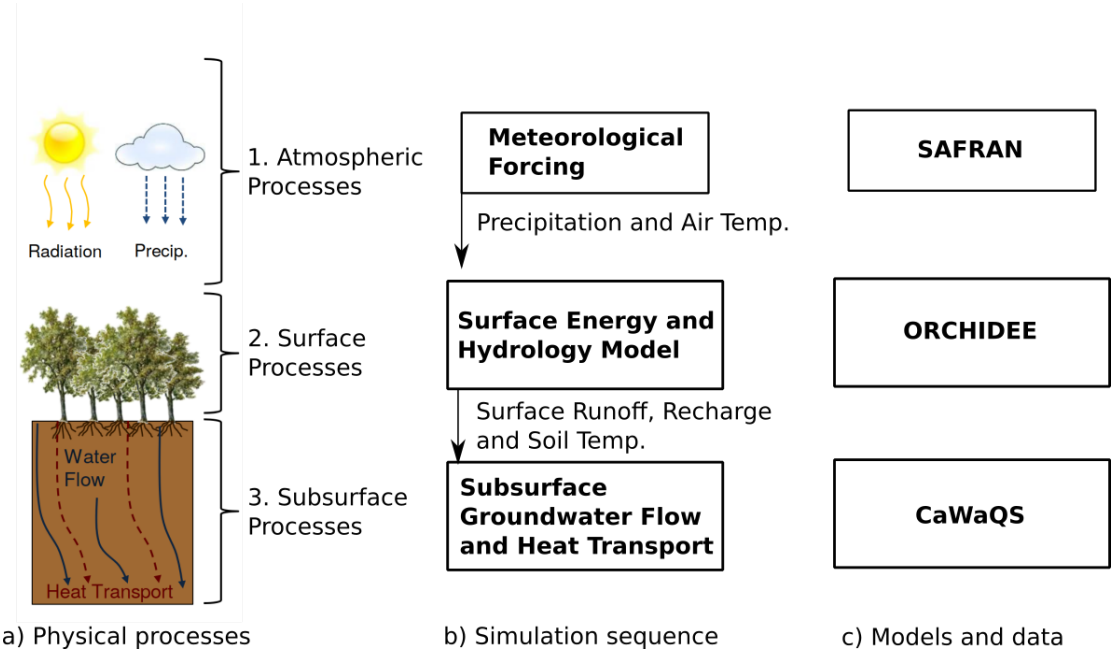

Figure 5.3 a) The atmospheric and surface processes that control thermal regimes, b) the flowchart for integrating SVAT models and groundwater flow and heat transport models) and c) The flow chart of ORCHIDEE-CaWaQS integration. (Figure adapted from Kurylyk et al. (2014).)

5.3 Conclusion

In this chapter, the ORCHIDEE and CaWaQS models are described in detail. In terms of water and energy fluxes, ORCHIDEE can simulate the surface hydrology, including the top of the unsaturated zone. It accounts for the surface processes with biomass activity, evapotranspiration, runoff generation, infiltration processes, and the topsoil moisture content. CaWaQS simulates the hydrosystem water fluxes without explicitly accounting for the biomass processes such as photosynthesis, transpiration etc. yet it simulates the river, stream-aquifer interactions. At the conceptual level, ORCHIDEE- and CaWaQS complement each other. It is possible to couple two models at the water

table interface by simulating the explicit evapotranspiration, infiltration, soil moisture content within ORCHIDEEand groundwater flow, river hydraulics, and exchanges at the interfaces within CaWaQS. The coupled framework is then used to calculate the mass and energy balance of the hydrosystem at the regional scale. The advantage of this framework is its capacity to simulate the processes of the hydrosystem explicitly.

Chapter 6

Application of ORCHIDEE-CaWaQS: hydrological modeling

6.1 Introduction

As evidenced in previous chapters, climate change has negative consequences on hydrosystems. These consequences include the modification of water and energy cycle processes: the spatio-temporal variability of recharge, depletion of the water resources, evapotranspiration (Famiglietti, 2014), deeper water table, river discharge, aquifer and river water temperatures. The future availability of groundwater resources is at risk due to the increased demand and global changes (Taylor et al., 2013; Kløve et al., 2014; Castle et al., 2014). In the future, aridity will increase in the regions that were previously humid, and temperate. In the Seine basin, this impact is expected to manifest itself by increasing river water temperatures and decreasing low flow, so that navigation in the basin becomes more difficult. Critical infrastructure that depends on sustained river water flow at a certain temperature (between 10-15°C), such as nuclear power plants or water treatment plants, are likely to be impacted. Indeed this impact is already documented in the case of nuclear power plants by Boogert and Dupont (2005). Heat waves and low water flow cause nuclear power plants to shut down and cause economic damage. Although the apparent risks of climate change on water resources are identified, the controlling dynamics of the water and energy balance are relatively unknown.

Understanding the water cycle relies on process-based models that explicitly simulate hydrosystem processes (de Marsily, 1986). However, process-based models traditionally focus on surface processes (Clark et al., 2015) or groundwater and river processes (Singh, 2014). Moreover, these models generally do not attempt to include heat

transport, although the apparent impact of climate change is tightly coupled with the energy balance (Anderson, 2005). In Chapter 4, we have seen that several modelling approaches are available to simulate the compartments of the hydrosystems. The common theme of these models is to simulate the water balance; however, assessing the climate change impacts also requires understanding the heat balance. On the other hand, simulating the heat balance of a hydrosystem requires the water balance and subsequent water flow fields to be established. This is because advective heat fluxes associated with water flow exert strong control on the heat balance.

Several coupling methodologies were developed to integrate groundwater models with surface water models (Barthel, 2014). Simultaneous integration of the models in the case of Maxwell et al. (2007) has advantages in terms of computation time and the possibility of studies of the groundwater feedback to the surface processes (Maxwell et al., 2014; Condon and Maxwell, 2015; Fan et al., 2007). A simultaneous integration approach was adopted by Rousset et al. (2004) to evaluate the water balance of the Seine hydrosystem and the surface heat balance, however the study did not include the Jurassic layer and no attempt to extend the heat balance estimation to river and aquifer system was made. A limitation of this approach is the difficulty and time investment required to integrate two independent models to simulate simultaneously. The second type of integration is sequential integration, where the results of surface model are forced as input to the groundwater model (Okkonen and Klove, 2011). This type of simulation is faster to adopt; however, the lack of feedback between the surface and groundwater components is a limitation. This limitation has implications, such as the water table evapotranspiration feedback observed in modern land surface models (Clark et al., 2015).

Aquifer recharge is one of the main challenging aspects of developing a groundwater model. Groundwater recharge depends on various factors, including surface morphology, soil composition, the thickness of the unsaturated zone or the depth of the water table, root zone and vegetation activity, land use, and regional and local climate. These factors are highly heterogeneous and contribute to the spatial and temporal variability of recharge. In the literature, various methods of recharge estimation at different tem-

poral and spatial scales are proposed (Healy and Scanlon, 2010). Many hydrological models depend on the water budget method for estimating the recharge at larger application scales. The inherent limitation of this approach is the uncertainties associated with actual evapotranspiration (AET), groundwater recharge, and surface runoff. Water budget methods include explicit or implicit (lumped) approaches. For example, standalone CaWaQS relies on a lumped production function that calculate the groundwater recharge, the surface runoff and actual evapotranspiration as a function of soil type and land use. However, lumped approaches are inherently limited to the conceptual understanding of the application area, and they are not suitable for studies of underlying physical processes that drive groundwater recharge, AET, or surface runoff. On the other hand, Soil-Vegetation-Atmosphere Transfer (SVAT) models aim to explicitly calculate the components of the water budget by a set of physical equations (Koster et al., 2000). Integrating SVAT into a groundwater model could improve the estimation of groundwater recharge and understanding of the underlying processes. This approach also has other benefits as state-of-the-art SVATs simultaneously estimate energy and carbon processes that could be coupled with groundwater models to study the energy balance or carbon dynamics in relation to groundwater; also improve the transferability of parameters to other similar catchments.

ORCHIDEE SVAT model (see Chapter 5) was selected for this study as it accounts for the explicit surface water balance processes and is tightly coupled with the energy processes at the near-surface with the actual evapotranspiration term. It simulates water budget and energy balance at the near-surface simultaneously and produces surface runoff, infiltration, actual evapotranspiration, and the temperature at the surface and within the soil column. Coupling the ORCHIDEE model with a groundwater model CaWaQS can alleviate some of the constraints in current groundwater models, such as distributed recharge and evapotranspiration estimation and coupled energy processes, which could be then used to force a heat transport simulation of the groundwater.

The Seine basin was previously simulated by ORCHIDEE (Otalora, 2016) with a much coarser forcing file, and no attempt was made to couple it with a groundwater model. Therefore, developing the model with a high-resolution meteorological forcing

and estimating the surface water budget and energy balance could pave the way to a full hydrosystem simulation. CaWaQS already simulates the Seine basin as validated in the previous studies (Flipo et al., 2020a). Therefore, this study aims to develop the hydrological coupling of two models to achieve a satisfactory water balance. Such coupled model can then be used for explicit heat transport simulations for the understanding of the energy balance of the Seine basin and also to test future climate change scenarios (Flipo et al., 2020a). The objectives of this work were: **(i)** Construct the Seine basin application in the ORCHIDEE model; **(ii)** Calibrate the surface water balance with the help of various boundary conditions (soil texture maps), and by constraining the soil hydrology, vegetation, and albedo parameters; **(iii)** Evaluate the performance of the calibrated ORCHIDEE model by the help of Leaf Area Index (LAI) and Actual evapotranspiration products; **(iv)** Couple the surface hydrological fluxes (runoff and recharge) to CaWaQS model and evaluate the coupled model performance.

6.2 Data and methods

In this section, the development of ORCHIDEE Seine model and the selection of soil and land cover maps, the CaWaQS Seine model are presented. The integration of two models and the calibration and evaluation procedures, the selected parameters are described.

6.2.1 Construction of the Seine model

The construction of the ORCHIDEE model and its application on the Seine hydrosystem contains multiple steps. SVAT models are data intensive and require information from multiple sources to simulate water and energy fluxes simultaneously. ORCHIDEE also requires input from multiple data streams:

- Meteorological forcing data
- Soil texture distribution map
- Vegetation distribution map

- Slope map
- Yearly carbon concentration

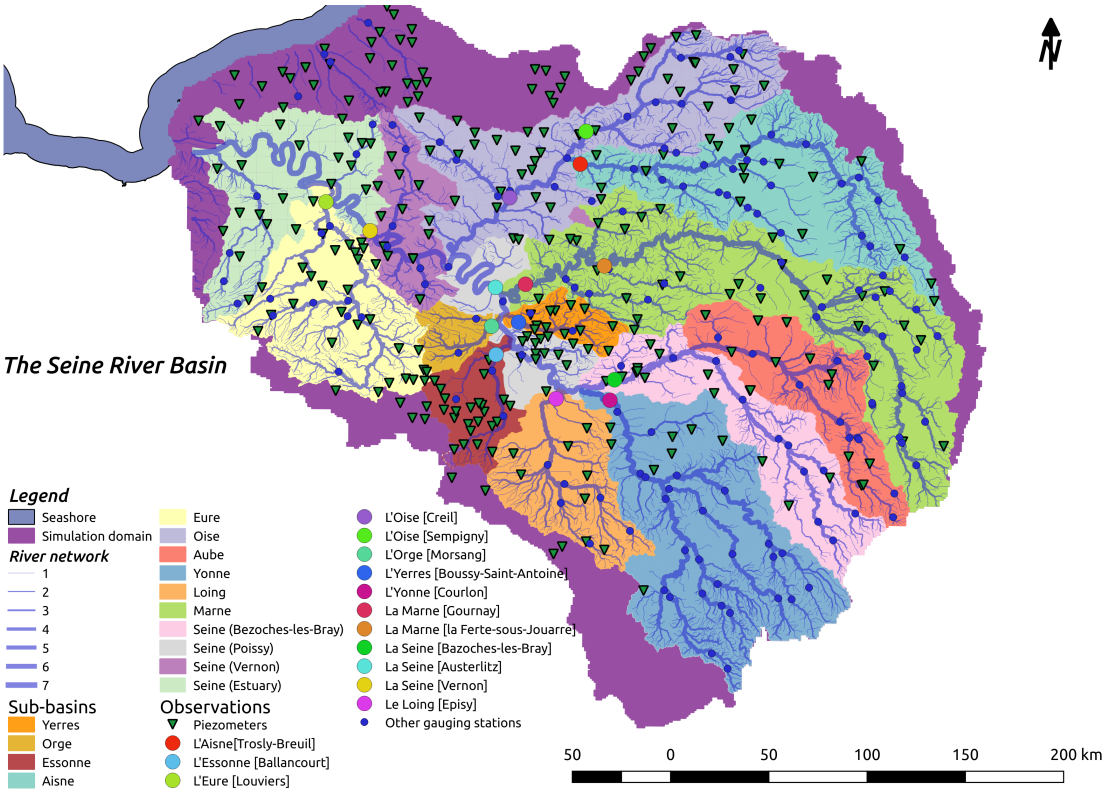

Figure 6.1 The simulated domain by ORCHIDEE. Main sub-basins in the basin are shown. River network is not simulated by ORCHIDEE. Evaluation data locations are noted: piezometers (triangle), and major gauging stations (circle).

Meteorological forcing data were obtained from the SAFRAN dataset (Vidal et al., 2010b; Quintana-Seguí et al., 2008; Durand et al., 1993). The meteorological data variables required by ORCHIDEE are precipitation (snow, rain), surface air temperature, surface air pressure, surface air humidity, wind speed, long-wave and short-wave radiation. At the France scale, Météo-France produces distributed meteorological forcing as a sub-product of global circulation models at 8km resolution. The resulting data are called SAFRAN (Système d'Analyse Fournissant des Renseignements Atmosphériques à la Neige) (Durand et al., 1993). SAFRAN is an analysis system using an optimal interpolation (OI) method to compute each value analysed by modifying the first-guess field with the weighted mean of the difference between observed and first-guess values at station locations within a search distance. The first guess comes from the large-scale

ARPEGE operational weather prediction model at a 0.25° resolution, and the observations come from Météo-France monitoring stations (n ≈ 4100 stations for precipitation and n ≈ 1100 stations for temperature over metropolitan France). The analysis is performed on climatological homogeneous areas, and the variables analysed are projected to an 8-km) regular grid accounting for elevation. The orography is set from a high-resolution 8 km × 8 km digital elevation model, and temperature and precipitation are determined with a vertical step of 300 m (Quintana-Seguí et al., 2008). SAFRAN is constructed on a dense observation network and comparisons with observations, including precipitation and temperature. Comparative studies between SAFRAN reanalysis and observations show a good match (Vidal et al., 2010b). For these reasons, SAFRAN was selected as the meteorological forcing in this study.

However, the SAFRAN dataset does not provide surface air pressure. This variable data was obtained from the MERRA (The Modern-Era Retrospective Analysis for Research and Applications) satellite product (Rienecker et al., 2011). This reanalysis data combines field observations with satellite observations. The MERRA product is produced at 0.5°-0.66° resolution and at 1 hour time step. The MERRA product was combined with SAFRAN data using the SAFRAN grid as a base for the MERRA dataset. Overlapping cells were identified, and the information was passed to the forcing files. In the cells where more than one MERRA cell was available, an area-weighted average was applied to the surface air pressure to obtain the pressure of that cell.

While preparing the Seine model, the SAFRAN dataset was masked over the Seine domain, resulting in 1490 active cells representing the basin (Figure 6.1). The SAFRAN cells overlaying on the Seine basin were identified and subsetted with the help of the GIS environment. The discretisation of the cell is the same as the SAFRAN meteorological data resolution, i.e. 8 km * 8 km. The resulting mesh contains 2650 cells with 1490 active cells representing the Seine catchment (Figure 6.1) .

6.2.2 Soil information

Soil surveys, in general, aim to map the distribution of clay, silt, and sand particles of the horizon. From the distribution of the three types of soil particles, the dominant

soil texture can be obtained via a lookup table (as in Figure 6.2). Different institutions provide several soil texture classes, though there are two commonly used classifications (the USDA and Europe soil classification). The soil classes obtained from these maps are linked to the soil hydraulic properties via pedo-transfer functions.

ORCHIDEE model requires a soil texture distribution map to assign each grid cell with a pre-defined set of soil hydrological and thermal parameters as a function of the soil texture. By default, the soil texture of ORCHIDEE can be assigned to two types of soil maps. First, the Zobler (Zobler, 1986) soil texture map with 1° resolution and 5 soil texture classes: Coarse, Medium to Coarse, Medium, Fine to Medium, and Fine. The second soil texture class is provided by Reynolds et al. (2000) at $5\mathrm{min}$ resolution based on the USDA soil classification system. The Reynolds map has 12 soil texture classes.

In this study 4 soil texture distribution maps were evaluated, including the default Reynolds map:

1. SoilGrids map (SP-MIP, Gudmundsson et al. (2019), (Hengl et al., 2017))., SoilGrids website) The database is at 250 m resolution horizontally and uses equidistant Equi7 grid projection. The soil predictions are derived from a major soil profile compilation set and with the help of machine learning techniques (Hengl et al., 2017). The SoilGrids database provides the global soil distribution and the fractions of sand, silt, and clay at 250 m resolution. The procedure describing how the USDA classes are obtained is described below.

2. INRA soil map: INRA InfoSoil soil map is developed as a part of the European Soil Database (ESDB, 2004). The goal of this database is to obtain the surface soil information, including the soil thickness, the dominant soil texture types, and the classification of soils based on FAO soil classification and the dominant land use. The database is developed at 1:1.000.000 scale with Lambert Azimuthal projection. The database provides the dominant soil texture types (varying sand, silt, and clay ratios) in 5 classes: very fine, fine, medium, medium coarse, and coarse soils. The method of conversion between European soil classes and USDA soil classes is described below.

3. Reynolds map (Reynolds et al., 2000): Reynolds map provides a global soil texture map. It converts the FAO soil map (1996) to USDA soil texture classes at 1°/12 resolution (≈ 9 km). It uses the plate carrée projection.

4. LUCAS map (Ballabio et al., 2016). The Land Use and Cover Area frame Statistical survey (LUCAS) aims to collect land use and land surface data. It uses a high number of soil survey data and combines the satellite products (SRTM, MODIS) to predict the soil textures. It provides soil texture predictions for the 23 European countries at 500 m resolution with Lambert Azimuthal projection.

LUCAS and Reynolds maps were already provided in the USDA soil texture class format, whereas, SoilGrids and INRA maps required pre-processing to obtain USDA soil texture class equivalent.

The distribution of the USDA soil texture classes from the SoilGrids map is obtained with the following methodology: The fractions of sand, silt, and clay over the Seine basin are obtained from the SoilGrids database. The zonal means of each particle size are obtained within 8 km grids. The USDA soil class distribution in the Seine basin is obtained from the ternary particle distribution diagram (Figure 6.2) provided by the "soiltexture" package in the R environment (R Core Team, 2017). The soil texture maps were prepared as the ORCHIDEE input with the help of "ncdf4" package in the R environment

To obtain the lookup table to prescribe the USDA soil texture classes distribution from the INRA InfoSoil map, the following methodology is used: The dominant soil textures described in the ESDB legend are obtained for each soil mapping unit. The soil textures provided in the ESDB legend (Very fine, fine, medium, medium coarse, coarse) are translated into the corresponding USDA soil classes via a lookup table based on superposing European soil classes on USDA soil classes (Figure 6.2, Table 6.1). However, it should be noted that this transformation does not depend on additional analysis, and it is subject to uncertainty. The soil map representing the Seine basin is obtained in the GIS environment and transferred to the ncdf file using the "ncdf4" package in the R environment.

Table 6.1 The lookup table used to transform European soil classification to USDA soil classification according to Figure 6.2

Soil no	European soil texture class	USDA soil texture
1	Very Fine	Clay
2	Fine	Sandy Clay
3	Medium Fine	Silty Loam
4	Medium	Loam
5	Coarse	Loamy Sand

The soil texture distribution maps subsetted for the Seine River basin are provided in Figure 6.3. These maps are used for the first four simulations of the calibration period. The Reynolds map contains predominantly Loam and Clay Loam soil textures and small patches of Loamy Sand and Sandy Loam. LUCAS and SoilGrids maps show a similar distribution of the soil textures spatially, but they differ in terms of soil textures. While SoilGrids has Silty Clay and Clay Loam soils, the LUCAS map has predominantly Silt Loam and Silt Clay Loam. Both maps contain a significant portion of Loam. The INRA map has Loam, Silty Clay, Silt Loam and Sandy loam soils; however, it shows little spatial resemblance towards the east compared to other maps.

The distribution of soil textures in the Seine basin sub-catchments is provided in Figure 6.4. Notably, The Eure has almost uniform soil texture distribution in the whole domain for some soil maps: for example, Reynolds and LUCAS maps. LUCAS and SoilGrids, and INRA maps have significant portions of silty soils in almost all catchments. Having silty soils, with relatively low hydraulic conductivity, can reduce infiltration. In the Reynolds map, no silty soils are present, and throughout sub-catchments of the Seine basin, Clay loam and Loam share the significant portion of the catchment.

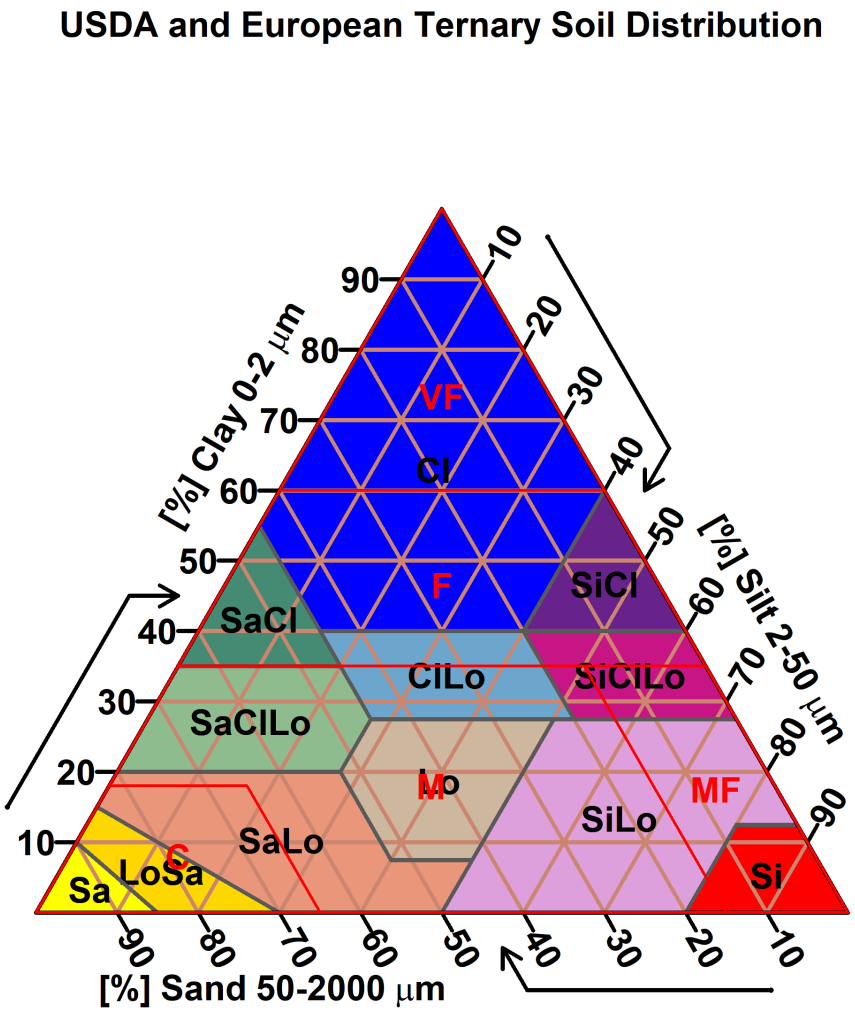

Figure 6.2 Ternary diagram of the USDA soil classification system (Grey) USDA, 1993) overlapped by European Ternary Diagram (red). (Cl = Clay, SiCl = Silt Clay, SaCl = Sandy clay, ClLo = Clay loam, SiClLo = Silty Clay Loam, SaClLo = Sandy Clay Loam, Lo = Loam, SiLo = Silty Loam, Si = Silt, SaLo = Sandy Loam, LoSa = Loamy Sand, Sa = Sand; VF = Very Fine, F = Fine, M = Medium, MF = Medium Fine, C = Coarse)

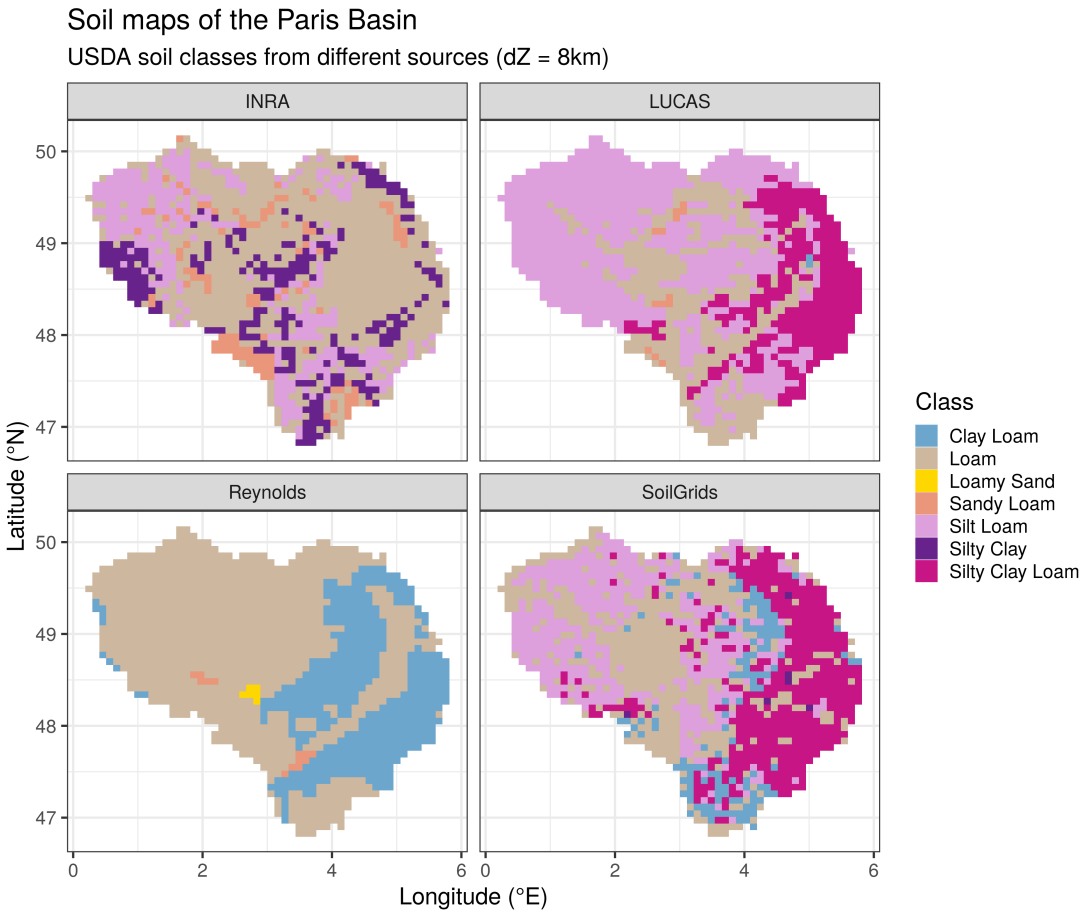

Figure 6.3 The soil classification maps from INRA, LUCAS, Reynolds, SoilGrids

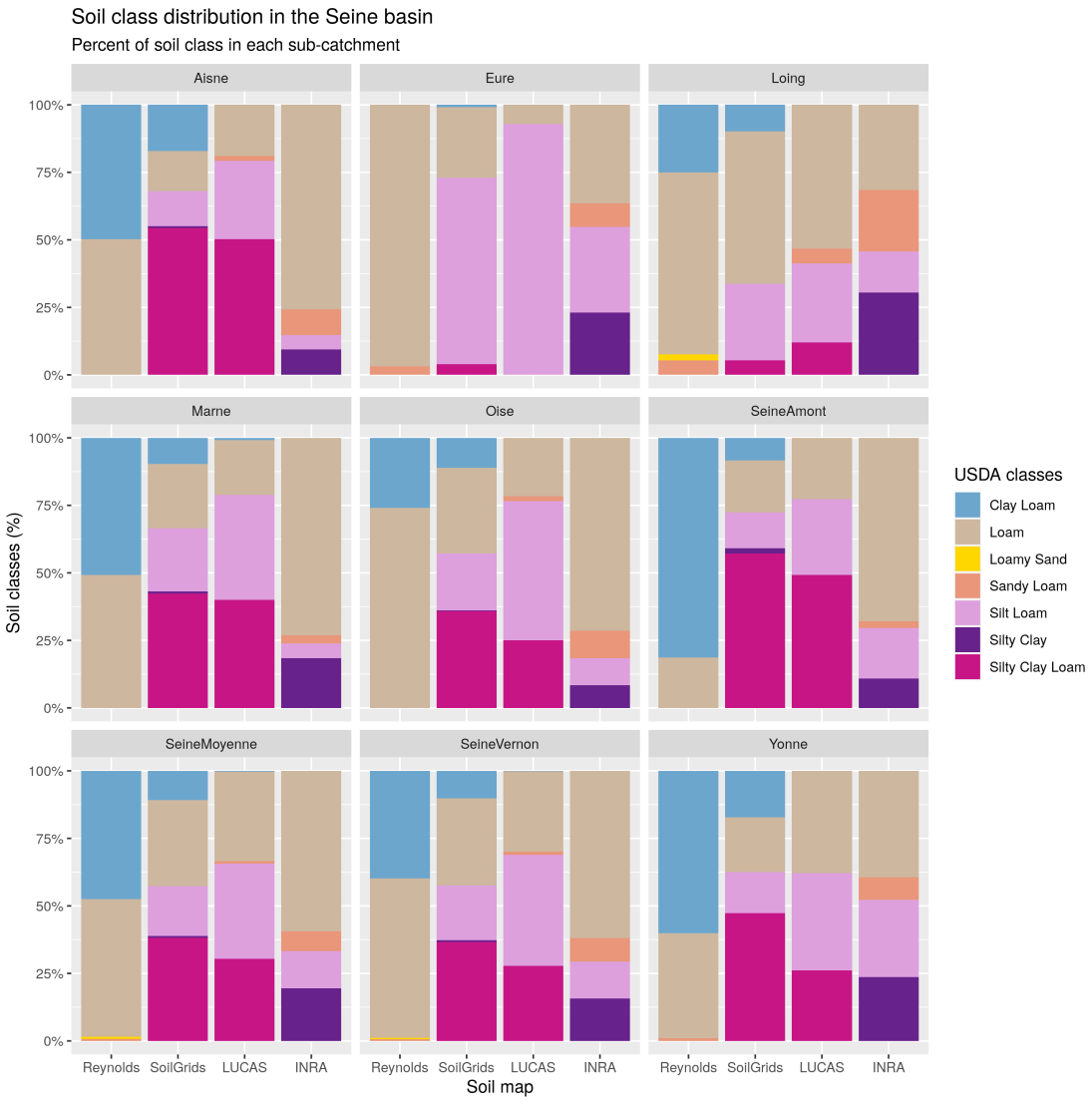

Figure 6.4 Soil distribution of different soil maps per sub-catchment in the Seine basin

6.2.3 Vegetation

The vegetation map in this application was obtained from the ESA CCI-LC (ESA-CCI Page) database. This product is generated from different global surface reflectance time series covering the 1992-2015 period. The pre-processing includes radiometric, geometric and atmospheric effects correction. Supervised and unsupervised classification algorithms were combined in an automated procedure to derive the land cover classes (ESA Land Cover, 2017). 22 primary and 16 sub-level land cover classes were defined based on the United Nations Land Cover Classification System (UN-LCCS, FAO webpage). The product was globally validated based on expert verification of a network of 2600 points (ESA Land Cover, 2017). The conversion procedure of the ESA CCI LC product into ORCHIDEE PFT classes is delineated by Lurton et al. (2020). The detailed documentation of the conversion can be found in the ORCHIDAS database. This procedure consists of aggregating 38 distinct land cover types into 15 PFT types. Figure 6.5 illustrates the distribution of land cover types from the ESA CCI LC product (2015). The PFT map based on the ESA-CCI map for the year 2015 is given in Figure 6.5. Mainly, the forested areas are aggregated into two PFT types. The forests in Western Europe consist of broadleaved summergreen and needle-leaved evergreen tree types. Agricultural crops and grasslands are represented by C3 type agricultural crops and grass types, respectively. The urban aggregation is handled by the bare soil PFT class.

This database, prepared by the ORCHIDAS team, is available in the IPSL repository. Spatially, high-resolution land cover representation (0.025°, 0.05°, 0.1° resolution) is available for the period 1992-2015 at the IPSL repository.

The variation of vegetation types can be seen in Figure 6.7. The dominant vegetation type in the basin is C3 type agricultural crops. C3 grass is the second abundant PFT class in the basin. Around 2% of the basin's surface area is covered by temperate trees forming the forestry in the basin. The portion of the forestry is relatively stable. Over the span of 24 years, the agricultural area distribution diminishes by around 2% after 2000. The reduction in the agricultural areas are due to urbanisation as the bare soil

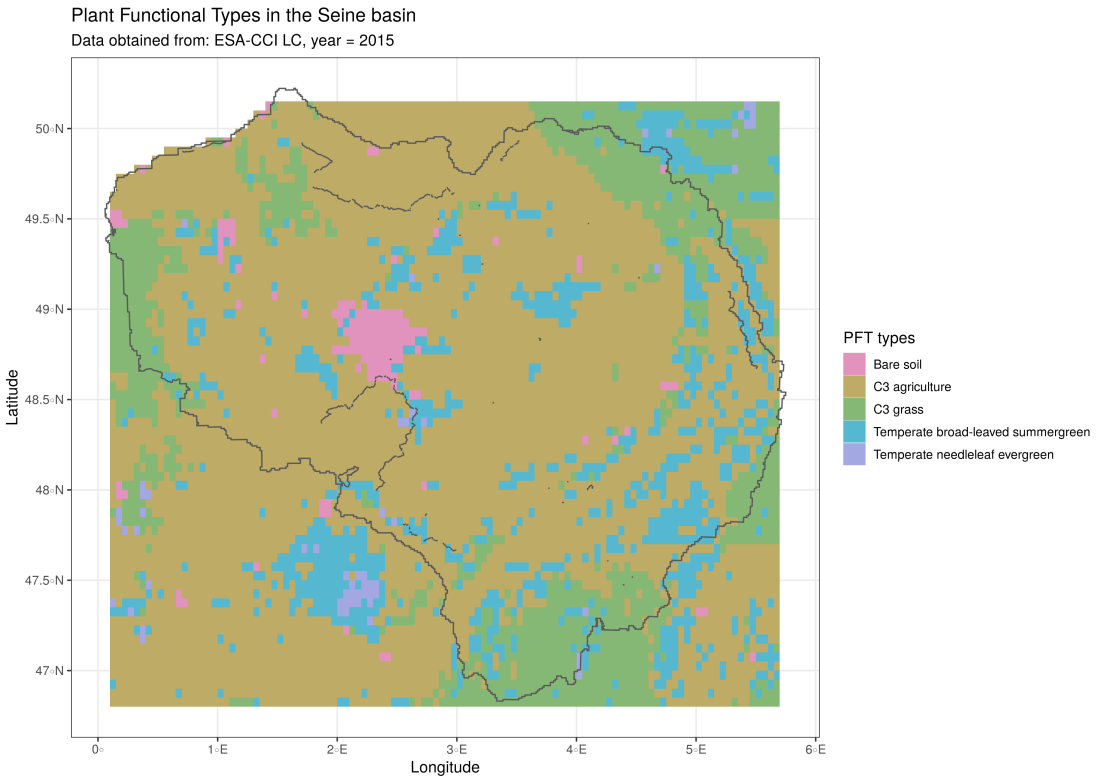

Figure 6.5 ESA-CCI 2015 land cover map over the ORCHIDEE Seine Basin grid (resolution = 300 m)

portion increases after the same year.

STOMATE was activated to include vegetation processes dynamically. It controls the transpiration via stomatal conductance, and the canopy layer capacity in terms of surface hydrology. The vegetation dynamics are calculated over time, and the corresponding LAI is updated at each time step of the STOMATE module. Vegetation parameters and how they are used within the ORCHIDEE model are described by Krinner et al. (2005). The vegetation parameters are obtained from Smith et al. (1998), and Sitch et al. (2003).

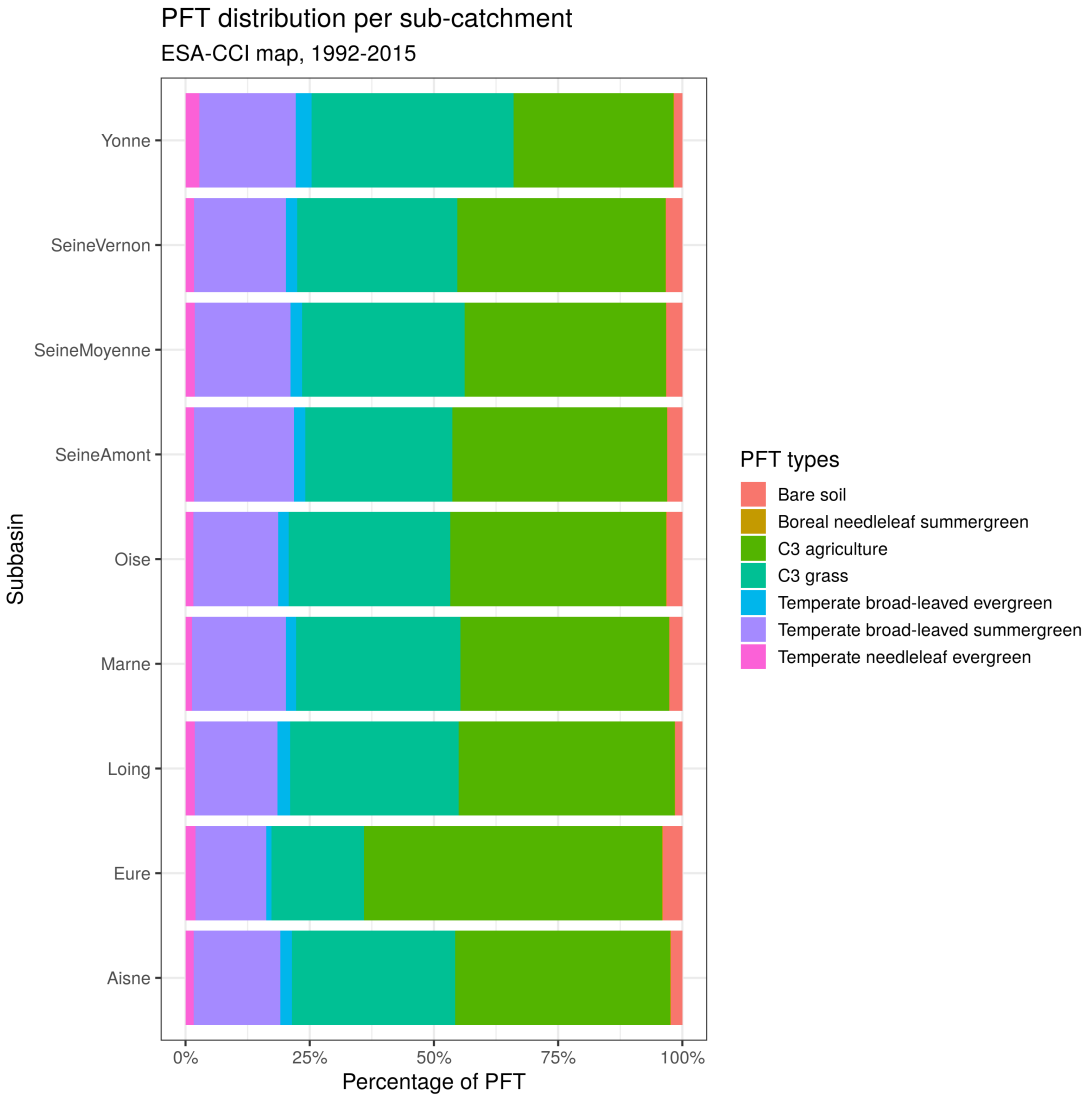

Figure 6.6 Distribution of vegetation by sub-catchment in the Seine basin

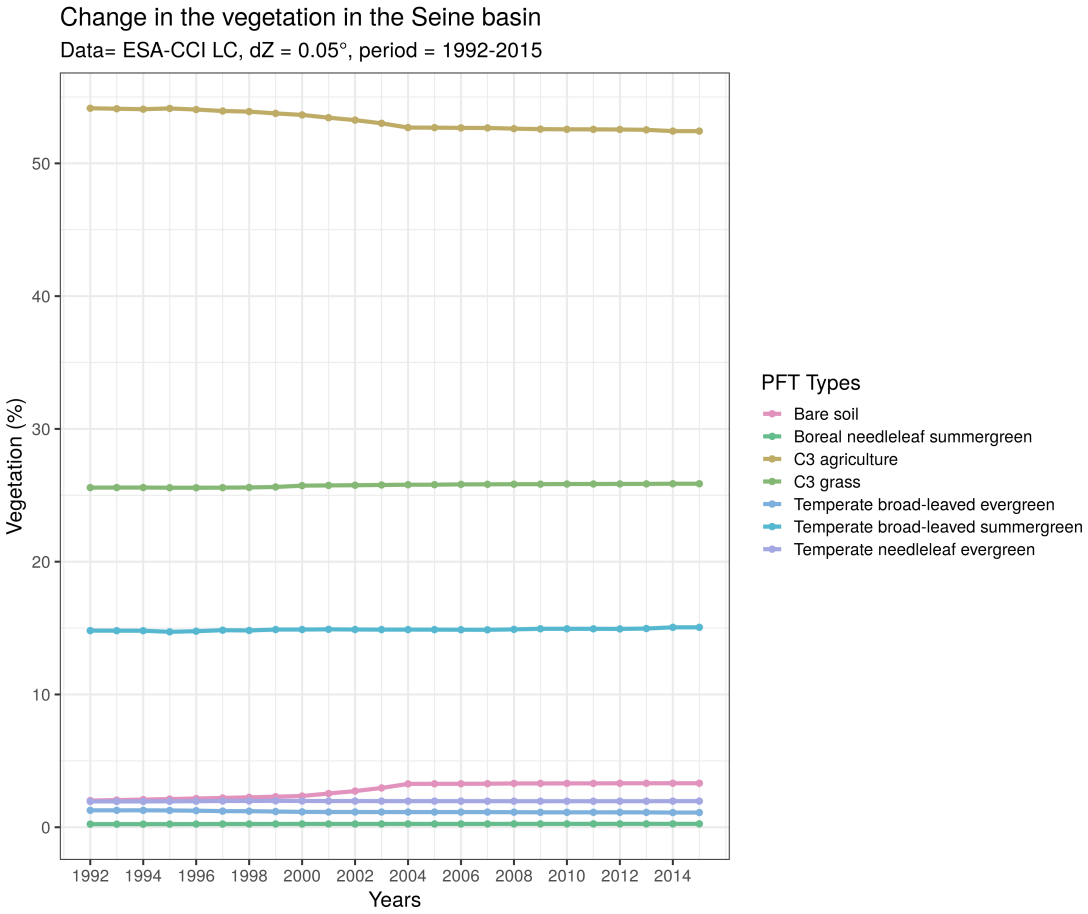

Figure 6.7 PFT type variation in the period 1992-2015 of the Seine Basin

6.2.4 Slope map

The slope map is obtained from IGN DEM at 25 m resolution (Figure 6.1). For each pixel, the slope in degrees is obtained and converted to a percentage through the QGIS environment. The slope of each grid is upscaled by averaging the slope of each pixel from 25 m to 8 km with bi-linear interpolation in the R environment with the "raster" package. The corresponding slope map is provided in Figure 6.8. The map currently used by other applications of ORCHIDEE (Otalora, 2016) is obtained from NGDC-etopo2 database at a coarser resolution (0.25° = 27 km).

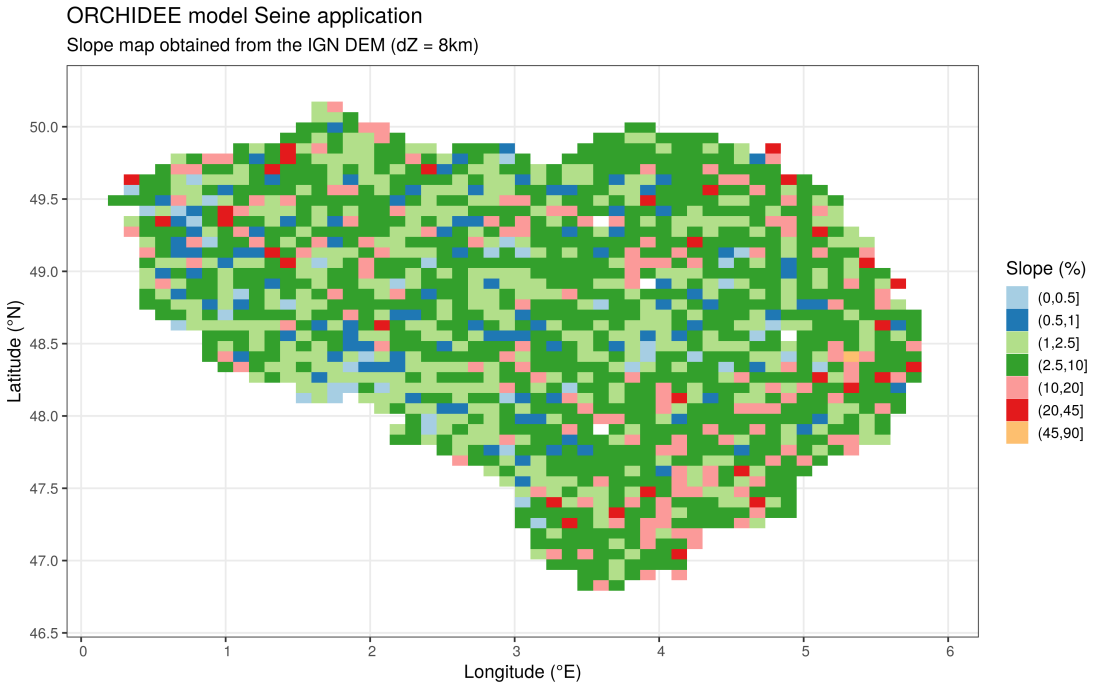

Figure 6.8 The slope map transformed from an IGN 25m DEM database

In the ORCHIDEE model, surface slope plays a role in the re-infiltration process. Cells with a lower than 0.5$\%$ slope reinfiltrate part of the runoff at the end of each time-step. This parameter is modifiable and is shown to influence the runoff - drainage partition (Tafasca et al., 2019).

6.2.5 Introduction of a new soil class: urban

The Seine basin is covered by a significant amount of urban agglomeration (Figure 6.5, noted Bare soil). The existence of urban areas modifies the hydrology at the surface. Mainly, the urban structures, pavements create an impermeable layer that diminishes the porosity, and conductivity of soils. It reduces soils capacity to infiltrate. Moreover, the construction of buildings settle on the foundation, and compress the soil, therefore reducing the porosity. Sewage systems in cities route collected precipitation directly to the river network. Precipitation events are therefore drained without contributing to the groundwater recharge. These modifications at surface change the streamflow dynamics at the outlet.

The hydrodynamics of urban hydrology, transport mechanisms (Sini et al., 1996) are complex, and the estimation of soil properties are difficult (De Kimpe and Morel, 2000). ORCHIDEE allows users to define or modify the soil hydraulic parameters to introduce new Pedo-transfer functions. In thus study, a new urban soil class was described. Two steps were taken:

- A soil texture map was developed in line with the land cover distribution (Figure 6.9)
- The saturated hydraulic conductivity, K_{sat} was modified to $7.5 * 10^{-8}\ \mathrm{m\,s^{-1}}$ (equivalent of $6.5\mathrm{mm\,y^{-1}}$) obtained from Berthier et al. (2004).

6.2.6 Water abstraction

The ORCHIDEE model does not explicitly account for the water abstractions, as it simulates a natural basin. The Seine basin, however, is dominated by agricultural and industrial applications that withdraw a considerable amount of water (see section 2.3.1). The agricultural withdrawals usually occur during the irrigation period, i.e. from June to September.

During the calibration period, the impact of the water withdrawals at the outlet of the main sub-catchments was taken into account. The water withdrawal data from the

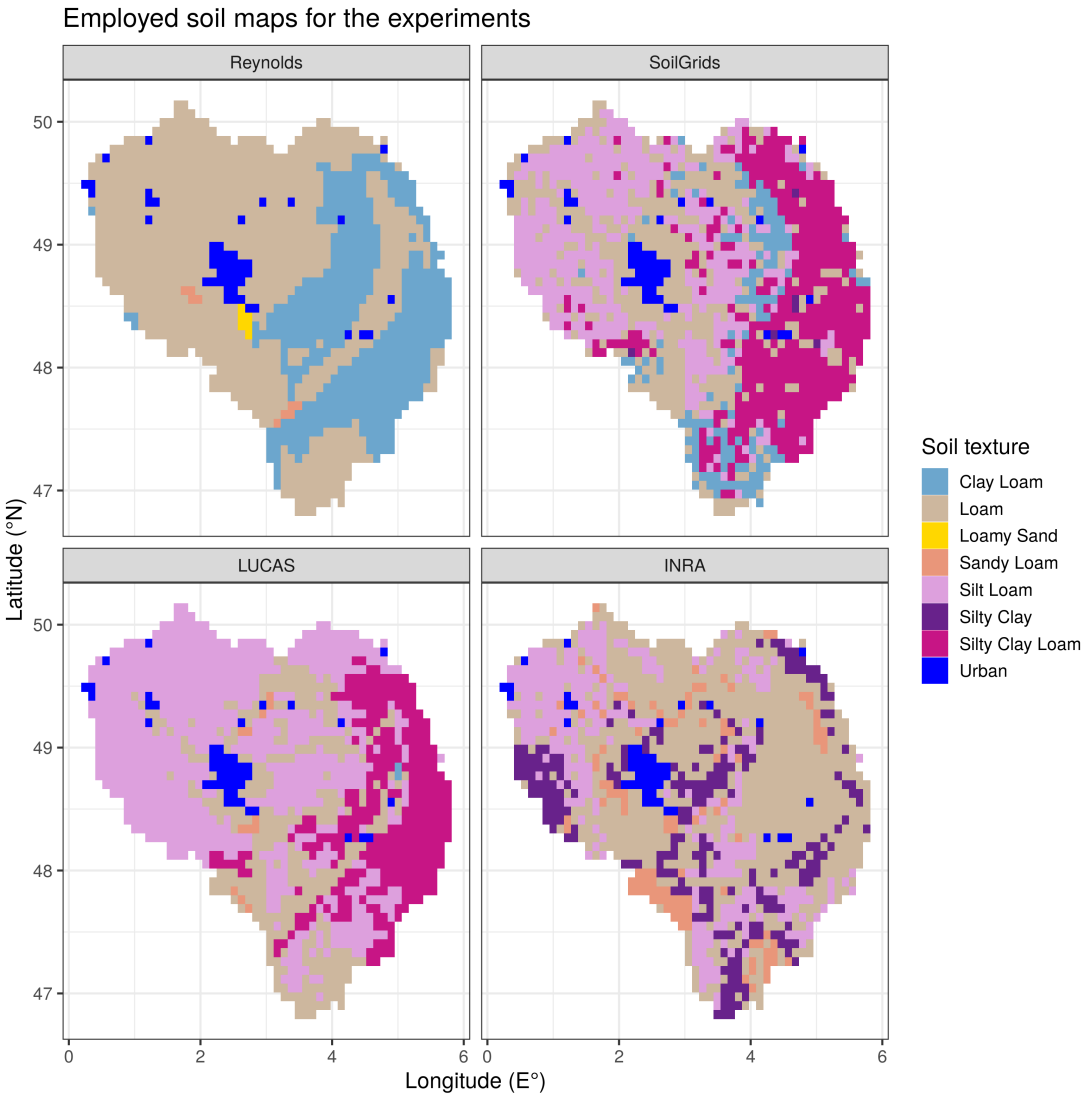

Figure 6.9 Various soil texture distribution maps with new urban soil texture class.

Seine basin water management agency (AESN, 2013) for domestic, industrial and agricultural needs were aggregated over the catchment. An average withdrawal rate is then obtained for the main catchment. The water abstraction data provided for the period 2008-2012 indicates that up to 37 $\mathrm{m^3\,s^{-1}}$ is abstracted from the catchment. The estimated groundwater withdrawal rate was then removed from the calculated total surface runoff calculated by ORCHIDEE; Then the bias on pluri-annual mean discharge was estimated. This effectively accounts for the water withdrawals from the basin that would otherwise cause a positive bias since ORCHIDEE only considers a natural basin without urban effects.

6.2.7 Technical considerations of the Seine application

A limitation is the uncertainties related to soil description. The basin is covered mainly by carbonates (over 60%). An significant limitation is the routing module. ORCHIDEE requires a routing map to simulate the effective rainfall routing; however, such a map is not available for the Seine basin. The routing module provides the fast reservoir and slow reservoir routing of the excess water with proper transit time. Otherwise, the estimated total runoff time series would not reflect the discharge at the outlets of the sub-catchments in the Seine basin.

The forcing data is also subject to uncertainties and bias related to model or instrument limitations. Different forcing data have been compared by Otalora (2016); however, the SAFRAN dataset was not tested.

6.2.7.1 Extending ORCHIDEE unsaturated zone to water table

A limitation of the ORCHIDEE implementation on the Seine River Basin, is that the unsaturated zone extends beyond the root zone (by default 2 meters) simulated by ORCHIDEE (Figure 6.10). There are several possible solutions to obtain the recharge from the infiltration. CaWaQS model uses a conceptual Nash-cascade reservoir solution to estimate the flow (Flipo et al., 2020a). Another possible solution is to use a 1-D vertical numerical model (Rivière et al., 2014) to estimate the fluxes at the water table by using the surface infiltration as forcing. The third solution is to transfer infiltration into recharge directly to the groundwater model, which is the case in this study, given that the basin has mostly 0-15 m unsaturated zone thickness. Considering the addition of a 1-D vertical model to transfer recharge creates additional computational burden, the third solution was selected within the scope of this study. However, it must be noted that lack of deeper water table has implications on the actual evapotranspiration (Fan et al., 2007).

In this application, we assume that the soil bottom of ORCHIDEE reaches the water table, so the drainage at the bottom directly contributes to the aquifer system as recharge. Similarly, the surface runoff estimated by ORCHIDEE is prescribed to

CaWaQS; therefore, the runoff is collected by CaWaQS and transferred to the river network. This approach was deemed best given that the complexity of the unsaturated zone is difficult to simulate at a high resolution without a high computational cost. Also, the unsaturated zone thickness varies spatially and temporally in the basin, and ORCHIDEE is not able to simulate a variably thick soil column yet.

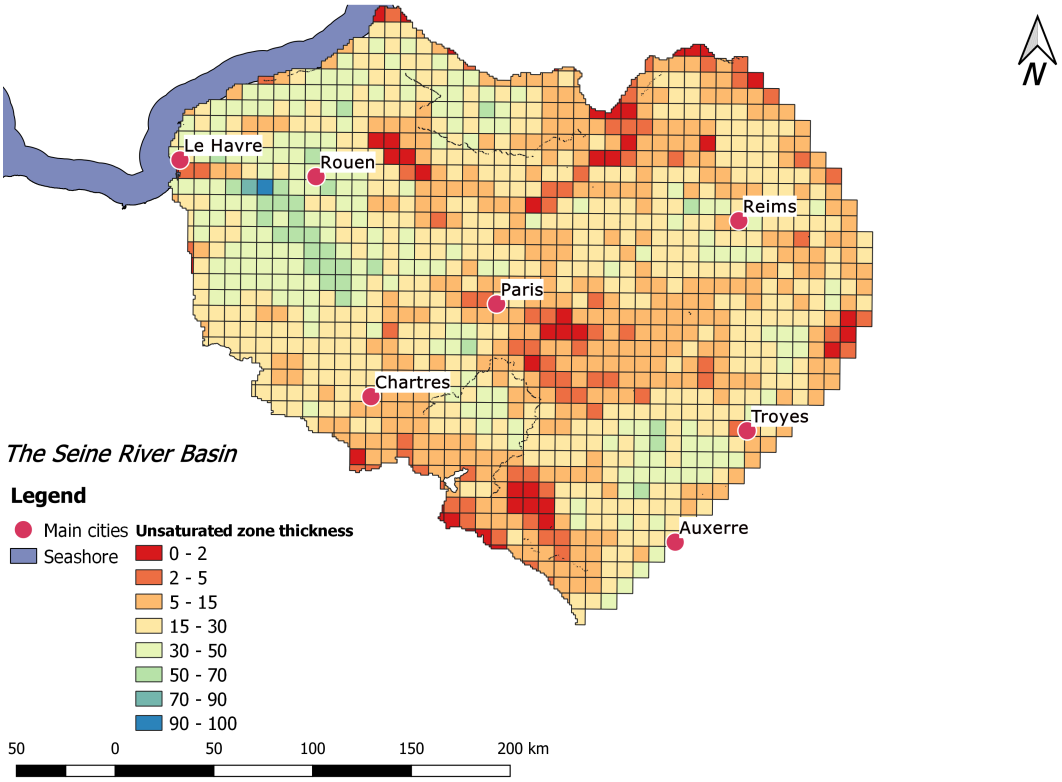

Figure 6.10 ORCHIDEE grid structure intersected with unsaturated zone thickness from a previously validated CaWaQS model application

6.2.8 CaWaQS setup

An existing CaWaQS application developed over the Seine basin, with the main aquifer units and 28375 km river network, (Flipo et al., 2023), was used in this study. The aquifer system (see Chapter 2) defined in this application includes 8 aquifer layers:

- The Alluvial layer mainly focused around the main tributaries of the river network, which consists of alluvial deposits
- The Beauce aquifer, including the Rupelian limestones
- The Brie aquifer ensemble of Priabinian Brie limestones and Fontainebleau sands
- The Champigny aquifer composed of Upper-Eocene Champigny limestones and Beauchamp sands
- The Lutetian aquifer composed of Lutetian limestones and Yprecian sands
- The Thanetian aquifer composed of Thanetian limestones
- The Upper Cretaceous Chalk aquifer
- The Jurassic layer ensemble, which combines various aquifer and aquitard layers that reach down to 2500m depth overlain on the Hercynian crystalline rock.

In this study, the river geometry, including reach length and width, was obtained from SYRAH-CE (Chandesris et al., 2008) database. The river network gathes water from three sources: the surface runoff, overflows from the aquifer that are considered as stream-aquifer exchanges on headwaters (Strahler order <= 2), and the river-aquifer exchanges in the river reaches with Strahler order above 3 where exchanges are calculated by the concept of conductance (Pryet et al., 2015). Due to the computation time concerns, explicit river-aquifer exchanges are limited to Strahler order above 2.

The parameter set defining the aquifer system (transmissivities, storage coefficient, drainance) and river network (conductance) were obtained from a previously calibrated application by Flipo et al. (2023). The hydrological conditions defined in the CaWaQS Seine model are:

- A no-flow boundary condition is imposed at the bottom and border limits of the domain, except where the mesh boundary corresponds to an adjacent river.
- Groundwater withdrawals are considered as a daily pumping rate inferred from the annual groundwater abstraction data obtained from AESN (AESN, 2013).
- Agricultural withdrawals are assumed to take place only during the summer period (i.e. bulk irrigation water volume is distributed as: 20% in May, 30% in June and July, and 20% in August).
- The coastal hydraulics are neglected; therefore, the basin outlet before estuaries at Vernon is set as the downstream outlet of the Seine basin.

6.2.9 Calibration strategy

ORCHIDEE application represents the surface water component of the integrated model. The calibration of the surface water component consists of simulating the discharge of each sub-catchment correctly. The objective functions used in this study consist of Root Mean Squared Error (RMSE), percent bias (BIAS), correlation coefficient (CC), Nash-Sutcliffe Efficiency (NSE), Kling-Gupta Efficiency (KGE) and the comparison of total surface runoff with reference observed discharge at each sub-catchment outlet. The performance of pluri-annual discharge was evaluated by the relative bias.

The calibration procedure was carried out manually. The principle goal of the calibration is to tune the parameters described in the following sections taking into account the surface component functioning. Statistical criteria were applied at each sub-catchment.

6.2.9.1 The theoretical background of pluri-annual water budget

Pluri-annual hydrosystem water budget was calculated to evaluate the model performance (Labarthe, 2016; Flipo et al., 2020a). The hydrosystem water balance is given by equation 3.10. The hydrosystem water balance over a given basin during a short time interval dt can be expressed as follows:

$$p(t) - aet(t) = q_{out}(t) - q_{bound}(t) + \frac{ds_{surf}(t)}{dt} + \frac{ds_{sub}(t)}{dt} \tag{6.1}$$

Where p(t) is the precipitation rate, aet(t) is the actual evapotranspiration rate, q_{out}(t) is the river discharge at the basin outlet, q_{bound}(t) is the incoming subsurface fluxes through the basin boundary, $\frac{ds_{surf}(t)}{dt}$ is the water storage variation in the surface storage and $\frac{ds_{sub}(t)}{dt}$ is the water storage variation in the subsurface in $\mathrm{m}^3\,\mathrm{s}^{-1}$, whereas the time interval dt is in seconds. The instantaneous surface water budget, in this case, is defined as follows:

$$p(t) - aet(t) = runoff(t) + recharge(t) + \frac{ds_{surf}(t)}{dt} \tag{6.2}$$

Over a sufficiently long time, the stock variations in the subsurface and surface components can be neglected, and the integrated surface water balance for a major hydro-climatic period yields:

$$P - AET \approxeq Q_{out} \tag{6.3}$$

where P and AET are the time-averaged precipitation and evapotranspiration in the watershed over a sufficiently large period of time, Q_{out} is the time-averaged total discharge at the basin outlet, and it is a combination of time-averaged surface runoff and baseflow. This equation makes it possible to calibrate the water fluxes with discharge data at the outlet of sub-basins and the basin, as the aquifer recharge and evapotranspiration can be constrained.

6.2.10 Validation criteria

6.2.10.1 Percent Bias (BIAS)

The bias, or mean error (BIAS) were computed for each sub-catchment through a term-by-term comparison of the relative error in the prediction with respect to the actual value of the mean discharge:

$$BIAS = 100 * \frac{\frac{1}{N}\sum_{t=1}^{N}(X_{sim}(t) - X_{obs}(t))}{X_{mean}} \tag{6.4}$$

where N is the number of values that can be compared, and X(t) is the variable simulated or observed (with indices sim or obs). The bias quantifies the relative mean difference between the simulated and observed time series. The optimal value is 0; while a positive value indicates an overestimation, a negative value indicates an underestimation.

6.2.10.2 Root mean squared error (RMSE)

The root mean squared error (RMSE) or the standard deviation is the mean of the squared differences between observed and calculated values. The measurement estimates the spread between the observed data and calculations. These criteria are used widely in groundwater studies, mainly to compare how the piezometric head estimations perform against the observed piezometric heads (Labarthe, 2016; Flipo et al., 2014; Gupta et al., 2014).

$$RMSE = \sqrt{\frac{\sum_{j=1}^{n}(Q_{obs} - Q_{sim})^2)}{n}} \tag{6.5}$$

where Q_{obs} is the observed value, Q_{sim} is the simulated value, and n is the number of days of simulation.

6.2.10.3 Correlation Coefficient (CC)

Correlation coefficient (CC) indicates the strength and direction of a linear relationship between two random variables. It is also referred to as *Pearson's product-moment correlation coefficient*.

$$CC = \frac{1}{N}\frac{\sum_{t=1}^{N}(X_{obs}(t) - X_{mean,obs}) * (X_{sim}(t) - X_{mean,sim})}{\sigma_{X_{obs}}\sigma_{X_{sim}}} \tag{6.6}$$

where is the standard deviation $\sigma = \sqrt{\frac{1}{N-1}(\sum_{t-1}^{N}(X(t) - X_{mean})^2)}$. The value of CC ($\rho$) varies between -1 and 1; a negative value indicates a negative linear correlation, and a positive value indicates a positive correlation. Values close to 0 indicate weak or no linear correlation between two variables. CC = 1 means perfect correlation.

6.2.10.4 Nash-Sutcliffe Efficiency (NSE) coefficient

The Nash-Sutcliffe (NSE) coefficient measures the model's performance against the overall mean flow.

$$R^2 = 1 - \frac{\sum_{j=1}^{n}(Q_{obs} - Q_{sim})^2)}{\sum_{j=1}^{n}(Q_{obs} - \bar{Q}_{obs})^2)} \tag{6.7}$$

where $\bar{Q}_{obs})^2$ is the mean observed flow rate, Q_{obs} and Q_{sim} are observed and simulated flow rates, respectively. The value R^2 varies between $-\infty$ and 1, where the value of 1 represents a perfect model fit. Values of 0 and below indicate that the model predicts no better than using the mean of the flows.

6.2.10.5 Kling-Gupta Efficiency (KGE) coefficient

The Kling-Gupta Efficiency (KGE) coefficient (Gupta et al., 2009) measures the model's performance by evaluating relative importance of its different components such as correlation, bias, and variability.

$$KGE = \sqrt{(CC - 1)^2 + (\frac{cd}{rd} - 1)^2 + (\frac{cm}{rm} - 1)} \tag{6.8}$$

where CC is the correlation coefficient, rm is the average of observed values, cm is the average of simulation values, rd is the standard deviation of observation values and cd is standard deviation of simulation values.

The KGE could vary between $-\infty$ and 1 where a value of 1 indicates perfect fit of simulated values to observed values. Values equal to 0 or below indicate that the model does not satisfactorily fit to observations.

6.2.11 Model evaluation and data

A total of 14 sub-catchments are present in the Seine basin (Figure 6.1). All of the basins except the Seine Estuary have gauging stations at the outlet of each catchment. The largest catchment is the Seine Vernon catchment, with over 63700 km^2 surface area. The discharge rate at this outlet ranges between 450-500 $\mathrm{m}^3\,\mathrm{s}^{-1}$ over the period

1980-2020 (AESN, 2013). The simulated discharge was compared with each discharge observation at selected gauging stations.

For each cell, the ORCHIDEE model calculates the water fluxes (evapotranspiration, runoff, drainage). The total runoff (runoff + drainage) is also given as an output from the model. Knowing the area of each grid, the volume of water that flows from each grid can be estimated. As the extent of each sub-catchment is known, the total runoff at the outlet of each catchment can be estimated. Over a sufficiently long time, the total runoff equals the effective precipitation and the discharge at the outlet. Therefore, the estimated flow from ORCHIDEE can be compared with the observed flow, and the model performance can be evaluated. The discharge stations with sufficient observations are selected. The observations are cleaned from artefacts.

6.2.11.1 Observed data

6.2.11.1.1 Discharge: In the Seine basin, there are 183 gauging stations in the basin. Each catchment is analysed for the availability of the possible observations at daily intervals. For the calibration of ORCHIDEE surface water balance, 14 stations at the outlets of major sub-catchments were selected (Figure 6.1). The observation data was obtained from Banque Hydro (Table 6.2)

The majority of the observations are obtained after the year 2001. Therefore, the period 2001-2018 was selected to test the model performance where the discharge data is available for most of the major sub-catchments except Yonne.

The evaluation of the coupled model (ORC-CaWaQS) will be done by estimating the KGE, CC, NSE criterias from 183 gauging stations throughout the basin.

6.2.11.1.2 Piezometers: A total of 267 piezometers are available from the Seine basin (Figure 6.1). The locations of piezometers are distributed throughout the basin, penetrating to various aquifer layers. The majority of the data was collected from 1980 onward. The provenance of the piezometer data was provided in Table 6.2.

The coupled model performance was evaluated against the piezometer observations. RMSE, KGE, CC, and mean error (ME) criteria was be calculated to evaluate the model

Table 6.2 List of evaluation data sets.

		Resolution		Coverage			
Variable	Data set	Spatial	Temporal	Spatial	Temporal	Uncertainty	References
Discharge (Q)	Eau France	Point	Daily	Seine Basin	1874-2018	20%	SANDRE
Piezometers	Eau France	Point	Daily	Seine Basin	1980-2018	<0.5m	SANDRE
ET	GLEAM-ET	0.25°	Monthly	Global	2003-2018	-0.41 to 0.65 mm y^{-1}	Martens et al. (2018)
LAI	GIMMS	1/12°	Monthly	Global	1982-2011	RMSE = 0.67	Zhu et al. (2013)

performance at each piezometer.

6.2.11.1.3 Remote sensing products: Several remotely sensed databases and their value-added products are used to evaluate the model performance. GLEAM v3.3b (Martens et al., 2018) dataset provides actual evapotranspiration (AET) and soil moisture value-added products. The dataset is developed using ECMWF and ERA5 reanalysis data for the period 2003-2018. The actual evapotranspiration and soil moisture products are obtained via the Priestley-Taylor evapotranspiration method combined with a water balance module and evaporative stress functions. The latest version takes advantage of the satellite data in addition to the reanalysis forcing data. The dataset is provided at 0.25° resolution at daily time steps. Although AET products provide a distributed data set to evaluate the model performance, uncertainties at finer scales could be significant (Long et al., 2014). Therefore, any model evaluation with the help of these products should consider the uncertainties in their assessments.

Leaf area index (LAI) is another critical vegetation variable for monitoring the global vegetation dynamics. In this study, a product from Zhu et al. (2013) is used, based on a neural network algorithm that combines 3rd generation Global Inventory Modeling and Mapping Studies (GIMMS) Normalized Difference Vegetation Index (NDVI3g) and high-quality Terra Moderate Resolution Imaging Spectroradiometer (MODIS) LAI for the period 1981-2015 in monthly time steps. Here, this database is used to evaluate the monthly variability of the simulated LAI from ORCHIDEE.

6.2.12 Calibration procedure

The calibration procedure primarily depends on the performance of the total surface runoff against the observed discharge in the main sub-catchments (Figure 6.1) of the

Seine Basin. A set of 13 experiments (Table 6.3) were developed with varying soil, vegetation, and albedo parameters that control the main components of the water cycle: evapotranspiration, drainage and surface runoff. In order to evaluate the performance of the energy balance and vegetation dynamics, we evaluate the model based on the evaluation data sets available in the literature (Table 6.2). Therefore the calibration procedure can be summarised into five steps:

1. Discharge calibration: the stream flow data at the main outlets of the Seine basin was used in the objective function (PBIAS). Streamflow data were obtained for 14 main sub-catchments of the Seine basin (see section 6.2.11.1). The simulated total surface runoff by ORCHIDEE was transformed into discharge at the outlet by the information of the catchment area (from $\mathrm{mm\,y^{-1}}$ to $\mathrm{m^3\,s^{-1}}$). Afterwards, a fixed water withdrawal rate (37 $\mathrm{m^3\,s^{-1}}$, see section 6.2.6) was applied to the simulated discharge by ORCHIDEE to compare against the pluri-annual mean observed discharge.

2. Validation of AET: while calibrating the surface water balance against the observed discharge, the performance of the energy balance was validated against the monthly mean AET estimated in the catchment of the GLEAMv3 dataset over the period 2003-2018.

3. Validation of LAI: in addition to stream flow and AET data, the performance of the vegetation dynamics, which is reflected in the simulation of LAI by ORCHIDEE, was compared to the GIMMS dataset. The monthly average LAI estimation by ORCHIDEE was compared to the validation dataset for the period 1982-2011.

4. Partition of the effective rainfall (total runoff): The partition of total runoff in the Seine basin is also an important catchment parameter since the proportion of recharge and runoff can greatly impact the GW dynamics and discharge simulated at the outlet. Previous studies have shown that about two-thirds of the effective rainfall recharges the aquifer (Flipo et al., 2023).

5. Coupled model validation: The best performing ORCHIDEE model was used to force the CaWaQS model to simulate the groundwater dynamics and discharge. The mean observed and simulated piezometric levels and discharge were compared; the $RMSE$, the NSE , MAE , and CC were calculated to evaluate the performance of the piezometric levels. Also, KGE , NSE , MAE , and CC were calculated to evaluate the performance of the coupled model against discharge observations.

In the initial set of simulations, we used the reference parameters provided in ORCHIDEE (tag2.2, rev6533), and used at a global scale for CMIP6. The simulations share the same meteorological forcing, soil texture classification and parameters, slope map, and vegetation map. The background albedo map was derived from the MODIS albedo dataset aggregated at 0.5° resolution.

The default parameter set and the variation of the ORCHIDEE parameters during surface water balance calibration are given in Table 6.3. The initial 4 simulations allow us to assess the influence of soil texture map on surface hydrology. STOMATE was deactivated for the initial four (EXP1-4) simulations. Instead, a LAI map, obtained from an existing 40-year global simulation performed in stand-alone mode at 0.5°resolution, was prescribed (as used at global scale for CMIP6 application). EXP5 uses a version of LAI estimation where the LAI is interpolated between the minimum and maximum LAI throughout the year. EXP6-13 uses the STOMATE module (Krinner et al., 2005) which simulates the vegetation dynamics at daily time steps. Therefore the three available options to calculate LAI could be addressed. These options are the prescribed monthly average LAI (defined by the global scale MODIS simulation) and the dynamic LAI simulated by the vegetation module STOMATE. EXP6-12 uses the same setup in soil texture map and vegetation dynamics. They differ only in various ORCHIDEE parameters that were found to be effective on surface water balance by previous sensitivity analyses (Raoult et al., 2021). These parameters include the saturated hydraulic conductivity (K_{sat}), the decay factor of the K_{sat} due to soil contraction (see Figure 5.1); the visible and near infrared leaf albedo and maximum LAI of the main PFTs in the basin. EXP12-13 evaluates the newly described Reynolds-Urban (EXP13) soil texture

map (as defined in subsection 6.2.5). The length warm-up period was also assessed by evaluating two state variables: soil moisture and soil temperature.

Table 6.3 Parameter set applied to the 10 experiments to calibrate the ORCHIDEE model (-: same value than the previous one, R: Reynolds, SG: SoilGrids, L: Lucas, I : INRA, pLAI: prescribed LAI, ST: STOMATE activated, TeBS: Temperature Boreal Summergreen Trees, TeBe: Temperate Boreal Evergreen Trees, NC3: Natural C_3 grass, AC3: Agricultural C_3 crops)

Experiment		EXP1	EXP2	EXP3	EXP4	EXP5	EXP6	EXP7	EXP8	EXP9	EXP10	EXP11	EXP12	EXP13
Soil distribution		I	SG	L	R	R	R	R	R	R	R	R	R	R-Urb
Vegetation model		pLAI	pLAI	pLAI	pLAI	iLAI	ST	ST	ST	ST	ST	ST	ST	ST
Parameter	Class													
c_K		2	-	-	-	-	-	4	-	-	10	-	4	-
K_{sat} ($m\,s^{-1}$)	Loamy Sand	4.05×10^{-5}	-	-	-	-	-	-	-	1.73×10^{-5}	-	-	-	-
	Loam	2.88×10^{-6}	-	-	-	-	-	-	-	1.50×10^{-6}	-	-	2×10^{-6}	-
	Clay Loam	7.22×10^{-7}	-	-	-	-	-	-	-	4.62×10^{-7}	-	-	-	-
Near-infrared leaf albedo	TeBE	0.22	-	-	-	-	-	-	0.2	-	-	-	-	-
	TeBS	0.22	-	-	-	-	-	-	0.2	-	-	-	-	-
	NC3	0.3	-	-	-	-	-	-	0.25	-	-	-	-	-
	AC3	0.3	-	-	-	-	-	-	0.1	-	-	-	-	-
Visible-light leaf albedo	TeBE	0.06	-	-	-	-	-	-	0.04	-	-	-	-	-
	TeBS	0.06	-	-	-	-	-	-	0.04	-	-	-	-	-
	NC3	0.1	-	-	-	-	-	-	0.05	-	-	-	-	-
	AC3	0.1	-	-	-	-	-	-	0.04	-	-	-	-	-
Maximum LAI	TeBE	4.5	-	-	-	-	-	-	-	-	-	5.5	4.5	-
	TeBS	4	-	-	-	-	-	-	-	-	-	5	4	-
	NC3	2	-	-	-	-	-	-	-	-	-	3	2	-
	AC3	2	-	-	-	-	-	-	-	-	-	3	2	-

After the best performing simulation in ORCHIDEE was selected, the simulated recharge (drainage) and surface runoff were extracted in daily time steps and used to force CaWaQS. No additional steps were taken to calibrate the groundwater and river parameters of CaWaQS for hydrology after the calibrated surface water balance was obtained. Moreover, no additional calibration steps were undertaken to calibrate the soil temperatures estimated by ORCHIDEE.

6.2.12.1 Calibration period

The calibration period 2001-2018 hydrological years was selected. The reason for this period is that the Seine basin was found to be under the influence of NAO (see Section 2.4). The climatological influence exerts a 17-year influence on the precipitation regime, which controls the groundwater storage and discharge regime in the basin. We assume no storage variation to evaluate the effective rainfall against discharge (see Section 6.2.9.1), so we limit the calibration period to a 17-year to avoid the impact of the NAO. The validation of the model against the LAI and AET products depends on the availability of these products. GIMMS LAI product is available in monthly averages

over the period 1982-2011, and GLEAMv3 AET product is available over the period 2003-2018. Therefore, these periods were used to evaluate the LAI and AET. One year of ORCHIDEE simulation takes around 10 minutes in a parallel structure with 32 cores of AMD Opteron (2.2GHz) and 32Gb memory for a simulation with 1490 active grid cells.

6.3 Results and discussion

ORCHIDEE model is implemented in the Seine River Basin. The warm-up period was evaluated in the first ten years (1980-1990) of the simulation period (1980-2018). The calibration procedure is presented and discussed. The performance of the calibrated model is compared to observations from the basin and the water balance of standalone CaWaQS to evaluate the partition of total runoff into surface runoff and drainage. The results are analysed for the water balance.

6.3.1 Surface water balance (ORCHIDEE)

6.3.1.1 Impact of the warm-up period in ORCHIDEE

The first four simulations use the same settings and meteorological forcing, except the soil maps differ. Firstly, the warm-up period is analysed. The variation of total soil moisture and soil temperature at 2 meters are shown in Figures 6.11 and 6.12, respectively. The soil moisture shows a distinct signal for each soil class as the soil properties change. In order to analyse the stability of the model after a certain period of time, each soil class from the 4 soil maps is plotted in Figure 6.3. The distinct soil moisture signal of each soil class can be observed in Figure 6.11. There is a dramatic variation from the first day of the simulation as the simulation continues for each soil. This variation is apparent in soils that do not store much water, such as Loamy sand. Total soil moisture is around 650 $\mathrm{kg\,m^{-2}}$ at the beginning of the simulation. After 3 years, the moisture signal gains cyclicity regarding the meteorological input. Thus in terms of water fluxes, at least 3 years of warm-up period is required for the ORCHIDEE model. A safety of additional 2 years could also be taken for vegetation-related water fluxes.

The soil temperature at a 2-meter depth shows two distinct signals (Figure 6.12). During the first 5 years, the trend is relatively flat. After 1986, a positive trend increased the mean soil temperatures by 1.5 $^{\circ}\mathrm{C}$. This is probably related to climate warming and can be verified by regression analysis with the surface temperatures. The yearly variation of soil temperatures is captured fairly well under different soil textures and soil distribution maps. A previous application on the Seine basin (Otalora, 2016) used

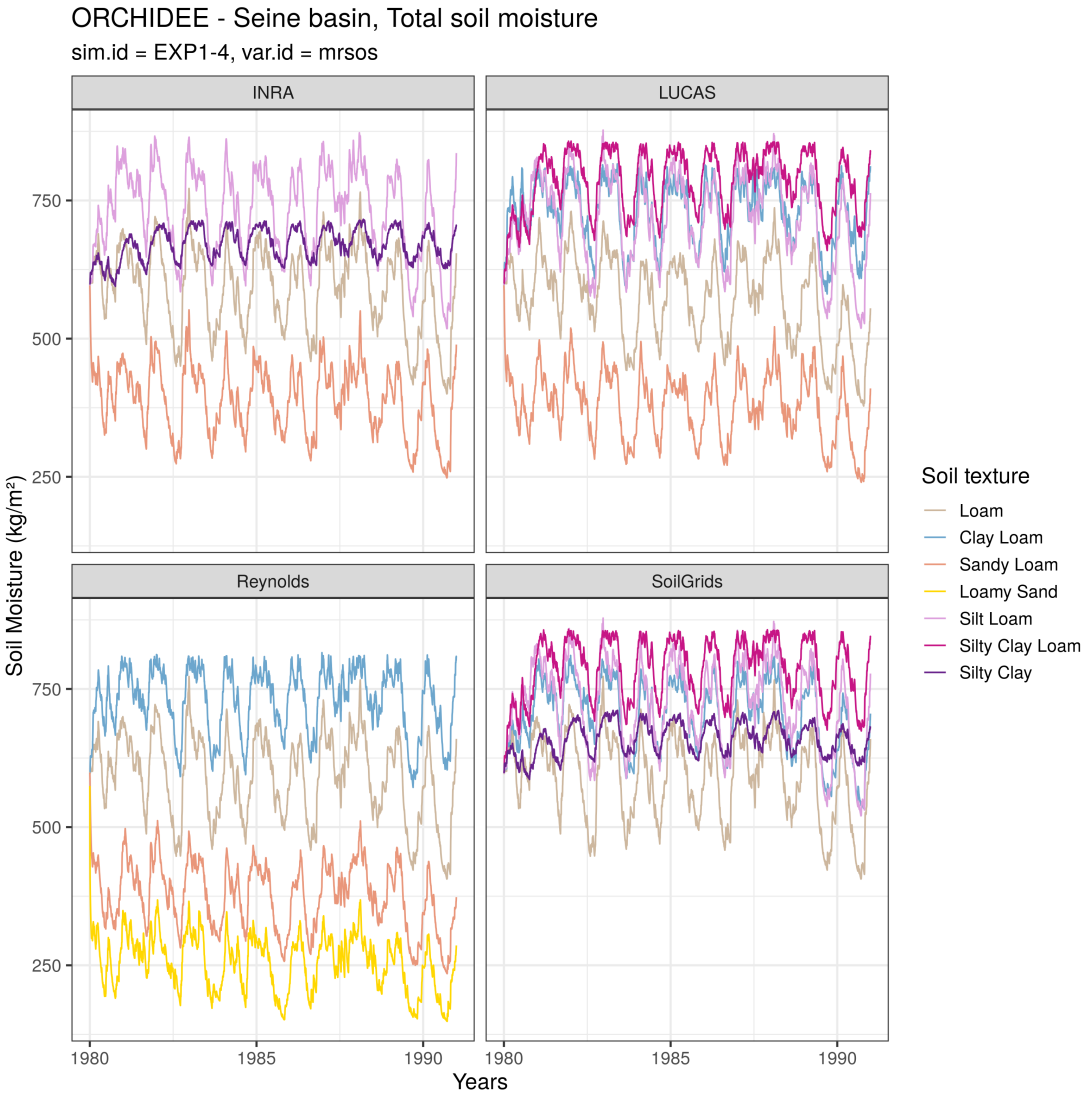

Figure 6.11 Evolution of soil moisture distribution over the period 1980-1990.

a 2-year spin-up period, which is sufficient to obtain a good initial state. Root zone soil moisture profiles for each soil type were tested to ensure each soil moisture profile reached stability with a constant precipitation test. Therefore, at least a 5-year warm-up period seems adequate to simulate the temperature and soil moisture dynamics.

6.3.1.2 Performance of pluri-annual discharge estimations

Figure 6.13 indicates how well the simulated total surface runoff at each sub-catchment performs against the observed mean discharge for the period 2001-2018. From EXP1-5, the estimations of discharge show significant positive bias (+25%). The positive bias mainly comes from the larger sub-catchments (Seine Vernon, Seine Moyenne). EXP6

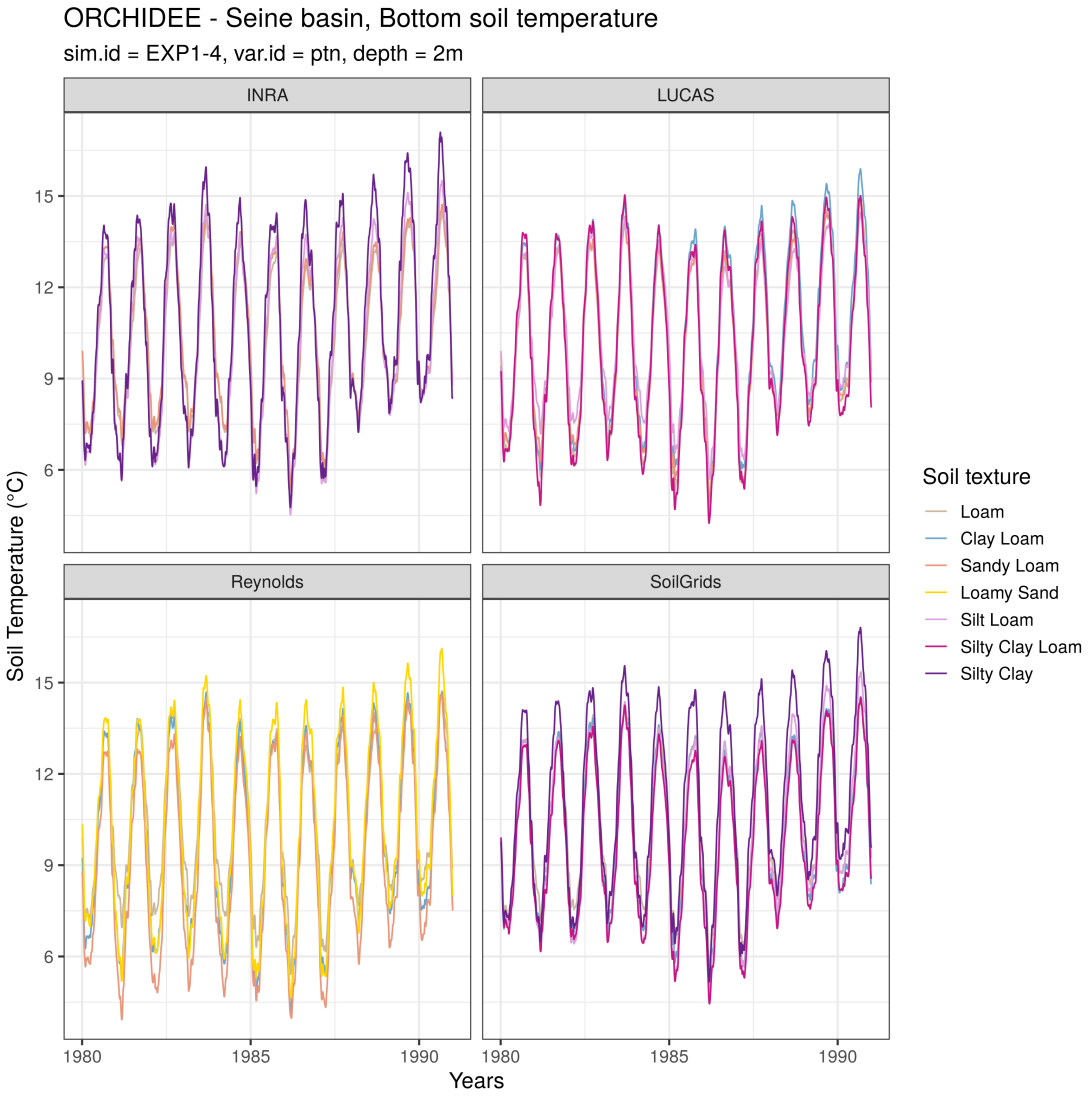

Figure 6.12 Evolution of soil temperature evolution over the period 1980-1990.

shows significant improvement to previous simulations after the STOMATE module was activated. Modifying c_K from 2 to 4 (Table 6.3) does not show a significant improvement. The performance of the mean discharge at the outlets improves greatly with the reduction of leaf albedo (EXP8). No significant variations were observed from EXP9-12 in terms of bias at the main outlets. The performance worsens slightly at the Vernon catchment with the introduction of the Reynolds-Urban soil texture map (EXP13).

Figure 6.14 represents the monthly variation of the total surface runoff at each sub-catchment of the Seine river basin. The mean monthly observed discharge was calculated from the mean discharge observations from each sub-catchment. Overall, the per-

formance of the discharge dynamics improves progressively with each iteration (from EXP1 to EXP11). The EXP1 performs the worst with respect to simulated dynamics in many sub-catchments. The abundance of silty soils in the INRA soil map (Figure 6.3) reduces the saturated hydraulic conductivity, which limits evapotranspiration. Texture maps with less silty soils, such as LUCAS and Reynolds, perform better than the INRA soil map. Overall, smaller catchments perform worse than larger catchments. ORCHIDEE cannot capture the winter flow (overestimation) or summer period (underestimation). This is partly due to sustained water flow in the river network by a set of water reservoirs available in the basin (see Chapter 2). It should be noted that ORCHIDEE standalone application does not consider the transit times as the routing scheme was not activated. Therefore, during the wet season, the simulated total surface runoff is systematically higher than the observed total surface runoff. Overall, the seasonal variation correlates well with the observed total surface runoff. INRA soil map shows deviation from other simulations, particularly in Yerres and Loing catchment.

The monthly discharge dynamics throughout the year with the exception of the Autumn season (Figure 6.14). This is mainly related to higher drainage at the bottom of the ORCHIDEE soil column. Drainage in ORCHIDEE is estimated as the excess water at the bottom of the soil column at the end of each time step. During summer the discharge at the outlet should be less than the observed discharges since the Seine basin baseflow is supported by water reservoirs and ORCHIDEE does not account for such modifications. In these experiments, the lower evapotranspiration (Figure 6.19) led to high amounts of infiltration in the soil column. During the dry season, the evapotranspiration values are lower than the observed data. Hence, excess drainage increases the overall estimated total surface runoff, as shown in Figure 6.13.

Estimated biases from the main sub-catchments of the basin from EXP11 are provided in Table 6.4. Notably, larger sub-catchments perform better in terms of bias, while smaller catchments perform worse. A special note should be put for Yerres, Orge and Essonne sub-catchments which show distinct monthly discharge dynamics compared to other sub-catchments (Figure 6.14). These basins are much smaller, and local heterogeneities and groundwater dynamics could be the controlling factor in the discharge

dynamics which were not possible to capture by the ORCHIDEE simulations.

Table 6.4 Results of the calculated percent bias for each sub-catchment from EXP11. The bias was estimated after the water withdrawal rates were applied to the simulated discharge.

	Station Name	Area (km^2)	Observed discharge ($m^3.s^{-1}$)	Simulated discharge ($m^3.s^{-1}$)	Bias(%)
1	Orge	936.47	4.07	3.71	-8.90
2	Yerres	1020.79	2.70	3.79	40.30
3	Essonne	1879.11	8.21	6.60	-19.60
4	Loing	7943.89	20.56	22.05	7.20
5	Yonne	5973.45	92.19	90.37	-2.00
6	Marne (Gournay)	4182.41	111.77	113.32	1.40
7	Aisne	12646.59	103.42	116.53	12.70
8	Oise (Creil)	10576.36	104.86	126.45	20.60
9	Eure	16774.74	25.25	26.85	6.30
10	Seine Bezoches-les-Bray	10151.05	79.74	82.72	3.70
11	Seine Poissy	44181.57	326.99	345.83	5.80
12	Seine Vernon	63771.94	482.48	498.1	3.1

The Seine basin implementation of the ORCHIDEE model is tested against the observed discharge at the Seine Vernon (Poses station) catchment (Figure 6.15) over the period 2009-2018. Notably, the daily simulated discharge records are much larger total surface runoff than the observed discharges at the Poses outlet. Since the routing was not available for this application, instantaneous transfer of the surface runoff performs poorly. However, the monthly averaged discharge estimations indicate that the model captures discharge dynamics and peak discharges fairly well.

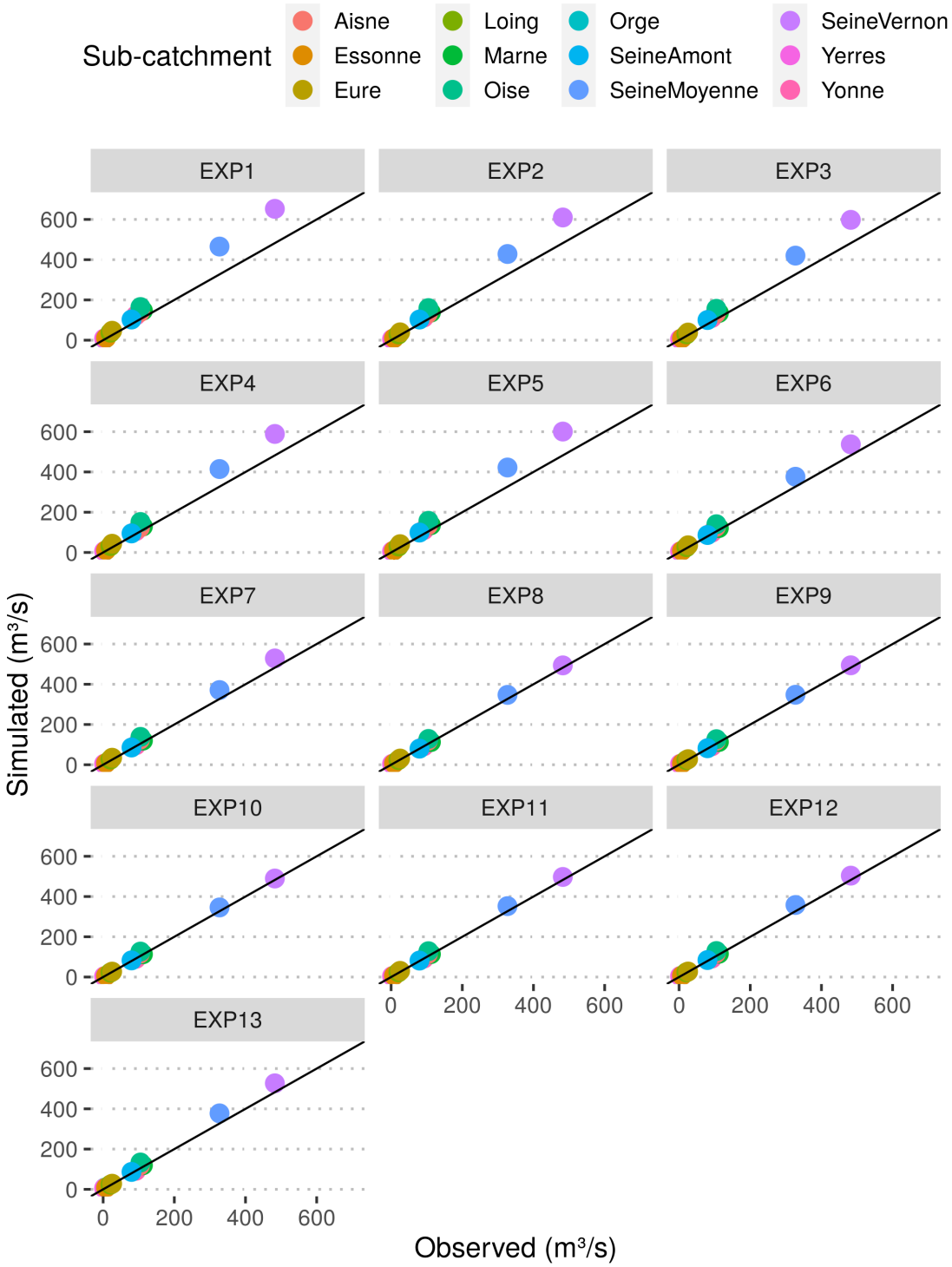

Figure 6.13 The comparison of pluri-annual mean discharge between simulated and observed of the experiments. Pluri-annual mean simulated fluxes were calculated and a withdraw rate was uniformly applied.

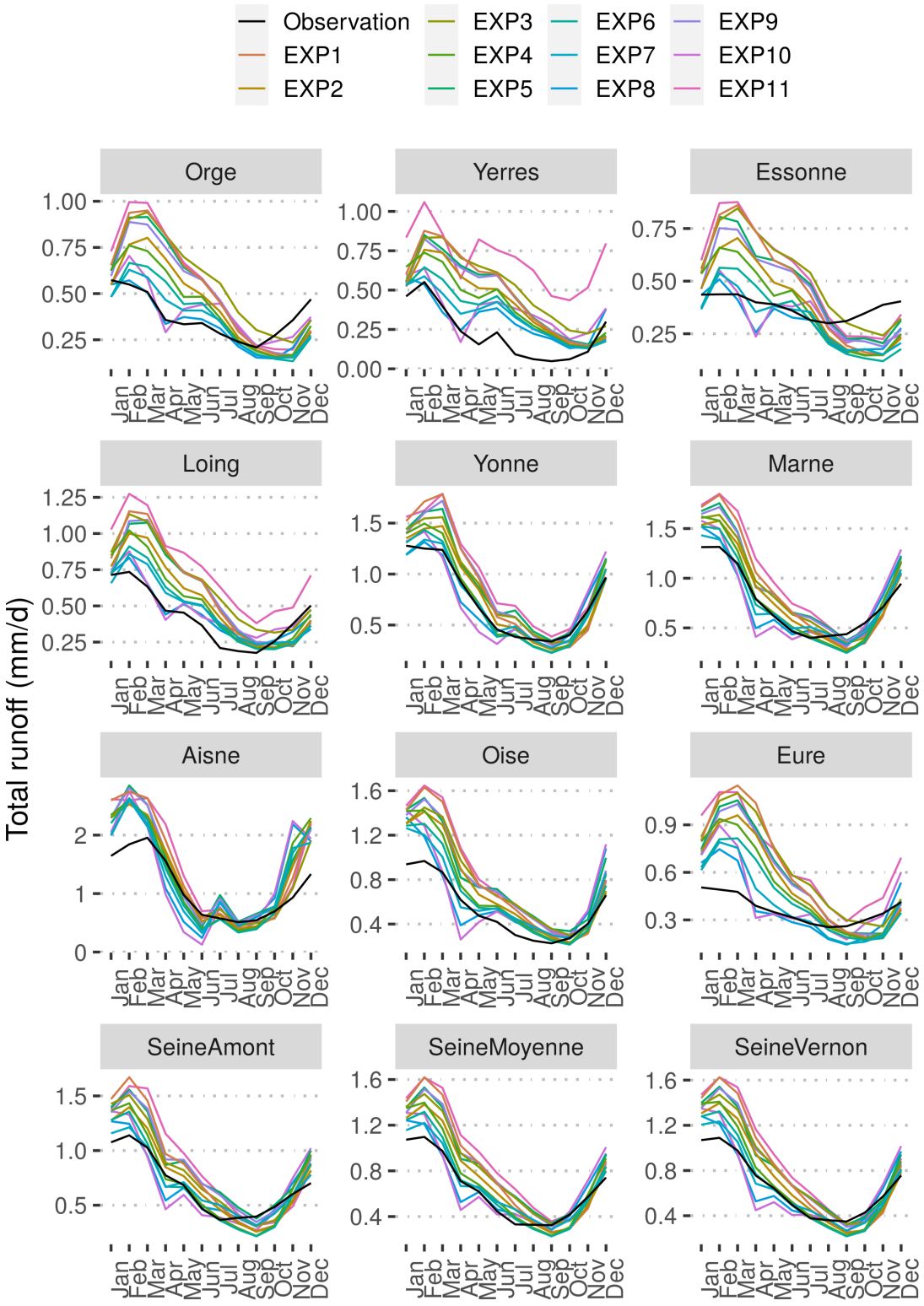

Figure 6.14 Monthly observed and simulated total (EXP1-11) surface runoff dynamics of in mm/d from main sub-catchments .

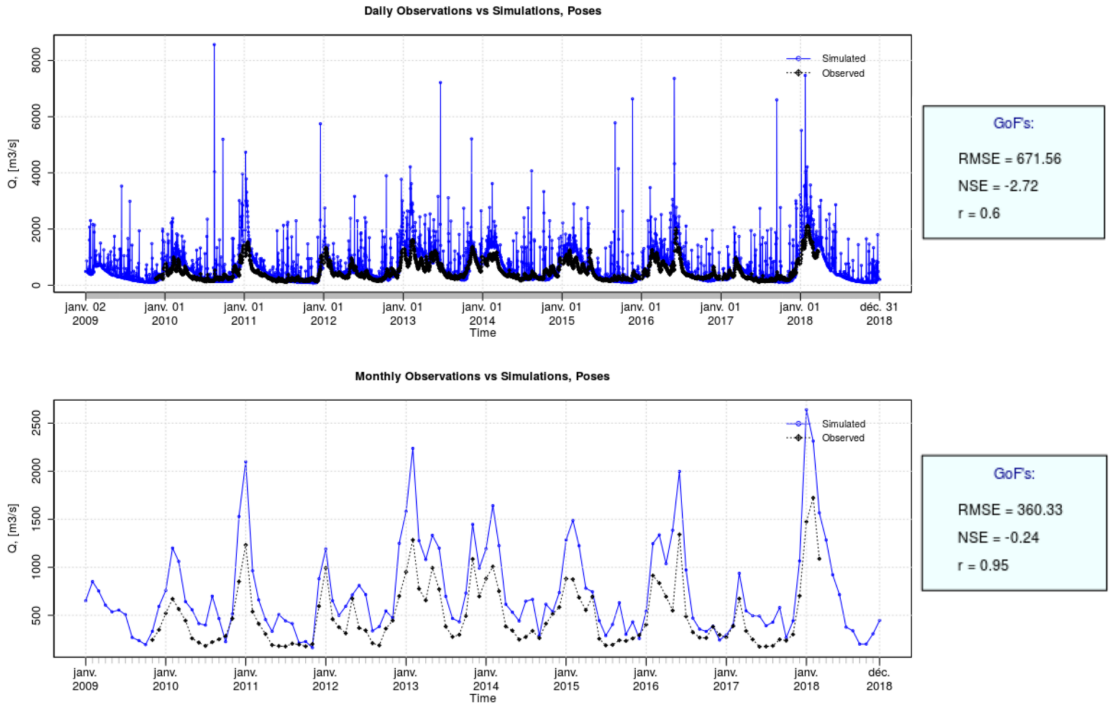

Figure 6.15 Comparison of observed discharge at Poses station with simulated total surface runoff fluxes from ORCHIDEE. The comparison shows the daily (upper figure) and 30-day moving averaged fluxes (lower figure).

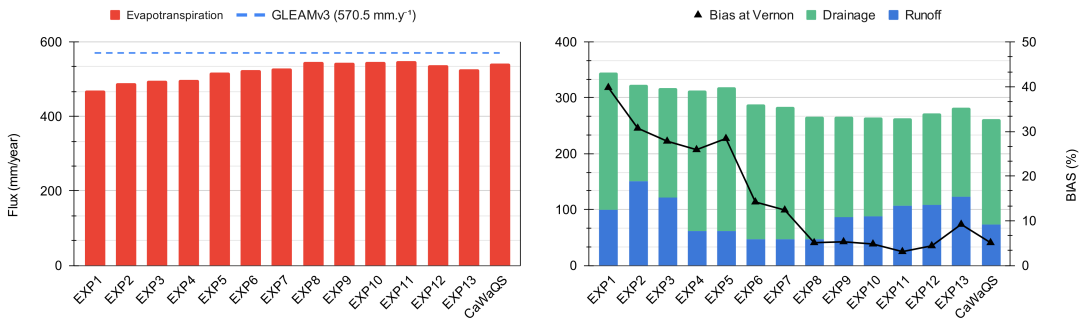

Figure 6.16 Mean yearly surface water budget components of EXP1-13 calculated by ORCHIDEE in $mm.y^{-1}$. Bias was calculated on the multi-year mean discharge at Vernon gauging station after the adjustments on the mean yearly water abstractions are taken into account . CaWaQS column represents the water balance calculated by CaWaQS-Seine application including water abstractions.

6.3.1.3 Pluri-annual water balance comparison

The simulated surface water balance with various parameter configurations (Table 6.3) is summarised as shown in Figure 6.16. The surface water balance shows the partitioning of the precipitation into actual evapotranspiration (AET), surface runoff and recharge (drainage). The first four simulations (EXP1-4) demonstrate the impact of the soil texture map from various sources on the surface water balance. The AET varies +6% (from 469 $mm.y^{-1}$ in INRA to 497 $mm.y^{-1}$ in Reynolds) with various soil texture maps. The increase of AET is directly reflected in the total surface runoff (or effective rainfall), where both recharge and surface runoff decrease. The soil texture map also modifies the partitioning of the effective rainfall into runoff and recharge. While with the SoilGrids map, the runoff forms almost 47% of the effective rainfall, the runoff decreases in EXP4 to 15%. The main difference between these soil types is the abundance of the silty soils in Soilgrids, unlike Reynolds maps. Similarly, the proportion of drainage is smaller in three simulations (EXP1-3), where silty soil is abundant. This is due to lower saturated hydraulic conductivity K_{sat} of these soil types, unlike Loam and Clay Loam classes. Therefore the existence of silty soils increases the surface runoff (Tafasca et al., 2019). Overall, the Reynolds soil texture map (EXP4) performs better, so this texture map was used for further optimisation.

EXP4, EXP5, and EXP6 share the same soil texture map, but how LAI is estimated

varies. The EXP4 has the LAI is prescribed from a previous GCM application (which has a coarser resolution); EXP5 uses interpolation between the minimum and maximum LAI; EXP6 uses the STOMATE module that simulates vegetation dynamics explicitly. The model's performance increases significantly with the use of the STOMATE (bias reduces from 25.9% to 14.2%). The performance of the bias slightly worsens in the EXP5 that uses LAI interpolation. The improvement in the performance comes from the increased AET due to higher LAI estimations. Increases in the LAI cause higher biomass activity. Additional transpiration was recorded as well. LAI is also connected to the root profile and the vegetation's capacity to withdraw water from the soil. The model response is quite similar under prescribed and interpolated LAI (with the latter having slightly less AET). Therefore, the STOMATE module was activated in other simulations for further calibration.

The introduction of a sharper vertical decay of K_{sat} below 30 cm in the soil column (from EXP6 to EXP7) showed a weak impact on the AET and the partition of runoff and recharge. The AET increased slightly (+4$mm.y^{-1}$), while the bias was reduced by 1.8%. This weak sensitivity of the deeper soil to surface AET shows the importance of the top 30 cm of the soil column for the vegetation processes and surface energy balance, as discussed by de Rosnay et al. (2000).

The implementation of lower NIR and VIS albedo (from EXP7 to EXP8) improves the bias at Vernon significantly (from 14% to 5.1%). The improvement on bias comes from the increase of AET (+16$mm.y^{-1}$ i.e; +5%). AET has increased due to lower albedo and higher available energy for evapotranspiration.

A decrease in K_{sat} of main soil texture types (from EXP8 to EXP9) shows a limited impact on the AET estimation; therefore, the bias on discharge did not improve. However, the partition of the effective rainfall varied significantly, so the portion of runoff increased considerably (from 18% to 33%). Similarly, a further increase in the soil decay factor to reduce K_{sat} below 30cm of the soil column (from EXP9 to EXP10) yielded very little impact on the overall partition of the surface water balance. An increase in the maximum LAI to increase vegetation activity shows very little impact (EXP11) on the AET. The portion of runoff increases slightly. Although the increase in maximum

LAI values shows a limited impact, increased values match the reported LAI ranges observed throughout the FluxNET network for similar biomes and climates (Krinner et al., 2005).

The EXP12 and EXP13 are two separate simulations; the main difference between them is the use of Urban soil texture class. The description of relatively impermeable urban soil texture causes a significant decrease in the AET (-10.7$mm.y^{-1}$). A portion of runoff increases by 5$\%$. The bias at Vernon increases from 4.4$\%$ to 9.2$\%$.

Overall, the bias at Vernon was reduced progressively from 39.8$\%$ at the initial simulation to 3.1$\%$. The overestimation of the discharge at Vernon is the result of an underestimation of AET (with respect to GLEAMv3 product with 570 $mm.y^{-1}$ overall AET in the basin). The dynamic estimation of LAI significantly improves the model performance. This could also be related to the coarse resolution of the prescribed LAI product. Although the impact of water withdrawals was taken into account, it should be noted that the Seine basin is heavily used for agriculture, and irrigation modifies the surface soil moisture profile significantly. This modification could lead to higher AET in the actual state of the basin. Moreover, processes such as harvesting and river water stage regulations were not simulated. Therefore a positive bias of 3.1$\%$ is quite satisfactory given that ORCHIDEE simulates a natural basin.

The proportion of recharge and surface runoff also plays a significant role in the water balance of the Seine basin. Previous studies indicated that approximately two-thirds of the effective rainfall translates into recharge in the aquifer (Flipo et al., 2023). Although the EXP11 performs slightly better than EXP10 in terms of bias and AET, the EXP10 has a recharge profile closer to the estimated effective rainfall partitioning (28.3$\%$). Therefore, EXP10 was selected to force the groundwater model CaWaQS .

The default ORCHIDEE model parameterisation is adapted for the global scale. Although various point scale studies explore the local scale parameter optimisation (Raoult et al., 2021; Bastrikov et al., 2018) or improve the terrestrial biosphere and energy processes (Peylin et al., 2016), regional scale parameterisations for the ORCHIDEE SVAT model is not yet available.

The regional scale parameter set might show variations from the global parame-

ter set. Therefore more studies are needed to estimate the regional parameterisation of SVAT models such as Xie et al. (2007) or Samaniego et al. (2010) to improve the applicability of SVAT models at regional setups.

6.3.1.4 Performance of various LAI estimation approaches

Figure 6.17 shows the bias of the spatial distribution of annual mean LAI and GIMMS LAI product averaged over the period 1982-2015. Four different ORCHIDEE simulations with distinct vegetation parameters were evaluated (Table 6.3). Overall, the monthly dynamics of various experiments perform quite well except for the prescribed LAI, which shows limited LAI during summer. The prescribed LAI shows a poor correlation with the observed LAI. During summer, LAI does not increase in the prescribed LAI, even though the basin is agriculturally dominated and vegetation activity is maximum due to growth in summer. This is probably due to the lack of refinement in the LAI map, which was obtained through a global 0.5°(≈55km) resolution simulation, whereas, in the Seine basin, we use 8 km resolution. The STOMATE module (EXP6) performs well in terms of seasonal dynamics. Similarly, the LAI interpolation method (iLAI) shows a sinusoidal signal, but can not capture the spring peak and winter lows. The combination of STOMATE with increased maximum LAI matches the spring LAI peak; however, LAI is overestimated. The overestimation during summer is expected because the LAI product tends to underestimate LAI during the summer season (Zhu et al., 2013). During winter, all the setups except iLAI underestimate LAI in the basin.

The distinct response by the various LAI estimation methods indicates that LAI is sensitive to the estimation method and maximum LAI parameter. However, compared to observation, additional work is needed to refine the minimum LAI to capture winter lows which, might have an impact on the winter evapotranspiration.

Figure 6.18 illustrates the seasonal variation of the simulated LAI vs observed LAI in the Seine basin from EXP6. The southern part is mainly covered by the Morvan Forest. Morvan Forest is dominated by temperate broad-leaved summer-green and evergreen species. Systematic underestimation of LAI in this section could be related to the parameterisation of the maximum and minimum LAI parameters that limit the LAI

estimations. In the Seine basin's agriculture-dominated regions, LAI is overestimated during the summer season. Further studies are required to regionalise the parameters of the PFT parameterisation to improve the vegetation dynamics and to understand them better.

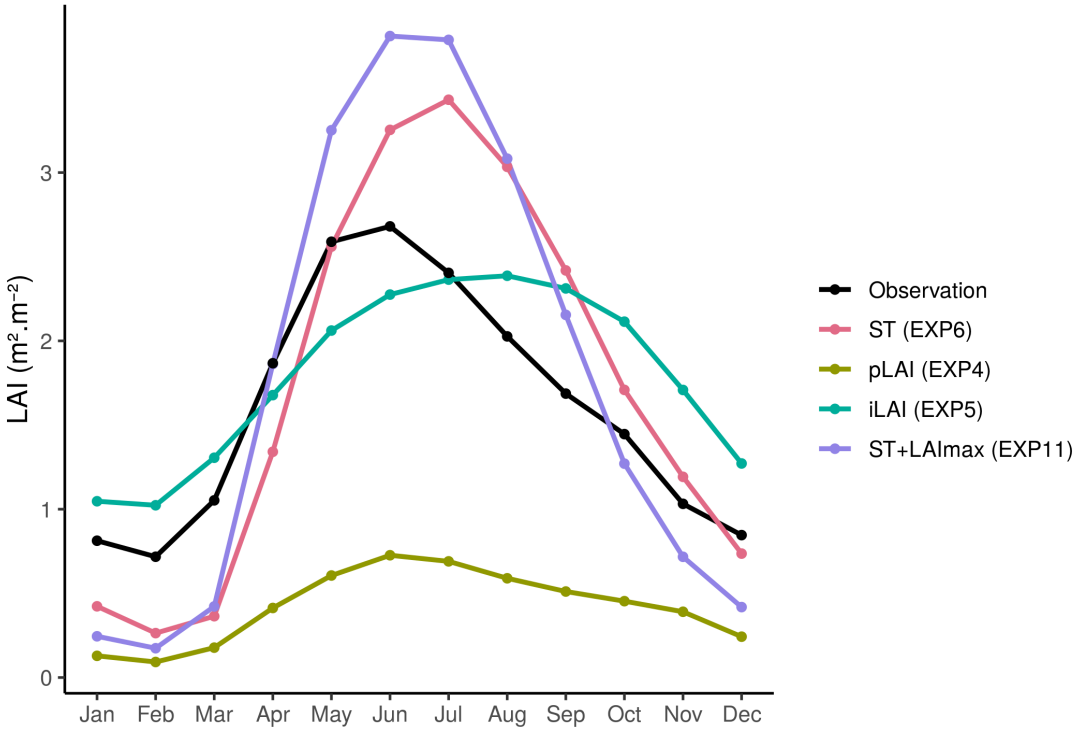

Figure 6.17 Monthly variation of LAI over the period 1982-2010. The comparison is between GIMMS-LAI product and the set of experiments

6.3.1.5 Comparison to GLEAMv3 product

The comparison of the seasonal dynamics between various ORCHIDEE simulations and the GLEAMv3 dataset is provided in Figure 6.19. AET was systematically underestimated during the summer season and overestimated during winter season. This underestimation is not directly related to the availability of the vegetation since LAI is overestimated during summer. Therefore, the current parameterisation of ORCHIDEE underestimates the AET, likely due to the water limitations in the soil, energy at the surface, or misrepresentation of the parameters at the regional scale. The evapotranspiration of the vegetated areas is tightly coupled to the availability of water at the top layers (de Rosnay et al., 2000), and both variables are linked through a stress factor as

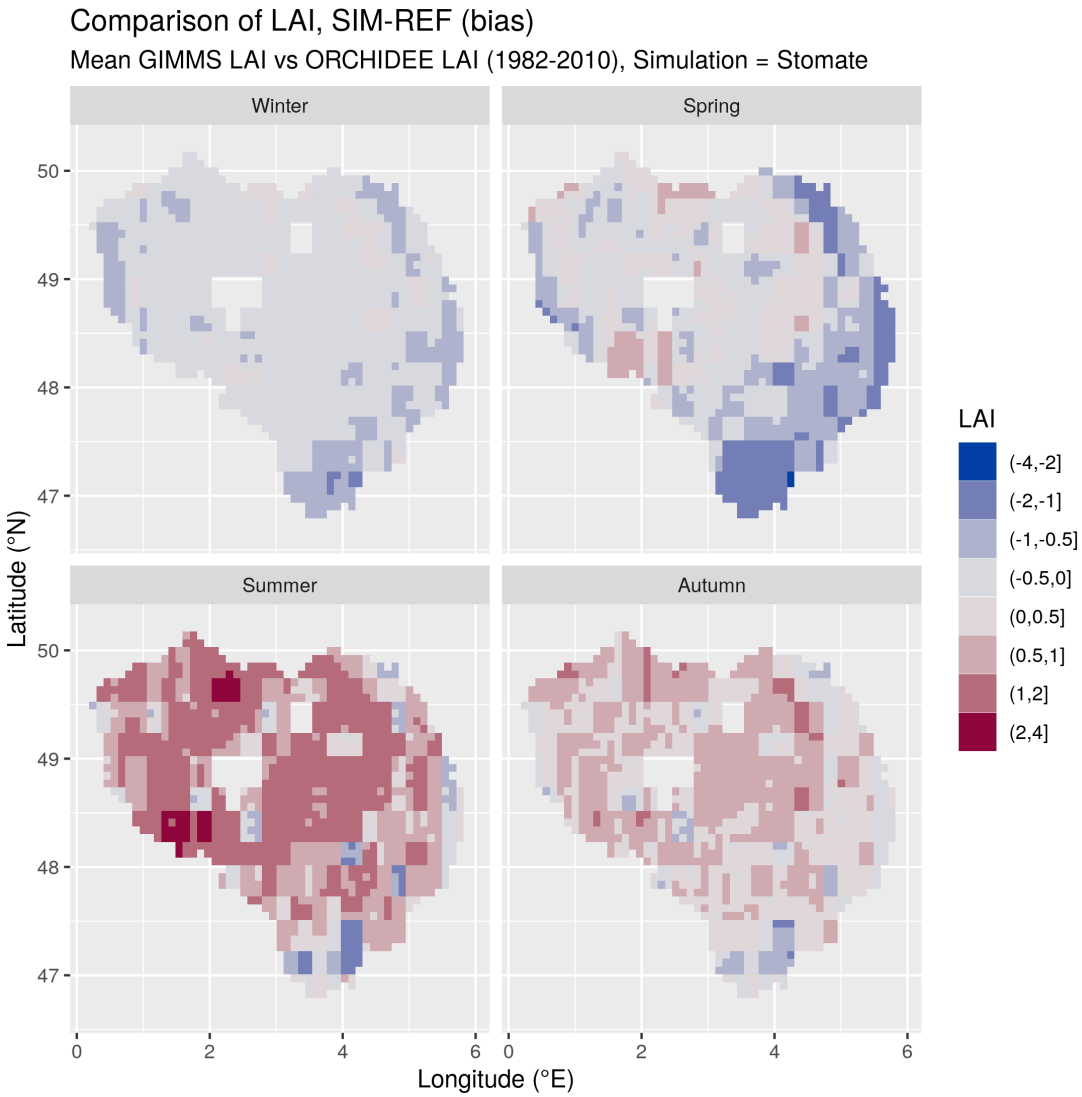

Figure 6.18 Monthly variation of LAI ($m^2.m^{-2}$over the period 1982-2010 from EXP6. The comparison is between GIMMS-LAI product and the set of experiments

a function of soil moisture. The soil moisture was found to be sufficient (above 80%) throughout the year. Therefore, the system is not limited by water availability but by the energy-related parameterisation in the application.

This was further evidenced in Figure 6.20. During summer, AET is systematically underestimated throughout the basin. The highest discrepancy between observed and simulated AET was partly in the forest-dominated areas (Morvan region in the south). Although LAI is overestimated throughout the basin during summer (Figure 6.18), AET was underestimated in the same regions (Figure 6.20). It should be noted that the largest AET underestimation was in the regions with underestimation of LAI (Morvan region), which indicates that LAI is also a factor in the underestimation of AET.

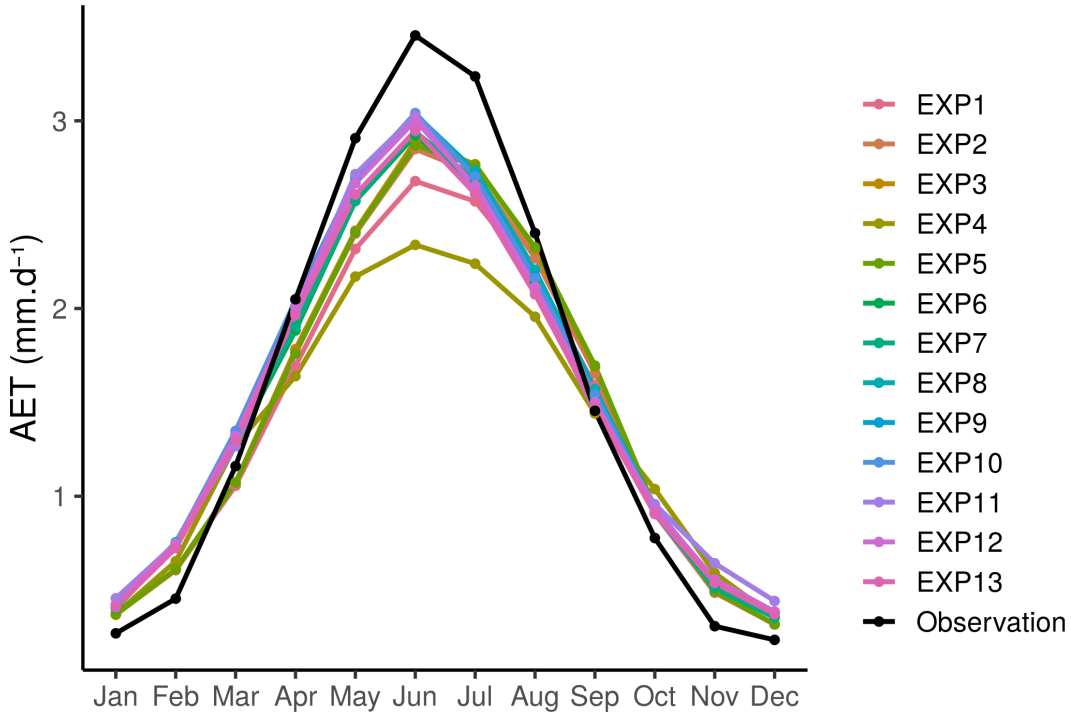

Figure 6.19 Monthly variation of actual evapotranspiration. The comparison is between GLEAM-AET product and the set of experiments

6.3.1.6 Impact of urban soil on simulated water fluxes

The monthly variation of the total surface runoff with the newly introduced Urban soil texture map and soil class is illustrated in Figure 6.21. A slight increase in the total surface runoff can be observed in the main sub-catchments downstream of Paris. The increase in runoff can be expected due to the introduction of impermeable soil, contrary to Loam. This modification has led to the reduction of K_{sat} by a factor. The largest impact of the new soil class is on the smaller catchments in proximity to the urban agglomeration (Orge, Yerres, Essonne). The largest discrepancy is observed in the Orge basin, which indicates that the evapotranspiration was very limited due to the impermeable layer. Another important aspect is that the introduction of the urban soil texture did not change the seasonality of the surface processes but merely led to an offset in proportion to the total runoff increase.

Although the K_{sat} was reduced in the new urban soil class, other soil hydraulic parameters were not modified (i.e. porosity, wilting point, α, n), which might also have

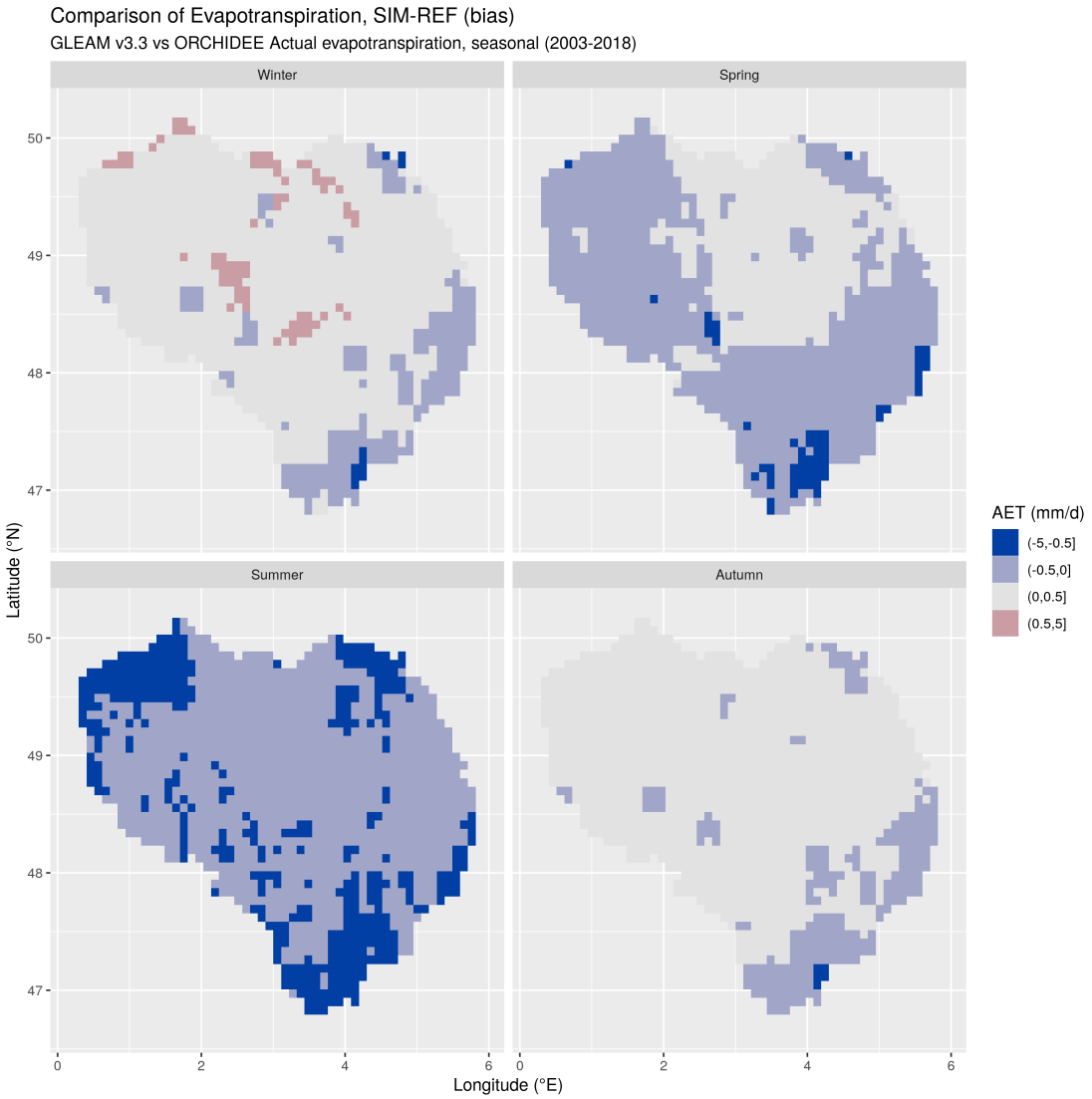

Figure 6.20 Monthly variation of actual evapotranspiration. The comparison is between GLEAMv3 product and EXP6 simulation in $mm.d^{-1}$

different ranges than currently defined values. As a first implementation, this method seems promising; however, cities show very distinct features which are very challenging to map. Sub-grid heterogeneity should be expected to be significant, and soil texture maps which include cities should aim to refine the texture map at a finer scale than $8\mathrm{km}$ resolution.

6.3.1.7 Surface water balance of the period 1985-2018

The water balance is obtained from the ORCHIDEE (EXP10) simulation and shown in Figure 6.22. The water balance and its components are shown in Figure 6.22. The basin has an average annual precipitation rate of 805 mm/year, and it is subject to large

temporal variability. This is influenced by the distance to the ocean and the elevation of the basin. The maximum and minimum precipitation range from 550 to 1100 mm/year. The proportion of snowfall is very limited in the basin.

The evapotranspiration is 565 mm y^{-1}; most evapotranspiration is due to transpiration fluxes. This is followed by bare soil evaporation and canopy losses in the basin. Transpiration accounts for approximately half of the evapotranspiration. Canopy losses do not vary greatly between years, with an average of 35 mm y^{-1}.

The effective rainfall is 241 mm y^{-1} and its partitioned into surface runoff and groundwater recharge. The groundwater recharge forms 71.7% of the effective rainfall (172mm y^{-1}). The surface runoff is 70 mm y^{-1}. The proportion of drainage throughout the years varies significantly with the variation of precipitation. The transpiration evolution show limited variation throughout the years.

6.3.1.8 Distributed recharge and runoff maps

The distributed recharge and runoff estimations obtained from EXP10 of the ORCHIDEE Seine application are given in Figure 6.23. Runoff estimations are strongly correlated with the soil map and the hydraulic conductivity associated with the soil classes. Most runoff comes from the Eastern sector of the catchment. The area is dominated by clay loam which has very limited hydraulic conductivity ($62\mathrm{mm/d}$). Limited runoff zones are the areas with Sandy Loam and Loamy Sand, which have less than $50\mathrm{mm/year}$ runoff throughout the year on average. Drainage patterns show a more even distribution than runoff fluxes. On average, there is $270\mathrm{mm/year}$ of drainage throughout the basin.

Most drainage comes from the Morvan region which is dominated by forests and where there is limited agricultural activity. The soil class in that region is Loam which has limited hydraulic conductivity. Also, the area receives the most rainfall in the Seine catchment (more than 1000mm y^{-1}.) Around 90% of the precipitation translates into the recharge in the southern part of the Seine catchment. Overall, $71,7\%$ of the effective precipitation translates into the recharge in the ORCHIDEE Seine application.

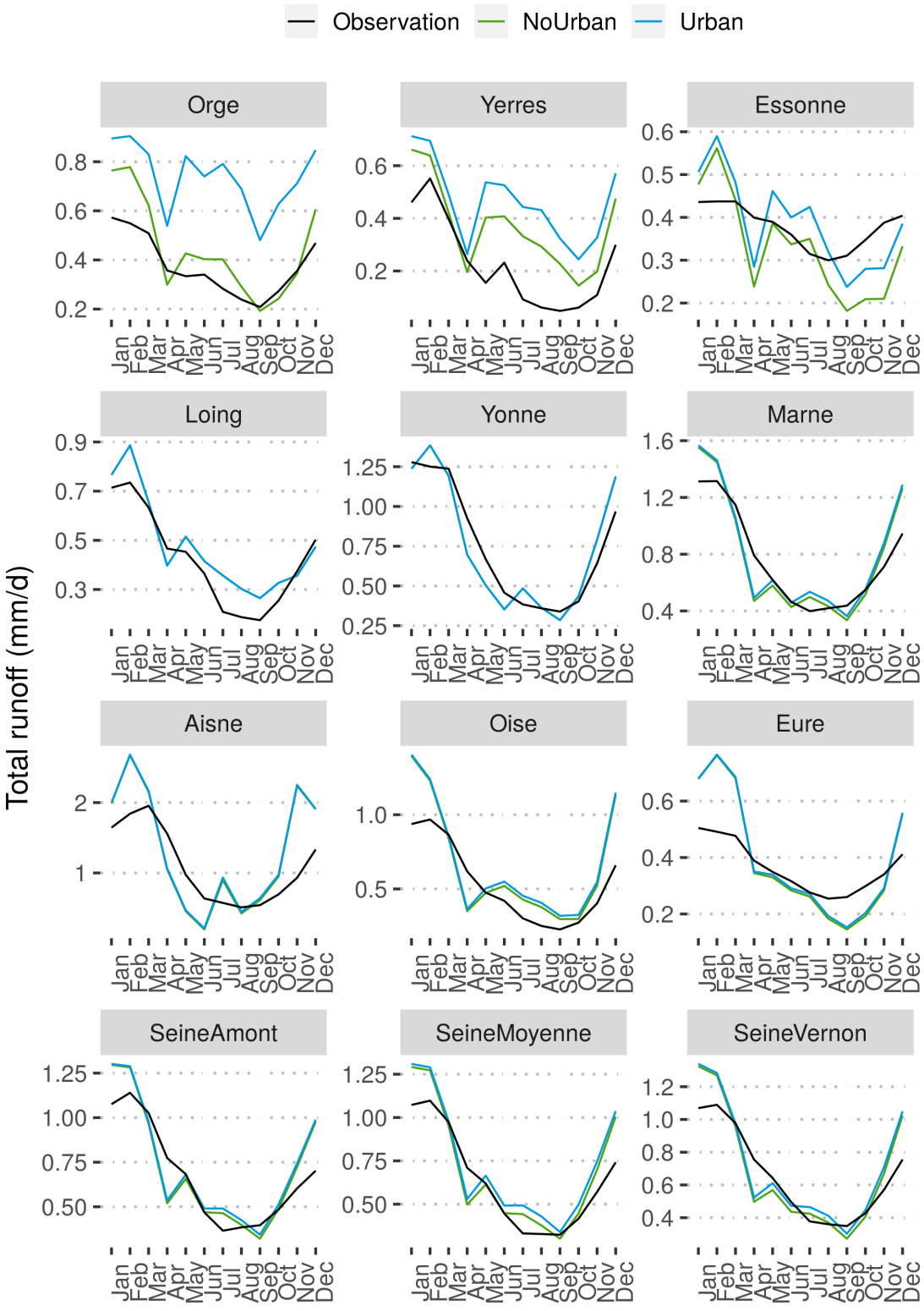

Figure 6.21 Monthly dynamics of the EXP12 (NoUrban) and EXP13 (Urban) compared to the observed discharge at the main sub-catchments of the Seine basin.

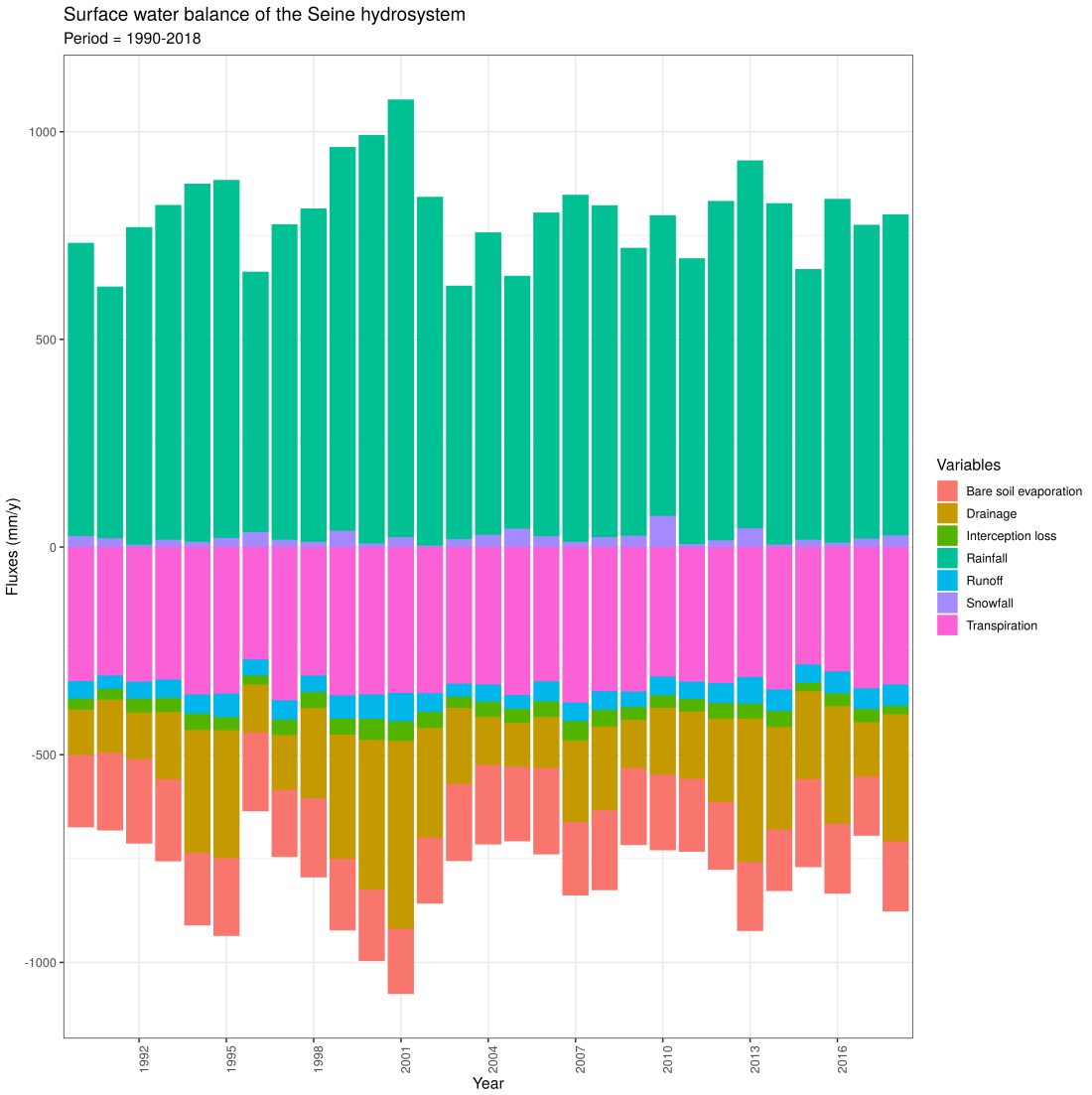

Figure 6.22 The surface water balance in the ORCHIDEE from EXP10. Positive scale shows the precipitation variation, whereas the negative scale shows the components of the surface water balance. Fluxues in $mm.y^{-1}$

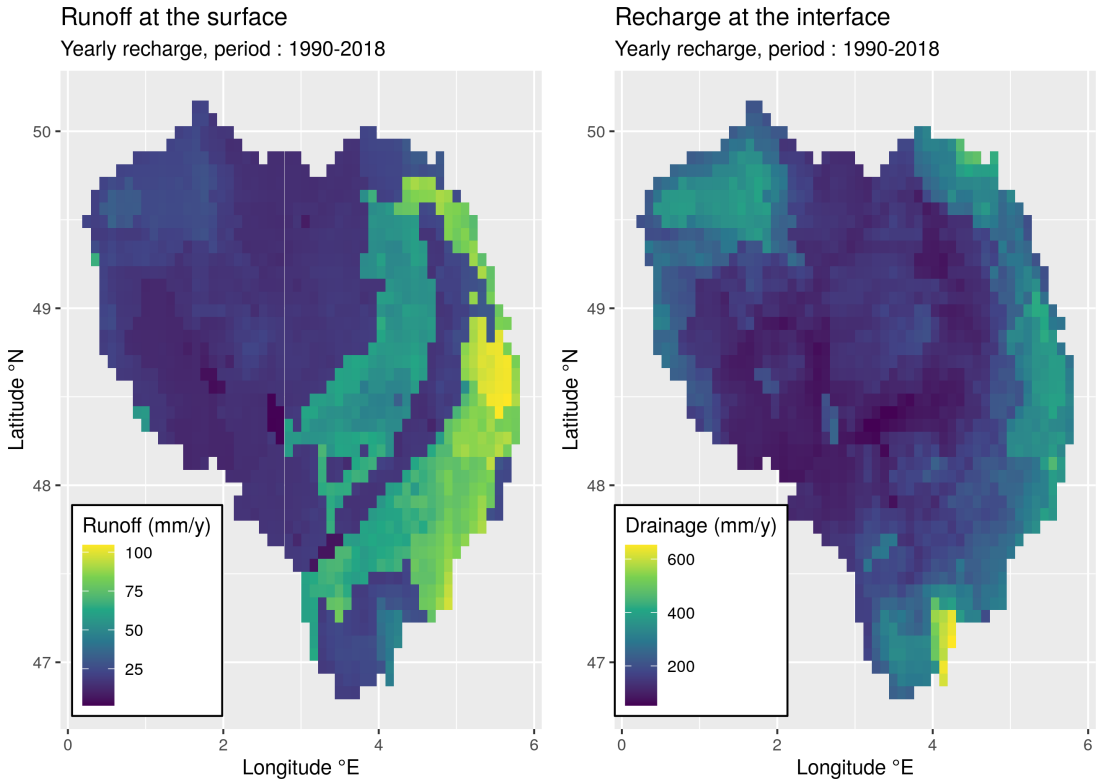

Figure 6.23 Distributed a) runoff, b) recharge maps obtained from the ORCHIDEE simulations. The yearly values are averaged for the period of 1990-2018.

6.3.2 ORCHIDEE-CaWaQS coupled application

After calibration of the surface water balance of the ORCHIDEE Seine application, the EXP10 was selected to force the CaWaQS model to simulate the aquifer system and river.

6.3.2.1 Performance of the discharge estimations

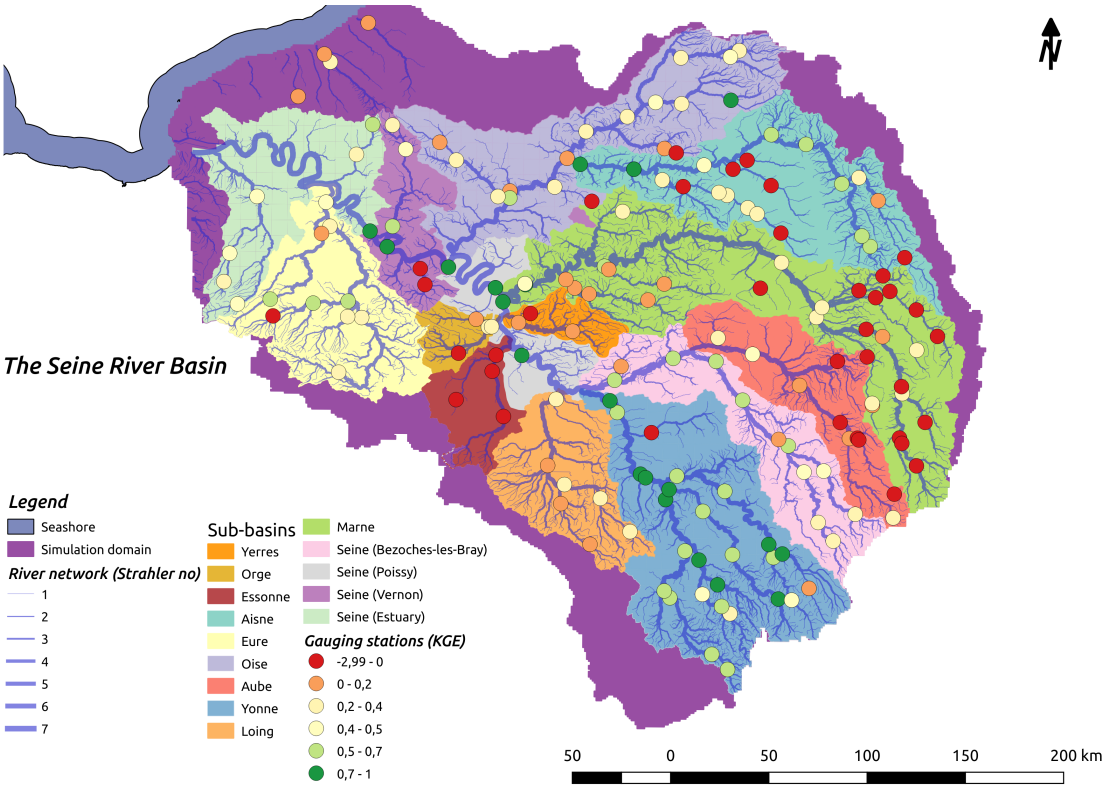

Figure 6.24 Spatial distribution of calculated KGE at the gauging stations simulated by ORCHIDEE-CaWaQs Seine application throughout the catchment. Coloured areas indicate the main sub-catchments of the basin. The thickness of river reaches varies as a function of Strahler order no.

The overall performance of the coupled ORCHIDEE-CaWaQS application was evaluated by KGE criteria applied at gauging stations throughout the basin (Figure 6.24). Main tributaries of the Seine basin show very good agreement with the observed flows in the basin. In the Seine river, KGE values range between 0.7 - 1. This performance is similar in the Marne, the Yonne, the Aisne, and the Oise. As the sub-catchment size decreases, the KGE also drops. Specifically, upstream of the Marne, in the Essone, the worst performing stations are seen (KGE $<$ 0). This indicates that forcing surface fluxes

via ORCHIDEE are not yet optimised for estimating fluxes at smaller reaches.

Two notable flood periods can be observed in Figure 6.25. Notably, during 2015 and 2017 two major floods have occurred. Flow records during these periods passed over $2000\mathrm{m}^3/\mathrm{s}$. The coupled simulation captures the dynamics of flood fairly well at the outlet of the Seine basin. At the outlet, the overall performance of the model during the period 2001-2018 is satisfactory, as the bias is 1.8%, and KGE is 0.77.

The overall comparison of the mean simulated and observed discharge in gauging stations at the outlet of main sub-catchments is shown in Figure 6.26. Overall, the comparison shows a systematic positive bias towards the simulated discharge estimations except in smaller catchments where the river dynamics could be different. This bias increases up to 12%. The systematic bias indicates that the amount of effective rainfall calculated by the surface module ORCHIDEE is higher than the previous effective rainfall used by the groundwater model (which was obtained by the surface module of CaWaQS using potential evapotranspiration estimations by the Penman method (Penman, 1948)). When the signal responses of the gauging stations are analysed (as illustrated in Figure 6.25), the seasonal responses are well captured, and there is no apparent phase shift between the responses. However, the magnitude of the high flow periods and the calculated base flow indicate that further refinement of the surface model is needed.

The main difference in the coupled framework is the absence of an unsaturated zone which impacts the transit time of the flow. In the standalone CaWaQS application, the effective rainfall is partitioned by the surface model with 7 parameters (Labarthe, 2016). This partitioning is part of the calibration of the groundwater model (Schuite et al., 2019; Flipo et al., 2020a), and it is used in the two-step calibration methodology (Flipo, 2013). Moreover, the unsaturated zone description in standalone CaWaQS introduces a series of Nash reservoirs (Nash, 1959; Besbes and De Marsily, 1984) which slows the water introduced to the aquifer system. In the case of CaWaQS forced by the ORCHIDEE SVAT model forcing, the partition of the effective rainfall is calculated by ORCHIDEE, as processes are represented physically. Also the absence of the unsaturated zone removes the unsaturated stock, and decreases the transit times of water (Labarthe, 2016). A coarser scale of applied surface fluxes without sub-grid hetero-

geneity of the unsaturated zone could be the reason for the reduced performance of the coupled model upstream.

At the main outlet, the model performs comparable to similar coupled approaches such as Rousset et al. (2004) or performs better than the ORCHIDEE application at lower resolutions (Otalora, 2016). The introduction of routing and groundwater dynamics via CaWaQS improved the flow dynamics. At smaller catchments, the local dynamics become more apparent and additional optimisation is required. The optimisation at smaller catchments could be achieved via novel SVAT optimisation approaches proposed by Ala-aho et al. (2017) to use PEST calibration or Demirel et al. (2018) to improve the spatial performance of SVATs.

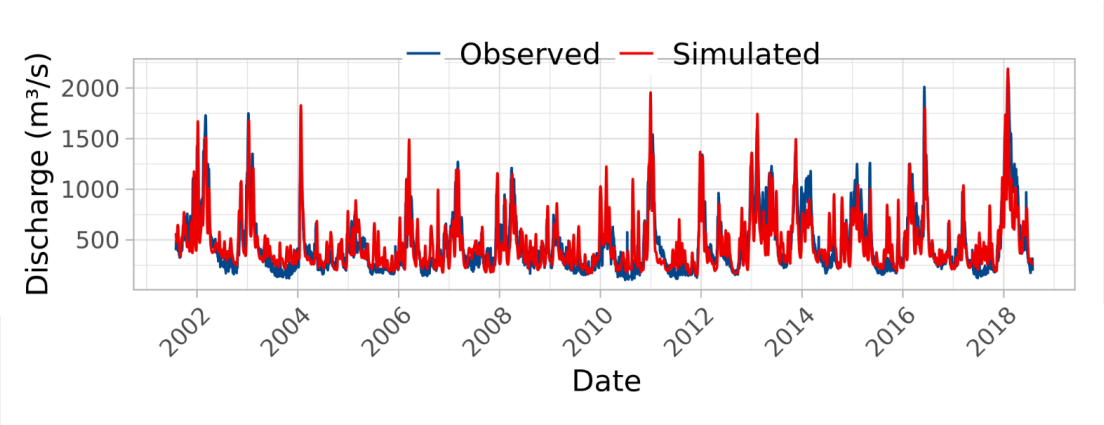

Figure 6.25 The simulated and observed discharges at the Vernon station. KGE= 0.77, Correlation coefficient: 0.82, PBIAS: 1.6%

6.3.2.2 Performance of piezometric heads

The calculation of the RMSE from the piezometric stations is shown in Figure 6.27. Overall, the median RMSE is 4.9 m from 267 piezometric stations from 8 aquifer layers in the basin. Overall, a number of piezometers show good evaluation in terms of the head estimations. Certain sectors have a very strong agreement. Especially, the Alluvium, the Beauce, and the Brie aquifers piezometers have good performance. Most of the piezometers in Lutetien and Thanetien aquifers show satisfactory performances. It should be noted that the Chalk (Craie) aquifer has the least performing piezometers. The piezometers near the Seine estuaries show poor performance overall, with the exception of a few notable piezometers. It could be related to the increased influence of

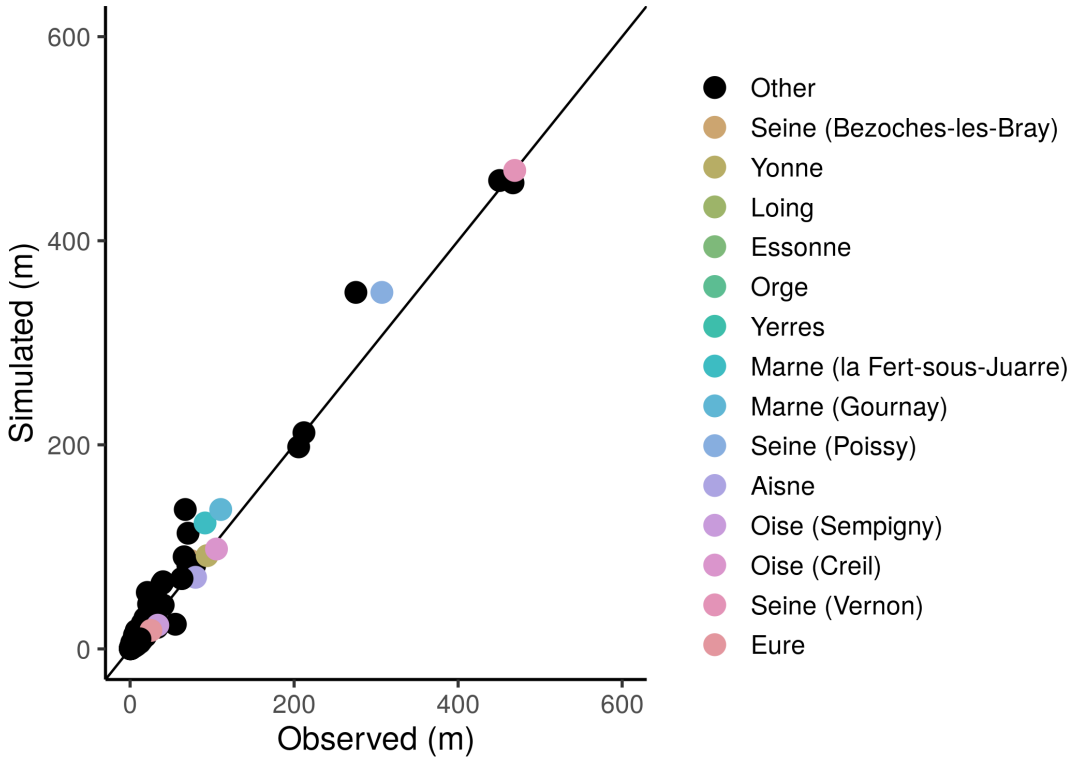

Figure 6.26 Comparison of the simulated and the observed discharges at each gauging station of the catchment. Period of averaging: 2001-2018

the oceanic hydraulics in the estuaries region. Towards the Eastern sector of the Chalk aquifer, better performing piezometers could be observed.

The comparison of the simulated and observed mean heads can be seen in Figure 6.28. Average simulated water levels show good agreement with the observed water levels in the aquifer system. A few outliers are present in the basin, mainly from the Chalk and Thanetian aquifers.

In the Beauce aquifer, the piezometers overall perform strongly; an example is shown in Figure 6.29. The simulation captures the head dynamics very well except for the local deviations. The local declines in the hydraulic heads can be observed in the period 2015-2016, and 2012-2013. Nevertheless, the model responds strongly to these decreases in the hydraulic heads.

In the case of the piezometer (Figure 6.30) within the Champigny aquifer, we observe relatively well-captured head dynamics with a positive bias. The decreasing water level trend until 2012 is very well captured. The coupled model adequately captured increasing water level dynamics after 2012.

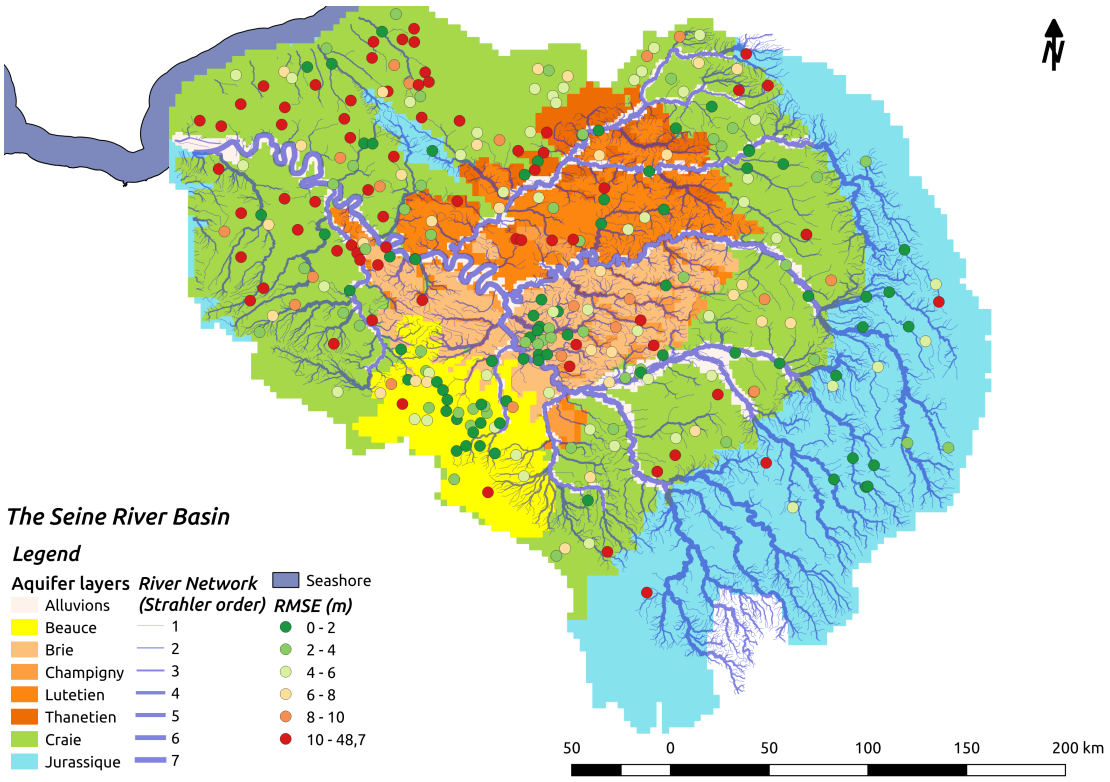

Figure 6.27 Spatial distribution of calculated RMSE on 292 piezometers over the period 2001-2018.

A notable piezometer in the Chalk aquifer is shown in Figure 6.31. The simulation captures the magnitude and dynamics of the hydraulic heads quite well. After a period of depletion until 2012, the water levels become relatively stable. This dynamic was very well captured by the simulation, which is reflected in the KGE (0.83) and CC (0.84) estimations.

In general, a positive bias is associated with the current application of the ORCHIDEE-CaWaQs on the Seine basin. There are a number of reasons for this behaviour. Firstly, the SVAT models tend to underestimate evapotranspiration (Wang et al., 2018b) as they do not have an adequate groundwater module integration (Clark et al., 2015), and the feedback between groundwater and evapotranspiration is not taken into account (Maxwell and Kollet, 2008b). Therefore, the effective rainfall estimations are generally higher than the conceptual solutions that are simulated by the standalone CaWaQs application (Flipo et al., 2020a). The second limitation is the lack of adequate unsaturated zone representation, which could attenuate the recharge signal. As observed in the Beauce aquifer (see Figure 6.29), the model responds to the variations in the hydraulic

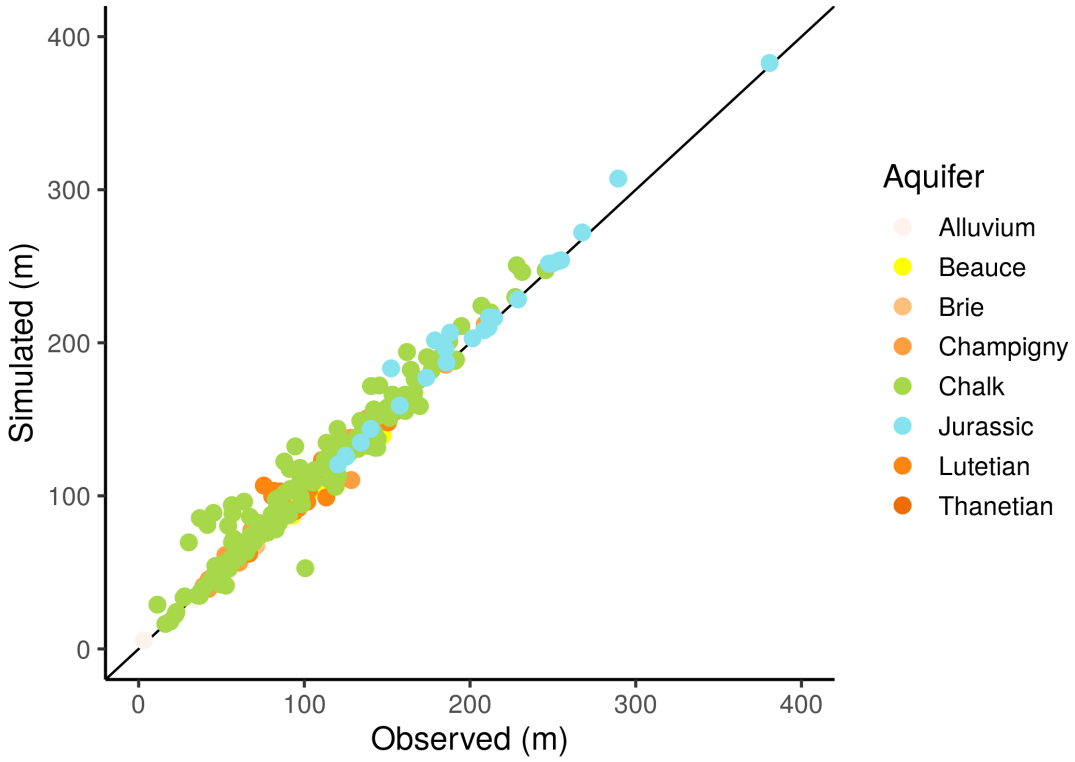

Figure 6.28 Comparison of the simulated and the observed piezometric heads at each observation well in the catchment.

heads, but stronger than the local variations. It is related to the direct translation of the infiltration estimated by the SVAT model as groundwater recharge to the aquifer.

Therefore, additional work is required to improve the coupled model performance, such as:

- Integration of the groundwater and SVAT models to fully simulate the hydrosystem and to have the feedback between groundwater-surface water as suggested by Clark et al. (2015); Maxwell et al. (2007); Fan et al. (2007).
- Refinement of the SVAT model to improve the estimation of evapotranspiration and to decrease the effective rainfall. Adaptation of the SVAT model to regional processes, i.e. urban zones and wetlands could improve the overall model performance.
- Introduction of variable thickness unsaturated zone in ORCHIDEE to represent the unsaturated zone stock variation and transit times.

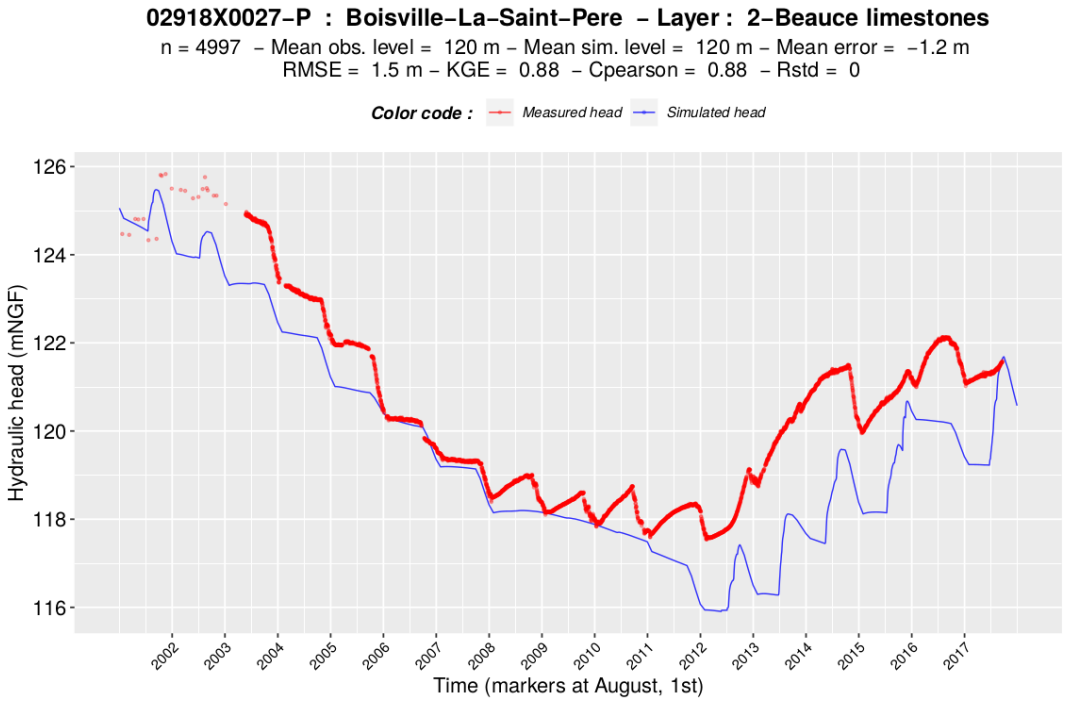

Figure 6.29 Time series illustration of hydraulic head during the examined period of the Beauce aquifer (Layer 2). The number of daily observations, RMSE, KGE, CC and standard deviation metrics are noted.

6.3.2.3 Performance of the coupled framework at Poses

The performance of discharge at the Poses sub-catchment was assessed to evaluate the coupled model with respect to standalone ORCHIDEE and CaWaQS applications. The comparison of flow dynamics calculated by three simulations and observation data is shown in Figure 6.32, and the associated performance statistics are provided in Table 6.5. Notably, the standalone ORCHIDEE model estimates larger discharges during high flow events and lower baseflow than the observation. This dynamic is expected as the total runoff is transferred to the outlet directly. The pre-calibrated standalone CaWaQS (green) simulation performs closest to the observations. The coupled model performs superior to standalone ORCHIDEE simulation after the surface runoff by ORCHIDEE routes through the aquifer system and the river network via CaWaQS . The flow dynamics are captured quite well by the coupled model (KGE = 0.77, NSE = 0.59). However, the performance is not yet close to the pre-calibrated CaWaQS model. Additional calibration and optimisation efforts are needed to improve the discharge dynamics of the model.

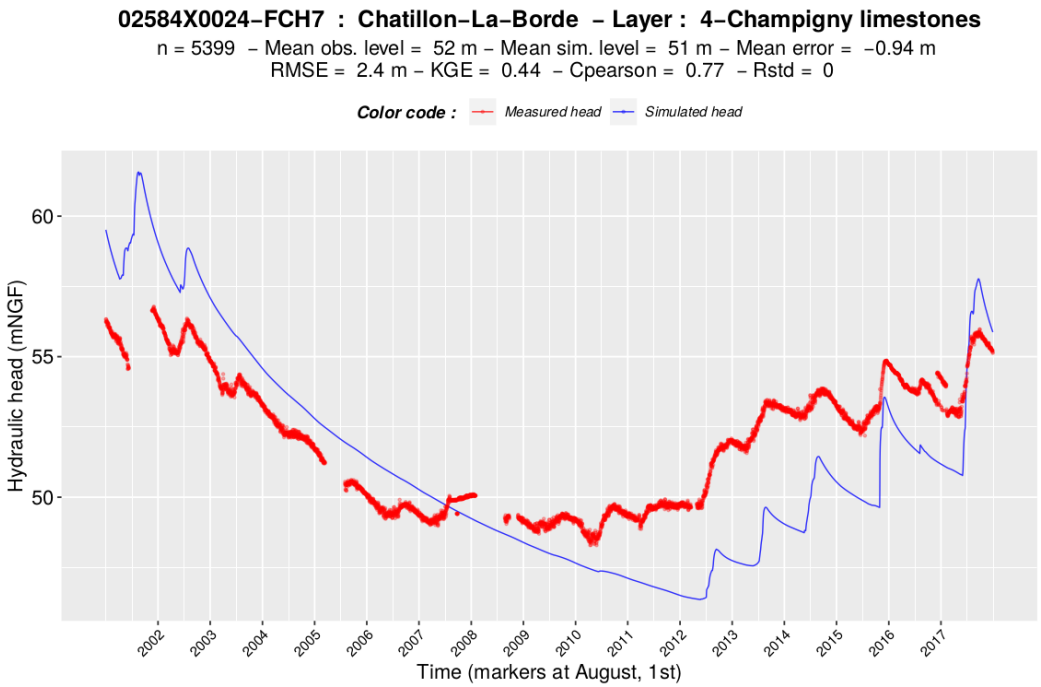

Figure 6.30 Time series illustration of hydraulic head during the examined period of the Champigny aquifer (Layer 4). The number of daily observations, RMSE, KGE, CC and standard deviation metrics are noted.

Table 6.5 Performance of standalone ORCHIDEE, CaWaQS and coupled ORC-CaW vs observations at Seine Vernon. PBIAS: Percent bias, KGE: Kling-Gupta Efficiency, NSE: Nash-Sutcliffe Efficiency, CC: Correlation coefficient. Period: 2001-2018.

Statistics	PBIAS	KGE	NSE	CC
CaWaQS (Standalone)	-4.2	0.83	0.82	0.91
ORCHIDEE (Standalone)	1.8	-0.53	-3.3	0.56
ORCHIDEE-CaWaQS (Coupled)	-0.2	0.77	0.59	0.82

6.4 Conclusions and perspectives

An ORCHIDEE SVAT model application is developed to simulate the surface water balance components. The surface water budget components were calibrated in the Seine basin by estimating pluri-annual discharge. The performance of LAI and AET was evaluated against the satellite products from GIMMSv3 (Zhu et al., 2013) and GLEAMv3 (Martens, 2019) products. A special attention was paid to the partition of the effective rainfall which was found to be around two-thirds recharge and one-third surface runoff (Flipo et al., 2023). The calibrated ORCHIDEE Seine model enabled the simulation of distributed recharge and runoff estimations with the help of ORCHIDEE. Estimated

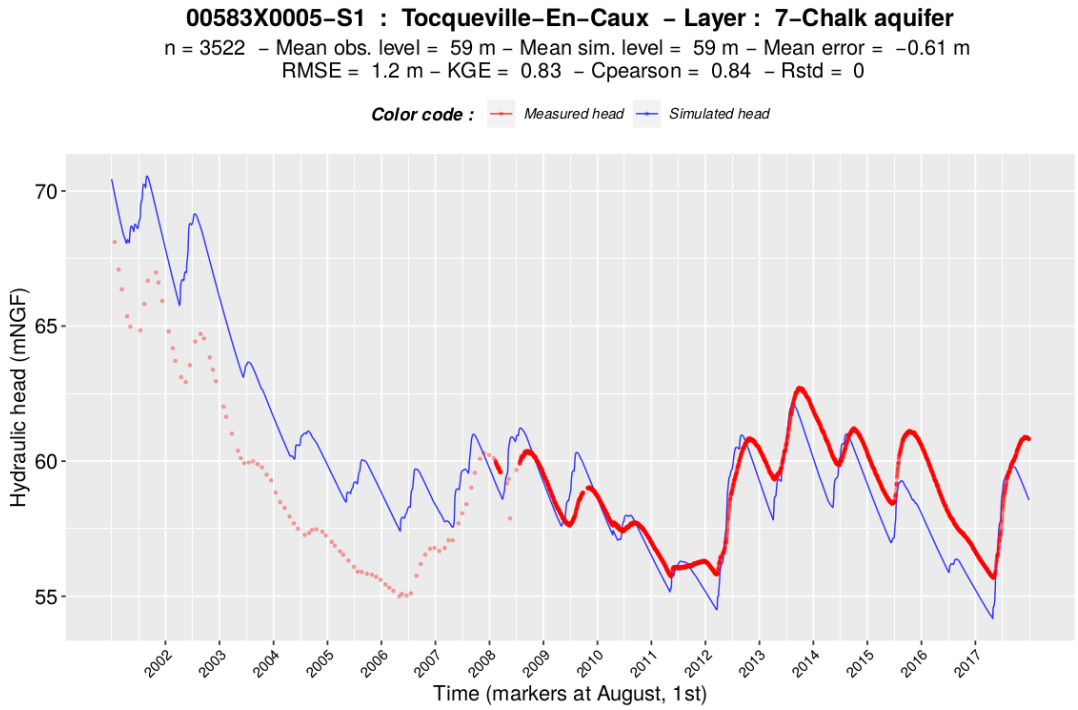

Figure 6.31 Time series illustration of hydraulic head during the examined period of the Chalk (Craie) aquifer (Layer 7). The number of daily observations, RMSE, KGE, CC and standard deviation metrics are noted.

surface runoff and recharge fluxes were used to force the groundwater model CaWaQS. The coupled model satisfactorily simulated the pluri-annual discharges in several main sub-catchments of the basin. Moreover, the coupled model can adequately simulate the water level dynamics in the aquifer system for at least half of the stations.

The surface water calibration shows that the soil texture maps shows weak sensitivities to evapotranspiration as documented in Tafasca et al. (2019). Significant improvements on bias were achieved by dynamically simulating the vegetation dynamics by STOMATE (Krinner et al., 2005). The evapotranspiration estimations were well within the uncertainty range provided by the GLEAM database (Martens et al., 2018). Although the LAI was overestimated in the catchment during the growth seasons, systematic underestimation of AET was documented. It should also be noted that SVAT models tend to underestimate the evapotranspiration fluxes, which in turn increase the effective rainfall (Wang et al., 2018b). At least 60 %of the actual evapotranspiration depends on the transpiration every year in the Seine basin. Therefore the summer underestimation of AET could be related to the vegetation representation and parameters.

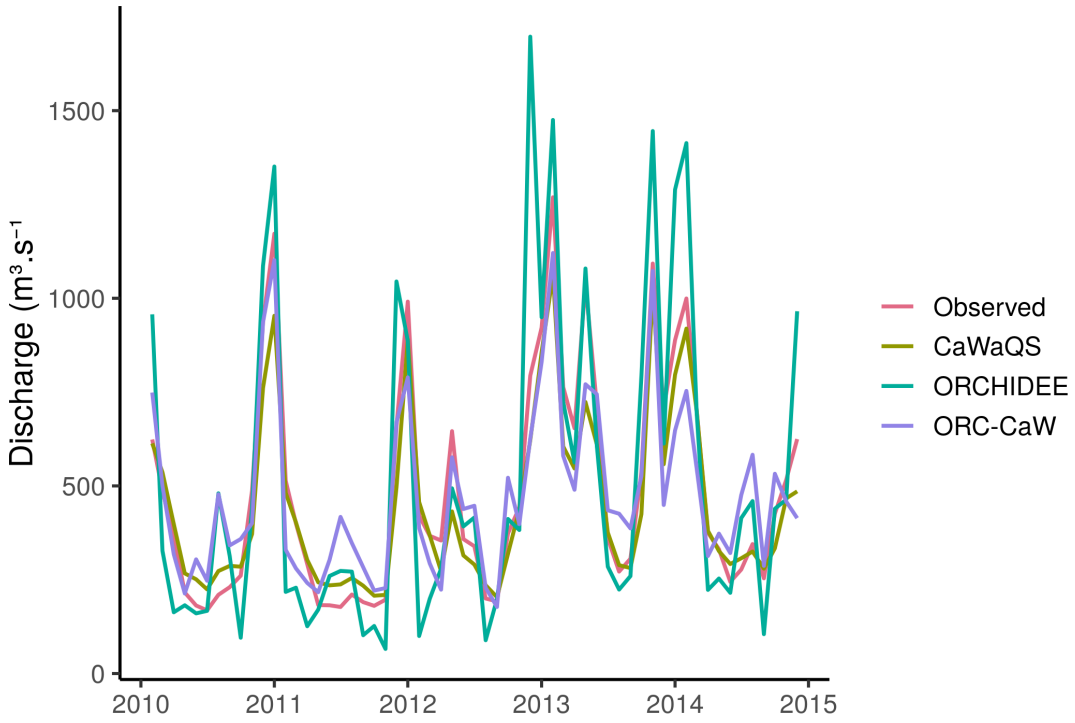

Figure 6.32 Comparison of standalone ORCHIDEE, standalone CaWaQS, the coupled model and the observed discharge at Seine Poses. A 30-day moving average was applied to discharge values

It is known that vegetation dynamics at a regional scale influence the soil moisture regimes (Loheide and Booth, 2011), heat waves (Stéfanon et al., 2012), riparian evapotranspiration (Loicq et al., 2018), and actual evapotranspiration (Garrigues et al., 2015). Further improvements on vegetation parameters at local and regional scales are necessary to understand their impact on hydrological fluxes (Grace and Williams, 2004). The AET could be improved by modifying the energy balance related parameter such as leaf albedo which caused the largest improvement of bias after the STOMATE module. Although sensitivity analyses were realised to understand the relative impact of various parameters (Raoult et al., 2021), additional work is needed to understand the cause of the AET underestimation which could lead to significant biases in future studies.

The spatial distribution of the simulated actual evapotranspiration captures the reference evapotranspiration satisfactorily. However, it should be noted that the evapotranspiration product is coarser than the resolution of the simulated domain. There is a high uncertainty linked to this resolution difference. During spring and summer, the actual

evapotranspiration is generally under-estimated with respect to the reference product. This could be related to the lack of water table dynamics of the current version of ORCHIDEE. It should be noted that the extended version of ORCHIDEE with wetland dynamics (including a water table) by Tootchifatidehi (2019) led to improved actual evapotranspiration estimations.

Based on the analysis, it could be concluded that the physically-based hydrological model ORCHIDEE can satisfactorily produce the actual evapotranspiration, runoff, recharge, and estimate the LAI within the range of uncertainty. The temporal dynamics of LAI are produced by the model through the STOMATE module, which simulates the dynamics of the vegetation, including several processes: photosynthesis, respiration, senescence, mortality, and litter dynamics. These processes are important for the estimation of LAI and vegetation cover, as well as the carbon processes. Therefore, the ORCHIDEE model could be extended with a groundwater module to study the dynamics of the vegetation with the impact on groundwater and vice versa.

During the surface water balance calibration, a new soil texture class "Urban" was introduced in ORCHIDEE and a soil texture map that specifies the urban zones was created. Initial simulations show that the introduction of an impermeable layer by Urban zone increases the surface runoff, however, for the practical goals of this study, the performance gets worse. Given the complexity of urban hydrological processes and difficulties associated with parameter estimation (De Kimpe and Morel, 2000), the urban soil map and soil properties of the new class should be further refined. Further investigation is required to include the anthropological impact by including the urban zones and their spatial and temporal variation in the ORCHIDEE model. Such endeavors could improve the regional simulation capabilities of the ORCHIDEE model at highly developed urban basins.

The river flow dynamics and routing in the ORCHIDEE model was not available in the current application. The performance of discharge improves significantly with the routing module in the ORCHIDEE-CaWaQS simulation. Although the performance is not captured as well as the pre-calibrated standalone CaWaQS model, the performance could be improved by regionalisation of the parameters (Samaniego et al., 2010;

Demirel et al., 2018) and the introduction of an unsaturated zone that represents the transit time delays. Because the main difference between the coupled model and standalone CaWaQS is the ability of CaWaQS to represent the unsaturated zone by a succession of Nash reservoirs which introduces transit time to groundwater recharge (Besbes and De Marsily, 1984). A variable thick unsaturated zone can also improve the groundwater dynamics since in the current application the recharge is transited into the aquifer system instantaneously which is not the case in the nature (Healy and Scanlon, 2010). There are attempts to include the routing module in ORCHIDEE to consider the travel times (Wang et al., 2018a; Nguyen-Quang et al., 2018).

Accurate estimation of recharge in groundwater modelling is a challenging task (Scanlon et al., 2002). Coupling two distributed models that simulate each component of the hydrosystem could help improve estimates of recharge and evapotranspiration. Additional benefits are a better understanding of the surface processes (vegetation dynamics) that impact the groundwater resources and possibility of scenario testing of climate change impact on groundwater resources. Previous observations show that the intensification of the hydrological cycle (Trenberth et al., 2007) impacts groundwater resources (Flipo et al., 2020b). This work provides that distributed estimates of recharge and runoff can be simulated reliably and produces accurate results.

Another aspect of the coupling framework is the performance of routing with the ORCHIDEE fluxes. The choice of routing module plays a significant role in the discharge simulation for SVAT models (Zhao et al., 2017). Representation of groundwater and routing within SVAT models is an active research area (Clark et al., 2015). We demonstrate that coupling SVAT model ORCHIDEE with CaWaQS improves the simulated discharge considerably. Future attempts to fully account for the groundwater and river processes in SVAT models is therefore important. Moreover, additional work is needed to fully integrate two models to simulate the hydrosystem simultaneously. This could improve understanding of the hydrosystem functioning by taking advantage of the full process representation, including the vegetation processes and actual evapotranspiration estimates with the groundwater feedback. Studies have shown that groundwater feedback has a strong link to regional evapotranspiration (Fan, 2015).

Previously, the CaWaQS model was applied to the Seine (Flipo et al., 2020a; Labarthe, 2016; Pryet et al., 2015) basin using the potential evapotranspiration estimations to calculate the effective rainfall which was then partitioned it into recharge and runoff via a production function and a Nash reservoir system. The proposed coupled model here successfully simulates by taking advantage of the distributed recharge and runoff forcing obtained by the ORCHIDEE Seine application. Therefore, the process based model can also be used to inform the groundwater model to simulate the hydrosystem adequately. It is also possible to extend this work to scenario testing to evaluate different climate and land use scenarios. Moreover, it will be possible to evaluate the spatial and temporal variation of recharge and runoff and its impact on the aquifer system within the coupled framework.

Chapter 7

Assessing water and energy fluxes in a regional hydrosystem: case study of the Seine basin

The calibration of the surface water balance and the evaluation of the coupled model were presented in Chapter 6. In this chapter, the complete heat and water balance using the coupled model ORCHIDEE-CaWaQS were developed. The results from this study were prepared in the form of a journal article. The paper is accepted by "Comptes Rendus: Geo-Hydrological Data and Models".

Kilic, D., Rivière, A., Gallois, N., Ducharne, A., Wang, S., Peylin, P., Flipo. N., submitted. Assessing water and energy fluxes in a regional hydrosystem: case study of the Seine basin

Abstract. While it is well accepted that climate change and growing water needs affect long-term sustainable water resources management, performing accurate simulations of water cycle and energy balance dynamics at regional scale remains a challenging task.

Traditional Soil-Vegetation-Atmosphere-Transfer (SVAT) models are used for numerical surface water and energy simulations. These models, by conception, do not account for the groundwater lower boundary that permits a full hydrosystem representation. Conversely, while addressing important features such as subsurface heterogeneity and river-aquifer exchanges, groundwater models often integrate overly simplified upper boundary conditions ignoring soil heating and the impacts of vegetation processes on radiation fluxes and root-zone uptakes. In this paper, one of the first attempts to jointly model water and energy fluxes with a special focus on both surface and ground-

water at the regional scale is proposed on the Seine hydrosystem (78,650 km^2), which overlays one of the main aquifer systems of Europe.

The tool couples the SVAT model ORCHIDEE and the process-based hydrological–hydrogeological model CaWaQS, which describes water fluxes, based on the blueprint published by de Marsily et al. (1978). An original transport library based on the resolution of the diffusion/advection transport equation was developed in order to simulate heat transfer in both 1D-river networks and pseudo-3D aquifer systems. In addition, an analytical solution is used to simulate heat transport through aquitards and streambeds. Simulated ORCHIDEE surface water and energy fluxes respectively feed fast surface runoff and slow recharge and then used as CaWaQS forcings to compute river discharges, hydraulic heads and temperature dynamics through space and time, within each of the hydrosystem compartments. The tool makes it possible to establish a fully consistent water and energy budget over a 17 yr-period. It also simulates temperature evolution in each aquifer and evaluates that river thermal regulation mostly relies by order of importance on short wave radiations (109.3 $\mathrm{W\,m^{-2}}$), groundwater fluxes (48.1 $\mathrm{W\,m^{-2}}$) and surface runoff (22.7 $\mathrm{W\,m^{-2}}$).

7.1 Introduction

Nowadays, "*the water we use comes to 95% from the renewable water cycle*" (de Marsily, 2020, 2009). Hydrosystems — defined as the overlapping combination of atmosphere, soil surface and subsurface where water flows — host the water cycle and are an essential resource for humans and ecosystems. Hydrosystems sustain the global ecology and meet the societal needs of drinking water, energy and food production. In terms of water resources, providing sufficient quantities for all requirements is not the only challenge. In order to be considered as a resource, the water quality, which encompasses physical, chemical and biological properties, is also essential. Our current understanding of hydrosystems is based primarily on numerical models (de Marsily, 1986) in which physical processes are simulated under a range of historical or potential conditions to quantify storage as well as fluxes within a given compartment or between multiple com-

partments of the system.

Climate change will modify the water cycle and energy balance processes (Taylor et al., 2013): soil infiltration, groundwater recharge (York et al., 2002), river discharge (Gudmundsson et al., 2021) and water temperature (Webb and Nobilis, 2007). Also, rising temperatures increase evaporative demand over land (Berg et al., 2016), which limits the amount of water for aquifer system recharge. Groundwater withdrawals, river uses and indirect effects of irrigation and land use changes (Wagener et al., 2010) also increase stresses on hydrosystems. Despite the importance of quantifying hydrosystem fluxes for water resources management, little is known about the prevalent temperature regime and heat fluxes of hydrosystems at the regional scale in the light of climate change (Taylor et al., 2013).

Many studies have been carried out regarding the effects of climate warming on stream temperature (Ducharne, 2008; Vliet et al., 2013; Webb et al., 2008) and aquatic species (Isaak et al., 2020). Groundwater temperature is influenced by the temperature of the infiltrating water and by the conduction of heat from the surface domain. Seasonal variations in shallow aquifers below urban areas coincide with various anthropogenic heat sources, such as sealed surfaces or subsurface building infrastructures for instance (Böttcher and Zosseder, 2022). This results in highly dynamic and complex thermal conditions, so that the the identification of influencing heat sources is not straightforward (Ferguson and Woodbury, 2007). From the land surface downward, the amplitude of groundwater temperatures decreases and average temperatures tend towards the yearly average ground surface temperature (Bense and Kooi, 2004). In areas with strong upward seepage, groundwater temperature is carried into streams. Therefore, groundwater seepage to streams is known to moderate summer and winter stream temperatures and to create so-called local thermal refugia (Kaandorp et al., 2019) and climate refugia (Briggs et al., 2018) for aquatic biota. Temperature is a major determinant for drinking water quality, since it influences physical, chemical and biological processes, such as absorption, decay (Monteiro et al., 2017), growth and competition (Prest et al., 2016). Water treatment processes are also influenced by water temperature, which must be between 10°C and 15°C to ensure the best potabilization conditions. Al-

though the link between energy and water fluxes is clear and the processes are well known (Anderson, 2005), studies on water resources include energy fluxes only *via* the evapotranspiration sink term of the water balance (Singh, 2014).

Understanding the coupled water and energy fluxes of a hydrosystem at the regional scale has benefits beyond understanding the physical processes. First, quantifying all fluxes at the hydrosystem scale allows decision makers to develop water policies (Flipo et al., 2021b) regarding water demand and energy generation or to mitigate the risks of contamination (Briggs et al., 2014b) or climate change (Taylor et al., 2013), and is therefore crucial. Especially, the impact of climate change on densely populated hydrosystems is highly uncertain while the demand for water and energy increase rapidly with population growth (de Marsily, 2009). Second, critical infrastructures such as nuclear power, water treatment plants depend on water temperature for cooling and uncertainties due to hydrological extremes (Boogert and Dupont, 2005) pose a risk within the water-energy-food nexus framework. Third, proper exploitation of geothermal sources, which has a great potential to replace fossil fuels, requires the heat budget estimation. Therefore, examining how water budget and subsurface energy may change in response to both climate-driven and anthropogenic effects is crucial to a holistic water management in terms of quantitative and qualitative issues.

Between the different approaches for water temperature modeling (see Caissie 2006), deterministic models offer the benefit of scenario testing for management purposes, which is critical in understanding the impact of climate change on river basins. Most attempts are local 0D models, often applied in many points (e.g. Bustillo et al. 2014), or 1D models mostly used in small river basins (e.g. Wondzell et al. 2019). Notable exceptions are the worldwide modelling of Van Vliet et al. (2012b); Vliet et al. (2013) and the high-resolution basin scale model of Beaufort et al. (2016a) in the Loire basin. In all these applications, groundwater temperature is never explicitly modelled, and groundwater contribution to river temperature is either overlooked or approximated by empirical relationships. The same applies to input heat fluxes from rainfall and/or surface runoff. Qiu et al. (2019) and Loinaz et al. (2013) attempted to simulate river temperatures explicitly, although these applications were limited to small watershed

scales. A challenge in the explicit simulation of river and groundwater temperatures is establishing the temperature of recharge and runoff.

To address these issues, a numerical tool has been developed to jointly model water and energy flows with a focus on surface and groundwater at the regional scale. The tool couples the SVAT (Soil-Vegetation-Atmosphere-Transfer) model ORCHIDEE and the hydrological–hydrogeological model CaWaQS. ORCHIDEE is capable of simulating coupled water and energy fluxes at surface. The novelty of our approach is to combine surface temperatures and recharge and runoff fluxes simulated by ORCHIDEE with the process based CaWaQS model to explicitly simulate river and aquifer water and heat fluxes. For this purpose, an original transport library based on the resolution of the diffusion/advection transport equation was developed to simulate heat transfer in both 1D river networks, and pseudo-3D aquifer systems. In addition, an analytical solution is used to simulate heat transport through aquitard layers and streambed.

We selected the Seine River basin to test our approach as its under increasing stress of climate change and it possesses distributed data sets for process-based models. The Seine River basin, one of the major aquifer systems in Europe, faces major water resource issues due to a variety of uses, *e.g.* drinking water, cooling and heating of buildings by geothermal or river-based energies, agricultural withdrawals, cooling of the nuclear power plants that provide electricity in the area, etc.

In the following, the numerical tool is first presented with a focus on SVAT-subsurface coupling. The calibration of surface water balance is demonstrated. Dynamics and orders of magnitude of water and heat budgets are detailed in the case of long-term simulations, to answer three research questions: **(i)** what is the hydrological and thermal functioning of the Seine hydrosystem in current climate conditions? **(ii)** what are the predominant heat sources in the Seine aquifer system and river network, resulting in the formation of extensive subsurface urban heat islands on groundwater temperature? **(iii)** what is the role of the surface runoff and river-aquifer exchanges in the river thermal load?

7.2 Material and methods

7.2.1 Study area: The Seine hydrosystem

The Seine basin ($\simeq$ 78,650 km^2) is entirely located within the sedimentary Paris basin in northern France. The geological settings consists of concentric tertiary sedimentary formations (alternating clay, sandstone and limestone), Cretaceous Chalk and Jurassic limestones lying on a basement of Hercynian crystalline rock formations, mainly outcropping at the extreme south-east (Morvan) and north-east (Ardennes) limits of the basin. The highest altitude is 856 m a.s.l and 90$\%$ of the basin is below 300 m. The river network shows gentle slopes and climate does not exhibit sharp geographical gradients.

The climatic regime of the basin is pluvial oceanic, modulated by seasonal variations in evapotranspiration. The mean annual precipitation rate is 825 mm over the 1980–2020 period (SAFRAN dataset, Vidal et al. (2010a)). Flow at the downstream Seine river was determined at the gauging station of Vernon before the estuary. The mean discharge at the station was 490 $\mathrm{m^3\,s^{-1}}$ over the 1980-2020 period (HYDRO database). Furthermore, variographic studies have shown the stationarity of both groundwater and river water stock over this time period (Flipo et al., 2012).

Currently, the Seine basin is the most urbanized and industrialized basin in France (Flipo et al., 2021b). It includes 17 million inhabitants (25$\%$ of the national population), with 10 million in the Paris conurbation alone, and 40$\%$ of national industrial activities, while a large zone around the huge Paris conurbation is oriented towards the mass production of cereals and industrial crops (Figure 7.1). This scale of activity creates an enormous energy demand which can be partially offset by exploiting geothermal energy (Bayer et al., 2019). However, this potential is yet to be quantified by estimating the energy budget of the aquifer system. Given the large population and food production of the Seine basin, water resources are of high strategic importance as about $1\ \mathrm{km^3}$ of groundwater is extracted every year over the whole basin (Flipo et al., 2023).

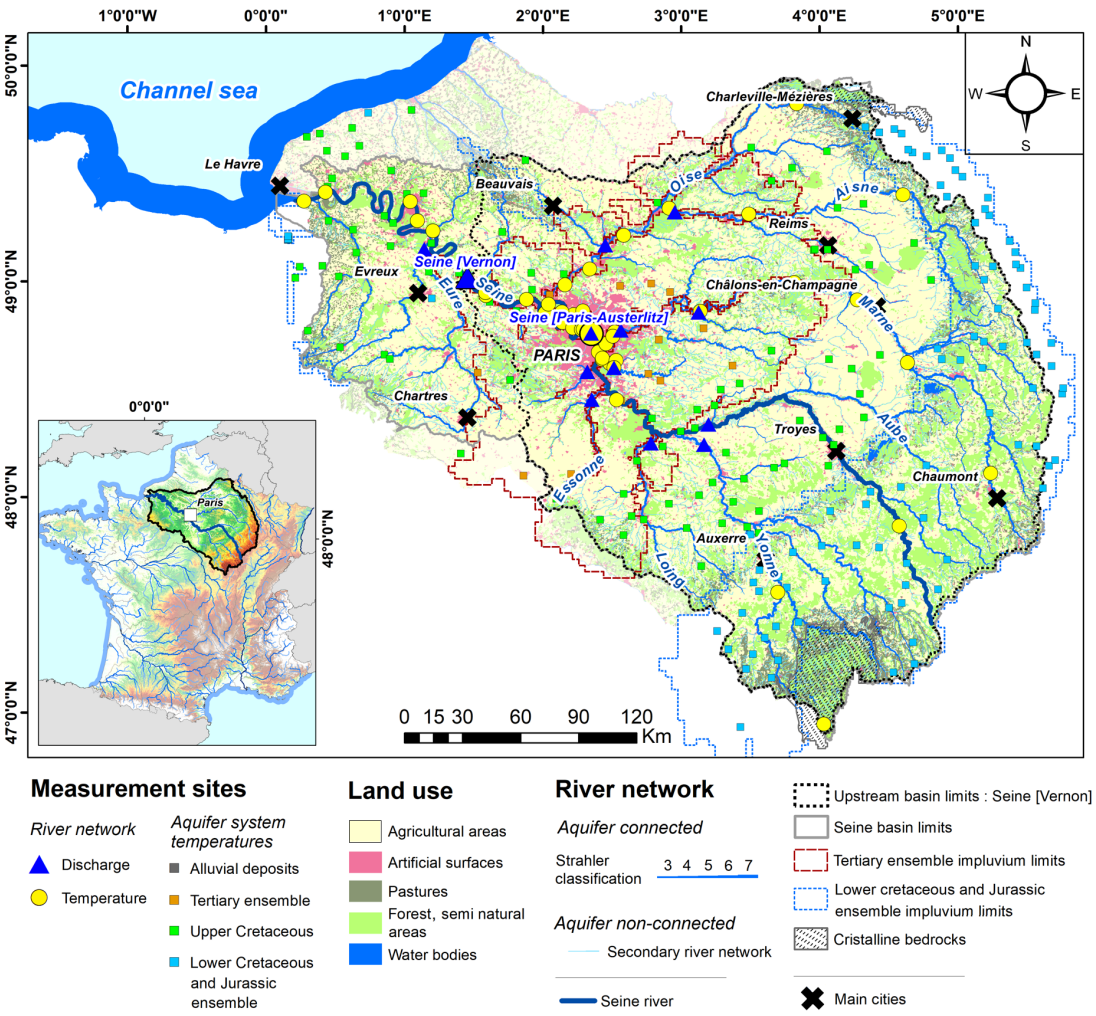

Figure 7.1 General overview of the Seine basin area ($\simeq$ 78,650 km^2). Land use as provided by the 2018 *CorineLandCover* database is used as map background. Triangles and square points represent river discharge and temperature measurements, respectively. Colored dashed lines indicate the extent of the entire aquifer system. Aquifer temperatures stations are grouped according to the main aquifer ensemble they are associated with.

7.2.2 Numerical tools and model development

7.2.2.1 ORCHIDEE (tag 2.2, rev. 6533)

ORCHIDEE is a SVAT model, initially designed to be coupled to an atmospheric global circulation model (Krinner et al., 2005), but it can also be used in stand-alone mode, using an input meteorological data set. ORCHIDEE tag 2.2 was developed as part of the IPSL-CM6 model (Boucher et al., 2020) to contribute to the sixth phase of the Coupled Model Intercomparison Project (CMIP6) (Eyring et al., 2016).

The horizontal resolution is imposed by the atmospheric grid, and the energy and

water budgets of the land surface are calculated in each grid-cell at a sub-hourly time step (15-min in the coupled model, 30-min in stand-alone mode) to properly account for the diurnal variations of incoming radiation. These budgets depend strongly on land cover, described in each grid-cell as a mosaic of 15 plant functional types (PFTs) including bare soil, evergreen and deciduous trees, C3 and C4 grasses and crops. All PFTs share the same equations but with different parameters. The proportion of each PFT is prescribed in each grid cell from land cover maps derived from satellite observations, with yearly updates (Lurton et al., 2020). Two options are compared in this work regarding the evolution of leaf area index (LAI), which can be either prescribed via input maps of monthly LAI, or calculated dynamically at a daily time step by the so-called STOMATE module, which redistributes the net primary production (photosynthesis minus autotrophic respiration) owing to PFT dependent rules of allocation and phenology.

The vertical soil moisture redistribution is modelled by a multi-layer solution of Richards equation, using a 2-m soil discretized into 11 soil layers, with free drainage as a bottom boundary condition. Infiltration and infiltration-excess surface runoff are derived from a Green-Ampt parametrization (D'Orgeval et al., 2008). The unsaturated values of hydraulic conductivity and diffusivity are given by the Van Genuchten-Mualem relationships. In each grid cell, the corresponding parameters (including saturated hydraulic conductivity K_{sat} and porosity) are deduced from soil texture as detailed in Tafasca et al. (2019). K_{sat} (in m s^{-1}) further undergoes a vertical exponential decay to account for the effects soil compaction and bioturbation:

$$K_{\mathrm{sat}}(z) = K^{*}_{\mathrm{sat}} \exp(-c_K(z - z_{\mathrm{lim}})), \tag{7.1}$$

where z is the depth below the soil surface (m), K^{*}_{sat} is the reference value of K_{sat} based on soil texture (m s^{-1}), z_{lim} is the depth at which the decrease of K_{sat} starts (by default equal to 0.3 m), and c_K is the decay factor (in m^{-1}, equal to 2 by default).

Evapotranspiration is composed of four sub-fluxes: sublimation, interception loss, soil evaporation, and transpiration, tightly coupled to photosynthesis. Soil evaporation

and transpiration depend on soil moisture via stress factors reducing the effective rates compared to the potential rate, which itself depends on an aerodynamic resistance (and stomatal resistance for transpiration) and the water vapor gradient between the surface and the atmosphere. Evapotranspiration E (in kg m^{-2} s^{-1}) and its energy equivalent, the latent heat flux (in W m^{-2}), couple the water and the energy budgets, calculated at the grid-cell scale given by:

$$C_p \frac{\partial T_s}{\partial t} = (1 - \alpha_s)\, R_{\mathrm{SWd}} + R_{\mathrm{LWd}} - \varepsilon \sigma T_s^4 - LE - H - G. \tag{7.2}$$

Surface temperature T_s is the prognostic variable (K), t is time (s), C_p is the heat capacity of the surface layer (J K^{-1} m^{-3}), while R_{SWd} and R_{LWd} are the input downward radiation fluxes (W m^{-2}) in the visible and infra-red wavelengths, respectively. Surface albedo α_s depends on the albedo of the soil and of each PFT, which are prescribed parameters, and on snow albedo, calculated as a function of snow age by a 3-layer snow module (Wang et al., 2013). Finally, L is the latent heat of vaporization (J kg^{-1}), H is the sensible heat flux (W m^{-2}), and G is the ground heat flux (W m^{-2}), which couples the surface energy budget to the soil temperature profile, resulting from a 1D heat diffusion equation. Soil freezing is neglected since the Seine River basin is predominantly temperate. The vertical discretization for heat diffusion is identical to that adopted for water down to 2 m, then further extended to 18 m where a zero heat flux is assumed. The soil thermal properties (heat capacity and conductivity) of each layer depend on soil moisture (assuming a uniform profile below 2m) and soil texture (Wang et al., 2016b).

7.2.2.2 CaWaQS (*v* 3.17)

Mostly relying on the former MODCOU-NEWSAM software (Ledoux et al., 1989) based on the blueprints of de Marsily et al. (1978), the physically-based CaWaQS3.x (Flipo et al., 2023, 2007a) computes, at a daily time-step, the main physical processes controlling the water budget and flow dynamics in each compartment of a hydrosystem. Each CaWaQS library deals with a specific compartment of a hydrosystem. This feature allows users to bypass certain modules when necessary and makes CaWaQS suitable for

coupled applications.

CaWaQS is capable of distributing forcing fluxes over its own grid, accepting forcing fluxes at various grid sizes. Forcing runoff fluxes are aggregated by CaWaQS to local sub-catchment areas and directly routed to the river network in which river discharges are simulated using a Muskingum scheme and water levels are simulated using a Manning-Strickler approach (Saleh et al., 2011). Saturated groundwater flows are numerically solved using a finite difference solution of the 2-D diffusivity equation on a multi-layered nested grid. Vertical exchanges between aquifer layers and stream-aquifer exchanges depend on drainance and conductance concepts respectively *i.e.* a 1-D steady-state approach, assumed to be linearly linked to the head difference between two aquifer layers or river water level-aquifer head difference (Flipo et al., 2014). Aquifer recharge from the unsaturated zone as well as anthropogenic withdrawals are treated as source terms.

Recent developments added a transport module, which simulates heat and solute transport in porous media (aquifer, pseudo-3D resolution) and the free surface compartment (river network, 1-D approach). Transport is described using the following advection-diffusion equation:

$$\nabla \left[\frac{\lambda}{\rho_w \, C_w} \nabla T_w - \, q \, T_w \right] = \frac{\rho \, C}{\rho_w \, C_w} \frac{\partial T_w}{\partial t}, \tag{7.3}$$

where T_w is the water temperature (K), q is the specific discharge ($\mathrm{m\,s^{-1}}$), λ is the thermal conductivity of the porous medium ($\mathrm{W\,m^{-1}\,K^{-1}}$), ρ_w and ρ are the densities of water and the porous medium (both in $\mathrm{kg\,m^{-3}}$), and C_w and C are the specific heat capacities of water and porous medium ($\mathrm{J\,kg^{-1}\,K^{-1}}$).

River-atmosphere heat exchanges are described based on an energy budget equation similar to equation 7.2 but for water temperature T_w; the various heat fluxes were calculated following Magnusson et al. (2012). Whilst the energy income from the sun is the largest source of energy for a river system, clouds, riparian vegetation and topography-related shading can reduce heat input significantly (Loicq et al., 2018). The limited permeability of aquitard layers constrains water flow to the vertical direction between

aquifers (de Marsily, 1986). Similarly, streambed flow is also dominated by vertical exchanges between the stream and its underlying aquifer layer. Consequently, heat flow between two adjacent aquifers separated by an aquitard layer or a streambed linking the river with the aquifer layer can be resolved by a 1-D analytical solution. In this study, the heat exchanges through aquitard layers and streambed were resolved by the analytical solution of Kurylyk et al. (2017) :

$$\alpha_i \frac{\partial^2 T_i(z,t)}{\partial z^2} - q \frac{\partial T_i(z,t)}{\partial z} = 0 \quad (i = 1,\, 2,\, ...,\, n-1) \tag{7.4}$$

where z is the depth (m), n is the number of layers, α_i is the bulk thermal conductivity λ of layer i divided by the volumetric heat capacity of water ($\mathrm{m^2\,s^{-1}}$), and T_i is temperature of layer i. This solution is an extension of the method initially proposed by Bredehoeft and Papaopulos (1965), to allow for variations in thermal conductivity with depth. The equation is based on four fundamental assumptions: **(i)** heat transfer is restricted to one dimension; **(ii)** Darcy flux is constant and uniform throughout each layer; **(iii)** temperature profiles are at steady-state during each time step; and **(iv)** properties are homogeneous within each layer.

The aquitard interface is a 3-layered system with 3 unknowns, i.e. the temperatures of the aquitard as well as of the top and bottom aquifers. The streambed interface is a 2-layered system with 3 unknowns, i.e. the streambed, river and aquifer temperatures. The analytical solution coefficients are incorporated as a term of the solution matrix of the porous media, thereby simultaneously resolving the heat transport in the aquitard. The river temperature in the previous time step is used to calculate the streambed temperature at the stream-aquifer interface. The streambed temperature calculated by the analytical solution is then used as the lower boundary of the river transport simulation.

7.2.2.3 Model coupling strategy

Coupling is achieved *via* an "offline" forcing procedure, whereby the models involved are sequentially run, thus only allowing one-way interaction, from ORCHIDEE to CaWaQS. To this end, selected ORCHIDEE simulation results are used as daily CaWaQS up-

per boundary conditions: drainage fluxes simulated by ORCHIDEE are prescribed as CaWaQS aquifer recharge, with a temperature equal to the one in the soil at 2-m, while surface runoff is routed to the river system, assuming its temperature is at equilibrium with the soil surface temperature (0.001m depth, top layer).

The correspondence between the ORCHIDEE grid mesh and and the elementary surface units of CaWaQS is handled by CaWaQS, *via* spatially weighted area-based arithmetic means. The coupled model scheme internally projects each element to its geographic coordinate and then passes the forcing flux information to the receiving model.

7.2.2.4 Numerical experiment design

The coupled tool was applied over the 2001-2018 period, which was noteworthy for remarkable flood events (*e.g.* winter/spring 2001, winter 2016-18) as well as extremely low-flow/drought periods and heat-waves (*e.g.* summer 2003, summer 2006-2007).

7.2.2.4.1 ORHIDEE setup ORCHIDEE is run over the Seine basin in stand-alone mode, forced with the SAFRAN meteorological data set (Vidal et al., 2010a). It provides the required atmospheric variables at an hourly time step, over a regular 8 x 8 km grid, which is therefore the horizontal resolution of the simulations. A total of 1,490 cells are used to described the simulated domain. A constant carbon-dioxide concentration (370 ppm) over the period 1980-2018 was applied.

The vegetation distribution map was derived at 0.5 degree resolution from the ESA-CCI Land Cover dataset at 300 m resolution, for the 1992-2015 period (see details in Lurton et al. (2020)). Vegetation distribution outside this period was set to that of the nearest available year with a constant vegetation distribution. For simulations with prescribed LAI, the monthly values were obtained from an existing 40-year global simulation performed in stand-alone mode at 0.5 ° (55 km resolution). The soil background albedo map was derived from the MODIS albedo dataset aggregated at 0.5 degree resolution. Soil texture distribution maps were obtained from four sources: Reynolds (Reynolds et al., 2000), SoilGrids (Hengl et al., 2017), LUCAS (Ballabio et al., 2016),

and INRA (Jolivet et al., 2006). The initial state was obtained after a five-year warm-up period (1980-1985) in order to reach the land surface model equilibrium state for soil moisture and soil temperature.

7.2.2.4.2 CaWaQS setup A pre-existing CaWaQS application over the Seine basin, which considers the main aquifer units in interaction with the Seine river and its main tributaries (Flipo et al., 2023), was used here. From the oldest to the most recent, these aquifers can be grouped according to the following four main ensembles: **(i)** an ensemble of aquifer and aquitard units, ranging from Lower Jurassic (Hettangian stage) to Lower Cretaceous (Albian stage), **(ii)** the large Upper Cretaceous chalk aquifer, **(iii)** a Tertiary aquifer complex including the five main aquifer layers dating from Palaeocene to Miocene stages and **(iv)** recent alluvial deposits (Pleistocene, Holocene). River geometry was obtained from the SYRAH-CE (Chandesris et al., 2008) database. River network water inputs account for subsurface runoff, overflows from aquifer to soil surface as well as river-aquifer exchanges. Mainly due to computation time concerns, river-aquifer exchange calculations were restrained to the main hydraulic network, which corresponds to river reaches with a Strahler order above or equal to 3 (Figure 7.1). The thermal parametrization (thermal conductivities, heat capacities and porosities) of the Seine basin was extracted from Dentzer (2016) and Rivière (2012). Heat transport was simulated in the river reaches with a Strahler order above or equal to 3 (Figure 7.1). Soil surface temperatures obtained from ORCHIDEE were prescribed to river reaches below Strahler order 3. The initial temperature state of the aquifer system was obtained by running the coupled model for 40 years by re-cycling 2 sets of 20-year simulations in the period 1985-2005.

CaWaQS forcings were defined as follows: **(i)** A no-flow boundary condition is imposed at the bottom and border limits of the domain, except where the mesh boundary corresponds to an adjacent river; **(ii)** Groundwater withdrawals are taken into account as a daily pumping rate, inferred from the annual groundwater abstraction data of the Seine basin water management agency (Agence de l'eau Seine-Normandie, AESN) for domestic, industrial and agricultural needs; **(iii)** Agricultural withdrawals are assumed

to take place only during the summer period (*i.e.* bulk irrigation water volume is distributed as: 20% in May, 30% in June and July, and 20% in August); **(iv)** A no-heat flux boundary condition is imposed for the horizontal borders; **(v)** A Dirichlet boundary condition is assigned to the top boundary of the groundwater system for transport; **(vi)** Geothermal fluxes are assumed for the bottom limit of the domain (75 mWm^{-2}, Dentzer (2016)).

7.2.2.5 Calibration protocol

7.2.2.5.1 Calibration strategy A two-step calibration procedure was used to calibrate the water and heat cycle of the Seine Hydrosystem. Considering the impact of North Atlantic Oscillation (NAO) on the groundwater and river stock variation (Flipo et al., 2012), a 17-year averaging period between 2001-2018 was selected to conduct the first step of the optimization procedure.

The surface hydrology calibration step consists of iterative trial-and-error adjustments of the ORCHIDEE parameters to minimize the bias between simulated and observed mean pluri-annual discharge at Vernon, the most downstream gauging station of the Seine before the estuary (Figure 7.1). The bias was calculated after the simulated pluri-annual mean discharge (estimated by total runoff times basin area) was corrected for yearly groundwater abstraction (annual average equivalent of 37 $\mathrm{m}^3\,\mathrm{s}^{-1}$ during 2008-2012, AESN) from the basin. Previous studies (Flipo et al., 2023) indicate that around two-thirds of effective rainfall contributes to aquifer recharge in the basin, and this ratio was also considered as a qualitative target for the calibration.

A set of 10 ORCHIDEE simulations were chosen to illustrate this iterative process (Table 7.1). Firstly, EXP1 to EXP4 allow us to assess the influence of the soil texture map (with a prescribed LAI map and default parameters, as used at global scale for CMIP6). Then, the two available options to account for LAI variations (prescribed map vs dynamic simulation by the STOMATE module) can be assessed by comparing EXP4 and EXP5. Finally, EXP5 to EXP10 only differ by some ORCHIDEE parameters found to be effective by several sensitivity analyses (e.g. Raoult et al. (2021)): the saturated hydraulic conductivity (K_{sat}) assigned to the dominant soil textures in the Seine River

basin (Loamy Sand, Loam, Clay Loam) and its decay factor c_K (Eq. 7.1); the visible and near-infrared leaf albedo and maximum LAI of the main PFTs in the basin. It must be noted that no calibration was carried out to improve the thermal fluxes. The temperatures of soil bottom and soil top layers were assumed to be at equilibrium with the recharge (drainage) and surface runoff temperatures, respectively.

CaWaQS parameterizations of river network and groundwater were taken from the pre-calibrated parameter set provided by Flipo et al. (2023). No additional calibration of the hydrological components and groundwater heat transport of CaWaQS were undertaken, but the river heat budget was calibrated by modifying the uniform shading factor ranging from 0% to 50% applied on the net incoming radiation on the river (Beaufort et al., 2016a). A 30 $\%$ uniform shading, consistent with reported shading factor values (Loicq et al., 2018), was selected after a series of simulations.

Table 7.1 Parameter set applied to the 10 experiments to calibrate the ORCHIDEE model (-: same value than the previous one, R: Reynolds, SG: SoilGrids, L: Lucas, I : INRA, pLAI: prescribed LAI, ST: STOMATE activated, TeBS: Temperature Boreal Summergreen Trees, TeBe: Temperate Boreal Evergreen Trees, NC3: Natural C_3 grass, AC3: Agricultural C_3 crops)

Experiment		EXP1	EXP2	EXP3	EXP4	EXP5	EXP6	EXP7	EXP8	EXP9	EXP10
Soil distribution		I	SG	L	R	R	R	R	R	R	R
Vegetation model		pLAI	pLAI	pLAI	pLAI	ST	ST	ST	ST	ST	ST
Parameter	Class										
c_K		2	-	-	-	-	4	-	-	10	-
K_{sat} ($m\,s^{-1}$)	Loamy Sand	4.05×10^{-5}	-	-	-	-	-	-	1.73×10^{-5}	-	-
	Loam	2.88×10^{-6}	-	-	-	-	-	-	1.50×10^{-6}	-	-
	Clay Loam	7.22×10^{-7}	-	-	-	-	-	-	4.62×10^{-7}	-	-
Near-infrared leaf albedo	TeBE	0.22	-	-	-	-	-	0.2	-	-	-
	TeBS	0.22	-	-	-	-	-	0.2	-	-	-
	NC3	0.3	-	-	-	-	-	0.25	-	-	-
	AC3	0.3	-	-	-	-	-	0.1	-	-	-
Visible-light leaf albedo	TeBE	0.06	-	-	-	-	-	0.04	-	-	-
	TeBS	0.06	-	-	-	-	-	0.04	-	-	-
	NC3	0.1	-	-	-	-	-	0.05	-	-	-
	AC3	0.1	-	-	-	-	-	0.04	-	-	-
Maximum LAI	TeBE	4.5	-	-	-	-	-	-	-	-	5.5
	TeBS	4	-	-	-	-	-	-	-	-	5
	NC3	2	-	-	-	-	-	-	-	-	3
	AC3	2	-	-	-	-	-	-	-	-	3

7.2.2.5.2 Evaluation strategy To validate the coupled model performance, the Seine basin hydrogeological and thermal application results were compared to a set of river discharge and water level monitoring wells as well as river and aquifer temperature data, distributed among the different aquifer units (Figure 7.1). The Kling-Gupta Efficiency

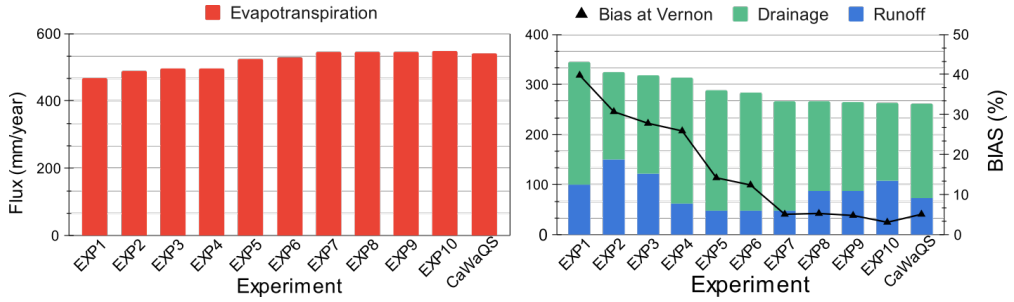

Figure 7.2 Mean yearly surface water budget components calculated by ORCHIDEE in mm y^{-1}. Bias was calculated on the multi-year mean discharge at Vernon gauging station after the adjustments on the mean yearly water abstractions are taken into account for EXP1-10. CaWaQS column represents the water balance calculated by the CaWaQS-Seine application including water abstractions.

coefficient (KGE), Root Mean Square Error ($RMSE$), Mean Absolute Error (MAE), Percent bias ($PBIAS$) and the Pearson correlation coefficient (CC) were used to quantitatively evaluate the misfit between simulated and observed values and dynamics.

Field data were collected between 2001-2018. The variables collected are discharge data from 183 gauging stations; hydraulic head data from 267 piezometers were used to evaluate the performance statistics of the hydrology. Discharge and hydraulic head time series data were obtained from publicly available ADES and HYDRO national datasets. River water temperature data were assembled from various agencies operating in the basin; the dataset comprises hourly and daily observations from 62 sites (Rivière et al., 2021). During the simulation period (2001-2018), 48 stations with hourly observations were selected. The aquifer temperature data used were obtained from the national ADES database. While providing a comprehensive amount of data, records are often incomplete and heterogeneous. The majority of the temperature data were collected on site while pumping, hence the depths of the temperature observations represent the depth of the screened well. A pre-processing was therefore applied to the dataset using the interquartile range (IQR) method, as described in Hemmerle et al. (2019). From the initial data set of 9,179 stations over the Seine-Normandy region, 211 stations with a minimum of 40 observations over the simulation period remained after the pre-processing.

7.3 Results and discussions

7.3.1 Calibration of the surface water cycle

The simulated water balance, shown in Figure 7.2, illustrates how the different parameter configurations (Table 7.1) influence the partitioning of the precipitation into actual evapotranspiration (AET), surface runoff and recharge (drainage). The first four simulations (EXP1-4) show the impact of the soil texture map, which induces a 6% variation of AET (mean values between 469 and 497 mm y^{-1}), also reflected in the total runoff (effective precipitation). Soil texture also impacts the partitioning of the total runoff between drainage and surface runoff, which varies between 20 and 47% of the total runoff between EXP4 (Reynolds) and EXP2 (SoilGrids), as the SoilGrids and INRA maps include a significant fraction of silty soils that increase the surface runoff at the expense of drainage (Tafasca et al., 2019). Eventually, the Vernon discharge bias decreases from 39.8 % in EXP1 to 25.9 % in EXP4, so we kept the Reynolds soil texture map for further optimization.

The dynamic calculation of the vegetation dynamics by the STOMATE module (EXP5) allows a further increase in AET (+26 mm y^{-1}) compared to simulations with prescribed LAI (EXP1-4). The reason is that STOMATE calculates a higher LAI than the prescribed one, increasing the AET via a larger biomass during the growth season. The resulting decrease in total runoff leads to a further reduction of the Vernon discharge bias decreases, from 25.9% to 14.2 %. The small decrease in the contribution of surface runoff to total runoff (-3%) can be attributed to the trade off between surface runoff and increased vegetation activity and water abstraction of roots in the topsoil. Reducing the NIR and VIS leaf albedo (from EXP6 to EXP7) also yielded a significant increase in AET (+ 16 mm y^{-1}, i.e. +5%), because it increases the net available energy. This brings a further reduction of the discharge bias at Vernon to 5.1% in EXP7.

In contrast, implementing a sharper vertical decay of K_{sat} below 30 cm in the soil column (from EXP5 to EXP6) showed a weak impact on all the studied variables: AET improved slightly by only 4 mm y^{-1}, the discharge bias by only 1.8 %, the partition of the total runoff, and the surface runoff fraction was hardly changed. This weak

sensitivity to modifications of the vertical K_{sat} profile shows the importance of the top $30\mathrm{cm}$ of the soil column on the water balance rather than deeper zones (de Rosnay et al., 2000). The decrease of K_{sat} for all the dominant soil textures (EXP7 to EXP8) had an even smaller impact on AET, total runoff thus on the discharge bias (even slightly worsened). Decreasing K_{sat}, however, showed a significant impact on the partition of total runoff, as it nearly doubled the contribution of surface runoff (from 18% to 33 $\%$). The additional decrease of K_{sat} in the bottom part of the soil by increasing the decay factor c_K to 10 (EXP9) had no impact on the water and energy budget, and the increase of maximum LAI (EXP 10) had a very limited effect on AET and total runoff although it increased the proportion of surface runoff (+ 10 $\%$). The maximum LAI values in all simulations including EXP10 match the reported LAI ranges observed throughout the FluxNET network for similar biomes and climates (Krinner et al., 2005). A detailed calibration of vegetation properties is beyond the scope of this study, although ways to improve the terrestrial biosphere and energy processes in SVAT models are active research domains (Peylin et al., 2016).

Eventually, these results show that the overestimation of discharge at the Vernon outlet resulted from an underestimated AET. A considerable improvement of the discharge bias came from the dynamic LAI calculations, which may partly be attributed to the coarse resolution of the input LAI map in pLAI simulations, and to a better seasonal cycle of LAI (comparison to GiMMS (Zhu et al., 2013) product not shown), more consistent with the SAFRAN meteorological forcing. Although groundwater withdrawals are taken into account in the calculation of the ORCHIDEE discharge bias (see section 7.2.2.5), the lack of irrigation in the simulations may also contribute to the underestimation of AET and the overestimation of river discharge since the enhancement of AET by surface water withdrawals is overlooked. Considering that ORCHIDEE simulates a natural basin contrary to heavily regulated and irrigated Seine basin, a 3.1% bias (EXP10) at the outlet of the basin (Vernon) is very satisfactory. However, when the proportions of infiltration and surface runoff are considered (see section 7.2.2.5), EXP9 performs better with nearly two-thirds of recharge contributing to total runoff.

7.3.2 Performance of the ORCHIDEE-CaWaQS coupled simulation

The best performing ORCHIDEE simulation in terms of river discharge bias and partitioning of effective rainfall (EXP9) was selected to force the CaWaQS simulation. A coupled simulation was performed over the 17 year period (August 2001 - July 2018). The simulated discharge compared satisfactorily with observed stream flow in 14 main sub-catchments, as illustrated at the outlet of the Seine basin (Vernon) in illustrated in Figure 7.3.a. Although low flows are slightly overestimated by the coupled model, it captures the yearly dynamics properly (KGE = 0.77, CC = 0.82) and mean volume ($PBIAS$ = 1.6%), given that the measurement error of river discharge can reach 20% (Sauer and Meyer, 1992).

Stream temperature is also well simulated along the Seine basin, as illustrated by Paris-Austerlitz station (Figure 7.3.b). The simulated temperatures match the observed ones (KGE = 0.97) with a $PBIAS$ of -0.3% and an $RMSE$ of 1.52°C, although simulated temperatures are generally underestimated in both summer and winter. Part of this uncertainty can be attributed to the uniform shading factor or the lack of urban structures that artificially modifies the heat regime on riverbanks (Ferguson and Woodbury, 2007). The model also uses a uniform and time-constant shading factor which deviates from the prevalent seasonal dynamics and spatial distribution of the vegetation in the Seine basin (Figure 7.1). Model performances respectively evaluated against stream and aquifer temperature probes over the simulation period are provided in Tables 7.2 and 7.3.

The dynamics of the heat transport in the river network is well represented (KGE > 0.7 for 90% of the stations) and MAE is lower than 2°C for 65% of the stations. 96% of the river temperature stations have an $RMSE$ lower than 4°C. Headwaters (< 10,000 km^2) show a higher mean $RMSE$ (2.58 °C) than downstream ($\geq$ 10,000 km^2) stations (1.58 °C). Prescribed temperatures on river reaches with a Strahler order below 3 strongly influence the river temperatures on headwaters and contribute to the higher RMSE because the proportion of reaches with a prescribed temperature is higher than downstream reaches. A relatively high $RMSE$ indicates a misfit between simulated

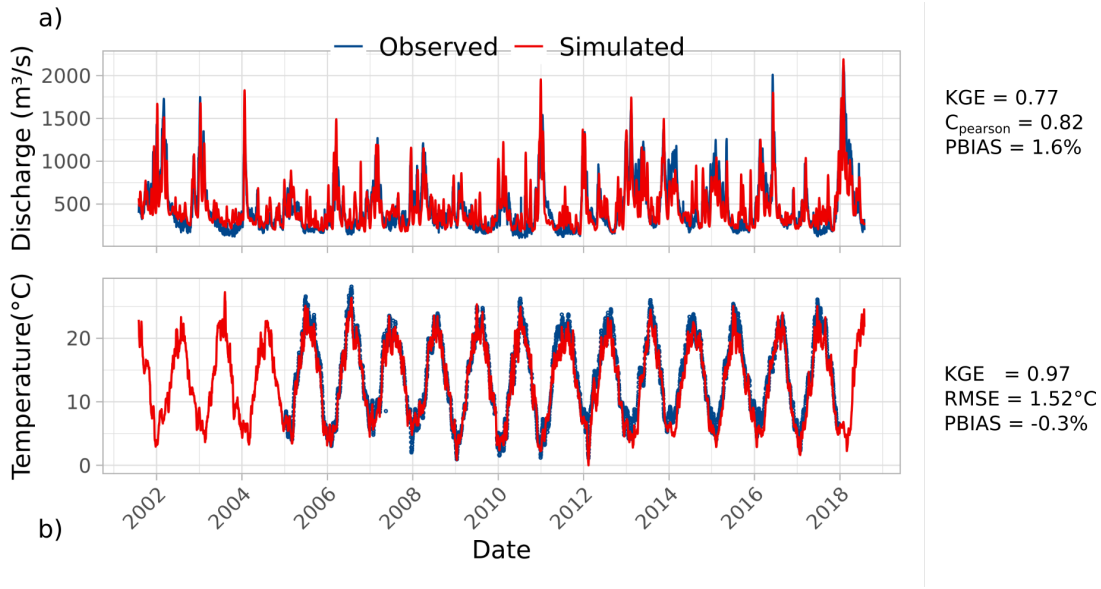

Figure 7.3 Comparison between a) simulated (red) and observed (blue) discharge at the outlet of Seine watershed (Vernon); b) simulated (red) and observed (blue) river temperature at Paris (Austerlitz). From August 2001 to July 2018. Years indicate 1st of January. KGE: Kling-Gupta Efficiency coefficient; CC: correlation coefficient; $PBIAS$: Percent bias; $RMSE$: Root mean squared error.

and observed temperatures at the daily scale. Overall the seasonal dynamics are well represented in the river network (Figure 7.3.b). Heat transport in the river performs comparably to other studies at the regional scale using the equilibrium temperature method (Beaufort et al., 2016a) in terms of $RMSE$.

The groundwater temperatures show a good fit as the $RMSE$ is below 2°C for 49% of the stations. The median $RMSE$ calculated for the aquifer observations was 2.12°C (ranging between 20.2 and 0.01°C). Stations with a larger than 10°C RMSE are focused on the Jurassic aquifer. This is largely due to a mismatch between the depth of the well and the depth of the cell. However, only 22% of the stations show a CC higher than 0.5. Only 3% of the stations show a KGE performance greater than 0.5. The limiting factor in terms of the dynamics is the lack of sufficient time series in the aquifer system. Regarding the assumptions for the estimates of the upper boundary conditions for heat transport in the groundwater system, simulated soil temperatures at 2m depth from ORCHIDEE were applied to the groundwater system top boundary, which are quite different from the actual temperatures of groundwater at the water table (Anderson, 2005).

Table 7.2 Statistical criteria (2001-2018 period) from 48 stream temperature probes distributed in the basin. Upper Table: Root Mean Square Error ($RMSE$), Mean Absolute Error (MAE). Lower table: Pearson correlation coefficient (CC), and Kling-Gupta Efficiency (KGE) coefficient.

	$RMSE$	MAE	$RMSE$	MAE
Value range [°C]	Station count [-]		Cumulative percentage [%]	
[0.0-2.0[	31	42	65	88
[2.0-4.0[	15	1	96	90
[4.0-6.0[	2	2	100	94
[6.0-8.0[	0	3	100	100
	CC	KGE	CC	KGE
Value range [-]	Station count [-]		Cumulative percentage [%]	
]0.7-1.0]	48	43	100	90
]0.5-0.7]	0	2	100	94
]0.4-0.5]	0	1	100	96
]0.2-0.4]	0	2	100	100

Table 7.3 Statistical criteria (2001-2018 period) from 211 aquifer temperature probes distributed in the basin. $RMSE$: Root Mean Square Error, MAE: Mean Absolute Error .

	$RMSE$	MAE	$RMSE$	MAE
Value range [°C]	Piezometer count [-]		Cumulative percentage [%]	
[0.0-2.0[	93	115	44	49
[2.0-4.0[	58	59	71	74
[4.0-6.0[	16	17	79	81
[6.0-8.0[	17	17	87	88
[8.0-10.0[	8	9	91	92
>=10	20	19	100	100

7.4 Hydrological and thermal functioning of the Seine Hydrosystem

The results of the best ORCHIDEE-CaWaQS simulation were used to compute the water budget (Figure 7.4) and the energy budget (Figure 7.5) of the whole Seine basin, including groundwater contributions, over the period 2001-2018.

7.4.1 Pluri-annual water budget

Figure 7.4 displays a pluri-annual water budget of the Seine basin. The AET represents 73.5% (559 mm y^{-1}) of the rainfall (760 mm y^{-1}). The remaining effective rainfall (201 mm y^{-1}) is partitioned into surface runoff and groundwater recharge, amounting to 34.6% and 65.3% of the effective rainfall, respectively. A total infiltration flow of 449.2 $m^3 s^{-1}$ transits through the unsaturated zone, recharging the whole aquifer sys-

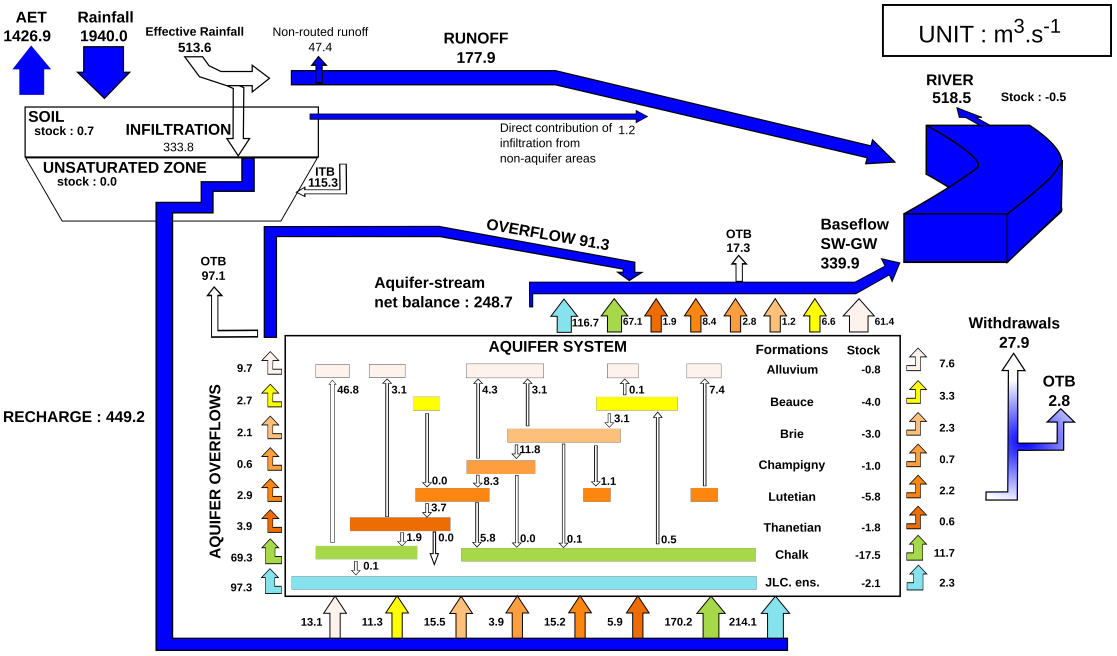

Figure 7.4 Water budget of the Seine hydrosystem over the period 2001-2018 as simulated by ORCHIDEE-CaWaQS application. Groundwater system encompasses the full extent of the aquifers. ITB: Infiltration flux for outcropping aquifer units beyond the Seine basin limits. Flows outside boundaries (OTB) are beyond the extent of the Seine basin. Flows are expressed in inter-annual average values in $\mathrm{m^3\,s^{-1}}$. Model layers : 'Alluvium': Alluvial deposits, 'Beauce': Beauce limestones ensemble, 'Brie': Brie limestones and Fontainebleau sands, 'Champigny': Champigny limestones, 'Lutetian': Lutetian limestones, 'Thanetian': Thanetian sands, 'Chalk' : Upper Cretaceous chalk aquifer, 'JLC. ens.': Lower Cretaceous and Jurassic ensemble.

tem. 27.8% of the aquifer recharge is lost through regional water fluxes across the Seine basin boundaries (21.6% of recharge) or withdrawn from the system by pumpings (6.2% of recharge). Within the Seine basin, river-aquifer exchanges for Strahler orders higher than 3 supply roughly half of the discharge (248.7 $\mathrm{m^3\,s^{-1}}$) recorded at the outlet of the river network (Figure 7.4). What is called overflow mostly corresponds to the drainage of the groundwater system by low Strahler orders (one and two). It therefore also corresponds to stream-aquifer exchanges, and amounts to 91.3 $\mathrm{m^3\,s^{-1}}$ (17.6% of total discharge). Finally, surface runoff contributes up to 177.9 $\mathrm{m^3\,s^{-1}}$ (34.4% of total discharge).

7.4.2 Pluri-annual heat budget

The pluri-annual heat budget over the period 2001-2018 is illustrated in Figure 7.5. The mean daily air temperature recorded is $10.6°\mathrm{C}$ in the Seine basin, and the simulated

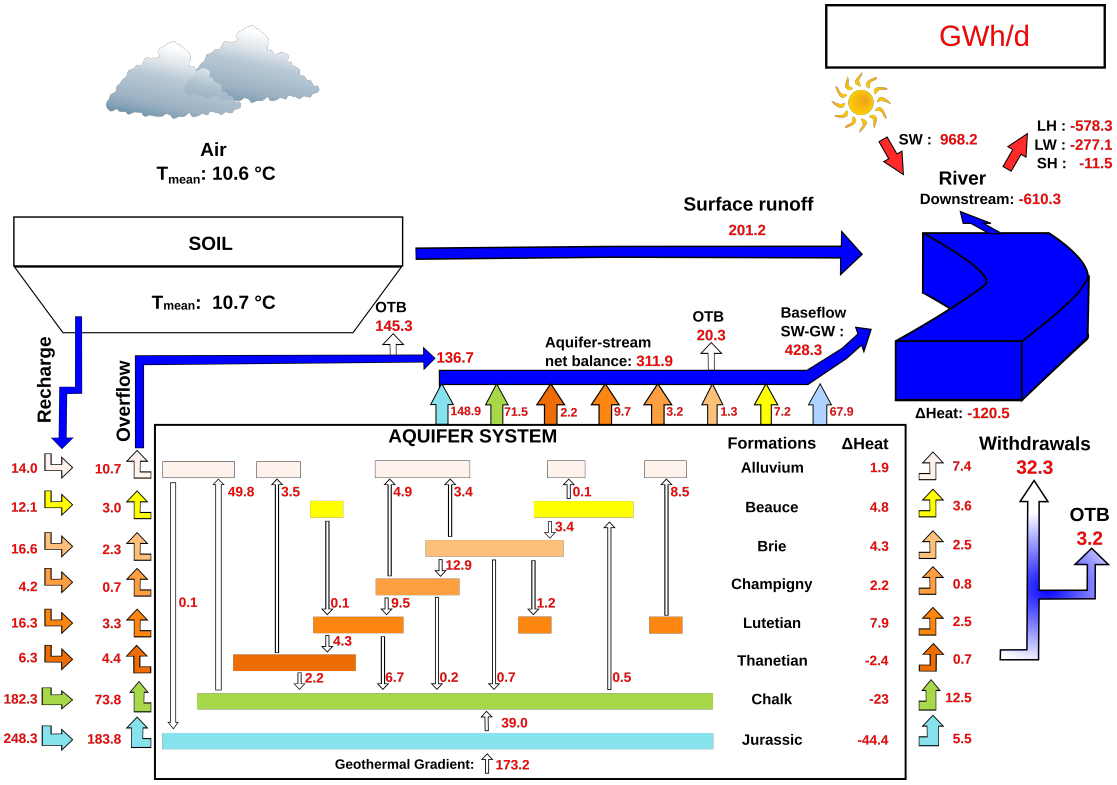

Figure 7.5 Heat budget of the Seine hydrosystem over the period 2001-2018 as simulated by ORCHIDEE-CaWaQS application. Groundwater system encompasses the entire aquifer extents. Flows outside boundaries are beyond the extent of the Seine basin. Energy amounts are expressed in multi-annual average values in $\mathrm{GW\,h}$ per day and mean annual daily air temperature and soil temperature at $2\,\mathrm{m}$ depth are shown in $^{\circ}\mathrm{C}$. $\Delta Heat$: net thermal load variation in the river network. SW: Net short-wave radiation, LW: Long-wave radiation, SH: Sensible heat, LH: Latent heat. Model layers : 'Alluvium': Alluvial deposits, 'Beauce': Beauce limestones ensemble, 'Brie': Brie limestones and Fontainebleau sands, 'Champigny': Champigny limestones, 'Lutetian': Lutetian limestones, 'Thanetian': Thanetian sands, 'Chalk' : Upper Cretaceous chalk aquifer, 'Jurassic': Lower Cretaceous and Jurassic ensemble.

mean daily soil surface temperature is $11.3^{\circ}\mathrm{C}$ (*i.e.* the temperature associated to surface runoff). Soil temperature at $2\mathrm{m}$ depth is estimated as $10.7^{\circ}\mathrm{C}$. The mean daily river temperature is estimated as $12.1^{\circ}\mathrm{C}$ (Figure 7.5). Yearly mean aquifer temperatures range between $10.6^{\circ}\mathrm{C}$ for the shallow alluvium aquifer and $23.8^{\circ}\mathrm{C}$ for the deeper Jurassic aquifer. The largest heat gains in the aquifer system are due to the recharge fluxes ($182.5\ \mathrm{TW\,h}$) and the geothermal gradient ($63.2\ \mathrm{TW\,h}$) at the bottom of the basin (Figure 7.5). The former represents advective fluxes while the latter represents conductive fluxes. The influence of advection diminishes with depth as expected, while conduction becomes the dominant thermal process. This is due to the decrease of water fluxes with

depth.

The main sources of surface advective heat losses are due to : **(i)** river-aquifer exchanges (113.8 $\mathrm{TW\,h}$), **(ii)** stream-aquifer exchanges for the secondary river network (Strahler orders 1 and 2) (*i.e.* overflow that amounts 102.9 $\mathrm{TW\,h}$), **(iii)** and withdrawals (11.8 $\mathrm{TW\,h}$). The aquifer system looses the most energy via the Jurassic, the Chalk and the alluvium aquifers. The Jurassic loses the largest advective heat fluxes via overflow and river-aquifer exchanges towards the surface (Figure 7.5). The Chalk aquifer and the alluvium are the second and third largest contributors to river via advective term. The Chalk aquifer is also the largest contributor to thermal losses due to water withdrawal (4.6 $\mathrm{TW\,h}$).

Energy from short-wave radiation (net radiation, 353.4 $\mathrm{TW\,h}$) is main non-advective source of heat gain in the river network annually (Figure 7.5), contributing 60$\%$ of the river thermal load during the study period. As evidenced in Figure 7.4, the river-aquifer exchanges for the simulated river (Strahler orders larger than 3) and overflow (Strahler orders 1 and 2) are the largest contributors to the river heat budget. The incidence of the hydrological regime on the heat balance in the river network is illustrated by the large advective heat flux via baseflow (156.3 $\mathrm{TW\,h}$ per year), which forms the second source of river heat gains. Surface runoff contributes 13$\%$ of the total thermal load in the river network. The largest non-advective heat losses in the river network are latent heat and long-wave radiation losses, accounting for 67$\%$ (211.0 $\mathrm{TW\,h}$) and 32 $\%$ (101.1 $\mathrm{TW\,h}$), respectively. Approximately 1$\%$ of total heat losses are due to sensible heat losses in the river.

7.4.3 Seasonal heat fluxes in the river network

Seasonal variations of each term of the heat balance in the river network are provided in Table 7.4. It is important to note that the heat exchanges between river and aquifer is not simulated by the model for the rivers with a Strahler orders lower than 3. This implies that the fluxes are not calculated on the same river extent as the other terms. Short-wave radiation is higher during summer and spring. It depends on the sunlight reaching to stream surface, albedo of water, and shading factor which limits the sunlight. The

shading factor can vary as a function of stream morphology, riparian vegetation, urban structures, or clouds (Loicq et al., 2018). The order of non-advective heat sinks does not vary seasonally, as latent heat is the largest heat sink in the system, followed by long-wave radiation, sensible heat and streambed conduction, respectively. Latent heat causes on average a 120.6 $\mathrm{W\,m^{-2}}$ heat loss during summer and 20.3 $\mathrm{W\,m^{-2}}$ heat loss during winter. From the simulation, heat fluxes related to conduction in the streambed are negligible when compared to other flux terms, regardless of the season.

Table 7.4 Seasonal heat fluxes ($\mathrm{W\,m^{-2}}$) in the Seine river network over the 2001-2018 period. The total river length is 28378 km, The total surface area of the river network is 369 km^2. The streambed fluxes are the heat exchanges between river and aquifer. Outflows are the heat loss of the river network via discharge. Negative sign (-) indicates loosing fluxes by the river. Inflows indicate the overflow towards the river network from the aquifer layer not linked to an active river-aquifer exchange calculation.

Process	Type	Winter	Spring	Summer	Autumn	Average
Short-wave radiation	Conductive	39.3	142.0	180.1	75.9	109.3
Long-wave radiation	Conductive	-16.1	-42.9	-44.6	-21.5	-31.3
Latent heat	Conductive	-20.3	-69.9	-120.6	-50.4	-65.3
Sensible heat	Conductive	-0.2	-1.7	-2.1	-1.1	-1.3
Streambed conduction	Conductive	0.4	-0.2	-0.7	-0.1	0.2
Surface runoff	Advective	13.3	18.9	37.9	20.8	22.7
Streambed advection	Advective	39.5	40.1	32.4	28.9	35.2
Inflows(Strahler order <3)	Advective	14.5	14.7	11.9	10.6	12.9
Outflows (Discharge)	Advective	69.1	101.5	96.2	63.2	82.5

Seasonally, heat gains in the Seine river are mainly controlled by the short-wave radiation and river-aquifer exchanges. During winter the net heat gains related to short-wave radiation decrease to only 22% of the heat gains during the summer period (Table 7.4). River-aquifer exchanges sustain the heat gains of the river network throughout seasons, and become the dominant heat source during winter. However, it must be noted that the coarse vertical discretization of the aquifer layers could lead to an overestimation of riverbed temperatures, inducing an overestimation in the streambed advection. This is the case with river cells adjacent to deeper aquifer layers such as the Jurassic layer. Advective heat flux contributions by each aquifer unit change every season due to river and riverbed temperature variations and the magnitude of the river-aquifer exchanges. Studies usually assume that the riverbed conduction contribution is negligible with respect to the advective heat input (Magnusson et al., 2012). Our study confirms

this statement as riverbed conduction reaches up to only 1.5% of river-aquifer advective fluxes.

Loinaz et al. (2013) has showed that at the catchment scale, river-aquifer exchanges contribute to a significant fraction of heat sources. Similarly, in the Seine basin, river-aquifer exchanges contribute significantly to the river energy budget. Locally, the river-aquifer exchanges can dominate the heat balance especially during the winter (Table 7.4). This can create a local cooling effect during summer or a warming effect during winter; an essential aspect of the river-aquifer exchanges that creates thermal refugia for fish species (Kaandorp et al., 2019). Also, local thermal variations in the river have implications for the industrial use of water and pollution (Prest et al., 2016).

Although a detailed sensitivity analysis was not feasible within the scope of this paper, a similar study at the regional scale in the Loire Basin reported that the dominant factors, in decreasing order of importance, were the shading factor, headwater temperatures, groundwater flow, discharge and river geomorphology, respectively (Beaufort et al., 2016a). Our approach differs from this study, which relied on an equilibrium temperature concept, by the way that the processes are treated explicitly and streambed temperature is estimated by an analytical solution in a distributed manner. We found that the river-atmosphere exchange had the largest impact on the river heat balance at regional scale.

7.4.4 Implications on the Water-Energy-Food Nexus

Water, food, and energy are the three essential elements that guarantee human survival and livelihood (De Amorim et al., 2018). The Water-Energy-Food Nexus (WEFN) has emerged since the early 2010's as a new approach to collectively manage three finite resources, whose accessibility is increasingly threatened by climate change, population growth, urbanization, and environmental concerns (Hoff, 2011).The need for a nexus approach has been motivated by the fact that there is a competition for water between water, food and energy production.

Our study shows that the Jurassic aquifer (Figure 7.5) has a good potential for the geothermal use. This fact is well known, Dogger aquifer (part of the Jurassic aquifer)

is exploited for more than 40 years via low temperature geothermal energy applications (Lopez et al., 2010). Paris basin has a great potential for geothermal energy production as annual thermal energy recycling is substantial (182.5 $\mathrm{TW\,h}$ via recharge and 63.2$\mathrm{TW\,h}$ via geothermal gradient annually). For comparison, France produced 548.6 $\mathrm{TW\,h}$ electricity in 2020 (NEA, 2020). Our findings indicate that the geothermal energy potential to offset part of this energy production is substantial. Further research is needed to assess the suitability of aquifer thermal energy systems (ATES) applications at shallower depths (Lee, 2010) in the Seine River basin.

Our coupled ORCHIDEE-CaWaQS model therefore opens the way for new research that integrates the WEFN in the sense that it can be used to assess the impact of energy and agricultural policies at the basin scale in a quantitative way, leveraging on previous studies describing the effect of agricultural practices on the Seine hydro-agrosystem with the ancestor of CaWaQS (Beaudoin et al., 2018).

7.5 Conclusions and perspectives

A first coupling model of water and energy fluxes at the regional scale (96,204 km^2) was carried out with a focus on the Seine hydrosystem in order to address the hydrological and thermal functioning of the hydrosystem and quantify the interactions between surface and subsurface compartments. The distribution of the thermal loads in the Seine hydrosystem including the aquifer system and the river network at the regional scale is quantified for the first time.

Overall, the coupled framework simulates the mean discharge at various sub-catchment scales in the Seine basin and hydraulic heads in the groundwater system adequately for the purposes of thermal transport simulation. For a first attempt of such a coupling between a SVAT (ORCHIDEE) and a hydrological model (CaWaQS), the platform performs satisfactorily for the simulation of both water fluxes and energy fluxes. The coupled ORCHIDEE-CaWaQS framework is designed to take advantage of broadly available gridded datasets from catchment to regional scales to estimate hydrosystem water and energy budgets. The transport module estimated the mean river temperatures

and aquifer temperatures adequately.

The findings presented herein have the potential to inform biological or water quality studies (Flipo et al., 2021b) on the Seine basin or engineering applications such as ATES to reduce the dependency on fossil fuel (Lee, 2010) by providing an insight into key physical processes driving the heat fluxes in the river network and the aquifer system. The impact of climate change on the share of energy fluxes at the regional basin scale will also be studied and provide useful information for adaptation and mitigation strategies. The model, for example, can be integrated in an ecohydrological model to estimate the impacts of thermal variability on fish or riparian habitat (Loinaz et al., 2014). These efforts can have policy implications by guiding environmental management agencies to prioritize their restoration and exploitation areas in the Seine basin. Future coupling with an agronomic model (Beaudoin et al., 2018) will also provide a complete picture within the WEFN framework (Garcia and You, 2016) at the regional scale, thereby improving our understanding of the competing aspects of limited resources.

Conflicts of interest

The authors declare no competing financial interest.

Dedication

The manuscript was written through contributions of all authors. All authors have given approval to the final version of the manuscript. **DK**: designed the research, developed the CaWaQS transport module, performed all simulations, analyzed the data and prepared the manuscript draft. **AR**: designed the research, developed CaWaQS transport module, designed the transport through streambed and aquitards interfaces, interpreted results, discussed findings, contributed and improved the manuscript. **NG**: developed the CaWaQS transport module and the required CaWaQS coupling functionalities, contributed to figures and improved the manuscript. **SW**: developed the CaWaQS transport module. **AD**: contributed to the design of the ORCHIDEE application, interpreted

ORCHIDEE results and discussed findings. **PP**: contributed to the design of the ORCHIDEE application, interpreted ORCHIDEE results and discussed findings. **NF**: designed the research, managed the development of CaWaQS, interpreted results, discussed findings and improved the manuscript, managed and ensured the funding of the project.

Acknowledgments

This work is a contribution to the PIREN Seine research program, which is part of the Zone Atelier Seine, included in the e-LTER network. We gratefully acknowledge the river temperature dataset provided by William Thomas. Groundwater withdrawals were obtained from Seine-Normandy Water Agency, over the 1994-2012 period.

Supplementary data

7.5.1 Performance of the ORCHIDEE-CaWaQS coupling: hydrology

Groundwater (GW) simulation shows satisfactory performance overall as the $RMSE$ and MSE are below 4 m in 40$\%$ and 44$\%$ of the stations, respectively. In terms of the regional scale aquifer dynamics 67$\%$ of the piezometers show a correlation (CC) larger than 0.5, whereas 25$\%$ of the piezometers exhibit a KGE larger than 0.5.

In the Vernon station (main catchment of the Seine basin), bias was estimated as 1.6 $\%$ with 0.77 KGE and 0.82 CC; the overall performance was satisfactory (Figure 7.3.a). Considering the sub-catchments, 6 out of 14 stations at the main sub-catchments show a KGE above 0.7 and 8 stations show a CC larger than 0.7. The estimated bias ranged between -12.6-23.8$\%$. At the basin scale, a total of 38.5 $\%$ of the stations show KGE values (not shown) larger than 0.5.

Table 7.5 Statistical criteria (2001-2018 period) from 267 piezometers distributed in the basin. Upper table: Root Mean Square Error ($RMSE$), Mean Absolute Error (MAE). Lower Table: Pearson correlation coefficient (CC), and Kling-Gupta Efficiency coefficient (KGE).

	RMSE	MAE	RMSE	MAE
Value range [m]	Piezometer count [-]		Cumulative percentage [%]	
[0.0-2.0[	61	83	23	25
[2.0-4.0[	47	64	40	44
[4.0-6.0[	45	59	57	62
[6.0-8.0[	30	41	68	75
[8.0-10.0[	20	23	76	82
>=10	64	61	100	100
	CC	KGE	CC	KGE
Value range [-]	Piezometer count [-]		Cumulative percentage [%]	
]0.7-1.0]	114	35	43	13
]0.5-0.7]	65	32	67	25
]0.4-0.5]	22	17	75	32
]0.2-0.4]	33	36	88	45
]0.0-0.2]	23	30	96	56
]-∞-0.0]	10	117	100	100

Chapter 8

An assessment of the water budget and energy balance of the Seine Basin: current and future trends

8.1 Introduction

Predicting the possible impact of climate change on water resources is one of the most difficult challenges faced by water managers. Assessment of the possible changes in the water cycle with respect to past trends and current hydrological conditions gained interest recently (Flipo et al., 2020a; Habets et al., 2013; Wu et al., 2020). While most of these studies focus on the possible changes associated with the water cycle, another set of uncertainties remains concerning water quality. Temperature is one of the main factors controlling a set of physical, chemical, and biological interactions in water resources that are key to water quality assessment. The risks posed by climate change on the water quality are often neglected due to difficulties associated with estimating river and aquifer temperature regimes. Future projections also often focus on surface water and neglect groundwater. This limited approach to assessing the water resources need to be addressed to improve our understanding of the impact of climate change on the energy balance of the hydrosystem.

An essential requirement for estimating the potential impact of climate change on the groundwater systems and river network is estimating the regional heat balance. Studies of heat balance often focus on either surface (Rousset et al., 2004) or river network (Beaufort et al., 2016a), while the aquifer system is often neglected. However, the surface temperature regime can significantly impact the aquifer system (Benz et al., 2017) with implications on the potability of water or on the water quality and the

ecology at the critical zone (Giardino and Houser, 2015; Gaillardet et al., 2018). With advancements in geothermal exploitation, the estimation of heat balance of the aquifer system explicitly became important (Lopez et al., 2010). Primarily urban agglomerations such as Paris depend on water temperature for district cooling (Térouanne et al., 2011), which is why future changes in the temperature regime should be quantified to mitigate potential negative scenarios. Therefore, there is a need to establish the heat balance of an hydrosystem explicitly to reconcile water quantity assessments with water quality to answer future challenges adequately.

A second requirement for estimating the impact of climate change on the energy balance of the hydrosystem is the estimation of water temperatures associated with groundwater recharge and surface runoff. Soil-Vegetation-Atmosphere-Transfer (SVATs) are developed as a lower boundary of atmospheric models and are often capable of simultaneously simulating the energy balance and water budget. As described in Chapter 5, ORCHIDEE is one of the SVAT models in the literature, and it is capable of simulating the soil temperatures as well as distributed evapotranspiration, surface runoff and recharge. Using the ORCHIDEE SVAT model, coupled with the groundwater model CaWaQS, can enable simulation of hydrosystem water budget and energy balance, with potential to represent the impact of future climate change adequately.

In addition to the choice of modelling capable of simulating hydrosystem water budget and energy balance, the need for high-resolution climate change scenarios adds another set of difficulties to future projection studies. Often, future climate projections rely on large-scale General Circulation Models (GCMs) that contain uncertainties and differences in model structure, parameterization and regionalization (Lehner et al., 2020). These models usually generate differing results on the precipitation and evapotranspiration. Moreover, such GCMs are usually at a global scale with very limited ability to adequately represent the regional meteorological variables (Dayon et al., 2015). In order to evaluate the impact of climate change on regional hydrosystems, reduction of uncertainties via bias correction is required. Therefore, the reanalysis products for climate projections at the regional scale require an appropriate bias correction capable of producing meteorological conditions in the study area and disaggregating the re-

gional application scale from the global scale. Recently, (Dayon et al., 2018) evaluated century-long global projections from CMIP5 by downscaling them at the France scale over the period 1990-2100. Subsequently, Flipo et al. (2020a) leveraged the regional scale climate projection data to evaluate the past, current and future trends of the water cycle in the Seine basin.

In this study, our goal is to extend the understanding of water cycle variations in the Seine basin by introducing a complete representation of the energy balance associated with the water cycle in the Seine basin. Therefore, our objective is to: **(i)**quantify the water cycle and energy budget in the Seine basin under the climate scenarios proposed by the IPCC for mid-century (2043-2060) and end-century (2083-2100); **(ii)**evaluate the temperature variations in the aquifer system; **(ii)**propose a future outlook of the energy balance of the Seine hydrosystem under different climate scenarios. To achieve these objectives, we adopt the bias corrected ISIMIP2b dataset (Frieler et al., 2017) for outputs of CMIP5 data. A previously calibrated ORCHIDEE-CaWaQS model (see chapter 7) was used.

8.2 Methods and materials

8.2.1 ORCHIDEE-CaWaQS Seine model

The detailed descriptions of ORCHIDEE and CaWaQS models were provided in Chapter 5. The Seine model developed in this application covers an area of 96200 km^2, whereas the Seine basin extent covers an area of 78,650 km^2. Similarly to Chapter 7, discharges and river-aquifer exchange are calculated in the main river network (i.e. river reaches with Strahler order 3-8). The model configuration and the grid structure were kept the same as in the previous Seine application (see chapter 7). The Seine application of the coupled framework was previously applied; the river discharges and water temperatures were satisfactorily estimated by the coupled framework. For instance, the Nash efficiency of discharge at the outlet of the Seine basin reaches 0.77, and the Kling-Gupta Efficiency calculated from water temperatures at Austerlitz station reaches 0.97.

The flowchart of the simulation protocol using the MIROC5 reanalysis data is shown in Figure 8.1. Step 1a and Step 1b were already done, and the downscaled GCM product was made available by the work of Bonnet (2018). The derived meteorological forcing from Step1b was used to force the ORCHIDEE-CaWaQS Seine model. The surface water budget and energy balance were estimated by the ORCHIDEE model. The coupling between ORCHIDEE and CaWaQS was established through the transfer of estimated recharge and surface runoff from ORCHIDEE to CaWaQS. We assume that temperature of recharge fluxes is at equilibrium with soil temperature at $2\mathrm{m}$ depth, whereas the surface runoff temperature is equal to the soil temperature of the first layer of ORCHIDEE ($0.001\mathrm{cm}$).

The variation from the previous application is that meteorological forcing variables were provided from a downscaled GCM product at the Seine basin scale instead of SAFRAN meteorological forcing.

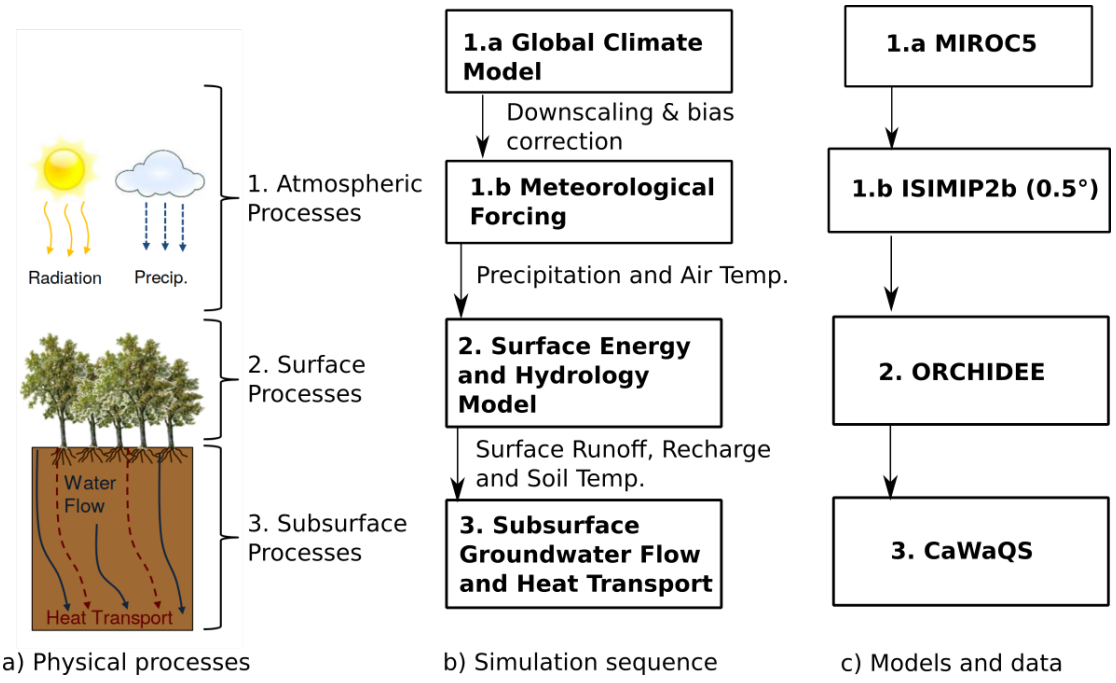

Figure 8.1 a) Physical processes that control the surface and subsurface temperature regimes; b) The flowchart that combines the atmospheric climate models used for future projections to surface and groundwater models c) The simulation protocol with models and data used in this application. (Step 1a.), Simulation of GCM model (Step1b) Downscaling of the GCM results at appropriate basin scale. (Step 2) Simulation of ORCHIDEE to estimate surface water budget and energy balance (Step 3) Simulation of CaWaQS coupled with the fluxes from ORCHIDEE. Adapted from Kurylyk et al. (2014).

8.2.2 Climate change scenarios

The international effort to quantify the effect of climate change on the global water cycle paved the way for the development of a series of successive climate model intercomparison projects. The fifth phase of the Coupled Model Intercomparison Project (CMIP5) provides a multi-model framework for climate simulation experiments that accounts for the past (up to pre-industrial), current, and future (up to the 22nd century) (Meehl et al., 2007; Taylor et al., 2012). Global Climate Models (GCMs) attempt to simulate all relevant physical processes to estimate the future climate states. A recent climate model intercomparison project (CMIP5) developed several scenarios that guide GCMs, as shown in Figure 8.2.

In this study, we use two climate data derived from the IPCC scenarios RCP8.5 (a.k.a. business-as-usual) and RCP6.0 (peak emissions at mid-century, slow adaptation). Radiative forces in RCP8.5 are expected to increase 8.5 $\mathrm{W\,m^{-2}}$, whereas in RCP6.0 scenario radiative forces increase 6.0 $\mathrm{W\,m^{-2}}$ (Van Vuuren et al., 2011).

GCMs differ in model structure, parameterisation and regionalisation (Hattermann et al., 2018, 2006), which might cause bias in the effect of climate scenario variation. These differences eventually lead to distinct climate predictions (Dayon et al., 2015). Climate impact studies at regional scale use an approach based on statistical downscaling of the GCM outputs (Maraun et al., 2010) or they may use output from regional climate models (Krysanova et al., 2017). Given the inherent differences of GCMs, selecting the appropriate climate projection output to estimate the regional projections becomes essential. Flipo et al. (2020a) recently analysed the future climate change impact on the Seine basin by using a downscaled GCM product to run the CaWaQS model. An analysis of the appropriateness of the GCM product for the Seine basin in the study found that the climate variables from MIROC5 GCM match the low-frequency SAFRAN reanalysis data. Therefore, we select MIROC5 GCM output from bias corrected ISIMIP2b database (Frieler et al., 2017) as the input for the coupled ORCHIDEE-CaWaQS Seine model application to estimate hydrological and temperature forecasts in the basin. The bias corrected variables are humidity, precipitation,

surface air pressure, short-wave and long wave radiation, near-surface wind speed and air temperature. The source code of the bias correction procedure and additional details could be found in Lange (2017).

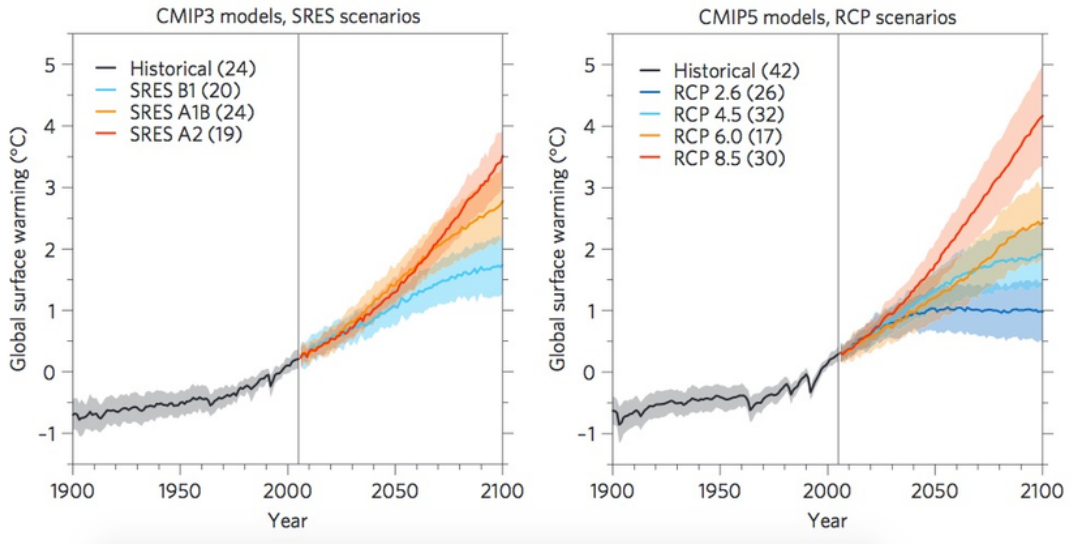

Figure 8.2 Global temperature change projections up to 2100 based on CMIP3 (left) and CMIP5 (right) frameworks. Lines represent the mean temperature anomaly increase based on the projections, and past observations (dark); shaded areas indicate the degree of uncertainty (source: IPCC (2019))

8.2.3 Experiments setup

A total of 5 simulations were developed to assess the current state, mid-century and end-century hydrological and thermal regimes of the Seine hydrosystem. When developing this application, a 17-year periodicity associated with the NAO was considered (Flipo et al., 2012). The period of 1993-2010 was selected to evaluate the current state of the hydrosystem.

In the current state, meteorological variables provided by SAFRAN (Vidal et al., 2010b) and MIROC data provided by the recent ISIMIP2b bias-corrected climate scenarios at 0.5°. Four simulations accounting for the RCP6.0 and RCP8.5 scenarios at mid-century (2043-2060) and end-century (2083-2100) were used to evaluate the future states of the Seine hydrosystem.

The main difference between the current state and future states are the following:

- The meteorological state of the hydrosystem changes with variable precipitation regimes and a higher average air temperature.

- The anthropogenic pressure on water resources is different in future scenarios. The methodology of future water withdrawal estimation is the same as Flipo et al. (2020a). In short, although the population in the basin is expected to increase by almost a third, the water usage in the basin was predicted to decrease by 16%due to an optimistic water usage optimisation and better agricultural practices via improved irrigation in the future.

Our study differs from Flipo et al. (2020a) in the estimation of future land use. While the former assumes a land cover change with increased urban cover due to population stresses, in this study, the land cover was assumed to be static until 2100 since ORCHIDEE does not consider urban zones yet. The meteorological forcing data were used to force the developed ORHCIDEE Seine model (detailed in chapter 7). Surface runoff, drainage, and soil temperatures at 0.5° were extracted from the ORCHIDEE model to force the CaWaQS model. The ORCHIDEE model was run over 1850-2005 period under past the past climate conditions. Using the results of this simulation as initial state, two IPCC scenarios (RCP6.0 and RCP8.5) were run over 2006-2100 period. Fluxes and temperatures of tranches of 30 years for current (1980-2010), mid-century (2030-2060), and end-century (2070-2100) were extracted from ORCHIDEE model to run the CaWaQS model initially. The resulting aquifer temperatures from the initial CaWaQS run was extracted to be recycled as the initial condition of the second set of simulations over the same period to estimate the heat balance under a good initial state assumption.

8.2.4 Analysis of hydrological and temperature regimes

Pluri-annual monthly average fluxes were calculated to evaluate the monthly variations of the hydrological and temperature regimes in the Seine basin. Reference simulations MIROC (MIROCREF) simulated to compare the future hydrosystem outlook to current hydrosystem state. Two future climate scenarios (RCP6.0 and RCP8.5) at mid-century

(2043-2060) and at end-century (2083-2100) were evaluated for the energy balance of the hydrosystem, the aquifer temperatures, river and riverbed temperature regimes. In order to assess the temperature regime, the water and riverbed temperature variations were compared to identify any significant changes. The aquifer temperatures under different scenarios were evaluated and the temperature change per decade of the aquifer layers were calculated.

8.3 Results and discussion

The evolution of the Seine basin from the current state (1993-2010) to mid-century (2043-2060) and end-century (2083-2100) was evaluated. The current state of the hydrosystem was simulated with ISIMIP2b MIROC5 with an assumption that GCM models contain a structural bias, causing variations from the actual state of the hydrosystem. The outlook of the thermal conditions in the basin are presented here. Detailed description of the energy balance and water budget of the Seine basin is provided in the Appendix B.

8.3.1 Projected changes in the Seine basin

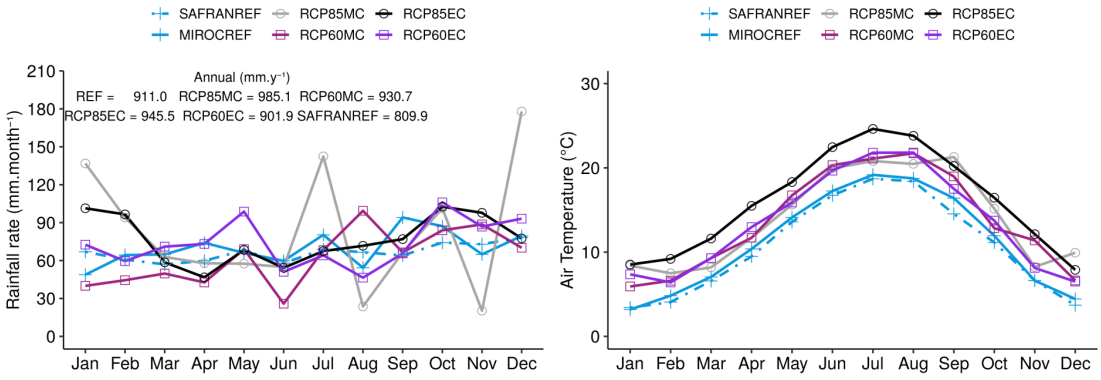

Figure 8.3 Changes in the regime of hydrological and energy fluxes. a) The monthly precipitation regime, b) the monthly air temperature regime at the surface boundary;

The changes in the precipitation regime and the annual mean precipitation of different scenarios are provided in Figure 8.3.a, where the precipitation regime is also compared to that of SAFRAN meteorological forcing (Vidal et al., 2010b) over the

same period. The main difference between MIROC and SAFRAN data in the 2000s is that SAFRAN records significantly more precipitation during the same period (+100 mm y^{-1}) MIROC has less precipitation in January, August, and November. The discrepancy decreases during May and June; however, MIROC has significantly more precipitation during Autumn.

The air temperatures of SAFRAN and MIROC data sets at the current state do not have any significant variation. The air temperature in MIROC is slightly higher temperature throughout the year.

At the mid-century, RCP6.0 and RCP8.5 scenarios show a stark contrast in precipitation regime; RCP60MC has 55 mm y^{-1} less than the RCP85MC scenario. This contrast comes from the wet season being less precipitous in RCP60MC, as there are much less rain events in December, January and July. In spring, RCP60MC shows higher precipitation. The summer and autumn seasons show changing trends in both scenarios, whereas large variability of RCP85MC is observed in the precipitation regime.

At the end-century, the discrepancy between RCP6.0 and RCP8.5 increases with a margin of 43.6 mm y^{-1}annually. The wet season becomes milder in RCP60EC, whereas an intensification of precipitation is observed in RCP85EC. Both scenarios predict less precipitation during the spring and summer seasons except for the RCP60 in May.

From the current state to the end-century, the annual precipitation is expected to increase in the Seine basin in the RCP8.5 scenario, whereas it decreases in RCP60 scenario.

Air temperatures increase progressively throughout the century (Figure 8.3.b). The sharpest increase is expected in the RCP85EC scenario, where the average air temperatures throughout the year rise at least 1.5°C up to 3°C in summer. RCP85MC, RCP60MC, and RCP60EC show similar air temperature regimes; therefore, the air temperature increases in the Seine basin slow down if the RCP6.0 scenario is realised by the end of the century. On average, air temperature increases 1.3°C by mid-century and 3.25°C by end-century in RCP85 scenario; air temperature increases 0.5°C by mid-century and 1.2°C by end-century in RCP60 scenario.

8.3.2 Changes in the temperature regime in the basin

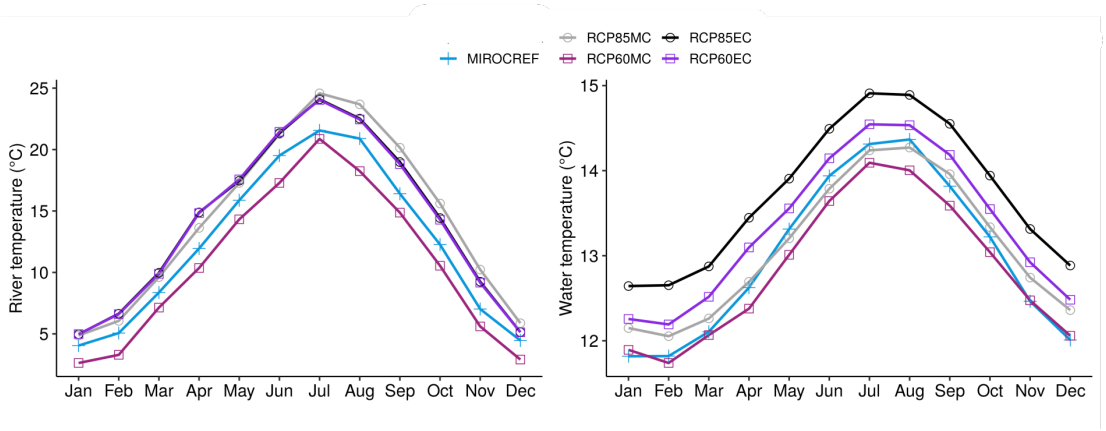

Figure 8.4 Changes in the temperature regime in the Seine hydrosystem. a) the average water temperatures in the Seine river, b) the riverbed temperatures at the river-aquifer interface.

The evolution of annual temperature regimes for the Seine for different periods is shown in Figure 8.4.a. A strong increase in temperature is observed in the function of time. In the case of the RCP6.0 scenario, the projections have a distinct temperature regime, which does not happen in the case of the RCP 8.5 scenario. These results are similar to the study of Rivière et al. (2021), who simulated future climate scenarios based on a machine learning approach. Rivière et al. (2021) show that the most impacted seasons are winter and summer. We show that winter and summer temperatures increase, average water temperatures increase at least 1.5°C. This phenomenon persists in the different projections but remains most visible in the scenarios with a high radiative forcing. Indeed, the projections are almost overlapping in spring, especially for the RCP 6.0 scenario. In the fall, a slight increase is observed for both scenarios. However, given the increase already observed between the periods 1870-1901 and 1995-2020, with an increase of about 2°C, water temperatures could continue to rise in the basin under a business-as-usual scenario.

Water temperatures in the Seine basin range between 5-22°C at the current temperature regime (Figure 8.4.a). The MIROC (MIROCREF) simulations shows the same trend, with no significant temperature variations throughout the year. A slight temperature decrease is observed in mid-century scenarios in the average temperatures. This

decrease could be linked to strong heat input from the aquifer given that the riverbed temperatures are slightly lower than MIROCREF scenario. Similarly, the RCP6.0 end-century (RCP60EC) simulation indicates that the Seine basin river water temperatures will not change significantly if this climate scenario is reached. Contrary to other scenarios RCP8.5 mid century (RCP85MC) and end-century (RCP85EC) simulation shows the most significant increase during spring and summer. Water temperature increase reaches up to 1.5°C in April. Unlike spring and summer temperatures, the winter water temperatures stay relatively the same in the future scenarios except for a slight average temperature increase in January and February.

The riverbed temperatures (Figure 8.4.b) show much less variation throughout the year when compared to water temperatures. At the riverbed, the temperatures range between 11.8-14.9°C. During winter, the riverbed temperatures are at least 6°C warmer than the river water temperatures. On the other hand temperatures show, on average, 5 °C lower riverbed temperatures than river water temperatures during summer. Mid-century temperatures show the same temperature regime in both scenarios (RCP85MC and RCP60MC). If the RCP6.0 scenario is realised, the riverbed temperatures increase on average at least 0.3°C. However, in the RCP8.5 scenario (RCP85EC) at the end of the century, the riverbed temperatures throughout the year increase at least 0.7°C. During winter, temperatures in the riverbed increase by 0.9°C. This temperature increase is reflected in the river water temperatures (Figure 8.4.a), which shows a higher temperature regime in the RCP85EC scenario.

8.3.3 Projected seasonal changes in the river heat fluxes

Projected changes in the heat balance of the river network are provided in Table 8.1. The short-wave radiation shows a significant increase at the end of the century in the RCP8.5 scenario. However, mid-century average short-wave radiation does not vary between scenarios. Latent heat and long-wave radiation are the largest two sinks of the river heat balance. An increase in the latent heat indicates that river evaporation intensifies by the end of the century in both scenarios.

At mid century, aquifer contribution and inflows through runoff do not vary sig-

Table 8.1 Heat fluxes ($\mathrm{W\,m^{-2}}$) in the Seine river network from current, mid-century and end-century scenarios. The total river length is 28378 km, The total surface area of the river network is 369 km^2. Outflows are the heat flow from the river network via discharge. Inflows indicate the overflow towards the river network from the aquifer layer not linked to an active river-aquifer exchange calculation. Reanalysis: MIROC5 forcing. Negative sign (-) indicates losing fluxes by the river. Units are $\mathrm{W\,m^{-2}}$.

			mid-century		end-century	
Name	Type	Reanalysis	RCP6.0	RCP8.5	RCP6.0	RCP8.5
Short-wave radiation	Conductive	124,30	125,10	124,10	126,60	129,70
Long-wave radiation	Conductive	-35,14	-34,75	-34,05	-36,17	-36,20
Latent heat	Conductive	-66,70	-65,60	-65,70	-66,70	-67,80
Sensible heat	Conductive	-1,30	-1,45	-1,01	-1,25	-1,50
Air–>water net flux	Conductive	21,16	23,30	22,89	22,45	24,20
Surface runoff	Advective	14,30	14,50	16,50	17,30	19,60
Streambed Conduction	Conductive	1,40	1,60	1,30	1,40	1,80
River-aquifer exchanges	Advective	34,02	33,03	33,57	35,33	37,48
GW–>SW net flux	Advective + Conductive	35,42	34,63	34,87	36,73	39,28
Inflows (upstream strahler order<=3)	Advective	7,47	8,38	8,28	9,19	11,01
Outflows (Discharge)	Advective	78,35	80.81	82.84	85.67	94.09

nificantly in both scenarios. However, a significant discrepancy occurs by the end of the century, where RCP8.5 river-aquifer exchanges intensify via higher river-aquifer water contribution to river. Contrary to RCP8.5, during the end-century, river-aquifer exchanges contribution in the RCP6.0 scenario falls below mid-century values due to lower precipitation and aquifer contribution to river baseflow.

Overall, the heat gains are largest in the RCP8.5 scenario, where these gains are reflected in the river and riverbed temperatures (Figure 8.4).

8.3.4 Projected changes in the energy balance

The heat balance of the Seine basin in its current state, mid-century and end-century scenarios are provided in Table 8.2. Surface heat balance is controlled mainly by the advective fluxes. The contribution of runoff and recharge in the aquifer and river heat budgets are proportional to changes in the water budget.

While being closely associated with water fluxes, advective fluxes could vary due to changes in the temperature regime. The heat load increase significantly via overflows and river aquifer exchanges in RCP6.0 and RCP8.5 scenarios throughout the century.

The thermal load of runoff increases significantly throughout the century in all scenarios. This could be related to increased surface runoff due to intense precipitation events in the climate scenarios (Figure 8.3). The largest heat contribution of recharge

Table 8.2 Estimation of the heat balance under the current state, mid-century, and end-century scenarios on the behaviour of the Seine hydrosystem. RV: Relative variation of scenarios from current reanalysis; RV*: Relative variation of GCM ref. from SAFRAN; Basin: Seine basin domain; ITB: Infiltration outside the basin boundaries; OTB: Outflows through the basin boundaries. Negative sign (-) indicates losses. Units are GWh/d

	Current	mid-century				end-century			
	GCM ref.	RCP6.0		RCP8.5		RCP6.0		RCP8.5	
Name	Reanalysis	Amount	RV	Amount	RV	Amount	RV	Amount	RV
Discharge at the outlet (Basin)	827,24	1140,81	37,9	1255,45	51,8	1269,98	53,5	16242,28	98,5
Runoff (Basin)	458,44	664,85	45,0	797,21	73,9	731,14	59,5	1066,41	132,6
Recharge (Basin)	391,52	543,99	38,9	539,01	37,7	649,36	65,9	744,66	90,2
Overflow (Basin)	-100,44	-144,69	44,1	-131,65	-31,1	-166,94	66,2	-177,26	76,5
River-aquifer exchanges (Basin)	-268,36	-331,26	23,4	-326,59	21,7	-371,90	38,6	-398,61	48,5
Withdrawals (Whole domain)	-39,56	-33,68	-14,9	-34,37	-13,1	-34,63	–12,4	-36,02	-8,9
Stock (Whole domain)	-1,25	–2,40	92,1	1,17	-193,4	-8,28	564,1	5,75	-561,3
ITB	147,30	197,95	34,4	196,36	33,3	231,93	57,5	262,25	78,0
OTB River-Aquifer	-19,24	-21,46	11,5	-20,45	6,3	-21,79	13,2	-23,42	21,7
OTB Overflow	-116,70	-163,40	40,0	-161,61	38,5	-194,06	66,3	-221,72	90,0

to aquifer heat balance is observed at the end of the century in RCP8.5 scenario. An increase in the heat contribution is due to a sharp change in air temperature trend by the end of the century (Figure 8.3).

Overall, strong perturbations in the heat balance of the aquifer system are observed throughout the century. Large variations in the heat balance is linked to the coarse scale (0.5°) of the ISIMIP2b meteorological forcing that shows large climatological variability. These results highlight the potential variability of the heat balance of the Seine aquifer system under various climate scenarios. This variability could significantly impact the spatial and temporal variation of the aquifer temperature regime, especially at the shallow depths.

Average soil and aquifer temperatures under various climate change scenarios are provided in Table 8.3. Soil temperatures show a significant increasing trend by the mid and end centuries. The average soil surface temperature was found to be 11.52°C over the period 1993-2010. By the mid-century, the average soil surface temperatures reach 12.97°C and 13.77°C for RCP60 and RCP85 scenarios, respectively. Climate change will cause significant soil warming by at least 1.4°C by the mid-century under limited adaptation and mitigation scenarios. Likewise, by the end-century, the surface temperatures reach an average of 14.08°C and 16.16°C for RCP60 and RCP85, respectively. An average temperature increase of 2.5°C to 4.5°C could tremendously impact the critical zone. A similar trend, albeit less severe, is also seen in the soil temper-

ature at a 2-meter depth. By mid-century, the average soil temperatures at 2-meter depth increased from 11.12°C to 12.58°C and 13.38°C for RCP60 and RCP85 scenarios. This trend continues in the second half of the century. The most significant soil temperature increase will be in the RCP85 scenario, where average temperatures will increase from 11.12°C to 15.68°C by the end-century. Aquifer temperatures show significant warming up throughout the century. The alluvium layer adjacent to the river network show an increase of more than 2.5°C under RCP85 scenario. Similar temperature trends are observed in shallow aquifer layers such as Beauce, Brie, Champigny at decreasing amounts. The slowest temperature increase was simulated in the Chalk and the Jurassic aquifer layers. In terms of temperature increase rates over the century, the alluvium layer warms up at a rate of 0.12 and 0.23°C per decade by mid century under RCP60 and RCP85 scenarios respectively. This trend gets stronger in the second half of the century, with 0.15 and 0.26°C per decade under RCP60 and RCP85 scenarios respectively. This temperature trend continues in deeper layers, albeit in decreasing order. The slowest temperature gradient was simulated in the Jurassic layer with approximately 0.02°C per decade. It must be noted that the Chalk layer has an average of 10.54 to 10.92°C under these simulations. Given that the Chalk layer is the layer that covers a large surface area of the basin, the average temperatures reflect the shallower parts of the aquifer. However, a longer initialisation of the model is needed to reflect the likely higher aquifer temperatures in the Chalk layer.

Overall, the continued trend of soil temperature increase will affect biogeochemical processes and vegetation dynamics (Kurylyk et al., 2014). Moreover, increased soil temperatures propagate to the aquifer system, which sustains the potable water and agricultural needs of the Seine basin. Therefore increases in groundwater temperature are evident, and its impact on the water quality remains an essential concern for the future state of the hydrosystem.

Table 8.3 Average soil temperatures (surface and soil at 2 meter depth) by simulated by ORCHIDEE and aquifer temperatures simulated by CaWaQS under different climate change scenarios. Values are given in °C. Current period is the average temperature over 1993-2010, Mid-century is the average temperature over 2043-2060, End-century is the average temperature over 2083-2100

	Current	Mid-century		End-century	
Near Surface	MIROCREF	RCP60MC	RCP85MC	RCP60EC	RCP85EC
Surface (0m)	11.52	12.97	13.77	14.08	16.16
Soil (2m)	11.12	12.58	13.38	13.78	15.68
Aquifer Layers					
Alluvium	11.18	11.80	12.35	12.56	13.65
Beauce	11.69	12.09	12.45	12.61	13.24
Brie	11.49	12.07	12.46	12.62	13.40
Champigny	11.44	11.75	11.98	12.06	12.48
Lutetian	11.38	11.55	11.68	11.74	11.97
Thanetian	11.08	11.36	11.56	11.65	12.00
Chalk	10.54	10.75	10.81	10.81	10.92
Jurassic	23.83	23.88	23.92	23.94	24.02

8.4 Conclusions and perspectives

Soil-Vegetation-Atmosphere Transfer (SVAT) and regional groundwater modelling are standard tools for estimating the water budget and the effects of future climate changes on water resources. Numerous Global Circulation Models (GCMs) are currently available to simulate numerous greenhouse gas (GHG) emissions scenarios (Taylor et al., 2012). With recent advancements in downscaling methods (Dayon et al., 2018) or bias corrected GCM products such as ISIMIP2b (Frieler et al., 2017) , studies of regional climate change on water resources became possible. In France, several studies estimated future climate changes in regional water resources using such GCM scenarios (Habets et al., 2013; Flipo et al., 2020a). However, these studies did not consider the changes in the heat balance and temperature regime of rivers. Here we made an initial attempt to estimate the water budget and energy balance of the Seine hydrosystem under future climate change scenarios using the coupled framework . Towards this goal, we used MIROC5 GCM meteorological forcing data, from the bias corrected ISIMIP2b product, which was recently identified as relevant in terms of hydroclimatic variability for the Seine basin (Flipo et al., 2020a).

This approach combines the ORCHIDEE SVAT model with the CaWaQS ground-

water model to simulate surface, groundwater and river hydrology coupled with heat transport. We developed two simulations to evaluate the current conditions (1993-2010) using MIROC5. Then four future climate conditions based on two RCP scenarios (RCP6.0 and RCP8.5) were developed over the mid-century (2043-2060) and end-century (2083-2100) conditions.

The preliminary results from the future climate scenario simulations show that future climate trends in the Seine basin indicate that the rainfall patterns show winter intensification of the water cycle, whereas the temperature trends keep increasing. Air temperature increases significantly impact the surface and soil temperatures at 2-meter depth. These changes at the near-surface propagate to deeper aquifer layers. The temperature increase is consistent for all aquifer layers ranging from 0.4°C to 2.50°C. The end-century RCP8.5 scenario proves to be challenging for the Seine basin as the intensification of water cycle becomes apparent with longer dry period and wetter wet period. Moreover, average river temperatures show increases linked to the increases in the riverbed temperature.

A permanent increase in the average temperatures in rivers negatively impacts the riverine habitat as the warming reduces the resilience of the river network. For example, in the business-as-usual scenario (RCP8.5), by the end of the century, rivers might not be able to provide thermal refugia (Briggs et al., 2012) for the fish species. Increased river temperatures would have grave consequences for the fish species (Isaak et al., 2012). Moreover, increased temperatures affect pollutant metabolism (Briggs et al., 2014a) as the Seine river is a source of significant diffuse and point nitrate supply (Beaudoin et al., 2018).

Temperature is one of the factors of eutrophication (Le Moal et al., 2019). Temperature is also a critical factor in aerobic respiration in the streambed, and higher temperatures could decrease the respiration rate (Vieweg et al., 2016; Bailey and Ahmadi, 2014). For example, bacterial growth is sensitive to water temperatures (Wang et al., 2018b) which could impact the dissolved oxygen profile in the river, and subsequently, the water quality. Varying riverbed temperatures and changes in the riverbed temperature regime could have lasting impacts on the temperature layers of the river water col-

umn. In the case of the Seine basin, the business-as-usual scenario (RCP8.5) poses risks and vulnerabilities by the end of the century in terms of water temperatures. Therefore, studies of biogeochemical aspects of rivers for water quality should include variable riverbed temperatures rather than assuming a steady state. Additional work should also be carried out to identify the 'hotspots' of higher thermal contribution from the riverbed to the river network.

The inherent limitations of climate projections and uncertainties of GCMs require ensemble studies where not one but multiple scenarios are tested from different models (Lehner et al., 2020). This approach is robust when handling the unknown future state of the climate. A significant limitation of this study was that climate change scenarios from one GCM (MIROC) were considered. However, to account for the bias from a particular model, multiple models should be run in an ensemble to estimate the impact and significance of climate change trends (Eyring et al., 2016).

Further studies are needed to detail the extent of the climate warming towards the shallow aquifer layers, which could impact the spatial and temporal variability of the riverbed and river water temperatures. Additionally, studies into the aquifer temperatures need better temperature observations at various aquifer layers and depths to understand the current temperatures of the aquifer system to calibrate the model and reduce uncertainties further. These preliminary results show that the coupled ORCHIDEE-CaWaQS framework is a promising tool to quantify the fluxes at various compartments of an hydrosystem, and it could be a useful regional modelling tool to understand better the impact of surface climate variability on river and groundwater resources. Such distributed approach can significantly improve our ability to map the spatial and temporal distribution of temperatures in rivers and aquifers.

Chapter 9

Conclusion and perspectives

9.1 Coupled water and energy budget at the regional scale

The question of energy fluxes within hydrosystems was first brought to the attention of the scientific community by ecological sciences. Their aim was to understand how water temperature can regulate the life cycle of fish communities. In order to achieve this, many studies were carried out on headwater streams, and thermal budgets were established based on measurements (Caissie, 2006; Webb et al., 2008). Later, modellers developed numerical tools for calculating energy fluxes at the watershed scale (Loinaz et al., 2013) and regional river basin, such as the Loire (Beaufort, 2015; Beaufort et al., 2016a; Loicq et al., 2018). One of the main drawbacks of these significant advances was the simple way groundwater is accounted for without explicit modelling of groundwater processes.

The objective of this thesis was to quantify the energy balance at the regional scale for the first time by including the groundwater processes and their interaction with other hydrosystem compartments. In this work, an attempt to explicitly integrate groundwater processes in the energy balance of a regional river basin was carried out. A coupled framework that relies on an off-line coupling of the SVAT ORCHIDEE (Krinner et al., 2005; Boucher et al., 2020) with the hydrological model CaWaQS (Flipo et al., 2007a, 2023; Labarthe, 2016) at the Seine basin scale was developed. In order to achieve this objective, methodological and technical developments were necessary:

- Development of heat transfer in CaWaQS, including the development of libttc, which is dedicated to the river and aquifer systems. An original approach for

transfer in aquitards and the river bed was also implemented based on Kurylyk et al. (2017);

- Setting up of a regional ORCHIDEE application rather than its usually global scale implementation;

- Development of a calibration strategy that relies on the step-wise approach proposed by Flipo et al. (2023). It was adapted to force ORCHIDEE to reproduce the share of the main hydrological fluxes, AET, runoff, and aquifer recharge, at the Seine basin scale and for 14 main sub-basins;

- Definition of the geothermal flux as a bottom boundary condition for the aquifer system, initialisation procedure of the thermal state of the aquifer system, and a first approach based on an assumption of homogeneous aquifer units for the calibration of thermal parameters.

The newly developed ORCHIDEE-CaWaQS simulation platform significantly improves our understanding of the role of groundwater in the thermal regulation of a regional river network. The controlling processes of the river and aquifer thermal loads in the Seine river basin, such as heat gains and losses of the aquifer system and river network via recharge, overflow, water withdrawals, river-aquifer exchanges, and river atmosphere exchanges, were quantified. The river thermal load is controlled by the short-wave radiation, river-aquifer exchanges, and surface runoff in the Seine basin by supplying 60%, 27% and 13% of total thermal gains, respectively. The Jurassic, the Chalk, and the Alluvium aquifers are the main contributors to the advective heat gains by the river network. Over the period of 2001-2018, the energy input from groundwater represented 156.6 $TWh.y^{-1}$, which is a significant contribution of energy inputs to the river network. The main energy input to the river network comes from short wave radiation (356.4 $TWh.y^{-1}$). When balance by losses at the air-water interface that includes latent heat, long-wave incident radiation and sensible heat are considered, the net energy input to the river through its free surface is (37.0 $TWh.y^{-1}$). Therefore, the main net energy input to the river network originates from the aquifer system. The

heat inputs from the river-aquifer exchanges play a key role in determining the water temperature throughout the Seine basin. These results contribute significantly to our understanding of how groundwater heat exchanges contribute to the river heat balance. Therefore, quantifying energy balance helps us to estimate the complete heat balance of the river network and aquifer system.

The coupling of the ORCHIDEE-CaWaQS model can simulate the hydrosystem water balance and energy budget adequately. The model performs satisfactorily in terms of discharge at the main sub-catchments of the basin, as well as most of the piezometers. Additional calibration work is needed to improve the performance of the model on headwaters. The off-line coupling of the two models is promising. However, limitations include the lack of variable unsaturated zone thickness, variable water table feedback to the atmosphere, and the lack of urban zones. A potential on-line coupling with the variable water table could improve both the hydrological and heat transport performance of the model. The implementation of the analytical solution to limit the computational time of simulating an additional variable (temperature) works satisfactorily. The combined use of the numerical solution and analytical solution enables us to estimate the temperatures at aquitards and the riverbed. The estimation of riverbed temperatures helps us to define the lower boundary of the river transport solution.

Estimating the future impacts of climate change on hydrosystems is one of the most pressing challenges for water resources managers. This challenge is due to the difficulties in quantifying the potential impact by appropriate tools that can adequately represent the future climate scenarios. In the last chapter of this thesis, we aim to reconcile this gap by combining the newly developed ORCHIDEE-CaWaQS coupled with CMIP5 projection in coherence with the previous work of Flipo et al. (2020a). The hydrosystem water and energy budget was quantified for two IPCC climate change projection scenarios (RCP6.0, RCP8.5). We estimated the current (1993-2010), mid-century (2043-2060) and end-century (2083-2100) budgets that could shed light on the potential future stresses on the Seine hydrosystem. The most striking result from our study is that under the business-as-usual scenario (RCP8.5) water temperatures increase at least 1°C. Moreover, the wet season intensifies, whereas the dry period becomes longer

in the RCP8.5 scenario in terms of discharges. The contribution of the river-aquifer exchanges might decrease significantly due to longer dry periods. Even if the RCP6.0 scenario is adapted, by the end of the century, the water temperatures would increase considerably. Finally, shallow aquifer temperatures increase considerably, ranging from 0.1-0.25°C per decade. An increase of this temperature trend in the second half of the century was also observed. These results would affect the critical zone with modifications to the pollution processes and the well-being of aquatic species in the basin. Moreover, under the business-as-usual scenario, the cooling and water treatment might become more challenging for industrial applications since warmer water temperatures increase the cost of cooling. Our findings can help the water managers and stakeholders develop necessary mitigation plans and identify vulnerability zones in the Seine basin.

9.2 Perspectives

Even though the performances of the ORCHIDEE-CaWaQS are remarkable, further improvements should be carried on:

- **vegetation modelling**. Our results indicate that a common limitation of the SVAT model application is the underestimation of AET. The dynamic calculation of vegetation processes performed superior to the prescription of LAI map derivated from large-scale applications. Further works should therefore be carried on to better simulates the vegetation growth dynamically;

- **hydrological modelling**. A key limitation of the hydrological model is that the vadose zone has a fixed geometry while its thickness varies daily and seasonally, depending mainly on the climate and anthropogenic stresses. Another limitation is the lack of feedback between the aquifer and the surface. As evidenced in the literature (Fan, 2015), the depth of the water table impacts the evapotranspiration at the surface and the vegetation activity. It could, in fact, reduce the uncertainties related to evapotranspiration and reduce the underestimation of AET during summer (Clark et al., 2015);

- **heat transfer**. Due to time constraints, a simple allocation approach of thermal

parameters per aquifer unit was selected. It is clearly an oversimplification of the problem at hand. Further work should be carried on to regionalise thermal parameters in each aquifer layer using the layer calibrated values as regularisation values;

- An important perspective of process-based modelling is the **transferability** of the parameters into other catchments. Specifically, explicit representation of physical processes should allow the parameters to be deployed in other catchment applications. For example, this modelling approach could be applied to another regional catchment, such as the Loire basin. It would be interesting to explore the validity of the parameters that represent the processes of the Seine hydrosystem in other catchments. The transferability also underlies the importance of understanding the sensitivity of the water cycle and energy balance processes to various parameters of the catchment.

- **The European Water Framework Directive (WFD)** (Council of European Union, 2000) encourages European countries to prioritise the development of predictive tools that link measures of ecological quality to physical and chemical conditions in a basin. Given that temperature is a key parameter of chemical and biological processes, the platform could be used to inform ecohydrology or agronomic models aiming at estimating the impacts of climate change. The quantification of water and energy fluxes paves the way to catchment scale studies of the hydrosystem functioning at various temporal and spatial scales. This has implications beyond the understanding of processes in the hydrosystem. In order to develop such tools, quantifying the water and energy budget of hydrosystems in a spatially distributed and integrated fashion proves to be an indispensable approach. The coupled model we present here could be used to inform policymakers on water quality monitoring and management especially in regional catchments (Chapman et al., 2016).

- **Water and energy consumption** is driven by many competing activities, including energy and food production. Water, energy, and food are limited resources,

and their production and use often overlap. Water-Energy-Food Nexus (WEFN) approach aims to reconcile the competing uses of these resources; however, modelling approaches that account for all three resources are met with various challenges (Garcia and You, 2016). Our tool that combines water and energy could be coupled with an agronomics and economics model to expand our understanding within the WEFN perspective. It would be particularly interesting to quantify potential future limitations on energy production or food production due to the anomalies in the water cycle and energy balance of the hydrosystem. Moreover, an economic impact assessment could be realised via an economic model, aiding the stakeholders and managers of an hydrosystem.

Bibliography

Addor, N. and Melsen, L. A.: Legacy, Rather Than Adequacy, Drives the Selection of Hydrological Models, Water Resources Research, 55, 378–390, doi:https://doi.org/10.1029/2018WR022958, 2019.

AESN: Etat des lieux du bassin de la Seine et des cours d'eau côtiers normands, Tech. rep., AESN, 2013.

Ala-aho, P., Soulsby, C., Wang, H., and Tetzlaff, D.: Integrated surface-subsurface model to investigate the role of groundwater in headwater catchment runoff generation: A minimalist approach to parameterisation, Journal of Hydrology, 547, 664–677, doi:10.1016/j.jhydrol.2017.02.023, 2017.

Allen, D. M.: Development and application of a process-based, basin-scale stream temperature model, Ph.D. thesis, Citeseer, 2008.

Anderson, C. H. and Bisal, F.: Snow Cover Effect on the Erodible Soil Fraction, Canadian Journal of Soil Science, 49, 287–296, doi:10.4141/cjss69-040, 1969.

Anderson, M. P.: Heat as a Ground Water Tracer, Ground Water, 43, 951–968, doi:10.1111/j.1745-6584.2005.00052.x, 2005.

André, L., Audigane, P., Azaroual, M., and Menjoz, A.: Numerical modeling of fluid–rock chemical interactions at the supercritical CO2–liquid interface during CO2 injection into a carbonate reservoir, the Dogger aquifer (Paris Basin, France), Energy Conversion and Management, 48, 1782–1797, doi:10.1016/j.enconman.2007.01.006, 2007.

Anibas, C., Fleckenstein, J. H., Volze, N., Buis, K., Verhoeven, R., Meire, P., and Batelaan, O.: Transient or steady-state? Using vertical temperature profiles to quantify groundwater-surface water exchange, Hydrological Processes, 23, 2165–2177, doi:10.1002/hyp.7289, 2009.

Anquetin, S., Braud, I., Vannier, O., Viallet, P., Boudevillain, B., Creutin, J.-D., and Manus, C.: Sensitivity of the hydrological response to the variability of rainfall fields and soils for the Gard 2002 flash-flood event, Journal of hydrology, 394, 134–147, 2010.

Aquanty: HydroGeoSphere User Manual, User Manual, Aquanty, 2015.

Arora, V., Seglenieks, F., Kouwen, N., and Soulis, E.: Scaling aspects of river flow routing, Hydrological Processes, 15, 461–477, doi:10.1002/hyp.161, 2001.

Arora, V. K., Chiew, F. H. S., and Grayson, R. B.: A river flow routing scheme for general circulation models, Journal of Geophysical Research: Atmospheres, 104, 14 347–14 357, doi:10.1029/1999JD900200, 1999.

Attard, G., Rossier, Y., Winiarski, T., and Eisenlohr, L.: Deterministic modeling of the impact of underground structures on urban groundwater temperature, Science of The Total Environment, 572, 986–994, doi:10.1016/j.scitotenv.2016.07.229, 2016.

Bailey, R. T. and Ahmadi, M.: Spatial and temporal variability of in-stream water quality parameter influence on dissolved oxygen and nitrate within a regional stream network, Ecological Modelling, 277, 87–96, doi:10.1016/j.ecolmodel.2014.01.015, 2014.

Ball, J. T., Woodrow, I. E., and Berry, J. A.: A Model Predicting Stomatal Conductance and its Contribution to the Control of Photosynthesis under Different Environmental Conditions, in: Progress in Photosynthesis Research: Volume 4 Proceedings of the VIIth International Congress on Photosynthesis Providence, Rhode Island, USA, August 10–15, 1986, edited by Biggins, J., pp. 221–224, Springer Netherlands, Dordrecht, doi:10.1007/978-94-017-0519-6_48, 1987.

Ballabio, C., Panagos, P., and Monatanarella, L.: Mapping topsoil physical prop-

erties at European scale using the LUCAS database, Geoderma, 261, 110–123, doi:10.1016/j.geoderma.2015.07.006, 2016.

Balsamo, G., Beljaars, A., Scipal, K., Viterbo, P., van den Hurk, B., Hirschi, M., and Betts, A. K.: A Revised Hydrology for the ECMWF Model: Verification from Field Site to Terrestrial Water Storage and Impact in the Integrated Forecast System, Journal of Hydrometeorology, 10, 623–643, doi:10.1175/2008JHM1068.1, 2009.

Barthel, R.: HESS Opinions "Integration of groundwater and surface water research: an interdisciplinary problem?", Hydrology and Earth System Sciences, 18, 2615–2628, doi:https://doi.org/10.5194/hess-18-2615-2014, 2014.

Bartholow, J.: The stream network temperature model (SNTEMP), Ecological Modelling, p. 4, 1996.

Bartholow, J.: Stream network and stream segment temperature models software, USGS Unnumbered Series, U.S. Geological Survey, Fort Collins, CO, 2010.

Bastrikov, V., MacBean, N., Cédric, B., Santaren, D., Kuppel, S., and Peylin, P.: Land surface model parameter optimisation using in situ flux data: comparison of gradient-based versus random search algorithms (a case study using ORCHIDEE v1.9.5.2), Geoscientific Model Development, 11, 4739–4754, doi:10.5194/gmd-11-4739-2018, 2018.

Bates, B., Kundzewicz, Z. W., and IPCC, eds.: Climate change and water, IPCC Technical Paper; 6, IPCC Secretariat, oCLC: 551335526, 2008.

Bayer, P., Attard, G., Blum, P., and Menberg, K.: The geothermal potential of cities, Renewable and Sustainable Energy Reviews, 106, 17–30, doi:10.1016/j.rser.2019.02.019, 2019.

Beaudoin, N., Gallois, N., Viennot, P., Le Bas, C., Puech, T., Schott, C., Buis, S., and Mary, B.: Evaluation of a spatialized agronomic model in predicting yield and N leaching at the scale of the Seine-Normandie Basin, Environmental Science and Pollution Research, 25, 23 529–23 558, doi:10.1007/s11356-016-7478-3, 2018.

Beaufort, A.: Modélisation physique de la température des cours d'eau à l'échelle régionale: application au bassin versant de la Loire, Ph.D. thesis, Université François Rabelais de Tours, 2015.

Beaufort, A., Curie, F., Moatar, F., Ducharne, A., Melin, E., and Thiery, D.: T-NET, a dynamic model for simulating daily stream temperature at the regional scale based on a network topology, Hydrological Processes, 30, 2196–2210, doi:10.1002/hyp.10787, 2016a.

Beaufort, A., Moatar, F., Curie, F., Ducharne, A., Bustillo, V., and Thiéry, D.: River Temperature Modelling by Strahler Order at the Regional Scale in the Loire River Basin, France: River Temperature Modelling by Strahler Order, River Research and Applications, 32, 597–609, doi:10.1002/rra.2888, 2016b.

Beaufort, A., Moatar, F., Sauquet, E., Loicq, P., and Hannah, D. M.: Influence of landscape and hydrological factors on stream–air temperature relationships at regional scale, Hydrological Processes, 34, 583–597, doi:10.1002/hyp.13608, 2020.

Bense, V. F. and Kooi, H.: Temporal and spatial variations of shallow subsurface temperature as a record of lateral variations in groundwater flow, Journal of Geophysical Research: Solid Earth, 109, doi:https://doi.org/10.1029/2003JB002782, 2004.

Benyahya, L., Caissie, D., St-Hilaire, A., Ouarda, T. B., and Bobée, B.: A Review of Statistical Water Temperature Models, Canadian Water Resources Journal, 32, 179–192, doi:10.4296/cwrj3203179, 2007.

Benyahya, L., Caissie, D., Satish, M. G., and El-Jabi, N.: Long-wave radiation and heat flux estimates within a small tributary in Catamaran Brook (New Brunswick, Canada), Hydrological Processes, 26, 475–484, 2012.

Benz, S. A., Bayer, P., and Blum, P.: Global patterns of shallow groundwater temperatures, Environmental Research Letters, 12, 034 005, doi:10.1088/1748-9326/aa5fb0, 2017.

Berg, A., Findell, K., Lintner, B., Giannini, A., Seneviratne, S., Hurk, B., Lorenz, R., Pitman, A., Hagemann, S., Meier, A., Cheruy, F., Ducharne, A., Malyshev, S., and Milly, P.: Land–atmosphere feedbacks amplify aridity increase over land under global warming, Nature Climate Change, 6, 869–874, doi:10.1038/nclimate3029, 2016.

Berthier, E., Andrieu, H., and Creutin, J.: The role of soil in the generation of urban runoff: development and evaluation of a 2D model, Journal of hydrology, 299, 252–266, 2004.

Besbes, M. and De Marsily, G.: From infiltration to recharge: use of a parametric transfer function, Journal of Hydrology, 74, 271–293, doi:10.1016/0022-1694(84)90019-2, 1984.

Best, M. J., Pryor, M., Clark, D. B., Rooney, G. G., Essery, R. L. H., Ménard, C. B., Edwards, J. M., Hendry, M. A., Porson, A., Gedney, N., Mercado, L. M., Sitch, S., Blyth, E., Boucher, O., Cox, P. M., Grimmond, C. S. B., and Harding, R. J.: The Joint UK Land Environment Simulator (JULES), model description – Part 1: Energy and water fluxes, Geoscientific Model Development, 4, 677–699, doi:10.5194/gmd-4-677-2011, 2011.

Beven, K.: A manifesto for the equifinality thesis, Journal of Hydrology, 320, 18–36, doi:10.1016/j.jhydrol.2005.07.007, 2006.

Beven, K. and Binley, A.: The future of distributed models: Model calibration and uncertainty prediction, Hydrological Processes, 6, 279–298, doi:10.1002/hyp.3360060305, 1992.

Beven, K. J. and Kirkby, M. J.: A physically based, variable contributing area model of basin hydrology / Un modèle à base physique de zone d'appel variable de l'hydrologie du bassin versant, Hydrological Sciences Bulletin, 24, 43–69, doi:10.1080/02626667909491834, 1979.

Bicknell, B. R., Imhoff, J. C., Kittle Jr, J. L., Donigian Jr, A. S., and Johanson, R. C.:

Hydrological simulation program-FORTRAN. user's manual for release 11, US EPA, 1996.

Billen, G., Garnier, J., Mouchel, J.-M., and Silvestre, M.: The Seine system: Introduction to a multidisciplinary approach of the functioning of a regional river system, Sciences of Total Environment, 375, 1–12, 2007.

Bisht, G., Huang, M., Zhou, T., Chen, X., Dai, H., Hammond, G. E., Riley, W. J., Downs, J. L., Liu, Y., and Zachara, J. M.: Coupling a three-dimensional subsurface flow and transport model with a land surface model to simulate stream–aquifer–land interactions (CP v1.0), Geoscientific Model Development, 10, 4539–4562, doi:10.5194/gmd-10-4539-2017, 2017.

Boé, J., Terray, L., Habets, F., and Martin, E.: Statistical and dynamical downscaling of the Seine basin climate for hydro-meteorological studies, International Journal of Climatology, 27, 1643–1655, doi:10.1002/joc.1602, 2007.

Bogan, T., Mohseni, O., and Stefan, H. G.: Stream temperature-equilibrium temperature relationship, Water Resources Research, 39, doi:10.1029/2003WR002034, 2003.

Bonan, G. B., Levis, S., Kergoat, L., and Oleson, K. W.: Landscapes as patches of plant functional types: An integrating concept for climate and ecosystem models: PLANT FUNCTIONAL TYPES AND CLIMATE MODELS, Global Biogeochemical Cycles, 16, 5–1–5–23, doi:10.1029/2000GB001360, 2002.

Bond, R. M., Stubblefield, A. P., and Van Kirk, R. W.: Sensitivity of summer stream temperatures to climate variability and riparian reforestation strategies, Journal of Hydrology: Regional Studies, 4, 267–279, doi:10.1016/j.ejrh.2015.07.002, 2015.

Bonnet, R.: Variations du cycle hydrologique continental en France des années 1850 à aujourd'hui, Ph.D. thesis, Université de Toulouse 3 Paul Sabatier, 2018.

Boogert, A. and Dupont, D.: The nature of supply side effects on electricity prices: The impact of water temperature, Economics Letters, 88, 121–125, doi:10.1016/j.econlet.2004.12.029, 2005.

Boucher, O., Servonnat, J., Albright, A. L., Aumont, O., Balkanski, Y., Bastrikov, V., Bekki, S., Bonnet, R., Bony, S., Bopp, L., Braconnot, P., Brockmann, P., Cadule, P., Caubel, A., Cheruy, F., Codron, F., Cozic, A., Cugnet, D., D'Andrea, F., Davini, P., Lavergne, C., Denvil, S., Deshayes, J., Devilliers, M., Ducharne, A., Dufresne, J., Dupont, E., Éthé, C., Fairhead, L., Falletti, L., Flavoni, S., Foujols, M., Gardoll, S., Gastineau, G., Ghattas, J., Grandpeix, J., Guenet, B., Guez, E., L., Guilyardi, E., Guimberteau, M., Hauglustaine, D., Hourdin, F., Idelkadi, A., Joussaume, S., Kageyama, M., Khodri, M., Krinner, G., Lebas, N., Guillaume, L., Lévy, C., Li, L., Lott, F., Lurton, T., Luyssaert, S., Madec, G., Madeleine, J., Maignan, F., Marchand, M., Marti, O., Mellul, L., Meurdesoif, Y., Mignot, J., Musat, I., Ottlé, C., Peylin, P., Planton, Y., Polcher, J., Rio, C., Rochetin, N., Rousset, C., Sepulchre, P., Sima, A., Swingedouw, D., Thiéblemont, R., Traore, A. K., Vancoppenolle, M., Vial, J., Vialard, J., Viovy, N., and Vuichard, N.: Presentation and Evaluation of the IPSL-CM6A-LR Climate Model, Journal of Advances in Modeling Earth Systems, 12, doi:10.1029/2019MS002010, 2020.

Bowen, I. S.: The Ratio of Heat Losses by Conduction and by Evaporation from any Water Surface, Phys. Rev., 27, 779–787, 1926.

Boyd, M. and Kasper, B.: Analytical Methods for Dynamic Open Channel Heat and Mass Transfer: Methodology for the Heat Source Model Version 7.0, Tech. rep., Oregon Department of Environmental Quality, Portland, OR, 2003.

Bras, R., Eagleson, P. S., Turner, E. K., and Parsons, R. M.: Hydrology, The forgotten Earth science, Eos, Transactions American Geophysical Union, 68, 227, doi:10.1029/EO068i016p00227, 1987.

Braud, I., Dantas-Antonino, A. C., Vauclin, M., Thony, J. L., and Ruelle, P.: A simple soil-plant-atmosphere transfer model (SiSPAT) development and field verification, Journal of Hydrology, 166, 213–250, doi:10.1016/0022-1694(94)05085-C, 1995.

Bredehoeft, J. D. and Papaopulos, I. S.: Rates of vertical groundwater movement

estimated from the Earth's thermal profile, Water Resources Research, 1, 325–328, doi:10.1029/WR001i002p00325, 1965.

Briggs, M. A., Lautz, L. K., and McKenzie, J. M.: A comparison of fibre-optic distributed temperature sensing to traditional methods of evaluating groundwater inflow to streams, Hydrological Processes, 26, 1277–1290, doi:10.1002/hyp.8200, 2012.

Briggs, M. A., Lautz, L. K., Buckley, S. F., and Lane, J. W.: Practical limitations on the use of diurnal temperature signals to quantify groundwater upwelling, Journal of Hydrology, doi:10.1016/j.jhydrol.2014.09.030, 2014a.

Briggs, M. A., Lautz, L. K., and Hare, D. K.: Residence time control on hot moments of net nitrate production and uptake in the hyporheic zone, Hydrological Processes, 28, 3741–3751, doi:10.1002/hyp.9921, 2014b.

Briggs, M. A., Johnson, Z. C., Snyder, C. D., Hitt, N. P., Kurylyk, B. L., Lautz, L., Irvine, D. J., Hurley, S. T., and Lane, J. W.: Inferring watershed hydraulics and cold-water habitat persistence using multi-year air and stream temperature signals, Science of The Total Environment, 636, 1117–1127, doi:10.1016/j.scitotenv.2018.04.344, 2018.

Brooks, R. and Corey, T.: Hydraulic properties of porous media, vol. 24 of *Hydrology Papers*, 37, Colorado State University, 1964.

Brown, G. W.: Predicting Temperatures of Small Streams, Water Resources Research, 5, 68–75, doi:10.1029/WR005i001p00068, 1969.

Brunner, G. W.: HEC-RAS River Analysis System. Hydraulic User's Manual. Version 1.0., Tech. rep., Hydrologic Engineering Center Davis, 1995.

Brunner, P., Cook, P., and Simmons, C.: Hydrogeologic controls on disconnection between surface water and groundwater, Water Resourses Research, 45, W01 422, doi:10.1029/2008WR006953, 2009.

Burns, E. R., Ingebritsen, S. E., Manga, M., and Williams, C. F.: Evaluating geothermal and hydrogeologic controls on regional groundwater temperature distribution, Water Resources Research, 52, 1328–1344, doi:10.1002/2015WR018204, 2016.

Burrus, J.: Contribution à l'étude du fonctionnement des systèmes pétroliers : apport d'une modélisation bidimensionnelle, Ph.D. thesis, Paris, ENMP, 1997.

Bustillo, V., Moatar, F., Ducharne, A., Thiéry, D., and Poirel, A.: A multimodel comparison for assessing water temperatures under changing climate conditions via the equilibrium temperature concept: case study of the Middle Loire River, France, Hydrological Processes, 28, 1507–1524, doi:10.1002/hyp.9683, 2014.

Böttcher, F. and Zosseder, K.: Thermal influences on groundwater in urban environments – A multivariate statistical analysis of the subsurface heat island effect in Munich, Science of The Total Environment, 810, 152 193, doi:10.1016/j.scitotenv.2021.152193, 2022.

Büttner, G., Feranec, J., Jaffrain, G., Mari, L., Maucha, G., and Soukup, T.: The Corine Land Cover 2000 Project, EARSeL eProceedings, p. 16, 2004.

Cabral, M. C., Garrote, L., Bras, R. L., and Entekhabi, D.: A kinematic model of infiltration and runoff generation in layered and sloped soils, Advances in Water Resources, 15, 311–324, doi:10.1016/0309-1708(92)90017-V, 1992.

Caissie, D.: The thermal regime of rivers: a review, Freshwater Biology, 51, 1389–1406, doi:0.1111/j.1365-2427.2006.01597.x, 2006.

Caissie, D., El-Jabi, N., and St-Hilaire, A.: Stochastic modelling of water temperatures in a small stream using air to water relations, Canadian Journal of Civil Engineering, 25, 250–260, doi:10.1139/l97-091, 1998.

Caissie, D., Satish, M. G., and El-Jabi, N.: Predicting water temperatures using a deterministic model: Application on Miramichi River catchments (New Brunswick, Canada), Journal of Hydrology, 336, 303–315, doi:10.1016/j.jhydrol.2007.01.008, 2007.

Caissie, D., Kurylyk, B. L., St-Hilaire, A., El-Jabi, N., and MacQuarrie, K.: Streambed temperature dynamics and corresponding heat fluxes in small

streams experiencing seasonal ice cover, Journal of Hydrology, 519, 1441–1452, doi:10.1016/j.jhydrol.2014.09.034, 2014.

Camporese, M., Paniconi, C., Putti, M., and Orlandini, S.: Surface-subsurface flow modeling with path-based runoff routing, boundary condition-based coupling, and assimilation of multisource observation data, Water Resources Research, 46, doi:10.1029/2008WR007536, 2010.

Campoy, A., Ducharne, A., Cheruy, F., Hourdin, F., Polcher, J., and Dupont, J. C.: Response of land surface fluxes and precipitation to different soil bottom hydrological conditions in a general circulation model, Journal of Geophysical Research: Atmospheres, 118, 10,725–10,739, doi:10.1002/jgrd.50627, 2013.

Carlaw, H. and Jaeger, J.: Conduction of Heat in Solids, Clarendon, Oxford, 1959.

Carsel, R. F. and Parrish, R. S.: Developing joint probability distributions of soil water retention characteristics, Water Resources Research, 24, 755–769, doi:10.1029/WR024i005p00755, 1988.

Castle, S. L., Thomas, B. F., Reager, J. T., Rodell, M., Swenson, S. C., and Famiglietti, J. S.: Groundwater depletion during drought threatens future water security of the Colorado River Basin, Geophysical Research Letters, 41, 5904–5911, doi:10.1002/2014GL061055, 2014.

Chandesris, A., Mengin, N., Malavoi, J. R., Souchon, Y., Pella, H., and Wasson, J. G.: Système relationnel d'audit de l'hydromorphologie des cours d'eau: principes et méthodes, Tech. rep., Irstea, URL `https://hal.inrae.fr/hal-02590482`, pp. 64 + Annexes, 2008.

Chapman, D. V., Bradley, C., Gettel, G. M., Hatvani, I. G., Hein, T., Kovács, J., Liska, I., Oliver, D. M., Tanos, P., Trásy, B., et al.: Developments in water quality monitoring and management in large river catchments using the Danube River as an example, Environmental Science and Policy, 64, 141–154, 2016.

Chapra, S., Pelletier, G., and Tao, H.: QUAL2K, A modeling framework for simulating river and stream water quality. Version, 2, 91, 2008.

Chow, V.: Open Channel Hydraulics, McGraw Hill Company Inc., New York., 1959.

Christensen, J. H. and Christensen, O. B.: Severe summertime flooding in Europe, Nature, 421, 805, doi:10.1038/421805a, 2003.

Christensen, O. B. and Christensen, J. H.: Intensification of extreme European summer precipitation in a warmer climate, Global and Planetary Change, 44, 107–117, doi:10.1016/j.gloplacha.2004.06.013, 2004.

Christensen, O. B., Christensen, J. H., Machenhauer, B., and Botzet, M.: Very High-Resolution Regional Climate Simulations over Scandinavia—Present Climate, Journal of Climate, 11, 3204–3229, doi:10.1175/1520-0442(1998)011<3204:VHRRCS>2.0.CO;2, 1998.

Clapp, R. B. and Hornberger, G. M.: Empirical equations for some soil hydraulic properties, Water Resources Research, 14, 601–604, doi:10.1029/WR014i004p00601, 1978.

Clark, M. P., Fan, Y., Lawrence, D. M., Adam, J. C., Bolster, D., Gochis, D. J., Hooper, R. P., Kumar, M., Leung, L. R., Mackay, D. S., Maxwell, R. M., Shen, C., Swenson, S. C., and Zeng, X.: Improving the representation of hydrologic processes in Earth System Models, Water Resources Research, 51, 5929–5956, doi:10.1002/2015WR017096, 2015.

Clarke, R. T.: Issues of experimental design for comparing the performance of hydrologic models, Water Resources Research, 44, doi:10.1029/2007WR005927, 2008.

Cluis, D. A.: Relationship between tream temperature and ambient air temperature, Hydrology Research, 3, 65–71, doi:10.2166/nh.1972.0004, 1972.

Cole, T. M. and Wells, S. A.: CE-QUAL-W2: A Two-dimensional, Laterally Averaged, Hydrodynamic and Water Quality Model, Version 3.5, Tech. rep., US Army Engineering and Research Development Center, Vicksburg, MS, 2006.

Condon, L. E. and Maxwell, R. M.: Evaluating the relationship between topography and groundwater using outputs from a continental-scale integrated hydrology model, Water Resources Research, 51, 6602–6621, doi:10.1002/2014WR016774, 2015.

Constantz, J., Stewart, A., Niswonger, R., and Sarma, L.: Analysis of temperature profiles for investigating stream losses beneath ephemeral channels, Water Resourses Research, 38-12, 1316, doi:10.1029/2001WR001221, 2002.

Council of European Union: Water Framework Directive (WFD) 2000/60/EC, https://www.eea.europa.eu/policy-documents/water-framework-directive-wfd-2000, Accessed on 03.10.2021, 2000.

Cox, M. M. and Bolte, J. P.: A spatially explicit network-based model for estimating stream temperature distribution, Environmental Modelling and Software, 22, 502–514, doi:10.1016/j.envsoft.2006.02.011, 2007.

Cucchi, K., Flipo, N., Rivière, A., and Rubin, Y.: Estimating hydrothermal properties and high-frequency fluxes from multiphysics measurements in the hyporheic zone, Advances in Water Resources, in prep.

Cunge, J. A.: On the subject of a flood propagation computation method (Muskingum method), Journal of Hydraulic Research, 7, 205–230, publisher: Taylor and Francis, 1969.

Dai, A., Qian, T., Trenberth, K. E., and Milliman, J. D.: Changes in Continental Freshwater Discharge from 1948 to 2004, Journal of Climate, 22, 2773–2792, doi:10.1175/2008JCLI2592.1, 2009.

Dai, Y., Zeng, X., Dickinson, R. E., Baker, I., Bonan, G. B., Bosilovich, M. G., Denning, A. S., Dirmeyer, P. A., Houser, P. R., Niu, G., Oleson, K. W., Schlosser, C. A., and Yang, Z.-L.: The Common Land Model, Bulletin of the American Meteorological Society, 84, 1013–1024, doi:10.1175/BAMS-84-8-1013, 2003.

Dai, Y., Xin, Q., Wei, N., Zhang, Y., Shangguan, W., Yuan, H., Zhang, S., Liu, S., and Lu, X.: A Global High-Resolution Data Set of Soil Hydraulic and Thermal Properties for Land Surface Modeling, Journal of Advances in Modeling Earth Systems, 11, 2996–3023, doi:10.1029/2019MS001784, 2019.

Dayon, G., Boé, J., and Martin, E.: Transferability in the future climate of a statistical downscaling method for precipitation in France, Journal of Geophysical Research, 120, 1023–1043, doi:10.1002/2014JD022236, 2015.

Dayon, G., Boé, J., Martin, E., and Gailhard, J.: Impacts of climate change on the hydrological cycle over France and associated uncertainties, Comptes Rendus - Geoscience, 350, 141–153, doi:10.1016/j.crte.2018.03.001, 2018.

De Amorim, W. S., Valduga, I. B., Ribeiro, J. M. P., Williamson, V. G., Krauser, G. E., Magtoto, M. K., de Andrade, J. B. S. O., et al.: The nexus between water, energy, and food in the context of the global risks: An analysis of the interactions between food, water, and energy security, Environmental Impact Assessment Review, 72, 1–11, doi:10.1016/j.eiar.2018.05.002, 2018.

De Kimpe, C. R. and Morel, J.-L.: Urban soil management: a growing concern, Soil science, 165, 31–40, 2000.

De la Torre, A. M.: Groundwater influence on soil moisture memory and land-atmosphere interactions over the Iberian Peninsula, Ph.D. thesis, Universidade de Santiago de Compostela, 2014.

De Maet, T., Cornaton, F., and Hanert, E.: A scalable coupled surface–subsurface flow model, Computers and Fluids, 116, 74–87, doi:10.1016/j.compfluid.2015.03.028, 2015.

de Marsily, G.: Quantitative Hydrogeology - Groundwater Hydrology for Engineers, Academic Press, London, 1986.

de Marsily, G.: L'eau, un trésor en partage, Quai des sciences, Dunod, 2009.

de Marsily, G.: Will we soon run out of water?, Annals of Nutrition and Metabolism, 76, 10–16, publisher: Karger Publishers, 2020.

de Marsily, G., Ledoux, E., Levassor, A., Poitrinal, D., and Salem, A.: Modelling of large multilayered theory and applications aquifer systems: Theory and Applications, Journal of Hydrology, 36, 1–34, 1978.

de Noblet-Ducoudré, N., Gervois, S., Ciais, P., Viovy, N., Brisson, N., Seguin, B., and Perrier, A.: Coupling the Soil-Vegetation-Atmosphere-Transfer Scheme ORCHIDEE to the agronomy model STICS to study the influence of croplands on the European carbon and water budgets, Agronomie, 24, 397–407, doi:10.1051/agro:2004038, 2004.

de Rosnay, P.: Integrated parameterization of irrigation in the land surface model ORCHIDEE. Validation over Indian Peninsula, Geophysical Research Letters, 30, doi:10.1029/2003GL018024, 2003.

de Rosnay, P. and Polcher, J.: Modelling root water uptake in a complex land surface scheme coupled to a GCM, Hydrology and Earth System Sciences, 2, 239–255, doi:10.5194/hess-2-239-1998, 1998.

de Rosnay, P., Bruen, M., and Polcher, J.: Sensitivity of surface fluxes to the number of layers in the soil model used in GCMs, Geophysical Research Letters, 27, 3329–3332, doi:10.1029/2000GL011574, 2000.

de Rosnay, P., Polcher, J., Bruen, M., and Laval, K.: Impact of a physically based soil water flow and soil-plant interaction representation for modeling large-scale land surface processes, Journal of Geophysical Research: Atmospheres, 107, ACL–3, doi:10.1029/2001JD000634, 2002.

De Vries, D. A.: Thermal Properties of Soils, Physics of Plant Environment, edited by Van Wijk, WR North-Holland Pub, Co, 1963.

Deardorff, J. W.: Efficient prediction of ground surface temperature and moisture, with inclusion of a layer of vegetation, Journal of Geophysical Research: Oceans, 83, 1889–1903, 1978.

Deas, M., Abbolt, A., and Bale, A.: Shasta river flow and temperature modeling project, Tech. rep., Watercourse Engineering, Inc, 2003.

Deltares, D.: Delft3D-FLOW Simulation of Multi-Dimensional Hydrodynamic Flows and Transport Phenomena Including Sediments, User Manual, Version, 2008.

Demirel, M. C., Mai, J., Mendiguren, G., Koch, J., Samaniego, L., and Stisen, S.: Combining satellite data and appropriate objective functions for improved spatial pattern performance of a distributed hydrologic model, Hydrology and Earth System Sciences, 22, 1299–1315, doi:10.5194/hess-22-1299-2018, 2018.

Dentzer, J.: Forçages environnementaux et contrôles structuraux sur le régime thermique actuel du bassin de Paris : enjeux pour la compréhension du potentiel géothermique en Ile-de-France, Ph.D. thesis, Université Pierre et Marie Curie - Paris VI, 2016.

DHI: FEFLOW Documentation, vol. 1-5, DHI-WASY, 2009.

DHI: MIKE SHE Reference Manual Vol.2, Tech. rep., DHI, 2017.

DHI, D.: Mike-11: a modelling system for rivers and channels, reference manual, DHI–Water and Development, Horsholm, Denmark, 2003.

Dickinson, E., Henderson-Sellers, A., and Kennedy, J.: Biosphere-atmosphere Transfer Scheme (BATS) Version 1e as Coupled to the NCAR Community Climate Model, Tech. rep., National Center for Atmospheric Research, Boulder, CO (United States)., doi:10.5065/D67W6959, 1993.

Dickinson, R. E., Henderson-Sellers, A., Rosenzweig, C., and Sellers, P. J.: Evapotranspiration models with canopy resistance for use in climate models, a review, Agricultural and Forest Meteorology, 54, 373–388, doi:10.1016/0168-1923(91)90014-H, 1991.

Dingman, S.: Physical Hydrology, Waveland Press, 2008.

Doble, R., Brunner, P., McCallum, J., and Cook, P. G.: An Analysis of River Bank Slope and Unsaturated Flow Effects on Bank Storage, Ground Water, 50, 77–86, doi:10.1111/j.1745-6584.2011.00821.x, 2012.

Domenico, P. A. and Schwartz, F. W.: Physical and chemical hydrogeology, vol. 506, Wiley New York, 1998.

Dooge, J.: The hydrologic cycle as a closed system, International Association of Scientific Hydrology. Bulletin, 13, 58–68, doi:10.1080/02626666809493568, 1968.

Dorchies, D., Thirel, G., Jay-Allemand, M., Chauveau, M., Dehay, F., Bourgin, P.-Y., Perrin, C., Jost, C., Rizzoli, J.-L., Demerliac, S., and Thépot, R.: Climate change impacts on multi-objective reservoir management: case study on the Seine River basin, France, International Journal of River Basin Management, 12, 265–283, doi:10.1080/15715124.2013.865636, 2014.

D'Orgeval, T., Polcher, J., and Li, L.: Uncertainties in modelling future hydrological change over West Africa, Climate Dynamics, 26, 93–108, doi:10.1007/s00382-005-0079-3, 2006.

D'Orgeval, T., Polcher, J., and de Rosnay, P.: Sensitivity of the West African hydrological cycle in ORCHIDEE to infiltration processes, Hydrology and Earth System Sciences, 12, 1387–1401, doi:10.5194/hess-12-1387-2008, 2008.

Douville, H., Royer, J. F., and Mahfouf, J. F.: A new snow parameterization for the Météo-France climate model, Climate Dynamics, 12, 21–35, doi:10.1007/BF00208760, 1995.

Ducharne, A.: Importance of stream temperature to climate change impact on water quality, Hydrology and Earth System Sciences Discussions, 4, 2425–2460, doi:https://doi.org/10.5194/hess-12-797-2008, 2008.

Ducharne, A.: The hydrol module of ORCHIDEE: scientific documentation, Tech. rep., Sorbonne University, CNRS, IPSL, 2018.

Ducharne, A. and Laval, K.: Influence of the Realistic Description of Soil Water-Holding Capacity on the Global Water Cycle in a GCM, Journal of Climate, 13, 4393–4413, doi:10.1175/1520-0442(2000)013<4393:IOTRDO>2.0.CO;2, 2000.

Ducharne, A., Koster, R. D., Suarez, M. J., Stieglitz, M., and Kumar, P.: A catchment-based approach to modeling land surface processes in a general circulation model: 2.

Parameter estimation and model demonstration, Journal of Geophysical Research: Atmospheres, 105, 24 823–24 838, doi:10.1029/2000JD900328, 2000.

Ducharne, A., Théry, S., Viennot, P., Ledoux, E., Gomez, E., and Déqué, M.: Influence du changement climatique sur l'hydrologie du bassin de la Seine, VertigO - la revue électronique en sciences de l'environnement, 4, doi:10.4000/vertigo.3845, 2003.

Ducharne, A., Baubion, C., Beaudoin, N., Benoit, M., Billen, G., Brisson, N., Garnier, J., Kieken, H., Lebonvallet, S., Ledoux, E., Mary, B., Mignolet, C., Poux, X., Sauboua, E., Schott, C., Théry, S., and Viennot, P.: Long term prospective of the Seine River system: Confronting climatic and direct anthropogenic changes, Science of The Total Environment, 375, 292–311, doi:10.1016/j.scitotenv.2006.12.011, 2007.

Ducharne, A., Habets, F., Déqué, M., Evaux, L., A., H., Lepaillier, A., Lepelletier, T., Martin, E., Oudin, L., Pagé, C., Ribstein, P., Sauquet, E., Thiéry, D., Terray, L., Viennot, P., Boé, J., Bourqui, M., Crespi, O., Gascoin, S., and Rieu, J.: Projet RExHySS : Impact du changement climatique sur les Ressources en eau et les Extrêmes Hydrologiques dans les bassins de la Seine et la Somme, Rapport d'étude, Ministère de l'Ecologie, de l'Energie, du Développement durable et de la Mer, 2009.

Ducharne, A., Arboleda-Obando, P., and Cheruy, F.: Effets de l'humectation des sols par les nappes sur la trajectoire du changement climatique dans le bassin de la Seine et en Europe, PIREN Seine, p. 17, 2020.

Ducoudré, N. I., Laval, K., and Perrier, A.: SECHIBA, a new Set of Parameterizations of the Hydrologic Exchanges at the Land Atmosphere Interface within the LMD Atmospheric General Circulation Model, Journal of Climate, 6, 248–273, URL http://www.jstor.org/stable/26197219, 1993.

Duethmann, D. and Blöschl, G.: Why has catchment evaporation increased in the past 40 years? A data-based study in Austria, Hydrology and Earth System Sciences, 22, 5143–5158, doi:10.5194/hess-22-5143-2018, 2018.

Dugdale, S. J., Hannah, D. M., and Malcolm, I. A.: River temperature modelling: A

review of process-based approaches and future directions, Earth-Science Reviews, 175, 97–113, doi:10.1016/j.earscirev.2017.10.009, 2017.

Dunne, T. and Black, R. D.: An Experimental Investigation of Runoff Production in Permeable Soils, Water Resources Research, 6, 478–490, doi:10.1029/WR006i002p00478, 1970.

Durand, Y., Brun, E., Merindol, L., Guyomarc'h, G., Lesaffre, B., and Martin, E.: A meteorological estimation of relevant parameters for snow models, Annals of Glaciology, 18, 65–71, doi:10.1017/S0260305500011277, 1993.

Dümenil, L. and Todini, E.: Chapter 9 - A rainfall–runoff scheme for use in the Hamburg climate model, in: Advances in Theoretical Hydrology, edited by O'Kane, J. P., European Geophysical Society Series on Hydrological Sciences, pp. 129–157, Elsevier, Amsterdam, doi:10.1016/B978-0-444-89831-9.50016-8, 1992.

Ek, M. B., Mitchell, K. E., Lin, Y., Rogers, E., Grunmann, P., Koren, V., Gayno, G., and Tarpley, J. D.: Implementation of Noah land surface model advances in the National Centers for Environmental Prediction operational mesoscale Eta model, Journal of Geophysical Research: Atmospheres, 108, doi:10.1029/2002JD003296, 2003.

ESA Land Cover, C.: Product User Guide Version 2.0, Esa [online] Available from: https://www. esa-landcover, 2017.

ESDB: The European Soil Database distribution version 2.0, Tech. rep., European Commission and the European Soil Bureau Network, CD-ROM, EUR 19945 EN, 2004.

Essery, R., Bunting, P., Rowlands, A., Rutter, N., Hardy, J., Melloh, R., Link, T., Marks, D., and Pomeroy, J.: Radiative Transfer Modeling of a Coniferous Canopy Characterized by Airborne Remote Sensing, Journal of Hydrometeorology, 9, 228–241, doi:10.1175/2007JHM870.1, 2008.

Eyring, V., Bony, S., Meehl, G. A., Senior, C. A., Stevens, B., Stouffer, R. J., and Taylor, K. E.: Overview of the Coupled Model Intercomparison Project Phase 6 (CMIP6) ex-

perimental design and organization, Geoscientific Model Development, 9, 1937–1958, doi:10.5194/gmd-9-1937-2016, publisher: Copernicus GmbH, 2016.

Fairbairn, D., Barbu, A. L., Napoly, A., Albergel, C., Mahfouf, J.-F., and Calvet, J.-C.: The effect of satellite-derived surface soil moisture and leaf area index land data assimilation on streamflow simulations over France, Hydrology and Earth System Sciences, 21, 2015–2033, doi:10.5194/hess-21-2015-2017, 2017.

Famiglietti, J. S.: The global groundwater crisis, Nature Climate Change, 4, 945–948, doi:10.1038/nclimate2425, 2014.

Famiglietti, J. S. and Rodell, M.: Water in the Balance, Science, 340, 1300–1301, doi:10.1126/science.1236460, 2013.

Famiglietti, J. S. and Wood, E. F.: Evapotranspiration and runoff from large land areas: Land surface hydrology for atmospheric general circulation models, Surveys in Geophysics, 12, 179–204, doi:10.1007/BF01903418, 1991.

Fan, Y.: Groundwater in the Earth's critical zone: Relevance to large-scale patterns and processes: Groundwater at large scales, Water Resources Research, 51, 3052–3069, doi:10.1002/2015WR017037, 2015.

Fan, Y., Miguez-Macho, G., Weaver, C. P., Walko, R., and Robock, A.: Incorporating water table dynamics in climate modeling: 1. Water table observations and equilibrium water table simulations, Journal of Geophysical Research: Atmospheres, 112, doi:10.1029/2006JD008111, 2007.

Feddes, R. A., Hoff, H., Bruen, M., Dawson, T., de Rosnay, P., Dirmeyer, P., Jackson, R. B., Kabat, P., Kleidon, A., Lilly, A., and Pitman, A. J.: Modeling Root Water Uptake in Hydrological and Climate Models, Bulletin of the American Meteorological Society, 82, 2797–2810, doi:10.1175/1520-0477(2001)082<2797:MRWUIH>2.3.CO;2, 2001.

Ferguson, G. and Woodbury, A. D.: Urban heat island in the subsurface, Geophysical Research Letters, 34, doi:10.1029/2007GL032324, 2007.

Fleckenstein, J. H., Krause, S., Hannah, D. M., and Boano, F.: Groundwater-surface water interactions: New methods and models to improve understanding of processes and dynamics, Advances in Water Resources, 33, 1291–1295, doi:10.1016/j.advwatres.2010.09.011, 2010.

Flipo, N.: Modélisation intégrée des transferts d'azote dans les aquifères et les rivières : Application au bassin du Grand Morin, Ph.D. thesis, Centre d'Informatique Géologique, Ecole Nationale Supérieure des Mines de Paris, 2005.

Flipo, N.: Modélisation des Hydrosystèmes Continentaux pour une Gestion Durable de la Ressource en Eau, Thèse d'habilitation, Paris ENSMP, 2013.

Flipo, N., Poulin, M., Even, S., and Ledoux, E.: Hydrological part of CAWAQS (Catchment Water Quality Simulator): fitting on a small sedimentary basin, SIL Proceedings, 1922-2010, 29, 768–772, doi:10.1080/03680770.2005.11902782, 2005.

Flipo, N., Even, S., Poulin, M., Théry, S., and Ledoux, E.: Modelling nitrate fluxes at the catchment scale using the integrated tool CAWAQS, Sciences of Total Environment, 375, 69–79, doi:10.1016/j.scitotenv.2006.12.016, 2007a.

Flipo, N., Jeannée, N., Poulin, M., Even, S., and Ledoux, E.: Assessment of nitrate pollution in the Grand Morin aquifers (France): Combined use of geostatistics and physically based modeling, Environmental Pollution, 146, 241–256, doi:10.1016/j.envpol.2006.03.056, 2007b.

Flipo, N., Monteil, C., Poulin, M., de Fouquet, C., and Krimissa, M.: Hybrid fitting of a hydrosystem model: long term insight into the Beauce aquifer functioning (France), Water Resourses Research, 48, W05 509, doi:10.1029/2011WR011092, 2012.

Flipo, N., Mouhri, A., Labarthe, B., Biancamaria, S., Rivière, A., and Weill, P.: Continental hydrosystem modelling : the concept of nested stream-aquifer interfaces, Hydrology and Earth System Sciences, 18, 3121–3149, doi:10-5194/hess-18-3121-2014, 2014.

Flipo, N., Rivière, A., Gallois, N., Labarthe, B., Baratelli, F., Wang, S., Maillot, M., Verbeke, T., Goblet, P., Jost, A., and Abasq, L.: CAtchment WAter Quality SImulator : CaWaQS, in: Rapports de synthèse de fin de phase VII du programme PIREN Seine, edited by Seine, P., vol. 4 of *Mesures hydrogéophysiques et biogéochimiques haute-fréquence et "time lapse" des interfaces nappe-rivière : évolution des ressources en eau*, pp. 11–46, PIREN-Seine, URL https://hal-mines-paristech.archives-ouvertes.fr/hal-02404683, 2019.

Flipo, N., Gallois, N., Labarthe, B., Baratelli, F., Viennot, P., Schuite, J., Rivière, A., Bonnet, R., and Boé, J.: The Seine River Basin, chap. Pluri-annual water budget on the Seine basin: past, current and future trends, pp. 59–89, Handbook of Environmental Chemistry, Springer, Cham, Switzerland, doi:10.1007/698_2019_392, 2020a.

Flipo, N., Lestel, L., Labadie, P., Meybeck, M., and Garnier, J.: The Seine River Basin, chap. Trajectories of the Seine River Basin, pp. 1–28, Handbook of Environmental Chemistry, Springer, Cham, Switzerland, doi:10.1007/698_2019_437, 2020b.

Flipo, N., Gallois, N., and Schuite, J.: Recalibration du modèle CaWaQS-Seine pour l'analyse du fonctionnement du bassin, Rapport technique d'étude R310521NFLI, Centre de Géosciences - ARMINES/MINES ParisTech, 2021a.

Flipo, N., Labadie, P., and Lestel, L., eds.: The Seine River Basin, Springer, Cham, Switzerland, doi:10.1007/978-3-030-54260-3, 2021b.

Flipo, N., Gallois, N., and Schuite, J.: Regional coupled surface-subsurface hydrological model fitting based on a spatially distributed minimalist reduction of frequency-domain discharge data, Geoscientific Model Development Discussions, 16, 353–381, doi:10.5194/gmd-2022-24, 2023.

Foreman, M., Lee, D., Morrison, J., Macdonald, S., Barnes, D., and Williams, I.: Simulations and retrospective analyses of fraser watershed flows and temperatures, Atmosphere-Ocean, 39, 89–105, doi:10.1080/07055900.2001.9649668, 2001.

Franks, S., Beven, K., Quinn, P., and Wright, I.: On the sensitivity of soil-vegetation-atmosphere transfer (SVAT) schemes: equifinality and the problem of robust calibration, Agricultural and Forest Meteorology, 86, 63–75, doi:10.1016/S0168-1923(96)02421-5, 1997.

Franks, S. W., Beven, K. J., and Gash, J. H. C.: Multi-objective conditioning of a simple SVAT model, Hydrology and Earth System Sciences, 3, 477–488, doi:10.5194/hess-3-477-1999, 1999.

Freeze, R. A. and Cherry, J. A.: Groundwater, Prentice-Hall, Englewood Cliffs, NJ, 604 pp., 1979.

Freeze, R. A. and Harlan, R.: Blueprint for a physically-based digitally simulated, hydrologic response model, Journal of Hydrology, 9, 237–258, doi:10.1016/0022-1694(69)90020-1, 1969.

Frieler, K., Lange, S., Piontek, F., Reyer, C. P., Schewe, J., Warszawski, L., Zhao, F., Chini, L., Denvil, S., Emanuel, K., et al.: Assessing the impacts of 1.5 C global warming–simulation protocol of the Inter-Sectoral Impact Model Intercomparison Project (ISIMIP2b), Geoscientific Model Development, 10, 4321–4345, 2017.

Furman, A.: Modeling Coupled Surface–Subsurface Flow Processes: A Review, Vadose Zone Journal, 7, 741, doi:10.2136/vzj2007.0065, 2008.

Gaillardet, J., Braud, I., Hankard, F., Anquetin, S., Bour, O., Dorfliger, N., de Dreuzy, J., Galle, S., Galy, C., Gogo, S., Gourcy, L., Habets, F., Laggoun, F., Longuevergne, L., Borgne, T. L., Naaim-Bouvet, F., Nord, G., Simonneaux, V., Six, D., Tallec, T., Valentin, C., Abril, G., Allemand, P., Arènes, A., Arfib, B., Arnaud, L., Arnaud, N., Arnaud, P., Audry, S., Comte, V. B., Batiot, C., Battais, A., Bellot, H., Bernard, E., Bertrand, C., Bessière, H., Binet, S., Bodin, J., Bodin, X., Boithias, L., Bouchez, J., Boudevillain, B., Moussa, I. B., Branger, F., Braun, J. J., Brunet, P., Caceres, B., Calmels, D., Cappelaere, B., Celle-Jeanton, H., Chabaux, F., Chalikakis, K., Champollion, C., Copard, Y., Cotel, C., Davy, P., Deline, P., Delrieu, G., Demarty, J., Dessert, C., Dumont, M., Emblanch, C., Ezzahar, J., Estèves, M., Favier, V., Faucheux, M., Filizola,

N., Flammarion, P., Floury, P., Fovet, O., Fournier, M., Francez, A. J., Gandois, L., Gascuel, C., Gayer, E., Genthon, C., Gérard, M. F., Gilbert, D., Gouttevin, I., Grippa, M., Gruau, G., Jardani, A., Jeanneau, L., Join, J. L., Jourde, H., Karbou, F., Labat, D., Lagadeuc, Y., Lajeunesse, E., Lastennet, R., Lavado, W., Lawin, E., Lebel, T., Bouteiller, C. L., Legout, C., Lejeune, Y., Meur, E. L., Moigne, N. L., Lions, J., Lucas, A., Malet, J. P., Marais-Sicre, C., Maréchal, J. C., Marlin, C., Martin, P., Martins, J., Martinez, J. M., Massei, N., Mauclerc, A., Mazzilli, N., Molénat, J., Moreira-Turcq, P., Mougin, E., Morin, S., Ngoupayou, J. N., Panthou, G., Peugeot, C., Picard, G., Pierret, M. C., Porel, G., Probst, A., Probst, J. L., Rabatel, A., Raclot, D., Ravanel, L., Rejiba, F., René, P., Ribolzi, O., Riotte, J., Rivière, A., Robain, H., Ruiz, L., Sanchez-Perez, J. M., Santini, W., Sauvage, S., Schoeneich, P., Seidel, J. L., Sekhar, M., Sengtaheuanghoung, O., Silvera, N., Steinmann, M., Soruco, A., Tallec, G., Thibert, E., Lao, D. V., Vincent, C., Viville, D., Wagnon, P., , and Zitouna, R.: OZCAR: the French network of Critical Zone Observatories, Vadose Zone Journal, 17, 180 067, doi:10.2136/vzj2018.04.0067, 2018.

Gallois, N. and Flipo, N.: Actualisation de l'application CaWaQS-Seine : Extension du système aquifère à la frange orientale du bassin et calibration de son comportement hydrodynamique, Rapport technique PIREN-Seine phase VIII, ARMINES/MINES ParisTech, PSL Universite - Centre de Géosciences, 2021.

Gallois, N. and Viennot, P.: Modélisation de la pollution diffuse d'origine agricole des grands aquifères du bassin Seine-Normandie : Actualisation des modélisations couplées STICS-MODCOU – Modélisation de scénarios agricoles sous changement climatique, Tech. rep., ARMINES/MINES ParisTech, 2018.

Gallois, N., Ledoux, E., and Flipo, N.: Mise à jour du modèle mathématique de l'hydrosystème de Volvic - Phase I : Migration de l'application numérique MODCOU-NEWSAM vers la plateforme de modélisation CaWaQS, Rapport technique d'étude, ARMINES/MINES ParisTech, PSL Universite - Centre de Géosciences, 2020a.

Gallois, N., Rivière, A., and Flipo, N.: Développements numériques au sein de la plate-

forme de modélisation des hydrosystèmes CaWaQS : Introduction des premières fonctionnalités de transport conservatif, Tech. rep., ARMINES, 2020b.

Gallois, N., Ledoux, E., and Flipo, N.: Mise à jour du modèle mathématique de l'hydrosystème de Volvic - Phase II : Actualisation de l'application numérique CaWaQS-Volvic : Scénarisations climatiques, Rapport technique d'étude, ARMINES/MINES ParisTech, PSL Universite - Centre de Géosciences, 2021.

Garcia, D. J. and You, F.: The water-energy-food nexus and process systems engineering: A new focus, Computers and Chemical Engineering, 91, 49–67, doi:10.1016/j.compchemeng.2016.03.003, 2016.

Garrigues, S., Olioso, A., Calvet, J. C., Martin, E., Lafont, S., Moulin, S., Chanzy, A., Marloie, O., Buis, S., Desfonds, V., Bertrand, N., and Renard, D.: Evaluation of land surface model simulations of evapotranspiration over a 12-year crop succession: impact of soil hydraulic and vegetation properties, Hydrology and Earth System Sciences, 19, 3109–3131, doi:10.5194/hess-19-3109-2015, 2015.

Gentine, P., D'Odorico, P., Lintner, B. R., Sivandran, G., and Salvucci, G.: Interdependence of climate, soil, and vegetation as constrained by the Budyko curve, Geophysical Research Letters, 39, doi:10.1029/2012GL053492, 2012.

Giardino, J. R. and Houser, C.: Principles and Dynamics of the Critical Zone, no. 19 in Developments in Earth Science Processes, Elsevier, 2015.

Giordano, M.: Global Groundwater? Issues and Solutions, Annual Review of Environment and Resources, 34, 153–178, doi:10.1146/annurev.environ.030308.100251, 2009.

Gomez, E.: Modélisation intégrée du transfert de nitrate à l'échelle régionale dans un système hydrologique. Application au bassin de la Seine, Ph.D. thesis, École Nationale Supérieure des Mines de Paris, 2002.

Gonçalvès, J., Violette, S., Robin, C., Pagel, M., Guillocheau, F., de Marsily, G., Bruel, D., and Ledoux, E.: 3-D modelling of salt and heat transport during the 248 m.y. evo-

lution of the Paris basin : diagenetic implications, Bulletin de la Société Géologique de France, 174, 429–439, doi:10.2113/174.5.429, 2003.

Goto, S., Yamano, M., and Kinoshita, M.: Thermal response of sediment with vertical fluid flow to periodic temperature variation at the surface, Journal of Geophysical Research: Solid Earth, 110, 1–11, doi:10.1029/2004JB003419, 2005.

Grace, J. and Williams, M.: Unsaturated-zone Modeling: Progress, Challenges and Applications, chap. Understanding and parameterizing the soil–water– atmosphere transfer through vegetation, pp. 73–94, Springer Science and Business Media, 2004.

Green, W. H. and Ampt, G. A.: Studies on Soil Phyics., The Journal of Agricultural Science, 4, 1–24, doi:10.1017/S0021859600001441, 1911.

Gringarten, A. C. and Sauty, J. P.: A theoretical study of heat extraction from aquifers with uniform regional flow, Journal of Geophysical Research, 80, 4956–4962, doi:10.1029/JB080i035p04956, 1975.

Gudmundsson, L., Leonard, M., Do, H. X., Westra, S., and Seneviratne, S. I.: Observed Trends in Global Indicators of Mean and Extreme Streamflow, Geophysical Research Letters, 46, 756–766, doi:10.1029/2018GL079725, 2019.

Gudmundsson, L., Boulange, J., Do, H. X., Gosling, S. N., Grillakis, M. G., Koutroulis, A. G., Leonard, M., Liu, J., and Müller, H.: Title: Globally observed trends in mean and extreme river flow attributed to climate change, Science, 371, 1159–1162, doi:10.1126/science.aba3996, 2021.

Gunduz, O.: Coupled flow and contaminant transport modeling, Ph.D. thesis, Georgia Institute of Technology, Georgia, 2004.

Gupta, H., Harald, K., and Martinez, G.: Decomposition of the mean squared error and NSE performance criteria : Implications for improving hydrological modelling, Journal of Hydrology, 377, 80–91, doi:10.1016/j.jhydrol.2009.08.003, 2009.

Gupta, H. V., Perrin, C., Blöschl, G., Montanari, A., Kumar, R., Clark, M., and Andréassian, V.: Large-sample hydrology: a need to balance depth with breadth, Hydrology and Earth System Sciences, 18, 463–477, doi:10.5194/hess-18-463-2014, 2014.

Gurdak, J. J.: Climate-induced pumping: Groundwater, Nature Geoscience, 10, 71–71, doi:10.1038/ngeo2885, 2017.

Haag, I. and Luce, A.: The integrated water balance and water temperature model LARSIM-WT, Hydrological Processes, 22, 1046–1056, doi:10.1002/hyp.6983, 2008.

Habets, F., Boone, A., Champeaux, J. L., Etchevers, P., Franchistéguy, L., Leblois, E., Ledoux, E., Le Moigne, P., Martin, E., Morel, S., Noilhan, J., Quintana Seguí, P., Rousset-Regimbeau, F., and Viennot, P.: The SAFRAN-ISBA-MODCOU hydrometeorological model applied over France, Journal of Geophysical Research: Atmospheres, 113, doi:10.1029/2007JD008548, 2008.

Habets, F., Boé, J., Déqué, M., Ducharne, A., Gascoin, S., Ali, H., Martin, E., Pagé, C., Sauquet, E., Terray, L., Thiéry, D., Oudin, L., and Viennot, P.: Impact of climate change on the hydrogeology of two basins in northern France, Climatic Change, 121, 771–785, doi:10.1007/s10584-013-0934-x, 2013.

Hannah, D. M., Webb, B. W., and Nobilis, F.: River and stream temperature: dynamics, processes, models and implications, Hydrological Processes, 22, 899–901, doi:10.1002/hyp.6997, 2008.

Hattermann, F., Krysanova, V., Habeck, A., and Bronstert, A.: Integrating wetlands and riparian zones in river basin modelling, Ecological Modelling, 199, 379–392, doi:10.1016/j.ecolmodel.2005.06.012, 2006.

Hattermann, F., Vetter, T., Breuer, L., Su, B., Daggupati, P., Donnelly, C., Fekete, B., Florke, F., Gosling, S., Hoffmann, P., Liersch, S., Masaki, Y., Motovilov, Y., Muller, C., Samaniego, L., Stacke, T., Wada, Y., Yang, T., and Krysnaova, V.: Sources of uncertainty in hydrological climate impact assessment: A cross-scale study, Environmental Research Letters, 13, 015 006, doi:10.1088/1748-9326/aa9938, 2018.

Haverkamp, R., Vauclin, M., Touma, J., Wierenga, P. J., and Vachaud, G.: A Comparison of Numerical Simulation Models For One-Dimensional Infiltration, Soil Science Society of America Journal, 41, 285, doi:10.2136/sssaj1977.03615995004100020024x, 1977.

Hayashi, M. and Rosenberry, D. O.: Effects of Ground Water Exchange on the Hydrology and Ecology of Surface Water, Groundwater, 40, 309–316, doi:10.1111/j.1745-6584.2002.tb02659.x, 2002.

Healy, R. W. and Scanlon, B. R.: Estimating Groundwater Recharge, Cambridge University Press, 2010.

Healy, R. W., Winter, T. C., LaBaugh, J. W., and Franke, O. L.: Water Budgets: Foundations for Effective Water-Resources and Environmental Management, Circular 1308, U.S. Geological Survey, Renton, 2007.

Hemmerle, H., Hale, S., Dressel, I., Benz, S. A., Attard, G., Blum, P., and Bayer, P.: Estimation of Groundwater Temperatures in Paris, France, Geofluids, 2019, e5246 307, doi:10.1155/2019/5246307, publisher: Hindawi, 2019.

Hengl, T., Jesus, J. M. d., Heuvelink, G. B. M., Gonzalez, M. R., Kilibarda, M., Blagotić, A., Shangguan, W., Wright, M. N., Geng, X., Bauer-Marschallinger, B., Guevara, M. A., Vargas, R., MacMillan, R. A., Batjes, N. H., Leenaars, J. G. B., Ribeiro, E., Wheeler, I., Mantel, S., and Kempen, B.: SoilGrids250m: Global gridded soil information based on machine learning, PLOS ONE, 12, e0169 748, doi:10.1371/journal.pone.0169748, publisher: Public Library of Science, 2017.

Hoff, H.: Understanding the nexus, The Bonn2011 Conference: The Water, Energy and Food Security Nexus., URL https://policycommons.net/artifacts/1359033/understanding-the-nexus/1972269/, accessed on 15.04.2022, 2011.

Honnorat, M., Marin, J., Monnier, J., and Lai, X.: Dassflow v1.0: a variational data

assimilation software for 2D river flows, Bulletin of Sociological Methodology/Bulletin de Méthodologie Sociologique, 37, 55–57, doi:10.1177/075910639203700105, 1992.

Hopmans, J. W., Šimunek, J., and Bristow, K. L.: Indirect estimation of soil thermal properties and water flux using heat pulse probe measurements: Geometry and dispersion effects, Water Resources Research, 38, 7–1–7–14, doi:10.1029/2000WR000071, 2002.

Horton, R. E.: The field, scope, and status of the science of hydrology, Eos, Transactions American Geophysical Union, 12, 189–202, doi:10.1029/TR012i001p00189-2, 1931.

Horton, R. E.: The Rôle of infiltration in the hydrologic cycle, Transactions, American Geophysical Union, 14, 446, doi:10.1029/TR014i001p00446, 1933.

Hughes, J. D.: Documentation for the MODFLOW 6 Groundwater Flow Model, Tech. rep., U.S. Geological Survey, Reston, VA, 2017.

Händel, F., Liedl, R., Fank, J., and Rock, G.: Regional modeling of geothermal energy systems in shallow aquifers: the Leibnitzer Feld case study (Austria), Environmental Earth Sciences, 70, 3433–3446, doi:10.1007/s12665-013-2469-x, 2013.

IPCC: Climate change 2007: the physical science basis ; contribution of Working Group I to the Fourth Assessment Report of the Intergovernmental Panel on Climate Change, UNEP, New York, 1st published edn., oCLC: 551019794, 2007.

IPCC: Climate Change and Land, Tech. rep., IPCC, 2019.

IPCC: Climate Change 2021: The Physical Science Basis. Contribution of Working Group I to the Sixth Assessment Report of the Intergovernmental Panel on Climate Change, vol. In Press, Cambridge University Press, Cambridge, United Kingdom and New York, NY, USA, doi:10.1017/9781009157896, 2021.

Isaak, D. J., Wollrab, S., Horan, D., and Chandler, G.: Climate change effects on stream and river temperatures across the northwest U.S. from 1980–2009 and implications for salmonid fishes, Climatic Change, 113, 499–524, doi:10.1007/s10584-011-0326-z, 2012.

Isaak, D. J., Luce, C. H., Horan, D. L., Chandler, G. L., Wollrab, S. P., Dubois, W. B., and Nagel, D. E.: Thermal Regimes of Perennial Rivers and Streams in the Western United States, JAWRA Journal of the American Water Resources Association, 56, 842–867, doi:10.1111/1752-1688.12864, 2020.

Ivanov, V. Y., Vivoni, E. R., Bras, R. L., and Entekhabi, D.: Catchment hydrologic response with a fully distributed triangulated irregular network model, Water Resources Research, 40, doi:10.1029/2004WR003218, 2004a.

Ivanov, V. Y., Vivoni, E. R., Bras, R. L., and Entekhabi, D.: Preserving high-resolution surface and rainfall data in operational-scale basin hydrology: a fully-distributed physically-based approach, Journal of Hydrology, 298, 80–111, doi:10.1016/j.jhydrol.2004.03.041, 2004b.

Jarvis, N. J.: A simple empirical model of root water uptake, Journal of Hydrology, 107, 57–72, doi:10.1016/0022-1694(89)90050-4, 1989.

Jensen, J. and Engesgaard, P.: Nonuniform Groundwater Discharge across a Streambed: Heat as a Tracer, Vadose Zone Journal, 10, 98–109, doi:10.2136/vzj2010.0005, 2011.

Johansen, O.: Thermal Conductivity of Soils, Tech. Rep. July, U.S. Army Cold Regions Research and Engineering Laboratory, doi:10.1063/1.1699752, 1977.

Jolivet, C., Boulonne, L., and Ratié, C.: Manuel du Réseau de Mesures de la Qualité des Sols, Unité InfoSol, INRA, Orléans, France, URL `https://hal.inrae.fr/hal-02818011`, accessed on 03.10.2021, 2006.

Jost, A.: Caractérisation des forçages climatiques et géomorphologiques des cinq derniers millions d'années et modélisation de leurs conséquences sur un système aquifère complexe: le bassin de Paris., Ph.D. thesis, Paris 6, Paris, 2006.

Jowett, I. G., Kingsland, S., and Collier, K. J.: WAIORA user guide: Water Allocation Impacts on River Attributes, version 2.0, Hamilton: NIWA, 2004.

Jung, M., Reichstein, M., Ciais, P., Seneviratne, S. I., Sheffield, J., Goulden, M. L., Bonan, G., Cescatti, A., Chen, J., de Jeu, R., Dolman, A. J., Eugster, W., Gerten, D.,

Gianelle, D., Gobron, N., Heinke, J., Kimball, J., Law, B. E., Montagnani, L., Mu, Q., Mueller, B., Oleson, K., Papale, D., Richardson, A. D., Roupsard, O., Running, S., Tomelleri, E., Viovy, N., Weber, U., Williams, C., Wood, E., Zaehle, S., and Zhang, K.: Recent decline in the global land evapotranspiration trend due to limited moisture supply, Nature, 467, 951–954, doi:10.1038/nature09396, 2010.

Kaandorp, V. P., Doornenbal, P. J., Kooi, H., Peter Broers, H., and de Louw, P. G. B.: Temperature buffering by groundwater in ecologically valuable lowland streams under current and future climate conditions, Journal of Hydrology X, 3, 100 031, doi:10.1016/j.hydroa.2019.100031, 2019.

Kalbus, E., Schmidt, C., Molson, J. W., Reinstorf, F., and Schirmer, M.: Influence of aquifer and streambed heterogeneity on the distribution of groundwater discharge, Hydrol. Earth Syst. Sci., 13, 69–77, doi:10.5194/hess-13-69-2009, 2009.

Kampf, S. K. and Burges, S. J.: A framework for classifying and comparing distributed hillslope and catchment hydrologic models, Water Resources Research, 43, doi:10.1029/2006WR005370, 2007.

Kendall, M. G.: Further contributions to the theory of paired comparisons, Biometrics, 11, 43–62, publisher: JSTOR, 1955.

Kilic, D., Rivière, A., Flipo, N., Ducharne, A., Ghattas, J., Raoult, N., , Peylin, P., Demarty, J., Cappelaere, B., Barral, H., Ansart, P., Blanchouin, A., Baudin, A., Marlot, L., and Goblet, P.: Sensitivity analysis of surface water balance in ORHCIDEE: Case study on the Avenelles basin, in: 3e Journées de Modélisation des Surfaces Continentales, p. 1, 2019.

Kilic, D., Rivière, A., Flipo, N., Ducharne, A., Peylin, P., and Goblet, P.: Integrated modeling of water and heat fluxes in the Seine hydrosystem, France, in: EGU General Assembly Conference Abstracts, pp. EGU21–4351, 2021a.

Kilic, D., Rivière, A., Flipo, N., Ducharne, A., Peylin, P., and Goblet, P.: Integrated

modeling of water and heat fluxes in the Seine hydrosystem, France, in: EGU General Assembly Conference Abstracts, pp. EGU21–4351, 2021b.

King, I. P.: Rma-11: A three-dimensional finite element model for water quality in estuaries and streams version 2.5, Dept. of Civil and Environmental Engineering, University of California Davis, California, Tech. Rep, 1997.

King, T. V. and Neilson, B. T.: Quantifying Reach-Average Effects of Hyporheic Exchange on Arctic River Temperatures in an Area of Continuous Permafrost, Water Resources Research, 55, 1951–1971, doi:10.1029/2018WR023463, 2019.

Kløve, B., Ala-Aho, P., Bertrand, G., Gurdak, J. J., Kupfersberger, H., Kværner, J., Muotka, T., Mykrä, H., Preda, E., Rossi, P., Uvo, C. B., Velasco, E., and Pulido-Velazquez, M.: Climate change impacts on groundwater and dependent ecosystems, Journal of Hydrology, 518, 250–266, doi:10.1016/j.jhydrol.2013.06.037, 2014.

Knijff, J. M. V. D., Younis, J., and Roo, A. P. J. D.: LISFLOOD: a GIS-based distributed model for river basin scale water balance and flood simulation, International Journal of Geographical Information Science, 24, 189–212, doi:10.1080/13658810802549154, 2010.

Knutti, R. and Sedláček, J.: Robustness and uncertainties in the new CMIP5 climate model projections, Nature Climate Change, 3, 369–373, doi:10.1038/nclimate1716, 2013.

Koster, R. D. and Suarez, M. J.: The components of a 'SVAT' scheme and their effects on a GCM's hydrological cycle, Advances in Water Resources, 17, 61–78, doi:10.1016/0309-1708(94)90024-8, 1994.

Koster, R. D., Suarez, M. J., Ducharne, A., Stieglitz, M., and Kumar, P.: A catchment-based approach to modeling land surface processes in a general circulation model: 1. Model structure, Journal of Geophysical Research: Atmospheres, 105, 24 809–24 822, doi:10.1029/2000JD900327, 2000.

Kowalczyk, E. A., Wang, Y. P., Law, R. M., Davies, H. L., McGregor, J. L., and Abramowitz, G.: The CSIRO Atmosphere Biosphere Land Exchange (CABLE) model for use in climate models and as an offline model, CSIRO Marine and Atmospheric Research Paper, p. 42, 2006.

Krause, S., Lewandowski, J., Grimm, N. B., Hannah, D. M., Pinay, G., McDonald, K., Martí, E., Argerich, A., Pfister, L., Klaus, J., Battin, T., Larned, S. T., Schelker, J., Fleckenstein, J., Schmidt, C., Rivett, M. O., Watts, G., Sabater, F., Sorolla, A., and Turk, V.: Ecohydrological interfaces as hot spots of ecosystem processes, Water Resources Research, 53, 6359–6376, doi:10.1002/2016WR019516, 2017.

Krinner, G., Viovy, N., de Noblet-Ducoudré, N., Ogée, J., Polcher, J., Friedlingstein, P., Ciais, P., Sitch, S., and Prentice, I. C.: A dynamic global vegetation model for studies of the coupled atmosphere-biosphere system, Global Biogeochemical Cycles, 19, 1–33, doi:10.1029/2003GB002199, 2005.

Krysanova, V., Vetter, T., Eisner, S., Huang, S., Pechlivanidis, I., Strauch, M., Gelfan, A., Kumar, R., Aich, V., Arheimer, B., Chamorro, A., Griensven, A. v., Kundu, D., Lobanova, A., Mishra, V., Plötner, S., Reinhardt, J., Seidou, O., Wang, X., Wortmann, M., Zeng, X., and Hattermann, F. F.: Intercomparison of regional-scale hydrological models and climate change impacts projected for 12 large river basins worldwide—a synthesis, Environmental Research Letters, 12, 105 002, doi:10.1088/1748-9326/aa8359, publisher: IOP Publishing, 2017.

Kundzewicz, Z. W., Mata, L. J., Arnell, N. W., Doll, P, P., Jimenez, B., Miller, K., Oki, T., Sen, Z., and Shiklomanov, Igor A., I.: The implications of projected climate change for freshwater resources and their management, Hydrological Sciences Journal, 53, 3–10, doi:10.1623/hysj.53.1.3, 2008.

Kupfersberger, H., Rock, G., and Draxler, J. C.: Inferring near surface soil temperature time series from different land uses to quantify the variation of heat fluxes into a shallow aquifer in Austria, Journal of Hydrology, 552, 564–577, doi:10.1016/j.jhydrol.2017.07.030, 2017.

Kurylyk, B. L., MacQuarrie, K., and McKenzie, J.: Climate change impacts on groundwater and soil temperatures in cold and temperate regions: Implications, mathematical theory, and emerging simulation tools, Earth Science Reviews, 138, 313–334, doi:10.1016/j.earscirev.2014.06.006, 2014.

Kurylyk, B. L., MacQuarrie, K. T. B., Caissie, D., and McKenzie, J. M.: Shallow groundwater thermal sensitivity to climate change and land cover disturbances: derivation of analytical expressions and implications for stream temperature modeling, Hydrology and Earth System Sciences, 19, 2469–2489, doi:10.5194/hess-19-2469-2015, 2015.

Kurylyk, B. L., Irvine, D. J., Carey, S. K., Briggs, M. A., Werkema, D. D., and Bonham, M.: Heat as a groundwater tracer in shallow and deep heterogeneous media: Analytical solution, spreadsheet tool, and field applications, Hydrological processes, 31, 2648–2661, doi:10.1002/hyp.11216, 2017.

Labarthe, B.: Quantification des échanges nappe-rivière au sein de l'hydrosystème Seine par modélisation multi-échelle, Ph.D. thesis, MINES ParisTech, PSL Research University, 2016.

Lange, S.: ISIMIP2b Bias-Correction Code, doi:10.5281/zenodo.1069050, URL `https://doi.org/10.5281/zenodo.1069050`, 2017.

Lavers, D. A., Hannah, D. M., and Bradley, C.: Connecting large-scale atmospheric circulation, river flow and groundwater levels in a chalk catchment in southern England, Journal of Hydrology, 523, 179–189, doi:10.1016/j.jhydrol.2015.01.060, 2015.

Le Lay, H., Thomas, Z., Rouault, F., Pichelin, P., and Moatar, F.: Characterization of Diffuse Groundwater Inflows into Stream Water (Part II: Quantifying Groundwater Inflows by Coupling FO-DTS and Vertical Flow Velocities), Water, 11, 2430, doi:10.3390/w11122430, 2019.

Le Moal, M., Gascuel-Odoux, C., Ménesguen, A., Souchon, Y., Étrillard, C., Levain, A., Moatar, F., Pannard, A., Souchu, P., Lefebvre, A., et al.: Eutrophica-

tion: a new wine in an old bottle?, Science of the Total Environment, 651, 1–11, doi:10.1016/j.scitotenv.2018.09.139, 2019.

LeBlanc, R. T., Brown, R. D., and FitzGibbon, J. E.: Modeling the Effects of Land Use Change on the Water Temperature in Unregulated Urban Streams, Journal of Environmental Management, 49, 445–469, doi:10.1006/jema.1996.0106, 1997.

Ledoux, E.: Modélisation intégrée des écoulements de surface et des écoulements souterrains sur un bassin hydrologique, Ph.D. thesis, ENSMP, UPMC, 1980.

Ledoux, E., Girard, G., de Marsily, G., Villeneuve, J. P., and Deschenes, J.: Spatially Distributed Modeling: Conceptual Approach, Coupling Surface Water And Groundwater, pp. 435–454, Springer Netherlands, Dordrecht, doi:https://doi.org/10.1007/978-94-009-2352-2_16, 1989.

Ledoux, E., Gomez, E., Monget, J., Viavattene, C., Viennot, P., Ducharne, A., Benoit, M., Mignolet, C., Schott, C., and Mary, B.: Agriculture and groundwater nitrate contamination in the Seine basin. The STICS-MODCOU modelling chain, STOTEN, 375, 33–47, doi:10.1016/j.scitotenv.2006.12.002, 2007.

Lee, K. S.: A Review on Concepts, Applications, and Models of Aquifer Thermal Energy Storage Systems, Energies, 3, 1320–1334, doi:10.3390/en3061320, number: 6 Publisher: Molecular Diversity Preservation International, 2010.

Lehner, F., Deser, C., Maher, N., Marotzke, J., Fischer, E. M., Brunner, L., Knutti, R., and Hawkins, E.: Partitioning climate projection uncertainty with multiple large ensembles and CMIP5/6, Earth System Dynamics, 11, 491–508, 2020.

Leij, F. J., Russell, W. B., and Lesch, S. M.: Closed-Form Expressions for Water Retention and Conductivity Data, Groundwater, 35, 848–858, doi:10.1111/j.1745-6584.1997.tb00153.x, 1997.

Lestel, L., Eschbach, D., Meybeck, M., and Gob, F.: The Evolution of the Seine Basin Water Bodies Through Historical Maps, in: The Seine River Basin, edited by Flipo, N., Labadie, P., and Lestel, L., vol. 90, pp. 29–57, Springer International Publishing, Cham,

doi:10.1007/698_2019_396, series Title: The Handbook of Environmental Chemistry, 2020.

Liang, X., Lettenmaier, D. P., Wood, E. F., and Burges, S. J.: A simple hydrologically based model of land surface water and energy fluxes for general circulation models, Journal of Geophysical Research, 99, 14 415, doi:10.1029/94JD00483, 1994.

Liu, J., Yang, H., Gosling, S. N., Kummu, M., Flörke, M., Pfister, S., Hanasaki, N., Wada, Y., Zhang, X., Zheng, C., et al.: Water scarcity assessments in the past, present, and future, Earth's future, 5, 545–559, doi:10.1002/2016EF000518, 2017.

Loheide, S. P. and Booth, E. G.: Effects of changing channel morphology on vegetation, groundwater, and soil moisture regimes in groundwater-dependent ecosystems, Geomorphology, 126, 364–376, doi:10.1016/j.geomorph.2010.04.016, 2011.

Loheide, S. P. and Gorelick, S. M.: A local-scale, high-resolution evapotranspiration mapping algorithm (ETMA) with hydroecological applications at riparian meadow restoration sites, Remote Sensing of Environment, 98, 182–200, doi:10.1016/j.rse.2005.07.003, 2005.

Loicq, P., Moatar, F., Jullian, Y., Dugdale, S. J., and Hannah, D. M.: Improving representation of riparian vegetation shading in a regional stream temperature model using LiDAR data, Science of The Total Environment, 624, 480–490, doi:10.1016/j.scitotenv.2017.12.129, 2018.

Loinaz, M. C., Kampp Davidsen, H., Butts, M., and Bauer-Gottwein, P.: Integrated flow and temperature modeling at the catchment scale, Journal of Hydrology, 495, 238–251, doi:10.1016/j.jhydrol.2013.04.039, 2013.

Loinaz, M. C., Gross, D., Unnasch, R., Butts, M., and Bauer-Gottwein, P.: Modeling ecohydrological impacts of land management and water use in the Silver Creek basin, Idaho: Ecohydrological impacts in Silver Creek, Journal of Geophysical Research: Biogeosciences, 119, 487–507, doi:10.1002/2012JG002133, 2014.

Long, D., Longuevergne, L., and Scanlon, B. R.: Uncertainty in evapotranspiration from land surface modeling, remote sensing, and GRACE satellites, Water Resources Research, 50, 1131–1151, doi:10.1002/2013WR014581, 2014.

Lopez, S., Hamm, V., Le Brun, M., Schaper, L., Boissier, F., Cotiche, C., and Giuglaris, E.: 40 years of Dogger aquifer management in Ile-de-France, Paris Basin, France, Geothermics, 39, 339–356, doi:10.1016/j.geothermics.2010.09.005, 2010.

Lurton, T., Balkanski, Y., Bastrikov, V., Bekki, S., Bopp, L., Braconnot, P., Brockmann, P., Cadule, P., Contoux, C., Cozic, A., Cugnet, D., Dufresne, J.-L., Éthé, C., Foujols, M.-A., Ghattas, J., Hauglustaine, D., Hu, R.-M., Kageyama, M., Khodri, M., Lebas, N., Guillaume, L., Marchand, M., Ottlé, C., Peylin, P., Sima, A., Szopa, S., Thiéblemont, R., Vuichard, N., and Boucher, O.: Implementation of the CMIP6 Forcing Data in the IPSL-CM6A-LR Model, Journal of Advances in Modeling Earth Systems, 12, e2019MS001 940, doi:https://doi.org/10.1029/2019MS001940, 2020.

Magnusson, J., Jonas, T., and Kirchner, J. W.: Temperature dynamics of a proglacial stream: Identifying dominant energy balance components and inferring spatially integrated hydraulic geometry, Water Resources Research, 48, doi:10.1029/2011WR011378, 2012.

Maillot, M.: Étude des remontées de nappe de Paris et de la Petite Couronne lors des épisodes de crue de la Seine et de la Marne, Ph.D. thesis, MINES ParisTech, 2019.

Manabe, S.: Climate and the ocean circulation, Monthly Weather Review, 97, 739–774, doi:10.1175/1520-0493(1969)097<0739:CATOC>2.3.CO;2, 1969.

Maraun, D., Wetterhall, F., Ireson, A. M., Chandler, R. E., Kendon, E. J., Widmann, M., Brienen, S., Rust, H. W., Sauter, T., Themeßl, M., Venema, V. K. C., Chun, K. P., Goodess, C. M., Jones, R. G., Onof, C., Vrac, M., and Thiele-Eich, I.: Precipitation downscaling under climate change: Recent developments to bridge the gap between dynamical models and the end user, Reviews of Geophysics, 48, RG3003, doi:10.1029/2009RG000314, 2010.

Marescaux, A., Thieu, V., Gypens, N., Silvestre, M., and Garnier, J.: Modeling inorganic carbon dynamics in the Seine River continuum in France, Hydrology and Earth System Sciences, 24, 2379–2398, doi:10.5194/hess-24-2379-2020, 2020.

Martens, B.: GLEAM - Global Land Evaporation Amsterdam Model, 2019.

Martens, B., De Jeu, R. A. M., Verhoest, N. E. C., Schuurmans, H., Kleijer, J., and Miralles, D. G.: Towards Estimating Land Evaporation at Field Scales Using GLEAM, Remote Sensing, 10, 1720, doi:10.3390/rs10111720, number: 11 Publisher: Multidisciplinary Digital Publishing Institute, 2018.

Massei, N., Laignel, B., Deloffre, J., Mesquita, J., Motelay, A., Lafite, R., and Durand, A.: Long-term hydrological changes of the Seine River flow (France) and their relation to the North Atlantic Oscillation over the period 1950-2008, Int. J. Climatol., 30, 2146–2154, doi:10.1002/joc.2022, 2010.

Masson-Delmotte, V., Zhai, P., Pörtner, H. O., Roberts, D., Skea, J., Shukla, P., Pirani, A., Moufouma-Okia, W., Péan, C., Pidcock, R., Connors, S., Matthews, J. B. R., Chen, Y., Zhou, X., Gomis, M. I., Lonnoy, E., Maycock, T., Tignor, M., and Waterfield, T., eds.: Global Warming of 1.5° C: An IPCC Special Report on the Impacts of Global Warming of 1.5° C Above Pre-industrial Levels and Related Global Greenhouse Gas Emission Pathways, in the Context of Strengthening the Global Response to the Threat of Climate Change, Sustainable Development, and Efforts to Eradicate Poverty, Intergovernmental Panel on Climate Change, 2018.

Maxwell, R. and Kollet, S.: Quantifying the effects of three-dimensional subsurface heterogeneity on Hortonian runoff processes using a coupled numerical, stochastic approach, Advances in Water Resources, 31, 807–817, doi:10.1016/j.advwatres.2008.01.020, 2008a.

Maxwell, R. M. and Condon, L. E.: Connections between groundwater flow and transpiration partitioning, Science, 353, 377–380, doi:10.1126/science.aaf7891, 2016.

Maxwell, R. M. and Kollet, S. J.: Interdependence of groundwater dynamics

and land-energy feedbacks under climate change, Nature Geoscience, 1, 665–669, doi:10.1038/ngeo315, 2008b.

Maxwell, R. M. and Miller, N. L.: Development of a Coupled Land Surface and Groundwater Model, Journal of Hydrometeorology, 6, 233–247, doi:10.1175/JHM422.1, 2005.

Maxwell, R. M., Chow, F. K., and Kollet, S. J.: The groundwater–land-surface–atmosphere connection: Soil moisture effects on the atmospheric boundary layer in fully-coupled simulations, Advances in Water Resources, 30, 2447–2466, doi:10.1016/j.advwatres.2007.05.018, 2007.

Maxwell, R. M., Putti, M., Meyerhoff, S., Delfs, J.-O., Ferguson, I. M., Ivanov, V., Kim, J., Kolditz, O., Kollet, S. J., Kumar, M., Lopez, S., Niu, J., Paniconi, C., Park, Y.-J., Phanikumar, M. S., Shen, C., Sudicky, E. A., and Sulis, M.: Surface-subsurface model intercomparison: A first set of benchmark results to diagnose integrated hydrology and feedbacks, Water Resources Research, 50, 1531–1549, doi:10.1002/2013WR013725, 2014.

McConnell, C. and Pingen, G.: Multi-Layer, Pseudo 3D Thermal Topology Optimization of Heat Sinks, in: Volume 7: Fluids and Heat Transfer, Parts A, B, C, and D, p. 2381, ASME, Houston, Texas, USA, doi:10.1115/IMECE2012-93093, 2012.

Meehl, G. A., Stocker, T. F., Collins, W. D., Friedlingstein, P., Gaye, A. T., Gregory, J. M., Kitoh, A., Knutti, R., Murphy, J. M., Noda, A., et al.: Global climate projections, in: Climate Change 2007: the physical science basis, pp. 747–846, Cambridge University Press, 2007.

Merlin, O., Stefan, V. G., Amazirh, A., Chanzy, A., Ceschia, E., Er-Raki, S., Gentine, P., Tallec, T., Ezzahar, J., Bircher, S., Beringer, J., and Khabba, S.: Modeling soil evaporation efficiency in a range of soil and atmospheric conditions using a meta-analysis approach, Water Resources Research, 52, 3663–3684, doi:10.1002/2015WR018233, 2016.

Meybeck, M.: Riverine quality at the Anthropocene: Propositions for global space and time analysis, illustrated by the Seine River, Aquatic Sciences, 64, 376–393, doi:10.1007/PL00012593, 2002.

Meybeck, M., de Marsily, G., and Fustec, E.: La Seine en son bassin: fonctionnement écologique d'un système fluvial anthropisé, Elsevier, 1998.

Miguez-Macho, G., Fan, Y., Weaver, C. P., Walko, R., and Robock, A.: Incorporating water table dynamics in climate modeling: 2. Formulation, validation, and soil moisture simulation, Journal of Geophysical Research: Atmospheres, 112, doi:10.1029/2006JD008112, 2007.

Milly, P. C. D. and Dunne, K. A.: Trends in evaporation and surface cooling in the Mississippi River Basin, Geophysical Research Letters, 28, 1219–1222, doi:10.1029/2000GL012321, 2001.

Milly, P. C. D., Wetherald, R. T., Dunne, K. A., and Delworth, T. L.: Increasing risk of great floods in a changing climate, Nature, 415, 514–517, doi:10.1038/415514a, 2002.

Milly, P. C. D., Malyshev, S. L., Shevliakova, E., Dunne, K. A., Findell, K. L., Gleeson, T., Liang, Z., Phillipps, P., Stouffer, R. J., and Swenson, S.: An Enhanced Model of Land Water and Energy for Global Hydrologic and Earth-System Studies, Journal of Hydrometeorology, 15, 1739–1761, doi:10.1175/JHM-D-13-0162.1, 2014.

Minaudo, C., Meybeck, M., Moatar, F., Gassama, N., and Curie, F.: Eutrophication mitigation in rivers: 30 years of trends in spatial and seasonal patterns of biogeochemistry of the Loire River (1980–2012), Biogeosciences, 12, 2549–2563, doi:https://doi.org/10.5194/bg-12-2549-2015, 2015.

Moatar, F. and Gailhard, J.: Water temperature behaviour in the River Loire since 1976 and 1881, Comptes Rendus Geoscience, 338, 319–328, doi:10.1016/j.crte.2006.02.011, 2006.

Moigne, P. L.: SURFEX Scientific Documentation, Tech. rep., CNRM, Météo-France, 2012.

Monninkhoff, B. L. and Li, Z.: Coupling FEFLOW and MIKE11 to optimise the flooding system of the Lower Havel polders in Germany, International Journal of Water, 2009.

Monteiro, L., Figueiredo, D., Covas, D., and Menaia, J.: Integrating water temperature in chlorine decay modelling: a case study, Urban Water Journal, 14, 1097–1101, doi:10.1080/1573062X.2017.1363249, 2017.

Monteith, J.: Evaporation and environment, Symposia of the Society for Experimental Biology, 19, 205–234, 1965.

Morin, G. and Paquet, P.: Modèle hydrologique CEQUEAU, Tech. Rep. R000926, Université du Québec, INRS-Eau, Terre et Environnement, Québec, 2007.

Motovilov, Y. G., Gottschalk, L., Engeland, K., and Belokurov, A.: ECOMAG: Regional model of hydrological cycle, Institute Report Series, p. 88, 1999.

Mualem, Y.: A new model for predicting the hydraulic conductivity of unsaturated porous media, Water Resources Research, 12, 513–522, doi:10.1029/WR012i003p00513, 1976.

Mueller, M. H., Huggenberger, P., and Epting, J.: Combining monitoring and modelling tools as a basis for city-scale concepts for a sustainable thermal management of urban groundwater resources, Science of The Total Environment, 627, 1121–1136, doi:10.1016/j.scitotenv.2018.01.250, 2018.

Nash, J. E.: Systematic determination of unit hydrograph parameters, Journal of Geophysical Research (1896-1977), 64, 111–115, doi:10.1029/JZ064i001p00111, 1959.

NEA: Nuclear Energy Data 2019, OECD, doi:https://doi.org/https://doi.org/10.1787/1786b86b-en-fr, URL https://www.oecd-ilibrary.org/content/publication/1786b86b-en-fr, 2020.

Nguyen-Quang, T., Polcher, J., Ducharne, A., Arsouze, T., Zhou, X., Schneider, A., and Fita, L.: ORCHIDEE-ROUTING: revising the river routing scheme using a high-

resolution hydrological database, Geoscientific Model Development, 11, 4965–4985, doi:10.5194/gmd-11-4965-2018, 2018.

Niu, G.-Y., Yang, Z.-L., Dickinson, R. E., Gulden, L. E., and Su, H.: Development of a simple groundwater model for use in climate models and evaluation with Gravity Recovery and Climate Experiment data, Journal of Geophysical Research: Atmospheres, 112, doi:10.1029/2006JD007522, 2007.

Noilhan, J., , and Lacarrere, P.: GCM grid-scale evaporation from mesoscale modeling, Journal of climate, 8, 206–223, 1995.

Okkonen, J. and Klove, B.: A sequential modelling approach to assess groundwater–surface water resources in a snow dominated region of Finland, Journal of Hydrology, 411, 91–107, doi:10.1016/j.jhydrol.2011.09.038, publisher: Elsevier, 2011.

Oleson, K. W., Lawrence, D. M., Flanner, M. G., Kluzek, E., Levis, S., Swenson, S. C., Thornton, E., Dai, A., Decker, M., Dickinson, R., Feddema, J., Heald, C. L., Lamarque, J.-F., Niu, G.-Y., Qian, T., Running, S., Sakaguchi, K., Slater, A., Stöckli, R., Wang, A., Yang, L., Zeng, X., and Zeng, X.: Technical Description of version 4.0 of the Community Land Model (CLM), Tech. rep., NCAR, 2010.

Otalora, M.: Simulating the Seine River discharge using the land surface model ORCHIDEE, Tech. rep., Université Pierre et Marie Curie, Paris 6, 2016.

Pal, J. S., Giorgi, F., Bi, X., Elguindi, N., Solmon, F., Gao, X., Rauscher, S. A., Francisco, R., Zakey, A., Winter, J., Ashfaq, M., Syed, F. S., Bell, J. L., Diffenbaugh, N. S., Karmacharya, J., Konaré, A., Martinez, D., da Rocha, R. P., Sloan, L. C., and Steiner, A. L.: Regional Climate Modeling for the Developing World: The ICTP RegCM3 and RegCNET, Bulletin of the American Meteorological Society, 88, 1395–1410, doi:10.1175/BAMS-88-9-1395, 2007.

Panday, S. and Huyakorn, P. S.: A fully coupled physically-based spatially-distributed model for evaluating surface/subsurface flow, Advances in Water Resources, 27, 361–382, doi:10.1016/j.advwatres.2004.02.016, 2004.

Pekárová, P., Miklánek, P., Halmová, D., Onderka, M., Pekár, J., Kučárová, K., Liová, S., and Škoda, P.: Long-term trend and multi-annual variability of water temperature in the pristine Bela River basin (Slovakia), Journal of Hydrology, 400, 333–340, doi:10.1016/j.jhydrol.2011.01.048, 2011.

Penman, H. L.: Natural evaporation from open water, bare soil and grass, Royal Society Publishing, 193, 120–147, doi:10.1098/rspa.1948.0037, 1948.

Peters-Lidard, C. D., Blackburn, E., Liang, X., and Wood, E. F.: The Effect of Soil Thermal Conductivity Parameterization on Surface Energy Fluxes and Temperatures, Journal of the Atmospheric Sciences, 55, 1209–1224, doi:10.1175/1520-0469(1998)055<1209:TEOSTC>2.0.CO;2, 1998.

Peterson, D. and Wilson, J.: Variably saturated flow between streams and aquifers, Tech Completion Rep 233, New Mexico Water Resources Research Institute, Socorro, 1988.

Peylin, P., C., B., MacBean, N., Leonard, S., Rayner, P., Kuppel, S., Koffi, E., Kane, A., Maignan, F., Chevallier, F., Ciais, P., and Prunet, P.: A new stepwise carbon cycle data assimilation system using multiple data streams to constrain the simulated land surface carbon cycle, Geoscientific Model Development, 9, 3321–3346, doi:10.5194/gmd-9-3321-2016, 2016.

Pielke, R. A.: Mesoscale Meteorological Modeling, Academic Press, 2013.

Pitman, A. J.: The evolution of, and revolution in, land surface schemes designed for climate models, International Journal of Climatology, 23, 479–510, doi:10.1002/joc.893, 2003.

Pokhrel, Y. N., Koirala, S., Yeh, P. J.-F., Hanasaki, N., Longuevergne, L., Kanae, S., and Oki, T.: Incorporation of groundwater pumping in a global Land Surface Model with the representation of human impacts, Water Resources Research, 51, 78–96, doi:10.1002/2014WR015602, 2015.

Prest, E. I., Hammes, F., van Loosdrecht, M. C. M., and Vrouwenvelder, J. S.: Bi-

ological Stability of Drinking Water: Controlling Factors, Methods, and Challenges, Frontiers in Microbiology, 7, doi:10.3389/fmicb.2016.00045, 2016.

Pryet, A., Labarthe, B., Saleh, F., Akopian, M., and Flipo, N.: Reporting of Stream-Aquifer Flow Distribution at the Regional Scale with a Distributed Process-Based Model, Water Resources Management, 29, 139–159, doi:10.1007/s11269-014-0832-7, 2015.

Qian, B., Gregorich, E. G., Gameda, S., Hopkins, D. W., and Wang, X. L.: Observed soil temperature trends associated with climate change in Canada, Journal of Geophysical Research: Atmospheres, 116, doi:10.1029/2010JD015012, 2011.

Qian, T., Dai, A., and Trenberth, K. E.: Hydroclimatic Trends in the Mississippi River Basin from 1948 to 2004, Journal of Climate, 20, 4599–4614, doi:10.1175/JCLI4262.1, 2007.

Qiu, H., Blaen, P., Comer-Warner, S., Hannah, D. M., Krause, S., and Phanikumar, M. S.: Evaluating a coupled phenology – surface energy balance model to understand stream – subsurface temperature dynamics in a mixed-use farmland catchment, Water Resources Research, doi:10.1029/2018WR023644, 2019.

Qu, Y. and Duffy, C. J.: A semidiscrete finite volume formulation for multiprocess watershed simulation, Water Resources Research, 43, doi:10.1029/2006WR005752, 2007.

Querner, E. P.: Description and application of the combined surface and groundwater flow model MOGROW, Journal of Hydrology, 192, 158–188, doi:10.1016/S0022-1694(96)03107-1, 1997.

Quintana-Seguí, P., Le Moigne, P., Durand, Y., Martin, E., Habets, F., Baillon, M., Canellas, C., Franchisteguy, L., and Morel, S.: Analysis of Near-Surface Atmospheric Variables: Validation of the SAFRAN Analysis over France, Journal of Applied Meteorology and Climatology, 47, 92–107, doi:10.1175/2007JAMC1636.1, publisher: American Meteorological Society, 2008.

R Core Team: R: A Language and Environment for Statistical Computing, URL https://www.r-project.org/, 2017.

Raoult, N., Ottlé, C., Peylin, P., Bastrikov, V., and Maugis, P.: Evaluating and Optimizing Surface Soil Moisture Drydowns in the ORCHIDEE Land Surface Model at In Situ Locations, Journal of Hydrometeorology, 22, 1025–1043, doi:10.1175/JHM-D-20-0115.1, 2021.

Renard, F. and Tognelli, A.: A new quasi-3D unsaturated–saturated hydrogeologic model of the Plateau de Saclay (France), Journal of Hydrology, 535, 495–508, doi:10.1016/j.jhydrol.2016.02.014, 2016.

Reynolds, C. A., Jackson, T. J., and Rawls, W. J.: Estimating soil water-holding capacities by linking the Food and Agriculture Organization Soil map of the world with global pedon databases and continuous pedotransfer functions, Water Resources Research, 36, 3653–3662, doi:10.1029/2000WR900130, 2000.

Richards, L. A.: Capillary conduction of liquids through porous mediums, Physics, 1, 318–333, doi:10.1063/1.1745010, 1931.

Richards, L. A. and Weaver, L. R.: Moisture retention by some irrigated soils as related to soil moisture tension, Journal of Agricultural Research, 69, 215–235, 1944.

Rienecker, M. M., Suarez, M. J., Gelaro, R., Todling, R., Bacmeister, J., Liu, E., Bosilovich, M. G., Schubert, S. D., Takacs, L., Kim, G.-K., Bloom, S., Chen, J., Collins, D., Conaty, A., da Silva, A., Gu, W., Joiner, J., Koster, R. D., Lucchesi, R., Molod, A., Owens, T., Pawson, S., Pegion, P., Redder, C. R., Reichle, R., Robertson, F. R., Ruddick, A. G., Sienkiewicz, M., and Woollen, J.: MERRA: NASA's Modern-Era Retrospective Analysis for Research and Applications, Journal of Climate, 24, 3624–3648, doi:10.1175/JCLI-D-11-00015.1, publisher: American Meteorological Society, 2011.

Rigon, R., Bertoldi, G., and Over, T. M.: GEOtop: A Distributed Hydrological Model with Coupled Water and Energy Budgets, Journal of Hydrometeorology, 7, 371–388, doi:10.1175/JHM497.1, 2006.

Ringard, J., Chiriaco, M., Bastin, S., and Habets, F.: Recent trends in climate variability at the local scale using 40 years of observations: the case of the Paris region of France, Atmospheric Chemistry and Physics, 19, 13 129–13 155, doi:https://doi.org/10.5194/acp-19-13129-2019, publisher: Copernicus GmbH, 2019.

Rivière, A.: Influences du pergélisol sur les écoulements souterrains et leurs échanges avec une rivière : étude numérique et expérimentale, Ph.D. thesis, Université Pierre et Marie Curie, Paris, 2012.

Rivière, A.: LIBTTC: Notice Technique v0.0.9, Tech. rep., MINES ParisTech, 2017.

Rivière, A., Ladet, D., Thomas, W., Le Breton, G., Ducharne, A., Oudin, L., and de France, D. I.: Projections des températures de l'eau de la Seine à Paris à l'horizon, PIREN Seine, URL `https://hal-mines-paristech.archives-ouvertes.fr/hal-03533469`, accessed on 21.02.2022, 2021.

Rivière, A., Gonçalvès, J., Jost, A., and Font, M.: Experimental and numerical assessment of transient stream–aquifer exchange during disconnection, Journal of Hydrology, 517, 574–583, doi:10.1016/j.jhydrol.2014.05.040, 2014.

Rivière, A., Gonçalvès, J., and Jost, A.: agnes-riviere/ginette: Ginette-2020-09, doi:10.5281/zenodo.4058821, 2020.

Rock, G. and Kupfersberger, H.: 3D modeling of groundwater heat transport in the shallow Westliches Leibnitzer Feld aquifer, Austria, Journal of Hydrology, 557, 668–678, doi:10.1016/j.jhydrol.2017.12.060, 2018.

Roulier, S., Baran, N., Mouvet, C., Stenemo, F., Morvan, X., Albrechtsen, H.-J., Clausen, L., and Jarvis, N.: Controls on atrazine leaching through a soil-unsaturated fractured limestone sequence at Brévilles, France, Journal of Contaminant Hydrology, 84, 81–105, doi:10.1016/j.jconhyd.2005.12.004, 2006.

Rousset, F., Habets, F., Gomez, E., Moigne, P. L., Morel, S., Noilhan, J., and Ledoux, E.: Hydrometeorological modeling of the Seine basin using the SAFRAN-

ISBA-MODCOU system, Journal of Geophysical Research: Atmospheres, 109, doi:10.1029/2003JD004403, 2004.

Rushton, K., Eilers, V., and Carter, R.: Improved soil moisture balance methodology for recharge estimation, Journal of Hydrology, 318, 379–399, doi:10.1016/j.jhydrol.2005.06.022, 2006.

Rutherford, J. C., Blackett, S., Blackett, C., Saito, L., and Davies-Colley, R. J.: Predicting the effects of shade on water temperature in small streams, New Zealand journal of marine and freshwater research, 31, 707–721, doi:10.1080/00288330.1997.9516801, 1997.

Saleh, F., Flipo, N., Habets, F., Ducharne, A., Oudin, L., Viennot, P., and Ledoux, E.: Modeling the impact of in-stream water level fluctuations on stream-aquifer interactions at the regional scale, Journal of Hydrology, 400, 490–500, doi:10.1016/j.jhydrol.2011.02.001, 2011.

Samaniego, L., Kumar, R., and Attinger, S.: Multiscale parameter regionalization of a grid-based hydrologic model at the mesoscale, Water Resources Research, 46, doi:10.1029/2008WR007327, 2010.

Sansone, A. L. and Lettenmaier, D. P.: A GIS-based temperature model for the prediction of maximum stream temperatures in the cascade mountain region, Technical 168, University of Washington, 2001.

Sauer, V. B. and Meyer, R.: Determination of error in individual discharge measurements, Tech. rep., US Geological Survey; Books and Open-File Reports Section [distributor], URL `https://pubs.er.usgs.gov/publication/ofr92144`, accessed on 04.03.2022, 1992.

Scanlon, B., Healy, R., and Cook, P.: Choosing appropriate techniques for quantifying groundwater recharge, Hydrogeology Journal, 10, 18–39, doi:10.1007/s10040-001-0176-2, 2002.

Schaap, M. G. and Leij, F. J.: Improved Prediction of Unsaturated Hydraulic Conductivity with the Mualem-van Genuchten Model, Soil Science Society of America Journal, 64, 843–851, doi:10.2136/sssaj2000.643843x, 2000.

Scheck-Wenderoth, M., Cacace, M., Maystrenko, Y. P., Cherubini, Y., Noack, V., Kaiser, B. O., Sippel, J., and Björn, L.: Models of heat transport in the Central European Basin System: Effective mechanisms at different scales, Marine and Petroleum Geology, 55, 315–331, doi:10.1016/j.marpetgeo.2014.03.009, 2014.

Schilling, O. S., Cook, P. G., and Brunner, P.: Beyond Classical Observations in Hydrogeology: The Advantages of Including Exchange Flux, Temperature, Tracer Concentration, Residence Time, and Soil Moisture Observations in Groundwater Model Calibration, Reviews of Geophysics, 57, 146–182, doi:10.1029/2018RG000619, 2019a.

Schilling, O. S., Park, Y.-J., Therrien, R., and Nagare, R. M.: Integrated Surface and Subsurface Hydrological Modeling with Snowmelt and Pore Water Freeze-Thaw, Groundwater, 57, 63–74, doi:10.1111/gwat.12841, 2019b.

Schuite, J., Flipo, N., Massei, N., Rivière, A., and Baratelli, F.: Improving the spectral analysis of hydrological signals to efficiently constrain watershed properties, Water Resources Research, doi:10.1029/2018WR024579, 2019.

Sen, P. K.: Estimates of the regression coefficient based on Kendall's tau, Journal of the American statistical association, 63, 1379–1389, doi:10.1080/01621459.1968.10480934, 1968.

Seneviratne, S. I., Corti, T., Davin, E. L., Hirschi, M., Jaeger, E. B., Lehner, I., Orlowsky, B., and Teuling, A. J.: Investigating soil moisture–climate interactions in a changing climate: A review, Earth-Science Reviews, 99, 125–161, doi:10.1016/j.earscirev.2010.02.004, 2010.

Seyedhashemi, H., Vidal, J.-P., Diamond, J. S., Thiéry, D., Monteil, C., Hendrickx, F., Maire, A., and Moatar, F.: Regional, multi-decadal analysis on the Loire River basin reveals that stream temperature increases faster than air temperature, Hydrology and Earth

System Sciences, 26, 2583–2603, doi:10.5194/hess-26-2583-2022, publisher: Copernicus GmbH, 2022.

Shan, C. and Bodvarsson, G.: An analytical solution for estimating percolation rate by fitting temperature profiles in the vadose zone, Journal of Contaminant Hydrology, 68, 83–95, doi:10.1016/S0169-7722(03)00126-8, 2004.

Shen, C. and Phanikumar, M. S.: A process-based, distributed hydrologic model based on a large-scale method for surface–subsurface coupling, Advances in Water Resources, 33, 1524–1541, doi:10.1016/j.advwatres.2010.09.002, 2010.

Shevliakova, E., Pacala, S. W., Malyshev, S., Hurtt, G. C., Milly, P. C. D., Caspersen, J. P., Sentman, L. T., Fisk, J. P., Wirth, C., and Crevoisier, C.: Carbon cycling under 300 years of land use change: Importance of the secondary vegetation sink, Global Biogeochemical Cycles, 23, doi:10.1029/2007GB003176, 2009.

Singh, A.: Groundwater resources management through the applications of simulation modeling: A review, Science of The Total Environment, 499, 414–423, doi:10.1016/j.scitotenv.2014.05.048, 2014.

Sini, J.-F., Anquetin, S., and Mestayer, P. G.: Pollutant dispersion and thermal effects in urban street canyons, Atmospheric environment, 30, 2659–2677, doi:10.1016/1352-2310(95)00321-5, 1996.

Sinokrot, B. A. and Stefan, H. G.: Stream temperature dynamics: Measurements and modeling, Water Resources Research, 29, 2299–2312, doi:10.1029/93WR00540, 1993.

Sitch, S., Smith, B., Prentice, I. C., Arneth, A., Bondeau, A., Cramer, W., Kaplan, J. O., Levis, S., Lucht, W., Sykes, M. T., Thonicke, K., and Venevsky, S.: Evaluation of ecosystem dynamics, plant geography and terrestrial carbon cycling in the LPJ dynamic global vegetation model, Global Change Biology, 9, 161–185, doi:10.1046/j.1365-2486.2003.00569.x, 2003.

Smith, T. M., Shugart, H. H., Woodward, F. I., and Keddy, P.: Plant functional types,

Trends in Plant Science, 3, 241–241, publisher: Kidlington, Oxford: Elsevier Science, Ltd., c1996-, 1998.

Sophocleous, M.: Interactions between groundwater and surface water: the state of the science, Hydrogeology Journal, 10, 52–67, doi:10.1007/s10040-001-0170-8, 2002.

Spanoudaki, K., Stamou, A. I., and Nanou-Giannarou, A.: Development and verification of a 3-D integrated surface water–groundwater model, Journal of Hydrology, 375, 410–427, doi:10.1016/j.jhydrol.2009.06.041, 2009.

Stallman, R.: Steady one-dimensional fluid flow in a semi-infinite porous medium with sinusoidal surface temperature, Journal of Geophysical Research, 70, 2821–2827, doi:10.1029/JZ070i012p02821, 1965.

Stamou, A. I., Memos, C. D., and Kapetanaki, M. E.: Modelling water renewal in a coastal embayment, Proceedings of the Institution of Civil Engineers - Maritime Engineering, 160, 93–104, doi:10.1680/maen.2007.160.3.93, 2007.

Stefan, H. G. and Preud'homme, E. B.: Stream temperature estimation from air temperature, Journal of the American Water Resources Association, 29, 27–45, doi:10.1111/j.1752-1688.1993.tb01502.x, 1993.

Sterling, S. M., Ducharne, A., and Polcher, J.: The impact of global land-cover change on the terrestrial water cycle, Nature Climate Change, 3, 385–390, doi:10.1038/nclimate1690, 2013.

Stocker, T., Qin, D., Plattner, G.-K., Tignor, M., Allen, S., Boschung, J., Nauels, A., Xia, Y., Bex, V., and Midgley, P., eds.: Climate Change 2013: The Physical Science Basis. Contribution of Working Group I to the Fifth Assessment Report of the Intergovernmental Panel on Climate Change, Cambridge University Press, Cambridge, United Kingdom and New York, NY, USA, 2013.

Stonestrom, D. A. and Constantz, J., eds.: Heat as a tool for studying the movement of ground water near streams, no. 1260 in Circular / U. S. Department of the Interior, U.S.

Geological Survey, U.S. Geological Survey, Information Services, Reston, Va, oCLC: 249104967, 2003.

Stéfanon, M., Drobinski, P., D'Andrea, F., and de Noblet-Ducoudré, N.: Effects of interactive vegetation phenology on the 2003 summer heat waves: Effects of phenology on heat waves, Journal of Geophysical Research: Atmospheres, 117, n/a–n/a, doi:10.1029/2012JD018187, 2012.

Sulis, M., Meyerhoff, S. B., Paniconi, C., Maxwell, R. M., Putti, M., and Kollet, S. J.: A comparison of two physics-based numerical models for simulating surface water–groundwater interactions, Advances in Water Resources, 33, 456–467, doi:10.1016/j.advwatres.2010.01.010, 2010.

Sun, N., Yearsley, J., Voisin, N., and Lettenmaier, D. P.: A spatially distributed model for the assessment of land use impacts on stream temperature in small urban watersheds, Hydrological Processes, 29, 2331–2345, doi:10.1002/hyp.10363, 2015.

Swain, E. D. and Wexler, E. J.: A coupled surface-water and ground-water flow model (MODBRANCH) for simulation of stream-aquifer interaction, Tech. rep., U.S. Geological Survey, doi:10.3133/twri06A6, 1996.

Tafasca, S., Ducharne, A., and Valentin, C.: Weak sensitivity of the terrestrial water budget to global soil texture maps in the ORCHIDEE land surface model, Hydrology and Earth System Sciences Discussions, pp. 1–20, doi:https://doi.org/10.5194/hess-2019-305, publisher: Copernicus GmbH, 2019.

Takata, K., Emori, S., and Watanabe, T.: Development of the minimal advanced treatments of surface interaction and runoff, Global and Planetary Change, 38, 209–222, doi:10.1016/S0921-8181(03)00030-4, 2003.

Tavakoly, A., Habets, F., Saleh, F., Yang, Z.-L., Bourgeouis, C., and Maidment, D.: An integrated framework to model nitrate contaminants with interactions of agriculture, groundwater, and surface water at regional scales: The STICS–EauDyssée cou-

pled models applied over the Seine River Basin, Journal of Hydrology, 568, 943–958, doi:10.1016/j.jhydrol.2018.11.061, publisher: Elsevier, 2019.

Taylor, C. A. and Stefan, H. G.: Shallow groundwater temperature response to climate change and urbanization, Journal of Hydrology, 375, 601–612, doi:10.1016/j.jhydrol.2009.07.009, 2009.

Taylor, K., Stouffer, R., and Meehl, G.: An overview of CMIP5 and the experiment design, Bulletin of the American Meteorological Society, 93, 485–498, doi:10.1175/BAMS-D-11-00094.1, 2012.

Taylor, R., Scanlon, B., Doll, P., Rodell, M., van Beek, R., Wada, Y., Longuevergne, L., Leblanc, M., Famiglietti, J., Konikow, L., Green, T., Chen, J., Taniguchi, M., Bierkens, M., MacDonald, A., Fan, Y., Maxwell, R., Yechieli, Y., Gurdak, J., Allen, D., Shamsudduha, M., Hiscock, K., Holman, I., and Treidel, H.: Ground water and climate change, Nature Climate Change, 3, 322–329, doi:10.1038/nclimate1744, 2013.

Térouanne, D., Gaschignard, V., Françoise, Y., and Veerapen, J. P.: Climespace-City of Paris: A District Cooling System to control impact of air-conditioning in Paris, Climespace Application File for the Global District Energy Climate Awards, 2011.

Terray, L. and Boé, J.: Quantifying 21st-century France climate change and related uncertainties, Comptes Rendus Geoscience, 345, 136–149, doi:10.1016/j.crte.2013.02.003, 2013.

Theurer, F. D., Voos, K. A., and Miller, W. J.: Instream water temperature model. Instream Flow Information Paper 16, Report 84/15, U.S. Geological Survey, 1984.

Thornthwaite, C. W.: An approach toward a rational classification of climate, Geographical review, 38, 55–94, doi:10.2307/210739, 1948.

Tian, Y., Zheng, Y., Wu, B., Wu, X., Liu, J., and Zheng, C.: Modeling surface water-groundwater interaction in arid and semi-arid regions with intensive agriculture, Environmental Modelling and Software, 63, 170–184, doi:10.1016/j.envsoft.2014.10.011, 2015.

Toffolon, M. and Piccolroaz, S.: A hybrid model for river water temperature as a function of air temperature and discharge, Environmental Research Letters, 10, 114 011, doi:10.1088/1748-9326/10/11/114011, 2015.

Tokuda, D., Kim, H., Yamazaki, D., and Oki, T.: Development of a Global River Water Temperature Model Considering Fluvial Dynamics and Seasonal Freeze-Thaw Cycle, Water Resources Research, 55, 1366–1383, doi:10.1029/2018WR023083, 2019.

Tootchifatidehi, A.: Development of a global wetland map and application to describe hillslope hydrology in the ORCHIDEE land surface model, Ph.D. thesis, Sorbonne Université, 2019.

Trenberth, K. E., Jones, P. D., Ambenje, P., Bojariu, R., Easterling, D., Tank, A. K., Parker, D., Renwick, J. A., Adler, R., Alexander, L., Alexandersson, H., Allan, R., Baldwin, M. P., Beniston, M., Bromwich, D., Camilloni, I., Cassou, C., Cayan, D. R., Chang, E. K. M., Christy, J., Dai, A., Deser, C., Dotzek, N., Fasullo, J., Fogt, R., Folland, C., Forster, P., Free, M., Frei, C., Gleason, B., Grieser, J., Groisman, P., Gulev, S., Kripalani, R., Kunkel, K., Marshall, G., Mears, C., Mote, P., Nakamura, H., Nicholls, N., Norris, J., Oki, T., Robertson, F. R., Rosenlof, K., Semazzi, F. H., Shea, D., Shepherd, J. M., Shepherd, T. G., Sherwood, S., Siegmund, P., Simmonds, I., Simmons, A., Thorncroft, C., Thorne, P., Uppala, S., Vose, R., Wang, B., Warren, S., Washington, R., Wheeler, M., Wielicki, B., Wong, T., Wuertz, D., Hoskins, B. J., Karl, T. R., and Jallow, B.: Observations: Surface and Atmospheric Climate Change, Tech. rep., IPCC, 2007.

Ukkola, A. M. and Prentice, I. C.: A worldwide analysis of trends in water-balance evapotranspiration, Hydrology and Earth System Sciences, 17, 4177–4187, doi:https://doi.org/10.5194/hess-17-4177-2013, 2013.

Van den Hoof, C., Hanert, E., and Vidale, P. L.: Simulating dynamic crop growth with an adapted land surface model – JULES-SUCROS: Model development and validation, Agricultural and Forest Meteorology, 151, 137–153, doi:10.1016/j.agrformet.2010.09.011, 2011.

Van Genuchten, M. T.: A Closed-form Equation for Predicting the Hydraulic Conductivity of Unsaturated Soils, Soil Science Society of America Journal, doi:10.2136/sssaj1980.03615995004400050002x, 1980.

Van Vliet, M. T. H., Yearsley, J. R., Franssen, W. H. P., Ludwig, F., Haddeland, I., Lettenmaier, D. P., and Kabat, P.: Coupled daily streamflow and water temperature modelling in large river basins, Hydrology and Earth System Sciences, 16, 4303–4321, doi:https://doi.org/10.5194/hess-16-4303-2012, publisher: Copernicus GmbH, 2012a.

Van Vliet, M. T. H., Yearsley, J. R., Ludwig, F., Vögele, S., Lettenmaier, D. P., and Kabat, P.: Vulnerability of US and European electricity supply to climate change, Nature Climate Change, 2, 676–681, doi:10.1038/nclimate1546, 2012b.

Van Vuuren, D. P., Edmonds, J., Kainuma, M., Riahi, K., Thomson, A., Hibbard, K., Hurtt, G. C., Kram, T., Krey, V., Lamarque, J.-F., et al.: The representative concentration pathways: an overview, Climatic change, 109, 5–31, 2011.

Vandenbohede, A., Louwyck, A., and Lebbe, L.: Conservative Solute Versus Heat Transport in Porous Media During Push-pull Tests, Transport in Porous Media, 76, 265–287, doi:10.1007/s11242-008-9246-4, 2009.

Vereecken, H., Weynants, M., Javaux, M., Pachepsky, Y., Schaap, M. G., and van Genuchten, M.: Using Pedotransfer Functions to Estimate the van Genuchten-Mualem Soil Hydraulic Properties: A Review, Vadose Zone Journal, 9, 795–820, doi:10.2136/vzj2010.0045, 2010.

Vidal, J.-P., Martin, E., Franchistéguy, L., Habets, F., Soubeyroux, J.-M., Blanchard, M., and Baillon, M.: Multilevel and multiscale drought reanalysis over France with the Safran-Isba-Modcou hydrometeorological suite, Hydrology and Earth System Sciences, 14, 459–478, doi:10.5194/hess-14-459-2010, 2010a.

Vidal, J.-P., Martin, E., Franchistéguy, L., Baillon, M., and Soubeyroux, J.-M.: A 50-year high-resolution atmospheric reanalysis over France with the Safran system, International Journal of Climatology, 30, 1627–1644, doi:10.1002/joc.2003, 2010b.

Vieweg, M., Kurz, M. J., Trauth, N., Fleckenstein, J. H., Musolff, A., and Schmidt, C.: Estimating time-variable aerobic respiration in the streambed by combining electrical conductivity and dissolved oxygen time series: Variable Respiration in the Streambed, Journal of Geophysical Research: Biogeosciences, 121, 2199–2215, doi:10.1002/2016JG003345, 2016.

Viviroli, D., Archer, D. R., Buytaert, W., Fowler, H. J., Greenwood, G. B., Hamlet, A. F., Huang, Y., Koboltschnig, G., Litaor, M. I., López-Moreno, J. I., Lorentz, S., Schädler, B., Schreier, H., Schwaiger, K., Vuille, M., and Woods, R.: Climate change and mountain water resources: overview and recommendations for research, management and policy, Hydrology and Earth System Sciences, 15, 471–504, doi:10.5194/hess-15-471-2011, 2011.

Vliet, M. T. V., Franssen, W. H., Yearsley, J. R., Ludwig, F., Haddeland, I., Lettenmaier, D. P., and Kabat, P.: Global river discharge and water temperature under climate change, Global Environmental Change, 23, 450–464, doi:10.1016/j.gloenvcha.2012.11.002, 2013.

Von Schuckmann, K., Cheng, L., Palmer, M. D., Hansen, J., Tassone, C., Aich, V., Adusumilli, S., Beltrami, H., Boyer, T., Cuesta-Valero, F. J., Desbruyères, D., Domingues, C., García-García, A., Gentine, P., Gilson, J., Gorfer, M., Haimberger, L., Ishii, M., Johnson, G. C., Killick, R., King, B. A., Kirchengast, G., Kolodziejczyk, N., Lyman, J., Marzeion, B., Mayer, M., Monier, M., Monselesan, D. P., Purkey, S., Roemmich, D., Schweiger, A., Seneviratne, S. I., Shepherd, A., Slater, D. A., Steiner, A. K., Straneo, F., Timmermans, M.-L., and Wijffels, S. E.: Heat stored in the Earth system: where does the energy go?, Earth System Science Data, 12, 2013–2041, doi:https://doi.org/10.5194/essd-12-2013-2020, publisher: Copernicus GmbH, 2020.

Voss, C. I.: SUTRA (Saturated-Unsaturated Transport). A Finite-Element Simulation Model for Saturated-Unsaturated, Fluid-Density-Dependent Ground-Water Flow with Energy Transport or Chemically-Reactive Single-Species Solute Transport., Tech. Rep. USGS/WRI/84-4369, Geological Survey Reston,VA; Water Resources Division, 1984.

Wada, Y., Van Beek, L., Van Kempen, C., Reckman, J., Vasak, S., and Bierkens, M.: Global depletion of groundwater resources, Geophysical Research Letters, 37, doi:10.1029/2010GL044571, 2010.

Wagener, T., Sivapalan, M., Troch, P., McGlynn, B., Harman, C., Gupta, H., Kumar, P., Rao, P., Basu, N., and Wilson, J.: The future of hydrology: An evolving science for a changing world, Water Resourses Research, 46, W05 301, doi:10.1029/2009WR008906, 2010.

Walko, R. L., Band, L. E., Baron, J., Kittel, T. G. F., Lammers, R., Lee, T. J., Ojima, D., Pielke, R. A., Taylor, C., Tague, C., Tremback, C. J., and Vidale, P. L.: Coupled Atmosphere–Biophysics–Hydrology Models for Environmental Modeling, Journal of Applied Meteorology, 39, 931–944, doi:10.1175/1520-0450(2000)039<0931:CABHMF>2.0.CO;2, 2000.

Wang, F., Cheruy, F., and Dufresne, J.-L.: The improvement of soil thermodynamics and its effects on land surface meteorology in the IPSL climate model, Geoscientific Model Development, 9, 363–381, doi:https://doi.org/10.5194/gmd-9-363-2016, 2016a.

Wang, F., Ducharne, A., Cheruy, F., Lo, M.-H., and Grandpeix, J.-Y.: Impact of a shallow groundwater table on the global water cycle in the IPSL land–atmosphere coupled model, Climate Dynamics, 50, 3505–3522, doi:10.1007/s00382-017-3820-9, 2018a.

Wang, F., Polcher, J., Peylin, P., and Bastrikov, V.: Assimilation of river discharge in a land surface model to improve estimates of the continental water cycles, Hydrology and Earth System Sciences, 22, 3863–3882, doi:10.5194/hess-22-3863-2018, 2018b.

Wang, S.: Simulation du métabolisme de la Seine par assimilation de données en continu, Ph.D. thesis, Université PSL, MINES ParisTech, France, 2019.

Wang, S., Jost, A., Labarthe, B., and Flipo, N.: Création du module Libwet de simulation des interactions gravières-aquifères., Rapport technique, PIREN-Seine, 2016b.

Wang, S., Flipo, N., and Romary, T.: Time-dependent global sensitivity analysis of the

C-RIVE biogeochemical model in contrasted hydrological and trophic contexts, Water Research, 144, 341–355, doi:10.1016/j.watres.2018.07.033, 2018c.

Wang, S., Flipo, N., Bordet, A., Bernier, J., Merchat, M., and Rocher, V.: Transport de chaleur par la Seine à la traversée de l'agglomération parisienne, Rapport d'étude, PIREN Seine, 2021.

Wang, T., Ottlé, C., Boone, A., Ciais, P., Brun, E., Morin, S., Krinner, G., Piao, S., and Peng, S.: Evaluation of an improved intermediate complexity snow scheme in the ORCHIDEE land surface model, Journal of Geophysical Research: Atmospheres, 118, 6064–6079, doi:10.1002/jgrd.50395, 2013.

Wang, Y. P., Kowalczyk, E., Leuning, R., Abramowitz, G., Raupach, M. R., Pak, B., van Gorsel, E., and Luhar, A.: Diagnosing errors in a land surface model (CABLE) in the time and frequency domains, Journal of Geophysical Research, 116, G01 034, doi:10.1029/2010JG001385, 2011.

Webb, B. and Zhang, Y.: Spatial and seasonal variability in the components of the river heat budget, Hydrological Processes, 11, 79–101, doi:10.1002/(SICI)1099-1085(199701)11:1<79::AID-HYP404>3.0.CO;2-N, 1997.

Webb, B., Hannah, D., Moore, R., Brown, L., and Nobilis, F.: Recent advances in stream and river temperature research, Hydrological Processes, 22, 902–918, doi:10.1002/hyp.6994, 2008.

Webb, B. W.: Trends in stream and river temperature, Hydrological Processes, 10, 205–226, doi:10.1002/(SICI)1099-1085(199602)10:2<205::AID-HYP358>3.0.CO;2-1, 1996.

Webb, B. W. and Nobilis, F.: Long-term changes in river temperature and the influence of climatic and hydrological factors,, Hydrological Sciences Journal, 52, 74–85, doi:10.1623/hysj.52.1.74, 2007.

Whitehead, P. G., Wilby, R. L., Battarbee, R. W., Kernan, M., and Wade, A. J.: A

review of the potential impacts of climate change on surface water quality, Hydrological Sciences Journal, 54, 101–123, doi:10.1623/hysj.54.1.101, 2009.

Winsemius, H. C.: Satellite data as complementary information for hydrological modelling, Ph.D. thesis, VSSD, Delft, oCLC: 436913625, 2009.

Winter, C., T., Harvey, J. W., Franke, O. L., and Alley, W. M.: Groundwater and Surface water: A single source, Circular, USGS, 1998.

Wondzell, S. M., Diabat, M., and Haggerty, R.: What matters most: are future stream temperatures more sensitive to changing air temperatures, discharge, or riparian vegetation?, JAWRA Journal of the American Water Resources Association, 55, 116–132, 2019.

Wood, E. F., Lettenmaier, D. P., and Zartarian, V. G.: A land-surface hydrology parameterization with subgrid variability for general circulation models, Journal of Geophysical Research, 97, 2717, doi:10.1029/91JD01786, 1992.

Woodside, W. and Messmer, J. H.: Thermal Conductivity of Porous Media .1. Unconsolidated Sands., Journal of Applied Physics, 32, 1688–1699, doi:10.1063/1.1728419, 1961.

Wool, T. A., Ambrose, R. B., and Martin, J. L.: WASP7 Temperature and Fecal Coliform Model Theory and User's Guide, US Environmental Protection Agency, EPA, 600, 2008.

Wosten, J., Pachepsky, Y., and Rawls, W. J.: Pedotransfer functions: bridging the gap between available basic soil data and missing soil hydraulic characteristics, Journal of Hydrology, 251, 123–150, doi:10.1016/S0022-1694(01)00464-4, publisher: Elsevier, 2001.

Wu, X., Ma, T., and Wang, Y.: Surface Water and Groundwater Interactions in Wetlands, Journal of Earth Science, 31, 1016–1028, doi:10.1007/s12583-020-1333-7, 2020.

Xie, Z., Yuan, F., Duan, Q., Zheng, J., Liang, M., and Chen, F.: Regional Parameter Estimation of the VIC Land Surface Model: Methodology and Application to River

Basins in China, Journal of Hydrometeorology, 8, 447–468, doi:10.1175/JHM568.1, publisher: American Meteorological Society Section: Journal of Hydrometeorology, 2007.

Yearsley, J.: A grid-based approach for simulating stream temperature: A grid-based approach for simulating stream temperature, Water Resources Research, 48, doi:10.1029/2011WR011515, 2012.

York, J. P., Person, M., Gutowski, W. J., and Winter, T. C.: Putting aquifers into atmospheric simulation models: An example from the Mill Creek Watershed, northeastern Kansas, Advances in Water Resources, 25, 221–238, doi:10.1016/S0309-1708(01)00021-5, publisher: Elsevier, 2002.

Zhan, H., Wen, Z., Huang, G., and Sun, D.: Analytical solution of two-dimensional solute transport in an aquifer–aquitard system, Journal of Contaminant Hydrology, 107, 162–174, doi:10.1016/j.jconhyd.2009.04.010, 2009.

Zhang, Y., Chen, W., and Cihlar, J.: A process-based model for quantifying the impact of climate change on permafrost thermal regimes, Journal of Geophysical Research: Atmospheres, 108, doi:10.1029/2002JD003354, 2003.

Zhang, Y., Liu, C., Tang, Y., and Yang, Y.: Trends in pan evaporation and reference and actual evapotranspiration across the Tibetan Plateau, Journal of Geophysical Research: Atmospheres, 112, doi:10.1029/2006JD008161, 2007.

Zhao, F., Veldkamp, T. I. E., Frieler, K., Schewe, J., Ostberg, S., Willner, S., Schauberger, B., Gosling, S. N., Schmied, H. M., Portmann, F. T., Leng, G., Huang, M., Liu, X., Tang, Q., Hanasaki, N., Biemans, H., Gerten, D., Satoh, Y., Pokhrel, Y., Stacke, T., Ciais, P., Chang, J., Ducharne, A., Guimberteau, M., Wada, Y., Kim, H., and Yamazaki, D.: The critical role of the routing scheme in simulating peak river discharge in global hydrological models, Environmental Research Letters, 12, 075 003, doi:10.1088/1748-9326/aa7250, publisher: IOP Publishing, 2017.

Zhou, X., Polcher, J., Yang, T., Hirabayashi, Y., and Nguyen-Quang, T.: Understanding

the water cycle over the upper Tarim Basin: retrospecting the estimated discharge bias to atmospheric variables and model structure, Hydrology and Earth System Sciences, 22, 6087–6108, doi:10.5194/hess-22-6087-2018, 2018.

Zhu, Z., Bi, J., Pan, Y., Ganguly, S., Anav, A., Xu, L., Samanta, A., Piao, S., Nemani, R. R., and Myneni, R. B.: Global Data Sets of Vegetation Leaf Area Index (LAI)3g and Fraction of Photosynthetically Active Radiation (FPAR)3g Derived from Global Inventory Modeling and Mapping Studies (GIMMS) Normalized Difference Vegetation Index (NDVI3g) for the Period 1981 to 2011, Remote Sensing, 5, 927–948, doi:10.3390/rs5020927, number: 2 Publisher: Multidisciplinary Digital Publishing Institute, 2013.

Zobler, L.: A world soil file grobal climate modeling, NASA Tech. Memo, 32, 1986.

Zweimüller, I., Zessner, M., and Hein, T.: Effects of climate change on nitrate loads in a large river: the Austrian Danube as example, Hydrological Processes, 22, 1022–1036, doi:10.1002/hyp.7000, 2008.

Šimůnek, J., van Genuchten, M. T., and Sejna, M.: The HYDRUS Software Package for Simulating Two- and Three-Dimensional Movement of Water, Heat, and Multiple Solutes in Variably-Saturated Media, Technical Manual, HYDRUS, 2011.

Appendices

Appendix A

Development of the heat transport in the CaWaQS platform

A.1 Introduction

La gestion durable de la ressource en eau, tant du point de vue de sa disponibilité, que de sa qualité physico-chimique et écologique, en passant par son potentiel de production d'énergie, sera sous-tendue dans le futur par notre capacité à anticiper les effets du changement climatique, l'évolution des demandes en eau et les nouveaux systèmes de gouvernance relatifs à la gestion des milieux anthropisés (gestion des infrastructures, politiques de développement territorial). Ainsi, il sera impératif de décrire aussi précisément que possible les évolutions temporelles et spatiales des transferts de solutés, de chaleur et d'eau dans les différents compartiments tout en tenant compte des changements globaux. Dans ce cadre, les équipes du PIREN-Seine développent un outil de modélisation intégrée visant à simuler des échanges thermiques entre l'atmosphère et la surface (sol, rivière et lac) et les systèmes aquifères.

Des premières simulations ont été mises en œuvre afin de prédire une évolution possible de l'hydrosystème Seine dans le futur (Flipo et al., 2020a; Ducharne et al., 2009; Ducharne, 2008; Boé et al., 2007). Cependant, la compréhension précise de l'impact du changement climatique sur le cycle de l'eau nécessite l'inclusion du bilan énergétique car les processus inhérents au cycle de l'eau sont dépendants de celui-ci (Maxwell and Kollet, 2008a).

Par conséquent, la compréhension actuelle du changement climatique nécessite une mise à jour des outils, précédemment déployés pour modéliser la ressource en eau et son devenir potentiel. C'est dans ce cadre que s'inscrit le développement du couplage

entre la plateforme ORCHIDEE (développée par l'IPSL (Krinner et al., 2005; Ducharne et al., 2000, 2020)) et la plateforme CaWaQS (développée par MINES ParisTech, PSL Université, (Flipo, 2005; Labarthe, 2016; Flipo et al., 2019; Gallois et al., 2020a). Le but de ce couplage est d'utiliser ORCHIDEE pour résoudre le bilan hydrique et énergétique des compartiments sol-végétation-atmosphère au pas de temps horaire ainsi que leur flux d'échange entre leurs différentes interface. CaWaQS sera utilisé pour le flux d'eau et d'energie dans les aquifères et les rivières. Ce couplage sera appliqué ultérieurement au bassin de la Seine. Un travail de déclinaison régionale d'ORCHIDEE à l'échelle du bassin de la Seine, non présenté ici, a d'ores-et-déjà été réalisé (Kilic et al., 2019, 2021a). Une recalibration récente des flux d'eau de l'application CaWaQS-Seine a été réalisée (Flipo et al., 2021a), ainsi que l'inclusion de l'ensemble du système aquifère de la frange orientale du bassin de la Seine (Gallois et al., 2021). Ce travail permettra donc de fermer le bilan énergétique en simulant le transport de chaleur dans l'aquifère et la rivière. L'apport d'énergie depuis la surface sera obtenu via le couplage d'ORCHIDEE avec CaWaQS .

Dans le cadre du PIREN-Seine, les efforts de modélisation autour de la question du transport à l'échelle du bassin de la Seine se sont historiquement concentrés sur la modélisation de la quantification de l'impact de la pollution d'origine agricole sur la contamination en nitrate du système aquifère (Gallois and Viennot, 2018; Beaudoin et al., 2018). Dans ce rapport, les développements et leur validation concernant le transport de chaleur sont décrits. Ces développements s'appuient sur les développement de la librairie libttc (Rivière, 2017) ainsi que les récentes améliorations opérées au sein de CaWaQS, en termes de couplage entre transport de matière et simulation de hydrodynamisme (Rivière, 2017; Gallois et al., 2020b). Après une brève introduction des outils du PIREN-Seine, une description détaillée des développements techniques sur le transport de chaleur dans l'aquifère et la rivière sera présentée.

A.2 Les outils de modélisation du transfert de chaleur dans les bassins

A.2.1 CaWaQS: CAtchment WAter Quality Simulator

La plateforme CaWaQS est un outil numérique permettant la simulation spatio-temporelle de flux d'eau à diverses échelles, en régime permanent et/ou transitoire, au sein d'un hydrosystème (Flipo, 2005; Labarthe, 2016; Flipo et al., 2019). Cet outil a hérité de nombreux concepts de la plate-forme de modélisation MODCOU-NEWSAM (de Marsily et al., 1978; Ledoux, 1980). Son application permet de couvrir un large éventail de problématiques, de la prospective sur les impacts du changement climatique sur la trajectoire hydrologique du bassin de la Seine (Flipo et al., 2020a), aux enjeux de remontées de nappe en agglomération parisienne (Maillot, 2019), en passant par l'étude d'impacts environnementaux autour de l'exploitation des gravières ou encore de la pollution diffuse d'origine agricole (Wang et al., 2016b).

CaWaQS couple un ensemble de bibliothèques autonomes (Labarthe, 2016; Flipo et al., 2019; Gallois et al., 2020b), offrant une structure modulaire à l'utilisateur qui peut sélectionner les compartiments de l'hydrosystème qu'il souhaite modéliser. Quatre librairies dédiées à ces compartiments constituent le cœur de la plateforme CaWaQS :

- *libfp*: (cf. Fig A.1.A) calcule le bilan hydrologique de la surface, au pas de temps journalier. Cette librairie estime l'évapotranspiration réelle et évalue le stock d'eau dans le sol. Le ruissellement et l'infiltration sont calculés à partir des précipitations et de l'évapotranspiration potentielle. Elle transfère également le ruissellement au réseau hydrographique, par méthode de routage instantané.

- *libhyd*: (cf. Fig A.1.B) simule les écoulements au sein du réseau rivière, selon le schéma de Muskingum (Cunge, 1969) (cf. Fig A.1.D). Le ruissellement produit localement est distribué, le long de chaque tronçon du réseau, de manière homogène. L'épaisseur de la colonne d'eau dans la rivière est calculée par la méthode de Manning-Strickler.

- *libnsat* simule le transfert vertical d'eau au sein de la zone non saturée, selon le concept de colonnes de réservoirs de Nash (Nash, 1959) (cf. Fig A.1.C). Ce com-

partiment est caractérisé par un ensemble de réservoirs successifs dont le temps de transit (coefficient de vidange) et l'épaisseur sont variables spatialement. Les flux calculés en base de ce compartiment sont, par suite transférés comme recharge à la zone saturée (aquifère), soit par transfert vertical direct ou après routage (Gallois et al., 2020a).

- *libaq*. Ce module simule (cf. Fig A.1.E) l'écoulement de l'eau dans un système aquifère multi-couche, selon une discrétisation semi-implicite, par différences finies. L'équation de diffusivité est résolue sous une forme pseudo-3D. Un support de cette résolution par maillage gigogne est possible pour affiner la résolution en relation avec les couches supérieures et inférieures. Le lien entre les couches du système aquifère est établi par le concept de drainance, analogue à celui de conductance, utilisé pour dans la simulation des échanges nappe-rivière.

Un ensemble de librairies complémentaires, permettent au logiciel de construire (*libio*, *libmesh*), interpoler (*libts*), gérer le temps (*libchronos*, *libts*), imprimer (*libprint*), coupler spatialement les flux entre compartiments (*libspa*) et résoudre des systèmes linéaires par la méthode du gradient conjugué (*libgc*).

L'ensemble des améliorations récentes, orientées simulation de flux d'eau, sont à la fois documentées dans Gallois et al. (2020a, 2021) (introduction de la notion de sous-bassin versants, de gouffres, d'infiltration rivière, court-circuits hydrauliques en système aquifère, etc.) et Gallois et al. (2020b) (injections de flux exogènes au réseau hydrographique). Des développements supplémentaires incluent également la possibilité de coupler CaWaQS avec un modèle de surface terrestre (LSM - *Land Surface Model*) en définissant les cartes de forçages de recharge et de ruissellement, de concentration et/ou de température à partir de ces modèles de surface. De plus, les développements récents de CaWaQS ont permis d'ajouter de nouvelles capacités telles que le transport de chaleur et de concentration dans la zone saturée et la composante rivière de CaWaQS qui fait l'objet de ce rapport.

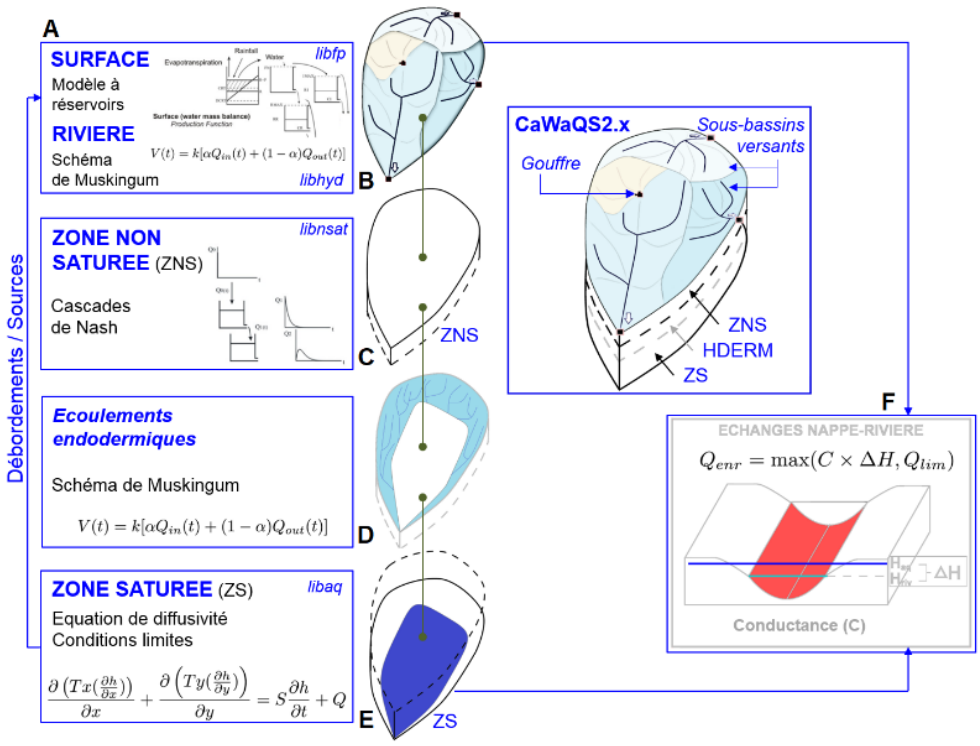

Figure A.1 Schématisation de la structure de la plate-forme CaWaQS3.X de modélisation de flux d'eau (d'après Gallois et al. (2020a)).

A.2.2 *libttc*: librairie de transport de chaleur et de solutés

A.2.2.1 Présentation

La librairie libttc (LIBrairie Transport Thermique et Concentration) simule le transport de chaleur et de soluté en milieu poreux (aquifères) et également en écoulement à surface libre (cours d'eau et rivières). Elle a été développée avec cinq buts principaux:

1. utiliser un formalisme commun pour le transfert de solutés et le transport de chaleur en milieu poreux (aquifère) ou en milieu eaux libre (rivière),

2. permettre une modélisation parallèle "multi-espèces". La librairie permet, en effet, le transport simultané dans les différents modules, de n espèces dissoutes, Cette fonctionnalité est essentielle, notamment, dans une optique future d'intégration du transport réactif imposant souvent des conditionnalités entre espèces,

3. simuler le transport sur un maillage irrégulier gigogne, tel qu'utilisé pour la modélisation de l'hydrodynamisme aquifère,

4. permettre un niveau de flexibilité additionnel sur le pas de temps de simulation. Celui-ci peut être, si nécessaire, différent de celui de servant aux calculs hydrodynamiques; ceci dans le but d'obtenir une meilleure représentation des processus avec la prise en compte de leur temps caractéristique,

5. coupler cette librairie avec différents codes résolvant les écoulements à surface libre (en rivière) ou en milieu poreux.

Table A.1 Paramètres utilisés pour la modélisation de transport. Les propriétés sont considérées homogènes

	Symbole et paramètres	Unités
ω	Porosité du milieu poreux	$[\mathrm{m}^3\,\mathrm{m}^{-3}]$
	Transport de chaleur	
T	Température	$[\mathrm{K}]$
λ_w	Conductivité thermique eau	$[\mathrm{W\,m^{-1}\,K^{-1}}]$
λ_s	Conductivité thermique solide	$[\mathrm{W\,m^{-1}\,K^{-1}}]$
λ	Conductivité thermique poreux	$[\mathrm{W\,m^{-1}\,K^{-1}}]$
c_{p_w}	Capacité calorifique spécifique eau	$[\mathrm{J\,kg^{-1}\,K^{-1}}]$
c_{p_s}	Capacité calorifique spécifique solide	$[\mathrm{J\,kg^{-1}\,K^{-1}}]$
c_p	Capacité calorifique spécifique poreux	$[\mathrm{J\,kg^{-1}\,K^{-1}}]$
ρ_w	Densité d'eau	$[\mathrm{kg\,m^{-3}}]$
ρ_s	Densité de solide	$[\mathrm{kg\,m^{-3}}]$
ρ	Densité du milieu poreux	$[\mathrm{kg\,m^{-3}}]$
β	Dispersivité thermique	$[\mathrm{m}]$
U	Vitesse de Darcy	$[\mathrm{m\,s^{-1}}]$
Q_{therm}	Terme source thermique	$[\mathrm{W\,m^{-2}}]$
	Transport de soluté	
C	Concentration	$[\mathrm{mg\,l^{-1}}]$
U	Vitesse de Darcy	$[\mathrm{m\,s^{-1}}]$
α	Dispersivité	$[\mathrm{m}]$
D_m	Le coefficient de diffusion effectif	$[\mathrm{m^2\,s^{-1}}]$
q_{solute}	Terme source soluté	$[\mathrm{mg\,l^{-1}\,s^{-1}}]$

L'algorithme de *libttc* s'appuie sur l'algorithme du code GINETTE (Rivière, 2012; Rivière et al., 2020). Cet algorithme permet de répondre à tous les objectifs de la librairie libttc. Il procure l'avantage d'appliquer les conditions aux limites aux faces des cellules peu importe son type et d'être très malléable à la fois en terme des processus décrit et la possibilité de modifier la valeur des paramètres si des couplages sont pris en compte. Compte tenu de l'analogie entre les équations (Eq. A.1) et (Eq. A.2), l'algorithme s'appuie sur l'écriture de l'équation de transport basée sur des

paramètres apparants, calculés selon le type de problème étudié (*i.e.* transport de soluté ou de chaleur). Le coefficient de diffusion thermique est analogue à celui du soluté $D_{therm} \Longleftrightarrow D_{solute}$ et le terme capacitif thermique est assimilable à celui des solutés $\frac{\rho c}{\rho_w c_w} \Longleftrightarrow \omega$.

$$\nabla \cdot (D_{therm} \nabla(T)) - \nabla \cdot (U\,T) = \frac{\rho c}{\rho_w c_w} \frac{\partial T}{\partial t} + \frac{Q_{therm}}{\rho_w c_w L} \tag{A.1}$$

$$\nabla \cdot (D_{solute} \nabla(C)) - \nabla \cdot (U\,C) = \omega \frac{\partial C}{\partial t} + q_{solute} \tag{A.2}$$

où T désigne la température du milieu poreux (K), D_{therm} le coefficient de dispersion thermique ($m^2\,s^{-1}$), U la vitesse de Darcy ($m\,s^{-1}$), ρ_w la masse volumique de l'eau ($kg\,m^{-3}$), c_{pw} la capacité calorifique massique de l'eau ($J\,K^{-1}\,kg^{-1}$) et L la longueur de la maille sur laquelle le flux de chaleur est injectée. Pour la transport de soluté, C désigne la concentration du soluté, ($\mathrm{mg\,l^{-1}}$), D_{therm} le coefficient de diffusion soluté ($\mathrm{m^2\,s^{-1}}$), U la vitesse de Darcy ($m\,s^{-1}$, ω la porosité ($\mathrm{m^3\,m^{-3}}$), q_{solute} le terme source de soluté ($\mathrm{mg\,l^{-1}\,s^{-1}}$). Pour le transport dans de l'eau libre, la valeur de la porosité est égale à 1. Ce qui permet à la librairie d'être utilisable à la fois en milieu poreux et en eau libre.

La librairie *libttc* est un ensemble de fonctions qui stockent la description des espèces simulées et de leur paramètres et résout le transport de chaleur et de soluté multi-espèces. Tout comme pour CaWaQS, la résolution du système linéaire correspondant au problème de transport est effectuée par *libgc*. Pour la discrétisation de l'équation de transport dans un schéma semi-implicite à différences finies, se référer à l'annexe. Les notations utilisées dans les équations (Eqs. A.1, A.2, A.3, A.4, A.5, A.6, A.7, A.8) de transport de chaleur advection-diffusion sont synthétisées dans le tableau A.1.

A.2.2.2 Spécificités du transport en aquifère

Les mécanismes qui contrôlent le transport de soluté et de chaleur en milieu poreux et en eau libre sont : l'advection, la dispersion hydrodynamique et la diffusion moléculaire (Eqs. A.1 et A.2). Le mécanisme d'advection correspond au déplacement du soluté

et de chaleur avec le mouvement du fluide. La vitesse d'advection est généralement considérée comme égale à la vitesse moyenne du fluide dans les pores (vitesse cinématique), si le soluté est considéré conservatif. La diffusion moléculaire correspond au transfert de soluté des zones à concentration élevée vers les zones à concentration faible induit par l'agitation moléculaire. Selon la loi de Fick, ce mécanisme est proportionnel au gradient de concentration et à un coefficient de diffusion propre au soluté. En milieu poreux, la diffusion est généralement plus faible que dans de l'eau libre du fait de la tortuosité. Le transfert par diffusion est alors contrôlé par le coefficient de diffusion effectif. Enfin, la dispersion hydrodynamique est due à l'hétérogénéité des vitesses microscopiques induite par la variabilité des ouvertures à l'échelle des pores et à plus large échelle. Elle entraîne un étalement du panache de soluté. Le transfert par dispersion peut être exprimé suivant une loi analogue à celle de Fick. Le flux dispersif est ainsi proportionnel au gradient de concentration et à une constante appelée coefficient de dispersion. Il est admis que ce coefficient est proportionnel à la vitesse moyenne du fluide et à un coefficient de dispersivité. Le coefficient de dispersion hydrodynamique D_{solute} ($\mathrm{m^2\,s^{-1}}$) est exprimé (Eq. A.3) en fonction de α, la dispersivité (m), et D_m le coefficient de diffusion effectif en $\mathrm{m^2\,s^{-1}}$.

$$D_{solute} = \alpha\, U + \omega\, D_m \tag{A.3}$$

Pour le transport de chaleur, le terme dispersif est exprimé grâce à la loi de Fourier, équivalente à la loi de Fick utilisée pour le transport de soluté. Contrairement au soluté qui diffuse uniquement dans l'eau par diffusion moléculaire, la diffusion thermique a lieu aussi bien dans l'eau que dans le milieu poreux. La diffusion équivalent thermique du milieu poreux dépend de la conductivité thermique λ, de la chaleur spécifique C_p ($\mathrm{J\,kg^{-1}\,K^{-1}}$) et de la masse volumique ($\mathrm{kg\,m^{-3}}$) du matériaux tel que D_{therm} (Eq. A.4) :

$$D_{therm} = \beta\, U + \frac{\lambda}{\rho_w C_{p_w}} \tag{A.4}$$

La capacité thermique volumique apparente du milieu poreux ($\mathrm{J\,m^{-3}\,K^{-1}}$) représente

la capacité du matériau à emmagasiner la chaleur et s'exprime avec la relation (Eq. A.5) (De Vries, 1963) :

$$\rho\, C_{p_m} = \omega\, (\rho_w\, C_{p_w})\, (1-\omega)(\rho_m\, C_{p_s}) \tag{A.5}$$

La chaleur a une capacité de diffusion beaucoup plus importante que le soluté. Ainsi, la diffusion moléculaire moyenne d'un soluté est inférieure de trois ordres de grandeur au coefficient de diffusion thermique dans l'eau et de quatre ordres à celui d'une roche sédimentaire ou de socle (Carlaw and Jaeger, 1959).

La conductivité thermique du milieu poreux λ ($\mathrm{W\,m^{-1}\,K^{-1}}$) représente la capacité du milieu poreux à conduire la chaleur. Différents modèles existent pour représenter la conductivité thermique apparente du milieu poreux λ:

- la moyenne pondérée:

$$\lambda = \omega\, \lambda_w + (1-\omega)\lambda_s \tag{A.6}$$

- la moyenne géométrique:

$$\lambda = \lambda_w^{\omega} + \lambda_s^{(1-\omega)} \tag{A.7}$$

- la moyenne harmonique:

$$\lambda = \frac{1}{\frac{\omega}{\lambda_w} + \frac{(1-\omega)}{\lambda_s}} \tag{A.8}$$

Woodside and Messmer (1961) ont montré que la moyenne géométrique (Eq. A.7) est appropriée pour représenter la dépendance de la conductivité thermique du solide sec à la porosité d'une roche consolidée. Les autres relations seraient plus représentatives de certains sédiments non consolidés.

L'effet de la dispersivité sur le transport de chaleur dans les milieux homogènes est encore débattu. Selon certains auteurs, les dispersivités de la chaleur et du soluté sont de même ordre de grandeur (de Marsily, 1986). Vandenbohede et al. (2009) suggèrent que la dispersivité thermique est plus faible que la dispersivité du soluté. Mais la plupart des auteurs ayant travaillé sur le transport de chaleur néglige en général la dispersion thermique par rapport à la conduction (Hopmans et al., 2002).

A.2.2.3 Spécificités du transport en surface libre

Dans cette section, le transport de chaleur dans le réseau hydrographique et le bilan des échanges thermiques entre eau et atmosphère sont décrits de façon synthétique. La description du transport de chaleur en rivière est présentée en section A.2.2 ainsi que dans le rapport de Wang et al. (2021), en ce qui concerne la modélisation du transport de chaleur à l'interface eau-air *via* la librairie *libseb*.

Pour avoir un bilan thermique complet sur une section de cours d'eau, l'équation de conservation de l'énergie est requise, sous la forme suivante (Sinokrot and Stefan, 1993; Wang et al., 2021) :

$$\frac{\partial(AT_w)}{\partial t} = -\frac{\partial(QT_w)}{\partial x} + AD_L\frac{\partial^2 T_w}{\partial x^2} + \frac{W\,H_{tot}}{\rho_w \cdot c_{pw}} + q_{inj}\,T_{inj} \tag{A.9}$$

où T_w désigne la température de l'eau (K), A la surface mouillée au centre de la section (m^2), D_L le coefficient de dispersion thermique longitudinal ($m^2\,s^{-1}$), ρ la masse volumique de l'eau ($kg\,m^{-3}$), c_{pw} la capacité calorifique massique de l'eau ($J\,K^{-1}\,kg^{-1}$), W la largeur au miroir de la section (m) et q_{inj} le débit d'eau linéique injecté ($m^3\,s^{-1}\,m^{-1}$), T_{inj} désigne la température de l'eau injectée (K). Le premier terme de la partie de droite représente le transport advectif et le second le transport diffusif. Quant au troisième terme de l'équation (A.9), comprenant H_{tot}, il correspond au flux énergétique total à l'interface air-eau, qu'il soit entrant ou sortant ($W\,m^{-2}$). Le dernier terme correspond quant à lui aux rejets directs en rivière.

A.2.2.3.1 Bilan des échanges thermiques eau/atmosphère à l'aide de la librairie *libseb*

À partir de données météorologiques spatio-temporelles, la librairie *libseb* calcule le bilan global des échanges thermiques à l'interface eau/atmosphère. Ce flux, noté H_{tot}, se décompose en quatre termes tel que :

$$H_{tot} = H_{sw} + H_{lw} + H_{lh} + H_{sh} \tag{A.10}$$

tel que H_{sw} désigne le flux dû au rayonnement solaire (ondes courtes) (Boyd and Kasper, 2003) , H_{lw} est le flux dû aux rayonnement par ondes longues (atmosphère/environnement) (Benyahya et al., 2012) , H_{lh} est le flux d'énergie par évapo-condensation (chaleur latente de transition de phase) (Dingman, 2008) et H_{sh} est le flux de chaleur par convecto-conduction (chaleur sensible) (Bowen, 1926). Les quatre flux du bilan d'énergie à l'interface air-eau sont détaillés dans le rapport PIREN-Seine de Wang et al. (2021).

On peut regrouper les flux latéraux ($q_{inj}\, T_{inj}$) ainsi que les flux d'énergie à l'interface air-eau ($\frac{W H_{tot}}{\rho_w \cdot c_{pw}}$) dans l'équation (A.9) afin de faciliter l'écriture de la discrétistaion numérique.

$$F_x = \frac{W H_{tot}}{\rho_w \cdot c_{pw}} + q_{inj}\, T_{inj} \tag{A.11}$$

La discrétisation suit un schéma semi-implicite (cf. Annexe) comme initialement réalisé entre Prose et *libttc* pour pour les espèces dissoutes (Wang, 2019) en remplaçant la vitesse par le débit (Eq. A.12).

$$\begin{aligned} &\frac{A_i^n T_i^n - A_i^{n-1} T_i^{n-1}}{\Delta t} + \theta \frac{Q_{i+\frac{1}{2}}^n T_i^n - Q_{i-\frac{1}{2}}^n T_{i-1}^n}{\Delta x} + (1-\theta) \frac{Q_{i+\frac{1}{2}}^{n-1} T_i^{n-1} - Q_{i-\frac{1}{2}}^{n-1} T_{i-1}^{n-1}}{\Delta x} \\ &= D_L (A_i^n \theta \frac{T_{i+1}^n - 2T_i^n + T_{i-1}^n}{\Delta x^2} + A_i^{n-1}(1-\theta) \frac{T_{i+1}^{n-1} - 2T_i^{n-1} + T_{i-1}^{n-1}}{\Delta x^2}) + \theta F_x^n + (1-\theta) F_x^{n-1} \end{aligned} \tag{A.12}$$

Dans cette équation, $i + \frac{1}{2}$ et $i - \frac{1}{2}$ représentent les indices des faces d'une section i. Les débits et les surfaces mouillées sont calculés par la librairie *libhyd*, *via* la méthode de Muskingum. Dans l'état d'implémentation actuel de la librairie *libttc*, un schéma pleinement implicite ($\theta = 1$) est utilisé.

A.3 Solution analytique des échanges thermiques cours d'eau-aquifère et aquifère-aquitard-aquifère

Le transport de chaleur entre la rivière et l'aquifère ainsi que l'interface aquifère-aquitard-aquifère a pu être trouvé en utilisant une solution analytique. Les solutions analytiques sont pratiques pour résoudre le transport de chaleur et estimer le flux de chaleur entre

des couches ayant des propriétés thermiques différentes. Bien qu'elles aient des limites, elles peuvent estimer suffisamment les débits verticaux entre le lit de la rivière et l'aquifère et à l'interface aquifère-aquitard-aquifère.

Several factors control the streambed temperature, such as the channel shape, stream water level, water flow, stream bank slope, stream bed hydraulic properties, groundwater table depth, aquifer hydraulic properties and aquifer geometric properties Peterson and Wilson (1988); Sophocleous (2002); Brunner et al. (2009); Doble et al. (2012). Inversement, la température du cours d'eau est également influencée par la température des aquifères en fonction de leur degré de connectivité.(Brunner et al., 2009; Rivière et al., 2014). Ces impacts créeraient effectivement des écarts entre les températures du cours d'eau et la température d'équilibre du cours d'eau. (Bogan et al., 2003). À l'échelle du tronçon, l'échange de chaleur par advection joue un rôle plus important lorsque les flux d'eaux souterraines sont importants (Constantz et al., 2002), à l'échelle régionale, les forces advectives et diffusives sont combinées. Pour la modélisation à l'échelle régionale, la largeur de la rivière est généralement beaucoup plus petite que la résolution du modèle. Par conséquent, la direction dominante de l'écoulement entre la rivière et l'aquifère est généralement verticale, ce qui convient au cadre de la solution analytique. À l'échelle du bassin versant, Loinaz et al. (2013) a utilisé une solution analytique en complément de l'application numérique à l'échelle du bassin versant pour estimer l'apport thermique des eaux souterraines. En outre, les solutions analytiques peuvent être utilisées de manière inversée pour estimer le débit de l'eau à l'interface entre le cours d'eau et l'aquifère dans de nombreuses études Stallman (1965); Anibas et al. (2009); Caissie et al. (2014); Jensen and Engesgaard (2011)). L'une de ces solutions est proposée et décrite en détail par Kurylyk et al. (2017); Shan and Bodvarsson (2004); Bredehoeft and Papaopulos (1965) qui sera utilisé dans ce modèle. La solution analytique proposée suppose un flux thermique vertical 1-D en régime permanent ; les propriétés thermiques sont supposées homogènes dans chaque couche ; et le flux de Darcy est constant et uniforme dans toutes les couches.

When the advective-conductive heat transport (Eq. A.1) is considered, in the steady state, the transport equation becomes Eq. A.26. Given that the bulk volumetric heat

capacity of the porous medium is A.5, a multi-layered heat transport in the porous medium has the boundary conditions:

$$T_1(z = 0) = T_0 \tag{A.13}$$

$$T_n(z = d_n) = T_B \tag{A.14}$$

where z is the depth, d_n is the bottom depth of the deepest layer, n is the number of layers, T_0 is the temperature of the top boundary condition, T_B is the temperature of the bottom boundary condition. At the interfaces of adjacent layers, the interface temperatures (T_L) must converge and be equal:

$$T_i(z = d_i) = T_{i+1}(z = d_i) = T_{Li}(i = 1, 2, ..., n - 1) \tag{A.15}$$

where d_i is the distance m of a layer *i* from the top boundary to the *i*th interface (Figure A.2). Also the total heat flux must be continuous and same across the layer interfaces. Therefore, the relationship of heat fluxes at the interface becomes:

$$\lambda_i \frac{dT_i(z = d_i)}{dz} = \lambda_i \frac{dT_{i+1}(z = d_i)}{dz}(i = 1, 2, ..., n - 1) \tag{A.16}$$

The steady-state heat transport equation A.26 is a homogeneous ordinary differential equation with a standard solution which contains two equation coefficients delineated in Kurylyk et al. (2017):

$$T_i(z) = C_{i1} \exp \frac{qz * \rho_w * C_w}{\lambda_i} + C_{i2}(i = 1, 2, ..., n - 1) \tag{A.17}$$

This is a n-layered system with 2n unknowns, and it has two specified boundary conditions (Equations A.13,A.14), n-1 interface conditions due to the continuity of the temperatures (Equation A.15) and n-1 interface conditions due to the continuity of heat fluxes (Equation A.16). Thus a system of of linear algebraic equations can be developed to solve 2n unknowns. For the heat transport in such a system, Shan and Bodvarsson (2004) obtained the coefficients below Kurylyk et al. (2017):

$$C_{i2} = \frac{\alpha T_0 - T_B}{\alpha - 1}(i = 1, 2, ..., n-1) \tag{A.18}$$

$$C_{1,1} = \frac{T_B - T_0}{\alpha - 1}(i = 1, 2, ..., n-1) \tag{A.19}$$

$$C_{i+1,1} = \exp qd_i(\frac{\rho_w C_w}{\lambda_i - \frac{\rho_w C_w}{\lambda_{i+1}}}) * C_{i,1}(i = 1, 2, ..., n-1) \tag{A.20}$$

Where the equation α is defined as

$$\alpha = \exp q \sum_{i=1}^{n}(\frac{b_i * \rho_w C_w}{\lambda_i}) \tag{A.21}$$

L'application conceptuelle de la solution analytique dans le modèle est décrite dans la figure A.2 ci-dessous. Pour le transport de chaleur aquifère-aquitard-aquifère, un schéma à 3 couches 2 inconnues (températures des couches aquifères supérieure et inférieure) est utilisé. Comme les températures sont estimées au centre de chaque couche aquifère, l'épaisseur de la couche est supposée être la distance du centre de la cellule au bord. Dans cette application, nous sommes intéressés par la température au centre de l'aquitard, donc la profondeur de la solution est $b_1 + b_2/2$.

Pour le transport de chaleur entre le cours d'eau, le lit du cours d'eau et l'aquifère, une solution à deux couches est utilisée. La température du cours d'eau est supposée être uniforme dans toute la colonne verticale. Par conséquent, la température au sommet du lit de la rivière est considérée comme suit T_0. Par conséquent, la profondeur d'intérêt de cette étude se situe à $b_1/2$ m. z_{bottom} signifie la température au centre de la couche aquifère sous le cours d'eau.

Dans l'application aquitard, une solution à 3 couches est utilisée. A chaque pas de temps, la température au centre de l'aquifère (z_{top}) au-dessus de l'aquitard et la température au centre de l'aquifère en dessous de l'aquitard (z_{bottom}) sont utilisées pour calculer la température de l'aquitard à la profondeur $b_1 + b_2/2$ m.

L'application de la solution analytique est intégrée dans la solution numérique. Ceci a été fait en incluant les températures de l'aquitard et du lit du cours d'eau comme une

inconnue, en fonction des coefficients calculés via la solution analytique dans la matrice des coefficients. Dans la solution de la température du lit de la rivière, puisque la température de la rivière est connue a priori, elle est ajoutée au côté droit de la solution. Cette approche était nécessaire afin de limiter le nombre de calculs effectués à chaque pas de temps, et d'effectuer les calculs nécessaires simultanément. On s'attend à ce que cette approche réduise le temps total de la simulation puisque le modèle régional est assez grand et coûteux numériquement.

Lorsque l'aquitard est défini dans la simulation, l'épaisseur de l'aquitard est insérée entre les couches aquifères et la conductivité thermique effective est ajustée avec l'épaisseur de la couche d'aquitard dans la solution numérique.

Une fois la température du lit de la rivière et de l'aquitard calculée au pas de temps t, la température du lit de la rivière est alors assignée comme limite inférieure du transport de chaleur de la rivière au pas de temps suivant $t + 1$.

Pour tester le cadre développé, un échantillon d'aquitard de $10\ \mathrm{m}$ d'épaisseur et 3 $\mathrm{W\,m^{-1}\,K^{-1}}$ est introduit entre deux couches aquifères, dont chacun a une épaisseur de $10\ \mathrm{m}$ et présente une conductivité thermique de 1,5 $\mathrm{W\,m^{-1}\,K^{-1}}$.

Une analyse de sensibilité robuste a été effectuée avec des conditions hydrologiques changeantes en appliquant des conditions de décharge et de recharge de l'aquifère à différentes vitesses de Darcy. Les vitesses variaient entre $1e^{-10}$ - $1e^{-2}$ $\mathrm{m\,s^{-1}}$ dans les deux directions ainsi que dans la condition d'absence d'écoulement. Le transport de chaleur a l'interface nappe-rivière et de l'aquitard dans CaWaQS à l'aide de la solution analytique est comparé à l'outil de tableur FLUX-LM fourni par Kurylyk et al. (2017)

A.4 Validation des développements

La librairie *libttc* a été couplée avec la librairie *libaq* dans le but de simuler le transport de chaleur et de solutés dans les aquifères. Bien que *libttc* résolve le transport de chaleur dans l'eau libre et dans un milieu poreux, l'objectif de ce test est de vérifier les calculs effectués par *libttc* couplée, au sein de CaWaQS3.X. Pour vérifier la fonctionnalité et la précision du problème de transport de chaleur, un ensemble de cas de tests a été réalisé.

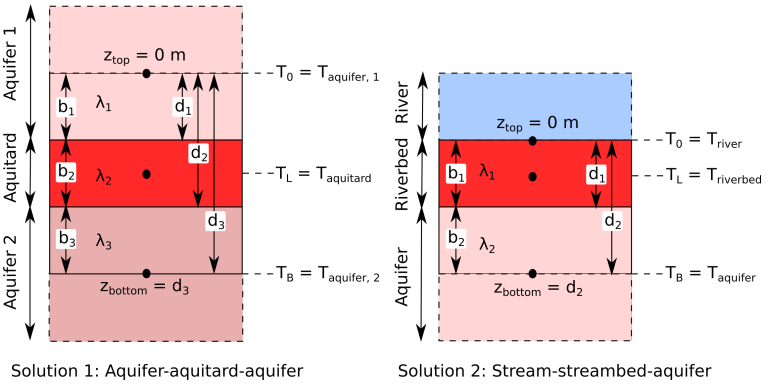

Figure A.2 La configuration de la solution analytique dans a) l'interface aquifère-aquitard-aquifère et b) l'interface nappe-rivière.

Il s'agit de résoudre le transport de chaleur en 1-D et 2-D, à la fois, en régime permanent et transitoire. Pour tous les tests présentés ici, un schéma implicite ($\theta = 1$) est utilisé.

La validation des cas test s'effectue en comparant les chroniques ou profils de températures simulés avec les résultats des solutions analytiques. Cinq critères sont utilisés pour évaluer quantitativement la performance du modèle : le biais, le coefficient de corrélation, l'erreur moyenne absolue (*Mean Absolute Error*; MAE), l'erreur moyenne quadratique (*Root Mean Square Error*; RMSE) et le KGE (*Kling-Gupta Efficiency*, Gupta et al. (2009)).

Les deux critères RMSE et MAE doivent tendre vers zéro pour une simulation précise. Le KGE est utilisé uniquement pour quantifier la pertinence des simulations transitoires. Il est basé sur le biais, le rapport des variances, et le coefficient de corrélation entre les variables observées et les variables simulées. Il repose sur la minimisation de la distance euclidienne des différentes composantes à leurs valeurs optimales.

Le coefficient de corrélation est défini par :

$$r = \frac{1}{n} \sum \frac{(V_{obs}(t) - \overline{V_{obs}}(t)) - (V_{sim}(t) - \overline{V_{sim}}(t))}{\sigma_{obs}\, \sigma_{sim}} \tag{A.22}$$

avec, les variables simulées (V_{sim}) et observées (V_{obs}), n le nombre d'échantillons, $\overline{V_{obs}}$ et $\overline{V_{sim}}$ sont la moyenne de la variable observée et simulée, et les écarts types σ_{obs} pour l'observation et σ_{sim} pour la simulation à l'instant t. Le MAE s'écrit :

$$MAE = \frac{1}{n}\sum(V_{obs}(t) - V_{sim}(t)) \tag{A.23}$$

Et le KGE:

$$KGE = 1 - \sqrt{(r-1)^2 + (\zeta - 1)^2 + (\upsilon - 1)^2} \tag{A.24}$$

avec, ζ le rapport des écarts types $\zeta = \sqrt{\frac{\sigma^2_{sim}}{\sigma^2_{obs}}}$ et υ le rapport des moyennes $\upsilon = \frac{\overline{V_{sim}(t))}}{\overline{V_{obs}(t))}}$.

A.4.1 Validation du transfert de chaleur en rivière

Les librairies *libseb* et *libttc* ont été implémentées dans le plateforme CaWaQS3.X. Un cas test bassin versant a été construit (Fig. A.3) afin d'y valider le transport de chaleur en rivière. Une simulation en conditions contrôlées a été mise en œuvre.

A.4.1.1 Description du cas test

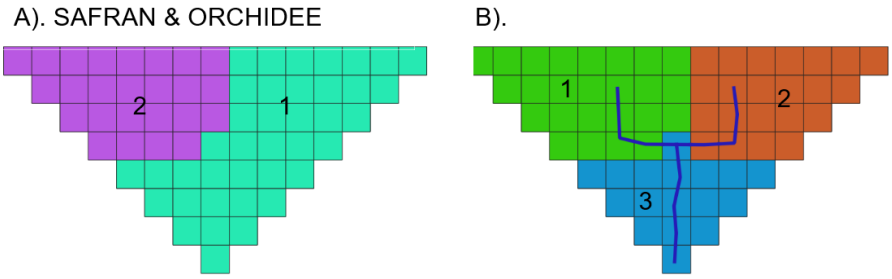

Figure A.3 Géométrie du cas-test : A). Couverture des mailles SAFRAN and ORCHIDEE, les zones 1 et 2 représentent des cellules SAFRAN différentes; B). Les lignes bleues correspondent aux tronçons de rivière; les sections (verte, bleue, rouge) correspondent aux unités de production d'eau et de chaleur dont les flux journaliers sont calculés par ORCHIDEE

Le bassin versant est composé de 64 mailles. Chaque maille a une surface de $1\ \mathrm{km}^2$. Trois tronçons de rivière sont définis, chacun étant associé à une unité de production d'eau et de chaleur (Fig. A.3B). Les flux d'eau journaliers (mm) sur le bassin versant sont calculés à l'aide du logiciel ORCHIDEE forcé par les données SAFRAN (Fig. A.3A). Ces flux d'eau sont utilisés par la librairie *libfp* pour produire les flux latéraux des tronçons de rivière.

Les températures de l'eau associées aux flux d'eau issus d'ORCHIDEE sont fixées à 298,22 K (25,07 °C). La température de l'eau dans les tronçons de rivière a été simulée pour une année hydraulique. Avec cette condition contrôlée, une solution théorique de 25,07 °C est attendue tout au long de la simulation.

A.4.1.2 Résultats

D'après les simulations, les températures de l'eau dans les trois tronçons de rivière sont toujours égales à 25,07 °C. Un exemple de sortie pour la maille à l'exutoire (tronçon de rivière 3) est montré dans la figure A.4. Le transport de chaleur en rivière dans le plate-forme CaWaQS3.X est ainsi validé pour une condition hydraulique transitoire.

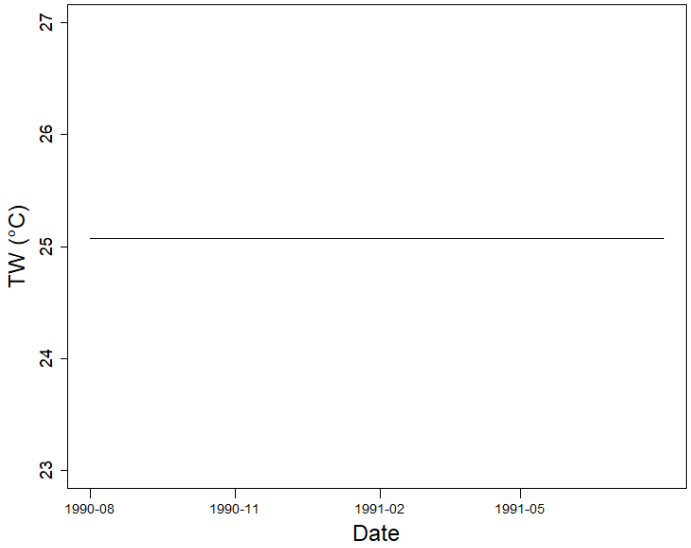

Figure A.4 Températures de l'eau simulées pour la maille à l'exutoire (tronçon de rivière 3)

A.4.2 Validation du transfert de chaleur en aquifère

A.4.2.1 Validation du transport conductif en régime permanent

Le transport de chaleur purement conductif en régime permanent s'écrit (Eq. A.25) :

$$D_{therm}\left(\frac{\partial^2 T}{\partial x^2}+\frac{\partial^2 T}{\partial y^2}\right)=0 \tag{A.25}$$

$$D_{therm}\left(\frac{\partial^2 T}{\partial x^2}+\frac{\partial^2 T}{\partial y^2}\right)-U\left(\frac{\%partialT}{\partial x}+\frac{\partial T}{\partial y}\right)=0 \tag{A.26}$$

Par conséquent, la chaleur en 1-D et 2-D évolue linéairement proportionnellement à D_{therm} (Stallman, 1965). Le premier cas de test développé pour vérifier la précision de la simulation du transport de chaleur est la diffusion en régime permanent dans une maillage gigogne.

A.4.2.1.1 Colonne 1-D avec maillage irrégulier Le premier cas (Fig. A.5) correspond au transport de chaleur utilisant la colonne verticale 1-D maillée, de façon irrégulière, à l'aide d'un maillage gigogne. Dans ce cas test, le domaine spatial construit traduit une colonne de sol verticale de 10 m d'épaisseur discrétisée par un maillage gigogne au centre. La taille des cellules est de 1 m, et le rapport de gigogne est de 1:2; au total, 12 cellules sont décrites.

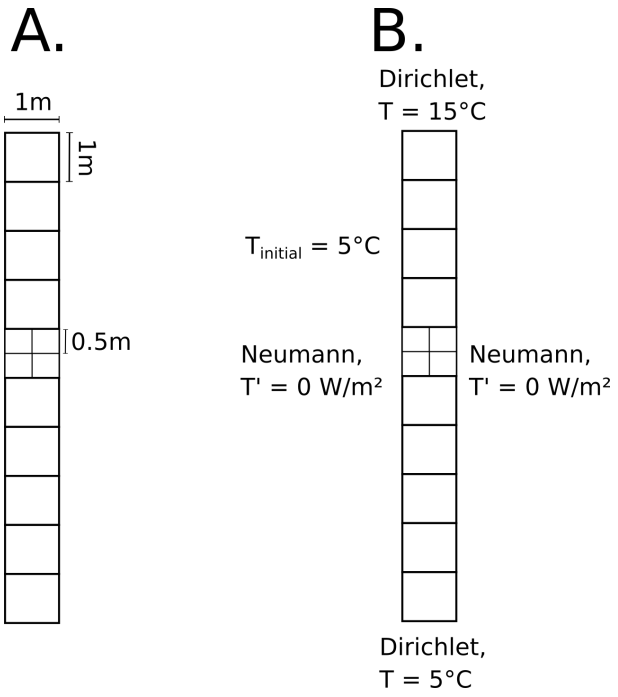

Figure A.5 A) La géométrie de la colonne de sol en 1-D. B) Températures initiales et conditions aux limites utilisées sur la colonne de sol.

Les conditions aux limites sur les côtés sont définies comme des conditions aux limites à flux nul (condition de Neumann). La condition en limite inférieure de la colonne (Fig. A.5.B) est fixée à 5 °C. Celle en limite supérieure l'est à 15 °C. La tempéra-

ture initiale de la colonne est uniforme de 5 °C. Les propriétés thermiques utilisées pour caractériser la colonne sont synthétisées dans le tableau A.2. Ces propriétés sont considérées homogènes sur l'ensemble du domaine.

Table A.2 Propriétés thermiques du problème du transport de la chaleur en colonne 1-D avec un maillage irrégulier

Paramètres et valeurs associées		Unités
ω	$0,15$	$[\mathrm{m^3\,m^{-3}}]$
λ_w	$0,570$	$[\mathrm{W\,m^{-1}\,K^{-1}}]$
λ_s	$7,61$	$[\mathrm{W\,m^{-1}\,K^{-1}}]$
c_{p_w}	4186	$[\mathrm{J\,kg^{-1}\,K^{-1}}]$
ρ_w	1000	$[\mathrm{kg\,m^{-3}}]$
c_{p_s}	900	$[\mathrm{J\,kg^{-1}\,K^{-1}}]$
ρ_w	2500	$[\mathrm{kg\,m^{-3}}]$
β	0	$[\mathrm{m}]$
U	0	$[\mathrm{m\,s^{-1}}]$

La figure A.6 montre la parfaite corrélation ($r = 1$) obtenue à l'issue de la simulation, entre, d'une part, la solution numérique du transport de chaleur par conduction, et d'autre part, la solution analytique associée. Des valeurs de RMSE et de MAE, toutes deux égales à 0 °C ont bien été déterminées. Le transport de chaleur par conduction en régime permanent pour la colonne de sol 1-D est, par conséquent, validé.

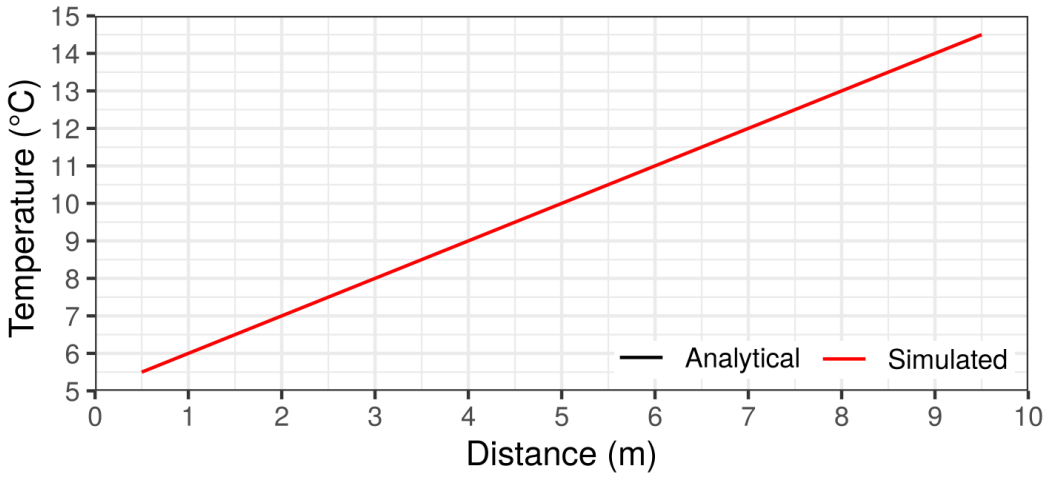

Figure A.6 Comparaison de la solution analytique (Stallman, 1965) et de la simulation CaWaQS3.X , dans le cas du transport de chaleur en colonne gigogne en 1-D.

A.4.2.1.2 Bassin avec un maillage régulier Le deuxième cas est associé au transport de chaleur dans un bassin versant d'une surface de 64 km^2. Un aquifère unique est représenté avec une résolution spatiale homogène de 1 km^2. Les conditions aux limites sur les faces Est et Ouest du bassin sont imposées à flux nul (conditions de Neumann). Les limites inférieures (resp. supérieures) de la colonne sont fixées à 5 °C (resp. 13 °C) (conditions de Dirichlet). Un problème de transport de chaleur par conduction pure dans la direction Nord-Sud est ainsi ici résolu. Une température initiale de 5 °C est attribuée à chaque cellule (Fig. A.7).

Les propriétés thermiques de la couche aquifère sont rassemblées dans le tableau A.3. De même que précédemment, les propriétés sont considérées homogènes sur l'ensemble de la couche.

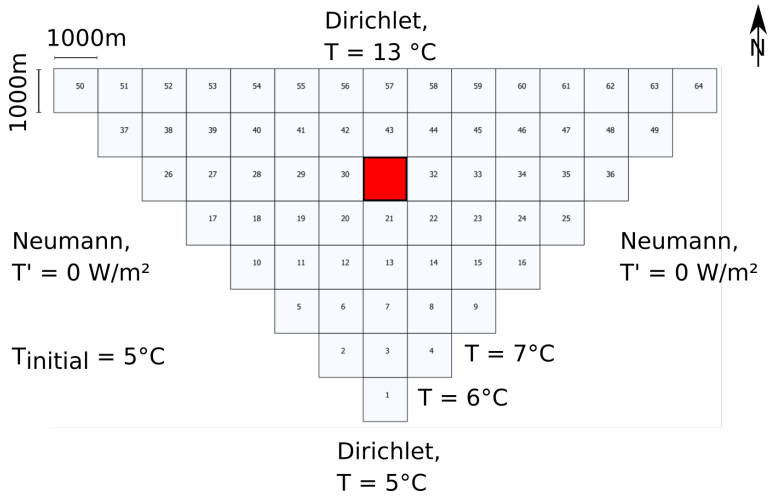

Figure A.7 Géométrie du cas test "bassin versant" et condition initiales et limites associées. La variation de température de la cellule rouge sera étudiée, par la suite, en section A.4.3.2.

Table A.3 Propriétés thermiques du problème du transport de la chaleur dans un bassin avec maillage régulier.

Paramètres	Valeurs	Unités	Paramètres	Valeurs	Unités
ω	0,15	$[\mathrm{m^3\,m^{-3}}]$	c_{p_s}	900	$[\mathrm{J\,kg^{-1}\,K^{-1}}]$
λ_w	0,570	$[\mathrm{W\,m^{-1}\,K^{-1}}]$	ρ_s	2500	$[\mathrm{kg\,m^{-3}}]$
λ_s	7,61	$[\mathrm{W\,m^{-1}\,K^{-1}}]$	β	0	$[\mathrm{m}]$
c_{p_w}	4186	$[\mathrm{J\,kg^{-1}\,K^{-1}}]$	U	0	$[\mathrm{m\,s^{-1}}]$
ρ_w	1000	$[\mathrm{kg\,m^{-3}}]$			

Un gradient de température Nord-Sud est correctement simulé par le modèle (Fig. A.8). Tel qu'attendu, en considérant une coupe transversale selon cette direction au centre de la couche, les résultats sont parfaitement alignés sur une droite dans le cas purement conductif. Ce cas test valide le transport de chaleur conductif en 2-D permanent.

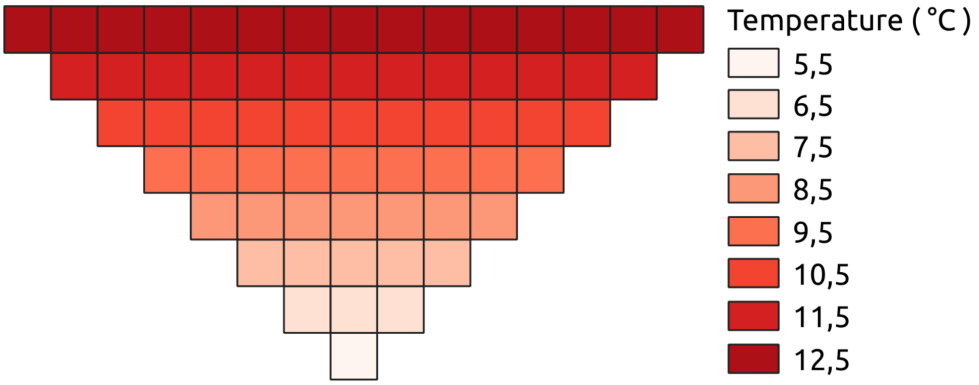

Figure A.8 Évolution de la température simulée en régime permanent, pour le bassin versant avec un flux de chaleur orienté Nord-Sud.

A.4.2.1.3 Milieu 2-D à maillage irrégulier Un troisième cas considère un problème de transport de chaleur conductif permanent, dans un milieu poreux idéalisé, à mailles irrégulières (Fig. A.9 variant entre 0,25 m et 1 m de côté). L'objectif est d'observer si une configuration de grille 2-D gigogne a un impact sur le transport de chaleur. Les conditions aux limites des faces Nord et Sud du milieu poreux sont définies comme des conditions aux limites à flux nul. La condition aux limites des faces Est des mailles sans voisins est fixée à 10 °C et la condition à la limite Ouest est fixée à 20 °C (Fig. A.9). Une température initiale de 5 °C est attribuée à chaque cellule. Les propriétés thermiques du milieu poreux sont répertoriées dans le tableau A.3. Les propriétés sont, ici encore, considérées homogènes.

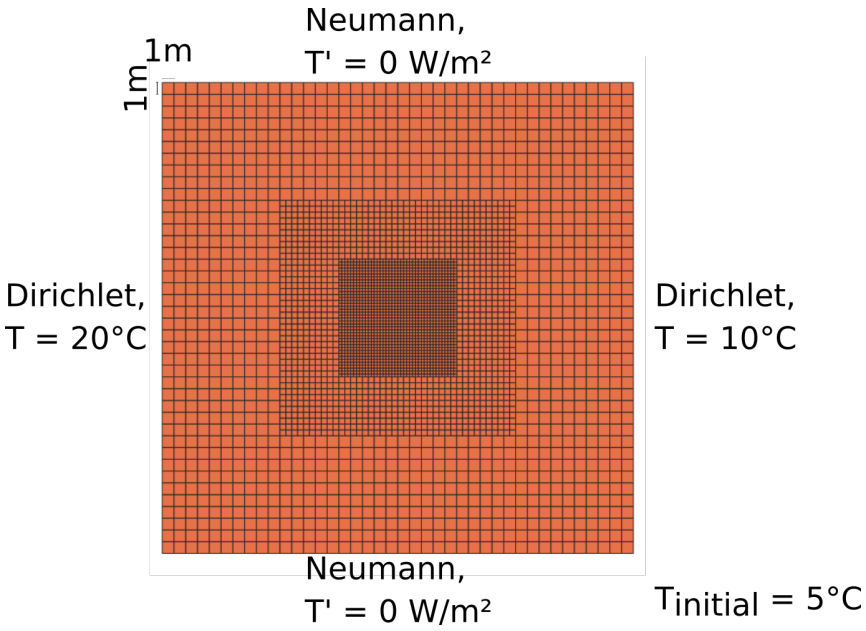

Figure A.9 Maillage irrégulier associé au cas de simulation test en milieu poreux. La résolution de la cellule est 1 m.

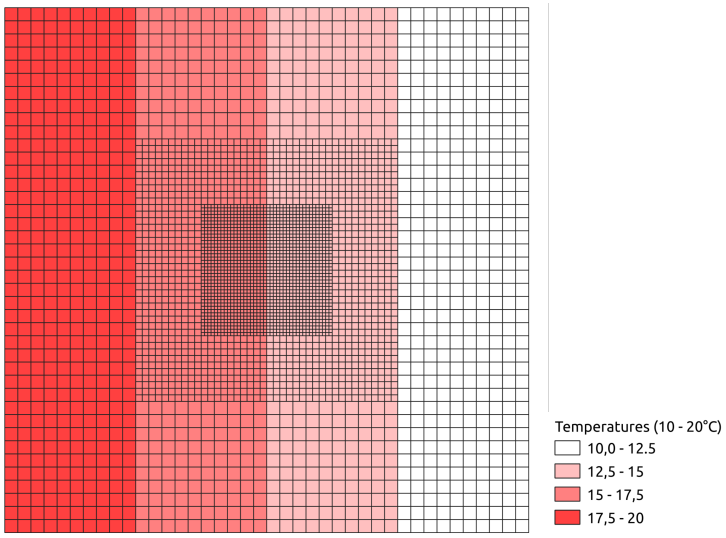

Figure A.10 Évolution de la température simulée en régime permanent pour le cas-test “bassin versant”.

Selon une coupe transversale à mi-domaine, orientée Ouest-Est, les résultats sont, à nouveau, en parfait accord avec la solution analytique, qui dans le cas d’une conduction pure se traduit par une simple droite (Fig. A.6). L’évolution de la température en régime permanent dans la dimension horizontale est satisfaisante, ce qui renforce encore la crédibilité de la résolution du transport de chaleur 2-D conductif en régime permanent par *libttc* intégrée dans CaWaQS3.X.

A.4.2.2 Validation du transport transitoire de chaleur conductif et advectif par comparaison avec la solution de Goto et al. (2005)

La réponse thermique d'une colonne de sédiments saturés en 1-D avec une vitesse donnée et une température variant périodiquement a une solution analytique (Goto et al., 2005; Stallman, 1965). Afin d'examiner la réponse du module de transport de chaleur, nous avons défini une colonne de sol, en utilisant une vitesse verticale fixe et une température périodiquement variable aux limites supérieures et inférieures. La géométrie de cette colonne est décrite en figure A.11.A.

Ces conditions aux limites imposent une réponse thermique verticale. Celle-ci dépend de la direction et de la vitesse de l'écoulement, de la diffusivité thermique du sédiment saturé et de la période de variation de la température de surface. La solution analytique de Goto et al. (2005) est utilisée pour estimer la variation de température en tout point de la colonne pour des vitesses ascendante et descendante, ainsi que pour un problème conductif pur. Les résultats de la solution numérique pour ces trois cas de transport de chaleur sont comparés aux solutions analytiques de Goto et al. (2005).

Si l'on considère un milieu poreux de profondeur z, la réponse thermique d'un milieu poreux homogène avec un écoulement vertical est exprimée par l'équation (Eq. A.27) (Stallman, 1965):

$$T(z,t) = \sum_i A_i \exp\left(\frac{vz}{2K_m} - \frac{z}{2K_m}\sqrt{\frac{\alpha_i + v^2}{2}}\right) \cos\left(\frac{2\pi\, t}{P_i} - \omega_i - \frac{z}{2K_m}\sqrt{\frac{\alpha_i - v^2}{2}}\right) \tag{A.27}$$

avec un temps t (s), une surface de A_i, une porosité ω_i, une conductivité thermique λ et une période de P_i. Le paramètre v est un produit de la vitesse d'écoulement du fluide U et de la capacité calorifique volumique de l'eau $\rho_w c_{p_w}$ et de celle du milieu poreux $\rho_s c_{p_m}$ défini comme suit :

$$v = \frac{\rho_w c_{p_w}}{\rho_m c_{p_m}} U \tag{A.28}$$

où ρ et c_p correspondent respectivement à la densité et la capacité thermique spé-

cifique du solide. Les indices w et m indiquent respectivement l'eau et le milieu poreux. α_i est une fonction de P_i, de K_m (diffusivité thermique du milieu poreux, $K_m = \frac{\lambda}{\rho_m C_{p_m}}$) et v.

$$\alpha_i = \sqrt{v^4 \left(1 + \frac{8\pi K_m}{P_i v^2}\right)} \tag{A.29}$$

Pour valider la solution numérique, on définit un milieu poreux de conductivité thermique égale à $1\ \mathrm{W\,m^{-1}\,K}$ et d'une capacité thermique de $4\,10^6\ \mathrm{J\,kg^{-1}\,K^{-1}}$. Une amplitude A_i de $1\ ^\circ\mathrm{C}$ avec une température moyenne de $11\ ^\circ\mathrm{C}$ et une période P_i de 30 jours a été choisie pour cette étude. 30 jours de simulation assureraient une propagation suffisante du transport de chaleur advectif et conductif dans une colonne de $10\ \mathrm{m}$ d'épaisseur. Les résultats de la simulation numérique sont ensuite comparés à la solution analytique du même milieu poreux. Les calculs de la solution analytique sont réalisés en utilisant le logiciel pyHeat (https://github.com/flipoyo/pyHeat).

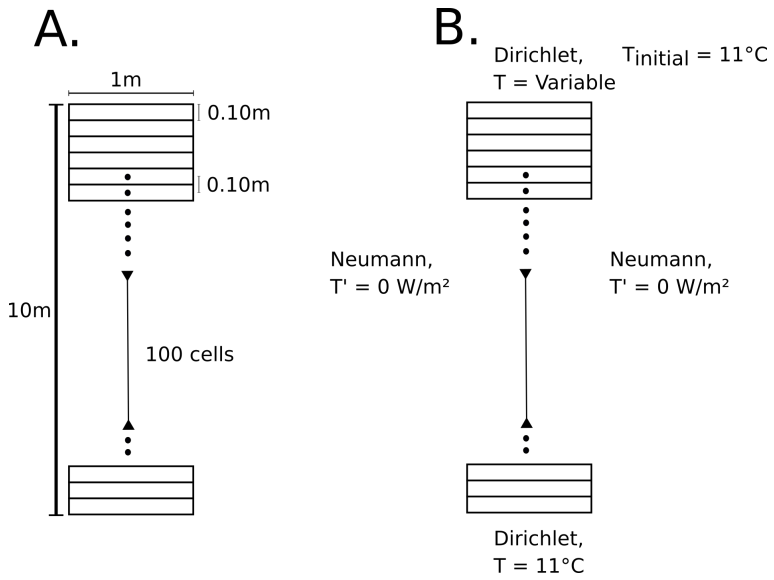

Figure A.11 A) Géométrie de la colonne de sol en 1-D. B) Températures initiales et conditions aux limites de la colonne de sol Goto et al. (2005).

Les propriétés thermiques du domaine simulé sont mentionnés en tableau A.4. Le vecteur vitesse est fixé et le signe positif indique une infiltration (flux d'eau descendant) alors que le signe négatif indique une exfiltration (flux d'eau ascendant). Dans le premier et le troisième cas, un écoulement vertical du fluide est appliqué dans le sédiment

homogène. Dans le second, il n'y a pas de flux vertical, le transport de chaleur est donc purement conductif. La conductivité thermique effective du milieu poreux est de $1\ \mathrm{W\,m^{-1}\,K^{-1}}$ (moyenne géométrique).

Table A.4 Propriétés thermiques de la colonne de sol utilisée pour les trois cas testés pour le transport de chaleur: 1) Flux advectif-conductif vers le bas, 2) Cas conductif pur, pas de flux d'eau, 3) Flux advectif-conductif vers le haut de la colonne.

Paramètres et valeurs associées		Unités
ω	0.15	$[\mathrm{m^3\,m^{-3}}]$
λ_w	0.570	$[\mathrm{W\,m^{-1}\,K^{-1}}]$
λ_s	1.104	$[\mathrm{W\,m^{-1}\,K^{-1}}]$
c_{p_w}	4186	$[\mathrm{J\,kg^{-1}\,K^{-1}}]$
ρ_w	1000	$[\mathrm{kg\,m^{-3}}]$
c_{p_s}	1674.39	$[\mathrm{J\,kg^{-1}\,K^{-1}}]$
ρ_w	2500	$[\mathrm{kg\,m^{-3}}]$
β	0	[m]

Le maillage, les conditions initiales et les conditions limites de la simulation sont données dans la figure A.11.B. Les conditions aux limites supérieures et inférieures sont définies comme des conditions de Dirichlet, tandis que les faces latérales sont définies comme des conditions de type Neumann à flux nul. Les valeurs des conditions initiales, les conditions aux limites supérieures et inférieures sont indiquées dans le tableau A.5.

Table A.5 Valeurs des conditions aux limites et initiales des trois cas tests. U_{cas1} est la simulation advectif-conductif avec un flux de l'eau descendant, U_{cas2} indique le test conductif pur, U_{cas3} est la simulation d'un flux de l'eau descendant. Les conditions aux limites et initiales thermiques $T_{initiale}$, $T_{surface}$, T_{bas} sont les mêmes pour les trois cas.

	paramètre et valeurs associées	unités
U_{cas1}	$1e^{-6}$	$[\mathrm{m\,s^{-1}}]$
U_{cas2}	0	$[\mathrm{m\,s^{-1}}]$
U_{cas3}	$-1e^{-6}$	$[\mathrm{m\,s^{-1}}]$
$T_{initiale}$	11	[°C]
$T_{surface}$	périodique de moyenne 11°C, d'amplitude 1°C et de période 30 jours	[°C]
T_{bas}	11	[°C]

La température initiale de la colonne est fixée à 11°C. Les côtés droit et gauche de la colonne de sol ont une condition limite de Neumann à flux nul. La condition limite supérieure est une température variable dans le temps avec une température moyenne de 11°C, une amplitude de 1°C et une période de 30 jours. La solution de Goto a pour hypothèse une colonne semi-infinie. La solution analytique a permis de calculer

la température à une profondeur de 10 m en utilisant les conditions citées ci-dessus. D'après ce calcul, la température est quasi constante et de 11°C. Cette température est imposée à la base de la colonne .

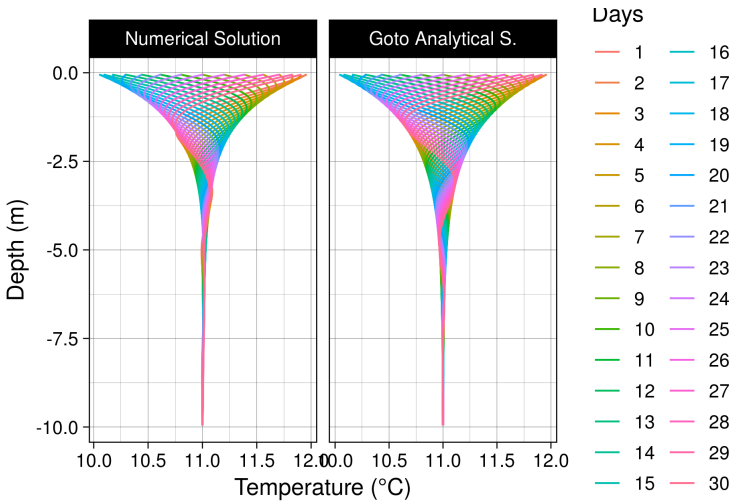

Figure A.12 Variations spatio-temporelles des réponses thermiques d'un flux de l'eau descendant (cas 1) dans la colonne de sol à partir a)de la solution numérique libttc, b) de la solution analytique Goto. Chaque ligne représente le profil de température d'un jour en différentes couleurs pendant la période de simulation.

Dans le cas 1, les profils de températures simulées sur une période de 30 jours sont représentés sur la figure A.12. Lorsque l'on compare la solution numérique et la solution analytique, les profils thermiques sont assez similaires. La propagation du flux de chaleur atteint jusqu'à 5m de profondeur dans les solutions numériques et analytiques.

Le critère statistiques de performance de la solution numérique par rapport à la solution analytique est donné dans le tableau A.6. On peut voir que la corrélation est très élevée, et que les valeurs MAE, et RMSE sont aussi basses que 0.023°C et que le kge est proche de 1.

Dans le cas 2 (simulation de conduction pure), la pénétration des variations de température atteint une profondeur de 2,5m en un mois. En dessous de 2,5m, la condition de surface n'a plus d'impact. Lorsque l'on compare la solution numérique et les solutions analytiques, les profils de température sont similaires. Les critères statistiques estimés pour ce cas peuvent être vus dans la tableau A.6. Nous observons une corrélation élevée ainsi que des valeurs MAE et RMSE assez faibles.

Table A.6 Performances de simulation: coefficient de corrélation, MAE (°C), RMSE (°C), biais (%), et KGE calculé pour les cas de test de la solution numérique vs Goto et al. (2005). 1) Cas 1 a un flux descendant avec une vitesse U de $1e{-}6\ \mathrm{m\,s^{-1}}$; 2) Cas 2 est une simulation en conductif pur $\mathrm{m\,s^{-1}}$; 3) Cas 3 a un flux ascendant U de $-1e{-}6\ \mathrm{m\,s^{-1}}$.

	Critères	Cas 1	Cas 2	Cas 3
1	Corrélation coeff.	0.988	0.998	0.998
2	MAE (°C)	0.020	0.002	0.001
3	RMSE (°C)	0.034	0.005	0.005
4	BIAIS (%)	0	0	0
5	KGE	0.938	0.987	0.956

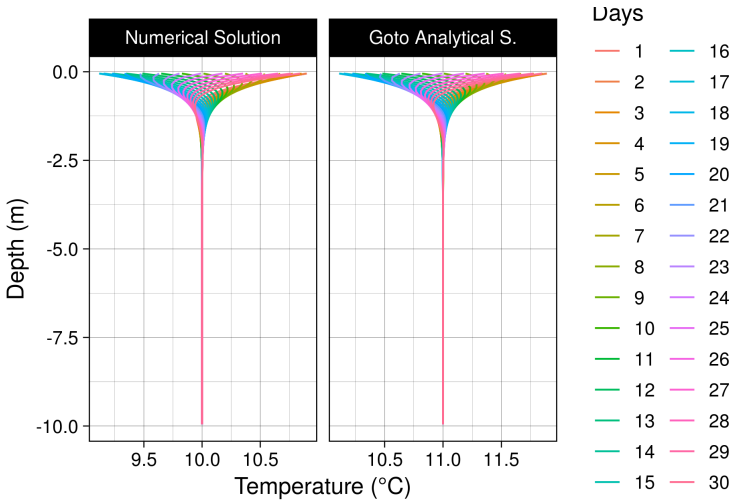

Figure A.13 Variations spatio-temporelles des réponses thermiques d'un flux de chaleur conductif pur (cas 2) dans la colonne de sol à partir de a)la solution numérique libttc, b) la solution analytique Goto. Chaque ligne représente le profil de température d'un jour en différentes couleurs pendant la période de simulation.

Le troisième cas (Fig. A.14) simule l'impact du flux vertical ascendant. La pénétration de la température de surface est entravée par l'advection de la température du bas de la colonne. Le profil de température devient linéaire à 1,3m de profondeur. Les critères statistiques sont donnés dans le tableau A.6. Comme dans les cas précédents, les critères statistiques montrent une bonne adéquation de la solution numérique avec la solution analytique. Nous observons un coefficient de corrélation élevé avec des valeurs MAE et RMSE limitées. Le KGE montre également une grande efficacité du modèle.

Les trois cas de transport de chaleur ont été testés et comparés avec une solution analytique pour valider le transport de chaleur simulé par la librairie libttc au sein de CaWaQS.

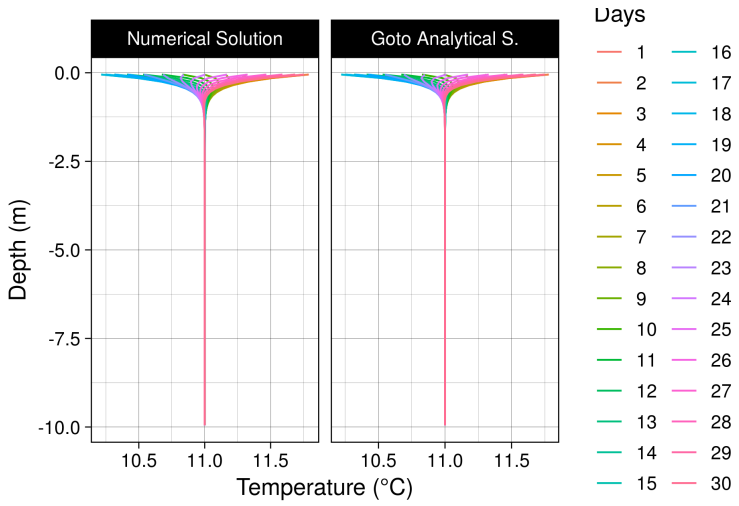

Figure A.14 Variations spatio-temporelles des réponses thermiques du flux de l'eau ascendant (cas 3) dans la colonne de sol à partir a) de la solution numérique libttc, b) de la solution analytique Goto. Chaque ligne représente le profil de température d'un jour en différentes couleurs pendant la période de simulation

Les simulations affichent de très bonnes performances : erreur absolue moyenne de 0.008°C, RMSE de 0.016°C, KGE moyen de 0.96.

A.4.3 Validation du transport de chaleur transitoire en régime hydraulique transitoire

Ce cas test comprend la variation de la température aux limites du modèle et la modification des vitesses d'eau au cours du temps. Deux cas tests sont développés:

1. le transport thermique transitoire dans la colonne de sol (Fig. A.11). Une variation de vitesse par paliers a été appliquée à la colonne de sol pour démontrer l'impact de la variation sur l'amplitude et la phase de la température.

2. la simulation d'un bassin avec conditions aux limites transitoires de température et de vitesse avec différents modes de transport de la chaleur.

A.4.3.1 Colonne Goto avec des flux d'eau variables

Le premier cas test transitoire s'appuie sur le cas du transfert de chaleur présenté par Goto et al. (2005), section A.4.2.2, p. 324, mais avec cette fois-ci des conditions hydrauliques variables. Les conditions initiales et aux limites sont donc présentées dans la Fig. A.15.

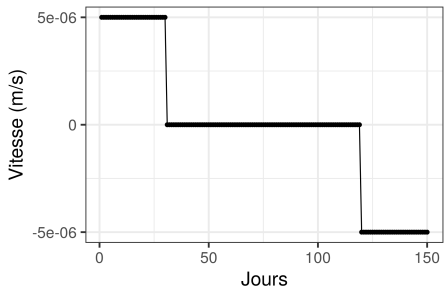

Figure A.15 Variations temporelles des d'un flux d'eau: Flux d'eau descendant jusqu'au jour 30, pas de flux d'eau entre le jour 30 et 60) et flux d'eau ascendant à partir du jour 60), dans la colonne de sol.

Une période totale de 90 jours est sélectionnée pour simuler le transport de chaleur dans la colonne verticale. Cette période est suffisante pour observer la propagation de la chaleur, car avec une vitesse de Darcy de $5\ 10^{-6}\mathrm{m\,s^{-1}}$, en 30 jours, la propagation de l'eau serait d'environ $12.5\mathrm{m}$. Il suffit de modifier l'amplitude de la température et d'observer la température des conditions limites réfléchies à certaines profondeurs. Pour observer la variation de la température, trois profondeurs sont choisies. Cette comparaison nous permettra de voir l'impact du transport advectif et des variations de la vitesse du flux d'eau sur le signal de température.

Table A.7 Propriétés thermiques d'une colonne de sol pour résoudre le transport de chaleur avec une hydraulique variable.

paramètres et valeurs associées		unités
ω	0.15	$[\mathrm{m^3\,m^{-3}}]$
λ_w	0.570	$[\mathrm{W\,m^{-1}\,K^{-1}}]$
λ_s	1.104	$[\mathrm{W\,m^{-1}\,K^{-1}}]$
c_{p_w}	4186	$[\mathrm{J\,kg^{-1}\,K^{-1}}]$
ρ_w	1000	$[\mathrm{kg\,m^{-3}}]$
c_{p_s}	1675.39	$[\mathrm{J\,kg^{-1}\,K^{-1}}]$
ρ_w	2500	$[\mathrm{kg\,m^{-3}}]$
β	0	$[\mathrm{m}]$

Un ensemble de simulations a été réalisé pour voir la convergence de la température dans le temps sur une durée de 150 jours avec la solution analytique de Goto pour une température moyenne de $11°\mathrm{C}$ une amplitude de $1°\mathrm{C}$ et une période de 30 jours (Figs. A.16, A.17, A.18).

À une profondeur de 0,5 m (Fig. A.16), nous observons que la température est

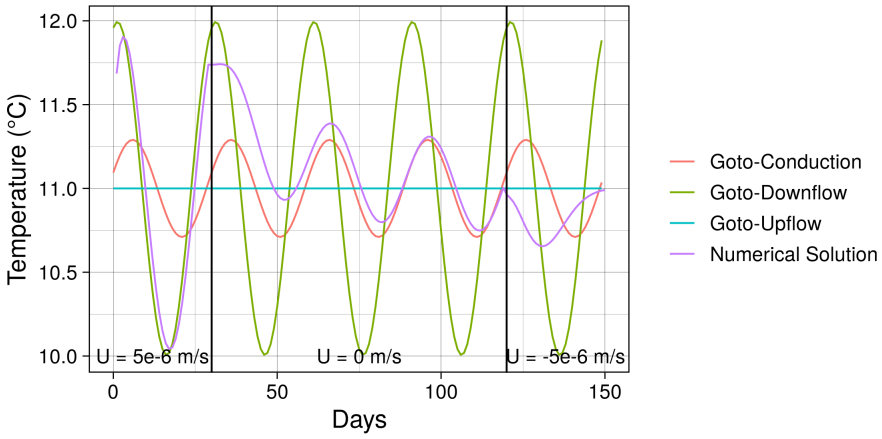

Figure A.16 Variations de température à $0.5\mathrm{m}$ profondeur. Goto-Conduction : Goto en conduction pur ; Goto-Downflow : Goto avec flux d'eau descendant ($U = 5\ 10^{-6}\mathrm{m\,s^{-1}}$). Goto-Upflow : Goto avec flux d'eau ascendant ($U = -5\ 10^{-6}\mathrm{m\,s^{-1}}$).

strictement corrélée avec la solution de Goto du flux d'eau descendant. Après 30 jours, la vitesse de Darcy devient 0 m/s et nous observons une atténuation de l'amplitude de la température dans la solution numérique. Elle converge vers la solution analytique du cas de conduction pure de Goto. Au jour 120, nous observons un autre changement de la vitesse de Darcy vers un flux ascendant, le signal de température récupère la température du fond de $11°\mathrm{C}$ après 30 jours. Cela est cohérent avec le temps de propagation de la température pour la vitesse de Darcy donnée.

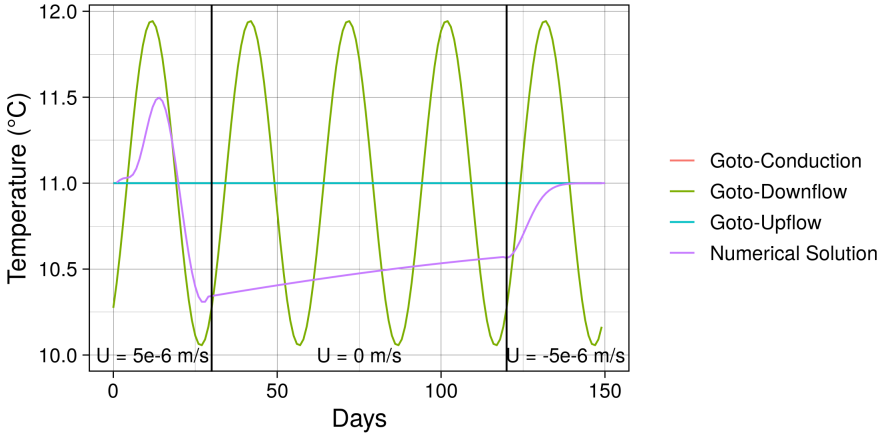

Figure A.17 Variations de température à $5\mathrm{m}$ profondeur. Goto-Conduction : Goto en conduction pur ; Goto-Downflow : Goto avec flux d'eau descendant ($U = 5\ 10^{-6}\mathrm{m\,s^{-1}}$). Goto-Upflow : Goto avec flux d'eau ascendant ($U = -5\ 10^{-6}\mathrm{m\,s^{-1}}$).

A $5\mathrm{m}$ de profondeur (Fig. A.17), nous observons une convergence similaire de la

température, avec un régime périodique qui se met en place pendant les 30 premiers jours de simulation.Durant les 90 jours suivants de régime conductif pur, la température progresse lentement avec pour cible la solution du régime conductif pur de $11°\mathrm{C}$. Cette température n'est pas atteinte du fait une conductivité thermique limitée qui ralentit la récupération du signal de température. Cependant, lorsque le flux d'eau s'inverse pour devenir ascendant au 120ème jour, il ne suffit alors que d'une quinzaine de jours pour que le température à -5 m atteigne la valeur de la condition limite de fond de $11°\mathrm{C}$.

Lorsque nous comparons la variation de la température dans le temps sur la figure A.18, une longueur d'onde sinusoïdale de 30 jours est trop courte pour montrer une variation de température suffisante à la profondeur de 9,5m. Les cas de conductivité pure et de flux d'eau ascendant montrent une température fixe de $11°\mathrm{C}$ à la profondeur de 9,5m. Dans le cas de la conductivité pure, la durée de simulation de 90 jours n'est pas suffisante pour atteindre une température permanente de $11°\mathrm{C}$.

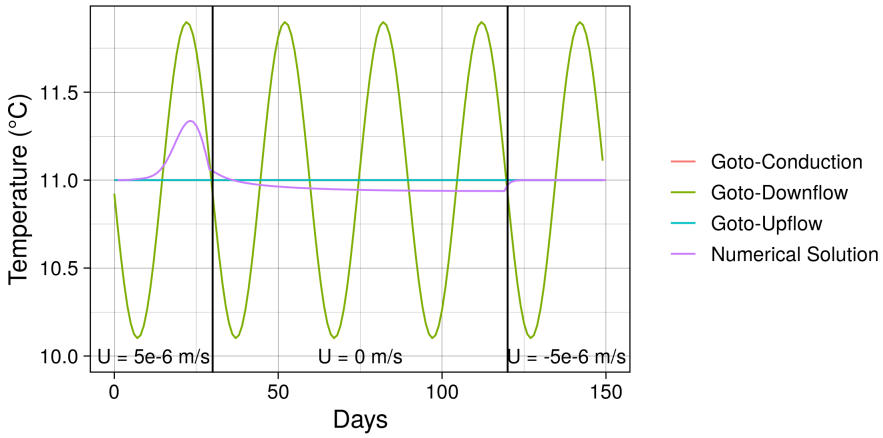

Figure A.18 Variations de température à 9.5 m profondeur. Goto-Conduction : Goto en conduction pur ; Goto-Downflow : Goto avec flux d'eau descendant ($U = 5\ 10^{-6}\mathrm{m\,s^{-1}}$). Goto-Upflow : Goto avec flux d'eau ascendant ($U = -5\ 10^{-6}\mathrm{m\,s^{-1}}$).

Globalement, les profils simulés à différentes profondeurs ont des comportements cohérents vis à vis des différentes solutions de Goto en régime hydraulique permanent. Les profils de température résultant à 0.5m, 5m et 9.5m de profondeur sont tracés sur la figure A.19. L'impact de la vitesse de l'eau sur l'amplitude des températures est clair. Une valeur élevée de la vitesse de Darcy avec un flux d'eau descendant permet à la température de surface de se propager dans le milieu.

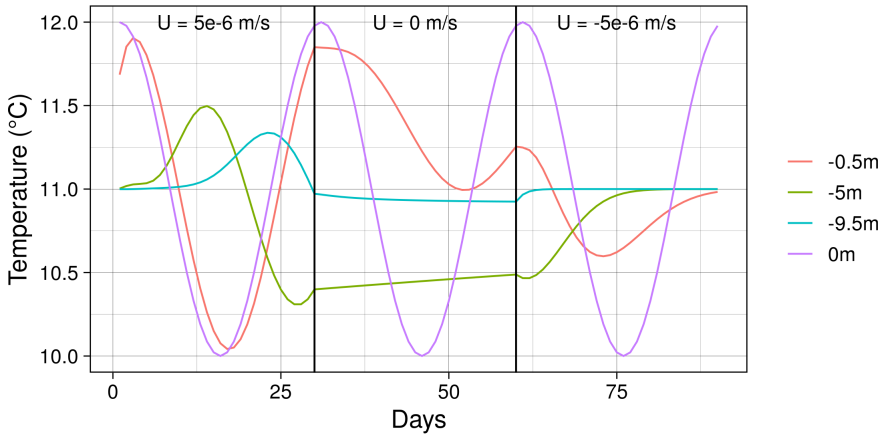

Figure A.19 Variations temporelles des réponses thermiques d'un flux de l'eau variable dans la colonne de sol à 0.5m, 5m, 9.5 m profondeur. La ligne violet indique la condition limite en haut de la colonne. Les lignes verticales indiquent les jours où la vitesse change.

Les températures à la profondeur de 0.5m imitent fortement le signal de la condition limite de surface après 4 jours. Ces 4 jours sont liés aux conditions homogènes initiales du modèle. De même, le signal de température à 5m de profondeur imite la condition limite supérieure avec un retard de 10 jours. Lorsque la vitesse devient nulle au 30e jour, il y a un fort découplage entre le signal de température de surface et celui des températures simulées à 0.5m et 5m de profondeur. Les températures à 0.5m ont un signal avec une plus faible amplitude. Les températures à 5m et 9.5m de profondeur tendent à revenir à des valeurs aux alentours de 11 °C en accord avec le régime conductif pur. Au jour 120, le champ de vitesse Darcy passe à une condition ascendante avec une vitesse de $5\ 10^{-6}\ \mathrm{m\,s^{-1}}$. Le flux vertical ascendant transporte une température de 11 °C. Les températures simulées à 0.5 m, 5 m et à 9.5m de profondeur tendent alors vers cette valeur. En 3 jours, la température à 9.5m de profondeur devient fixe à 11°C. En 12 jours, la température de 5m converge vers cette valeur et celle à la profondeur de 0.5 m converge vers cette valeur à la fin de la simulation.

A.4.3.2 Régime transitoire pour le bassin

Ce cas reprend le cas test de l'aquifère triangulaire de 64 km^2 présenté section A.4.2.1.2, p. 320, en imposant des conditions limites de températures et hydrauliques variables

pendant une année de simulation. Il a pour objectif de simuler l'impact d'une limite avec une température fluctuante sur les résultats précédemment exposés. Le domaine simulé étant très grand, la conductivité thermique est multipliée par un facteur 2 pour pouvoir observer la variation de température dûe à la conduction.

Les conditions aux limites de température sur les faces Est et Ouest du bassin sont définies comme des conditions aux limites à flux nul. La condition aux limites Nord est périodique de température moyenne 13°C, avec une amplitude de 1°C, et une période de 30 jours. Les conditions aux limites sur les faces sud sont définies comme des limites de Dirichlet de 5°C au point le plus au sud et augmentent linéairement vers le Nord. Une température initiale de 5°C est attribuée à toutes les cellules.

Pour les conditions hydrauliques, un champs de vitesses uniformes sur la colonne et variables dans le temps est imposé (Fig. A.20). Quatre expériences sont menées, EXP 1, 2, 3, 4. L'EXP1and2 a une vitesse uniforme de $1e{-}4\mathrm{m\,s^{-1}}$ où elle ne change pas au cours du temps. L'EXP1 a un écoulement dans la direction Sud-Nord, la direction s'inverse pour l'EXP2. Des vitesses variables sont appliquées dans EXP3-4. La variation représente une vitesse ascendante (Sud-Nord) qui s'inverse pour devenir descendante (Nord-Sud) en passant par un palier conductif c'est à dire une vitesse nulle. Chaque palier dure 120 jours. Dans EXP3 la vitesse vaut $10^{-6}\mathrm{m\,s^{-1}}$, alors qu'elle vaut $10^{-5}\mathrm{m\,s^{-1}}$ dans EXP4.

Trois cas avec les quatre régimes de vitesses EXP1, EXP2, EXP3, EXP4 sont simulés. Chaque cas a un type spécifique de transport de chaleur activé. Le premier cas est "Advectif" où seul le transport de chaleur advectif est activé dans le bassin. Le second cas est "Conductif" où la composante advectif est annulée et où seule la conduction pure est activée. Le troisième cas simule l'advection et la conduction où les deux composantes du transport de chaleur sont activées. Par conséquent, la "Conduction + Advection" est le signal combiné des cas "Conduction" et "Advection".

L'évolution de la température de la cellule 30 (Fig. A.7) obtenue à partir des simulations des deux premières expériences (EXP1 et EXP2) est illustré sur la figure A.21. Dans les deux expériences, nous observons une contribution presque insignifiante de la conduction. Une légère modification de la température due à la conduction est visible

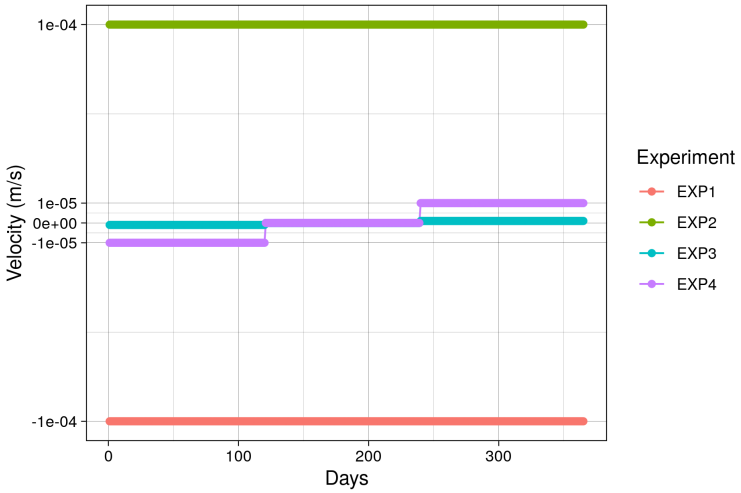

Figure A.20 Variation de la vitesse pour 1 an de période de simulation. Une fort vitesse de Darcy uniforme est appliquée dans EXP1and2. Tous les 120 jours, la vitesse est modifiée de manière progressive pour l'EXP3-4. EXP3 signifie une simulation avec un écoulement de l'eau plus lent dans la direction Nord-Sud. EXP4 signifie une simulation avec un flux d'eau plus fort. L'EXP4 est censée être dominée le terme advectif.

avec ses ondulations dans l'EXP2. Le même phénomène n'est pas visible dans l'EXP1 puisque la température du fond ne varie pas dans le temps (fixée à 5°C). Sur une période d'un an, nous observons qu'en cas d'advection pure (ligne bleue), la température de la cellule rouge atteint la même température que la condition limite du fond dans l'EXP1. Cependant, dans le cas "Conduction + Advection", avec l'effet de la conduction, la température ne descend qu'à 8°C au lieu de 5°C. Dans le cas EXP2, nous observons le réchauffement de la cellule du fait de la température plus élevée de l'eau circulant du Nord au Sud. Dans le cas de l'advection pure (ligne bleue), nous observons que la température atteint la température de la condition limite de 13°C. Mais la distance empêche la variation de température à la condition limite avec une amplitude de 1°C d'avoir une influence sur l'advection.

Les troisième et quatrième expériences sont présentées dans la figure A.22. Les températures simulées avec seulement le flux advectif est une vitesse allant du Sud vers le Nord Dans le cas de l'EXP3, la vitesse est inférieure d'un facteur de magnitude à celle de l'EXP4. L'impact de la différence de vitesses est clairement visible lorsque les deux profils de température sont comparés. L'impact de l'advection est beaucoup plus apparent dans l'EXP4. Alors que l'advection dans EXP3 a un impact sur les tem-

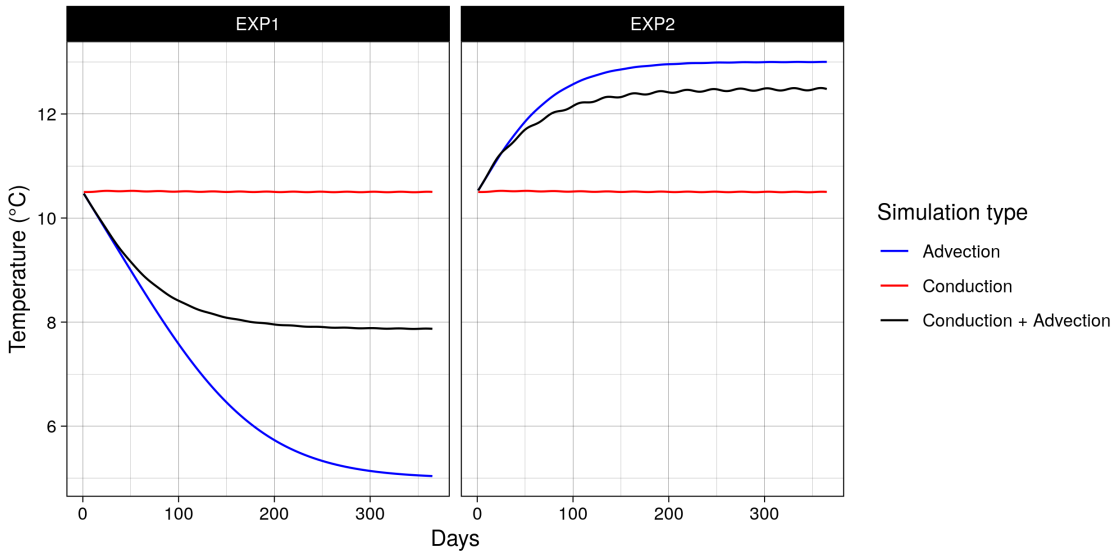

Figure A.21 Évolution de la température de la cellule rouge du cas synthétique aquifère triangulaire (Fig. A.7). EXP1 a une vitesse de $1e{-}4\mathrm{m\,s^{-1}}$ vers Sud-Nord, et EXP2 a une vitesse de $1e{-}4\mathrm{m\,s^{-1}}$ vers Nord-Sud. a) Advection signifie une simulation avec seulement le transport de chaleur advectif activé, b) Conduction signifie une simulation avec seulement le transport de chaleur conductif activé, c) Advection + Conduction signifie une simulation avec les deux composantes du transport de chaleur activées.

pératures jusqu'à 0,02°C, dans EXP4, les températures varient jusqu'à 0.4°C sur une période de 120 jours. Dans le cas advectif pur, lorsque la vitesse est nulle, le modèle représente bien une température constante qui correspond à un flux de chaleur nul. Le cas "Advection + Conduction" représente bien un flux de chaleur conductif à cette même période. En conséquence, la température n'y est pas constante lorsque la vitesse est nulle.

La conduction pure quant à elle ne modifie pas la température de manière significative. Ceci est dû à la taille du domaine simulé, plus le domaine de simulation est grand, plus l'impact du transport conductif diminue. Les ondulations de température pendant la période de simulation proviennent de la variation de température à la frontière nord du domaine simulé. Globalement, le transport de chaleur dans les différents modes de transport sont testés et il semble fonctionner de manière satisfaisante.

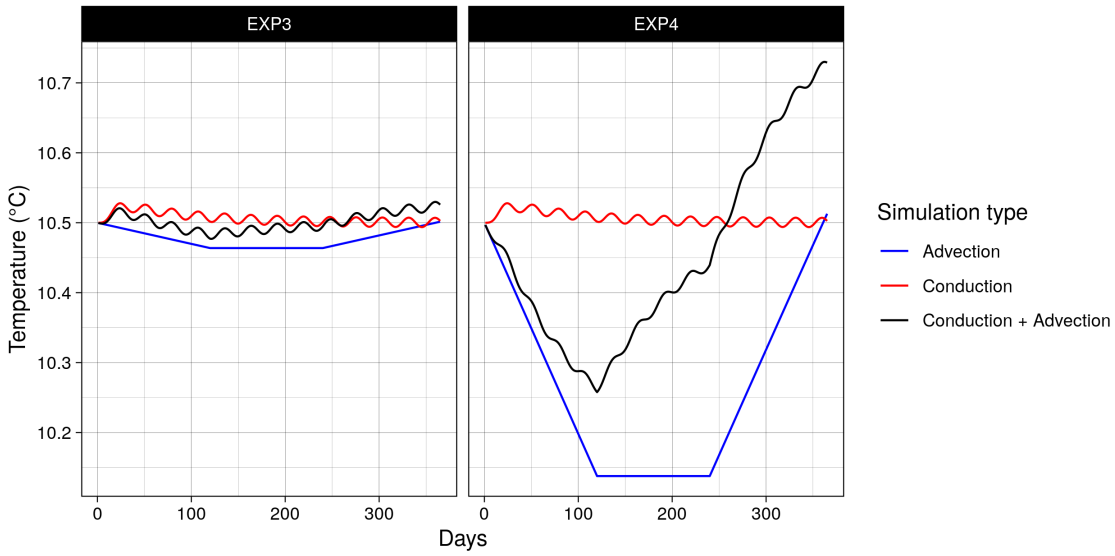

Figure A.22 Évolution de la température de la cellule rouge du cas synthétique aquifère triangulaire (Fig. A.7). EXP3 a une vitesse de $1e{-}6\,\mathrm{m\,s^{-1}}$ dans différentes directions, et EXP4 a une vitesse de $1e{-}5\,\mathrm{m\,s^{-1}}$. a) Advection signifie une simulation avec seulement le transport de chaleur advectif activé, b) Conduction signifie une simulation avec seulement le transport de chaleur conductif activé, c) Advection + Conduction signifie une simulation avec les deux composantes du transport de chaleur activées.

A.4.4 Validation du transport de chaleur au travers du lit de la rivière et au travers des aquitard

La solution analytique mise en œuvre dans la libttc est testée et les résultats sont donnés pour le lit du cours d'eau (Figure A.23) et l'aquitard (Figure A.24). Des profils de température synthétiques ont été générés en utilisant les propriétés thermiques et les valeurs d'épaisseur décrites dans la sous-section A.3. Les flux de Darcy varient de $1e^{-2}\,\mathrm{m\,s^{-1}}$ à $1e{-}10\,\mathrm{m\,s^{-1}}$ dans les deux conditions de décharge et de recharge. Dans la simulation à deux couches (streambed-aquifer), la courbure du profil de température est contrôlée par les valeurs de conductivité thermique changeantes jusqu'à la profondeur de la couche donnée. Le même mécanisme est observé dans la solution à trois couches (aquifère-aquitard-aquifère). La troisième couche supplémentaire change la courbe par la profondeur, modifie le profil de température.

Trois paramètres contrôlent le transport de chaleur dans le lit de la rivière et l'aquitard : l'épaisseur, la conductivité thermique et la vitesse de Darcy. La gamme optimale des

vitesses de Darcy change avec l'augmentation de la profondeur ou la modification des conductivités thermiques. Dans les deux milieux, la vitesse de Darcy optimale se situe entre $1e^{-6}\mathrm{m\,s^{-1}}$ et $-1e{-}6\mathrm{m\,s^{-1}}$. Si les vitesses sont supérieures à cette plage, la température de l'aquitard ou du lit de la rivière est égale à celle de la couche supérieure ou inférieure.

La RMSE de la température calculée par CaWaQS et le tableur FLUX-LM à la profondeur d'intérêt se situe entre $3e^{-3}$ et $3e^{-6}$°C pour les interfaces rivière-aquifère et aquifère-aquitard-aquifère.

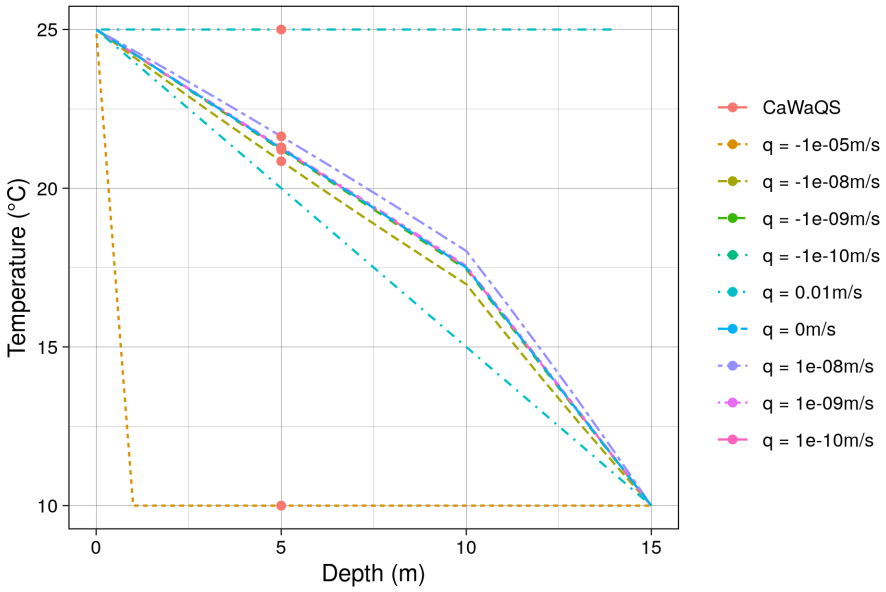

Figure A.23 Résultats de la solution de transport de chaleur au centre de la cellule du lit de la rivière en utilisant différents champs d'écoulement. Les points rouges sont le résultat de la simulation CaWaQS avec les mêmes températures limites du cours d'eau et de l'aquifère.

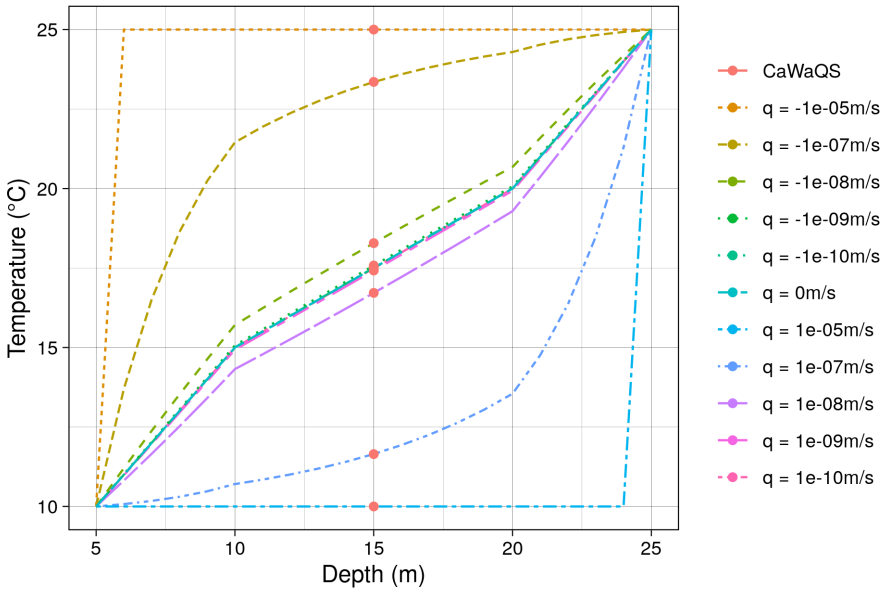

Figure A.24 Résultats de la solution de transport de chaleur au centre de la cellule aquitard en utilisant différents champs d'écoulement. Les points rouges sont le résultat de la simulation CaWaQS avec les mêmes températures limites de l'aquifère.

Conclusion

Ce rapport expose le développement et le test de la simulation du transfert de chaleur dans la plateforme de simulation des hydrosystèmes CaWaQS. Ce travail a nécessité de transformer et de développer la librairie de calcul, libttc, dédiée à la résolution du transport de chaleur et de soluté en milieu poreux et également pour les écoulements à surface libre. Libttc a ensuite été couplé au sein de la plateforme CaWaQS pour représenter les flux de chaleur au sein d'un aquifère monocouche. La mise en oeuvre du transport d'énergie en rivière a quant à elle nécessité de développer une autre librairie, libseb, dédiée au transfert d'énergie entre la surface libre des rivières et cours d'eau et l'atmosphère.

Un autre aspect crucial du transport de solutés et de chaleur en simultané dans les hydrosytèmes est l'interaction entre les unités aquifère et l'interface nappe-rivière. Pour calculer l'interaction entre les systèmes, une solution analytique (Kurylyk et al., 2017; Shan and Bodvarsson, 2004; Bredehoeft and Papaopulos, 1965) a été incorporée dans le module de transport. Cette méthode permet de calculer l'influence des flux advectifs et des flux conductifs via le terme du nombre de Peclet au niveau de l'aquitard et de l'interface rivière-aquifère. L'utilisation d'une telle équation permettrait une estimation efficace du flux thermique sans coût de calcul supplémentaire associé à la solution numérique aux interfaces des composants de l'hydrosystème.

L'hypothèse faite avec cette approche est que le transport de chaleur est strictement vertical, et que le flux de Darcy est constant et uniforme à travers les couches 1-D. Les profils de température sont acceptés en régime permanent et les propriétés thermiques sont homogènes dans chaque couche. A l'échelle d'un tronçon, le flux thermique horizontal est significatif dans la zone hyporhéique mais à l'échelle régionale, le flux thermique peut être accepté comme vertical car le gradient horizontal de vitesse peut être négatif. Pour le flux thermique aquifère-aquitard-aquifère, l'hypothèse d'un flux thermique vertical se vérifie car la perméabilité est très limitée dans l'aquitard. Par conséquent, la solution proposée est appropriée pour estimer le transport de chaleur aux interfaces.

Une fois finalisés, ces développements permettront de simuler pour la première fois les flux de chaleur au sein de l'hydrosystème Seine. Cela sera réalisé en couplant ORCHIDEE et CaWaQS, ORCHIDEE permettant de forcer CaWaQS. Une première version de ce couplage a déjà été réalisée par Kilic et al. (2021a) pour ce qui concerne le bilan hydrologique. Ce couplage va être amélioré avec l'introduction du transport de la chaleur. Les résultats de simulation permettront d'obtenir une cartographie fonctionnelle hydro-thermique des masses d'eau et une évaluation de leur sensibilité aux changements globaux en mobilisant différents scénarios climatiques du GIEC (Masson-Delmotte et al., 2018).

La dernière amélioration du couplage entre ORCHIDEE et CAWAQS sera la prise en compte les rétroactions des états de surface des sols et des nappes grâce à un couplage directe entre ORCHIDEE et CAWAQS. Ceci ouvrira également des perspectives d'amélioration des simulations du carbonne grâce à un couplage d'ORCHIDEE, CAWAQS et River-strahler.

Prises dans leur ensemble, les avancées techniques centrées autour de la thématique de transport, illustrées dans ce rapport, laissent entrevoir de nombreuses opportunités quant à l'extension des champs d'application de la plateforme CaWaQS3.X , outil de modélisation de la plate-forme de simulations des hydrosystèmes du PIREN Seine. Les développements actuels permettent le transport de multiples solutés et de chaleur dans les hydrosystèmes dans une même simulation. A terme, ces fonctionnalités permettront le couplage avec la plateforme Riverstrahler comme l'amélioration des simulations biogéochimiques avec la simulation de l'évolution des solutés en fonction de la températures comme par exemple dans le cas de la dénitrification (Wang et al., 2018c) ainsi que l'amélioration de la simulation du cycle du carbone (Marescaux et al., 2020).

Appendix B

Water and energy budgets from MIROC reanalysis simulations

Table B.1 The water balance of the hydrosystem from current, mid-century, and end-century simulations described in Chapter 8. Fluxes are defined in $m^3\,s^{-1}$.

	Current	Mid-century		End-century	
Name	MIROC	6,00	8,5	6,0	8,5
Precipitation (Model Scale)	2325.45	2375.74	2302.22	2514.60	2405.86
Evapotranspiration (Model Scale)	1429.48	2302.22	1204.59	1355.96	1183.40
Discharge at the outlet (Basin Scale)	723.74	918.13	957.60	961.35	1111.44
Runoff (Basin Scale)	396.11	510.24	576.27	516.88	656.86
Recharge (Basin Scale)	350.46	430.429	400.98	469.06	472.719
Overflow (Basin Scale)	94.86	134.02	121.26	153.72	161.63
River-aquifer exchanges (Basin Scale)	232.76	273.87	260.08	290.75	292.95
ITB	131.85	156.63	146.07	167.53	166.48
OTB River-Aquifer	-16.77	-18.51	-17.26	-18.14	-18.84
OTB Overflow	-104.46	-129.29	-120.23	-140.18	-140.75
Balance	-0.02	-0.02	0.02	-0.01	0

Table B.2 The water balance the aquifer layers from current, mid-century, and end-century simulations described in Chapter 8. Fluxes are defined in $m^3\ s^{-1}$.

	Current	Mid-century		End-century	
Name	MIROC	6,0	8,5	6,0	8,5
Recharge (Model Scale)	482.31	587.06	547.06	636.59	639.19
Allu	26.91	33.39	30.93	36.36	36.94
Beau	29.77	37.56	35.64	40.23	43.53
Brie	27.91	35.25	32.68	37.87	39.48
Chapigny	6.73	8.48	7.8	9.26	9.4
Lutetian	35.74	45.64	43.16	51.28	52.61
Thanetian	14.98	19.08	18.16	21.59	22.06
Craie	222.43	266.57	247.04	287.5	290.51
Jurassic	117.84	141.09	131.66	152.5	144.67
Overflow (Model Scale)	-199.32	-263.31	-241.49	-293.90	-302.38
Allu	-13.15	-15.94	-14.76	-17.34	-17.89
Beau	-8.46	-13.81	-12.8	-15.57	-18.05
Brie	-4.95	-8.12	-7.05	-9.17	-10.28
Chapigny	-0.43	-0.86	-0.68	-1.18	-1.25
Lutetian	-9.28	-14.37	-12.92	-17.57	-18.93
Thanetian	-10.2	-13.51	-12.74	-15.74	-16.25
Craie	-90.6	-117.45	-106.84	-131.65	-135.67
Jurassic	-62.26	-79.25	-73.7	-85.69	-84.06
River-Aquifer (Model Scale)	-249.53	-292.38	-277.34	-308.89	-311.79
Allu	-87.02	-102.68	-97.81	-108.77	-110.94
Beau	-12.03	-14.52	-14.09	-15.33	-16.4
Brie	-2.14	-2.56	-2.49	-2.67	-2.94
Chapigny	-5.4	-7.28	-6.81	-7.85	-8.33
Lutetian	-12.57	-14.6	-13.93	-15.75	-16.11
Thanetian	-2.53	-2.78	-2.73	-2.94	-2.99
Craie	-75.12	-86.23	-81.56	-91.18	-92.7
Jurassic	-52.72	-61.73	-57.92	-64.4	-61.38
Withdraval	-32.99	-27.69	-27.66	-27.66	-27.66
Allu	-8.04	-7.31	-7.31	-7.31	-7.31
Beau	-4.29	-3.4	-3.4	-3.4	-3.4
Brie	-2.55	-2.08	-2.05	-2.05	-2.05
Chapigny	-0.7	-0.48	-0.48	-0.48	-0.48
Lutetian	-2.21	-1.85	-1.85	-1.85	-1.85
Thanetian	-0.69	-0.55	-0.55	-0.55	-0.55
Craie	-12.2	-10.47	-10.47	-10.47	-10.47
Jurassic	-2.31	-1.55	-1.55	-1.55	-1.55
Stock change	-0.48	-3.7	-0.55	-6.13	2.63
Allu	0.01	0	0.03	0.06	0.06
Beau	-0.33	-0.51	-0.11	-0.37	0.18
Brie	-0.27	-0.89	-0.53	-1.23	-0.6
Chapigny	0.3	0.16	0.36	0.14	0.34
Lutetian	-1.31	-2.67	-2.84	-3.12	-2.05
Thanetian	-0.08	-0.56	-0.52	-0.51	-0.32
Craie	1.64	-0.76	1.44	-0.34	2.62
Jurassic	-0.44	1.53	1.61	-0.77	2.4

Table B.3 Intra-aquifer exchanges of the aquifer system from current, mid-century, and end-century simulations described in Chapter 8.Fluxes are defined in $m^3\ s^{-1}$.

	Current	Mid-century		End-century	
Name	MIROC	6,0	8,5	6,0	8,5
Intra-Aquifer (Model Scale)					
Alluvium-Beauce	0.15	0.17	0.17	0.19	0.2
Alluvium-Brie	4.69	5.84	5.6	6.3	6.68
Alluvium-Champigny	6.24	7.34	7.11	7.72	7.92
Alluvium-Lutetian	10.93	13.01	12.5	13.63	14.19
Alluvium-Thanetian	3.85	4.16	4.07	4.38	4.46
Alluvium-Chalk	55.43	62.02	59.47	64.78	65.7
Alluvium-Jurassic	0	0	0	0	0
Beauce-Brie	-4.58	-5.38	-5.24	-5.69	-6
Beauce-Champigny	-0.04	-0.04	-0.04	-0.04	-0.04
Beauce-Lutetian	-0.01	-0.01	-0.01	-0.01	-0.01
Beauce-Thanetian	0	0	0	0	0
Beauce-Chalk	0.1	0.29	0.23	0.37	0.39
Beauce-Jurassic	0	0	0	0	0
Brie-Champigny	-16.43	-19.54	-18.63	-20.48	-21.2
Brie-Lutetian	-1.44	-1.63	-1.58	-1.67	-1.76
Brie-Thanetian	0	0	0	0	0
Brie-Chalk	-0.03	0.02	0.01	0.03	0.03
Brie-Jurassic	0	0	0	0	0
Champigny-Lutetian	-10.72	-7.46	-11.75	-12.68	-12.99
Champigny-Thanetian	0	0	0	0	0
Champigny-Chalk	-0.01	-0.01	0	-0.01	-0.01
Champigny-Jurassic	0	0	0	0	0
Lutetian-Thanetian	-4.95	-5.58	-5.44	-5.96	-6.18
Lutetian-Chalk	-6.64	-7.46	-7.01	-7.77	-8.05
Lutetian-Jurasic	0	0	0	0	0
Thanetian-Chalk	-2.59	-3.09	-2.97	-3.44	-3.68
Thanetian-Jurassic	0	0	0	0	0
Chalk-Jurassic	0.11	0.1	0.11	0.09	0.09

Table B.4 Heat balance of the hydrosystem from current, mid-century, and end-century simulations described in Chapter 8. Heat flow amounts are defined in GWh/d.

	Current	Mid-century		End-century	
Name	MIROC	6,0	8,5	6,0	8,5
Discharge at the outlet (Basin Scale)	827.24	1140.81	1255.45	1269.98	1642.28
Runoff (Basin Scale)	458.44	664.85	797.21	731.14	1066.41
Recharge (Basin Scale)	391.52	543.99	539.01	649.36	744.66
Overflow (Basin Scale)	100.44	144.69	131.65	166.94	177.26
River-aquifer exchanges (Basin Scale)	268.36	331.26	326.59	371.90	398.61
ITB	147.30	197.95	196.36	231.93	262.25
OTB river-aq	-19.24	-21.46	-20.45	-21.79	-23.42
OTB overflow	-116.70	-163.40	-161.61	-194.06	-221.72
Withdrawals	-39.56	-33.68	-34.37	-34.63	-36.02
Stock change	-1.25	-2.40	1.17	-8.28	5.75

Table B.5 Heat balance of the aquifer layers from current, mid-century, and end-century simulations described in Chapter 8. Heat flow amounts are defined in GWh/d.

	Current	Mid-century		End-century	
Name	MIROC	6,0	8,5	6,0	8,5
Recharge (Model Scale)					
Allu	30.06	42.20	41.58	50.34	58.19
Beau	33.26	47.47	47.91	55.69	68.57
Brie	31.18	44.55	43.93	52.43	62.19
Chapigny	7.52	10.72	10.48	12.82	14.81
Lutetian	39.93	57.68	58.02	70.99	82.88
Thanetian	16.74	24.11	24.41	29.89	34.75
Craie	248.49	336.90	332.07	398.01	457.63
Jurassic	131.65	178.31	176.98	211.12	227.90
Overflow (Model Scale)					
Allu	-14.77	-18.90	-18.31	-21.88	-24.53
Beau	-9.93	-16.77	-16.01	-19.72	-24.01
Brie	-5.71	-9.84	-8.83	-11.63	-13.84
Chapigny	-0.49	-1.02	-0.82	-1.43	-1.57
Lutetian	-10.61	-16.67	-15.16	-20.72	-22.77
Thanetian	-11.36	-15.42	-14.80	-18.42	-19.60
Craie	-95.92	-126.80	-116.00	-142.96	-148.79
Jurassic	-149.04	-190.14	-177.14	-206.09	-202.82
River-Aquifer (Model Scale)					
Allu	-104.24	-108.08	-107.71	-123.19	-135.20
Beau	-14.11	-17.54	-17.50	-19.35	-21.67
Brie	-2.50	-3.18	-3.21	-3.52	-4.15
Chapigny	-6.23	-8.81	-8.55	-10.04	-11.33
Lutetian	-14.42	-16.92	-16.51	-18.92	-20.03
Thanetian	-2.81	-3.13	-3.17	-3.50	-3.72
Craie	-79.77	-92.92	-88.87	-99.52	-102.58
Jurassic	-95.22	-111.73	-106.23	-120.85	-115.97
Withdraval					
Allu	-9.03	-8.67	-9.07	-9.22	-10.02
Beau	-5.04	-4.13	-4.25	-4.31	-4.52
Brie	-2.94	-2.52	-2.57	-2.60	-2.76
Chapigny	-0.80	-0.57	-0.58	-0.58	-0.60
Lutetian	-2.53	-2.15	-2.17	-2.18	-2.23
Thanetian	-0.77	-0.63	-0.64	-0.64	-0.66
Craie	-12.92	-11.30	-11.37	-11.37	-11.48
Jurassic	-5.53	-3.72	-3.73	-3.73	-3.74
Stock change					
Allu	0.01	0.00	0.04	0.08	0.08
Beau	-0.39	-0.62	-0.14	-0.47	0.24
Brie	-0.31	-1.08	-0.66	-1.56	-0.81
Chapigny	0.34	0.19	0.43	0.17	0.43
Lutetian	-1.50	-3.10	-3.33	-3.68	-2.47
Thanetian	-0.09	-0.64	-0.60	-0.60	-0.39
Craie	1.74	-0.82	1.56	-0.37	2.87
Jurassic	-1.05	3.67	3.87	-1.85	5.79

Table B.6 Intra-aquifer heat exchanges and the geothermal gradient of the hydrosystem from current, mid-century, and end-century simulations described in Chapter 8. Fluxes are defined in GWh/d.

	Current	Mid-century		End-century	
Name	MIROC	RCP6.0	RCP8,5	RCP6,0	RCP8,5
Alluvium-Beauce	0.18	0.21	0.21	0.24	0.27
Alluvium-Brie	5.41	7.08	7.01	7.99	9.00
Alluvium-Champigny	7.17	8.67	8.56	9.36	9.93
Alluvium-Lutetian	12.49	15.09	14.67	16.07	17.07
Alluvium-Thanetian	4.29	4.75	4.73	5.13	5.38
Alluvium-Chalk	58.68	66.96	64.57	70.35	72.05
Alluvium-Jurassic	0.00	0.00	0.00	0.00	0.00
Beauce-Brie	-5.38	-6.53	-6.55	-7.21	-7.98
Beauce-Champigny	-0.05	-0.05	-0.05	-0.05	-0.05
Beauce-Lutetian	-0.01	-0.01	-0.01	-0.01	-0.01
Beauce-Thanetian	0.00	0.00	0.00	0.00	0.00
Beauce-Chalk	0.11	0.31	0.25	0.40	0.43
Beauce-Jurassic	0.00	0.00	0.00	0.00	0.00
Brie-Champigny	-18.97	-23.69	-23.33	-25.97	-28.55
Brie-Lutetian	-1.66	-1.98	-1.98	-2.12	-2.37
Brie-Thanetian	0.00	0.00	0.00	0.00	0.00
Brie-Chalk	-0.03	0.02	0.01	0.03	0.03
Brie-Jurassic	0.00	0.00	0.00	0.00	0.00
Champigny-Lutetian	-12.32	-8.81	-14.14	-15.37	-16.29
Champigny-Thanetian	0.00	0.00	0.00	0.00	0.00
Champigny-Chalk	-0.01	-0.01	0.00	-0.01	-0.01
Champigny-Jurassic	0.00	0.00	0.00	0.00	0.00
Lutetian-Thanetian	-5.66	-6.47	-6.38	-7.03	-7.43
Lutetian-Chalk	-7.59	-8.65	-8.23	-9.16	-9.68
Lutetian-Jurasic	0.00	0.00	0.00	0.00	0.00
Thanetian-Chalk	-2.88	-3.53	-3.45	-4.03	-4.44
Thanetian-Jurassic	0.00	0.00	0.00	0.00	0.00
Chalk-Jurassic	0.26	0.24	0.26	0.22	0.22
Geothermal Gradient					
Jurassic	173,20	173,20	173,20	173,20	173,20

RÉSUMÉ

La gestion des ressources en eau et de l'environnement est une tâche difficile. Sous l'effet du changement climatique, la gestion deviendra encore plus difficile. En ce qui concerne l'environnement, le changement climatique présente un risque pour les systèmes aquatiques ainsi que pour l'écologie du bassin. Notre compréhension des ressources en eau provient des modèles hydrologiques. Grâce à ces modèles, nous pouvons estimer le bilan hydrique d'une zone d'étude et également utiliser ces modèles pour comprendre le transport des polluants afin de protéger l'environnement. Jusqu'à récemment, les modèles hydrologiques ne comprenaient que les processus d'écoulement de l'eau. Cependant, le changement climatique se manifeste par l'augmentation de la chaleur et des températures dans l'atmosphère. L'impact de l'atmosphère sur les systèmes fluviaux et les ressources en eau souterraine est encore incertain. Cette thèse de doctorat vise à combler cette lacune dans la littérature qui est le manque de quantification de l'impact du changement climatique sur la rivière et les ressources en eau souterraine. Pour cela, nous combinons deux modèles qui simulent la surface proche (ORCHIDEE), les eaux souterraines et la rivière (CaWaQS) pour estimer le bilan hydrique et le bilan énergétique. Nous appliquons notre modèle au bassin de la Seine, qui fournit de l'eau à plus de 16 millions de personnes. Nous projetons également notre approche combinée aux conditions climatiques futures afin d'évaluer les changements possibles dans les régimes de débit et de température de l'eau dans le bassin de la Seine.

MOTS CLÉS

Modèlisation intégrée, Flux d'eau, Flux de chaleur, Le bassin de la Seine, Couplage

ABSTRACT

Water resources and environmental management are challenging tasks. Under the impact of climate change, management will become even more difficult. With respect to the environment, climate change poses risk to aquatic systems as well as the ecology of the basin. Our understanding of water resources comes from hydrological models. Using such models we can estimate the water budget of a study area and also use these models to understand the transport of pollutants for environmental protection. Until recently, the hydrological models included only the processes of water flow. However, climate change shows itself by the increases in the heat and temperatures in the atmosphere. The impact of the atmosphere on river systems and groundwater resources is still uncertain. This PhD thesis aims to address this gap in the literature which is the lack of quantification of the impact of climate change on the river and groundwater resources. To achieve this, we combine two models that simulate near surface (ORCHIDEE), groundwater and river (CaWaQS) to estimate the water budget and energy balance. We apply our model to the Seine basin, which supplies water to more than 16 million people. We also project our combined approach to future climate conditions to assess the possible changes in the water flow and temperature regimes in the Seine basin

KEYWORDS

Integrated model, Water fluxes, Heat fluxes, the Seine basin, Coupling